

Fossil sites at risk
in India p. 22

Engineered enzyme
forges fused rings p. 71

An earlier start for Stone Age
humans pp. 86, 90, & 95

Science

\$15
6 APRIL 2018
sciencemag.org

AAAS

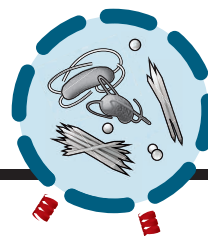
PRZEWALSKI'S HORSES

Ancient genomes illuminate
early horse domestication p. 111



CONTENTS

6 APRIL 2018 • VOLUME 360 • ISSUE 6384



33 & 49

Repairing a leaky membrane



18

NEWS

IN BRIEF

10 News at a glance

IN DEPTH

12 IN ITS SECOND YEAR, MARCH FOR SCIENCE GROWS UP

This year's event, set for 14 April, is only one element in a global pro-science movement *By J. Mervis*

13 UNIVERSITY IS QUICK TO DISCLOSE MISCONDUCT

The Ohio State University wins plaudits for unusually rapid transparency *By A. McCook*

14 HUMANE STUDIES OF OCTOPUSES GET A BOOST

By identifying effective anesthetics, findings aid compliance with regulations *By D. Staaf*

► PODCAST

16 ROCKY START FOR CHINA'S JAMES WATSON CENTER

A new center named for the Nobel laureate faces funding and mission challenges *By D. Normile*

17 NIH LOOKS TO PUNISH REVIEWERS WHO VIOLATE CONFIDENTIALITY

Agency re-reviewed dozens of funding proposals after officials discovered a violation of the rules *By J. Brainard*

FEATURES

18 A DELICATE BALANCE

Routinely giving antibiotics to premature babies may do more harm than good *By M. Broadfoot*

22 EDGE OF EXTINCTION

India's paleontologists are struggling to save fossil sites—and their own discipline *By S. Kumar*

24 A one-man fossil rescue mission

By S. Kumar

INSIGHTS

LETTERS

26 NEXTGEN VOICES: A POSTDOC'S PURPOSE

PERSPECTIVES

28 MICROPLASTICS RESEARCH—FROM SINK TO SOURCE

Microplastics are ubiquitous not just in the ocean but also on land and in freshwater systems *By C. M. Rochman*

30 SUPPORTING RECOVERY FROM BRAIN INJURY

A window of therapeutic opportunity could widen beyond the initial phase of brain injury *By S. Rumpel*

► RESEARCH ARTICLE P. 50

31 LATTICES FOR FRACTIONAL CHERN INSULATORS

Topological order beyond Landau levels is seen in encapsulated bilayer graphene *By C. Repellin and N. Regnault*

► REPORT P. 62

33 ESCRTS OFFER REPAIR SERVICE

A cellular membrane remodeling machinery repairs damaged organelles *By M. G. Gutierrez and J. G. Carlton*

► RESEARCH ARTICLE P. 49

34 UP CLOSE WITH HERPESVIRUSES

Two high-resolution structures reveal how ~3000 proteins are arranged in the herpes simplex virus capsid

By E. E. Heldwein

► RESEARCH ARTICLES PP. 47 & 48

36 LRRK2 KINASE IN PARKINSON'S DISEASE

Defects in vesicular trafficking and immune responses are found in Parkinson's disease *By D. R. Alessi and E. Sammler*

POLICY FORUM

38 TESTING INTERNATIONAL EDUCATION ASSESSMENTS

Rankings get headlines, but often mislead *By J. D. Singer and H. I. Braun*



Editor-in-Chief Jeremy Berg

Executive Editor Monica M. Bradford **News Editor** Tim Appenzeller

Deputy Editors Lisa D. Chong, Andrew M. Sugden(UK), Valda J. Vinson, Jake S. Yeston

Research and Insights

DEPUTY EDITOR, EMERITUS Barbara R. Jasny **SR. EDITORS** Gemma Alderton(UK), Caroline Ash(UK), Julia Fahrenkamp-Uppenbrink(UK), Pamela J. Hines, Stella M. Hurtleby(UK), Paula A. Kiberstis, Marc S. Lavine(Canada), Steve Mao, Ian S. Osborne(UK), Beverly A. Purnell, L. Bryan Ray, H. Jesse Smith, Jelena Stajic, Peter Stern(UK), Phillip D. Szuromi, Sacha Vignieri, Brad Wible, Laura M. Zahn **ASSOCIATE EDITORS** Michael A. Funk, Brent Grocholski, Priscilla N. Kelly, Seth Thomas Scanlon(UK), Keith T. Smith(UK) **ASSOCIATE BOOK REVIEW EDITOR** Valerie B. Thompson **LETTERS EDITOR** Jennifer Sills **LEAD CONTENT PRODUCTION EDITORS** Harry Jach, Lauren Kmec **CONTENT PRODUCTION EDITORS** Amelia Beyna, Jeffrey E. Cook, Amber Esplin, Chris Filiatreau, Cynthia Howe, Catherine Wolner **SR. EDITORIAL COORDINATORS** Carolyn Kyle, Beverly Shields **EDITORIAL COORDINATORS** Aneera Dobbins, Joi S. Granger, Jeffrey Hearn, Lisa Johnson, Maryrose Madrid, Scott Miller, Jerry Richardson, Anita Wynn **PUBLICATIONS ASSISTANTS** Ope Martins, Nida Masiulis, Dona Mathieu, Hilary Stewart(UK), Alana Warnke, Alice Whaley(UK), Brian White **EXECUTIVE ASSISTANT** Jessica Slater **ADMINISTRATIVE SUPPORT** Janet Clements(UK), Lizzanne Newton(UK)

News

NEWS MANAGING EDITOR John Travis **INTERNATIONAL EDITOR** Richard Stone **DEPUTY NEWS EDITORS** Elizabeth Culotta, Martin Enserink(Europe), David Grimm, Eric Hand, David Malakoff, Leslie Roberts **SR. CORRESPONDENTS** Daniel Cley(UK), Jeffrey Mervis, Elizabeth Pennisi **ASSOCIATE EDITORS** Jeffrey Brainard, Catherine Matatic **NEWS WRITERS** Adrian Cho, Jon Cohen, Jennifer Couzin-Frankel, Jocelyn Kaiser, Kelly Servick, Robert F. Service, Erik Stokstad(Cambridge, UK), Paul Voosen, Meredith Wadman **INTERNS** Roni Dengler, Katie Langin, Matt Warren **CONTRIBUTING CORRESPONDENTS** John Bohannon, Warren Cornwall, Ann Gibbons, Mara Hvistendahl, Sam Kean, Eli Kintisch, Kai Kupferschmidt(Berlin), Andrew Lawler, Mitch Leslie, Eliot Marshall, Virginia Morell, Dennis Normile(Shanghai), Charles Piller, Tania Rabesandratana(London), Emily Underwood, Gretchen Vogel(Berlin), Lizzie Wade(Mexico City) **CAREERS** Donisha Adams, Rachel Bernstein(Editor), Maggie Kuo **COPY EDITORS** Dorie Cheylen, Julia Cole (Senior Copy Editor), Cyra Master (Copy Chief) **ADMINISTRATIVE SUPPORT** Meagan Weiland

Executive Publisher Rush D. Holt

Publisher Bill Moran **Chief Digital Media Officer** Josh Freeman

DIRECTOR, BUSINESS STRATEGY AND PORTFOLIO MANAGEMENT Sarah Whalen **DIRECTOR, PRODUCT AND CUSTOM PUBLISHING** Will Schweitzer **MANAGER, PRODUCT DEVELOPMENT** Hannah Heckner **BUSINESS SYSTEMS AND FINANCIAL ANALYSIS** DIRECTOR Randy Yi **DIRECTOR, BUSINESS OPERATIONS & ANALYST** Eric Knott **SENIOR SYSTEMS ANALYST** Nicole Mehmedovich **SENIOR BUSINESS ANALYST** Cory Lipman **MANAGER, BUSINESS OPERATIONS** Jessica Tierney **BUSINESS ANALYSTS** Meron Kebede, Sandy Kim, Jourdan Stewart **FINANCIAL ANALYST** Julian Iriarte **ADVERTISING SYSTEM ADMINISTRATOR** Tina Burks **SALES COORDINATOR** Shirley Young **DIRECTOR, COPYRIGHT, LICENSING, SPECIAL PROJECTS** Emilie David **DIGITAL PRODUCT ASSOCIATE** Michael Hardesty **RIGHTS AND PERMISSIONS ASSOCIATE** Elizabeth Sandler **RIGHTS, CONTRACTS, AND LICENSING ASSOCIATE** Lili Catlett **RIGHTS & PERMISSIONS ASSISTANT** Alexander Lee

MARKETING MANAGER, PUBLISHING Shawana Arnold **MARKETING ASSOCIATE** Steven Goodman **SENIOR ART ASSOCIATES** Paula Fry **ART ASSOCIATE** Kim Huynh

INTERIM DIRECTOR, INSTITUTIONAL LICENSING Iquo Edim **ASSOCIATE DIRECTOR, RESEARCH & DEVELOPMENT** Elisabeth Leonard **SENIOR INSTITUTIONAL LICENSING MANAGER** Ryan Rexroth **INSTITUTIONAL LICENSING MANAGERS** Marco Castellani, Chris Murawski **SENIOR OPERATIONS ANALYST** Lana Guz **MANAGER, AGENT RELATIONS & CUSTOMER SUCCESS** Judy Lillibridge

WEB TECHNOLOGIES TECHNICAL DIRECTOR David Levy **TECHNICAL MANAGER** Chris Coleman **PORTFOLIO MANAGER** Trista Smith **PROJECT MANAGER** Tara Kelly, Dean Robbins **DEVELOPERS** Elissa Heller, Ryan Jensen, Brandon Morrison

DIGITAL MEDIA DIRECTOR OF ANALYTICS Enrique Gonzales **SR. MULTIMEDIA PRODUCER** Sarah Crespi **MANAGING DIGITAL PRODUCER** Kara Estelle-Powers **PRODUCER** Liana Birke **VIDEO PRODUCERS** Chris Burns, Nguyễn Khôi Nguyễn **DIGITAL SOCIAL MEDIA PRODUCER** Brice Russ

DIGITAL/PRINT STRATEGY MANAGER Jason Hillman **QUALITY TECHNICAL MANAGER** Marcus Spiegler **DIGITAL PRODUCTION MANAGER** Lisa Stanford **ASSISTANT MANAGER DIGITAL/PRINT** Rebecca Doshi **SENIOR CONTENT SPECIALISTS** Steve Forrester, Antoinette Hodal, Lori Murphy, Anthony Rosen **CONTENT SPECIALISTS** Jacob Hedrick, Kimberley Oster

DESIGN DIRECTOR Beth Rakouskas **DESIGN MANAGING EDITOR** Marcy Atarod **SENIOR DESIGNER** Chrystal Smith **DESIGNER** Christina Aycock **GRAPHICS MANAGING EDITOR** Alberto Cuadra **GRAPHICS EDITOR** Nirja Desai **SENIOR SCIENTIFIC ILLUSTRATORS** Valerie Altounian, Chris Bickel, Katharine Sutfitt **SCIENTIFIC ILLUSTRATOR** Alice Kitterman **INTERACTIVE GRAPHICS EDITOR** Jia You **SENIOR GRAPHICS SPECIALISTS** Holly Bishop, Nathalie Cary **PHOTOGRAPHY MANAGING EDITOR** William Douthitt **PHOTO EDITOR** Emily Petersen **IMAGE RIGHTS AND FINANCIAL MANAGER** Jessica Adams **INTERN** Mike Shanahan

SENIOR EDITOR, CUSTOM PUBLISHING Sean Sanders: 202-326-6430 **ASSISTANT EDITOR, CUSTOM PUBLISHING** Jackie Oberst: 202-326-6463 **ASSOCIATE DIRECTOR, BUSINESS DEVELOPMENT** Justin Sawyers: 202-326-7061 science_advertising@aaas.org **ADVERTISING PRODUCTION OPERATIONS MANAGER** Deborah Tompkins **SR. PRODUCTION SPECIALIST/GRAPHIC DESIGNER** Amy Hardcastle **SR. TRAFFIC ASSOCIATE** Christine Hall **DIRECTOR OF BUSINESS DEVELOPMENT AND ACADEMIC PUBLISHING RELATIONS, ASIA** Xiaoying Chu: +86-131 6136 3212, xchu@aaas.org **COLLABORATION/CUSTOM PUBLICATIONS/JAPAN** Adarsh Sandhu + 81532-81-5142 asandhu@aaas.org **EAST COAST/E. CANADA** Laurie Faraday: 508-747-9395, FAX 617-507-8189 **WEST COAST/W. CANADA** Lynne Stickrod: 415-931-9782, FAX 415-520-6940 **MIDWEST** Jeffrey Dembski: 847-498-4520 x3005, Steven Loerch: 847-498-4520 x3006 **UK EUROPE/ASIA** Roger Goncalves: TEL/FAX +41 43 243 1358 **JAPAN** Kaoru Sasaki (Tokyo): + 81 (3) 6459 4174 ksasaki@aaas.org

GLOBAL SALES DIRECTOR ADVERTISING AND CUSTOM PUBLISHING Tracy Holmes: +44 (0) 1223 326525 **CLASSIFIED** advertise@sciencecareers.org **SALES MANAGER, US, CANADA AND LATIN AMERICA** SCIENCE CAREERS Claudia Paulsen-Young: 202-326-6577 **EUROPE/ROW SALES** Sarah Lelarge **SALES ADMIN ASSISTANT** Kelly Grace +44 (0)1223 326528 **JAPAN** Miyuki Tani(Osaka): +81 (6) 6202 6272 mtani@aaas.org **CHINA/TAIWAN** Xiaoying Chu: +86-131-6136 3212, xchu@aaas.org **GLOBAL MARKETING MANAGER** Allison Pritchard **DIGITAL MARKETING ASSOCIATE** Aimee Aponte

AAAS BOARD OF DIRECTORS, CHAIR Susan Hockfield **PRESIDENT** Margaret A. Hamburg **PRESIDENT-ELECT** Steven Chu **TREASURER** Carolyn N. Ainslie **CHIEF EXECUTIVE OFFICER** Rush D. Holt **BOARD** Cynthia M. Beall, May R. Berenbaum, Rosina M. Bierbaum, Kaye Husbands Fealing, Stephen P.A. Fodor, S. James Gates, Jr., Michael S. Gazzaniga, Laura H. Greene, Robert B. Millard, Mercedes Pascual, William D. Provine

SUBSCRIPTION SERVICES For change of address, missing issues, new orders and renewals, and payment questions: 866-434-AAAS (2227) or 202-326-6417, FAX 202-842-1065. Mailing addresses: AAAS, P.O. Box 96178, Washington, DC 20090-6178 or AAAS Member Services, 1200 New York Avenue, NW, Washington, DC 20005

INSTITUTIONAL SITE LICENSES 202-326-6730 **REPRINTS:** Author Inquiries 800-635-7181 **COMMERCIAL INQUIRIES** 803-359-4578 **PERMISSIONS** 202-326-6765, permissions@aaas.org **AAAS Member Central Support** 866-434-2227 www.aaas.org/membercentral

Science serves as a forum for discussion of important issues related to the advancement of science by publishing material on which a consensus has been reached as well as including the presentation of minority or conflicting points of view. Accordingly, all articles published in Science—including editorials, news and comment, and book reviews—are signed and reflect the individual views of the authors and not official points of view adopted by AAAS or the institutions with which the authors are affiliated.

INFORMATION FOR AUTHORS See www.sciencemag.org/authors/science-information-authors

BOARD OF REVIEWING EDITORS (Statistics board members indicated with \$)

Adriano Aguzzi, *U. Hospital Zürich*
Takuzo Aida, *U. of Tokyo*
Leslie Aiello, *Wenner-Gren Foundation*
Judith Allen, *U. of Manchester*
Sebastian Amigorena, *Institut Curie*
Meinrat O. Andrae, *Max Planck Inst. Mainz*
Paola Ariotti, *Harvard U.*
Johan Auwerx, *EPFL*
David Awschalom, *U. of Chicago*
Clare Baker, *U. of Cambridge*
Nenad Ban, *ETH Zürich*
Franz Bauer, *Pontificia Universidad Católica de Chile*
Ray H. Baughman, *U. of Texas at Dallas*
Carlo Beenakker, *Leiden U.*
Kamran Behnia, *ESPCI*
Yasmine Belkaid, *NIAD, NIH*
Philip Benfey, *Duke U.*
Gabriele Bergers, *VIB*
Bradley Bernstein, *Massachusetts General Hospital*
Peer Bork, *EMBL*
Chris Bowler, *Ecole Normale Supérieure*
Ian Boyd, *U. of St. Andrews*
Emily Brodsky, *U. of California, Santa Cruz*
Ron Brookmeyer, *U. of California, Los Angeles (\$)*
Christian Büchel, *UKE Hamburg*
Dennis Burton, *The Scripps Res. Inst.*
Carter Tribley Butts, *U. of California, Irvine*
Gyorgy Buzsaki, *New York U. School of Medicine*
Blanche Capel, *Duke U.*
Mats Carlsson, *U. of Oslo*
Ib Chorkendorff, *Denmark TU*
James J. Collins, *MIT*
Robert Cook-Deegan, *Arizona State U.*
Lisa Coussens, *Oregon Health & Science U.*
Alan Cowman, *Walter & Eliza Hall Inst.*
Roberta Croce, *VU Amsterdam*
Janet Currie, *Princeton U.*
Jeff L. Dangl, *U. of North Carolina*
Tom Daniel, *U. of Washington*
Chiara Daraio, *Caltech*
Nicolas Daughas, *U. of Chicago*
Frans de Waal, *Emory U.*
Stanislas Dehaene, *Collège de France*
Robert Desimone, *MIT*
Claude Desplan, *New York U.*
Sandra Díaz, *Universidad Nacional de Córdoba*
Dennis Discher, *U. of Penn.*
Gerald W. Dorn II, *Washington U. in St. Louis*
Jennifer A. Doudna, *U. of California, Berkeley*
Bruce Dunn, *U. of California, Los Angeles*
William Dunphy, *Caltech*
Christopher Dye, *WHO*
Todd Ehlers, *U. of Tübingen*
Jennifer Elisseeff, *Johns Hopkins U.*
Tim Elston, *U. of North Carolina at Chapel Hill*
Barry Everitt, *U. of Cambridge*
Vanessa Ezenwa, *U. of Georgia*
Ernst Fehr, *U. of Zürich*
Michael Feuer, *The George Washington U.*
Toren Finkel, *NHLBI, NIH*
Kate Fitzgerald, *U. of Massachusetts*
Peter Fratzl, *Max Planck Inst. Potsdam*
Elaine Fuchs, *Rockefeller U.*
Eileen Furlong, *EMBL*
Jay Gallagher, *U. of Wisconsin*
Daniel Geschwind, *U. of California, Los Angeles*
Karl-Heinz Glassmeier, *TU Braunschweig*
Ramon Gonzalez, *Rice U.*
Elizabeth Grove, *U. of Chicago*
Nicolas Gruber, *ETH Zürich*
Kip Guy, *U. of Kentucky College of Pharmacy*
Taekjip Ha, *Johns Hopkins U.*
Christian Haass, *Ludwig Maximilians U.*
Sharon Hammes-Schiffer, *U. of Illinois at Urbana-Champaign*
Wolf-Dietrich Hardt, *ETH Zürich*
Michael Hasselmo, *Boston U.*
Martin Heimann, *Max Planck Inst. Jena*
Ykä Helariutta, *U. of Cambridge*
Janet G. Hering, *Eawag*
Kai-Uwe Hinrichs, *U. of Bremen*
David Hodell, *U. of Cambridge*
Lora Hooper, *UT Southwestern Medical Ctr. at Dallas*
Fred Hughson, *Princeton U.*
Randall Hulet, *Rice U.*
Auke Ijspeert, *EPFL*
Akiko Iwasaki, *Yale U.*
Stephen Jackson, *USGS and U. of Arizona*
Seema Jayachandran, *Northwestern U.*
Kai Johnson, *EPFL*
Peter Jonas, *Inst. of Science & Technology Austria*
Matt Kaeblerlein, *U. of Washington*
William Kaelin Jr., *Dana-Farber Cancer Inst.*
Daniel Kammen, *U. of California, Berkeley*
Abby Kavner, *U. of California, Los Angeles*
Masashi Kawasaki, *U. of Tokyo*
V. Narry Kim, *Seoul Nat. U.*
Robert Kingston, *Harvard Medical School*
Etienne Koechlin, *Ecole Normale Supérieure*
Alexander Kolodkin, *Johns Hopkins U.*
Thomas Langer, *U. of Cologne*
Mitchell A. Lazar, *U. of Penn.*
David Lazer, *Harvard U.*
Thomas Lecuit, *IDM*
Stanley Lemon, *U. of North Carolina at Chapel Hill*
Ottoline Leyser, *U. of Cambridge*
Wendell Lim, *U. of California, San Francisco*
Marcia C. Linn, *U. of California, Berkeley*
Jianguo Liu, *Michigan State U.*
Luis Liz-Marzán, *CIC biomaGUNE*
Jonathan Losos, *Harvard U.*
Ke Lu, *Chinese Acad. of Sciences*
Christian Lüscher, *U. of Geneva*
Laura Machesky, *Cancer Research UK Beatson Inst.*
Anne Magurran, *U. of St. Andrews*
Oscar Marin, *King's College London*
Charles Marshall, *U. of California, Berkeley*
Christopher Marx, *U. of Idaho*
C. Robertson McClung, *Dartmouth College*
Draigo Medellin, *U. of Mexico*
Graham Medley, *London School of Hygiene & Tropical Med.*
Jane Memmott, *U. of Bristol*
Tom Misteli, *NCI, NIH*
Yasushi Miyashita, *U. of Tokyo*
Mary Ann Moran, *U. of Georgia*
Richard Morris, *U. of Edinburgh*
Alison Motsinger-Reif, *NC State U. (\$)*
Daniel Neumark, *U. of California, Berkeley*
Kitty Nijmeijer, *TU Eindhoven*
Helga Nowotny, *Austrian Council*
Rachel O'Reilly, *U. of Warwick*
Harry Orr, *U. of Minnesota*
Pilar Ossorio, *U. of Wisconsin*
Andrew Oswald, *U. of Warwick*
Isabella Pagano, *Istituto Nazionale di Astrofisica*
Margaret Palmer, *U. of Maryland*
Steve Palumbi, *Stanford U.*
Jane Parker, *Max Planck Inst. Cologne*
Giovanni Parmigiani, *Dana-Farber Cancer Inst. (\$)*
John H. J. Petrini, *Memorial Sloan Kettering*
Samuel Pfaff, *Salk Inst. for Biological Studies*
Kathrin Plath, *U. of California, Los Angeles*
Martin Plenio, *Ulm U.*
Albert Polman, *FOM Institute for AMOLF*
Elvira Poloczanska, *Alfred-Wegener-Inst.*
Philippe Poulin, *CNRS*
Jonathan Pritchard, *Stanford U.*
David Randall, *Colorado State U.*
Sarah Reisman, *Caltech*
Félix A. Rey, *Institut Pasteur*
Trevor Robbins, *U. of Cambridge*
Amy Rosenzweig, *Northwestern U.*
Mike Ryan, *U. of Texas at Austin*
Mitinori Saitou, *Kyoto U.*
Shimon Sakaguchi, *Osaka U.*
Miquel Salmeron, *Lawrence Berkeley Nat. Lab*
Nitin Samarth, *Penn. State U.*
Jürgen Sandkühler, *Medical U. of Vienna*
Alexander Schlier, *Harvard U.*
Wolfram Schlenker, *Columbia U.*
Susannah Scott, *U. of California, Santa Barbara*
Vladimir Shalaev, *Purdue U.*
Beth Shapiro, *U. of California, Santa Cruz*
Jay Shendure, *U. of Washington*
Brian Shoichet, *U. of California, San Francisco*
Robert Siliciano, *Johns Hopkins U. School of Medicine*
Uri Simonsohn, *U. of Penn.*
Alison Smith, *John Innes Centre*
Richard Smith, *U. of North Carolina at Chapel Hill (\$)*
Mark Smyth, *QIMR Berghofer*
Pam Soltis, *U. of Florida*
John Speakman, *U. of Aberdeen*
Tara Spire-Jones, *U. of Edinburgh*
Allan C. Spradling, *Carnegie Institution for Science*
Eric Steig, *U. of Washington*
Paula Stephan, *Georgia State U.*
V. S. Subrahmanian, *U. of Maryland*
Ira Tabas, *Columbia U.*
Sarah Teichmann, *U. of Cambridge*
Shubha Tole, *Tata Inst. of Fundamental Research*
Wim van der Putten, *Netherlands Inst. of Ecology*
Bert Vogelstein, *Johns Hopkins U.*
David Wallach, *Weizmann Inst. of Science*
Jane-Ling Wang, *U. of California, Davis (\$)*
David Waxman, *Fudan U.*
Jonathan Weissman, *U. of California, San Francisco*
Chris Wikle, *U. of Missouri (\$)*
Terrie Williams, *U. of California, Santa Cruz*
Ian A. Wilson, *The Scripps Res. Inst. (\$)*
Timothy D. Wilson, *U. of Virginia*
Yu Xie, *Princeton U.*
Jan Zaenen, *Leiden U.*
Kenneth Zaret, *U. of Penn. School of Medicine*
Jonathan Zehr, *U. of California, Santa Cruz*
Maria Zuber, *MIT*

Science for state legislatures

Next week on 14 April, the March for Science will once again demonstrate the widespread public support for science around the world. Nowhere is this message more needed than in Washington, D.C., where the federal government continues to ignore the value of independent science advice to inform decision-making. Given this lack of expertise at the national level, it is critical to bolster the role of science in policy-making at the state government level. Here, California can lead by example.

Lawmakers must often evaluate scientific and technical information when making decisions, but such information can easily be misused, misrepresented, or ignored. Forty-five years ago, the American Association for the Advancement of Science (AAAS, the publisher of *Science*) launched its Science and Technology (S&T) Policy Fellowship Program, which has since enabled thousands of Ph.D. scientists, engineers, and physicians to work for a year for the U.S. government. Many of these fellows switched careers to populate the government, thereby connecting the scientific community to critical societal issues. Can the impact of these national-level fellows be mimicked at the state level? Nearly a decade ago, a similar program was created for the California state legislature—the California S&T Policy Fellows Program (on whose advisory committee we serve)—which could inspire other states to develop similar fellowships.

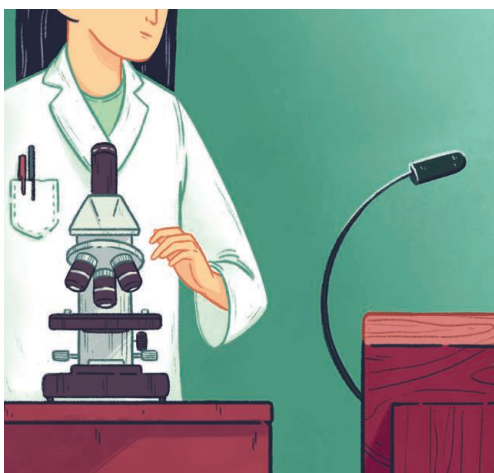
California's economy is larger than that of all but five nations, and its legislature is composed of a Senate with 40 members and an Assembly with 80 members. The state's economy is highly dependent on S&T, but there have been few individuals with a science or technology background associated with its legislature. Consequently, in 2009, the Gordon and Betty Moore Foundation provided a grant to the California Council on S&T to implement an annual S&T Fellowship Program. Each year, this program selects, trains, and places 10 Ph.D.'s or M.D.'s as California S&T Policy Fellows who serve as full-time legislative staff for a year.

A key metric for determining the effectiveness of the Fellows is evidence that their input directly affected legislation. In a recent survey of 67 former California S&T Policy Fellows, 56% reported that they provided input related to incorrect technical interpretations that resulted in weekly or monthly course corrections by legislative offices. Former legislators revealed that working with the Fellows added value to their offices in many ways, including proposing ideas for bills that relate to high-value job creation. The Fellows also helped policy-makers understand “science as a second language.” It is particularly impressive that 47% of the Fellows were hired into the state legislature after completing their 1-year fellowship; another 9% were hired into executive branch offices in California.*

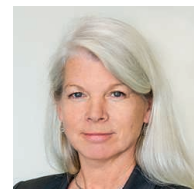
We and other scientists who have been involved with the California S&T Policy Fellows Program from the start find it both sobering and instructive to recall the difficulty in finding places for the initial 10 Fellows. The good news is that attitudes have changed since 2009, and Fellows are now in great demand. Moreover, because of daily contact with these knowledgeable individuals, both the legislature's appreciation of scientists and its use of science for decision-making have dramatically improved.

The establishment of S&T fellowship programs in other states could greatly increase evidence-based policy-making and not only benefit state policy-makers but also help to inform national policy-making and society as a whole. The California S&T Policy Fellows are currently supported on an annual basis through gifts from supportive individuals and private foundations. Many more funders should invest in “spreading scientists” to government at the state level to convey the benefits of science to society, especially when such critical advice at the national level seems sidelined. The federal government could certainly use some good role models right now.

– Mary E. Maxon and Bruce Alberts



“The Fellows also helped policy-makers understand ‘science as a second language.’”



Mary E. Maxon is the associate laboratory director for biosciences at the Lawrence Berkeley National Laboratory, Berkeley, CA, USA. memaxon@lbl.gov



Bruce Alberts is the chancellor's leadership chair for science and education in the Department of Biochemistry and Biophysics at the University of California, San Francisco, CA, USA. He is a former editor-in-chief of Science. balberts@ucsf.edu

*B. Alberts et al., *Proc. Natl. Acad. Sci. U.S.A.* **115**, 1952 (2018).

“Ernie Moniz and Steve Chu are geekier by a factor of 10, but the message is the same.”

Audience member, quoted by E&E News, reacting to U.S. Energy Secretary Rick Perry's speech supporting basic research funding, as his predecessors did.

IN BRIEF

Edited by Jeffrey Brainard

AIR QUALITY

United States to ease car emission rules



The administration will rewrite fuel economy standards designed to cut carbon emissions.

U.S. President Donald Trump's administration last week announced it intends to roll back tough auto mileage standards championed by former President Barack Obama to combat climate change. The standards, released in 2012, called for doubling the average fuel economy of new cars and light trucks, to 23.2 kilometers per liter by 2025. The Environmental Protection Agency (EPA) estimated the rules would prevent about 6 billion tons of carbon emissions by 2025. But on 2 April, EPA Administrator Scott Pruitt said the agency would rewrite the standards, arguing that Obama's EPA "made assumptions ... that didn't comport with reality, and set the standards too high." In a formal finding, Pruitt argued the standards downplay costs and are too optimistic about the deployment of new technologies and consumer demand for electric vehicles. Clean car advocates disputed many of Pruitt's claims, noting that auto sales have been strong despite stiffer tailpipe rules. "Backing off now is irresponsible and unwarranted," said Luke Tonachel of the Natural Resources Defense Council in Washington, D.C. Pruitt's move could also set up a legal clash with California state regulators, who have embraced the Obama-era standards and say they want to keep them.

France plans to compete in AI

COMPUTER SCIENCE | French President Emmanuel Macron on 29 March announced a plan to turn his country into a world leader for research and innovation in artificial intelligence (AI), a field dominated by the United States and China. It calls for a €1.5 billion investment through 2022, a handful of specialized institutes, a focus on ethics and open data, and recruitment of foreign researchers and French scientists working abroad. Like Macron's 2017 climate research initiative, "Make Our Planet Great Again," the AI plan is aimed at curbing the hemorrhage of talented researchers from France. The measures are largely based on recommendations in a new report by France's star mathematician Cédric Villani, a member of Parliament who belongs to Macron's political bloc. The European Union is set to unveil its own AI strategy on 25 April.

Uproar over 'alien' skeleton study

RESEARCH ETHICS | Chilean scientists have questioned the legal and ethical basis for a study published in *Genome Research* last month, which sequenced DNA from a 15-centimeter-tall skeleton found in the country's Atacama Desert in 2003. Ufologists have long claimed its origin is extra-terrestrial, but the study's authors, based at Stanford University in Palo Alto, California, and the University of California, San Francisco, concluded it was a human fetus with several genetic mutations. Critics now say the research was unethical because grave robbers likely removed the skeleton from its resting place, and some scientists are calling for the paper's retraction. In a statement, the editors of *Genome Research* stood behind the paper but acknowledged the need for "further discussion and agreement on rules of usage" for human remains. The Chilean government has said it will investigate how the remains were first uncovered.

Upright walking started early

ANTHROPOLOGY | Early members of the human family, or hominins, were walking upright with an efficient, straight-legged gait some 4.4 million years ago, new

research indicates. Some previous studies have portrayed early human ancestors as weird walkers, swaying from side to side; and paleoanthropologists have argued that hominins such as the famous 3.1-million-year-old Lucy weren't graceful on the ground because they retained traits for climbing trees, such as long fingers and opposable toes. But other scientists contend that natural selection would have quickly favored adaptations for efficient walking, given the dangers on the ground. To test these hypotheses, researchers compared how modern humans, apes, and monkeys use their hips, leg bones, and muscles when they walk—and then used those data to reconstruct how ancient hominins would have walked. Lucy and other members of *Australopithecus* likely had the same range of motion as modern humans do, they report in this week's issue of the *Proceedings of the National Academy of Sciences*.

Can you guess the mix in a mutt?

ANIMAL BEHAVIOR | It's not hard to tell a poodle by its curls, a greyhound by its deep narrow chest, or a pug by its flattened snout. But can people guess the ancestors of mixed-breed dogs? Researchers working with Darwin's Dogs, a citizen science effort focused on the genetics of canine behavior, want to know. On 16 April, they'll launch the MuttMix project, where volunteers try to identify the top three breeds in the ancestry of dogs that have undergone genetic tests. The project's leader, bioinformatician Elinor

Karlsson of the University of Massachusetts Medical School in Worcester, says the data will help her team assess how people perceive and react to dogs based on preconceptions about breed characteristics, and how much of dog behavior is driven by the way we tend to treat and train them.

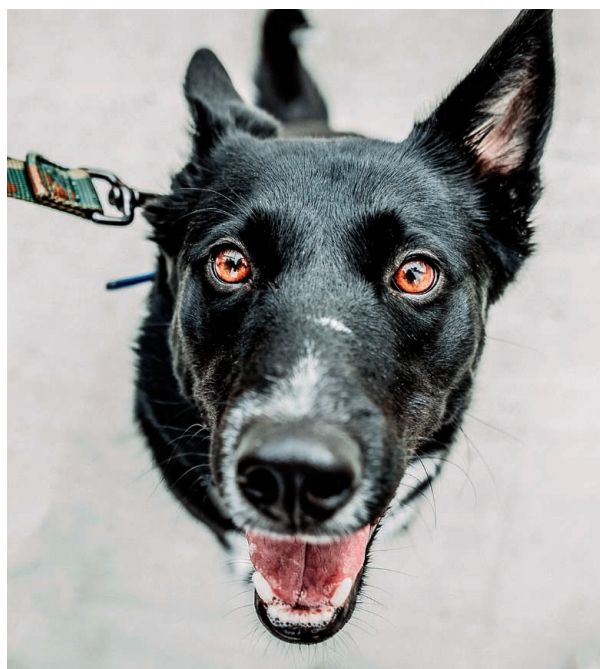
French balk at journal fees

ACADEMIC PUBLISHING | After 13 months of negotiations with German publisher SpringerNature, about 100 French universities, institutes, and hospitals won't renew their contract for almost 1200 Springer journals. The group, united in a consortium named Couperin.org, refuses to pay "ever more astronomical sums" for the subscriptions, which are a "threat to research," says a strident 30 March press release. Prices should go down, says chief negotiator Sandrine Malotiaux, because authors of 8% of Springer's 2017 papers paid to make them open access (OA), up from 3% in 2014. A SpringerNature spokesperson says the company is "disappointed," but that journal prices already factor into OA papers. Consortium members will retain access to the journals pending further talks.

Biobank studies to be blended

BIOMEDICINE | At least 60 studies around the world have enrolled, or plan to enroll, at least 100,000 people and follow them for years to study links between genes, lifestyle, and health. Last week, researchers met in Durham, North Carolina, to

discuss how to share data across these large cohort studies, sometimes called biobanks. Ranging from the UK Biobank (500,000 participants) to India's Barshi cohort (21,000 and counting), these studies already span more than 25 million people and have plans to enroll up to 36 million. Study leaders from 25 nations talked about data security, DNA sequencing strategies, assays that could be used across cohorts, and possible pilot projects, such as testing participants for inherited cancer genes. The participants may eventually share anonymized data about individuals as part of what they're calling "a global platform for translational research."



Our perception of mixed-breed dogs may influence their behavior.

How to use CO₂, not waste it

Every year humanity wastes billions of metric tons of carbon dioxide (CO₂) emitted from burning fossil fuels—but what if we could turn it into something useful? By adding electricity, water, and a variety of catalysts, scientists can reduce CO₂ into short molecules such as methane, which can then be used to produce fuels and consumable plastics. Writing last week in *Joule*, researchers explored the future of these technologies, and *Science* talked with one of the authors, materials scientist and graduate student Phil De Luna at the University of Toronto in Canada, to find out more. A longer version of this interview is available at <https://scim.ag/CO2recycling>.

Q: Why CO₂ recycling?

A: I could imagine a day when the entire energy mix is fueled by renewable energy sources, and then ... CO₂ becomes a way to store renewable energy, in chemical form, over long periods of time, in a stable way. And that's kind of the goal—to have CO₂ be a carrier of energy rather than just being a waste or an emission. ... The idea stems from artificial photosynthesis: Whereas nature has been able to take light, CO₂, and water and create food, we're looking at ways of engineering devices to take CO₂, renewable energy, and water and reduce that into more value-added products.

Q: Are any recycling technologies available to use now?

A: The scale-up and the advancements that have been happening in the last couple of years are really quite incredible. In terms of how close we are to industrial impact—it's really a matter of maybe 5 to 10 years.

Q: Which technology will ultimately win out?

A: At the end of the day, it's always going to be the market—which technology can get enough industrial sponsorship and acceptance from industry. ... These large energy companies are looking for ways to diversify their portfolios and technology. And this idea ... fits perfectly into what they're skilled at, and it really hedges the bets against becoming irrelevant.

S **SCIENCEMAG.ORG/NEWS**
Read more news from *Science* online.



IN DEPTH

SCIENCE ACTIVISM

In its second year, March for Science grows up

This year's event, set for 14 April, is only one element in a global pro-science movement

By **Jeffrey Mervis**

The March for Science, which drew more than a million people to streets around the world last April in reaction to the policies of newly elected U.S. President Donald Trump, shows signs of becoming a movement. This year's events, set for 14 April, will likely feature fewer sites and smaller crowds, both at the flagship march in Washington, D.C., and elsewhere. Even so, the movement is morphing from a single day of grassroots mass protest into sustained global expressions of support for science.

The ad hoc, all-volunteer body that coordinated last year's events has grown into an international organization with a paid staff of 10 and a mailing list of 230,000. (AAAS, which publishes *Science*, is a major sponsor.) Its activities now include online petitions to legislators on timely topics (a letter last week urged Congress to support research on gun violence), a Vote for Science campaign that highlights a different issue each month, and an upcoming national summit for local activists. Next month, the group will award its first cohort of small grants to seed a handful of grassroots projects.

Last year's march took place on Earth Day; this year, the organizers decided to avoid that overlap. "Earth Day is a very

powerful event, and we decided to let it stand on its own," says Caroline Weinberg, one of the founders of the March for Science and the interim executive director of the overall organization.

Many of the hundreds of groups that sprang up outside Washington, D.C., to organize the 2017 marches are diversifying. Some have tapped into the enthusiasm, and contributions, from last year's march to create nonprofit organizations that have become year-round advocates for science in their communities. Few of this year's marches are likely to match last year's numbers, but that prospect doesn't bother Weinberg, who is based in New York City, where another large event is in the works. "Last year the goal was to get people out in support of science," Weinberg says. "This year, we are trying to put more emphasis on direct advocacy."

With U.S. midterm elections looming in November, many groups say electing more science-friendly candidates to local, state, and federal offices is a high priority. In San Diego, California, march organizers received "requests from three different groups to set up voter registration booths, and we said yes to all of them," says Navid Zohoury, co-lead organizer of the event and a chemist at Inova Diagnostics, a local biotech company. "Voter registration is playing a much bigger role for us this year."

But Weinberg notes that "voting in November can't be your only activity." San Diego for Science, a nonprofit that evolved from last year's march there, is also promoting an initiative launched by the city's Fleet Science Center. Dubbed "Two Scientists Walk Into a Bar," it features pairs of scientists talking with patrons in 25 bars for 2 hours about whatever is on their minds. "We're trying to demystify science," says Zohoury, who hopes the trademarked "Two Scientists" will become a nationwide phenomenon.

In Oklahoma City, science advocates won't be staging a march on 14 April. Last month, organizers rescheduled their event for the fall in anticipation of a statewide teachers strike that began this week. Now, a Vote for Science fair will be used as "a lead-up to the general election," with demonstrators making their presence felt at the state capital, says Jocelyn Barton, a clinical psychologist and president of the local March for Science group. An April march would also have strained the capacity of that group's more activist members, she admits. The strike "is where all the energy is right now," she says.

Many other sites have altered their march plans, as well. Some have shifted from a march to a rally or fairlike event to keep costs down or because other events claimed their preferred venues. Others have succumbed to "march fatigue" after a year of activism in reaction to the Trump administration.

March for Science organizers want next week's event to leave a legacy beyond abandoned signs.

There are now marches “going on practically every weekend, so burnout is definitely a factor,” says Mark Shapiro, a retired physicist at California State University in Fullerton, who this year is reprising his role as lead organizer of the Fullerton march. The effort required takes its toll on volunteers, he notes: His march is the only one scheduled this year for Orange County, which hosted four last year.

European organizers are also expecting many fewer marches, and some countries won't be holding any. “Fake news everywhere, poor budgets, little recognition from the society: It's all exhausting,” says Léa Verdière, a graduate student in biology at the University of Rennes in France who heads the team planning a 3-hour march there. “Ironically, those are also some of the reasons why we will march.”

Randy Caldwell, an organizer in Munich, Germany, says his city's marchers want to highlight the value of science to society, rather than simply attacking its critics. It will be “more of a pro-fest than a protest,” Caldwell says. The lack of strong support for the event from any of the city's major

will help focus attention on the problems facing the nation's academic scientists. “Nothing has changed for good, only bad,” since last year's event, says Camilo Alcantara Concepción, biology professor at the University of Guanajuato in Mexico. Some cities will be seeing their first science marches.

Elsewhere, however, local organizers are starting to discuss whether a march is the best vehicle to sustain support for science. “We might be in a transition year,” says Angela Jordan, president of the March for Science in Mobile, Alabama. “Last year we marched and heard from speakers,” says Jordan, a research development coordinator at the University of South Alabama there. “This year we want it to be more of a science festival,” with interactive events for the public and posters from winning student science fair projects supplementing the rally.

National organizers have also spent months thinking about ways to complement next week's march on the National Mall in Washington, D.C., which will feature such speakers as oceanographer and climate advocate David Titley, dancer and chemist Crystal Dilworth, astrophysicist Hakeem Oluseyi, and public health policy professor Susan Sorenson. In July, U.S. organizers hope to ride the growing wave of science activism with a 3-day “March for Science Summit” in Chicago, Illinois. The meeting “is all about skill-building” for outreach, organizing, and advocacy, says Stephanie Fine Sasse, a national staffer based in San Francisco, California, who's leading the planning. She'd like participants to “leave the meeting with the feeling that they can do something they couldn't do before.”

Fine Sasse is also coordinating the group's first wave of community grants. The initial commitment of \$10,000 comes from the sales of a book, *Science Not Silence: Voices from the March for Science Movement*, that captured the 2017 march in words and pictures. She hopes additional fundraising will allow the grants programs to grow.

Despite the changing shape of the March for Science, its leaders think the name will remain relevant. “Over time it may become a metaphor,” Fine Sasse says. “But for now, the March for Science serves its purpose as a branding tool and a way to gain visibility.” ■

With reporting by Dennis Normile in Shanghai, China; Lizzie Wade in Mexico City; and Hinnerk Feldwisch-Drentrup in Berlin.

RESEARCH INTEGRITY

University is quick to disclose misconduct

The Ohio State University wins plaudits for unusually rapid transparency

By **Alison McCook**, *Retraction Watch*

In an unusual move, The Ohio State University (OSU) in Columbus last week released a detailed account of the scientific misbehavior of one of its former faculty members. The 75-page report was damning: It concluded that cancer researcher Ching-Shih Chen—once lauded as an “Innovator of the Year” and the winner of millions of dollars in federal funding—had committed misconduct in eight papers. The problems prompted the university to suspend a clinical trial of an anticancer compound Chen had identified, and led to his resignation last September.

Typically, the public might not have learned any of these worrying details for months or years. Most institutions conduct misconduct investigations privately and then—if the federal government funded any of the affected research—forward the results to the relevant funding agencies. The agencies can then take their time in deciding how to respond, and when to release the findings.

In this case, however, OSU officials opted to short-circuit that process. In their report, they announced Chen was guilty of “deviating from the accepted practices of image handling and figure generation and intentionally falsifying data” in 14 instances. OSU recommended all eight affected papers be retracted immediately.

The report's release won praise from advocates of transparency. But the applause came in the wake of criticism of how OSU has handled other recent cases of alleged and proven misconduct. In 2011, for example, federal officials asked the university to redo an investigation of a pharmacy researcher, according to *The Columbus Dispatch*. The school had initially concluded that problems with some published images



Organizers of the San Diego, California, march participate in public outreach events, such as the trademarked “Two Scientists Walk Into a Bar” initiative.

universities, he adds, “shows why marching on is so important.”

Australian organizers are expecting about the same number of local marches as last year, and hoping for the same positive public reaction. “We encourage everyone to come out and show their support,” says Taylor Szyszka, a graduate biochemistry student at the University of Sydney and spokesperson for the March for Science Australia.

Mexican organizers hope the growing number of marches, from 12 to at least 14,

were due to the researcher's disorganization, but the re-examination concluded they were the result of misconduct. Last year, a former associate professor resigned after an investigation into a now-retracted paper that incorrectly reported injuries related to the CrossFit workout program, prompting lawsuits.

And in March 2017, *The New York Times* reported that OSU had conducted at least five probes of Carlo Croce, a star oncologist whose published findings have been called into question. To date, he has retracted eight papers and issued 15 corrections. The university has not censured Croce, but school officials, stung by the article, hired a law firm to conduct a review of how the institution dealt with allegations of research misconduct, including those against Croce. The school has declined to share the full report, but did release a summary that stated OSU had "reached reasoned and supportable conclusions" about Croce's work. Croce, meanwhile, is suing *The New York Times* for defamation.

OSU's proactive disclosure about Chen was a turnabout. The findings were likely to affect many co-authors and others, so the school saw no reason to wait, says Jennifer Yucel, the university's research integrity officer. "We thought it was very important for the community to have this information," she says. OSU is sending its findings to the federal Office of Research Integrity (ORI), which handles misconduct cases involving researchers funded by the National In-

stitutes of Health, as Chen was. But ORI "can't overturn the institution's determination," Yucel notes. Plus, she adds, "There is a push for better transparency and better understanding of these investigations."

The move was part of OSU's ongoing efforts to find better ways to tackle research integrity problems, says Susan Garfinkel, the university's assistant vice president for research compliance, who oversaw investigations at ORI until last year. "It's not surprising that any major institution wants to be proactive in managing these [misconduct] problems," which exist at many institutions, Garfinkel says. "In fact, it's what everyone should be doing."

OSU is also sponsoring a 1-day summit on research integrity this fall for researchers, funders, publishers, and others. It is also providing electronic lab notebooks to all researchers and instructors, to ease record keeping and make researchers' tracks easier to follow.

C. K. Gunsalus, director of the National Center for Professional & Research Ethics at the University of Illinois in Urbana, says OSU officials may have decided on openness because it was the best way to burnish their public image. But, she says, "It's to their credit that they're making their judgment on their own standards" and not waiting for ORI to validate their findings. She can recall just "a handful of times" that other universities have opted for such prompt transparency.

Unfortunately, Gunsalus doesn't expect many other institutions to follow suit. "I wish I thought so," she says. But "institutions right now are sufficiently risk-averse and publicity-aware," Gunsalus says. "If they can avoid releasing [investigation reports], they do."

Chen, meanwhile, has also resigned from Academia Sinica in Taiwan, where he directed the academy's Institute of Biological Chemistry from 2014 to 2017, according to the *Taipei Times*. That institution is planning its own investigation of his work.

The suspended clinical trial involving Chen's anticancer compound can resume, according to an outside consultant that examined the issue. The consultant concluded that, despite the flawed papers, the trial could proceed "without any risk to patients." ■

Alison McCook is the editor of Retraction Watch, which produced this story as part of a collaboration with Science.

ANIMAL RESEARCH

Humane studies of octopuses get a boost

By identifying effective anesthetics, findings aid compliance with regulations

By Danna Staaf

"You're doing your surgery, but you don't know if the animal still feels it and you've just stolen its ability to respond," says biologist Robyn Crook of San Francisco State University (SFSU) in California. Until recently, researchers working with octopuses, squids, and other cephalopods routinely faced this dilemma, an ethical and, in some cases, legal challenge to studying these intelligent creatures in the laboratory. But Crook has now shown that both ordinary alcohol and magnesium chloride are effective anesthetics—crucial information for scientists pursuing cephalopod research.

Cephalopods might not seem to be ideal laboratory animals. They're exclusively marine, so a complex seawater system is needed to keep them alive, and they're disinclined to stay put—octopuses can escape through minuscule holes, while squids may jet right out of their tanks. But their unique biology and behavior have made them indispensable to researchers in many fields. Studies of the squid's giant axon helped spawn modern neuroscience decades ago, and the light organ of the bobtail squid (*Euprymna scolopes*) powered a revolution in the study of symbiotic host-microbe interactions. Today, some researchers are studying how the animals accomplish their striking feats of regeneration, while others use them in ecotoxicology studies; cephalopods even guide research into the origins of consciousness.

Because of their complex brains, cephalopods became the first invertebrates to be protected by laboratory animal laws. In 1991, the Canadian Council on Animal Care decided to extend the standards for vertebrate care to cephalopods, meaning, among other things, that researchers have to get ethical approval for their studies and must use anesthesia,

"We thought it was very important for the community to have this information."

Jennifer Yucel, The Ohio State University



Investigators concluded cancer researcher Ching-Shih Chen had committed misconduct in eight papers.



The algae octopus (*Abdopus aculeatus*) was one of three subjects in a study of anesthesia.

when possible, for procedures that could cause pain. Since then, the United Kingdom, New Zealand, and some Australian states have passed similar regulations. The biggest expansion of cephalopod rights came in 2013, when an EU-wide directive gave them the same protections as vertebrates in scientific studies in 28 countries.

Although the new regulations create extra hurdles, EU researchers have generally been able to continue their work, says Graziano Fiorito, a cephalopod neuroscientist at the Anton Dohrn Zoological Station in Naples, Italy. “We can do whatever research is scientifically, logically justifiable,” he says.

But a crucial question remained: Do the anesthetics widely used in cephalopods actually work? Most researchers use either ethanol or magnesium chloride because they immobilize cephalopods quickly and the animals soon recover without lasting effects. But paralysis isn’t the same as anesthesia, and previous studies of cephalopod anesthesia all used behavioral indicators as a measure of efficacy. None addressed the question of whether the animals were unconscious or felt pain, Crook says.

At workshops, European researchers raised what Jennifer Mather, a cephalopod ethologist at the University of Lethbridge in Canada, calls “the horrible specter” that the drugs might be mere muscle relaxants, blocking motion but not sensation. In 2017, Crook, who was already studying the response of the cephalopod nervous system to pain and injury, returned home from one of these workshops determined to set the specter to rest.

Her team recorded nerve signals from three cephalopod species: a cuttlefish and two species of octopus. The experimental technique relied on the pallial nerve, which

lies just inside the cephalopod mantle cavity, transmitting signals from the mantle to the brain and back. Exposed and accessible, the nerve can be hooked up to an electrode noninvasively. Even so, the procedure isn’t always easy: “The octopuses like to pull out the electrode,” says collaborator Samantha Brophy of SFSU, and cuttlefish research “is like working with a cat,” says another SFSU collaborator, Hanna Butler-Struben. “You can’t really force them to do anything.”

Once the electrodes were hooked up, the team added anesthetics to the seawater in the animals’ tanks, then pinched their skin lightly at regular intervals—not exactly a painful stimulus, but enough to produce a nerve signal in a conscious animal. As the anesthetized animals lost their physical responsiveness, the scientists wanted to see whether signals that mark the brain’s ability to perceive sensations also disappeared.

Magnesium chloride and ethanol both passed the test in all three species—though each with its own caveat. Magnesium chloride cut off an animal’s physical responses to stimuli 15 minutes before it deadened the signals for sensation, leaving the animal temporarily in a vulnerable state of appearing anesthetized when it wasn’t yet. “That was a real eye-opener for us,” Crook says. “That changed our practices in the lab.” Ethanol shut down both movement and sensation simultaneously—although not before causing the animals to tense and rub their tentacles in typical cleaning behavior, a sign of irritation. That’s not a big surprise, Fiorito says: “If I put ethanol in your eye, even in solution, you’re not going to be in a good state.”

The team also tested ether, which caused anesthesia but had a much longer recovery period. It’s also hazardous for researchers, so Crook’s team recommends against its

use. Another drug candidate, MS-222, failed to cause anesthesia in a lower dose but was fatal in a higher one. A bath in chilled seawater, another proposed method, didn’t cause anesthesia either. (On the other hand, they found that injections with lidocaine and magnesium chloride readily triggered local anesthesia, which might be useful in some experiments.)

The data, published 20 February in *Frontiers in Physiology*, come as a welcome relief to many scientists. “This is what we needed,” Mather says. “I care about my animals and I want to see them properly cared for.” Fiorito notes, however, that nerve signals don’t give the full picture. Additional research “should show the real mechanism of the molecule used, and what receptors are silenced so that the animal can actually be in an anesthetized state.”

Cephalopod research is not regulated in the United States, but most researchers, including Crook, already use magnesium chloride or ethanol as anesthetics when needed. Whether to implement official rules is under debate. In January, the Association for Assessment and Accreditation of Laboratory Animal Care International proposed altering its definition of “laboratory animal” to include cephalopods, but the Federation of American Societies for Experimental Biology opposed the change.

Brophy points out that the new data will make it easier for researchers to follow their consciences, regardless of what regulations require. “You can treat cephalopods humanely when you’re doing research with them,” she says. “And that should always be a standard, I believe.” ■

Danna Staaf is a science journalist in San Jose, California, and the author of *Squid Empire: The Rise and Fall of the Cephalopods*.

RESEARCH INSTITUTES

Rocky start for China's James Watson center

A new center named for the Nobel laureate faces funding and mission challenges

By **Dennis Normile**, in Shanghai, China

There was no mistaking the guest of honor at a 16 March event in the southern Chinese city of Shenzhen. James Watson, the Nobel laureate who turns 90 this week, was front and center on a red-carpeted stage before an enormous rendering of a futuristic complex dubbed The CheerLand-Watson Center for Life Sciences and Technology, intended to rival prestigious biomedical research centers in the West. Flanking him were local officials, including a vice-mayor of Shenzhen, and the chairman and CEO of China's CheerLand Investment Group, which is bankrolling the effort to launch the center.

Despite the glitzy ceremony, which included an evening-gown clad announcer and a half-day conference on precision medicine, the ambitious effort is raising eyebrows—and doubts. “I left Shenzhen rather pessimistic that the institute would ever be built,” says Watson, who wonders whether

within a year and eventually employ 1000 researchers, Liu says.

Watson got involved in fall 2016, when the head of Cold Spring Harbor Asia, CSHL's outpost in Suzhou, China, led a small delegation to the New York campus. Among the attendees were CheerLand representatives and Fu Xinyuan, a biochemist at the Southern University of Science and Technology (SUSTech) in Shenzhen. Fu was born in China but served on the faculty at Yale University and other U.S. institutions. His dream, he says, was to build an institute in China that would be as international as Yale and Harvard University, with researchers from all over the world. Fu jokes he pointed out to Watson that there was no institute bearing his name, even though one in London is dedicated to Francis Crick, Watson's partner in the discovery of the helical structure of DNA.

Watson was intrigued. “I thought China might be the place to develop cheaper drugs,” he says. He also thought that “China may be the future, so I wanted to see it.”

CheerLand stepped forward as a bene-

authorities—in a letter Fu made available to *Science*—seeking support for “The James Watson Center for Life Sciences and Technology.” Watson wrote that he wanted the center to be the only such institute in China bearing his name. He would serve as “Permanent Honorary Chairman” and lead the center's “conceptualization, design, recruitment, and scientific research strategies.”

Shenzhen awarded the nascent institute land rights to 16 hectares for 30 years. But misunderstandings arose. Watson thought the center would focus on cancer drug discovery. But an announcement on the website of Shenzhen's Dapeng New District, where the center is located, makes one mention of cancer cell immunotherapy, while identifying “precision medicine” as a main focus. Aside from the land, Watson says his name “hasn't drawn any money from Shenzhen.”

Fu says Watson was “a little naïve,” in his expectations, and that Shenzhen will want stronger evidence of an economic benefit before committing more money.

Liu says he envisions a nonprofit research effort with government support, but with another arm that would commercialize results for investors. He says CheerLand is putting up \$45 million for the first phase of construction and recruitment. But that is just an initial investment that will help raise money from other parties, says John Ma, director of investment at CheerLand's New York City office. “We are confident that the Shenzhen government will help.” (*Science* was unable to reach Shenzhen officials for confirmation.)

The CheerLand-Watson Center will need a lot of help to live up to Liu's dream of making it “bigger than Cold Spring Harbor Laboratory.” Li Guanglei, a CheerLand official handling government relations, says they are applying for two grants from the Shenzhen municipal government that could bring in up to \$6 million annually for research over 5 years, and are continuing to negotiate for unrestricted ongoing support. For comparison, CSHL has a staff of about 1100 and in 2017 spent \$148 million on its research and educational activities.

“I wish these people luck,” says Watson, who will keep working with CheerLand for the time being. But “I don't think this particular effort is going to happen unless somebody comes forward with a lot of money.” ■

With reporting by *Bian Huihui*.



A Shenzhen, China, research center named for James Watson will be impressive—if it gets built.

the necessary funding will materialize. The research agenda is also veering away from what he expected.

The institute's backers insist the project is going forward. “Within 5 years, the center will be having a very strong economic and social impact, not only in China but worldwide,” says Liu Ruyin, CheerLand's CEO in Beijing. Modeled after the Cold Spring Harbor Laboratory (CSHL) in New York where Watson served more than 4 decades as director, president, and chancellor, the center is supposed to start operations

factor. Founded in 2012 by a group of Chinese investors in the British Virgin Islands, CheerLand has real estate holdings and biotech and health care investments in the United States and China. It has forged partnerships with research institutions, notably a precision medicine institute at SUSTech. CheerLand agreed to fly Watson to China and pay him a consulting fee he describes as “commensurate with my status.”

Watson visited Shenzhen in April 2017 to see possible sites for the laboratory. After returning home, he wrote Shenzhen



PEER REVIEW

NIH looks to punish reviewers who violate confidentiality

Agency re-reviewed dozens of funding proposals after officials discovered a violation of the rules

By Jeffrey Brainard

When a grant application to the U.S. National Institutes of Health (NIH) in Bethesda, Maryland, goes through peer review, the entire process is supposed to be shrouded in secrecy. But late last year, NIH officials disclosed that someone involved in the proposal review process had violated confidentiality rules designed to protect its integrity. As a result, the agency announced that it would re-review dozens of applications that might have been compromised.

Now, NIH says it has completed re-evaluating 60 applications—and has begun taking disciplinary action against researchers who broke its rules. It has also cast a broader net for violations.

“We are beginning a process of really coming down on reviewers and applicants who do anything to break confidentiality of review,” Richard Nakamura, director of NIH’s Center for Scientific Review (CSR), which manages most of NIH’s proposal reviews, said last week. Targets could include “applicants who try to influence reviewers ... [or] try to get favors from reviewers.”

“We hope that in the next few months we will have several cases” of violations that can be shared publicly, Nakamura told *Science* at a 26 March meeting of CSR’s advisory council. He said such cases are “rare, but it is very important that we make [them] even more rare.”

This year, CSR recruited more than 18,000 researchers to serve on its dozens of review panels, which score more than 61,000 applications for funding. Every reviewer is required to sign a statement certifying that they have read and will abide by NIH’s confidentiality rules, which bar “disclosing, in any manner, information about the committee deliberations, discussions, evaluations, or documents to anyone who has not been officially designated to participate in the peer review meeting.”

Michael Lauer, NIH’s deputy director for extramural research, disclosed in a 22 December 2017 blog post that those rules had been violated. He and other NIH officials have declined to say how the agency discovered the violations or how many grant applications, peer reviewers, or review panels were involved. And they were mum on what punishments they had in mind for anyone who violated the rules.

The National Institutes of Health says it will crack down on anyone who tries to manipulate peer review.

But some details emerged at last week’s CSR advisory council meeting. The 60 proposals that NIH asked a new group of reviewers to rescore were originally handled by a single review panel during a single round of reviews, Nakamura said. “There was an attempt to influence the outcome of the review,” he said. The effect on the outcome “was sufficiently ambiguous that we felt it was necessary to redo the reviews.”

Nakamura also described the types of violations of confidentiality NIH has detected. They included “reciprocal favors,” he said. He didn’t elaborate, but the term typically means that an applicant offered a favor to a reviewer in exchange for a favorable evaluation of a proposal, or vice versa.

In at least one case, an applicant learned the “initial scores” given to a proposal, Nakamura said, and the names of the reviewers assigned to a proposal before a review meeting took place. Both details are supposed to be secret. Nakamura also reported that a scientific review officer—an NIH staff member who helps run a review panel—inappropriately changed the score that peer reviewers had given a proposal.

As for disciplining those involved, Nakamura said, “We try to do something that’s fairly graded in this process.” NIH rules suggest possible sanctions could include suspending or barring violators from obtaining federal research funds.

As it continues to investigate confidentiality breaches, NIH has been emphasizing its rules for protecting the integrity of peer review. “In the past year there has been an internal decision to pursue more cases and publicize them more,” Nakamura said. “What we’re trying to do is to be more assertive more broadly on violations of appropriate behavior in peer review.”

Members of the CSR council generally encouraged NIH to provide more training for reviewers about the rules. Some suggested, though, that rule-breaking was tacitly encouraged by the practices on some standing review panels, and that educational efforts would be needed to change that culture.

“One thing I’ve seen is that members of study sections will go have a drink [after the meeting], and they’ll be sitting around and discussing what happened,” said council member José López of the University of Washington in Seattle. “But then other people [not on the review panel] join, and the discussion continues. ... If everyone does it, then it seems OK. It really needs a cultural change at the level of the study section.” ■

A DELICATE BALANCE

Routinely giving antibiotics to premature babies may do more harm than good *By Marla Broadfoot*

Should she change the dose of steroids? Administer a diuretic? Remove the feeding tube? Rachel Greenberg makes hundreds of crucial decisions while shuffling through the dimly lit bays of the neonatal intensive care unit (NICU) at Duke University Medical Center in Durham, North Carolina. As she checks on the little ones entrusted to her care, some babies fuss in open cribs beneath mobiles emitting soothing tones; the smallest, weighing less than half a kilogram, slumber in cases of clear plastic. In the corners, computer monitors silently shout messages such as “Wash your hands!”

Near the end of Greenberg's rounds, the young neonatologist visits one of the newest arrivals, a baby girl with mahogany skin and wisps of black hair, recently transferred from a community hospital. She was born 4 weeks too early, and though she's faring better than most in the NICU, a note in her chart concerns Greenberg.


Doctors at the community hospital had given the baby antibiotics without testing for an infection. Greenberg wonders whether the drugs were necessary. She had run a blood culture herself and found no bacteria. Maybe the baby never had an infection. Or maybe she had, and the antibiotics were working. With no way to know, Greenberg continues the medication.

Like that baby, the vast majority of the nearly half-million infants born prematurely in the United States are given antibiotics, even without evidence of infection. Many preemies are kept on the drugs after blood tests say they are not sick. Yet that practice, once considered the best way to protect a hospital's most vulnerable patients, is now being challenged. “We're beginning to recognize that the risk of giving that antibiotic may actually outweigh the benefit,” says Josef Neu, a neonatologist at the University of Florida in Gainesville.

Some studies suggest that even while helping fight certain infections, those drugs may encourage others by wiping out an in-

fant's developing gut microbiome—those trillions of resident microbes with functions as diverse as synthesizing vitamins and bolstering our immune systems. By disrupting that microbial ecosystem, blanket antibiotic dosing of babies, particularly preemies, may promote a host of problems later in life, such as asthma and obesity. And recent research indicates that long after preemies leave the NICU, they can harbor many antibiotic-resistant microorganisms, potentially endangering not only themselves, but also the wider population.

In all corners of medicine, doctors are waking up to the dangers of antibiotic overuse. But change is coming slowly to the NICU. Another message that pops up on the monitors at Duke is: “Antibiotics are not always the answer!” Yet many neonatologists hesitate to alter their habits, unable to shake the fear that a baby may die on their watch. “We are working to change our perception ... to fight the belief that antibiotics are always the safe thing to do,” Greenberg says.



Antibiotics can help fragile premature babies survive. But they may have a cost later in life.

Neu hopes to provide hard evidence with a small clinical trial: A random selection of premature infants who would have been given antibiotics automatically will instead be placed in a nontreatment control group. For 2 years, his team will track the microbiomes and health of the preemies. Some of Neu's colleagues feel uneasy about withholding antibiotics, but he says answers are needed. "What can we do to use these antibiotics more intelligently? This is, I think, one of our biggest conundrums in neonatal intensive care right now."

TODAY, BABIES BORN as early as 28 weeks routinely survive, as do more than half of those born at 24 weeks (although often with significant disabilities). Much of the credit goes to antibiotics, which have thwarted infections such as sepsis and group B strep that a preemie's immature immune system could not have fought on its own. Those successes spurred a steady increase in routine antibiotic use in the NICU. At last count, three of

the top four drugs prescribed in the NICU were antibiotics.

Over time, however, scientists began noticing that antibiotics can increase babies' risk of the very afflictions the drugs aim to protect against—such as fungal infections, late-onset sepsis, and a deadly intestinal disorder called necrotizing enterocolitis. In a seminal 2009 study in *Pediatrics*, for example, Greenberg's colleague Michael Cotten showed that each additional day of antibiotics significantly increased the odds that a preemie would develop necrotizing enterocolitis or die.

Researchers are still debating when the first microbes colonize us—in utero or during birth—but Greenberg and many others worry that early use of antibiotics in infants disrupts the establishment of those indispensable residents. The gut microbiome is practically an organ unto itself, weighing about as much as the liver. It is thought to play a critical role in priming the immune system, and it produces just as many neurotransmitters as the human brain. Ge-

netic and environmental factors, including antibiotics, shape its makeup early in life. Then, around age 3, a quasi-stability sets in and we are "stuck with that architecture," says Gautam Dantas, a microbiologist at Washington University in St. Louis, Missouri.

Dantas recently began tracing those dynamics in premature babies, whose microbiomes are just being established. In stool samples of premature infants from the St. Louis Children's Hospital, he was shocked to discover that every child had been exposed to antibiotics. As a result, none of the samples could serve as controls. Instead, he compared stool samples from preemies who had been exposed to antibiotics for just a few days to stool from those exposed for a few months. He found that babies on long-term antibiotics had only a 10th of the bacterial diversity. In addition, their dominant denizens were a "who's-who list of bad gut pathogens," he says. "Our speculation is that because of all the high antibiotic pressure, those are the only bugs that can survive, and they probably are coming in from surfaces in the NICU."

Over the past 2 years, Dantas has traced what happened to those impoverished microbiomes after the babies left the hospital. He showed that at first, the preemies' microbiomes remained stunted. But by 4 to 6 months of age they had become just as diverse as those of full-term babies. Dantas speculates, though, that the preemies "may never truly catch up" because they lacked a normal microbial complement at times when they reached key developmental milestones.

them when an infant shows up in the NICU. That's what Neu's trial aims to do. At first, he says, the university's institutional review board balked at his proposal for a randomized control trial, questioning whether he could get enough parents to consent to withholding medication from their premature babies. But he says parents are generally receptive to the study once they understand that the mom or the baby will definitely receive antibiotics if either is at very high risk of infection.

An early barrage of antibiotics

Premature babies often receive multiple medications. Three of the four most prescribed are antibiotics (red), which are routinely given even when no infection is present.



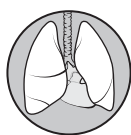
1. Ampicillin

Broad-spectrum antibiotic that treats bacterial infections



2. Gentamicin

Antibiotic that treats gram-negative bacteria



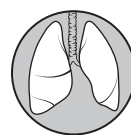
3. Caffeine

Stimulant that treats apnea and aids breathing



4. Vancomycin

Antibiotic that treats gram-positive bacteria



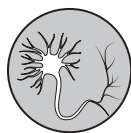
5. Beractant

Surfactant that helps lungs function normally



6. Furosemide

Diuretic that helps reduce extra fluid in the body



7. Fentanyl

Strong, short-acting narcotic that relieves pain



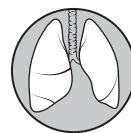
8. Dopamine

Increases blood pressure, and helps heart beat stronger



9. Midazolam

Sedative that helps reduce stress



10. Calfactant

Surfactant that helps lungs function normally

That legacy might explain a growing number of suggestive links between early use of antibiotics and disorders such as asthma, autoimmune disease, and obesity. For example, in a retrospective analysis of medical records from 64,580 children, those exposed to antibiotics in their first 24 months were at higher risk of early childhood obesity.

Dantas found another disturbing consequence when he examined the microbiomes of 2-year-olds who had been exposed to antibiotics in the NICU: microbes resistant to every antibiotic he tested, even colistin, one of the last-resort drugs. Their guts had basically become a breeding ground for antibiotic-resistant microorganisms. "The picture may not be completely grim, but it's not rosy for sure," he says. "I understand there's a risk of infection, but I just haven't seen compelling data or evidence that showed a clear benefit of those drugs."

MANY SCIENTISTS THINK the only way to understand the real impact of antibiotics on preemies is to stop automatically giving

Neu and his team plan to enroll 150 premature infants. However, the study, launched last year, has had a slow start. Physicians, not parents, have proved to be the biggest roadblock, Neu says. Doctors taking part in the study often put an infant on antibiotics at the first sign of illness, even if the baby had been randomized to the control group. Some colleagues have told him they can't worry about a later risk of asthma or obesity when their patient might not make it out of the NICU alive.

A better test for infection could help change that mindset. Blood cultures aren't foolproof and can take 24 to 48 hours. By then a preemie is likely to be on antibiotics already. "We don't have great tests beyond the blood culture to tell us who's got an infection," Cotten says. "And when a kid is falling apart over days in front of you, you worry that infection is the cause and you worry that your blood culture wasn't sensitive enough ... so you feel like you have to treat."

Neonatologist Karen Puopolo of the Children's Hospital of Philadelphia in Penn-

sylvania recently developed a fast way to screen for serious bacterial infections in full-term infants. Her algorithm is based on gestational age; maternal risk factors, such as when the amniotic sac ruptured; and the infant's clinical exam. According to a recent study in multiple hospitals, Puopolo's sepsis calculator cut the percentage of babies given antibiotics in half, and hundreds of other hospitals are now using it. But she says developing a similar tool for preemies has proved tricky because the standard risk factors would predict that most of them have an infection.

However, Puopolo discovered one factor that could distinguish between preemies at high and low risk of infection: whether they were delivered vaginally or by cesarean (C-section). Infants delivered early because of maternal health problems—such as preeclampsia, cancer, or severe kidney disease—account for about a third of all preterm births. Those babies are typically born by "elective" C-section, which doesn't expose them to risk of infection from bacteria in the birth canal. Using data from 5300 premature babies in the NICU at Brigham and Women's Hospital in Boston, Puopolo showed that those born via C-section had one-twelfth the incidence of sepsis. "That is a distinction that neonatologists know, but they haven't been using that knowledge in how they treat babies," Puopolo says. Last year, she worked with Cotten to look at the use of antibiotics in 15,000 late preterm and full-term babies. Many low-risk babies—defined primarily as those born through C-section—were not only put on antibiotics, but also kept on them for more than a week.

Still, the trend may be changing. Over the past decade, Cotten and Greenberg have tracked antibiotic use and infant health at Duke and 12 other NICUs. In forthcoming research, they found that the number of premature babies kept on antibiotics after a negative blood culture dropped from 50% in 2008 to 36% in 2014, the most recent year for which such data are available. That drop did not come with an increase in death or infection; if anything, Greenberg says, it may have improved outcomes.

Doctors are not the only ones starting to pay attention. Over the past year, Cotten has had several families ask him whether putting their preemie on antibiotics is a good idea—a question he hadn't heard in almost 30 years on the job. "The public is starting to ask, parents are starting to ask," he says. "I think ... the message is getting out." ■

Marla Broadfoot is a science journalist based in Wendell, North Carolina.



EDGE OF EXTINCTION

India's paleontologists are struggling to save fossil sites—and their own discipline

By **Sanjay Kumar**, in Lucknow and Dhar, India

Last December, paleontologist Guntupalli V. R. Prasad and his team were hunting for signs of dinosaur nests buried in a limestone hillock near Bagh, a town in central India's Madhya Pradesh state. They found trouble instead.

As the group from the University of Delhi fanned out along a formation skirting a farm, several people from a nearby village gathered to confront them. Locals often assume that outsiders prowling their land are government officials bent on appropriating tracts for a pittance in order to develop them, Prasad says. When he started to explain, a man cut him short and told his fellow villagers, "Your land is gone now." Tempers flared, and the scientists, fearing for their safety, beat a retreat.

It wasn't always like that, Prasad says. But land grabs by companies, often aided by local officials, have escalated in India. Now, he says, "Suspicion and hostility deny us access to fossil sites and seriously harm our work."

Lack of access is just one of the prob-

lems India's paleontologists face. "India has some of the world's greatest paleontological resources," says Nigel Hughes, a paleobiologist at the University of California, Riverside, whose findings in the Himalayas have illuminated trilobite evolution. But Indian officials have done little to support a field widely viewed as impractical and esoteric.

With few legal protections, sites often fall victim to looting and development. And although funds are scarce for all science in India, the plight of paleontology is particularly acute. Little money is available for excavations and for acquiring and curating specimens, and the country lacks a national institution in which its natural heritage can be studied and preserved.

All of this discourages young people from entering the field. Cash-strapped universities are curtailing or axing paleontology courses, says Ashok Sahni, of Panjab University in Chandigarh, a leading figure in Indian paleontology. Sahni, best known for his finds of dinosaur nesting sites in Jabalpur and insects trapped in amber in Vastan,

in Gujarat state, says he has watched waves of colleagues retire—with few young talents stepping in to replace them. "There is no critical mass of researchers left," he says. "Indian paleontology is dying."

THE FIRST DINOSAUR FOSSILS found in Asia, belonging to a kind of sauropod, were unearthed in 1828 in Jabalpur, in central India's Narmada Valley. Ever since, the subcontinent has yielded a stream of important finds, from some of the earliest plant remains through the reign of dinosaurs to a skull of the human ancestor *Homo erectus*. "Right from the time when photosynthesis started to the Quaternary [epoch], we have it all, continuous," Sahni says.

Much of that fossil richness reflects India's long, solitary march after it broke loose from the supercontinent Gondwanaland, starting some 150 million years ago. During 100 million years of drifting, the land mass acquired a set of plant and animal species, including many dinosaurs, that mix distinctive features with ones



Downloaded from <http://science.sciencemag.org/> on April 5, 2018

IMAGES: (LEFT TO RIGHT) GUNTUPALLI V. R. PRASAD; WALTER MYERS/SCIENCE SOURCE



<https://www.sciencemag.org/> on April 5, 2018

seen elsewhere. Then, 50 million to 60 million years ago, India began colliding with Asia, and along the swampy edges of the vanishing ocean between the land masses, new mammals emerged, including ancestral horses, primates, and whales.

Now, that rich legacy is colliding with the realities of present-day India. Take a site in Himachal Pradesh state where, in the late 1960s, an expedition by Panjab University and Yale University excavated a trove of humanoid fossils, including the most complete jaw ever found of a colossal extinct ape, *Gigantopithecus bilaspurensis*. The discovery helped flesh out a species known previously only through teeth and fragmentary jaws. Today's paleontologists would love to excavate further at the site, Sahni says. But it "has been completely flattened"—turned into farm fields, with many of its fossils lost or sold. To India's paleontologists, that is a familiar story.

In the early 1980s, for example, blasting at a cement factory in Balasinor in Gujarat revealed what the workers believed

were ancient cannon balls. A team led by Dhananjay Mohabey, a paleontologist then at the Geological Survey of India in Kolkata, realized they were dinosaur eggs. Mohabey and his colleagues soon uncovered thousands more in hundreds of nests, as well as many other fossils. Examining one Cretaceous period clutch in 2010, Jeffrey Wilson of the University of Michigan in Ann Arbor discerned what appeared to be snake bones. He and Mohabey recovered more fossil fragments and confirmed that a rare snake (*Sanajeh indicus*) had perished while coiled around a dinosaur egg. It was the first evidence, Mohabey says, of snakes preying on dinosaur hatchlings.

Mohabey and others have since documented seven dinosaur species that nested in the area. (In a separate find in Balasinor, other researchers unearthed the skeleton of a horned carnivore called *Rajasaurus narmadensis*—the royal Narmada dinosaur.) But locals and visitors soon began pillaging the sites. In the 1980s, dinosaur eggs were sold on the street for pennies.

India's fossil legacy includes an ichthyosaur, excavated in 2016 (left), and a distinctive sauropod, *Isisaurus colberti* (right), shown roaming central India in the late Cretaceous, 65 million to 100 million years ago.

In 1997, local authorities designated 29 hectares encompassing the nesting sites as the Balasinor Dinosaur Fossil Park in Raiyoli. But poaching continued largely unabated in the park and outside its boundaries, Mohabey says. Even now, the park is not fully fenced and the museum building, ready since 2011, is still not open. "I have myself seen a beautiful dinosaur nest just disappear from the Raiyoli park despite our efforts to hide it from the public gaze," says Aaliya Farhat Babi, a local princess who moonlights as a fossil conservationist. "The eggs were meticulously taken out as if by some expert."

The obliteration of the Balasinor fossil beds is almost complete, Mohabey says. "The majority of critical fossils are lost forever," he says. "Sometimes I literally wish I had not have discovered the site."

A one-man fossil rescue mission

In a country where fossils are at risk from neglect and looting (see main story, p. 22), Vishal Verma runs risks of his own to save them. In 2007, for instance, the high school physics teacher borrowed \$300 and rented a small truck to haul a 2-ton rock from a site in the fossil-rich Narmada Valley, in central India's Madhya Pradesh state. The rock enclosed an exquisite nest of dinosaur eggs, and Verma wanted to save it from poachers. After a 150-kilometer ride to a museum in the town of Mandu, the truck's chassis gave out. The nest was undamaged and is now on display in the museum (which Verma had helped set up). But its rescuer was left with a crushing debt—to his relatives and friends and

Verma sometimes pays villagers for fossils, which makes some experts squeamish. They say the payments could encourage poaching and illicit fossil sales. And they point out that contextual information is lost when a fossil is removed from a site without adequate study. Verma says he doesn't excavate; he and his team just collect surface finds, which they document beforehand. He adds that in the absence of regulations protecting the fossils, he doesn't see any other way to secure important specimens. "If I don't pay them, somebody else will take them and these fossils will just disappear," he says. Prasad agrees that the payments are acceptable—as long as Verma doesn't



Dinosaur eggs from the Narmada Valley of Madhya Pradesh state in India are easy prey for poachers.

the truck's owner—that took years to repay. He contemplated suicide. "Darkness overshadowed my eyes," he says.

Once Verma recovered from his depression, he says, the misadventure strengthened his resolve to protect Narmada's diverse fossil sites. Crisscrossing the valley over the past 2 decades, Verma has rescued dozens of fossilized dinosaur nests and hundreds of eggs, along with thousands of other specimens, including rare extinct sharks and a fossilized gymnosperm forest. What others call his "fossil madness" consumed most of his salary over those years.

"Verma is doing a great service with his crusade against pilferage of fossils, and by bringing many new fossil finds to the notice of trained paleontologists," says Guntupalli V. R. Prasad, a paleontologist at the University of Delhi who has co-authored several papers with Verma. "He does more field work than any paleontologist."

"anticipate anything in return."

A few paleontologists even say they owe their careers to Verma. "I don't think my Ph.D. is possible without him," says Harsha Dhiman, a graduate student at the University of Delhi. Verma helped her locate scientifically valuable dinosaur nests, she says, adding that on many occasions he kept her spirits up in grueling field conditions. He's a "paleontology ambassador as well as a savior."

Verma's crusade has also won over local authorities. Relying on his expertise and collections, municipalities established the Ashmadha Fossil Museum in Mandu in 1999 and a fossil museum in the Ralamandal Wildlife Sanctuary in 2013. And an unofficial tribute to Verma is in the works. Madhya Pradesh has set aside roughly 90 hectares for a National Dinosaur Fossil Park in Bagh. When it opens, perhaps in a few years, Verma's fossils will be on prominent display in the park's museum. —Sanjay Kumar

INDIA'S NATIONAL SHRUG toward its fossil riches began decades ago. Paleontology lost prestige in a scandal that erupted in 1989, when John Talent, a geologist at Macquarie University in Sydney, Australia, accused an Indian paleontologist of fraudulent activities over 25 years. Writing in *Nature*, Talent asserted that Vishwa Jit Gupta, a paleontologist then at Panjab University, had claimed discoveries that could not be confirmed later. Talent also charged that Gupta described as "Indian" specimens that had actually been dug up elsewhere. (Ammonoids that Gupta claimed had been found in the Himalayas were actually from Morocco.) Gupta "inundated geological and biogeographical literature of the Himalayas with a blizzard of disinformation so extensive as to render the literature almost useless," Talent wrote.

Gupta's university briefly suspended him, but he held onto his position after a long court battle and retired in 2002. India's paleontology community has struggled to regain respect—and public confidence—ever since then.

Government neglect has been a much bigger problem, however, as officials and legislators have largely ignored pleas to protect sites. "Legally, it's a free-for-all," says Rajeev Pattanayak, a paleontologist at Panjab University. Without laws, he notes, there is no way to crack down on poachers. "We do not even have a system of permits for excavation or collection of fossils in India," adds Sunil Bajpai, a paleontologist at the Indian Institute of Technology in Roorkee and director of the Birbal Sahni Institute of Palaeosciences (BIPS) in Lucknow.

The absence of legal protections for fossils also allows landowners to arbitrarily shut down access to sites. One coveted locale is a lignite coal mine in Vastan. "I always call Vastan not a coal mine, but a fossil gold mine," Sahni says. The mine has coughed up some of the oldest fossils of mammals in South Asia, including evidence that horses arose on the subcontinent some 54 million years ago before spreading to other continents—a pioneering find by Bajpai and his colleagues at BIPS. Another team found more than 100 insect species in 50-million-year-old amber in that mine and others. The Vastan mine "was like a Garden of Eden where you could find entirely unexpected things," Sahni says.

For many years, he says, mining officials allowed him and his colleagues to collect there. But since 2015, the mine has arbitrarily barred them, Sahni says. And some mines have destroyed fossil sites. In the Babiya Hills of Kutch, lignite mines have dumped waste rock on key localities for early whale fossils. Last year, Bajpai vis-

ited one site he'd excavated only to find that mining waste had "destroyed half the locality."

Even after fossils are excavated and taken to museums, they are still at risk, Prasad says. "The biggest question before me is what will I do with my type specimens once I retire," he says. Prasad has ruled out donating his type specimens—which defined new species of dinosaurs and early mammals—to his own University of Delhi, one of the best in the nation. In the cash-starved geology department, "all major instruments are out of order." Faculty positions are perennially vacant, Prasad says, and there is scant money for expeditions or for training budding scientists. Other universities face conditions that are even more dire, he says. The bottom line is that far too often, "once people retire, their collections are simply thrown away by the new people or they rot unknown in some storage."

Nor would Prasad hand his type specimens over to the Geological Survey, he says, even though it is the next logical choice after his university. At the Geological Survey's museum, he claims, the specimens would be locked away—and inaccessible to researchers. "I strongly believe that our natural heritage should remain within the country," Prasad says. But at the moment, he sees no choice for his fossils but to "deposit them in a well-curated museum abroad with a research tradition and good conservation practices."

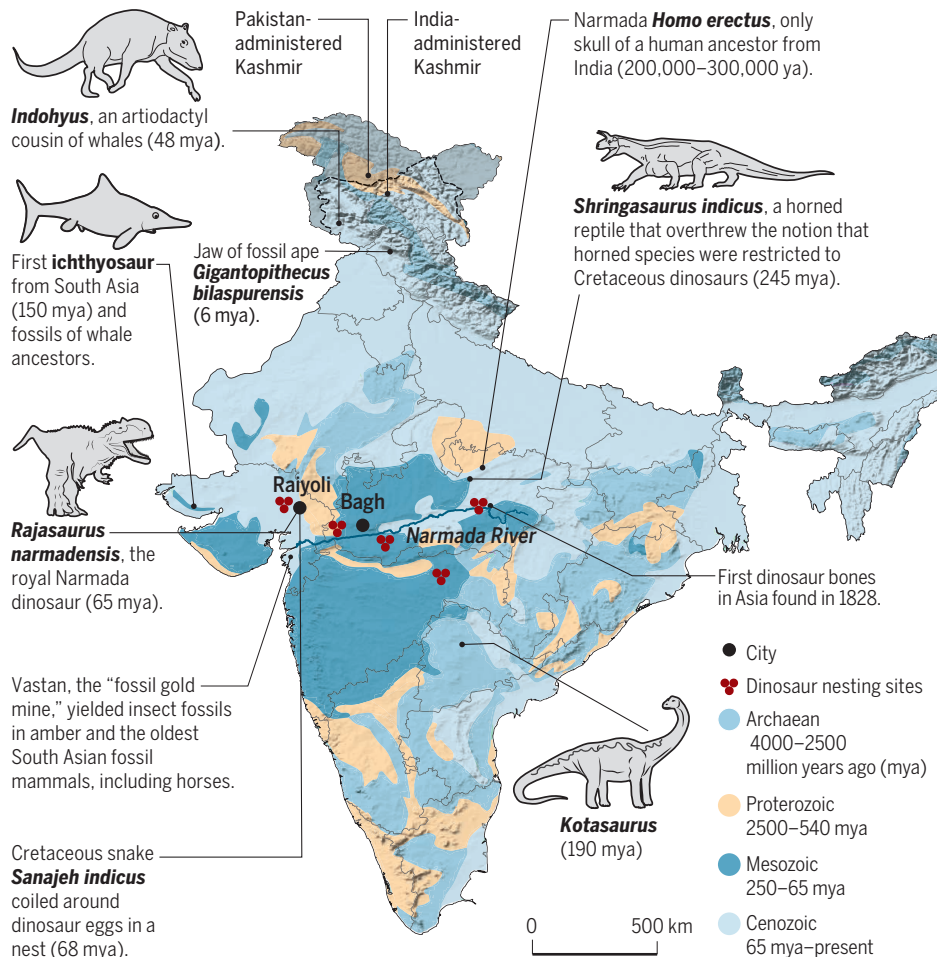
As a remedy for the crisis, Indian and foreign scientists have lobbied for the creation of a Smithsonian-style institution. "India critically needs a national repository for scientifically important fossils," Hughes says. A comprehensive fossil repository, Sahni adds, would be indispensable not only for public education, but also for the discipline. "Suppose we get a sample from Vastan: an ankle bone of a rabbit. How will you identify it? In France, Germany, and [the] U.S. you have active people working on this and they have each bone of each living animal. So, they can compare. But in India, we have nothing like this," he says. "It's a big loss to our science."

Indian officials appear to be unmoved. The government is "agnostic vis-a-vis the various science disciplines," says Ashutosh Sharma, secretary of the Department of Science & Technology in New Delhi, which funds much of India's basic research. His agency would be willing to "fill any policy gaps," he says, but it has not seen a need for a special effort to rejuvenate paleontology.

THE FLAME of Indian paleontology may be guttering, but a few recent developments have buoyed spirits. In February 2016, a

A subcontinent's fossil riches

Diverse geology and a complex history, including 100 million years as an island continent, help explain the diversity of fossils in India. Fossil sites have little protection, however, and paleontology is poorly funded.



team from the University of Delhi, Kutch University, and the universities of Kiel and Erlangen-Nuremberg in Germany unveiled a 150-million-year-old, nearly complete skeleton of an ichthyosaurus. Found in Lodai village in Gujarat, the specimen of the marine reptile is "the first intact and near complete fossil skeleton of an extinct Jurassic reptile from South Asia," says Prasad, who led the excavation.

Another big find came last August, when the Indian Statistical Institute in Kolkata, which maintains a vaunted paleontology section, announced that its researchers had unearthed at least seven specimens of a 245-million-year-old long-horned reptile from the Satpura Gondwana Basin in Madhya Pradesh. The Triassic period find, which they have named *Shringasaurus indicus*, overturned the notion that horned species were exclusive to dinosaurs of the Cretaceous period, some 100 million years later.

At least one venerated institution is hoping for a revival. BIPS, founded in 1946—making it one of the oldest institutions in

the country—is expanding. The institute once focused exclusively on paleobotany. Thanks to a hefty budget boost from the Indian government, it's broadening to cover all paleosciences. New lab facilities, a museum, and a fossil repository are under construction. The aim, says Bajpai, is to turn the institute into "one of the best labs in earth sciences in India"—and perhaps a national repository for India's most important fossil collections.

But Sahni and others say their field needs something that is even more important, and harder to provide, than adequate funding and legal protection for sites. India needs to instill in the public a respect for the country's paleontological riches. And that's intertwined with improving livelihoods in rural India—and creating economic incentives to preserve fossil sites. "Unless people have a stake in protecting sites," Sahni says, "they will continue to get destroyed." ■

Sanjay Kumar is a science journalist in New Delhi.

INSIGHTS



LETTERS

NEXTGEN VOICES

A postdoc's purpose

We gave young scientists this challenge: **What is the purpose of a postdoc?**

Address this question by writing a job advertisement for the perfect postdoc position. We received responses from scientists around the world representing a variety of fields. Some wrote advertisements for their ideal postdoc job and benefits, no matter how fantastical. Others felt that the perfect postdoc position is the one that is most realistically described to job seekers. —**Jennifer Sills**

The idealists

Want to conduct cutting-edge research, without becoming a cog in the machine? We have the perfect postdoc position for you! Our lab is making the world a better place through high-impact science and individualized mentoring. We offer compensation that reflects your advanced degree, making roommates and leftover seminar-pizza completely optional. Not from this country? No problem! We'll sponsor your visa for as long as you need. Postdocs with families are supported with paid parental leave and excellent child care assistance. Focus on your science, not your working conditions—all benefits are contractually guaranteed through a strong postdoc union.

Carolyn Adams Brotherton

Department of Microbiology, University of Washington, Seattle, WA 98195, USA. Email: cbrother@uw.edu

This postdoc position will include hands-on training divided into 6 months each of full-time technical practice, administrative and management roles, teaching, and grant writing and budgeting. Candidates who complete all short-term training fellowships will be promoted to professorship. Say goodbye to jobs that require you to juggle all of these roles simultaneously while you worry about securing the next fellowship position. Join our team and find your work-life balance.

Saima Naz

Lahore, Punjab, Pakistan. Email: saimanaz85@gmail.com

The candidate for this 3-year postdoc should have a relevant publication record. We give more weight to papers available online as preprints than to those under review. Selected candidates will be invited to visit

the lab, where they'll be given the opportunity to speak individually with each lab member. The successful candidate will be encouraged to collaborate with other labs, co-mentor young students, write his or her own grants, and take independent projects with him or her when the fellowship ends.

Syed Shan-e-Ali Zaidi

eLife Ambassador, Gembloux Agro-Bio Tech, University of Liège, Gembloux, 5030 Namur, Belgium. Email: shan.e.ali@outlook.com

The Knownforhermentorship Lab at the University of Beachfront Paradise is looking for highly motivated and creative postdoctoral fellows. We are particularly interested in developing an outside-the-box yet somehow sure-to-not-be-scooped application immediately translatable to benefit humanity. The successful applicants will use a slight tweak on the techniques they spent 5 years of graduate school learning to tell a story sure to leave reviewers breathless and h-indexes soaring. Candidates will retain the emotional capital to develop and maintain meaningful relationships outside the lab. Additionally, the adviser will respect and support the trainees' ongoing journey toward gainful employment at the next stage of their careers. As such, experiences leading to outside-the-bench experience will be highly encouraged.

Allison F. Dennis

The Program in Cell, Molecular, Developmental Biology, and Biophysics (CMDB), Johns Hopkins University, Baltimore, MD 21218, USA. Email: adennis16@jhu.edu

Seeking a professional in curiosity to complement a vibrant and diverse academic community. Tasks consist of

research, teaching, service, and active preparation for a fruitful career. Ample access provided to mentoring by senior scientists and experts outside of academia, as well as training and funding for research, conference participation, and leadership development. Fair compensation and employee benefits offered, including health care and social security. The successful candidate will be a self-motivated critical thinker with an open mind, patience, integrity, and exceptional learning strategies. Desired qualifications include enthusiasm, adaptability, high frustration tolerance, and excellent communication skills.

Anni Hämäläinen

École d'Optométrie, University of Montréal, Montréal, QC H3T 1P1, Canada, and Canadian Association of Postdoctoral Scholars.
Email: anni.hamalainen@umontreal.ca

Approaching 40 and still without a tenured position? Join our Ivy League university and let the Matthew effect boost your career. We are a cronyism-free workplace. You are encouraged to pursue your own research interests. Your publication output is more important for us than any teaching or administrative obligations. Our prestigious location incurs high living costs, but you can work remotely and enjoy more time with your family.

Wadim Strielkowski

Department of Agricultural and Resource Economics, University of California, Berkeley, Berkeley, CA 94720, USA. Email: strielkowski@berkeley.edu

Are you responsible and ready to move forward in your career and contribute to your lab? Are you an independent thinker who is clear-eyed about the questions in your field? Apply for a postdoc position to enhance your skills, practice writing papers, and apply for funding with a safety net in case you fail. As you mentor Ph.D. students and answer their questions, you'll be pushed to think like a professor, preparing you for your next step.

Ming-Ju Amy Lyu

Department of Plant Systems Biology, Shanghai Institute of Plant Physiology and Ecology, Chinese Academy of Sciences, Shanghai 200032, China.
Email: lvmj@sjp.ac.cn

Calling freshly minted Ph.D.s—you tired, poor, huddled masses! Through the trenches of graduate school, you have emerged victorious. Do you desire a bounty of rest and riches? This position is not for you. If you seek instead to stretch and challenge your abilities as a person of science, apply now. Responsibilities: Pretend you are starting your Ph.D. over, and you are your own adviser. Benefits:

Health care, professional development opportunities, and a journey toward the pinnacle of understanding. Skills required: In the spirit of Einstein, no special talents required—only passionate curiosity.

J. K. Wenderott

Department of Materials Science and Engineering, University of Michigan, Ann Arbor, MI 48109, USA.
Email: jillkw@umich.edu

We are seeking an adventurous postdoc to work in a high-risk project in Mordor University's Volcanology Department. Requirements: Diplomatic skills to deal with hobbits, high elves, wizards, and ginormous red eyes. Fluent in uruk-hai with persuasive grant-conjuration skills. The candidate will be required to lead and train goblins and naughty trolls through state-of-the-art projects. The candidate will enjoy networking opportunities in the Minas Tirith Lava and Fire Annual Meeting. Master magic along with data analysis!

Cristina Espinosa-Diez

Oregon Health and Science University, Portland, OR 97239, USA. Email: espinosm@ohsu.edu

The realists

Position: Postdoctoral position under Nobel Prize-winning PI performing groundbreaking, world-changing research. Very high pay with competitive benefits. Guaranteed faculty position at prestigious university upon successful completion of short, 6-month postdoctoral tenure. High-impact factor publications and suitable authorship position. Ample funds devoted to conference travel with many networking opportunities. Freedom to pursue personal research endeavors. Direct, hands-on training with newest and most important techniques in the field. Wanted: Hardworking, knowledgeable Ph.D. graduate who realizes this offer does not exist.

Kyle Isaacson

Department of Bioengineering, University of Utah, Salt Lake City, UT 84112, USA.
Email: kyle.isaacson@utah.edu

Seeking candidate to fill postdoctoral research position. Responsibilities include full-time research, full-time grant application writing, full-time mentorship of graduate students, and a willful ignorance about the fact that you should be paid more for this. Candidates should be proficient in whatever skills the PI suddenly decides that he or she needs in the group, regardless of the research history of either the candidate or the group. Benefits include technically not being unemployed and being able to mumble

vague affirmations about how the position will help in a future career, despite empirical evidence to the contrary for all but a few.

Yifan Li

Berkeley, CA 94703, USA. Email: yili91@gmail.com

The National Institute of Looking Deep into Things is searching for a highly motivated postdoc who can pretend to be able to do everything. Your responsibilities lie in doing what we ask you to do—or not—as long as at the end of each week you report doing a lot. Benefits: Minimum financial coverage until the unlikely day when you find a place to pursue your real passion and curiosity. Apply now!

Ebrahim Hassan

Institute of Virology, Medical Center University of Freiburg, 79104 Freiburg, Germany.
Email: ebrahim.hassan@uniklinik-freiburg.de

New lab seeks deeply purposeful scholar comfortable with the menial tasks that comprise postdoctoral training. The successful candidate will seek to work for long stretches without supervision, interspersed with intense bouts of micromanagement. The postdoc will somehow intuit when to submit to the ideas of the Principal Investigator and when to think with fierce independence. Such training will yield the mental toughness needed for success against the background dysfunction present in both private- and public-sector workplaces. Highly specific career goals and hardheaded open-mindedness will both be considered a plus.

J. Steen Hoyer

Department of Ecology, Evolution, and Natural Resources, Rutgers University, New Brunswick, NJ 08901, USA. Email: j.s.hoyer@wustl.edu

We are currently seeking a deity-in-training to fill the honorable position of postdoctoral researcher under our esteemed Principal Investigator. Daily responsibilities include maintaining a positive workplace culture by facilitating the caffeination of graduate students and tending to the undergraduates with regular watering and pruning. Qualified candidates should be capable of transmuting their flesh into that of a rhino's, gritting their teeth with the force of an alligator, and generating new ideas on demand. Benefits include socially preparing yourself for life on Mars, learning how to sleep sitting up, and being first author whenever you roll above a five on a six-sided die.

Joseph Michael Cusimano

College of Pharmacy, The Ohio State University, Columbus, OH 43210, USA.
Email: joecusi@hotmail.com

10.1126/science.aat6008



Plastic fragments, including microplastics, are now ubiquitous on land, in freshwaters, and in the ocean.

they encouraged scientists to include the fate, contamination, and effects of microplastics on Earth's natural cycles, ecosystems, and organisms in their studies of plastic pollution.

What resulted was a scientific explosion. Over the past 14 years, researchers have documented and studied microplastics across the globe, resulting in tremendous advances regarding the sources, fate, and effects of microplastics and their associated chemicals. Several hundred scientific publications now show that microplastics contaminate the world's oceans, including marine species at every level of the food chain, from pole to pole and from the surface to the seafloor. Yet, scientists have only just begun to document and study microplastics in freshwater and terrestrial systems.

Microplastics were first reported in freshwater lakes in 2013 (4). Since then, microplastics have been reported on freshwater beaches, in lakes, or in rivers in Africa, Europe, Asia, North America, and South America (5). Just like in the marine realm, microplastics are common in freshwater systems at a global scale. Although contamination tends to be greater near large population centers, microplastics—often in the form of microfibers—have also been found in remote locations (6), perhaps as a result of atmospheric deposition (7). Microplastic concentrations in freshwater ecosystems are highly variable, and even though these systems are less dilute than oceans, concentrations reported thus far appear to be in a range similar to those in the marine environment (5). Microplastic contamination, as seen in marine animals, has also been reported in freshwater animals, including insects, worms, clams, fish, and birds.

Researchers generally seem to expect the effects of microplastics on freshwater organisms to be similar to those on marine organisms. In fact, scientists have been testing impacts of microplastics on freshwater animals for many years because several of them—such as Japanese medaka, zebrafish, *Daphnia*, and *Ceriodaphnia*—are standard toxicity test species. As a result, impacts from exposure to microplastics have been demonstrated in freshwater plants, invertebrates, and several species of fish (5). Still, the research remains young, and most studies of freshwater systems and organisms aim to better understand the sources of microplastics to the environment and their effects on animals in general. Given that freshwater ecosystems are highly diverse, with roughly as many fish species as in the oceans, researchers must also ask questions about the unique fate and effects of microplastics in

PERSPECTIVES

POLLUTION

Microplastics research—from sink to source

Microplastics are ubiquitous not just in the ocean but also on land and in freshwater systems

By Chelsea M. Rochman

Research on microplastic pollution (small particles of plastic <5 mm in size) has long focused on their largest sink: the ocean. More recently, however, researchers have expanded their focus to include freshwater and terrestrial environments. This is a welcome development, given that an estimated 80% of microplastic pollution in the ocean comes from land (1) and that rivers are one of the dominant pathways for microplastics to reach the oceans (2). Like other persistent pollutants, such as polychlorinated biphe-

nyls (PCBs), microplastics are now recognized as being distributed across the globe. Detailed understanding of the fate and impacts of this ubiquitous environmental contaminant will thus require a concerted effort among scientists with expertise beyond the marine sciences.

Scientists sporadically reported the presence of small plastic particles in the ocean as early as the 1970s, but research into their distribution and impacts effectively began in 2004 with a pioneering study led by marine ecologist Richard Thompson (3). To describe small plastic particles and differentiate them from large plastic debris such as fishing nets, bottles, and bags, the authors dubbed them “microplastics.” Recognizing that microplastics were both widespread and potentially unique in their impact on the environment,

Department of Ecology and Evolutionary Biology,
University of Toronto, Toronto, ON M5S 3B2, Canada.
Email: chelsea.rochman@utoronto.ca

these vulnerable ecosystems themselves.

Research on microplastics is even more limited for terrestrial environments. Despite a call for more research in terrestrial systems in 2012 (8), only a handful of studies have since sought to quantify microplastics in terrestrial birds (9), soils (10, 11), dust (including tire dust) (12), and atmospheric fallout (7). The discovery that microplastics can undergo atmospheric transport contributed appreciably to the current understanding of their global transport (7). To predict effects on wildlife, a few researchers have exposed insects, nematodes, and earthworms to microplastics in a laboratory setting. These studies have shown how microplastics may be transported through soils (13) and incorporated into habitats (10), as well as how they affect the feeding behavior and health of various terrestrial invertebrates (14).

Soils may act as an important long-term sink for microplastics (8). This has been demonstrated via the presence of plastic microfibers and fragments in sewage sludge that is widely applied on vast expanses of agricultural land (11). Other large-scale sources of microplastics in soils are the weathering and disintegration of protective plastic sheeting (plasticulture) over agricultural fields and the fragmentation of plastic litter and plastic items in landfills. To better understand microplastics as an emerging global contaminant, further field sampling should aim to measure the extent of the contamination on land. Models and laboratory and field experiments should aim to better understand the

sources, fate, and effects of microplastics in terrestrial biomes.

Studies of terrestrial and freshwater ecosystems will continue to be particularly helpful for elucidating sources of microplastic pollution to the environment. This is because freshwater and terrestrial ecosystems are direct receivers of treated and untreated urban, industrial, and agricultural waste. The plastics in these environments therefore more readily reveal their original source than in the open ocean, where particles tend to be weathered, fouled, and highly fragmented.

For example, plastic microbeads from personal care products were first reported in the freshwater Laurentian Great Lakes (4), leading to legislation aimed at eliminating this source of microplastics in several regions (including the United States, Canada, and Taiwan). Moreover, a study from 2005 demonstrated that synthetic fibers are spread on soils when sewage sludge is applied (11). This study proposed synthetic fibers as an indicator of the land application of sludge, but also led researchers to conclude that laundry effluent is an important source of microfibers to the environment (15).

In general, freshwater and terrestrial studies have helped increase understanding of microplastic sources to the environment. Moreover, the current evidence suggests that microplastic contamination is as ubiquitous on land and in freshwater as in the marine environment (see the figure). But little is known about its fate and effects in freshwater and terrestrial ecosystems, which

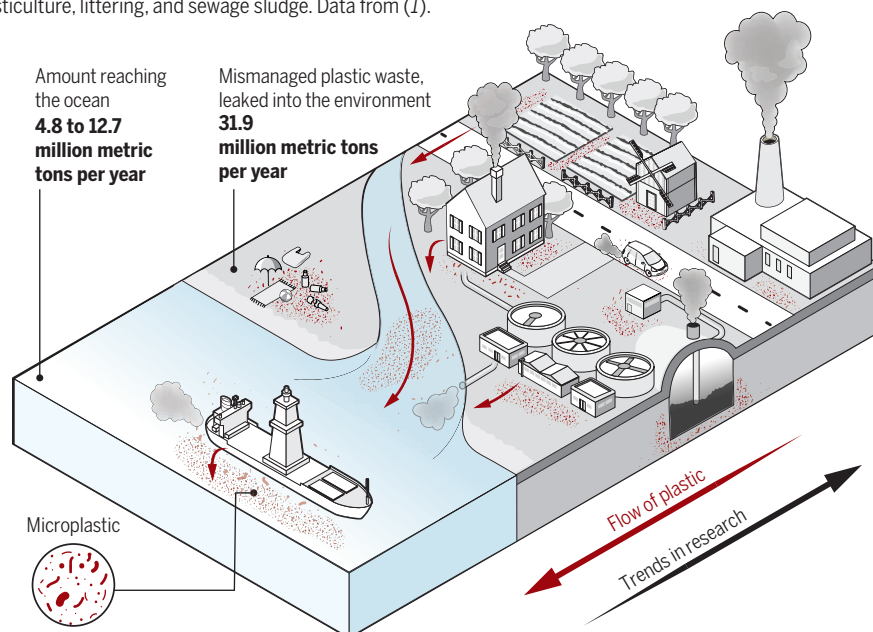
are governed by physical, chemical, and biological processes that differ from those in the marine realm. Progress in these systems can be accelerated by building on more than a decade of focused research on microplastics in marine ecosystems. For example, well-developed methods for sampling, extracting, and quantifying microplastics can be applied. Moreover, the same chemicals used to detect microplastics in marine environments can be applied in all environments.

Microplastic fate and impacts may vary across these systems, however. For example, there may be differences in how microplastics are transported in freshwater bodies because of differences in salinity, temperature, and current patterns. In terrestrial systems, atmospheric circulation may be responsible for long-range atmospheric transport of microplastics, similar to other persistent chemical contaminants. Exposure of and effects on organisms may also vary owing to differences in physiology. For example, marine fish drink water to maintain osmotic balance, whereas freshwater fish absorb water through their skin and gills; this should lead to different amounts of microplastic ingestion for identical concentrations of microplastics. Thus, these systems bring new challenges that must be considered, even as scientists apply knowledge of microplastics in the oceans to fast-track understanding of microplastics in fresh water and on land.

Even though the oceans cover more than 70% of our planet, the biodiversity in freshwater and terrestrial systems combined is more than five times greater than in the ocean. Researchers often ask questions about impacts to human health as a result of microplastics in seafood, yet microplastics in dust, groundwater, and agricultural soils may also be of great importance. As such, microplastic research must be global and include a greater understanding of the scale, fate, and effects of microplastic pollution at all stages, from its sources via freshwater and terrestrial ecosystems to its ocean sink. ■

Microplastics everywhere

High amounts of microplastics have been found not just in the sea and on beaches, but also in rivers and soils around the world, demonstrating how pervasive this modern pollution is. Sources include leakage from landfills, plasticulture, littering, and sewage sludge. Data from (1).



REFERENCES

1. J. Jambeck et al., *Science* **347**, 768 (2015).
2. L. C. M. Lebreton et al., *Nat. Commun.* **8**, 15611 (2017).
3. R. C. Thompson et al., *Science* **304**, 838 (2004).
4. M. Eriksen et al., *Mar. Pollut. Bull.* **77**, 177 (2013).
5. D. Erkes-Medrano et al., *Water Res.* **75**, 63 (2015).
6. C. M. Free et al., *Mar. Pollut. Bull.* **85**, 156 (2014).
7. R. Dris et al., *Mar. Pollut. Bull.* **104**, 290 (2016).
8. M. C. Rillig, *Environ. Sci. Technol.* **46**, 6453 (2012).
9. S. Zhao et al., *Sci. Total Environ.* **550**, 1110 (2016).
10. E. Huerta Lwanga et al., *Environ. Pollut.* **220**, 523 (2017).
11. K. A. V. Zubris, B. K. Richards, *Environ. Pollut.* **138**, 201 (2005).
12. P. J. Kole et al., *Int. J. Environ. Res. Public Health* **14**, 1265 (2017).
13. M. C. Rillig et al., *Sci. Rep.* **7**, 1362 (2017).
14. E. Huerta Lwanga et al., *Environ. Sci. Technol.* **50**, 2685 (2016).
15. M. A. Browne et al., *Environ. Sci. Technol.* **45**, 9175 (2011).

10.1126/science.aar7734

NEUROSCIENCE

Supporting recovery from brain injury

A window of therapeutic opportunity could widen beyond the initial phase of brain injury

By **Simon Rumpel**

The beauty and intricacy of the human brain is unfortunately also mirrored by its vulnerability. Damage to the brain is typically permanent. Because cells of the adult brain, apart from rare exceptions, no longer divide, there is essentially no regrowth of damaged brain tissue. Acquired brain injury in the majority of cases occurs directly through traumatic events such as an accident involving a blow to the head or indirectly through interruption of the blood supply, namely a stroke. Brain injury is a major burden, with an estimated 1.7 million people in the United States suffering a traumatic brain injury and nearly

800,000 Americans suffering a stroke each year (1, 2). However, current treatment options for such brain injuries are still limited and are focused on the first hours after the insult. On page 50 of this issue, Abe *et al.* (3) describe a new approach in mouse and primate models that aims to enhance the ability of the brain to regain functionality in the days and weeks after brain injury.

As an organ with a disproportionately large energy consumption (~20% of the total energy is used by the brain, which is only ~2% of human body weight), normal brain function ceases within seconds after interruption of blood supply. Typically, a blood clot blocks the blood flow in the case of an ischemic stroke; less frequently, a blood vessel bursts, leading to hemorrhagic stroke.

Within minutes, neurons will be permanently damaged and undergo cell death during the next hours, often involving a phase of neuronal hyperactivity (4). Apart from the neurons located within the core area immediately affected by trauma or loss of blood supply, additional loss of neurons is also observed in the surrounding brain areas, the so-called penumbra (see the figure). Here, a temporarily decreased blood flow and pathologically increased neuronal activity spreading over from the core area endangers neighboring neurons.

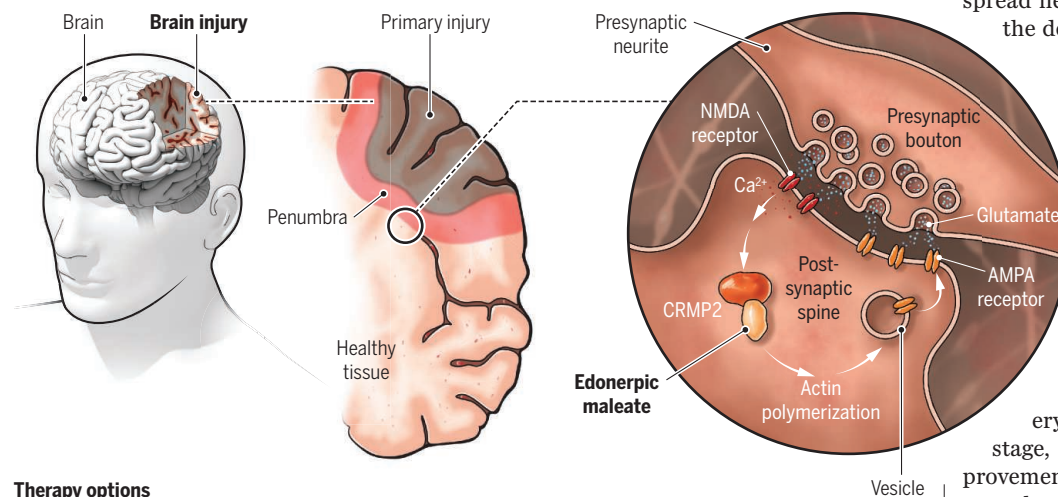
The size and location of the affected brain area varies substantially among individuals and therefore so does the degree of resulting functional impairment. A stroke, for example, is often recognized by the sudden development of deficits in the motor control of limbs and loss of control of facial muscles and speech production. The phase of acute injury to the brain lasts a few hours and, in a fraction of cases—typically involving large trauma or widespread hemorrhagic bleeding—can lead to the death of the patient.

The acute phase is immediately followed by a recovery phase that is characterized by a spontaneous lessening of behavioral impairments that can last for weeks to many months. During this recovery phase, cascades of molecular alterations are observed that reflect changes in gene expression, increased release of growth factors, and regrowth of neuronal processes. The recovery phase transitions to the chronic stage, when the rate of functional improvements does not increase and in many cases leaves affected persons with lifelong impairments associated with considerable loss in quality of life.

Therefore, therapeutic options to mitigate the consequences of brain injury are of prime importance; however, current options are still limited. In the case of an ischemic stroke, the infusion of tissue plasminogen activator—in order to attempt to dissolve the blood clot and to allow fast

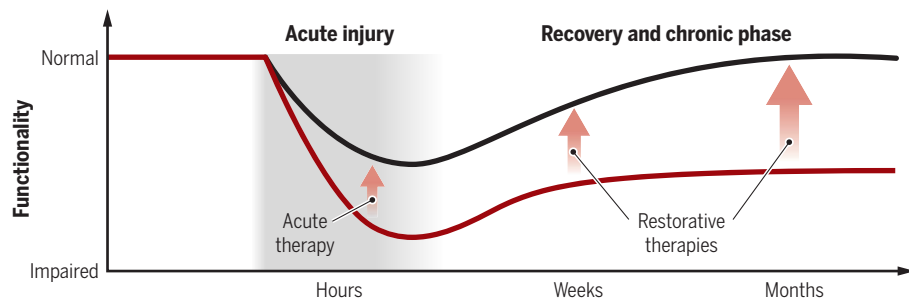
Functional recovery from brain injury

During the first few hours of acute brain injury, brain cells are damaged and permanently lost, resulting in sudden loss of functionality. Plastic remodeling of synaptic connections mediates spontaneous relief from impairment during the recovery phase, which often remains incomplete. NMDA, *N*-methyl-D-aspartate.



Therapy options

Acute therapy options aim to limit the damage to the brain. Restorative therapies hold the promise to offer additional treatment opportunities at later time points, supporting the brain's ability to recover.



Institute of Physiology, Focus Program Translational Neurosciences, University Medical Center of the Johannes Gutenberg University Mainz, Hanns-Dieter-Hüsch Weg 19 55128 Mainz, Germany. Email: sirumpel@uni-mainz.de

reperfusion—remains the standard therapy (5). Current complementary therapies aim to protect neurons in the penumbra and restrain brain damage to the core area (6). Importantly, the time for these therapies to be administered is limited to a narrow window during the acute phase of the insult, and therefore, patients often remain untreated when received at the hospital after the acute phase. Therefore, therapies that support the spontaneous recovery of the brain during later phases after the injury are a long-sought objective (7).

What are the mechanisms that help the brain in many cases to spontaneously recover at least partially from functional impairments? The neurons of the brain make an estimated 10^{13} synaptic connections and thereby create a highly complex network. A single neuron in the cortex, the outer shell of the brain, receives signals from a few thousand neurons and in turn sends out signals to a similarly large number of downstream neurons. Despite that in the adult brain the number of neurons is largely constant, the connections among them are not

“...a new approach in mouse and primate models...aims to enhance the ability of the brain to regain functionality in the days and weeks after brain injury.”

hardwired. Brain circuits have the ability to undergo plastic remodeling by building new and eliminating old synapses as well as adapting the strength of persistent connections (8). This synaptic plasticity is believed to mediate cognitive processes such as the storage of information during memory formation in healthy conditions, but after brain injury, synaptic plasticity helps to reconfigure neuronal circuits and thus to regain functionality (9, 10). An emerging picture from longitudinal imaging studies in animal models is that neuronal microcircuits display a substantial level of dynamic remodeling even under conditions that do not require behaviorally or pathologically induced adaptation and thus represents a fundamental property of the brain (11).

The molecular mechanisms underlying plastic changes of synapses have been under intense investigation for decades. A major finding was that the receptors for neurotransmitters at the synapse are not fixed but undergo continuous and tightly regulated turnover that allows fast in-

creases or decreases in total receptor number and thus connection strength (12, 13). The study by Abe *et al.* identifies edonergic maleate as a small-molecule drug that is able to positively modulate the potential of synaptic connections to undergo plasticity after brain injury and to increase the rate of spontaneous functional recovery. As a mechanism of action, the authors provide evidence that edonergic maleate binds to CRMP2 (collapsin-response-mediator-protein 2) and thereby promotes activity-dependent incorporation of AMPA-type neurotransmitter receptors into synapses, mediating an increased potential for functional recovery. Enhanced rates of functional recovery were observed in motor tasks after experimentally induced brain injury in mice as well as in nonhuman primates (after the induction of a stroke). Importantly, administration of edonergic maleate occurred during the recovery phase in the days after the insult and not during the few hours in the acute phase of brain injury, providing a treatment opportunity beyond the acute phase.

It will be interesting to test the translational potential of the findings obtained in the animal models in humans. Although this often proves challenging, edonergic maleate has been used previously in human phase II studies (for example, ClinicalTrials.gov ID NCT02079909) in a different therapeutic context, and thus, important steps in terms of safety evaluation have been taken already. Therefore, edonergic maleate provides a promising treatment option for brain injury after the acute phase and joins other approaches, including small-molecule candidates, antibodies, growth factors, and brain stimulation (7, 14, 15). ■

REFERENCES

1. E. J. Benjamin *et al.*, *Circulation* **135**, e146 (2017).
2. M. Faul *et al.*, *Traumatic brain injury in the United States: Emergency department visits, hospitalizations and deaths 2002–2006* (Centers for Disease Control and Prevention, National Center for Injury Prevention and Control, 2010).
3. H. Abe *et al.*, *Science* **360**, 50 (2018).
4. T. W. Lai, S. Zhang, Y. T. Wang, *Prog. Neurobiol.* **115**, 157 (2014).
5. National Institute of Neurological Disorders and Stroke rt-PA Stroke Study Group, *N. Engl. J. Med.* **333**, 1581 (1995).
6. M. D. Ginsberg, *Neuropharmacology* **55**, 363 (2008).
7. S. C. Cramer, *J. Stroke* **20**, 57 (2018).
8. D. B. Chklovskii, B. W. Mel, K. Svoboda, *Nature* **431**, 782 (2004).
9. S. Rumpel, J. LeDoux, A. Zador, *Science* **308**, 83 (2005).
10. S. C. Cramer, *Ann. Neurol.* **63**, 272 (2008).
11. A. R. Chambers, S. Rumpel, *Neuroscience* **357**, 172 (2017).
12. R. Malinow, R. C. Malenka, *Annu. Rev. Neurosci.* **25**, 103 (2002).
13. D. S. Bredt, R. A. Nicoll, *Neuron* **40**, 361 (2003).
14. Cumberland Consensus Working Group *et al.*, *Neurorehabil. Neural Repair* **23**, 97 (2009).
15. Z. G. Zhang, M. Chopp, *Trends Mol. Med.* **21**, 543 (2015).

10.1126/science.aat2450

TOPOLOGICAL MATTER

Lattices for fractional Chern insulators

Topological order beyond Landau levels is seen in encapsulated bilayer graphene

By Cécile Repellin¹ and Nicolas Regnault²

Individual electrons are elementary particles, but in some solid-state systems, electrons can act collectively as though they had a fraction of an electron's charge. This emergent behavior is spectacularly observed in two-dimensional (2D) electron gases as the fractional quantum Hall (FQH) effect in the form of a fractional quantized transverse (or Hall) conductivity and in shot-noise experiments. These experiments require low temperatures and very large magnetic fields in order to create strong electron interactions. This latter condition now appears not to be as essential as originally thought. On page 62 of this issue, Spanton *et al.* (1) report on an experimental platform based on bilayer graphene that forms a moiré pattern with an encapsulating hexagonal boron nitride layer. They observed incompressible phases with a fractional filling of the band structure with a nonzero Chern number (it has quantized properties robust to local perturbations, or topologically invariant). Some of which have no analog in traditional FQH systems (see the figure).

Many materials naturally exhibit topological properties. For example, microscopic properties such as spin-orbit coupling and ferromagnetic exchange may strongly affect a semiconductor's band structure and lead to a nonzero quantized Hall conductivity, as well as other topological phenomena. This paradigm has ignited the quest for entirely new fractional phases that rely explicitly on the presence of an underlying lattice, dubbed

¹Department of Physics, Massachusetts Institute of Technology, Cambridge, MA 02139, USA. ²Laboratoire Pierre Aigrain, Département de Physique de l'École Normale Supérieure, Paris Sciences et Lettres Research University, Université Paris Diderot, Sorbonne Paris Cité, Sorbonne Universités, Université Pierre et Marie Curie Université Paris 06, CNRS, 75005 Paris, France. Email: regnault@lpa.ens.fr

fractional Chern insulators (FCIs). Although band-structure engineering has led to the synthesis of an ever-growing number of topological materials, including the realization of the integer quantum Hall effect in the absence of a magnetic field, FCIs require the strength of electron-electron interactions to overcome band dispersion and disorder—an important experimental challenge.

A strong analogy can be drawn between the Bloch bands of a band insulator and the Landau levels of a 2D electron gas subject to a magnetic field. The band gap in the former can be compared with the cyclotron energy separating each level in the latter. A fully filled Landau level has a quantized Hall conductivity of one in units of e^2/h , where e is the electron charge and h is Planck's constant. The seminal work of Haldane (2) showed that a filled Bloch band can also have a nonzero quantized Hall conductivity. This integer, the Chern number (C), is a topological invariant, and for a single Landau level, $C = 1$. When the lowest band has $C = 1$ and is partially filled, it may form an incompressible quantum liquid akin to the FQH effect under well-tuned microscopic conditions. These states are the simplest examples of FCIs, and their existence was predicted by analytical and numerical studies (3, 4).

However, FCIs are not merely mimicking FQH physics but feature distinctive properties. Some of these stem from simple energetic arguments. In contrast to Landau levels, Chern bands have a finite dispersion whose competition with interactions may lead to interesting phase transitions between FCIs and symmetry-broken phases. Additionally, band gaps are not fixed by an external magnetic field but result from the microscopic details of the lattice, so a material could be designed in which FCI states may be observed at higher temperatures.

More profound differences occur that require an understanding of Chern insulators beyond energetics. A vector field analogous to the magnetic field, the Berry curvature, may be defined across the lattice Brillouin zone. Although a magnetic field is generally spatially uniform, the distribution of the Berry curvature in momentum space depends on microscopic details and affects the stability of an FCI. Another exciting perspective of these lattice systems is the possibility of a band with $C > 1$, a property that does not exist in a continuum system unless a degree of freedom is added. In the presence of strong interactions, $C > 1$ FCIs with no FQH counterpart may be formed at fractional filling.

Experimental studies of lattice effects in topological systems have been limited to probing the single-particle physics of Chern insulators. The realization of a Chern insulator in magnetically doped thin films with

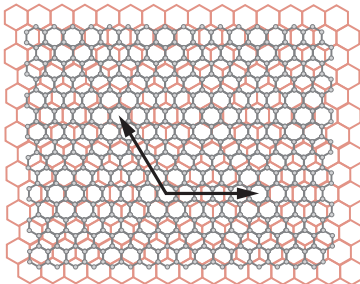
strong spin-orbit coupling was an important milestone (5). Cold atomic gases have also provided a rather controlled setting in which to realize lattice models with artificial gauge fields created through laser-assisted tunneling (6) or shaking (7) and to measure the Berry curvature of Chern bands (8). The realization of incompressible phases at fractional filling has been limited to traditional FQH systems, leaving experimentally unexplored the phases in which both lattice and interactions play a starring role.

Topological order and symmetry

The Bloch bands of a moiré pattern superlattice acquires topological character when a large external magnetic field is applied.

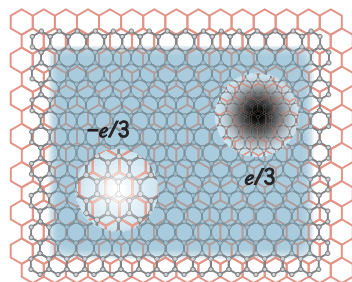
Moiré lattice

Spanton *et al.* used the slight mismatch between the lattice constants of graphene and hexagonal boron nitride to create a moiré pattern at their interface.

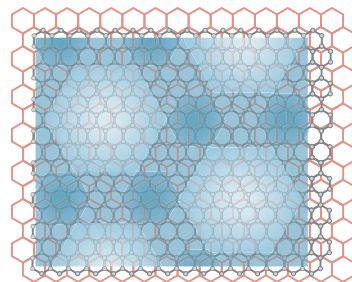


Band insulators

At $\nu = 1/3$ filling of a band, the competition between electron-electron interactions and band dispersion leads to the emergence of two incompressible phases.



The fractional Chern insulator is akin to the Laughlin state of the fractional quantum Hall effect and carries $+e/3$ and $-e/3$ charge excitations.



The symmetry-broken Chern insulator phase has an electronic density pattern with a periodicity three times the lattice constant of the moiré pattern.

Spanton *et al.* have proposed and implemented a setup for measuring FCI phenomena with no direct FQH equivalent. They encapsulated a bilayer graphene heterostructure in hexagonal boron nitride gate dielectrics and closely aligned the graphene with one of the dielectrics to obtain a moiré pattern. This superlattice generates Bloch bands whose nontrivial topology is created by an external high magnetic field. They measured the penetration field capacitance, which accesses whether the bulk of the system is gapped, and reported several incompressible phases at fractional filling ν .

Spanton *et al.* explored the interplay between lattice effects and strong electronic correlations in their bilayer graphene material. They observed incompressible phases with a fractional filling of the band structure, some of which have no analog in traditional FQH systems. They convincingly identified as FCIs some of the incompressible states by carefully comparing experimental results and theoretical expectations. Notably, they identified the $\nu = 1/3$ Laughlin state (9), but also a state at $\nu = 2/3$ filling of a $C = 2$ band, a $C > 1$ FCI. Although an incompressible state can be observed at $\nu = 2/3$ in a FQH bilayer, the unusual effect of lattice translations makes the observed $C = 2$ FCI a richer state.

Spanton *et al.* also reported the observation of interaction-driven symmetry-breaking phases at fractional filling. Interestingly, the competition between these phases and the FCIs is well captured by the authors' rather simple modeling of the device. They have used state-of-the-art numerical techniques (namely, infinite density matrix renormalization group) to explore this transition, and their numerical results are a key asset to corroborate the observation of the various fractional phases.

An interesting development would be to remove the need for such a high magnetic field, which is feasible in principle but requires more microscopic ingredients at the lattice level. In a different direction, even more exotic features such as non-Abelian excitations are predicted to be pinned by lattice dislocations in a $C > 1$ FCI. Being able to engineer various lattices and their defects would permit the testing of the most intriguing of these theoretical predictions. ■

REFERENCES

1. E. M. Spanton *et al.*, *Science* **360**, 62 (2018).
2. F. D. M. Haldane, *Phys. Rev. Lett.* **61**, 2015 (1988).
3. E. J. Bergholtz, Zhao Liu, *Int. J. Mod. Phys. B* **27**, 1330017 (2013).
4. S. A. Parameswaran, R. Roy, S. L. Sondhi, *Comp. Rendus Phys.* **14**, 816 (2013).
5. Cui-Zu Chang *et al.*, *Science* **340**, 167 (2013).
6. M. Aidelsburger *et al.*, *Nat. Phys.* **11**, 162 (2015).
7. G. Jotzu *et al.*, *Nature* **515**, 237 (2014).
8. N. Flaschner *et al.*, *Science* **352**, 1091 (2016).
9. R. B. Laughlin, *Phys. Rev. Lett.* **50**, 1395 (1983).

10.1126/science.aar5675

ESCRTs offer repair service

A cellular membrane remodeling machinery repairs damaged organelles

By **Maximiliano G. Gutierrez**¹
and **Jeremy G. Carlton**^{1,2}

Repair or replace? Be it our stereos, our saucepans, or our socks, today's society encourages us to shun the repairman and toss damaged goods. Our cells face similar decisions when dealing with damaged organelles. Although they can be degraded through the process of autophagy, it seems that cells do not always go straight for the bin and instead employ some nifty tricks to stitch damaged organelles back together. On page 49 of this issue, Skowrya *et al.* (7) expose an unexpected role for the endosomal sorting complex required for transport (ESCRT)-III machinery in repairing damaged endolysosomes, which has important consequences for the maintenance of organelle function and cell survival.

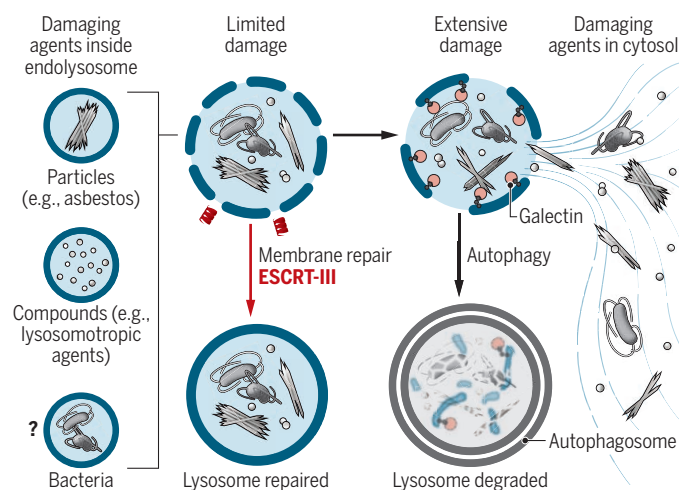
All cells sample their environment by taking in material from the outside world. Internalized content is delivered to endosomes, a series of membrane-bound compartments that sort and process internalized material. Through luminal acidification and the acquisition of proteolytic enzymes, endosomes can mature into endolysosomes to degrade this content and release nutrients into the cell. However, internalized materials can actually damage these organelles: Particulate matter such as uric acid crystals or asbestos fibers can puncture endosomal membranes, lysosomotropic chemicals can polymerize in the endolysosomal lumen and disrupt membranes, and a number of pathogens actively destroy these membranes to access the cytosol. Cells unable to repair damaged endolysosomes can die and trigger inflammation. Thus, maintaining the integrity of these organelles is essential for ensuring cellular viability and limiting tissue damage. Autophagy is an intracellular pathway that degrades and recycles cellular components. In this process,

old or damaged organelles are sealed away from bulk cytoplasm inside newly built autophagosomes. Fusion of autophagosomes with endolysosomes allows proteolytic degradation of the engulfed content.

A variety of multiprotein complexes exist on endosomes to coordinate cargo sorting with membrane remodeling. For degradative sorting, an important process is generating intra-endosomal vesicles into which cargo destined for degradation is incorporated. To effect this, the ESCRT machinery captures these

Maintaining lysosome function

During limited damage, endolysosome membranes can be repaired by ESCRT-III. If damage becomes extensive, then selective autophagy is initiated, resulting in a loss of functional lysosomes.



cargos and soluble ESCRT-III components polymerize into spiral filaments that remodel endosomal membranes to allow intra-endosomal vesicle biogenesis to occur (2).

In a series of live-cell imaging experiments, Skowrya *et al.* showed that ESCRT-III components were rapidly recruited to endolysosomes when cells were treated with lysosomotropic agents. The authors visualized endolysosomal damage and, upon ESCRT-III recruitment, observed repair and recovery of function. However, ESCRT proteins could only repair small holes, whereas larger ruptures triggered autophagic degradation through recruitment of cytosolic galectins (proteins that bind sugars present on the inner leaflet of endosomes that are exposed upon organelle damage). ESCRT-III

recruitment was insensitive to disruption of the autophagy system and occurred more rapidly than galectin recruitment. These data nicely separate the fates of differentially damaged endolysosomes and present ESCRT-III as a repair kit, patching small ruptures before they can expand and compromise function (see the figure). Patched endolysosomes maintained their biochemical activity, saving the cell from investing resources in disposing of them and synthesizing new ones.

Mechanistically, the nature of the recruitment signal that triggers ESCRT-III assembly at damaged endolysosomes awaits identification. Apoptosis-linked gene-2 (ALG-2)-interacting protein X (ALIX) and tumor susceptibility gene 101 (TSG101), both upstream ESCRT components, played redundant roles in recruitment. However, these proteins are typically adaptors, linking ESCRT-III to preexisting localization cues,

and it is not yet clear what stabilizes these factors upon endolysosomal damage. ALG-2, a calcium- and ALIX-binding protein that assists in the recruitment of ESCRT-III to small plasma membrane ruptures (3, 4), was co-recruited to damaged endolysosomes, suggesting that calcium leakage from these organelles could trigger ESCRT-III assembly.

Also unknown is the membrane topology at the site of repair. ESCRT-III usually acts to sever cytoplasm-filled membranous stalks (2), a topology that does not obviously fit the expected geometry of ruptures in single-membraned organelles. During plasma membrane repair, damaged regions being repaired by ESCRT-III were proposed to bud away from the cytoplasm (3). However, in vitro assembly studies (5) and deep-etch microscopy (6) have shown that ESCRT-III filaments can also form planar spiral arrays. One possibility is that these arrays plug the holes and provide a platform to flow membrane in from intact regions. When considering the fate of damaged endolysosomes, it is also not obvious how cells differentiate between small and large ruptures; restriction of the size of an ESCRT-III spiral could provide a simple means to selectively plug small holes with larger holes remaining open to permit galectin-mediated initiation of autophagy. These data suggest that the roles of ESCRT in the degradative pathway are twofold: to sort cargo into this route and to ensure that endolysosomes are competent to degrade these cargos.

¹The Francis Crick Institute, 1 Midland Road, London NW1 1AT, UK. ²School of Cancer and Pharmaceutical Sciences, King's College London, London SE1 1UL, UK. Email: max.g@crick.ac.uk; jeremy.carlton@crick.ac.uk

This study opens many questions regarding the physiological and pathophysiological roles of this pathway. Are lysosomes inherently unstable and in need of continual repair? That the authors observed a gradual depletion of functional lysosomes in ESCRT-silenced cells indicates that this is the case. Upon extensive damage, leakage of endolysosomal contents into the cytosol can trigger lysosomal cell death (7). Thus, the ESCRT-machinery likely plays important housekeeping roles in maintaining organelle number and protecting against this form of cell death.

The findings of Skowrya *et al.* may be relevant for the regulation of the innate immune response. Many internalized pathogens damage phagosomal membranes to gain access to the cytosol. Keeping bacteria in intact phagosomes facilitates their elimination by endolysosomal degradation. In the case of *Salmonella* and *Mycobacteria*, current models implicate membrane influx from fusion with endosomes as well as autophagosomes in maintaining these pathogens in sealed compartments (8, 9). It will be interesting to understand whether ESCRT-III functions alongside these mechanisms to protect cells from infection.

ESCRT-dependent endolysosomal sealing could also be linked to the adaptive immune response. Immune cells such as dendritic cells have evolved mechanisms to activate a tailored immune response by displaying peptides from foreign proteins on their cell surface. If self-proteins found inappropriately in the cytosol are presented as foreign, this will trigger an unwanted autoimmune response. One can imagine how endolysosomal repair could restrict cross-presentation of self-antigens from lysosomal material and inappropriate immune system activation.

Skowrya *et al.* add a new process to the variety of membrane remodeling functions performed by ESCRT-III. As well as showing how resourceful cells are at repurposing existing machineries, the amazing repair mechanisms that cells have evolved to maintain organelle integrity are highlighted. ■

REFERENCES AND NOTES

1. M. L. Skowrya *et al.*, *Science* **360**, eaar5078 (2018).
2. J. Schöneberg *et al.*, *Nat. Rev. Mol. Cell Biol.* **18**, 5 (2017).
3. A. J. Jimenez *et al.*, *Science* **343**, 1247136 (2014).
4. L. L. Scheffer *et al.*, *Nat. Commun.* **5**, 5646 (2014).
5. N. Chiaruttini *et al.*, *Cell* **163**, 866 (2015).
6. P. I. Hanson *et al.*, *J. Cell Biol.* **180**, 389 (2008).
7. S. Aits, M. Jäätelä, *J. Cell Sci.* **126**, 1905 (2013).
8. L. Schnettger *et al.*, *Cell Host Microbe* **21**, 619 (2017).
9. S. Kreibich *et al.*, *Cell Host Microbe* **18**, 527 (2015).

ACKNOWLEDGMENTS

J.G.C. is a Wellcome Trust Senior Research Fellow (206346/Z/17/Z). M.G.G. is supported by the Francis Crick Institute and receives core funding from Cancer Research UK (FC001092), Medical Research Council (FC001092), and Wellcome Trust (FC001092).

10.1126/science.aat2630

BIOCHEMISTRY

Up close with herpesviruses

Two high-resolution structures reveal how ~3000 proteins are arranged in the herpes simplex virus capsid

By Ekaterina E. Heldwein

Viral capsids are marvels of biological engineering. They are sturdy enough to withstand pressure exerted by the tightly packed genomes inside yet can come apart or loosen easily to release the viral genome once the virus penetrates the cell. They are also great examples of genetic economy. Because of the limited coding capacity of viruses, capsids are built by using a few proteins over and over. As a result, capsids are symmetrical. Capsids of many viruses, such as herpesviruses, have icosahedral symmetry, which means nearly spherical soccer ball-like particles with 20 triangular faces and 12 vertices. Reports in

are formed by the major capsid protein VP5; each hexon is also decorated with a hexameric crown composed of small capsid protein VP26. Instead of a 12th penton, there is a portal composed of 12 copies of the protein UL6, which is necessary for DNA packaging.

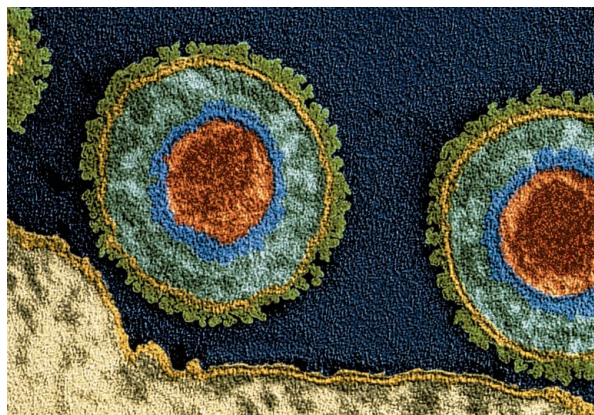
Gluing together these hexons and pentons are 320 triplexes, heterotrimers of two VP23 proteins and one VP19C protein. Each vertex is further decorated with two additional proteins, UL25 and UL17, which are essential for reinforcing the capsids (3) so that they can withstand several atmospheres of pressure generated by the large genomes (4) without bursting apart. UL25 also anchors the tegument layer of the herpesviral particle (5). Tegument, a component specific to herpes-

viruses, consists of multiple copies of several proteins that serve to regulate gene expression, evade the innate immune response, and hijack host trafficking machinery. By bringing these proteins into the cell along with the capsid, the virus can manipulate the cell even before viral genes are expressed.

How do 3000 protein copies build this massive structure, and how are tegument proteins anchored on the capsid? Until very recently, cryogenic-electron microscopy (cryo-EM) reconstructions of herpesvirus capsids were limited to a resolution

of ~7 Å (6), at which helices appear as tubes. At this resolution, it is difficult to identify proteins accurately and impossible to map their interactions precisely. By contrast, capsid reconstructions at a resolution of 3.5 Å would allow side chains of individual amino acids to be seen, and all proteins can be traced from scratch.

Within the past few months, capsid reconstructions of two herpesviruses, Kaposi's sarcoma-associated herpesvirus (KSHV) at 4.2 Å (7) and human cytomegalovirus (HCMV) at 3.9 Å (8), have been published. The HSV reconstructions by Yuan *et al.* and Dai and Zhou now use clever tactics to push the resolution further. Even with state-of-the-art data collection, traditional reconstruction strategies initially yielded only ~4-Å resolu-



A false-colored electron micrograph of HSV-1 virions shows the capsid (orange) coated with tegument (blue and teal) and surrounded by a lipid envelope (yellow).

this issue by Yuan *et al.* on page 48 (1) and Dai and Zhou on page 47 (2) reveal in detail how ~3000 protein copies are arranged in the 130-nm-diameter structure of the herpes simplex virus (HSV) capsid (see the figure).

Herpesviruses are a large family of viruses that collectively infect nearly all species of vertebrates and even invertebrates such as mollusks. Several of these viruses infect humans for life, causing symptoms that range from cold sores and genital lesions to encephalitis and cancers. Herpesvirus capsids consist of 150 hexameric blocks (hexons) and 11 pentameric blocks (pentons). Both blocks

Department of Molecular Biology and Microbiology, Tufts University School of Medicine, Boston, MA 02111, USA.
Email: katya.heldwein@tufts.edu

tion in both cases. One problem is that images need to be corrected for defocus in order to avoid loss of high-resolution information. To overcome this problem, both teams used local rather than uniform defocus correction for different regions of each particle.

Another problem is that because of their large size, herpesvirus capsids deviate from strictly icosahedral symmetry. Thus, standard icosahedral reconstruction strategies limit the resolution by effectively averaging out high-resolution details. Realizing this and modifying reconstruction protocols to loosen the icosahedral symmetry restraints allowed the authors to go beyond the 4-Å limit. Together, the two papers expand the frontiers of knowledge in two complementary ways.

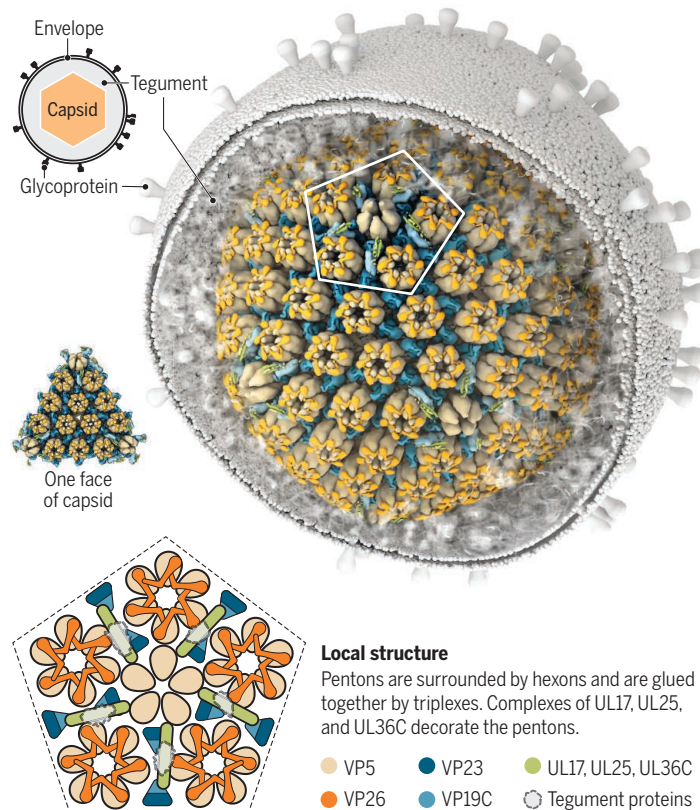
Yuan *et al.* report the reconstruction of HSV-2 B-capsids, purified from the nuclei of infected cells. B-capsids contain scaffold proteins rather than viral genomes and are thought to be either capsid assembly intermediates (9) or dead ends (10). At 3.1 Å—the highest resolution thus far for any large virus—the structure reveals intricate details of the capsid architecture. The authors achieved this in part through use of a new block-based reconstruction method that better accounts for lack of strict icosahedral symmetry.

Dai and Zhou report the 3.5-Å reconstruction of mature, genome-filled capsids (C-capsids) from HSV-1 imaged within whole viral particles (virions) (see the photo and figure). Imaging capsids within virions precludes the loss of UL25, UL17, and the tegument, which often occurs during purification. By visualizing the interface between the capsid and the surrounding tegument layer of the virion, the authors clarified how the tegument layer is anchored on the capsid. Given the many technical challenges associated with cryo-EM imaging of ~210-nm-diameter viral particles, this reconstruction is an impressive accomplishment.

Both reports provide the detailed view of the extensive noncovalent and covalent interactions, particularly the disulfide bonds (17), that stabilize the hexons, the pentons, and the triplexes and glue them together within capsids. This knowledge can now be used to clarify the capsid assembly pathway and de-

Zooming in on virus structure

The HSV capsid is an icosahedron with 20 faces and 12 vertices. Two high-resolution structures show how ~3000 proteins that form pentons, hexons, and triplexes are arranged within the HSV capsid. One structure also shows how the tegument is anchored to the pentons.



sign small-molecule compounds that inhibit viral replication by interrupting capsid assembly, potentially yielding new antivirals.

Another major finding in both reports is that herpesvirus capsid proteins have a great deal of conformational diversity, which means that no protein copies within the asymmetric unit are exactly the same. This is particularly true of VP5. VP5 was expected to adopt one conformation in pentons and a different one in hexons to form optimal interactions in these two different oligomeric structures. However, even within hexons, VP5 adopts different conformations depending on whether its neighbors are pentons or hexons. Such location-specific conformational adaptations ensure optimal interactions yet also result in the final capsid being quasi-symmetrical.

Although the quasi-icosahedral symmetry observed in herpesvirus capsids could be due to their large size, a lack of perfect symmetry has also been observed in viruses with smaller capsids (12). Thus, intrinsic structural flexibility may be an important characteristic of viral capsids.

The two reconstructions share many common features. But whereas Yuan *et al.*'s

reconstruction of purified B-capsids reveals some additional features, likely owing to the higher resolution, Dai and Zhou's reconstruction of C-capsids also reveals the detailed structure of the capsid-associated complex formed by auxiliary capsid proteins UL17 and UL25 and the C terminus of tegument protein UL36. The structure shows that these three proteins form a central five-helix bundle that anchors UL36 to the capsid and allows it to serve as a hub for tegument recruitment. By contributing to this helical bundle, UL36 also helps recruit UL25 and UL17 to the capsid, reinforcing capsid structure. The detailed structure of this complex will enable mechanistic exploration of its multiple roles in viral replication.

Despite the stunning amount of information provided by the two reconstructions, neither study could resolve the distinct portal vertex, which is the DNA gateway into the capsid. Although the reconstructions suggest that B- and C-capsids have similar overall structures, they do not address the question of what structural features

ensure that C-capsids rather than A- and B-capsids mature into viral particles (10). Refining our understanding of morphogenesis will require identification and isolation of additional capsid intermediates. The technological advances that enabled Yuan *et al.* and Dai and Zhou to overcome the challenges of large size, imperfect symmetry, and in situ imaging open doors to further breakthroughs. ■

REFERENCES AND NOTES

1. S. Yuan *et al.*, *Science* **360**, eaao7283 (2018).
2. X. Dai, Z. H. Zhou, *Science* **360**, eaao7298 (2018).
3. U. Sae-Ueng *et al.*, *Nucleic Acids Res.* **42**, 9096 (2015).
4. D. W. Bauer *et al.*, *J. Am. Chem. Soc.* **135**, 12126 (2013).
5. K. E. Coller *et al.*, *J. Virol.* **81**, 11790 (2007).
6. A. Huet *et al.*, *Nat. Struct. Mol. Biol.* **23**, 531 (2016).
7. X. Dai *et al.*, *Nature* **553**, 521 (2018).
8. X. Yu *et al.*, *Science* **356**, 1350 (2017).
9. R. Tandon *et al.*, *Viruses-Basel* **7**, 899 (2015).
10. J. D. Heming *et al.*, *Adv. Anat. Embryol. Cell Biol.* **223**, 119 (2017).
11. R. Szczepaniak *et al.*, *J. Virol.* **85**, 8625 (2011).
12. M. C. Morais, *Proc. Natl. Acad. Sci. U.S.A.* **113**, 11390 (2016).

ACKNOWLEDGMENTS

I thank G. Smith for helpful comments on the manuscript. I acknowledge the funding support of the NIH grant 1R01GM111795, Investigators in Pathogenesis award from Burroughs Wellcome Fund, and the Howard Hughes Medical Institute Faculty Scholar Award.

10.1126/science.aat3990

NEURODEGENERATION

LRRK2 kinase in Parkinson's disease

Defects in vesicular trafficking and immune responses are found in Parkinson's disease

By **Dario R. Alessi¹** and **Esther Sammler^{1,2}**

Despite intensive research, attempts to pause or even just slow the progression of Parkinson's disease (PD) have thus far failed. Although most cases of PD are idiopathic and with largely unknown aetiology, mutations in ~20 genes, including *LRRK2* (leucine-rich repeat kinase 2), cause rare genetic Parkinsonism. All pathogenic mutations in *LRRK2* result in hyperactivation of the LRRK2 kinase, offering the prospect of elaborating disease-modifying treatments. Indeed, LRRK2 inhibitors have entered phase 1 clinical trials. Data are also emerging for LRRK2 involvement in idiopathic PD, suggesting that inhibitors may benefit patients beyond those carrying *LRRK2* mutations. Recent

advances point toward a role for LRRK2 in regulating autophagy, an intracellular process that delivers cytoplasmic constituents to the lysosome for degradation and recycling. LRRK2 phosphorylates a subgroup of RAB proteins and regulates their ability to bind cognate effector proteins. Additionally, LRRK2 is highly expressed in immune cells. Intriguing research indicates that, in early life, increased LRRK2 activity may protect against opportunistic pathogenic infection but then later increases the risk of developing PD, a concept called antagonistic pleiotropy.

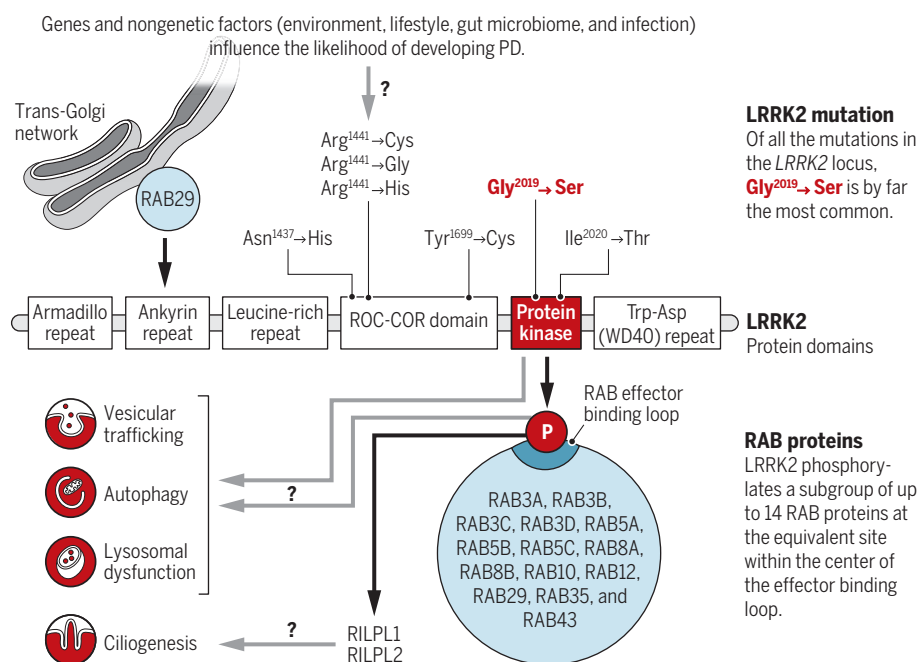
Autosomal dominant missense mutations within the *LRRK2* gene account for 1 to 2% of all cases of PD, and a much higher proportion in some populations (Ashkenazi Jews and North African Berbers) (1).

LRRK2-associated PD closely resembles idiopathic disease in terms of late age of onset, signs, and symptoms (1). The penetrance of *LRRK2* mutations is incomplete and dependent on age and specific mutation. For example, most carriers of the common Gly²⁰¹⁹→Ser (G2019S) mutation may never develop disease (penetrance as low as 24%), whereas the Arg¹⁴⁴¹→Gly (R1441G) mutation appears to be more penetrant (up to 95% in later life) (2, 3). Variations at the *LRRK2* locus also mildly increase the risk for idiopathic PD (1, 3). LRRK2 is a large protein (2527 residues) that, in addition to its kinase domain, possesses a second enzymatic guanosine triphosphatase (GTPase) domain (ROC-COR domain) as well as other motifs (see the figure). The pathogenic mutations cluster within the GTPase (for example, R1441G) as well as kinase (for example, G2019S) domains and stimulate protein kinase activity. The G2019S mutation results in a moderate increase in kinase activity (about twofold). Pathogenic mutations in the GTPase domain enhance GTP binding and stimulate LRRK2 activity to a greater extent than those in the kinase domain (around fourfold) through interactions with the RAB29 protein and the Golgi apparatus (4, 5).

Much research, based on studying localization and verifying consequences of manipulating the expression of wild-type and mutant forms of LRRK2, reveals that it plays a major role in vesicular membranes, as well as autophagy and lysosome function (6). The role of LRRK2 in vesicular membranes could be mediated by the ability of LRRK2 to phosphorylate a subgroup of RAB GTPases, including RAB8A (Thr⁷³) and RAB10 (Thr⁷³), at highly conserved sites located in the center of the effector binding motif (7, 8). RAB proteins are master regulators of membrane trafficking, orchestrating vesicle formation and vesicle movement along actin and tubulin networks, as well as membrane docking and fusion; all important aspects of autophagy and lysosome biology. Consistent with RAB proteins comprising relevant substrates for PD, all the

LRRK2 signaling pathway

Mutations that activate LRRK2 kinase activity are associated with Parkinson's disease (PD). LRRK2 phosphorylates a subgroup of RAB GTPases that regulate various cellular processes, including vesicular trafficking and immune responses. LRRK2 is a possible therapeutic target for PD.



¹Medical Research Council (MRC) Protein Phosphorylation and Ubiquitylation Unit, School of Life Sciences, University of Dundee, Dundee DD1 5EH, UK. ²Department of Neurology, School of Medicine, Dundee, Ninewells Hospital, Dundee DD1 9SY, UK. Email: d.r.alessi@dundee.ac.uk; e.m.sammler@dundee.ac.uk

pathogenic LRRK2 mutants tested enhance RAB phosphorylation in vivo (7, 8).

LRRK2 phosphorylation of RAB8A and RAB10 does not affect GTPase activity but instead prevents binding to well-characterized effectors, including the guanosine diphosphate–dissociation inhibitor and the guanine nucleotide exchange factor rabin-8 (7, 8). This is likely to affect localization and the GTP-loaded state of RAB proteins. Recent work revealed that the poorly studied proteins RAB-interacting lysosomal-like protein 1 (RILPL1) and RILPL2, previously implicated in regulating ciliary membrane content, specifically bind to RAB8A and RAB10 once they have been phosphorylated by LRRK2 (8). Interestingly, pathogenic *LRRK2* mutations inhibit primary cilia formation induced by serum starvation (8), but it remains to be established whether this is mediated through LRRK2-phosphorylated RAB8A–RAB10 interaction with RILPL1 and RILPL2.

There is mounting evidence that disruption of RAB biology and membrane trafficking is involved in PD. Loss-of-function mutations in RAB39B and complex genetic changes within the Parkinson disease 16 (*PARK16*) locus encompassing *RAB29*, as well as mutations in the genes encoding at least three other components of the membrane trafficking machinery [vacuolar protein sorting-associated protein 35 (VPS35), VPS13C, and DnaJ homolog subfamily C member 6] are causally linked to PD (3, 4). Loss-of-function mutations in PTEN-induced putative kinase 1 (PINK1) are associated with young-onset recessive PD. PINK1 indirectly controls the phosphorylation of certain RAB GTPases, including RAB8A, at a site (Ser¹³³) distinct from that of LRRK2-mediated phosphorylation (9). Furthermore, various RAB proteins, including LRRK2 substrates RAB3A and RAB8A, promote vesicular trafficking from the endoplasmic reticulum to the Golgi apparatus and thereby attenuate cytotoxicity linked to aggregated α -synuclein, a factor that is frequently associated with PD (10).

Inflammation plays an important role in the development of PD. LRRK2 is highly expressed in macrophages, monocytes, and neutrophils, suggesting that it functions in the defense against intracellular pathogens. In humans, single-nucleotide polymorphisms within or close to the *LRRK2* gene have been linked to inflammatory conditions, including ulcerative colitis and Crohn's disease, and also increased susceptibility to leprosy infection (11). In mice, LRRK2 is required for mucosal immunity against the opportunist

pathogen *Listeria monocytogenes* and colocalizes with intracellular *Salmonella typhimurium* during bacterial infection in macrophages (12). The LRRK2 kinase is most closely related to the receptor-interacting protein (RIP) kinases, which are key regulators of inflammasomes. Inflammasomes are multiprotein signaling complexes that assemble upon stimulation of the innate immune system by pathogens or toxins and play a crucial role in the inflammatory response and host defense (12). LRRK2 may participate in modulating inflammasome assembly. Mice lacking LRRK2 or treated with an LRRK2 inhibitor exhibit an impaired ability to clear *S. typhimurium* infection (13). By contrast,

“...increased LRRK2 activity may protect against opportunistic pathogenic infection but then later increases the risk of developing PD, a concept called antagonistic pleiotropy.”

mice expressing the kinase-activating G2019S LRRK2 mutant are protected from infection (13). Moreover, in response to *S. typhimurium* infection, LRRK2 interacts with and reportedly phosphorylates the inflammasome protein NLRC4 (NLR family CARD domain-containing protein 4) at a critical residue (Ser⁵³³) required for its assembly into inflammasomes (13). This leads to the activation of caspase 1, which processes and produces a variety of proinflammatory agents such as interleukin-1 β , that if sustained over a long time could lead to neuroinflammation and increased PD susceptibility. Therefore, current understanding suggests that activation of LRRK2 by mutation promotes proinflammatory responses offering protection against infection and survival benefit earlier in life, before PD strikes.

Highly potent, selective, and brain penetrant LRRK2 inhibitors have been reported. Such drugs could benefit not only individuals bearing *LRRK2* mutations but also other patients in whom LRRK2 activity is driving the disease. Much research is taking place to develop tests to interrogate LRRK2 activity and function in patients. This includes studying LRRK2 autophosphorylation and RAB protein phosphorylation in neutrophils, monocytes, and cerebrospinal fluid. Several pharmaceutical companies are in late stages of preclinical evaluation of LRRK2 inhibitors, and one has recently completed a phase 1 clinical trial in healthy volunteers. Studies

in LRRK2-deficient rodents and nonhuman primates treated with LRRK2 inhibitors highlighted potential toxicity concerns in lung and kidney, resulting from loss of LRRK2 kinase activity that might be linked with altered autophagy and lysosome biology (14, 15). Therefore, lung and kidney function will need to be closely monitored in LRRK2 inhibitor clinical trials. Given the challenges of translating findings in immunity from mice to humans, LRRK2 inhibitor clinical trials present an opportunity for refining our understanding of LRRK2 in human immune function. Above all, it will be important to establish whether LRRK2 inhibition increases the risk of opportunistic infections.

LRRK2 lies at the nexus of an emerging signaling network of high relevance for understanding and developing treatments for PD. It will be essential to define in clearer detail the upstream and downstream components of this pathway. Understanding the interplay between LRRK2-mediated immune defense mechanisms and PD will undoubtedly reveal fascinating biology.

Reports of monozygotic *LRRK2* mutation-carrying twins discordant for PD and the incomplete penetrance of *LRRK2* mutations highlight the importance of environment (for example, exposure to toxins, herbicides, pesticides, and fungicides), lifestyle (for example, smoking, exercise, diet), gut microbiome, and infection in the development of LRRK2-dependent PD. It is possible that these factors synergize with genetic mutations. In the future, aligning mechanistic insight into disease pathways with genetics and clinical phenotyping could define the roles that LRRK2 signaling plays in idiopathic PD. This will help justify the use of LRRK2 inhibitors in more patients. However, for now, the most exciting question will be whether LRRK2 inhibitors have disease-modifying effects in PD patients with *LRRK2* mutations. ■

REFERENCES

1. C. Paisán-Ruiz et al., *J. Parkinsons Dis.* **3**, 85 (2013).
2. A. J. Lee et al., *Mov. Disord.* **32**, 1432 (2017).
3. A. Domingo, C. Klein, *Handb. Clin. Neurol.* **147**, 211 (2018).
4. E. Purlyte et al., *EMBO J.* **37**, 1 (2018).
5. Z. Liu et al., *Hum. Mol. Genet.* **27**, 385 (2018).
6. D. A. Roosen, M. R. Cookson, *Mol. Neurodegener.* **11**, 73 (2016).
7. M. Steger et al., *eLife* **5**, e12813 (2016).
8. M. Steger et al., *eLife* **6**, e31012 (2017).
9. Y.-C. Lai et al., *EMBO J.* **34**, 2840 (2015).
10. A. A. Cooper et al., *Science* **313**, 324 (2006).
11. N. L. Dzamko, *Adv. Neurobiol.* **14**, 123 (2017).
12. M. Lamkanfi, V. M. Dixit, *Nature* **548**, 534 (2017).
13. W. Liu et al., *J. Exp. Med.* **214**, 3051 (2017).
14. M. A. S. Baptista et al., *PLOS ONE* **8**, e80705 (2013).
15. R. N. Fujiet al., *Sci. Transl. Med.* **7**, 273ra15 (2015).

10.1126/science.aar5683



POLICY FORUM

EDUCATION

Testing international education assessments

Rankings get headlines, but often mislead

By **Judith D. Singer¹** and **Henry I. Braun²**

News stories on international large-scale education assessments (ILSAs) tend to highlight the performance of the media outlet's home country in comparison with the highest-scoring nations (in recent years, typically located in East Asia). Low (or declining) rankings can be so alarming that policy-makers leap to remedies—often ill-founded—on the basis of what they conclude is the “secret sauce” behind the top performers’ scores. As statisticians studying the methods and policy uses of ILSAs (1), we believe the obsession with rankings—and the inevitable attempts to mimic specific features of the top performing systems—not only misleads, it diverts attention from more constructive uses of ILSA data. We highlight below the perils of drawing strong policy inferences from such highly aggregated data, illustrate benefits of conducting more nuanced analyses of ILSA data both within and across countries, and offer concrete suggestions for improving future ILSAs.

Despite our critiques, ILSAs’ high costs, and policy-makers’ often misguided inferences, we certainly do not believe that ILSAs—such as Programme for International Student Assessment (PISA), Trends in International Mathematics and Science Study (TIMSS), or Progress in International Reading Literacy Study (PIRLS)—should be abandoned. ILSAs provide a unique reference framework for understanding national results and patterns of relationships. As such, they can be invaluable for mobilizing a country’s political will to invest resources in education. ILSA data have also served as the foundation for hundreds of secondary analyses that have addressed important education policy questions. But to fulfill their promise, changes are needed in their interpretation, dissemination, and analysis and in the strategies used to design future assessments.

UNPACKING EAST ASIAN SUCCESSES

In 2012, the seven jurisdictions with the highest mean mathematics PISA scores were Shanghai, Singapore, Hong Kong, Taiwan, South Korea, Macau, and Japan. Before concluding that adopting any feature of East Asian education—such as mastery textbooks, the “solution du jour” recently

adopted by Great Britain (2)—would improve the test scores of students elsewhere, consider the following.

ILSA samples aren’t necessarily representative of a jurisdiction’s relevant age (or grade) group. PISA defines its target population as “15-year-olds enrolled in education institutions full-time.” Until recently, China had an internal passport system in which migrants from the countryside could not enroll in urban schools. In 2014, the Organization for Economic Cooperation and Development (OECD), which sponsors PISA, admitted that the 2012 Shanghai sample excluded 27% of 15-year-olds (in the United States, the comparable statistic was ~11%) (3). Less-developed OECD countries, such as Mexico and Turkey, have similar problems because as many as 40% of their 15-year-olds have already dropped out. The full consequences of these exclusions for country-level means is not known, but it is likely that excluded students come from the lower end of the achievement distribution.

Results from single cities (such as Shanghai), city states (such as Singapore), or countries with national education systems (such as France) aren’t comparable with those from countries with decentralized systems (such as the United States, Canada, and Germany). For decentralized systems, country-level summaries are almost meaningless because they conceal substantial within-country heterogeneity in policies and practices. In 2015, for example, Massachusetts participated in PISA as a separate jurisdiction. Its mean reading score was statistically indistinguishable from those of the top performing East Asian nations; its mean mathematics score was more

¹Harvard University, Cambridge, MA, USA. ²Boston College, Chestnut Hill, MA, USA. Email: judith_singer@harvard.edu

middling, but if the state were treated as a country, it would still have ranked 12th (4).

The number of credible school-based predictors of student test scores always exceeds the number of countries assessed. Even as ILSA coverage expands, most include 50 to 75 countries or jurisdictions. Education experts could suggest 50 to 75 credible predictors of country-level test scores: Mastery textbooks? Teacher training? Teaching methods? Peer effects? With as many plausible predictors as there are countries in any analysis, it's impossible to conclude whether any particular feature of an education system—even one highly correlated with country-level mean test scores—definitively explains differences in student performance.

Test scores are also affected by many factors outside of school, so it's a mistake to treat test scores as unconditionally valid indicators of the quality of an education system. For example, in East Asia, as elsewhere, private tutoring is widespread. Korea is the most prominent example, where approximately half the 2012 PISA participants reported receiving private tutoring, often focused on test preparation. Overall, expenditures on private tutoring added 2.6% of gross domestic product to the government's contribution of 3.5% toward education (5). One plausible interpretation of Korea's and other East Asian jurisdictions' ILSA results is that they are not a result of the public education systems but rather this substantial private investment.

Student motivation to take low-stakes assessments varies across countries. ILSA scores have no consequences for individuals, so students must be motivated to do their best. It's plausible that students from East Asian cultures score higher partially because they're conditioned to perform their best on any test, even a low-stakes ILSA.

Rankings are derived from country-level means, and the corresponding confidence intervals are sufficiently wide that countries with substantially different ranks may be statistically indistinguishable. For example, in PISA 2015, Canada ranked 10th in mathematics, but its 95% confidence interval overlaps with Korea (ranked 7th) and Germany (ranked 16th) (6). Over time, rankings are also affected by which jurisdictions take part in a particular ILSA administration, so that a country's ranking can shift even when its performance remains stable.

Even if no single critique “explains away” the strong performance of students in East Asian countries, this constellation of concerns calls into question any simplistic conclusion based on rankings. Yet as long as ILSA results are primarily reported as league tables, a mix of nationalism, fears about global competitiveness, and human nature inevitably lead policy-makers in

countries with poor or declining performance toward unitary “silver bullet” solutions based on highly aggregated data.

MORE PROMISING NUANCED ANALYSES

We see much more promise in analyses of ILSA data disaggregated to levels below the country, be it by geographic region, province, or state, or by school or student characteristics. The best of these analyses incorporate a second data source now common in ILSAs: background questionnaires filled out by students, parents, teachers, and/or principals.

Jerrim (7), for example, used 2012 PISA data from Australia to probe the East Asian success stories. The subgroup of second-generation immigrants from top-performing East Asian countries had scores comparable with those East Asian countries, despite attending Australian schools that generally had much lower scores. Even acknowledging that immigrants are not a random sample of individuals from the originating country, this analysis suggests that family factors play a substantial role in ILSA test score differences and illustrates insights that come from within-country analyses.

Within-country analyses, of course, do not require ILSA data. The promise of ILSAs comes from comparing within-country analyses across countries. For example, Schmidt and McKnight (8) found that countries that have less curricular coverage of particular topics—for example, the United States does not emphasize physical sciences in curricula before high school—have poorer performance on those topical dimensions of TIMSS than countries whose curriculum covers more of that content (such as Korea). Secondary analyses such as these abound but rarely have the same impact as the initial league tables because these results typically appear long after the data release, sometimes after the next round of ILSA rankings has been released.

Another persistent analytic challenge is the construction of indicators of background characteristics that are equally reliable and valid across countries and cultures. Creating comparable composites—for example, of socioeconomic status (SES)—is even harder. PISA's SES indicator, the International Socio-Economic Index of Occupational Status, faces multiple obstacles, including varying views of parental occupational status (such as the relative status of engineers, doctors, and teachers differs across countries) and whether the items combined (for example, having a desk at home or a cellphone) really tap into a common underlying variable across countries (1).

Despite cross-cultural equivalence challenges, we find three types of cross-country comparisons of within-country analyses especially promising because—even when they

do not yield causal inferences, and they usually do not—they can suggest interesting hypotheses worthy of further study.

Benchmark within-country relationships across culturally similar countries. Consider two illustrative comparisons of 2012 PISA mathematics scores: (i) Hong Kong and Taiwan have very similar means, but the strength of the relationship between students' scores and SES is three times greater in Taiwan than in Hong Kong; and (ii) Canada's mean is 37 points higher than that of the United States, but the relationship between scores and SES is noticeably weaker in Canada than in the United States (9). We believe that benchmarking analyses such as these are more likely than league tables to lead countries with less equitable systems (here, Taiwan and the United States) to experiment with strategies their neighbors have used to improve educational equity.

A focus on the distribution of achievement within countries is needed. Recognizing the limitations of comparing means, ILSA league tables are increasingly supplemented with the percentages of students in each jurisdiction with especially high or low scores. For example, only 9% of U.S. students scored in the top two categories on the 2012 PISA mathematics assessment. By comparison, five OECD countries and six participating jurisdictions had more than double that percentage (9). Although these percentages are imprecise (as we explain above, regarding country-level means), differences of this magnitude suggest that the United States might consider experimenting with different approaches to offer high-achieving students appropriately challenging learning opportunities.

Comparing within-country natural experiments across countries would also be valuable. Natural experiments provide a credible basis for causal inference when researchers can effectively argue that the assignment of individuals to “treatments” is approximately random. Natural experiments that use ILSA data go a step further by assessing—using a common outcome—whether similar treatment effects are found in multiple jurisdictions. Bedard and Dhuey (10), for example, examined the effect of age at kindergarten entry on student achievement. Younger students—in both fourth and eighth grades—scored significantly poorer, on average, than their older peers, across a wide range of countries, demonstrating that despite the hope that differences by age within grade would fade over time, they do persist into adolescence. This suggests the need to study further the long-term effects of school entry policies on student outcomes and, perhaps, experiment with alternative policies (for example, allowing parents to wait another

year before enrolling a child who would otherwise be especially young for his or her grade).

FIVE SUGGESTIONS FOR IMPROVEMENT

ILSAs have improved considerably since the First International Mathematics Study of 1964: The tests are better; cross-cultural equivalence is a recognized, if not fully realized, priority; test administration and scoring methods have been upgraded; and sampling strategies and analytic approaches have been enhanced. But opportunities for improvement remain. We offer five concrete suggestions that we believe are most likely to yield payoffs commensurate with the increased costs associated with each.

ILSA sponsors—OECD for PISA and the Programme for the International Assessment of Adult Competencies (PIAAC), and the International Association for the Evaluation of Educational Achievement (IEA) for TIMSS and PIRLS—should develop communications materials and strategies that de-emphasize rankings. There is no doubt that country rankings (league tables) are a major driver of ILSA-related publicity. All ILSAs have governing boards of representatives from participating countries that play a major role in setting ILSA policies; these boards, if they had the political will, could press sponsors to disseminate results by using strategies that make it easier for the media to do a better job of reporting results and presenting balanced interpretations.

For example, when the U.S. National Center for Education Statistics released data from 2014 PIAAC—the U.S. ranked 13th—they color-coded the graphs to help readers compare the United States to three groups of countries: the seven with means that were significantly higher, the eight with means that were statistically indistinguishable (some higher; some lower), and the six with means that were significantly lower (11). Statistics Canada's comparable PIAAC report presented graphs of country-level means accompanied by 95% confidence intervals and box plots displaying each country's 5th, 25th, 75th, and 95th percentiles; they also displayed the results for Canada as a country and for each of its 10 provinces (12). Individual jurisdictions are particularly well positioned to present data this way because they can use their home country as the focal anchor.

National statistical agencies should facilitate linking their ILSA data to other data sources. Many secondary analyses of ILSA data would benefit from better measures of background characteristics, especially SES. In economically well-developed countries where census data are routinely collected (including most OECD countries), reliable indicators of school and community charac-

teristics collected for other purposes could be linked to ILSA data. These indicators would be more accurate and fine-grained than anything currently available in ILSAs. Countries with national registration systems (such as Norway and Sweden) have even greater opportunities. Sweden's National Agency for Education, for example, linked TIMSS scores to students' school grades, finding a strong positive correlation (13). This lends greater credibility to the validity claims of these low-stakes assessments, at least in Sweden and perhaps in other Scandinavian countries.

Capitalizing on the move to digitally based assessments (DBAs) should be a priority. ILSAs are shifting to computerized administration (as are many national assessments). DBAs will improve administration and data processing and can enhance accuracy through adaptive testing, which tailors successive questions to the current estimate of a student's proficiency level. Log files documenting participant interactions with the assessment can be used to study response patterns and their relationships to student effort and performance (1).

Piloting the addition of longitudinal components to current cross-sectional designs would also be helpful. Learning is about change, not status. To compare student performance and credibly identify its predictors both within and across education systems, longitudinal studies are essential (14). Realizing the benefits of longitudinal data, many countries track their students: some are based on ILSA samples (for example, Denmark and Switzerland have followed PISA participants), whereas others are homegrown (such as the Early Childhood Longitudinal Study in the United States and the National Educational Panel Study in Germany). Although country-specific tests can, in principle, be linked to ILSAs across countries for particular ages or grades, the linkages have been too weak to support cross-country analyses of within-country longitudinal data. Of course, there are some reasonable objections to this suggestion: (i) longitudinal tracking is expensive, (ii) attrition is a major concern, and (iii) it isn't clear that the knowledge gain would be worth the cost. But the only way to address these concerns is to try some pilots and use the experience to better gauge costs against benefits. We believe the move to DBAs may make experimentation with longitudinal extensions feasible and worthwhile.

An alternative that has achieved some success is tracking a particular cohort by drawing (different) random samples of that cohort over time so as to construct "pseudo-panel" data. For example, the PISA cohort of 15-year-olds is contained within the PIAAC population of 20- to 25-year-olds 10 years later. A

related approach is to use a differences-in-differences methodology to make putative causal inferences from such data. The core idea is to relate, at the country level, changes over time in explanatory factors to corresponding changes in test performance.

Findings from ILSA analyses should be used to stimulate randomized field trials (RFTs) that test the effects of specific interventions. This is less about improving ILSAs per se and more about appropriate steps after ILSA analyses suggest potential policy interventions. Of our five suggestions, we believe that this one is most likely to yield improvements in education policy. OECD and IEA have conducted RFTs investigating the effects of various features of ILSA design (such as modes of administration), but to our knowledge, none have suggested that countries use the results of ILSA analyses—that, at best, raise interesting questions—to sponsor RFTs in order to rigorously test the putative causal effects of policies identified through analyses of ILSA data.

Despite their many problems, ILSAs are—and should be—here to stay. They can serve as powerful instruments of change, although the nature and extent of their influence varies by country and over time (15). But to truly fulfill their promise, the ILSA community should begin planning trials and experiments with these and other strategies (1). ■

REFERENCES AND NOTES

1. J. D. Singer, H. I. Braun, N. Chudowsky, *Methods and Policy Uses of International Large-Scale Assessments: Report of a Workshop* (National Academy of Education, 2018).
2. www.gov.uk/government/news/south-asian-method-of-teaching-maths-to-be-rolled-out-in-schools.
3. www.washingtonpost.com/news/answer-sheet/wp/2014/03/20/so-how-overblown-were-no-1-shang-hais-pisa-results/?utm_term=.8a534d0df0a7.
4. www.oecd.org/pisa/PISA-2015-United-States-MA.pdf.
5. H. Park et al., *Ann. Rev. Soc.* **42**, 231 (2016).
6. https://nces.ed.gov/surveys/pisa/pisa2015/pisa-2015highlights_5.asp.
7. J. Jerrim, *Oxford Rev. of Ed.* **41**, 310 (2015).
8. W. H. Schmidt, C. C. McKnight, *Science* **282**, 1830 (1998).
9. OECD, *PISA 2012 Results: Excellence through Equity (Volume II). Giving Every Student the Chance to Succeed* (OECD Publishing, 2013).
10. K. Bedard, E. Dhuey, *Quart. J. Econ.* **121**, 1437 (2006).
11. <https://nces.ed.gov/fastfacts/display.asp?id=69>.
12. www.cmec.ca/Publications/Lists/Publications/Attachments/362/PIAAC_PSE_CMEC_2016_EN.pdf.
13. TIMSS, *TIMSS Advanced och Betygen* (in Swedish) (National Agency for Education, 2017).
14. J. D. Singer, J. B. Willett, *Applied Longitudinal Data Analysis: Modeling Change and Event Occurrence* (Oxford Univ. Press, 2003).
15. J. Ritzen, in *The Role of International Large-Scale Assessments: Perspectives from Technology, Economy, and Educational Research*, M. Von Davier, E. Gonzalez, I. Kirsch, K. Yamamoto, Eds. (Springer, 2013).

ACKNOWLEDGMENTS

The ideas here were stimulated by workshops on the methods and policy uses of international large-scale assessments supported by the Institute of Education Sciences, U.S. Department of Education, through grant R305U150003 to the National Academy of Education. The opinions expressed are those of the authors and do not represent views of the Institute or the U.S. Department of Education. We thank N. Chudowsky and two anonymous referees for helpful comments.

10.1126/science.aar4952



Jane Goodall observes a pair of chimpanzees in Tanzania in 1987.

BOOKS *et al.*

FIELD RESEARCH

Revisiting a tragedy at Gombe

Haunting clues suggest psychological distress preceded a researcher's 1969 death at Goodall's African research center

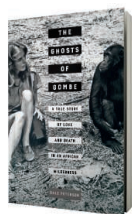
By **Malissa Stark-Rodenburg**

“Every individual matters. Every individual has a role to play. Every individual makes a difference,” wrote Jane Goodall in her 2003 story collection, *With Love*. In his new book, *The Ghosts of Gombe*, Goodall's official biographer, Dale Peterson, captures that same sentiment, examining the individuals who made her research possible and recounting the mysterious death of a woman at the Gombe Stream Research Centre in 1969.

The book follows several young researchers who made their way to the center in the late 1960s under varying personal circumstances. Carole Gale, a 19-year-old American, offered to volunteer at the center while she was studying in Nairobi at the Friends World Institute. Geza Teleki, a 25-year-old Hungarian anthropology graduate student at Penn State, arrived in Africa hoping to study under the Kenyan paleoanthropologist Louis Leakey. Through a series of misunderstandings, he found himself spending time with Goodall, who arranged for him to work at Gombe. Ruth Davis, age 25, was working as

a typist in the United States after graduating from George Washington University, when Teleki (with whom she had had a romantic relationship) encouraged her to take a job that he arranged for her.

When they arrived, the methods used to study chimps were still very similar to those pioneered by Goodall in the early 1960s. (Goodall was living in Ngorongoro during this period but still visited the camp a few times each year.) Chimps were lured into camp with bananas, where scientists diligently recorded everything they observed. Their notes were typed up later and entered into what was known as the “A-record.”



The Ghosts of Gombe
A True Story of Love
and Death in an
African Wilderness
Dale Peterson
University of California
Press, 2018. 232 pp.

It was Teleki, Gale, and Davis who persuaded Goodall to let them follow the chimps into the forest and observe them in their natural environment. (Data collected from such expeditions were recorded in the “B-record.”)

“The A-record observations in camp were based on watching chimps act on an artificial, human-created stage in front of a human audience,” observes Peterson. “Everyone who did the B-record follows ... recognized that in leaving the human stage and the human audience, they were entering the chimpanzee world and beginning to consider or imagine what it might be like to be an ape, a nonhuman ape, in an ape's world.”

A wealth of new behaviors were revealed during these expeditions, including the process by which chimpanzees overthrow a leader, as well as actions the researchers likened to acts of warfare. Teleki, Gale, and Davis bonded over their observations during the evenings, sharing the conflicted emotions they felt about their work—loving the chimps, on the one hand, while trying to remain objective scientific observers, on the other.

On 12 July 1969, Davis set out on a B-record follow and never returned. She was found dead at the base of a waterfall 6 days later. Was it an accident? Was she pushed? Did she jump?

At this point in the story, Peterson shifts focus from the chimps to the relationships between the researchers. Thoroughly, he scrutinizes letters Davis sent to her parents and to Teleki (who had returned to America by then). He analyzes the audio records she made on her final outing and collects personal accounts from her peers, which reveal that she had become withdrawn from the group in the months before her death.

“Such interior tectonics took place in a situational context: of isolation and intensity,” writes Peterson in an attempt to explain the emotions that can arise during remote field work. But how does an experienced young explorer end up dead at the base of a waterfall?

Peterson ultimately concludes that Davis's fall was neither a straightforward accident nor a suicide, although he does point to her mental state as a factor in her death. “Ruth's failure to find an intimate connection within that tiny human community was compensated for in part by her success in knowing the chimps and her sense of discovering an intimate belonging with them,” he writes. She believed that she was capable of traversing the same treacherous paths that they traveled, he speculates—an error that she paid for with her life.

It's challenging to put together a complete picture so long after the events, but Peterson uses letters, camp records, and personal accounts to tell the story artfully. He relays information from his interviewees warily, knowing how memory works, especially when it comes to emotional experiences.

Jane Goodall has spent a lifetime trying to understand the behaviors and relationships of the apes in Tanzania. With *The Ghosts of Gombe*, Dale Peterson has attempted to do the same for the people who made her research possible. It is the similarities between these two endeavors that make his book a worthwhile read. ■

The reviewer is a freelance science writer based in Denver, CO, USA. Email: mrodenb1@jhu.edu

10.1126/science.aas9266

SCIENCE FICTION

2001, 50 years later

A new book celebrates the making of the iconic space odyssey and its enigmatic director

By J. P. Telotte

Fifty years after its appearance, *2001: A Space Odyssey* remains a film that commands attention. This is partly because of its status as the most influential science fiction movie ever made; partly because of the ever-growing reputation of its director, Stanley Kubrick; and partly because it has always been a work that confounds easy interpretation—and so readily opens itself to multiple interpretations.

Michael Benson's *Space Odyssey*, an epic-like account of the film's planning, making,

of the genre, tellingly titled "The Imagination of Disaster."

Benson recounts how Kubrick sought to stake out a different path for the genre. He cites the director's first letter to noted British science fiction writer Arthur C. Clarke, wherein Kubrick declared that he wanted to do "the proverbial 'really good' science fiction movie" and wanted Clarke as a collaborator. This path would steer clear of what Kubrick's wife Christiane termed "little green men stuff," while seeking inspiration in Homer, his *Odyssey*, and the "archetypal workings of human mythological yearnings."



Stanley Kubrick (right) gives direction to actor Gary Lockwood on the set of *2001: A Space Odyssey*.

and reception, will hardly answer all of the questions that haunt it, but his thoroughly researched, multivoiced narrative should become essential reading for anyone wanting to penetrate the mysteries that continue to swirl around this work and its creator.

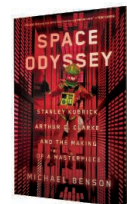
Before *2001*, the science fiction film had largely been a form modeled on pulp science fiction. Such films usually featured adventuring in outer space, alien invasion, or monstrous encounters. Just 2 years before its release in 1968, the writer and filmmaker Susan Sontag published her influential—and largely dismissive—overview

Benson provides a detailed account of how this ambitious aim was accompanied by prodigious preproduction research, attention to accuracy in the smallest details, and advice from top experts in various fields. In addition to Clarke, Kubrick sought the assistance of special effects figures Con Pederson and Douglas Trumbull, space flight consultant Frederick Ordway, actor/choreographer Dan Richter, production designer Tony Masters, cinematographer Geoffrey Unsworth, and many others, all of whom participated in what Benson terms "a kind of extended collective improvisation."

While emphasizing this "collective" product, Benson never loses sight of Kubrick's orchestrating hand—or mind. He emphasizes others' impressions of the director, as when

Space Odyssey
Stanley Kubrick, Arthur C. Clarke, and the Making of a Masterpiece

Michael Benson
Simon & Schuster,
2018. 525 pp.



publicist Roger Caras declared him "a genius," when Clarke called him "perhaps the most intelligent person I've ever met," and when cinematographer John Alcott suggested that, if he hadn't been a director, he would have been "the greatest lighting cameraman in the world." The image that emerges is of a person who could bring together great talent, who encouraged a "creative ferment," but who also exercised great control over his films.

As Clarke and Kubrick brainstormed about the general format and specific plot details of *2001*, and Clarke worked on a novelization originally intended to help sell the project to a studio and later to publicize the forthcoming film, Benson reveals that the cast and crew "never had a finished script," that there was no agreed-upon ending, and that major elements of the film changed from day to day.

Those changes were both big and small and reflected a constant sharpening of Kubrick's ideas. As his conception of his astronauts' electronic assistant changed from robot to computer and from guardian to flawed killer, a new view of humanity's relationship to electronic intelligence emerged. And as Kubrick sought an image sufficiently evocative of alien presence, the mysterious monolith that instigates *2001*'s journey changed from a crystal pyramid to a black slab, which he felt was easier to work with, while still being suggestive of the unknown.

Kubrick's original plans to use a voice-over narration for various parts of the film—exposition laboriously crafted by Clarke—also changed dramatically over time. *2001* ultimately became a "largely nonverbal work" that depended on mysterious and evocative images for much of its impact.

While Benson's *Space Odyssey* is hardly a gloss on those haunting images, nor a full accounting of the film's impact or Kubrick's directorial manner, it is a compelling point of access for those who want to further explore the mysteries of this film and its gifted director. A rigorously researched effort, the book gives voice to many of those involved in *2001*'s making, a number of whom expressed that the experience changed their lives. Without trying to be a biography, it also grants us much insight into the enigmatic director of one of the most compelling science fiction visions in the history of the cinema. ■

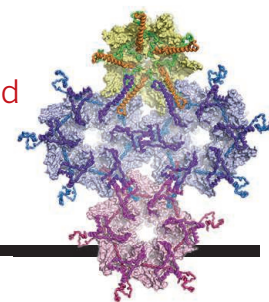
The reviewer is on the faculty of the School of Literature, Media, and Communication, Georgia Institute of Technology, Atlanta, GA 30332, USA. Email: jay.telotte@lmc.gatech.edu

10.1126/science.aat1489

RESEARCH

Herpesvirus capsid in high resolution

Yuan et al., p. 48



IN SCIENCE JOURNALS

Edited by **Stella Hurtley**



EVOLUTIONARY BIOLOGY

On the evolution of baleen whales

Baleen whales include the largest animals that have ever lived, but their evolutionary history has been difficult to decipher because of conflicting evidence from genes and morphology. Árnason *et al.* conducted whole-genome sequencing of the blue whale and five other baleen species to reconstruct their evolutionary history in detail. All existing species originated within the past 10 million years as global climates progressively cooled toward the poles. Taxonomic relationships are complicated by evidence of gene flow and hybridization among species facilitated by the absence of geographic barriers. Speciation occurred within an interwoven network of co-occurring lineages, rather than the classical Darwinian pattern of bifurcating trees that is characteristic of most animals. —JJ

Sci. Adv. 10.1126/sciadv.aap9873 (2018).

Gene flow among baleen whales is complex.

EMERGING INFECTIONS

Postnatal perturbation by Zika virus

Much of the concern surrounding Zika virus infections focuses on fetuses infected in utero. Mavigner *et al.* reasoned that this neurotropic virus may have deleterious effects even after birth. They found that infant rhesus macaques infected with Zika

virus had peripheral and central nervous system pathology. The infected animals had structural and functional brain abnormalities and altered emotional responses. These differences persisted months after the virus had been cleared. Thus, infants and young children exposed to Zika virus should perhaps undergo more than just routine monitoring. —LP

Sci. Transl. Med. 10, eaao6975 (2018).

SOLAR CELLS

Light relaxes hybrid perovskites

Ion migration in organic-inorganic perovskite solar cells limits device stability and performance. Tsai *et al.* found that a cesium-doped lead triiodide perovskite with mixed organic cations underwent a uniform lattice expansion after 180 min

of exposure at 1 sun of illumination. This structural change reduced the energy barriers for charge carriers at the contacts of solar cells. The resulting increase in power conversion efficiency from 18.5 to 20.5% was maintained for more than 1500 hours of illumination.

—PDS

Science, this issue p. 67

STEM CELLS

Signaling hematopoietic stem cells from afar

Throughout our entire life span, hematopoietic stem cells (HSCs) generate all of our blood cells. The bone marrow microenvironment, or niche, is key to activating stem cell activity. Decker *et al.* now show that thrombopoietin generated in the liver, but not from the local bone marrow niche, maintains HSCs in vivo in mice. Thus, systemic endocrine factors are needed to maintain somatic stem cells from a distance. These findings may be important when considering how to stimulate HSCs for therapeutic use. —BAP

Science, this issue p. 106

TOPOLOGICAL MATTER

Beyond fractional quantum Hall

Unlike most electronic topological phenomena, the fractional quantum Hall effect requires correlations among electrons. Spanton *et al.* describe a class of related but even more unusual states, the fractional Chern insulators (see the Perspective by Repellin and Regnault). They observed these states in

samples of bilayer graphene, where one of the graphene layers was misaligned by a small angle with respect to an adjoining layer of hexagonal boron nitride. The misalignment created a superlattice potential and topologically nontrivial bands, which had a fractional filling, thanks to strong electronic interactions. The findings expand the class of correlated topological states, which have been predicted to harbor exotic excitations. —JS

Science, this issue p. 62;
see also p. 31

MOLECULAR BIOLOGY

Live imaging of DNA loop extrusion

To spatially organize chromosomes, ring-shaped protein complexes including condensin and cohesin have been hypothesized to extrude DNA loops. Condensin has been shown to exhibit a DNA-translocating motor function, but extrusion has not been observed directly. Using single-molecule imaging, Ganji *et al.* visualized in real time a condensin-mediated, adenosine triphosphate-dependent, fast DNA loop extrusion process. Loop extrusion occurred asymmetrically, with condensin reeling in only one end of the DNA. These data provide unambiguous evidence of a loop extrusion mechanism for chromosome organization. —SYM

Science, this issue p. 102

ANCIENT GENOMES

Revisiting the origins of modern horses

The domestication of horses was very important in the history of humankind. However, the ancestry of modern horses and the location and timing of their emergence remain unclear. Gaunitz *et al.* generated 42 ancient-horse genomes. Their source samples included the Botai archaeological site in Central

Asia, considered to include the earliest domesticated horses. Unexpectedly, Botai horses were the ancestors not of modern domestic horses, but rather of modern Przewalski's horses. Thus, in contrast to current thinking on horse domestication, modern horses may have been domesticated in other, more Western, centers of origin. —LMZ

Science, this issue p. 111

NEUROSCIENCE

A small molecule for stroke therapy

Better therapies for motor impairments after stroke are greatly needed. In mice and nonhuman primates, Abe *et al.* found that edonergic maleate enhanced synaptic plasticity and functional recovery after a traumatic insult to the brain (see the Perspective by Rumpel). This recovery of motor function was accompanied by functional reorganization of the cortex. —PRS

Science, this issue p. 50;
see also p. 30

NITROGEN CYCLE

Freed from a rocky embrace

Nitrogen availability is a central controller of terrestrial plant growth and, thereby, of the carbon cycle and global climate change. It has been widely assumed that the atmosphere is the main source of terrestrial nitrogen input. Surprisingly, Houlton *et al.* now show that bedrock is just as large a nitrogen source across major sectors of the global terrestrial environment. They used three diverse and largely independent assessments of the nitrogen mobility and reactivity of rocks in the surface environment. These approaches yielded convergent estimates pointing to the equal importance of the atmosphere and bedrock as nitrogen sources. —HJS

Science, this issue p. 58

IN OTHER JOURNALS

Edited by **Caroline Ash**
and **Jesse Smith**

PLANT SCIENCE

Specializations for alpine living

Alpine plants called saxifrages have distinctive features that allow them to survive subzero temperatures and desiccating conditions. These plants' leaves are small, spiny, and succulent, and they ooze material from hydathode glands around their perimeter that forms a shiny crust on the leaf surface. Wightman *et al.* show that *Saxifraga scardica* from the Balkans also has a distinctive transparent leaf margin that apparently deflects incident light into inner, photosynthetic layers of the leaf. Such anatomy may be an adaptation to the diminished light environments in craggy alpine topography. Raman spectroscopy revealed that different saxifrage species secrete different combinations of materials. *S. scardica* secretions are composed of calcite and vaterite. The latter is a metastable calcium carbonate polymorph that is rare in nature and has features that might make it useful as a drug-delivery vehicle. —PJH

Flora 10.1016/j.flora.2018.02.006 (2018).

Transparent leaf margins channel
light into saxifrage leaves.



METABOLISM

Refining diabetes into five types

Diabetes has traditionally been classified as either type 1 or type 2. Ahlqvist *et al.* analyzed nearly 15,000 Scandinavian patients to refine the conventional diabetes classification system. Using six biological parameters and phenotype-based

clustering, the researchers found that patients were stratified into five subgroups. These subgroups differed in genetic associations, disease progression, and medical outcomes. For example, individuals in the insulin-deficient subgroup were more susceptible to developing retinopathy. In contrast, the patients who were most resistant to insulin were more prone

Aging muscle
doesn't waste away in
active individuals.



AGING

Aging muscle: Use it or lose it

It is perhaps not muscle that disappears as we age, but our preference and capacity for exercise. Pollock *et al.* examined the vastus lateralis muscle (part of the quadriceps) in a set of about a hundred 55- to 79-year-olds who cycled more than 100 miles a week. They analyzed muscle fiber type, fiber size, adenosine triphosphatase activity, capillary density, and abundance of mitochondrial proteins. The one measured parameter that showed a statistically significant change with age was a decrease in capillary density. Thus, in this cohort of recreational distance cyclists, where sedentary behavior was taken out of the mix, there was little deterioration of muscle caused by inherent aging processes.

—LBR

Aging Cell 10.1111/ace.12735 (2018).

to developing diabetic kidney disease than other subgroups. Updating the diabetes classification may help predict and assist those patients at greatest risk for complications and improve personalized care. —PNK

Lancet Diabetes Endocrinol. 10.1016/S2213-8587(18)30051-2 (2018).

CANCER

Tumor-agnostic therapy gets on TRK

In precision oncology, treatment is tailored to match the specific mutations that drive tumor growth. To date, this targeted approach has emphasized highly recurrent mutations specific to certain tumor types—for example, the BRAF mutations that occur in about 40% of melanomas. This paradigm of tumor type-specific therapy is changing, however, with the recognition that diverse tumor types can share the same low-frequency mutations. Recent clinical work illustrates the promise of “tumor-agnostic” targeted therapy. Drilon *et al.* studied 55 patients with 17

distinct tumor types that harbored rare chromosomal fusions involving tropomyosin receptor kinase (TRK) genes. They found that larotrectinib, a TRK inhibitor, produced durable responses in about 70% of the patients, regardless of their tumor's tissue of origin. —PAK

New Engl. J. Med. 378, 731 (2018).

MATERIALS SCIENCE

A revealing view of oxides

Oxide layers provide a protective barrier coating for underlying metals, although, if damaged, they can accelerate underlying degradation such as corrosion in pitted areas or intergranular cracking. However, oxide layers often do not flow the same way as the underlying metal when stressed. Yang *et al.* used electron microscopy in an oxygen environment to probe the deformation of aluminum, a tricky problem because of the speed at which alumina forms. As two welded tips were pulled apart, the alumina showed liquid-like flow behavior that could match the movement of the underlying aluminum. At high deformation rates, where

fresh aluminum was exposed, the authors observed self-healing of the coating through the seamless coalescence of new oxide islands. —MSL

Nano Lett. 10.1021/acs.nanolett.8b00068 (2018).

EDUCATION

A balance between content and process

Process of science (POS) skills, such as communication, experimental design, and data analysis, are critical components of STEM (science, technology, engineering, and math) curricula. Balanced with teaching content, how much time should be spent on teaching POS, and which POS skills should be prioritized? Addis and Powell-Coffman surveyed faculty and students across six science disciplines on time allotted to POS and which POS skills were most important. Whereas students approved of time spent on POS, faculty found this same amount of time to be insufficient. Students and faculty agreed that the POS skills of problem-solving, critical

thinking, and communication were important but disagreed about several others, suggesting a disconnect in the way that these two groups define specific POS skills. Findings from this study will help inform future curriculum development. —MMC

J. Coll. Sci. Teach. 47, 72 (2018).

PEROVSKITE MATERIALS

Layers for red luminescence

Two-dimensional organic-inorganic perovskites differ from their three-dimensional counterparts by having a quantum well structure that can alter their luminescent properties. Typically, these materials are formed by replacing A-site cations such as cesium with larger organic cations. Nazarenko *et al.* found that lead halide with two smaller cations, formamide (FA) and guanidinium (G)—FAGPbI₄—exhibited red photoluminescence at room temperature and was stable up to 255°C. The material is also photoconductive. —PDS

J. Am. Chem. Soc. 10.1021/jacs.8b00194 (2018).

ALSO IN SCIENCE JOURNALS

Edited by Stella Hurtley

STRUCTURAL BIOLOGY

Focusing in on herpesvirus

The herpesvirus family includes herpes simplex virus type 1 (HSV-1), which causes cold sores, and type 2 (HSV-2), which causes genital herpes. Herpesviruses comprise a large DNA genome enclosed in a large and complex protein cage called a capsid (see the Perspective by Heldwein). Dai and Zhou used electron microscopy to determine a high-resolution structure of the HSV-1 capsid bound to the tegument proteins that occupy the space between the capsid and the nuclear envelope. The structure suggests how these components may play a role in viral transport. Yuan *et al.* describe a higher-resolution structure of an HSV-2 capsid, providing insight into how the shell assembles and is stabilized. —VV

Science, this issue p. 47, p. 48; see also p. 34

CELL BIOLOGY

A quick fix for leaky endosomes

Cells internalize diverse material through various forms of endocytosis into an extensive endolysosomal network. Protecting the integrity of endolysosomal membranes in both physiological and pathophysiological contexts is critical to cell health. Skowrya *et al.* describe a role for the ESCRT (endosomal sorting complex required for transport) machinery on endolysosomal organelles during membrane repair (see the Perspective by Gutierrez and Carlton). The ESCRTs act as first responders to repair limited membrane damage and thereby restore compartmental integrity and function. This ESCRT activity is distinct from organelle disposal pathways. These findings will be important in understanding cellular

responses to invading pathogens and potentially disruptive proinflammatory particulates. —SMH

Science, this issue p. 49; see also p. 33

BIOCATALYSIS

Double rings made with heme

Cyclic organic structures with adjacent three-carbon rings—bicyclobutanes—are useful starting materials for chemical and materials synthesis owing to their extreme ring strain. Constructing these molecules is a challenging task for organic chemists, especially if a single stereoisomer is desired. Chen *et al.* engineered a heme-containing enzyme to catalyze sequential carbene insertion reactions using an alkyne substrate. Starting with an enzyme that could only catalyze a single carbene insertion, a series of mutations led to variants that catalyzed efficient, stereoselective production of bicyclobutanes. By using a less reactive alkyne substrate and screening more variants with active site mutations, the authors found enzymes that stop at either enantiomer of the intermediate cyclopropene. —MAF

Science, this issue p. 71

ORGANIC CHEMISTRY

A sulfur matchmaker for fluorine coupling

Fluorination is a burgeoning technique for fine-tuning the properties of pharmaceutical compounds. Unfortunately, the cross-coupling reactions widely used to make carbon-carbon bonds in drug research can be tripped up by fluorine substituents. Merchant *et al.* report a class of easily prepared, solid sulfone compounds that engage in nickel-catalyzed coupling of their fluoroalkyl groups with aryl zinc reagents. These sulfones

considerably simplify the synthetic routes to fluorinated analogs that would previously have required multistep strategies focused strictly on the fluorination protocol. —JSY

Science, this issue p. 75

NEURODEVELOPMENT

Embryonic hints of adult diversity

The adult brain contains dozens of different types of interneurons that control and refine neuronal circuits. Mi *et al.* used single-cell transcriptomics to investigate when these subtypes emerge during interneuron development in the mouse. Transcriptomes of embryonic interneurons showed similarities to adult classes of differentiated interneurons, thus dividing the immature embryonic interneurons themselves into classes. Nearly a dozen classes of embryonic neurons could be identified soon after their last mitosis by transcriptomic similarity with known classes of adult cortical interneurons. Thus, the fate of embryonic interneurons can be read in their transcriptomes well before the neurons migrate and reach their final sites of differentiation and circuit integration. —PJH

Science, this issue p. 81

PALEOANTHROPOLOGY

The Middle Stone Age in Africa

The Olorgesailie basin in the southern Kenya rift valley contains sediments dating back to 1.2 million years ago, preserving a long archaeological record of human activity and environmental conditions. Three papers present the oldest East African evidence of the Middle Stone Age (MSA) and elucidate the system of technology and behavior associated with the origin of *Homo sapiens*. Potts

et al. present evidence for the demise of Acheulean technology that preceded the MSA and describe variations in late Acheulean hominin behavior that anticipate MSA characteristics. The transition to the MSA was accompanied by turnover of large mammals and large-scale landscape change. Brooks *et al.* establish that ~320,000 to 305,000 years ago, the populations in eastern Africa underwent a technological shift upon procurement of distantly sourced obsidian for toolmaking, indicating the early development of social exchange. Deino *et al.* provide the chronological underpinning for these discoveries. —AMS

Science, this issue p. 86, p. 90, p. 95

STEM CELLS

Staging quiescent cells

Tissue-specific stem cells either divide or wait in a quiescent state until needed by the body. Quiescent stem cells have been thought to reside in the G₀ stage before activating to reenter the cell cycle. However, Otsuki and Brand now show that most quiescent stem cells in the *Drosophila* brain are arrested in G₂. Cells in the two phases display differences; for example, G₂ stem cells awaken more quickly than G₀ stem cells, with the conserved pseudokinase Tribbles playing a regulatory role. Elucidating the different pathways and mechanisms underlying quiescence could help to inform regenerative drug design. —BAP

Science, this issue p. 99

POLLUTION

Microplastics everywhere

Over the past decade and a half, numerous studies have shown that marine environments are contaminated with small pieces of plastic (microplastics) that are finding their way into sea salt

and seafood. In a Perspective, Rochman highlights recent work into microplastic pollution of freshwater and land environments. Microplastic contamination is just as ubiquitous in these environments as in the ocean, yet knowledge is much more limited. Research on freshwater and land contamination with microplastics will be crucial for understanding the sources and transport of microplastics to the sea, as well as for elucidating the distinct processes and impacts in these environments themselves. —JFU

Science, this issue p. 28

NEURODEGENERATION

A target in Parkinson's disease?

The kinase LRRK2 is activated by mutation in a subset of patients with Parkinson's disease, making it a possible therapeutic target. In a Perspective, Alessi and Sammler discuss the possible mechanisms leading to Parkinson's disease in patients with LRRK2 activation. In particular, the authors describe the role of LRRK2 in regulating diverse RAB guanosine triphosphatases, which are important in intracellular vesicular transport. Furthermore, the role of LRRK2 in inflammation is discussed as a possible common pathogenic mechanism in Parkinson's disease. —GKA

Science, this issue p. 36

NEUROSCIENCE

From Nogo to go

Recovery of motor function after spinal cord injury is limited by multiple inhibitors of axonal regeneration, such as the myelin-associated protein Nogo. Sekine *et al.* found that ORL1, a receptor for the opioid peptide nociceptin, also blocked axonal regeneration through mechanisms that partially depended on the Nogo receptor NgR1. In mice, an ORL1 antagonist improved motor function recovery and axonal regeneration after spinal cord injury. These effects were

accentuated in *Ngr1*-deficient mice, suggesting a possible clinical benefit to using a combination of ORL1 and NgR1 blockers to treat spinal cord injury. —WW

Sci. Signal. **11**, eaao4180 (2018).

RESEARCH ARTICLE SUMMARY

STRUCTURAL BIOLOGY

Structure of the herpes simplex virus 1 capsid with associated tegument protein complexes

Xinghong Dai and Z. Hong Zhou*

INTRODUCTION: Since Hippocrates first described the cutaneous spreading of herpes simplex lesions, many other diseases—chickenpox, infectious mononucleosis, nasopharyngeal carcinoma, and Kaposi's sarcoma—have been found to be associated with the nine known human herpesviruses. Among them, herpes simplex virus type 1 (HSV-1, causes cold sores), type 2 (HSV-2, causes genital herpes), and varicella-zoster virus (causes chickenpox and shingles)—which all belong to the α -herpesvirus subfamily—can establish lifelong latent infection within our peripheral nervous system.

Structure of the HSV-1 capsid with capsid-associated tegument proteins.

Surface view of a 4.2-Å resolution map of the icosahedral capsid, with a single facet shown in color. The structure of the vertex region (magnified view) was improved to 3.5-Å resolution by subparticle refinement. P, peripentonal; C, center; E, edge; Ta to Te, heterotrimeric triplexes composed of Tri1, Tri2A, and Tri2B.

RATIONALE: A prominent feature of these neurotropic viruses is the long-range (up to tens of centimeters) axonal retrograde transport of the DNA-containing viral capsid from nerve endings at sites of infection (such as the lips) to neuronal cell bodies at the ganglia to establish latency or, upon reactivation, anterograde transport of the progeny viral particles from the ganglia to nerve terminals, resulting in reinfection of the dermis. Capsid-associated tegument complexes (CATCs) have been demonstrated to be involved in this cytoskeleton-dependent capsid transport. Because of the large

size (~1300 Å) of HSV-1 particles, it has been difficult to obtain atomic structures of the HSV-1 capsid and CATC; consequently, the structural bases underlying α -herpesviruses' remarkable capability of long-range neuronal transport and many other aspects of its life cycle are poorly understood.

RESULTS: By using cryo-electron microscopy, we obtained an atomic model of the HSV-1 capsid with CATC, comprising multiple conformers of the capsid proteins VP5, VP19c, VP23, and VP26 and tegument proteins pUL17, pUL25, and pUL36. Crowning every capsid vertex

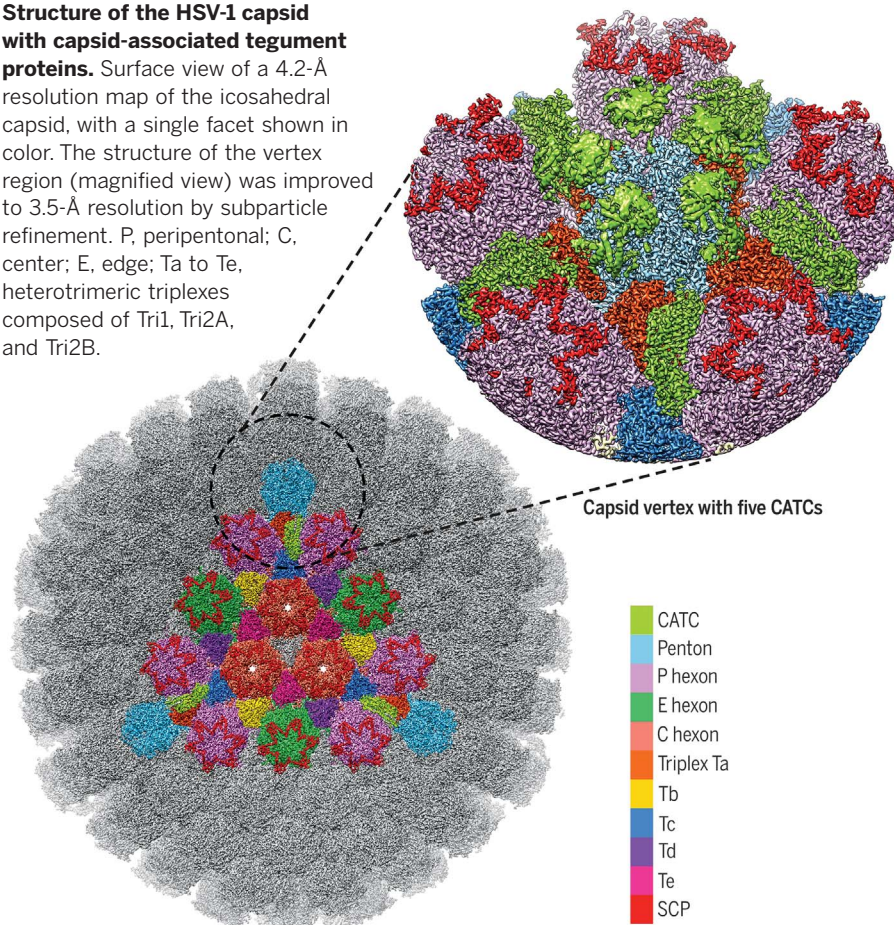
are five copies of heteropentameric CATC. The pUL17 monomer in each CATC bridges over triplexes Ta and Tc on the capsid surface and supports a coiled-coil helix bundle of a pUL25

dimer and a pUL36 dimer, thus positioning their flexible domains for potential involvement in nuclear egress and axonal transport of the capsid. The single C-terminal helix of pUL36 resolved in the CATC links the capsid to the outer tegument and envelope: As the largest tegument protein in all herpesviruses and essential for virion formation, pUL36 has been shown to interact extensively with other tegument proteins, which in turn interact with envelope glycoproteins. Architectural similarities between herpesvirus triplex proteins and auxiliary cementing protein gpD in bacteriophage λ , in addition to the bacteriophage HK97 gp5-like folds in their major capsid proteins and structural similarities in their DNA packaging and delivery apparatuses, indicate that the commonality between bacteriophages and herpesviruses extends to their auxiliary components. Notwithstanding this broad evolutionary conservation, comparison of HSV-1 capsid proteins with those of other herpesviruses revealed extraordinary structural diversities in the forms of domain insertion and conformation polymorphism, not only for tegument interactions but also for DNA encapsulation.

CONCLUSION: Our structure of the HSV-1 capsid with capsid-associated tegument proteins provides mechanistic insights into multiple aspects of the viral life cycle, including capsid assembly, nuclear egress, acquisition of tegument and envelope, and axonal transport in neuronal cells. The numerous molecular interactions and atomic details embodied in the structure make it a much-sought-after atlas for the search of antivirals targeting these critical steps of HSV-1 lytic replication. ■

The list of author affiliations is available in the full article online.

*Corresponding author. Email: hong.zhou@ucla.edu
Cite this article as X. Dai and Z. H. Zhou, *Science* 360, eaao7298 (2018). DOI: 10.1126/science.aao7298



RESEARCH ARTICLE

STRUCTURAL BIOLOGY

Structure of the herpes simplex virus 1 capsid with associated tegument protein complexes

Xinghong Dai^{1,2} and Z. Hong Zhou^{1,2*}

Herpes simplex viruses (HSVs) rely on capsid-associated tegument complex (CATC) for long-range axonal transport of their genome-containing capsids between sites of infection and neuronal cell bodies. Here we report cryo-electron microscopy structures of the HSV-1 capsid with CATC up to 3.5-angstrom resolution and atomic models of multiple conformers of capsid proteins VP5, VP19c, VP23, and VP26 and tegument proteins pUL17, pUL25, and pUL36. Crowning every capsid vertex are five copies of heteropentameric CATC, each containing a pUL17 monomer supporting the coiled-coil helix bundle of a pUL25 dimer and a pUL36 dimer, thus positioning their flexible domains for potential involvement in nuclear capsid egress and axonal capsid transport. Notwithstanding newly discovered fold conservation between triplex proteins and bacteriophage λ protein gpD and the previously recognized bacteriophage HK97 gp5-like fold in VP5, HSV-1 capsid proteins exhibit extraordinary diversity in forms of domain insertion and conformational polymorphism, not only for interactions with tegument proteins but also for encapsulation of large genomes.

The Herpesviridae family is associated with herpes lesions at the lips (cold sores) and the genitalia as well as many other diseases—chickenpox, infectious mononucleosis, nasopharyngeal carcinoma, and Kaposi's sarcoma (1). The nine known human herpesviruses span all three herpesvirus subfamilies— α -, β -, and γ -herpesviruses—and are grouped on the basis of their biological properties, including differences in tissue tropism. Viruses in the α -herpesvirus subfamily, including herpes simplex virus type 1 (HSV-1, causes cold sores) and type 2 (HSV-2, causes genital herpes) and varicella-zoster virus (causes chickenpox and shingles), can establish lifelong latent infections within the peripheral nervous systems of their hosts. The DNA-containing capsids of these neurotropic viruses undergo long-range (up to tens of centimeters) axonal retrograde transport from nerve endings at sites of infection (such as the lips) to neuronal cell bodies at the ganglia to establish latency. Upon reactivation, anterograde transport of the progeny viral particles from the ganglia to nerve terminals results in reinfection of the dermis. Capsid-bound tegument proteins are involved in this cytoskeleton-dependent capsid transport (2–7). Densities of tegument proteins have been visualized at the icosahedral vertices of the HSV-1 capsid by cryo-electron microscopy (cryo-EM) (8), leading to designations such as C-capsid-specific component

(9), capsid vertex-specific component (10), and, more generally across different subfamilies of herpesviruses, the capsid-associated tegument complex (CATC) (11). Molecular labeling, together with the fitting of crystallographic models into subnanometer resolution cryo-EM structures, has shown that CATC from α -herpesviruses contains at least pUL25 and pUL17 (10–14) and possibly pUL36 (15–17), all of which are essential for viral propagation. However, the CATC in the nonneurotropic β -herpesvirus human cytomegalovirus (HCMV) bears neither compositional nor structural similarities to that in α -herpesviruses. The β -herpesvirus-specific tegument protein pp150 forms a spherical net securing the capsid (18–20) that is pressurized by a viral double-stranded DNA (dsDNA) genome of 235 kb, 50% larger than that of HSV-1. Capsid proteins are more conserved than tegument proteins, with herpesviruses across different subfamilies all containing homologous capsid proteins, though the level of conservation varies greatly in both sequence and function.

In the absence of atomic structures of the HSV-1 capsid and CATC, the structural bases underlying long-range neuronal transport and aspects of genome packaging are poorly understood. Because of the large size (~1300 Å) of HSV-1 particles, the progress toward an atomic description of HSV-1 has been astonishingly slow, with the highest resolution as yet being 6.8 Å (17), which is insufficient for de novo atomic modeling.

Overall structures

To obtain an atomic description of the HSV-1 capsid and its associated tegument proteins, we imagined intact HSV-1 virions by electron-counting

cryo-EM (fig. S1) and obtained a three-dimensional icosahedral reconstruction at an effective resolution of 4.2 Å by combining 23,800 virion particles (Fig. 1A and fig. S2A). Like earlier reconstructions at lower resolution [for example, (17, 21)], our density map only reveals the icosahedrally ordered components of the virion, including a triangulation number (T) = 16 capsid containing pentons, 3 quasi-equivalent hexons (P, peripentonal; E, edge; and C, center), 6 quasi-equivalent triplexes (Ta to Tf), and 12 star-shaped CATC densities, each crowning a penton at the icosahedral vertex (Figs. 1, A to C, and 2A). Through a subparticle-refinement procedure, we further improved the structure of the vertex region containing CATC to 3.5-Å resolution (fig. S2, A and B). High-resolution features resolved in our cryo-EM map, such as amino acid side chains (Movies 1 and 2 and figs. S3 to S5), enabled us to build atomic models for both the capsid and CATC (Fig. 1D). The atomic models for the capsid proteins are all built de novo, including 16 copies of the major capsid protein (MCP) VP5, 10 copies of the triplex dimer protein (Tri2) VP23, 5 copies of the triplex monomer protein (Tri1) VP19c, and 15 copies of the smallest capsid protein (SCP) VP26, amounting to more than 28,000 residues in total.

Structure of the CATC

Surrounding each capsid vertex, five CATC densities form a five-pointed star crowning the penton (Fig. 2A). The relative density values of CATC versus its underlying triplexes are similar (Movie 2 and fig. S2B), suggesting nearly full occupancy of CATC, in contrast to the low occupancy of CATC in the virion of γ -herpesvirus Kaposi's sarcoma-associated herpesvirus (KSHV) (11). Each CATC contains a triplex-binding region bridging triplexes Ta and Tc, an extended five-helix bundle, and a bi-lobed head region that lies in the space between two neighboring penton MCPs (Fig. 2, B to E). The triplex-binding region and the five-helix bundle are well resolved (fig. S5), but the bi-lobed head region is not and requires low-pass filtering to 6-Å resolution for interpretation, indicating its higher level of flexibility (fig. S2B). Nonetheless, the clearly resolved secondary structures in the head region enabled reliable fitting of two copies of the crystal structure of the pUL25 C-terminal fragment [amino acids 134 to 580, Protein Data Bank (PDB) 2F5U] (22) (Fig. 2C and Movie 3), inconsistent with the assignment of one pUL25 and one pUL36 to the corresponding bi-lobed densities in a previous cryo-EM reconstruction of HSV-1 at 6.8-Å resolution (17). Our CATC model comprises these fitted dimer structures of the pUL25 head domain and de novo atomic models for the triplex-binding region and the five-helix bundle. We can model near full-length pUL17, two copies of N-terminal pUL25 (~90 amino acids), and two copies of C-terminal pUL36 (pUL36ct) (amino acids 3092 to 3139) (Fig. 1D).

The 696-amino acid-long pUL17 monomer comprises an eight-stranded β barrel at the N terminus (“front barrel”), a seven-stranded β barrel at the C terminus (“back barrel”), and a helix-rich middle segment that enwraps the β barrels

¹Department of Microbiology, Immunology, and Molecular Genetics, University of California, Los Angeles, Los Angeles, CA 90095, USA. ²California NanoSystems Institute, University of California, Los Angeles, Los Angeles, CA 90095, USA.

*Corresponding author. Email: hong.zhou@ucla.edu

to form two lobes (labeled “front” and “back”) (Fig. 2F and Movie 4). A small helical domain extends from between the two lobes (the “hump”). A helix extending from the front lobe (“extended helix,” amino acids 241 to 266) is the fifth helix of

the five-helix bundle and guides the positioning of the pUL25-pUL36 helix bundle (Fig. 2, E and F). The hump on one side and the P hexon on the other further anchor and stabilize the helix bundle (Fig. 2D). Overall, the position of the CATC is con-

strained by triplexes Ta and Tc and the P hexon tower (Fig. 2D and fig. S6).

The two subunits of the pUL25 dimer in CATC differ in structural details but bear the same domain organization, consisting of an N-terminal

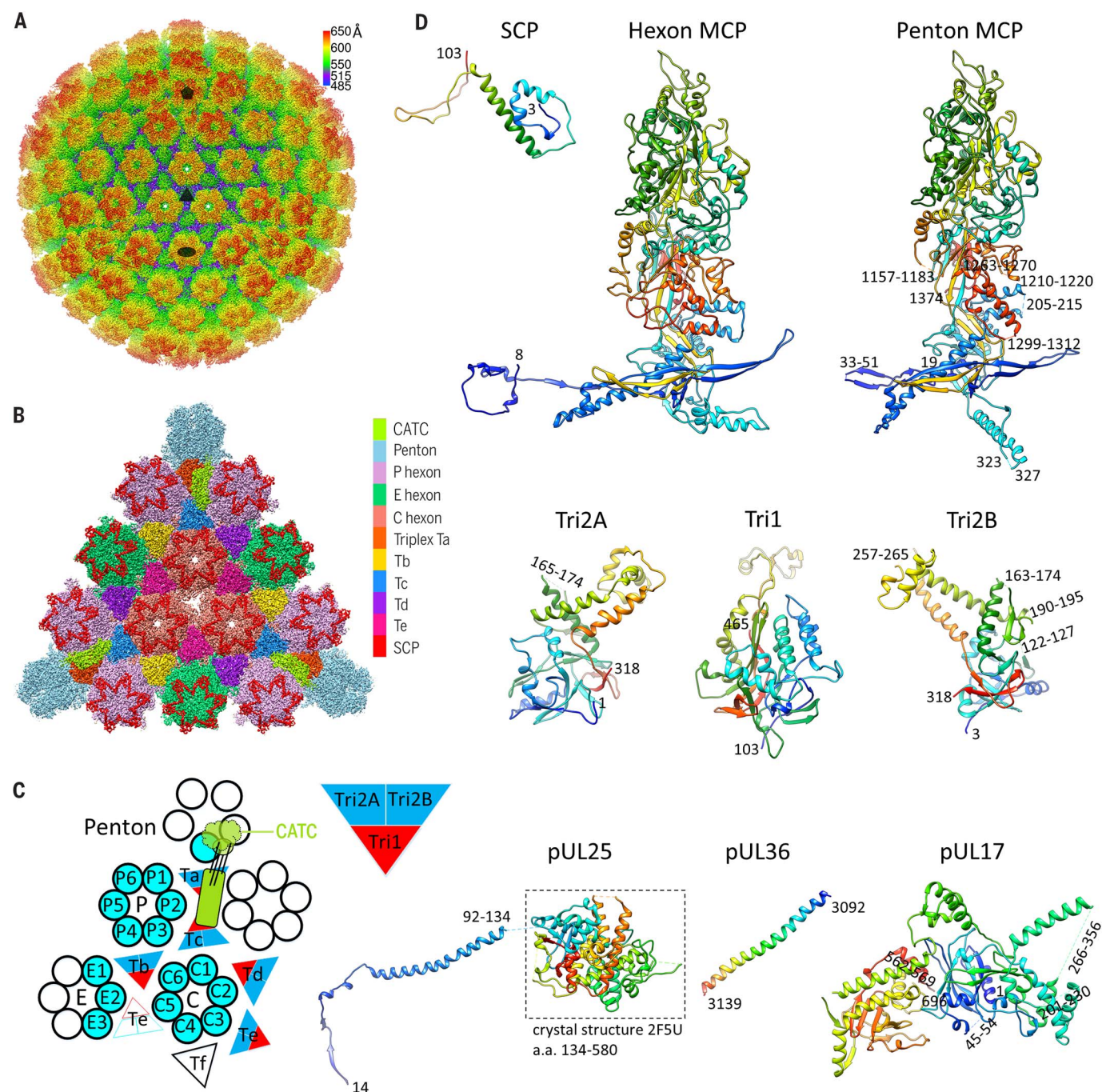


Fig. 1. Cryo-EM reconstruction and atomic modeling of the HSV-1 capsid.

(A) Radially colored cryo-EM density map of the HSV-1 capsid viewed along a threefold axis. Fivefold, threefold, and twofold axes are denoted by a pentagon, triangle, and oval, respectively. (B) Magnified view of one facet of the icosahedral capsid with structural components differentially colored. The density of triplex Tf at the center is not shown. (C) A schematic representation of one asymmetric unit (shaded) of the capsid. An extra copy of triplex Te

(unshaded) from an adjacent asymmetric unit is shown to depict that triplex pair Tb-Te has a similar configuration as Ta-Tc, thus providing a second potential binding site for the CATC (11, 17). The enlarged red and blue triangle shows the heterotrimeric nature of a triplex. a.a., amino acid. (D) Atomic models of individual capsid or tegument proteins in rainbow-colored ribbon (from blue at the N terminus to red at the C terminus). Numbers denote chain termini or flexible segments that are not modeled. a.a., amino acid.

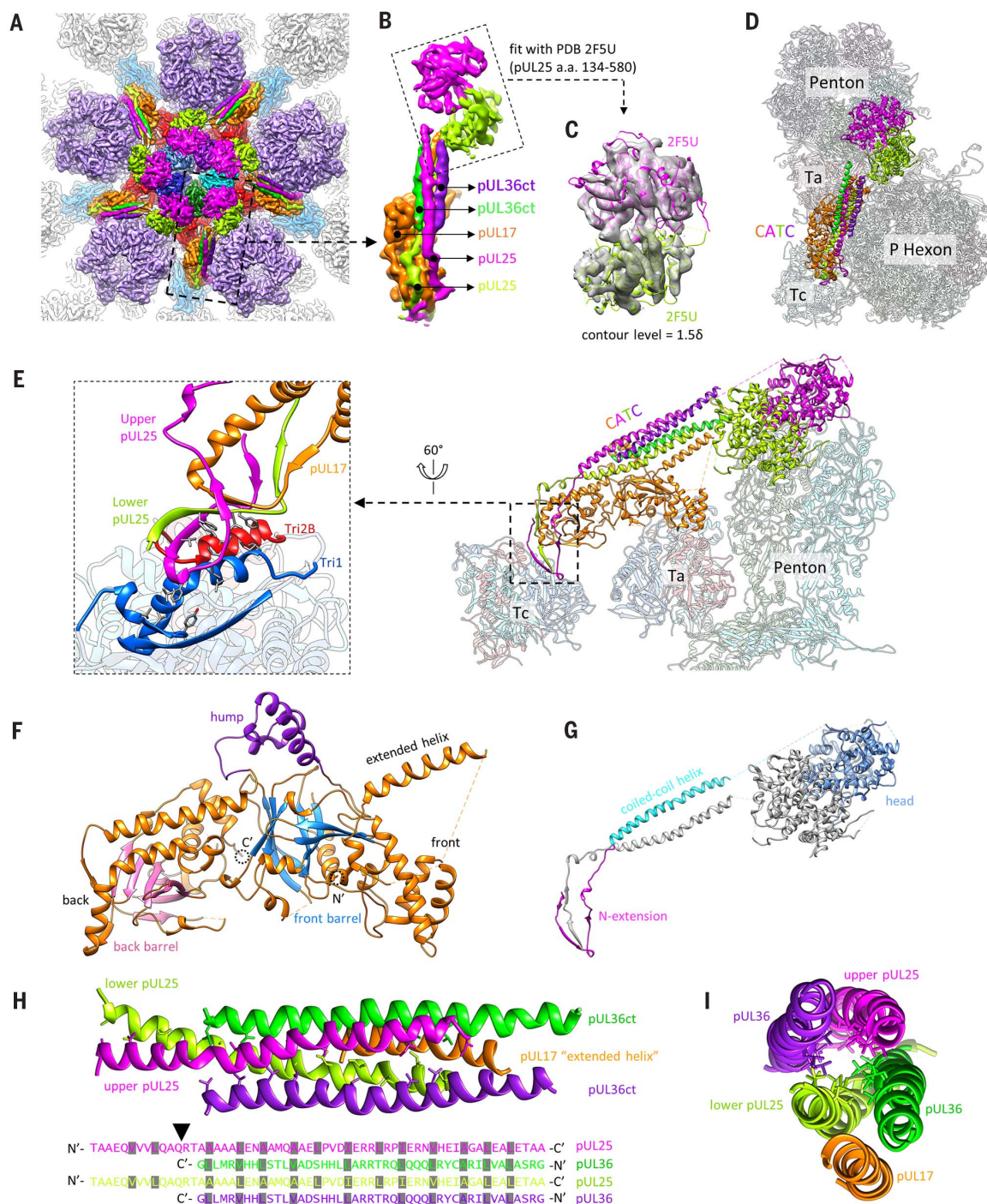


Fig. 2. Structure of the CATC. (A) Cryo-EM densities of the CATC surrounding a penton vertex. The density map was low-pass filtered to 6-Å resolution to show the flexible pUL25 head region. (B) Magnified view of a segmented-out CATC unit from the dashed square in (A), showing its composition. (C) Fitting of two copies of pUL25 C-terminal region crystal structure (PDB 2F5U) (22) into the bi-lobed head region of CATC. The contour level for the pUL25 head region in (A) to (C) was 1.5 δ (where δ is the standard deviation) and that of the rest was 3 δ . (D and E) Top view (D) and side view (E) of CATC interacting with underlying capsid components, shown with atomic models. On the left in

(E) is a magnified view of the interface between the CATC and triplex Tc. Hydrophobic side chains of the pUL25 dimer, Tri1, and Tri2B involved in the interactions are highlighted. (F and G) Domain organization of pUL17 (F) and pUL25 (G). (H and I) The five-helix bundle viewed from the top of the capsid (H) or along the center of the coiled coil (I). In (H), side chains are shown for hydrophobic residues in the center of the helix bundle (top), with their identities marked (grayed) in the sequence (bottom). The arrowhead in (H) points to the position in the pUL25 sequence where the hydrophobic residue distribution pattern breaks. N', N terminus; C', C terminus.

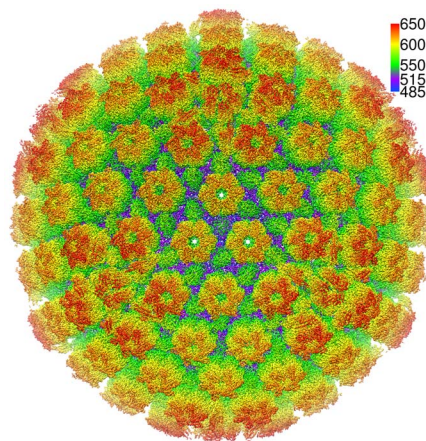
β -strand domain (N extension, amino acids 1 to 47) that interacts with pUL17, a coiled-coil helix domain (48 to 94), and the C-terminal head domain (134 to 580) (Fig. 2G and Movie 4). The N extensions of the two pUL25 monomers intertwine with each other and with the back lobe of pUL17: Three β strands (amino acids 3 to 5, 10 to 14, 24 to 26) of the upper pUL25, two β strands (14 to 20, 26 to 28) of the lower pUL25, and two β strands (503 to 505, 510 to 512) of pUL17 together form two small β sheets (Fig. 2E, magnified view). In this way, the two differently folded N extensions of the pUL25 dimer work together to fasten the coiled-coil helix bundle to pUL17. The N extensions of the two pUL25 molecules also insert a number of hydrophobic side chains (Phe⁷, Leu¹⁰, Val¹², Phe¹⁸, and Val²⁰ of the upper pUL25 and Phe¹⁸ and Val²⁰ of the lower pUL25) into two hydrophobic clefts of triplex Tc, one at the interface between Tri1 and Tri2B and the other on the surface of Tri1 (Fig. 2E, magnified view). Notably, only pUL25 residues are directly involved in triplex Tc binding, as opposed to previous suggestions that pUL17 directly interacts with both Ta and Tc—a reasonable interpretation when amino acid residues were not resolved (17).

Our identification of two copies of pUL36ct in the helix bundle of the CATC is supported by side-chain densities resolved in the 3.5-Å resolution subparticle reconstruction map (fig. S5). It is also consistent with biochemical data showing that the C-terminal 62-amino acid segment of pUL36 (also termed VP1/2) is essential for the association of pUL36 with the capsid and that this capsid association requires interaction with pUL25 in both pseudorabies virus (PRV) and HSV-1 (23, 24). In our model, the pUL36ct dimer joins the pUL25 dimer to form a four-helix coiled coil, which in turn rests on the extended helix of pUL17, giving rise to the five-helix bundle (Fig. 2, H and I, and Movie 4). Within the pUL25-pUL36ct four-helix coiled coil, hydrophobic side chains (predominantly leucine) are spaced every three or four residues in all four helices, similar to those in a leucine zipper (Fig. 2H). There is a break in this pattern of hydrophobic residues at position Gln⁵⁸, Arg⁵⁹ in pUL25 (arrowhead in Fig. 2H) where pUL36ct incorporates into the CATC. The bundling with pUL36ct may also stabilize the pUL25 dimer and likely the entire CATC, as previous cryo-EM reconstruction of a pUL36-deletion mutant of HSV-1 showed diminished CATC densities (16). The extensive interactions among all five subunits of CATC suggest that they likely coassemble in the nucleus and act together as a functional unit in binding the capsid, consistent with their detections in capsids purified from the host-cell nucleus (10, 25).

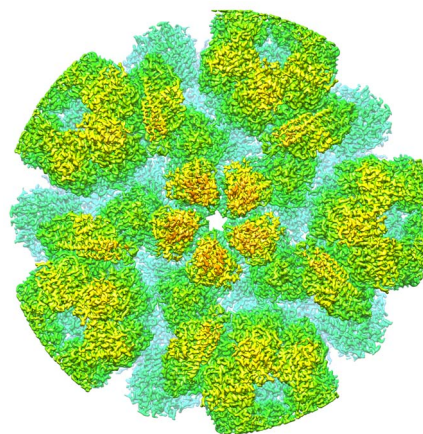
Bacteriophage-related motif and α -herpesvirus-specific features of the triplex

Protruding from the floor of the canyons between towering capsomers are six quasi-equivalent triplexes Ta to Tf (Figs. 1, B and C, and 3, A and B), with only Ta and Tc providing the platform for CATC binding (Movie 4). Each triplex is a hetero-

trimer consisting of one Tri1 (VP19c) and two conformers of Tri2 (VP23)—Tri2A and Tri2B (Fig. 3, C to F). The sequence of HSV-1 Tri1 protein VP19c is about 40% longer than those of the Tri1 homologs in both β - and γ -herpesviruses, whereas the Tri2 protein sequences are similar in length across the three herpesvirus subfamilies. The two Tri2 subunits in each triplex interact through their embracing-arm domains (amino acids 145 to 289) (Fig. 3H). The embracing-arm domains are structurally variable between the two subunits, whereas their trunk domains (1 to 144, 290 to 318) are constant (Fig. 3G). This Tri2A-Tri2B dimer is bound by the third-wheel domain (103 to 356, 412 to 465) of the Tri1 monomer from the side and latched at the top by a 55-amino acid insertional-arm domain (357 to 411) of Tri1 (Fig. 3I). Near the bottom of this heterotrimeric interface, an intermolecular disulfide bond formed between Cys²⁶⁶ of Tri1 and Cys²⁹⁸ of Tri2B likely further stabilizes the triplex (Fig. 3I, magnified view, and fig. S4).



Movie 1. Overall structure and high-resolution features of the HSV-1 capsid icosahedral reconstruction.



Movie 2. High-resolution features in the 3.5-Å resolution subparticle reconstruction of the HSV-1 capsid vertex region.

Despite no recognizable similarity between the Tri1 (VP19c) and Tri2 (VP23) protein sequences, the third-wheel domain of Tri1 and the trunk domain of Tri2 both predominantly contain two β barrels, giving rise to the homotrimeric appearance of the triplex when viewed from the inside of the capsid (Fig. 3J). Notably, the arrangement of the two β barrels in both Tri1 and Tri2 closely resembles the homotrimeric cementing proteins of dsDNA bacteriophages, such as gpD in phage λ (Fig. 3J and fig. S7). Indeed, side-by-side comparison of the chain tracing in gpD (26), Tri1, and Tri2 reveals identical topology of their β strands (Fig. 3K). This observation suggests that HSV-1 Tri1 and Tri2 evolved from an ancestral gene shared by phage λ gpD. Perhaps a gene-duplication event in the herpesvirus ancestor led to divergent evolution of Tri1 and Tri2. For example, whereas each subunit of the gpD trimer contributes an N-terminal extension to augment a β sheet on the capsid surface (27), the two Tri2 subunits in the herpesvirus triplex do not have such a capsid-binding N-terminal extension. Instead, the Tri1 monomer inserts its N-terminal extension (N anchor) through the capsid floor and folds into a tri-lobed structure inside the capsid (Fig. 3, C, D, and L) (20, 28), anchoring the entire triplex. Selection pressure to mediate binding of divergent tegument proteins outside the capsid and to accommodate genomes of varying sizes inside the capsid could have also forced Tri1 to diverge on both its outer and inner sides. Indeed, the Tri1 insertional arm, which emanates from a topologically similar location on one of the two β barrels as that of the Tri2 embracing arm, is the most externally located and is completely missing in HCMV Tri1 (20) and KSHV Tri1 (28). Likewise, the genome-facing N anchor of HSV-1 Tri1 is substantially longer than (102 versus 44 amino acids), and not as rigid as, that of HCMV (20).

HSV-1-specific features in the SCP and MCP

Like that of HCMV or KSHV (20, 28), the HSV-1 MCP (VP5) subunit can be thought of as an extensive elaboration on a central bacteriophage HK97 gp5-like (“Johnson”) fold (amino acids 51 to 193, 232 to 298, 365 to 396, 1061 to 1113), with six additional domains, including the N lasso (1 to 50), dimerization (299 to 364), helix-hairpin (194 to 231), channel (407 to 480, 1335 to 1374), buttress (397 to 406, 1048 to 1060, 1114 to 1334) and upper (481 to 1047) domains (Fig. 4A).

The upper domain of MCP (MCPud) provides the binding site for SCP (VP26) (Fig. 4B), which is the most divergent, both structurally and functionally, capsid protein across all herpesvirus subfamilies. Our atomic model of the 112-amino acid SCP monomer encompasses residues 3 to 103 and consists of a helix-rich N-terminal domain (amino acids 1 to 71) featuring the characteristic “stem helix” involved in MCPud binding (29) and the C-terminal hairpin-loop domain (72 to 112). Six SCP subunits form a gear-shaped hexameric ring crowning each hexon, with their hairpin-loop domains bridging the gaps between adjacent hexon MCP upper domains (Fig. 4, B and C).

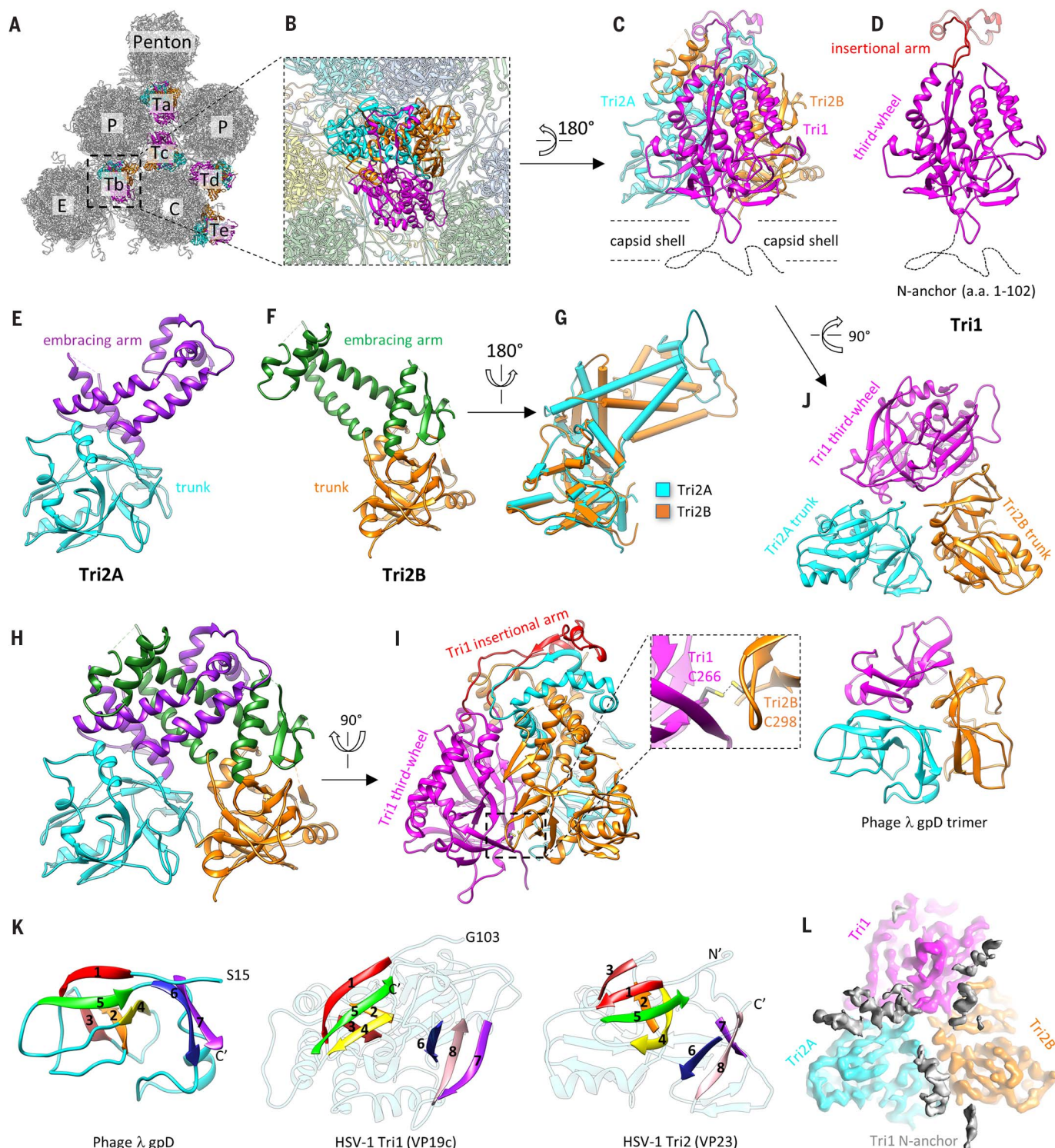


Fig. 3. Structure of the triplex. (A) Distribution of triplexes in the MCP network. (B) Magnified view of a triplex Tb as viewed from the outside of the capsid. (C to F) Detailed structures of triplex Tb (C) and its components Tri1 (D), Tri2A (E), and Tri2B (F). Dotted curves in (C) and (D) denote the N-terminal region of Tri1 that was not modeled because of its flexibility. (G) Superposition of Tri2A and Tri2B showing constant trunk domains and conformational differences in their embracing-arm domains. (H) Tri2A and Tri2B embrace each other with their embracing-arm domains to form a dimer. (I) The Tri1 insertional arm binding on top of the Tri2 dimer and

the Tri1-Tri2B intermolecular disulfide bond (shown in magnified view) stabilize the triplex structure. (J) Architectural similarities between HSV-1 triplex (top) and the gpD trimer of phage λ (bottom, PDB 1C5E) (26). Both are viewed from the inside of the capsid. (K) Same topology of β strands among gpD, Tri1, and Tri2. Corresponding β strands are colored in the same way and numbered one to eight, from N' to C'. (L) Cryo-EM density of triplex Tb in the same orientation as (J), showing the tri-lobed density of the flexible Tri1 N anchor (gray), which penetrates through the capsid floor and anchors the entire triplex to the capsid shell, as depicted in (C).

This “cross-linking” interaction of SCP resembles that of the 170-amino acid SCP-homolog ORF65 in γ -herpesvirus KSHV and thus likely has a similar function in stabilizing the hexons of the capsid (29). This is consistent with the previous observation that the VP26 null mutation resulted in decreased production of infectious virus in the nervous system of infected mice, though it had little effect in cell culture (30). Notably, the 75-amino acid SCP-homolog UL48.5 in β -herpesvirus HCMV completely lacks the C-terminal cross-linking moiety found in HSV-1 and KSHV but has evolved to stabilize the capsid by mediating the binding of a β -herpesvirus-specific tegument protein pp150 (19, 20).

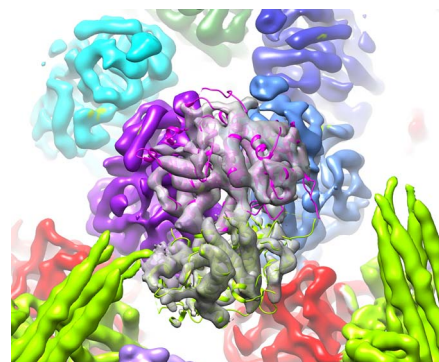
As in HCMV and KSHV (20, 28), three types of MCP-MCP interactions form a hierarchical network of interactions on the HSV-1 capsid floor (Fig. 4, D and E, and Movie 5). The type I interaction is intracapsomeric β augmentation between adjacent MCPs within a capsomer, as exemplified by P2 and P3 MCPs in Fig. 4F: Two β strands in the N arm of P2, two β strands in the E loop, and one β strand in the dimerization domain of P3 together form a five-stranded β sheet. Type II and type III interactions are intercapsomeric interactions involving the dimerization and N-lasso domains, respectively. As exemplified in Fig. 4, G and H, the C5 N lasso extends and lashes around the P2 N arm and P3 E loop and the P2 N lasso extends and lashes around the C5 N arm and C6 E loop to form a pair of type III interactions related by a local twofold axis. These type III interactions are built on and likely strengthen the type I interactions, as the C5 N lasso contributes two β strands to augment the existing five-stranded β sheet from P2 and P3's type I interaction into a seven-stranded β sheet (Fig. 4, F and H), as does the P2 N lasso to C5 and C6 (Fig. 4H). Furthermore, a type II interaction is formed by the dimerization domains of P3 and C6 pairing with one another around the local twofold axis with hydrophobic residues (Fig. 4I) and secures the pair of type III interactions among P2, P3, C5, and C6 (Fig. 4G).

The network interactions of the penton and its surrounding P hexons (Fig. 4J and Movie 5) are different from those of other hexons (Fig. 4G) in two ways. First, the N-terminal regions of penton MCP and P6 MCP refold and lose the canonical N-lasso structure of the hexon MCP (Fig. 4K). As a result, the penton neither lashes nor is lashed by adjacent P hexons. Second, the dimerization domain of penton MCP, as well as that of P1 MCP, refold from the helix-turn-helix structure in a canonical type II interaction (Fig. 4I) into a single long helix (Fig. 4J and fig. S8). The two resulting helices interact through a series of interdigitated leucine residues (that is, hydrophobic interactions) buried within the interface and a series of hydrogen-bonded arginine and glutamate residues lining the inner surface of the capsid (fig. S8). Five such helix pairs radiate from the penton channel and give rise to a star-shaped appearance (Fig. 4L and Movie 5) not seen in the capsids of β - (20) and γ -herpesviruses (29) and even the closely related α -herpesvirus PRV (17), thus providing an extra-

ordinary example of structural diversification of the HSV-1 capsid.

Discussion

Our observation of architectural similarities between herpesvirus triplex proteins and auxiliary cementing protein gpD in bacteriophage λ , in addition to earlier identifications of bacteriophage HK97 gp5-like folds in their major capsid proteins (27, 31) and structural similarities in their DNA packaging and delivery apparatuses (32), indicates that the commonality between bacteriophages and herpesviruses extends to their auxiliary components. Nonetheless, evolution seems to have driven the diversification of capsid-fortifying strategies in these viruses to accommodate differently sized genomes. Whereas a gpD-like cementing protein might have been replaced during evolution by autocatalytic chemical cross-linking of capsid proteins in HK97 (27, 33, 34), the much larger genome of herpesvirus necessitates more extensive involvement of the triplex in building a larger-sized capsid—indeed, the triplex coassembles with MCP as a major building block of the procapsid in herpesvirus (35–37), in contrast to the gpD trimer, which is an auxiliary addition to the matured phage λ capsid after genome packaging (27).



Movie 3. Fitting of two copies of the pUL25 C-terminal region crystal structure into the bi-lobed head region of CATC.

Together with the above, the model of an HSV-1 particle presented here provides not only the basis for understanding capsid assembly but also mechanistic insights into previously unexplained aspects of the viral life cycle. We show that CATC is a complex of tegument proteins pUL17, pUL25, and pUL36, which have been suggested to play multiple roles, including reinforcement of the capsid (38), retrograde transport of the incoming viral capsid during initial infection (3, 5, 7, 39, 40), ejection of the viral genome through the nuclear pore (41–43), and nuclear and cytoplasmic egress of the progeny viral particles (25, 44–49). CATC binds only the Ta-Tc triplex pair near two P hexons but not the other quasi-equivalent Tb-Te triplex pair near one C hexon and one E hexon (Fig. 1C), where the slightly different geometry of the C hexon presents a steric hindrance to CATC binding (fig. S9), as also revealed in the 6.8-Å resolu-

tion HSV-1 structure (17). This stringent selection of binding site suggests high rigidity of the CATC, which can be attributed to the characteristic of the pUL17 structure—two rigidity-promoting β barrels stuffed beneath the length-defining, helix-rich middle segment. The specificity of CATC binding might also have functional implications in ensuring the right timing for nuclear egress of capsid, a function that has been associated primarily with pUL25 for its interaction with the pUL31 component of the nuclear egress complex (44–48). In the host-cell nucleus, CATC must select mature capsids over immature ones (procapsids) for nuclear egress; the geometry of neighboring capsomers and triplexes in the spherical procapsid differs from that in the angularized mature capsid (35), preventing premature association of CATC to the procapsids. The structural constraints on CATC binding also raise the question of whether it can bind to the portal vertex. Although icosahedral reconstruction precludes knowledge of the geometry surrounding the portal, functional studies have shown an essential role of pUL25 in HSV-1 genome release (41–43), arguing for CATC's existence at the portal vertex.

The bundling of pUL36ct with the pUL25 coiled-coil helix provides an anchoring point for the recruitment of pUL36 and, in turn, pUL36-binding tegument proteins, such as the conserved pUL37 (50, 51) and pUL48 (VP16) (52), both of which can interact with cytoplasmic tails of viral glycoproteins to facilitate virion envelopment (53–56). In this regard, pUL36 is a pivot connecting herpesvirus capsid assembly and primary tegumentation in the host-cell nucleus to its secondary tegumentation (49) and envelopment in cytoplasm, and our structure provides the first atomic view of the early steps in this cascade of events leading to the morphogenesis of herpesvirus virion. Beyond its C-terminal helix resolved here, the central one-third of pUL36 also dimerizes to form a coiled-coil helix bundle (57). Intriguingly, this structural organization of the CATC is somewhat reminiscent of cellular motor proteins, which all contain a coiled-coil helix bundle joining their cytoskeleton-binding globular head domains with their cargo-binding domains (58–60). The involvement of CATC in cytoskeleton-dependent α -herpesvirus capsid transport, through either direct or indirect interactions with cellular motor proteins (2–7, 39, 40), now opens the door for new inquiries into the remarkable ability of long-range axonal transport of these neurotropic viruses.

Materials and Methods

Virus culture and purification

Vero cells (ATCC CCL-81) were cultured in Dulbecco's modified Eagle medium (DMEM) supplemented with 10% fetal bovine serum (FBS) to 100% confluence and inoculated with HSV-1 (strain KOS, ATCC VR-1493) at a multiplicity of infection (MOI) of ~ 0.01 . At 3 days postinfection, the culture media were collected and centrifuged at 8000g for 15 min to remove cell debris. Viral particles were pelleted by centrifuging at 80,000g for 1 hour, resuspended in phosphate-buffered saline (PBS, pH 7.4), and then purified by centrifuging through a 15 to 50%

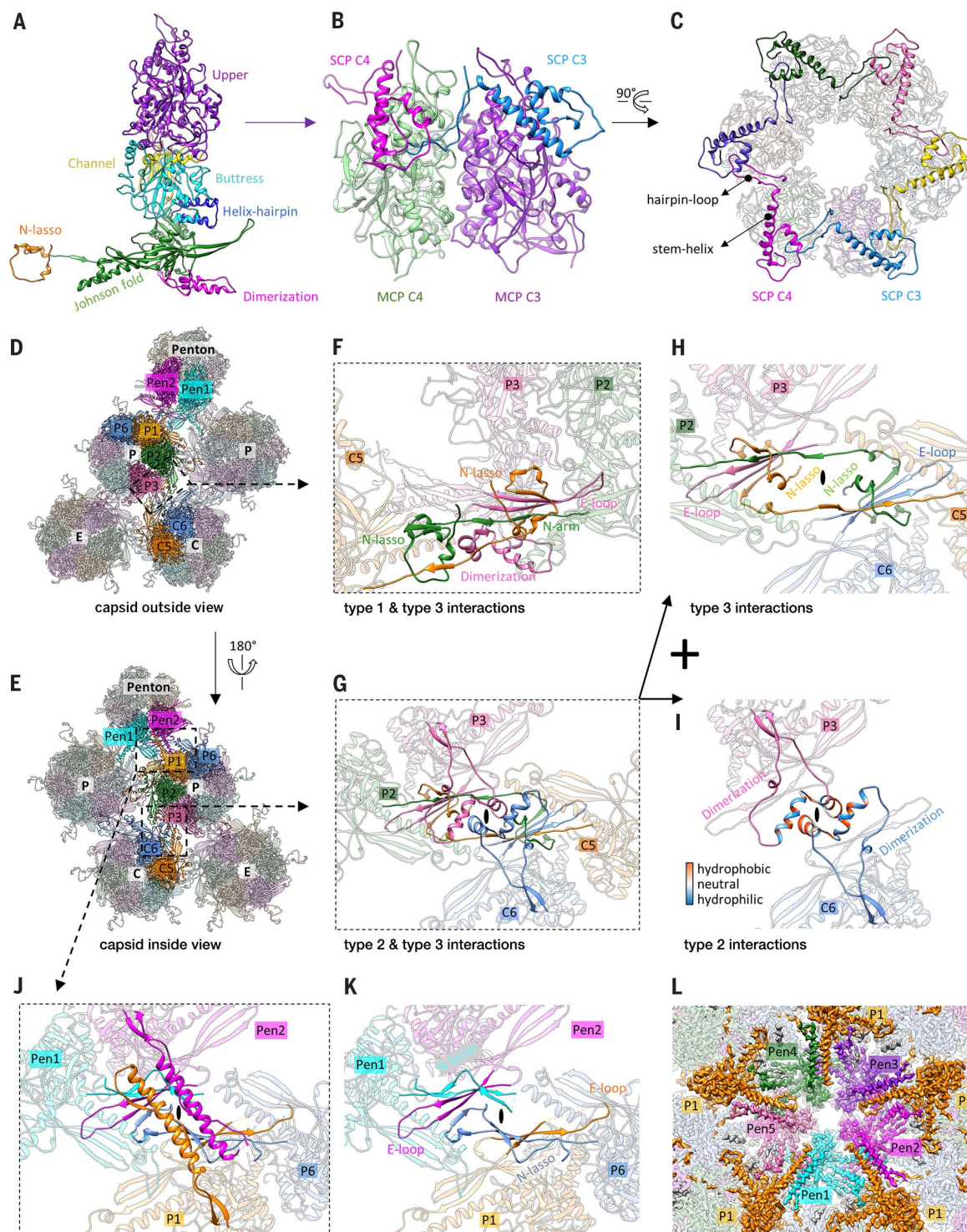


Fig. 4. SCP and MCP network interactions. (A) Domain organization in a hexon MCP. (B and C) SCP binds the upper domain of hexon MCP (B), and six copies of SCP form a gear-shaped ring crowning and stabilizing the hexon (C). (D and E) Part of the MCP network viewed from the outside (D) or the inside (E) of the capsid. Pen, penton. (F to I) Three types of network interactions among hexon MCPs. (H) and (I) show the individual structures that make up (G). The type I interaction is an intracapsomeric augmentation of β strands from adjacent MCPs [P2 and P3 in (F)] in the same capsomer. Type II and type III are intercapsomeric interactions among two pairs of MCPs [P2-P3 and C5-C6 in (G)] diagonally across the local twofold axis [ovals in (G) to (I)].

The type III interaction builds on and fortifies the type I interaction [see C5 N lasso in (F)]. The two dimerization domains joined by a type II interaction (I) also sit atop a pair of type III interactions, when looking from the inside of the capsid (G), and prevent the two N lassos [C5 and P2 N lassos in (G) and (H)] from unwinding. (J and K) Interactions between penton MCPs and the P1 and P6 hexon MCPs are different from the canonical hexon MCP network interactions [compare (J) and (G), (K) and (H)]. (L) Cryo-EM density at the penton area viewed from the inside of the capsid. The five copies of penton MCP are differently colored, whereas all P1 MCPs are colored in gold.

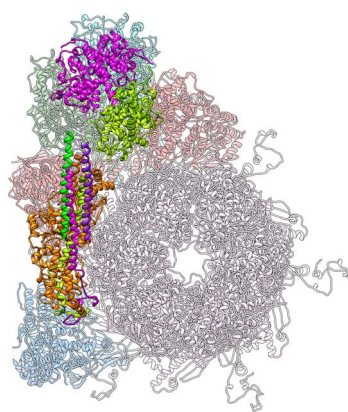
(w/v) sucrose density gradient at 80,000g for 1 hour. Two bands in the density gradient were usually identified. The lower band contained more noninfectious, enveloped particles lacking nucleocapsid and thus was discarded. The upper band was collected, diluted with PBS, and pelleted by centrifuging at 80,000g for 1 hour. For a 1-liter start volume of viral culture, the purified HSV-1 virions were resuspended in 30 μ l PBS and subjected to cryo-EM sample preparation.

Cryo-EM sample preparation and data collection

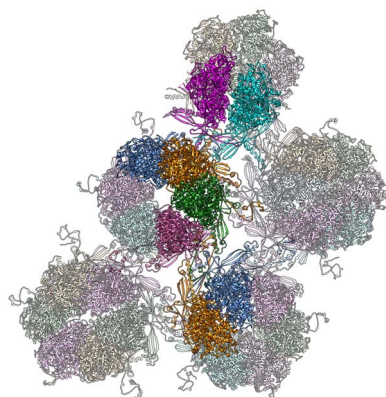
To best preserve the structural integrity of the capsid-associated tegument proteins, we decided to image intact virions instead of detergent-treated ones, which would have the benefits of reduced sample thickness and better contrast as demonstrated in the study of HCMV (20). For cryo-EM sample preparation, 2.5 μ l of purified HSV-1 virion was applied to a glow-discharged Quantifoil R2/1 Cu grid. The grid was manually blotted with filter paper to remove excess sample and flash-frozen in liquid ethane with a homemade plunger freezing apparatus. The frozen-hydrated grids were loaded into an FEI Titan Krios electron microscope operated at 300 kV for automated image acquisition with Leginon (61). A total of about 8000 movies were acquired with a Gatan K2 Summit direct electron detection camera operated in super-resolution electron-counting mode at a nominal magnification of $\times 14,000$, giving a pixel size of 1.03 \AA per pixel. The dose rate on the camera was set to $\sim 8e$ per physical pixel per second and the total exposure time for each movie was 13 s fractionated into 26 frames with 0.5-s exposure time for each frame. Frame images in each movie were aligned and averaged to produce a single micrograph after correction of beam-induced drift using the GPU-accelerated motion correction program (62).

Image processing

Defocus values of micrographs were determined by *CTFFIND3* (63) to be in the range of -1 to $-3 \mu\text{m}$. A total of 45,530 particles (1440 by 1440 pixels) were manually picked from 7356 selected micrographs using *boxer* in EMAN (64). The particle images were binned 8x, 4x, or 2x stepwise to speed up the data processing. Orientation and center parameters for each particle image were determined and refined with the common-line based IMIRS program (65, 66), and 3D reconstruction was done with GPU-accelerated *eLite3D* (67). In the initial step, only data lower than 30- \AA resolution were used, and no CTF correction was applied. On the basis of the reported phase residue (PR) value distribution, 28,042 high-quality particles were selected out and divided into two random halves for further refinement. After convergence of refinement for both halves, an FSC curve was calculated and the resolution was determined to be 4.2 \AA on the basis of the gold-standard FSC = 0.143 criterion (68). In the final step, the two halves of the data set were combined, and a total of 23,800 particles were used to calculate the final density map. A B-factor of



Movie 4. Structure of the CATC and its interactions with the underlying capsid components.



Movie 5. MCP network interactions in the capsid floor.

-200 \AA^2 was applied to sharpen the density map for model building and structure analysis.

Local averaging and atomic model building

Quasi-equivalent copies of MCP C1 to C6, or triplexes Tb to Te, in an asymmetric unit were segmented out in cuboid, fitted to each other, and averaged in Chimera (69) to further improve quality of the density map and facilitate backbone tracing for atomic model building. Ab initio models were built manually in Coot (70), with the local-averaged maps by the following standard modeling procedure: First, the density was traced by the Baton mode tool in Coot; the amino acid residues were then registered to this Baton model; and the geometry of the full atomic model was then regularized manually in Coot and finally iteratively refined with Phenix real space refinement program (71). For the MCP upper domain, its existing crystal structure (PDB 1NO7) (72) was fitted into the cryo-EM density map to guide backbone tracing of this region. The atomic models were then fitted into every quasi-equivalent position in the asymmetric unit and manually adjusted to account for minor structural variations.

Because of the limited resolution of the penton area, model building for the penton MCP and the CATC was not as straightforward as for the above-described other capsid proteins, including hexon MCPs, SCPs, and triplex proteins, and additional strategies had to be used. Briefly, fitting of C1 hexon MCP model into the penton of a low-pass filtered density map indicated that only their floor regions have substantial structural differences, but their tower regions are structurally similar. The floor region of penton MCP has adequate quality for de novo modeling, and this model was combined with the model of the C1 hexon MCP tower to generate a chimera atomic model of the penton MCP.

Each CATC density contains a triplex-binding region bridging triplexes Ta and Tc, and a bi-lobed head region situated above penton MCPs, joined by a coiled-coil five-helix bundle. The triplex-binding region and the five-helix bundle are well resolved, whereas the bi-lobed head region is only discernable when low-pass filtered to 6- \AA resolution. To model the triplex-binding region, which was known to be mainly occupied by a pUL17 monomer (10), we first traced its contiguous, nonbranching density segments and then used sequence-based secondary structure prediction of pUL17 as a roadmap to determine how to join these segments. Correct chain tracing of pUL17 is cross-validated by the good match of predicted secondary structures and those resolved in the density map.

To model the pUL25 of CATC, we first fitted two copies of the crystal structure of pUL25 C-terminal region (PDB 2F5U) (22) into the bi-lobed head region in the low-pass filtered map. These two fitted structures were combined with de novo models of two pUL25 N-terminal segments, each spanning a helix in the five-helix bundle and an extended loop in the triplex-binding region, to produce the full atomic model of the two pUL25 subunits. De novo modeling of the two remaining helices in the five-helix bundle as pUL36ct was straightforward in Coot, thanks to their simple structure as a contiguous helix.

In total, we built atomic models for a total of 51 unique conformers of the four capsid proteins and three tegument proteins: 15 hexon MCP (amino acids 8 to 1374), 1 penton MCP (19 to 33, 51 to 205, 215 to 323, 327 to 411, 430 to 1157, 1183 to 1210, 1220 to 1263, 1270 to 1299, 1312 to 1374), 15 hexon SCP (3 to 103), 5 Tri1 (103 to 465), 10 Tri2 (1 to 165, 174 to 318 of Tri2A; 3 to 122, 127 to 163, 174 to 190, 195 to 257, 265 to 318 of Tri2B), 1 pUL17 (1 to 45, 54 to 201, 230 to 266, 356 to 562, 569 to 696), 2 pUL25 (1 to 94 for one copy, 13 to 92 for the other copy, and each chimerized with PDB 2F5U resolving 134 to 577), and 2 pUL36 (3092 to 3139). As the last step, the refined atomic models of all individual conformers were combined and refined together in Phenix to resolve intermolecular clashes at the interface.

Subparticle refinement and model improvement

Because of the large size of the HSV-1 capsid, any overall particle deformation and the defocus

gradient across the particle (that is, the Ewald sphere effect) (73) would result in considerable dampening of the high-resolution information in conventional icosahedral reconstruction by treating the particle as a whole. Both effects are the most severe in the capsid vertex region, limiting attainable resolution of the penton and the CATC. To further improve resolution of the vertex region, we applied a subparticle refinement and reconstruction procedure considering both local variations (74) and defocus gradient. Specifically, icosahedral orientation and center parameters of each particle image determined above were used to guide extraction of all vertex regions as subparticles with their defocus values adjusted according to their locations on each particle. The orientation and center parameters of these subparticles were locally refined with Relion (75), and, by imposing C5 symmetry, we obtained a final reconstruction at 3.5-Å resolution on the basis of the gold-standard FSC = 0.143 criterion (68). Atomic models of components in the vertex region (including hexon MCPs P1, P2, and P6; penton MCP; triplex Ta; and the CATC) were fitted into the refined subparticle map, manually checked in Coot, and refined with Phenix. Overall, our models built from the 4.2-Å resolution icosahedral map match well with the improved subparticle map at 3.5-Å resolution, indicative of good quality and validity of our original models.

REFERENCES AND NOTES

- Pellett, B. Roizman, in *Fields Virology*, D. Knipe, P. Howley, Eds. (Lippincott Williams and Wilkins, Philadelphia, 2013), vol. 2, pp. 1802–1822.
- G. A. Smith, L. W. Enquist, Break ins and break outs: Viral interactions with the cytoskeleton of mammalian cells. *Annu. Rev. Cell Dev. Biol.* **18**, 135–161 (2002). doi: [10.1146/annurev.cellbio.18.012502.105920](#); pmid: [12142276](#)
- G. W. Luxton et al., Targeting of herpesvirus capsid transport in axons is coupled to association with specific sets of tegument proteins. *Proc. Natl. Acad. Sci. U.S.A.* **102**, 5832–5837 (2005). doi: [10.1073/pnas.0500803102](#); pmid: [15795370](#)
- G. W. Luxton, J. I. Lee, S. Haverlock-Moyns, J. M. Schober, G. A. Smith, The pseudorabies virus VP1/2 tegument protein is required for intracellular capsid transport. *J. Virol.* **80**, 201–209 (2006). doi: [10.1128/JVI.80.1.201-209.2006](#); pmid: [16352544](#)
- S. E. Antinone, G. A. Smith, Retrograde axon transport of herpes simplex virus and pseudorabies virus: A live-cell comparative analysis. *J. Virol.* **84**, 1504–1512 (2010). doi: [10.1128/JVI.02029-09](#); pmid: [19923187](#)
- S. V. Zaichick, K. P. Bohannon, G. A. Smith, Alphaherpesviruses and the cytoskeleton in neuronal infections. *Viruses* **3**, 941–981 (2011). doi: [10.3390/v3070941](#); pmid: [21994765](#)
- S. V. Zaichick et al., The herpesvirus VP1/2 protein is an effector of dynein-mediated capsid transport and neuroinvasion. *Cell Host Microbe* **13**, 193–203 (2013). doi: [10.1016/j.chom.2013.01.009](#); pmid: [23414759](#)
- Z. H. Zhou, D. H. Chen, J. Jakana, F. J. Rixon, W. Chiu, Visualization of tegument-capsid interactions and DNA in intact herpes simplex virus type 1 virions. *J. Virol.* **73**, 3210–3218 (1999). pmid: [10074174](#)
- B. L. Trus et al., Allosteric signaling and a nuclear exit strategy: Binding of UL25/UL17 heterodimers to DNA-filled HSV-1 capsids. *Mol. Cell* **26**, 479–489 (2007). doi: [10.1016/j.molcel.2007.04.010](#); pmid: [17531807](#)
- K. Toropova, J. B. Huffman, F. L. Homa, J. F. Conway, The herpes simplex virus 1 UL17 protein is the second constituent of the capsid vertex-specific component required for DNA packaging and retention. *J. Virol.* **85**, 7513–7522 (2011). doi: [10.1128/JVI.00837-11](#); pmid: [21627258](#)
- X. Dai, D. Gong, T. T. Wu, R. Sun, Z. H. Zhou, Organization of capsid-associated tegument components in Kaposi's sarcoma-associated herpesvirus. *J. Virol.* **88**, 12694–12702 (2014). doi: [10.1128/JVI.01509-14](#); pmid: [25142590](#)
- J. F. Conway et al., Labeling and localization of the herpes simplex virus capsid protein UL25 and its interaction with the two triplexes closest to the penton. *J. Mol. Biol.* **397**, 575–586 (2010). doi: [10.1016/j.jmb.2010.01.043](#); pmid: [20109467](#)
- S. K. Cockrell, J. B. Huffman, K. Toropova, J. F. Conway, F. L. Homa, Residues of the UL25 protein of herpes simplex virus that are required for its stable interaction with capsids. *J. Virol.* **85**, 4875–4887 (2011). doi: [10.1128/JVI.00242-11](#); pmid: [21411517](#)
- F. L. Homa et al., Structure of the pseudorabies virus capsid: Comparison with herpes simplex virus type 1 and differential binding of essential minor proteins. *J. Mol. Biol.* **425**, 3415–3428 (2013). doi: [10.1016/j.jmb.2013.06.034](#); pmid: [23827137](#)
- G. Cardone et al., The UL36 tegument protein of herpes simplex virus 1 has a composite binding site at the capsid vertices. *J. Virol.* **86**, 4058–4064 (2012). doi: [10.1128/JVI.00012-12](#); pmid: [22345483](#)
- W. H. Fan et al., The large tegument protein pUL36 is essential for formation of the capsid vertex-specific component at the capsid-tegument interface of herpes simplex virus 1. *J. Virol.* **89**, 1502–1511 (2015). doi: [10.1128/JVI.02887-14](#); pmid: [25410861](#)
- A. Huet et al., Extensive subunit contacts underpin herpesvirus capsid stability and interior-to-exterior allostery. *Nat. Struct. Mol. Biol.* **23**, 531–539 (2016). doi: [10.1038/nmsb.3212](#); pmid: [2711889](#)
- X. Yu et al., Biochemical and structural characterization of the capsid-bound tegument proteins of human cytomegalovirus. *J. Struct. Biol.* **174**, 451–460 (2011). doi: [10.1016/j.jsb.2011.03.006](#); pmid: [21459145](#)
- X. Dai et al., The smallest capsid protein mediates binding of the essential tegument protein pp150 to stabilize DNA-containing capsids in human cytomegalovirus. *PLOS Pathog.* **9**, e1003525 (2013). doi: [10.1371/journal.ppat.1003525](#); pmid: [23966856](#)
- X. Yu, J. Jih, J. Jiang, Z. H. Zhou, Atomic structure of the human cytomegalovirus capsid with its securing tegument layer of pp150. *Science* **356**, eaam6892 (2017). doi: [10.1126/science.aam6892](#); pmid: [28663444](#)
- Z. H. Zhou et al., Seeing the herpesvirus capsid at 8.5 Å. *Science* **288**, 877–880 (2000). doi: [10.1126/science.288.5467.877](#); pmid: [10797014](#)
- B. R. Bowman et al., Structural characterization of the UL25 DNA-packaging protein from herpes simplex virus type 1. *J. Virol.* **80**, 2309–2317 (2006). doi: [10.1128/JVI.80.5.2309-2317.2006](#); pmid: [16474137](#)
- J. I. Lee, G. W. Luxton, G. A. Smith, Identification of an essential domain in the herpesvirus VP1/2 tegument protein: The carboxy terminus directs incorporation into capsid assemblies. *J. Virol.* **80**, 12086–12094 (2006). doi: [10.1128/JVI.01184-06](#); pmid: [17005660](#)
- K. E. Coller, J. I. Lee, A. Ueda, G. A. Smith, The capsid and tegument of the alphaherpesviruses are linked by an interaction between the UL25 and VP1/2 proteins. *J. Virol.* **81**, 11790–11797 (2007). doi: [10.1128/JVI.01113-07](#); pmid: [17715218](#)
- M. Leelawong, J. I. Lee, G. A. Smith, Nuclear egress of pseudorabies virus capsids is enhanced by a subspecies of the large tegument protein that is lost upon cytoplasmic maturation. *J. Virol.* **86**, 6303–6314 (2012). doi: [10.1128/JVI.07051-11](#); pmid: [22438563](#)
- F. Yang et al., Novel fold and capsid-binding properties of the λ-phage display platform protein gpD. *Nat. Struct. Biol.* **7**, 230–237 (2000). doi: [10.1038/73347](#); pmid: [10700283](#)
- G. C. Lander et al., Bacteriophage lambda stabilization by auxiliary protein gpD: Timing, location, and mechanism of attachment determined by cryo-EM. *Structure* **16**, 1399–1406 (2008). doi: [10.1016/j.str.2008.05.016](#); pmid: [18786402](#)
- X. Dai et al., Structure and mutagenesis reveal essential capsid protein interactions for KSHV replication. *Nature* **553**, 521–525 (2018). doi: [10.1038/nature25438](#); pmid: [29342139](#)
- X. Dai et al., CryoEM and mutagenesis reveal that the smallest capsid protein cements and stabilizes Kaposi's sarcoma-associated herpesvirus capsid. *Proc. Natl. Acad. Sci. U.S.A.* **112**, E649–E656 (2015). doi: [10.1073/pnas.1420317112](#); pmid: [25646489](#)
- P. Desai, N. A. DeLuca, S. Person, Herpes simplex virus type 1 VP26 is not essential for replication in cell culture but influences production of infectious virus in the nervous system of infected mice. *Virology* **247**, 115–124 (1998). doi: [10.1006/viro.1998.9230](#); pmid: [9683577](#)
- M. L. Baker, W. Jiang, F. J. Rixon, W. Chiu, Common ancestry of herpesviruses and tailed DNA bacteriophages. *J. Virol.* **79**, 14967–14970 (2005). doi: [10.1128/JVI.79.23.14967-14970.2005](#); pmid: [16282496](#)
- F. J. Rixon, M. F. Schmid, Structural similarities in DNA packaging and delivery apparatuses in herpesvirus and dsDNA bacteriophages. *Curr. Opin. Virol.* **5**, 105–110 (2014). doi: [10.1016/j.coviro.2014.02.003](#); pmid: [24747680](#)
- R. L. Duda, Protein chainmail: Catenated protein in viral capsids. *Cell* **94**, 55–60 (1998). doi: [10.1016/S0092-8674\(00\)81221-0](#); pmid: [9674427](#)
- W. R. Wikoff et al., Topologically linked protein rings in the bacteriophage HK97 capsid. *Science* **289**, 2129–2133 (2000). doi: [10.1126/science.289.5487.2129](#); pmid: [11000116](#)
- A. A. Aksyuk et al., Subassemblies and asymmetry in assembly of herpes simplex virus procapsid. *mBio* **6**, e01525–e15 (2015). doi: [10.1128/mBio.01525-15](#); pmid: [26443463](#)
- J. V. Spencer, W. W. Newcomb, D. R. Thomsen, F. L. Homa, J. C. Brown, Assembly of the herpes simplex virus capsid: Preformed triplexes bind to the nascent capsid. *J. Virol.* **72**, 3944–3951 (1998). pmid: [9557680](#)
- B. L. Trus et al., The herpes simplex virus procapsid: Structure, conformational changes upon maturation, and roles of the triplex proteins VP19c and VP23 in assembly. *J. Mol. Biol.* **263**, 447–462 (1996). doi: [10.1016/S0022-2836\(96\)80018-0](#); pmid: [8918600](#)
- J. Snijder et al., Vertex-specific proteins pUL17 and pUL25 mechanically reinforce herpes simplex virus capsids. *J. Virol.* **91**, e00123-17 (2017). doi: [10.1128/JVI.00123-17](#); pmid: [28381566](#)
- H. Granzow, B. G. Klupp, T. C. Mettenleiter, Entry of pseudorabies virus: An immunogold-labeling study. *J. Virol.* **79**, 3200–3205 (2005). doi: [10.1128/JVI.79.5.3200-3205.2005](#); pmid: [15709042](#)
- M. McElwee, F. Beilstein, M. Labetoulle, F. J. Rixon, D. Pasdeloup, Dyx11/1BPAG1 promotes plus-end-directed transport of herpes simplex virus 1 capsids on microtubules during entry. *J. Virol.* **87**, 11008–11018 (2013). doi: [10.1128/JVI.01633-13](#); pmid: [23903849](#)
- V. G. Preston, J. Murray, C. M. Preston, I. M. McDougall, N. D. Stow, The UL25 gene product of herpes simplex virus type 1 is involved in uncoating of the viral genome. *J. Virol.* **82**, 6654–6666 (2008). doi: [10.1128/JVI.00257-08](#); pmid: [18448531](#)
- D. Pasdeloup, D. Blondel, A. L. Isidro, F. J. Rixon, Herpesvirus capsid association with the nuclear pore complex and viral DNA release involve the nucleoporin CAN/Nup214 and the capsid protein pUL25. *J. Virol.* **83**, 6610–6623 (2009). doi: [10.1128/JVI.02655-08](#); pmid: [19386703](#)
- J. B. Huffman et al., The C terminus of the herpes simplex virus UL25 protein is required for release of viral genomes from capsids bound to nuclear pores. *J. Virol.* **91**, e00641-17 (2017). doi: [10.1128/JVI.00641-17](#); pmid: [28490590](#)
- B. G. Klupp, H. Granzow, G. M. Keil, T. C. Mettenleiter, The capsid-associated UL25 protein of the alphaherpesvirus pseudorabies virus is nonessential for cleavage and encapsidation of genomic DNA but is required for nuclear egress of capsids. *J. Virol.* **80**, 6235–6246 (2006). doi: [10.1128/JVI.02662-05](#); pmid: [16775311](#)
- K. Yang, J. D. Baines, Selection of HSV capsids for envelopment involves interaction between capsid surface components pUL31, pUL17, and pUL25. *Proc. Natl. Acad. Sci. U.S.A.* **108**, 14276–14281 (2011). doi: [10.1073/pnas.1108564108](#); pmid: [21821792](#)
- M. Leelawong, D. Guo, G. A. Smith, A physical link between the pseudorabies virus capsid and the nuclear egress complex. *J. Virol.* **85**, 11675–11684 (2011). doi: [10.1128/JVI.05614-11](#); pmid: [21880751](#)
- T. C. Mettenleiter, F. Müller, H. Granzow, B. G. Klupp, The way out: What we know and do not know about herpesvirus nuclear egress. *Cell. Microbiol.* **15**, 170–178 (2013). doi: [10.1111/cmi.12044](#); pmid: [23057731](#)
- W. W. Newcomb et al., The primary enveloped virion of herpes simplex virus 1: Its role in nuclear egress. *mBio* **8**, e00825-17 (2017). doi: [10.1128/mBio.00825-17](#); pmid: [28611252](#)
- P. J. Desai, A null mutation in the UL36 gene of herpes simplex virus type 1 results in accumulation of unenveloped DNA-filled capsids in the cytoplasm of infected cells. *J. Virol.* **74**, 11608–11618 (2000). doi: [10.1128/JVI.74.24.11608-11618.2000](#); pmid: [11090159](#)

50. B. G. Klupp, W. Fuchs, H. Granzow, R. Nixdorf, T. C. Mettenleiter, Pseudorabies virus UL36 tegument protein physically interacts with the UL37 protein. *J. Virol.* **76**, 3065–3071 (2002). doi: [10.1128/JVI.76.6.3065-3071.2002](https://doi.org/10.1128/JVI.76.6.3065-3071.2002); pmid: [11861875](https://pubmed.ncbi.nlm.nih.gov/11861875/)
51. B. Mijatov, A. L. Cunningham, R. J. Diefenbach, Residues F593 and E596 of HSV-1 tegument protein pUL36 (VP1/2) mediate binding of tegument protein pUL37. *Virology* **368**, 26–31 (2007). doi: [10.1016/j.virol.2007.07.005](https://doi.org/10.1016/j.virol.2007.07.005); pmid: [17651773](https://pubmed.ncbi.nlm.nih.gov/17651773/)
52. D. H. Ko, A. L. Cunningham, R. J. Diefenbach, The major determinant for addition of tegument protein pUL48 (VP16) to capsids in herpes simplex virus type 1 is the presence of the major tegument protein pUL36 (VP1/2). *J. Virol.* **84**, 1397–1405 (2010). doi: [10.1128/JVI.01721-09](https://doi.org/10.1128/JVI.01721-09); pmid: [19923173](https://pubmed.ncbi.nlm.nih.gov/19923173/)
53. Q. Zhu, R. J. Courtney, Chemical cross-linking of virion envelope and tegument proteins of herpes simplex virus type 1. *Virology* **204**, 590–599 (1994). doi: [10.1006/viro.1994.1573](https://doi.org/10.1006/viro.1994.1573); pmid: [7941326](https://pubmed.ncbi.nlm.nih.gov/7941326/)
54. S. T. Gross, C. A. Harley, D. W. Wilson, The cytoplasmic tail of herpes simplex virus glycoprotein H binds to the tegument protein VP16 in vitro and in vivo. *Virology* **317**, 1–12 (2003). doi: [10.1016/j.virol.2003.08.023](https://doi.org/10.1016/j.virol.2003.08.023); pmid: [14675620](https://pubmed.ncbi.nlm.nih.gov/14675620/)
55. D. E. Kamen, S. T. Gross, M. E. Girvin, D. W. Wilson, Structural basis for the physiological temperature dependence of the association of VP16 with the cytoplasmic tail of herpes simplex virus glycoprotein H. *J. Virol.* **79**, 6134–6141 (2005). doi: [10.1128/JVI.79.10.6134-6141.2005](https://doi.org/10.1128/JVI.79.10.6134-6141.2005); pmid: [15857998](https://pubmed.ncbi.nlm.nih.gov/15857998/)
56. N. Jambunathan *et al.*, Herpes simplex virus 1 protein UL37 interacts with viral glycoprotein gK and membrane protein UL20 and functions in cytoplasmic virion envelopment. *J. Virol.* **88**, 5927–5935 (2014). doi: [10.1128/JVI.00278-14](https://doi.org/10.1128/JVI.00278-14); pmid: [24600000](https://pubmed.ncbi.nlm.nih.gov/24600000/)
57. N. Scrima *et al.*, Insights into herpesvirus tegument organization from structural analyses of the 970 central residues of HSV-1 UL36 protein. *J. Biol. Chem.* **290**, 8820–8833 (2015). doi: [10.1074/jbc.M114.612838](https://doi.org/10.1074/jbc.M114.612838); pmid: [25678705](https://pubmed.ncbi.nlm.nih.gov/25678705/)
58. G. Woehlke, M. Schliwa, Walking on two heads: The many talents of kinesin. *Nat. Rev. Mol. Cell Biol.* **1**, 50–58 (2000). doi: [10.1038/35036069](https://doi.org/10.1038/35036069); pmid: [11413489](https://pubmed.ncbi.nlm.nih.gov/11413489/)
59. N. Hirokawa *et al.*, Submolecular domains of bovine brain kinesin identified by electron microscopy and monoclonal antibody decoration. *Cell* **56**, 867–878 (1989). doi: [10.1016/0092-8674\(89\)90691-0](https://doi.org/10.1016/0092-8674(89)90691-0); pmid: [2522351](https://pubmed.ncbi.nlm.nih.gov/2522351/)
60. F. J. Kull, E. P. Sablin, R. Lau, R. J. Fletterick, R. D. Vale, Crystal structure of the kinesin motor domain reveals a structural similarity to myosin. *Nature* **380**, 550–555 (1996). doi: [10.1038/380550a0](https://doi.org/10.1038/380550a0); pmid: [8606779](https://pubmed.ncbi.nlm.nih.gov/8606779/)
61. C. Suloway *et al.*, Automated molecular microscopy: The new Leginon system. *J. Struct. Biol.* **151**, 41–60 (2005). doi: [10.1016/j.jsb.2005.03.010](https://doi.org/10.1016/j.jsb.2005.03.010); pmid: [15890530](https://pubmed.ncbi.nlm.nih.gov/15890530/)
62. X. Li *et al.*, Electron counting and beam-induced motion correction enable near-atomic-resolution single-particle cryo-EM. *Nat. Methods* **10**, 584–590 (2013). doi: [10.1038/nmeth.2472](https://doi.org/10.1038/nmeth.2472); pmid: [23644547](https://pubmed.ncbi.nlm.nih.gov/23644547/)
63. J. A. Mindell, N. Grigorieff, Accurate determination of local defocus and specimen tilt in electron microscopy. *J. Struct. Biol.* **142**, 334–347 (2003). doi: [10.1016/S1047-8477\(03\)00069-8](https://doi.org/10.1016/S1047-8477(03)00069-8); pmid: [12781660](https://pubmed.ncbi.nlm.nih.gov/12781660/)
64. S. J. Ludtke, P. R. Baldwin, W. Chiu, EMAN: Semiautomated software for high-resolution single-particle reconstructions. *J. Struct. Biol.* **128**, 82–97 (1999). doi: [10.1006/jsbi.1999.4174](https://doi.org/10.1006/jsbi.1999.4174); pmid: [10600563](https://pubmed.ncbi.nlm.nih.gov/10600563/)
65. Y. Liang, E. Y. Ke, Z. H. Zhou, IMIRS: A high-resolution 3D reconstruction package integrated with a relational image database. *J. Struct. Biol.* **137**, 292–304 (2002). doi: [10.1016/S1047-8477\(02\)00014-X](https://doi.org/10.1016/S1047-8477(02)00014-X); pmid: [12096897](https://pubmed.ncbi.nlm.nih.gov/12096897/)
66. H. Liu *et al.*, Symmetry-adapted spherical harmonics method for high-resolution 3D single-particle reconstructions. *J. Struct. Biol.* **161**, 64–73 (2008). doi: [10.1016/j.jsb.2007.09.016](https://doi.org/10.1016/j.jsb.2007.09.016); pmid: [17977017](https://pubmed.ncbi.nlm.nih.gov/17977017/)
67. X. Zhang, X. Zhang, Z. H. Zhou, Low cost, high performance GPU computing solution for atomic resolution cryoEM single-particle reconstruction. *J. Struct. Biol.* **172**, 400–406 (2010). doi: [10.1016/j.jsb.2010.05.006](https://doi.org/10.1016/j.jsb.2010.05.006); pmid: [20493949](https://pubmed.ncbi.nlm.nih.gov/20493949/)
68. P. B. Rosenthal, R. Henderson, Optimal determination of particle orientation, absolute hand, and contrast loss in single-particle electron cryomicroscopy. *J. Mol. Biol.* **333**, 721–745 (2003). doi: [10.1016/j.jmb.2003.07.013](https://doi.org/10.1016/j.jmb.2003.07.013); pmid: [14568533](https://pubmed.ncbi.nlm.nih.gov/14568533/)
69. E. F. Pettersen *et al.*, UCSF Chimera—a visualization system for exploratory research and analysis. *J. Comput. Chem.* **25**, 1605–1612 (2004). doi: [10.1002/jcc.20084](https://doi.org/10.1002/jcc.20084); pmid: [15264254](https://pubmed.ncbi.nlm.nih.gov/15264254/)
70. P. Emsley, B. Lohkamp, W. G. Scott, K. Cowtan, Features and development of Coot. *Acta Crystallogr. D Biol. Crystallogr.* **66**, 486–501 (2010). doi: [10.1107/S0907444910007493](https://doi.org/10.1107/S0907444910007493); pmid: [20383002](https://pubmed.ncbi.nlm.nih.gov/20383002/)
71. P. D. Adams *et al.*, PHENIX: A comprehensive Python-based system for macromolecular structure solution. *Acta Crystallogr. D Biol. Crystallogr.* **66**, 213–221 (2010). doi: [10.1107/S0907444909052925](https://doi.org/10.1107/S0907444909052925); pmid: [20124702](https://pubmed.ncbi.nlm.nih.gov/20124702/)
72. B. R. Bowman, M. L. Baker, F. J. Rixon, W. Chiu, F. A. Quiocho, Structure of the herpesvirus major capsid protein. *EMBO J.* **22**, 757–765 (2003). doi: [10.1093/emboj/cdg086](https://doi.org/10.1093/emboj/cdg086); pmid: [12574112](https://pubmed.ncbi.nlm.nih.gov/12574112/)
73. X. Zhang, Z. H. Zhou, Limiting factors in atomic resolution cryo electron microscopy: No simple tricks. *J. Struct. Biol.* **175**, 253–263 (2011). doi: [10.1016/j.jsb.2011.05.004](https://doi.org/10.1016/j.jsb.2011.05.004); pmid: [21627992](https://pubmed.ncbi.nlm.nih.gov/21627992/)
74. S. L. Ilca *et al.*, Localized reconstruction of subunits from electron cryomicroscopy images of macromolecular complexes. *Nat. Commun.* **6**, 8843 (2015). doi: [10.1038/ncomms9843](https://doi.org/10.1038/ncomms9843); pmid: [26534841](https://pubmed.ncbi.nlm.nih.gov/26534841/)
75. S. H. Scheres, RELION: Implementation of a Bayesian approach to cryo-EM structure determination. *J. Struct. Biol.* **180**, 519–530 (2012). doi: [10.1016/j.jsb.2012.09.006](https://doi.org/10.1016/j.jsb.2012.09.006); pmid: [23000701](https://pubmed.ncbi.nlm.nih.gov/23000701/)

ACKNOWLEDGMENTS

We thank S. Shivakoti for assistance in sample preparation, X. Zhang and Y. Liu for assistance in data processing, J. Jih for advice in modeling and movie production, L. J. Wang for assistance in figure preparation, and both L. J. Wang and S. Ye for critical reading of the manuscript. **Funding:** This project was supported in part by grants from the NIH (GM071940, DE025567, and AI094386). We acknowledge the use of instruments at the Electron Imaging Center for Nanomachines [supported by the University of California, Los Angeles, and by instrumentation grants from the NIH (1S100D018111, 1U24GM116792) and NSF (DBI-1338135, DMR-1548924)]. X.D. was supported in part by fellowships from the China Scholarship Council. **Author contributions:** Z.H.Z. and X.D. conceived the project, performed the experiment, interpreted the data, and wrote the paper. **Competing interests:** None declared. **Data and materials availability:** Coordinates and EM maps are available at the PDB and the Electron Microscopy Data Bank (EMDB), respectively, under the accession numbers PDB 6CGR, EMD-7472, and EMD-7473. All other data to support the conclusions are in the main paper or supplementary materials.

SUPPLEMENTARY MATERIALS

www.sciencemag.org/content/360/6384/eaao7298/suppl/DC1
Figs. S1 to S9
References (76, 77)

21 August 2017; accepted 23 February 2018
10.1126/science.aao7298

RESEARCH ARTICLE SUMMARY

STRUCTURAL BIOLOGY

Cryo-EM structure of a herpesvirus capsid at 3.1 Å

Shuai Yuan,* Jialing Wang,* Dongjie Zhu,* Nan Wang, Qiang Gao, Wenyuan Chen, Hao Tang, Junzhi Wang,† Xinzheng Zhang,† Hongrong Liu,† Zihe Rao,† Xiangxi Wang†

INTRODUCTION: Herpes simplex virus type 2 (HSV-2) is a sexually transmitted virus and is the leading causative agent of genital ulcer disease (GUD) worldwide. Patients with HSV-2 have a higher risk of acquiring human immunodeficiency virus (HIV) infection. HSV-2, as well as the closely related herpes simplex virus 1 (HSV-1), are simplexviruses with a natural-host range restricted to humans, belonging to the family of *Herpesviridae*, whose other members are responsible for a number of diseases, including congenital disorders (e.g., human cytomegalovirus) and even cancers (e.g., Epstein-Barr virus

and Kaposi sarcoma herpesvirus). HSVs' ability to establish a lifelong latent infection within hosts and recurrent reactivation from latency make them highly effective pathogens with seropositivity rates close to 100% in adult populations.

RATIONALE: The herpesvirus virion is genetically and structurally one of the largest and most complex viruses known. It has a $T = 16$ (triangulation number) icosahedral capsid with a diameter of ~125 nm that not only protects the viral genome physically from damage but

also plays an important role in the release of viral genome into the nucleus of the host cell. HSV capsid assembly requires the ordered packing of about 4000 protein subunits into the hexons, pentons, and triplexes that comprise the capsid. Previous studies have suggested that the directionality of triplexes on the capsid shell and disulfide bond formation between capsid proteins contribute to HSV capsid assembly, but in the absence of an atomic description of HSV capsids, the molecular basis that drives capsid assembly has remained elusive.

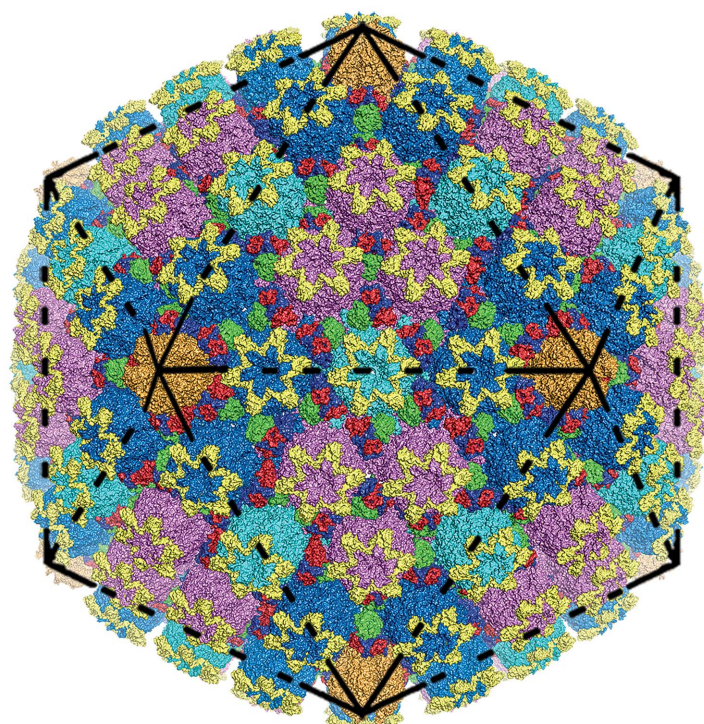
RESULTS: By using a “block-based” image reconstruction approach combined with a

ON OUR WEBSITE

Read the full article at <http://dx.doi.org/10.1126/science.aao7283>

Ewald sphere correction, we have visualized the HSV capsid at 3.1-Å resolution by cryo-electron microscopy (cryo-EM) and have built an atomic structure, which includes 28,138 residues in the asymmetric unit, belonging to 46 different conformers of four capsid proteins (VP5, VP23, VP19C, and VP26). These organize into three types of hexons (central, peripentonal, and edge) that contain the major capsid protein VP5 and the small capsid protein VP26, pentons made up of VP5, and triplexes composed of VP23 and VP19C. Acting as core organizers, VP5 proteins form extensive intermolecular networks, involving disulfide bonds (25 per asymmetric unit) and noncovalent interactions, with VP26 proteins and triplexes, that underpin capsid stability and assembly. Together with previous low-resolution structural results, we propose a model for the ordered assembly of the capsid using basic assembly units (a triplex and its covalently linked lasso triangle formed by three VP5s), which then cluster into higher-order structures conforming to twofold symmetry and guide nascent assembly intermediates into the correct $T = 16$ geometry.

CONCLUSION: The marked improvement in the resolution of the structure of the herpesvirus capsid determined by cryo-EM allows the first steps toward understanding the drivers of assembly and the basis of stability of the capsid. In addition, the atomic structure could guide rational design of therapeutic agents for treating tumors and therapeutic strategies against HSV. ■



A 3.1-Å structure of HSV-2 B capsid. Surface representation of HSV-2's 1250-Å-wide capsid. Black lines represent particle icosahedral facets.

The list of author affiliations is available in the full article online.

*These authors contributed equally to this work.

†Corresponding author. Email: xiangxi@ibp.ac.cn (X.W.); hrliu@hunn.edu.cn (H.L.); xzhang@ibp.ac.cn (X.Z.); wangjz@nicpbp.org.cn (J.-Z.W.); raozh@tsinghua.edu.cn (Z.R.)

Cite this article as S. Yuan *et al.*, *Science* **360**, eaao7283 (2018). DOI: 10.1126/science.aao7283

RESEARCH ARTICLE

STRUCTURAL BIOLOGY

Cryo-EM structure of a herpesvirus capsid at 3.1 Å

Shuai Yuan,^{1,2*} Jialing Wang,^{1,2*} Dongjie Zhu,^{1,6*} Nan Wang,^{1,2} Qiang Gao,^{1,5}
Wenyuan Chen,³ Hao Tang,³ Junzhi Wang,^{4†} Xinzhen Zhang,^{1,2†} Hongrong Liu,^{3†}
Zihe Rao,^{1,2,7,8,9†} Xiangxi Wang^{1,2†}

Structurally and genetically, human herpesviruses are among the largest and most complex of viruses. Using cryo-electron microscopy (cryo-EM) with an optimized image reconstruction strategy, we report the herpes simplex virus type 2 (HSV-2) capsid structure at 3.1 angstroms, which is built up of about 3000 proteins organized into three types of hexons (central, peripentonal, and edge), pentons, and triplexes. Both hexons and pentons contain the major capsid protein, VP5; hexons also contain a small capsid protein, VP26; and triplexes comprise VP23 and VP19C. Acting as core organizers, VP5 proteins form extensive intermolecular networks, involving multiple disulfide bonds (about 1500 in total) and noncovalent interactions, with VP26 proteins and triplexes that underpin capsid stability and assembly. Conformational adaptations of these proteins induced by their microenvironments lead to 46 different conformers that assemble into a massive quasymmetric shell, exemplifying the structural and functional complexity of HSV.

Herpesviridae is a large family of double-stranded DNA (dsDNA) viruses that cause a number of diseases such as encephalitis, oral and genital blisters, congenital disorders, and even cancers (1). During the course of these infections, a key survival tactic of herpesvirus is to establish a chronic latent infection within the host (2). Consequently, herpesviruses are highly persistent pathogens with seropositivity rates close to 100% in adult populations (3). Herpes simplex virus type 2 (HSV-2) is a sexually transmitted virus and is currently the leading causative agent of genital ulcer disease (GUD) worldwide. Patients with HSV-2 have a higher risk of acquiring human immunodeficiency virus (HIV) infection (4–6).

The herpesvirus virion is one of the largest viruses known and is genetically and structurally one of the most complex. It has a diameter of ~200 nm and comprises four structurally distinct

layers: a glycoprotein-bound envelope, an amorphous protein layer called the tegument, an icosahedral capsid, and at the core a large DNA genome. The capsid not only protects the viral genome from damage but also plays an important role in the release of viral genome into the nucleus of the host cell (7). The capsid initially assembles as a precursor procapsid that matures during DNA packing (8–10). The assembly of a procapsid requires components of the capsid shell and inner scaffold protein, pre-VP22a, a major component of the procapsid that is not present in the mature virion. After that, the procapsid matures through a major structural transformation triggered by limited cleavage of the C-terminal 25 amino acids of scaffold proteins, which are then removed, possibly during entry of DNA into the capsid (8, 11).

Three distinct types of capsids—called A, B, and C capsids—have been detected in lysates of infected cells (12). A capsids are empty and result from abortive DNA packing, B capsids contain a core of scaffold proteins, but no DNA, and C capsids, also known as mature capsids, are fully packed with DNA. B capsids retain a cleaved form of the scaffold proteins, suggesting that the capsid is either in the process of packaging or that the scaffold was not removed in time to allow DNA packaging (13). B capsids may be intermediates in viral assembly or abortive capsid forms generated as a result of unsuccessful proteolytic digestion of scaffold proteins or a failed attempt to package viral DNA. All three types of capsids have icosahedrally symmetric shells (triangulation number of $T = 16$) composed primarily of 955 copies of the 150-kDa major capsid protein, VP5, arranged as 150 hexons (on the triangular edges and faces) and 11 pentons

(on all but one vertex) (14). Other critical components include the dodecameric pUL6 portal complex, which occupies the twelfth vertex; 320 copies of the “triplex” that consists of two copies of VP23 and one copy of VP19C and connects adjacent capsomers located on the capsid (15); 900 copies of VP26, which is one of the components of the outer surface of hexons but not pentons (16). Compared with A and B capsids, C capsids have substantially higher occupancy of the capsid vertex-specific component (CVSC) (a putative heterotrimer consisting of the pUL17, pUL25, and pUL36 proteins) that binds specifically to triplexes adjacent to pentons (17). In addition to the shell proteins mentioned above, B capsids contain a large amount of the scaffold protein VP22a, which is produced by the UL26.5 gene, and smaller amounts of the two proteins coded by the UL26 gene (18). The UL26-encoded protease cleaves itself between amino acids 247 and 248, which separates pUL26 into an N-terminal domain bearing the protease called VP24 and a C-terminal domain called VP21 (19). The pathway for the assembly of mature capsids of herpesvirus has striking parallels with those of dsDNA bacteriophages (20). Furthermore, herpesviruses, although more complex, share the canonical HK97 capsid protein fold with the dsDNA tailed bacteriophage, indicative of common ancestry (21).

Efforts of many investigators over two decades have pushed the resolution of cryo-electron microscopy (cryo-EM) analysis of herpesvirus capsid from 15 to 6 Å (14, 15, 22–24). More recently, a 3.9-Å structure of human cytomegalovirus (HCMV) (a member of the *Herpesvirinae* family belonging to the β -herpesvirinae subfamily) capsid was reported (25). We have determined the structure of HSV-2 B capsid to 3.1 Å by using a combination of “block-based” reconstruction and accurate Ewald sphere corrections and have built reliable atomic models for the capsid, which provide insights into its stability and assembly.

Characterization and structure determination

HSV-2 (MS strain) was grown in Vero cells at 37°C and purified by a series of ultracentrifugation steps (see materials and methods). Because the cryo-EM imaging of such large intact HSV virions (>200 nm in diameter) would lead to low signal-to-noise ratios and a depth-of-field gradient through the virions, we purified HSV-2 capsids in the presence of detergents. Three types of capsid of HSV-2 were separated by ultracentrifugation and characterized as 713S A capsid; 924S B capsid and 1205S C capsid (fig. S1). Cryo-EM micrographs of the purified HSV-2 A, B, and C capsids were recorded using an FEI Titan Krios electron microscope equipped with a Falcon detector (fig. S1). A comparison of reconstructions of these three particle types at 8-Å resolution reveals an overall similar morphology for A, B, and C capsids. But, the presence of a scaffold core with a diameter of ~660 Å is observed in the B capsid. Further, in the C capsid, the dsDNA, seen as regularly spaced density shells (~25 Å apart), and the CVSC are observed (Fig. 1A).

¹National Laboratory of Macromolecules, Institute of Biophysics, Chinese Academy of Sciences, Beijing, 100101, China. ²University of Chinese Academy of Sciences, Beijing, 100049, China. ³College of Physics and Information Science, Synergetic Innovation Center for Quantum Effects and Applications, Hunan Normal University, Changsha, 410081, Hunan, China. ⁴National Institutes for Food and Drug Control, No. 2, Tiantanxili, Beijing, 100050, China. ⁵Sinovac Biotech Co., Ltd., Beijing, 100085, China. ⁶School of Life Science, University of Science and Technology of China, Hefei, 230026, China. ⁷Shanghai Institute for Advanced Immunochemical Studies, ShanghaiTech University, Shanghai, 201210, China. ⁸State Key Laboratory of Medicinal Chemical Biology, Nankai University, Tianjin 300353, China. ⁹Laboratory of Structural Biology, School of Medicine, Tsinghua University, Beijing, 100084, China.

*These authors contributed equally to this work.

†Corresponding author. Email: xiangxi@ibp.ac.cn (X.X.W.); hrlui@hnu.edu.cn (H.L.); xzhang@ibp.ac.cn (X.Z.); wangjiz@nicb.org.cn (J.-Z.W.); raozh@tsinghua.edu.cn (Z.R.)

Normal reconstruction strategies yield a reconstruction of ~4-Å resolution with icosahedral symmetry imposed. There are two bottlenecks that limit the cryo-EM resolution of this 1250-Å-diameter virus. First, the complex architecture of the virus does not strictly conform to the icosahedral symmetry. This could be due to the intrinsic structural flexibility associated with the particle or structural perturbation caused by ultracentrifugation during the purification process. Second, the gradient in defocus through the capsid arising from the large size of the virus limits the attainable resolution. To overcome these two problems, we developed a reconstruction method named block-based reconstruction, which together with accurate Ewald sphere corrections (see materials and methods), resulted in a 3.1-Å structure of B capsid (Fourier shell correlation = 0.143 criterion) (26) after processing 45,000 particles (Fig. 1B and fig. S2). The backbone of the polypeptide, as well as many side chains, was clearly defined (Fig. 1C), allowing an atomic model of the HSV capsid shell comprising the four capsid proteins VP5, VP26, VP23, and VP19C to be built de novo (figs. S3 to S5). The model was refined and validated using standard x-ray crystallographic metrics (table S1). An asymmetric unit consists of 16 copies of VP5—which exist in a C-Hex (central hexon), a P-Hex (peripentonal hexon), one-half of an E-Hex (edge hexon) and one-fifth of a Pen—and 15 copies of VP26 and 5^L/₃ triplexes (Ta, Tb, Tc, Td, Te, and one-third of Tf, located at the threefold axis) (Fig. 1B). In our atomic model, the asymmetric unit contains all 16 copies of VP5, 15 copies of VP26, and 5 triplexes (Ta, Tb, Tc, Td, and Te) (fig. S2C). The Tf triplex is on the icosahedral threefold axis; thus, densities for Tf were destroyed during the icosahedral averaging (fig. S2C).

VP5 structure and protrusion features

The 150-kDa major capsid protein (VP5) forms both the hexons and pentons and acts as a core organizer in the assembly of the capsids. None of the 16 copies of VP5 in the asymmetric unit are identical (fig. S6), suggesting that the microenvironments surrounding each subunit in the $T = 16$ icosahedral capsid are not strictly equivalent, which is consistent with the basis of quasi-equivalent packing. Structure-based phylogenetic analysis using Structure Homology Program (SHP) software places P1 and P6 (subunits from C-Hex, P-Hex, E-Hex, and Pen denoted as C1 to C6, P1 to P6, E1 to E6, and Pen1 to Pen5, respectively) between typical hexon- and penton-type VP5s (Fig. 2A) (27). As the major capsid protein in HCMV, each VP5 can be divided into seven domains: upper (residues 482 to 1047), channel (residues 407 to 481 and 1332 to 1374), buttress (residues 1123 to 1331), helix-hairpin (residues 195 to 237), Johnson-fold [residues 71 to 194, 238 to 294, 372 to 406, and 1048 to 1122, a characteristic fold first identified in bacteriophage HK97 gp5 (28)], dimerization (residues 295 to 371), and N-lasso (residues 1 to 70), which constitute three sections: upper, middle (channel, buttress, and helix-hairpin) and lower (Johnson-fold,

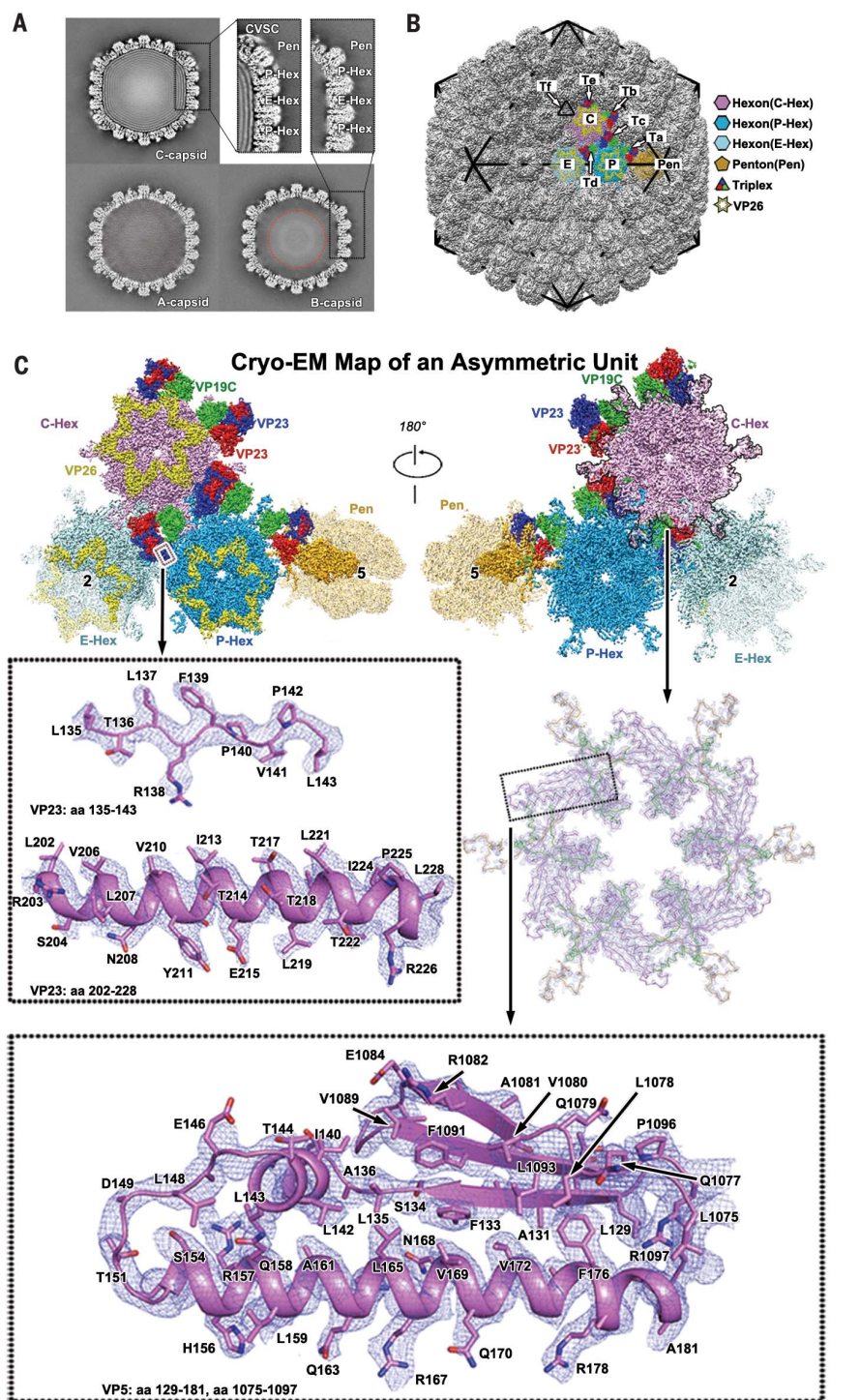


Fig. 1. Architecture of the HSV-2 B capsid. (A) Central slices of HSV-2 A-, B- and C-capsid reconstructions at 8 Å. The insets show dsDNA density and CVSC density. The scaffold core is marked with a red dotted circle. P-Hex (peripentonal), C-Hex (central), E-Hex (edge), and Pen (penton) denote hexons and pentons, respectively. (B) Locations of the various components of the capsid in the cryo-EM map of HSV-2 B capsid. Black lines, particle facets. The threefold icosahedral symmetry axis is marked as a triangle. P (peripentonal), C (center), and E (edge) denote hexons, and Ta to Tf denote triplexes. (C) Cryo-EM map of an asymmetric unit and local electron density maps are shown. The inset shows the density maps (mesh) and atomic models of VP5 and VP23, which illustrate side-chain features. Residues with side chains are labeled; aa denotes amino acids. Single-letter abbreviations for the amino acid residues are as follows: A, Ala; C, Cys; D, Asp; E, Glu; F, Phe; G, Gly; H, His; I, Ile; K, Lys; L, Leu; M, Met; N, Asn; P, Pro; Q, Gln; R, Arg; S, Ser; T, Thr; V, Val; W, Trp; and Y, Tyr.

dimerization, and N-lasso) (Fig. 2B and fig. S7). The upper and middle sections make up the capsid protrusions, whereas the lower section forms the capsid floor (Fig. 2, B and C). A comparison of typical hexon- and penton-type VP5s shows highly conserved upper and middle domains but reveals a conformational change in the lower section that has implications for the differences in assemblies of the penton and the hexon (Fig. 2B). The conformational changes include a $\sim 20^\circ$ counterclockwise rotation of the central helix and a $\sim 25^\circ$ clockwise rotation of the E loop, which straightens the subunit and increases the curvature of the lower shell of the penton. In addition, in the penton, the refolding of the N-lasso leads to formation of a β -hairpin (β A2 and β B1), decreasing its protrusion by ~ 25 Å

in comparison with hexon-VP5, whereas reorganization of the dimerization domain creates a 41-Å-long helix (α N), lining the inner capsid surface beneath the penton, yielding a comparatively slim penton with a greater height of ~ 170 Å and a reduced external diameter of ~ 160 Å at the “lower” end, relative to those in the hexon (Fig. 2, B and C, and Movie 1).

Despite the overall similarities between the channel domains, the axial channels comprising the β -sheet ring within hexons and pentons show distinct differences. The narrowest region of the hexon channel has an internal diameter of ~ 10 Å, whereas the penton channel is completely blocked by five histidine residues (His 419) (Fig. 2C); this contrasts with the HCMV penton, which has a ~ 14 -Å-diameter channel (fig. S8). Further, the

hexon channel is remarkably negatively charged (fig. S8). In contrast, the bottom of the penton channel presents more positive charges, indicating a possible role for this region in interactions with the genomic DNA (fig. S8). The electrostatic surface properties of the channel of the hexon and penton are appreciably different in HCMV, suggesting a distinctive role for the hexon channel in accommodating DNA (25). In addition to the channel domain, the upper domains of hexons and pentons make different contacts (fig. S9).

Adaptations of P-Hex

While surrounding the penton, P-Hex is also adjacent to neighboring hexons (Fig. 3A). Given the fact that the penton exhibits a distinct pattern of assembly compared with the typical hexon, subunits within P-Hex have to adopt conformational changes to allow three distinct interactions: with typical hexons, with pentons, and with themselves (Fig. 3A). Overall, the structure of the P-Hex resembles that of the typical hexon, with an indistinguishable external surface but with differences in the inner protein shell (Fig. 3B). Among the six copies of VP5 of the P-Hex, four are similar to the typical hexon-type VP5, whereas P1 and P6, adjacent to the penton, exhibit notable conformational changes at the N-lasso and dimerization domains (Fig. 3B and Movie 1). A superposition of P1 as well as P6 onto C1 and Pen1 shows that P6 is similar to Pen1 around the dimerization domain, where they both have a 41-Å-long helix, whereas the N-lasso domain of P6 is more similar to that of C1. Conversely, P1 and C1 share common structural features at the dimerization domain, whereas P1 adopts an analogous fold to the N-lasso domain of Pen1 (Fig. 3C). These adaptations in P1 and P6 contribute to enhanced interactions of P-Hex with the penton. Although the penton VP5 (Pen5) loses its lasso to an adjacent P6 (P-Hex), it establishes new quasi-equivalent twofold interactions with a P1 N-lasso domain, which would normally clasp a neighboring penton VP5 (Pen1) but instead adopts a short

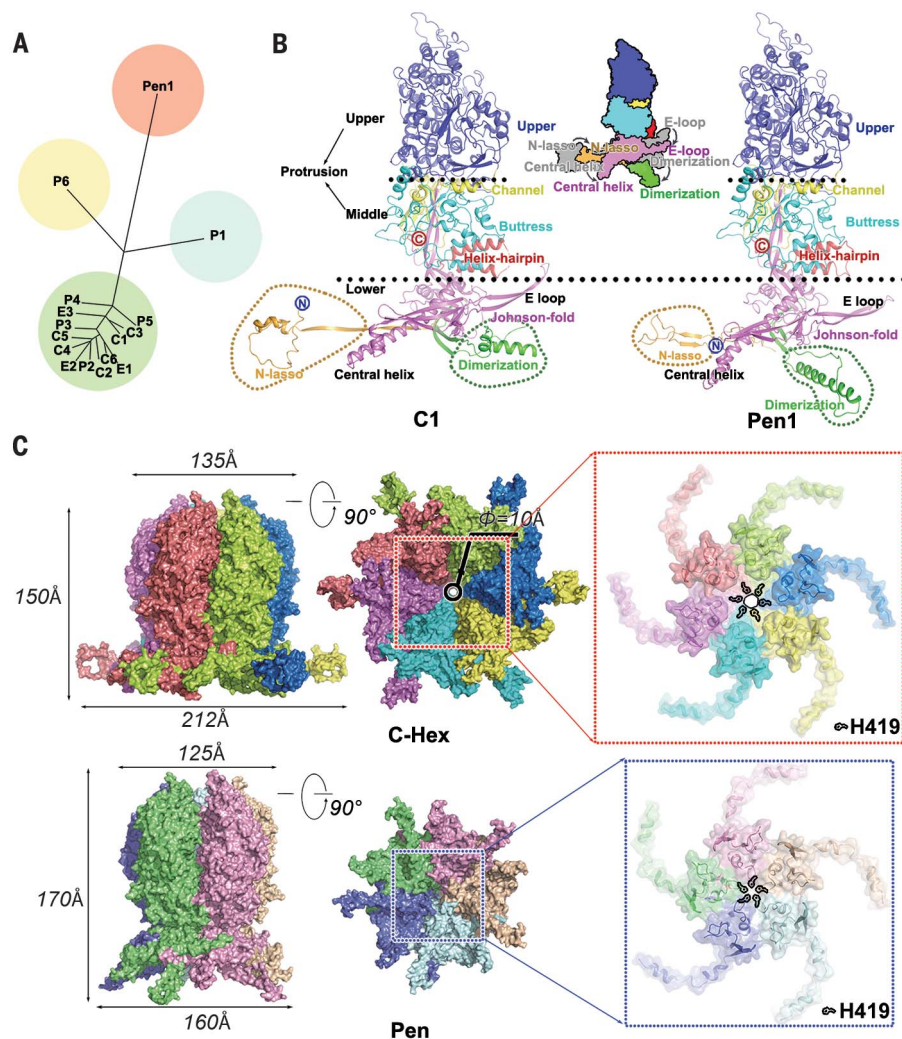
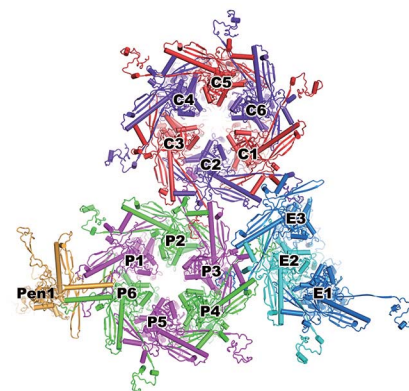


Fig. 2. Structure and organization of VP5. (A) Structure-based phylogenetic tree of 16 copies of VP5 present in an asymmetric unit. (B) Ribbon diagram of the typical hexon- and penton-VP5. N and C termini are labeled, and major conformational changes are marked with dashed lines. A model shown in the middle depicts the conformational changes. The upper and middle sections make up the capsid protrusions. (C) Comparison of the surface of C-Hex (up) and the Pen (down); side view (left) and top view (middle) are shown. Each subunit is depicted in a different color. Insets illustrate the differences in the central channel. The residues lining the narrowest region of the central channel are marked and labeled.



Movie 1. Structures of four types of VP5 conformers. Atomic models of the four types of VP5 conformers are colored by domain. The domains with significant conformational changes are highlighted.

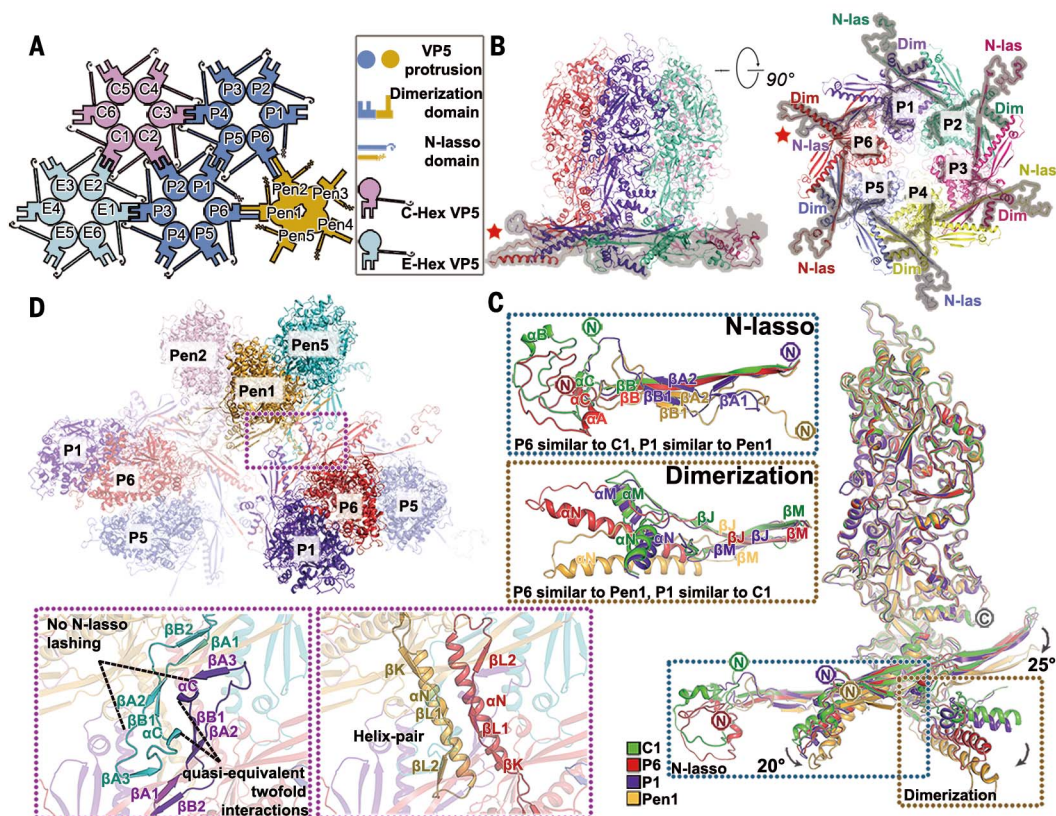
Fig. 3. Conformational adaptations of P-Hex.

(A) Schematic diagram of the binding mode of different capsomers. Domains with significant conformational differences (dimerization and N-lasso domains) in the floor of the capsid are highlighted.

(B) Ribbon diagram of the side view (left) and the bottom view (right) of P-Hex. The N-lasso and dimerization domains are labeled and highlighted. The red star indicates the region where the conformational adaptations occur.

(C) A superposition of C1, P1, P6, and Pen1. At N-lasso domain, P6 is similar to C1, and P1 is similar to penton-VP5. P1 and C1 share common structural features near the dimerization domain; P6 adopts folds similar to those of penton-VP5.

(D) Overview of penton, P1, P6, and P5. The insets demonstrate how the local geometry changes near the fivefold axis. The Pen5 VP5 establishes new quasi-equivalent twofold interactions with a P1 N-lasso domain instead of its lasso to an adjacent P6. A novel helix pair is formed by two long α N helices from the dimerization domain of Pen1 and P6.



N-lasso fold (Fig. 3D). In addition, a novel helix pair comprising two long α N helices from the dimerization domain of Pen1 and P-Hex (formed by β A2 and β B1 from P1 and β D, β E, and β L1 from P6) form quasi-equivalent twofold interactions, further strengthening the contacts between the penton and P-Hex (Fig. 4C). Hexon-hexon interactions occur between four VP5s and are characterized by the lassoing of the N-lasso domain of P3 and C3 and the quasi-equivalent dimerization between the two pairs of helices (α M and α N) in the dimerization domain of P2 and C2 (Fig. 4D). The N-lasso (e.g., C3) protrudes out and clasps β B (P3' N-lasso), and β D and β E (P2's E loop) across a quasi-twofold axis (Fig. 4D). In the same place, β A joins β B, β D, and β E to form a four-stranded β sheet (Fig. 4D). In addition, three sets of N-lasso interactions form an enclosed triangle around quasi-threefold axes, firmly connecting three hexons (Fig. 4E). Overall, hexon-hexon contact areas are ~35% larger than penton-hexon interaction areas, probably accounting for the vulnerability of pentonal vertices in HSV capsids (29).

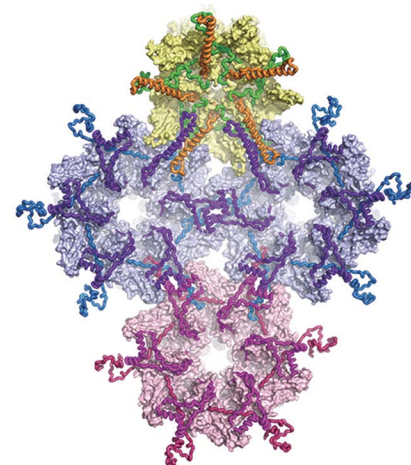
Extensive interactions at the inner capsid surface

The HSV capsid shell is assembled via extensive interactions of the lower sections of VP5, including both intracapsomer and intercapsomer interactions (Fig. 4 and Movie 2). In the penton, an archetypal example is between Pen4 and Pen5. β strands (β B1 and β A2) from Pen4's N-lasso domain, together with β strands (β D and β E) from Pen5's E loop and β L1 from Pen5's dimerization domain, form a five-stranded β sheet, which is further stabilized by Pen5's α N (Fig. 4A). In the hexon, β B from P3' and β D, β E, and β L from P2' make up a four-stranded β sheet (Fig. 4B). Two types of intercapsomer interactions, Pen-P-Hex and hexon-hexon, are observed. Regarding the former, a helix pair comprising two long α N helices from the dimerization domain of a penton subunit and an opposing P-Hex subunit (P6) is further stabilized by two adjacent central helices (α G), firmly holding the penton and the P-Hex together (Fig. 4C). Additionally, Pen1's α E and P1's α F form a small helix pair, as do Pen5's α F and P6's α E (Fig. 4C). Moreover, two sets of five-stranded β sheet beneath the helix pair from the

Pen (formed by β A2 and β B1 from Pen5 and β D, β E, and β L1 from Pen1) and P-Hex (formed by β A2 and β B1 from P1 and β D, β E, and β L1 from P6) form quasi-equivalent twofold interactions, further strengthening the contacts between the penton and P-Hex (Fig. 4C). Hexon-hexon interactions occur between four VP5s and are characterized by the lassoing of the N-lasso domain of P3 and C3 and the quasi-equivalent dimerization between the two pairs of helices (α M and α N) in the dimerization domain of P2 and C2 (Fig. 4D). The N-lasso (e.g., C3) protrudes out and clasps β B (P3' N-lasso), and β D and β E (P2's E loop) across a quasi-twofold axis (Fig. 4D). In the same place, β A joins β B, β D, and β E to form a four-stranded β sheet (Fig. 4D). In addition, three sets of N-lasso interactions form an enclosed triangle around quasi-threefold axes, firmly connecting three hexons (Fig. 4E). Overall, hexon-hexon contact areas are ~35% larger than penton-hexon interaction areas, probably accounting for the vulnerability of pentonal vertices in HSV capsids (29).

VP26 caps hexons only

VP26 (112 residues in length), one of the components of the outer surface of HSV capsids, is ~50% larger than its homolog SCP in HCMV. Unlike HCMV, where SCPs bind both hexons and pentons (30), VP26 only caps hexons (Fig. 5A) in HSV. VP26 of HSV exhibits no significant structural similarity with SCP. VP26 comprises an N-terminal domain of an "M" loop plus α A and



Movie 2. Extensive interactions at the inner capsid surface.

One copy of the penton, two copies of the P-Hex, and one copy of the C-Hex are shown. Each subunit participating in the interactions is outlined in different colors. Major secondary structural elements are also labeled in different colors based on the subunits that they come from.

a C-terminal domain of α B along with a long insertion loop. The two domains are connected by the extension loop (Fig. 5A). The C-terminal domain plays essential roles in capping hexons through two regions: (i) α B and one half of the

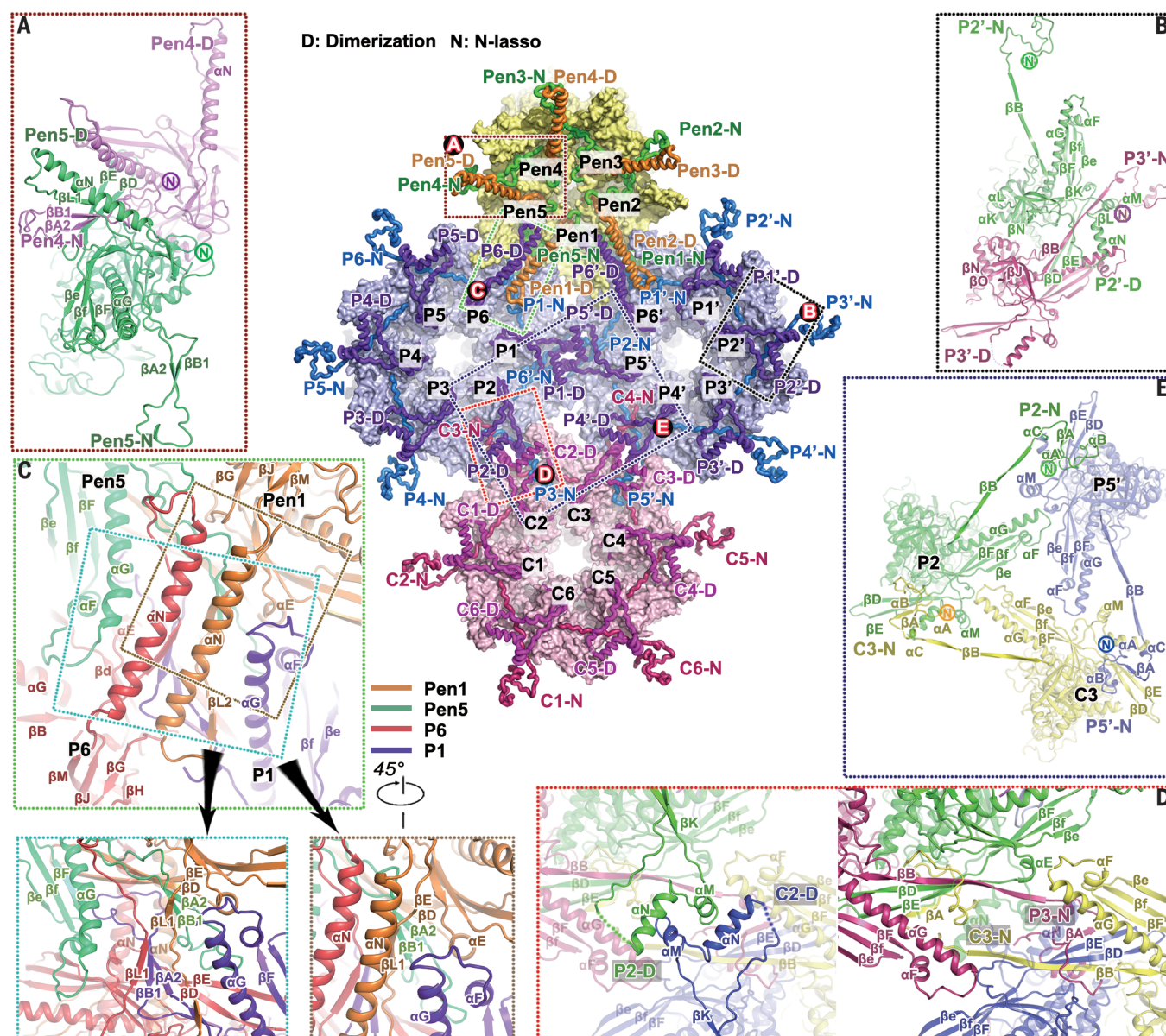


Fig. 4. Overview of the interactions at the inner capsid surface.

A schematic representation of the inner surface of the capsid structure is shown. The N-lasso domain and the dimerization domain of each subunit are shown as cartoons, whereas the remaining structure is rendered as a surface. One copy of the Pen, two copies of the P-Hex, and one copy of the

C-Hex are shown. The view is from the inside of the capsid. (A to E) Enlarged views of the interactions (boxed) are shown with secondary structural elements colored and labeled. Each subunit participating in the interactions is depicted in a different color and labeled. (A) and (B) are intracapsomer interactions; (C) to (E) are intercapsomer interactions.

insertion loop insert into the cleft formed by two adjacent hexon-VP5 upper domains and make hydrophobic interactions; (ii) the second half of the insertion loop accesses a shallow cleft in the adjacent hexon-VP5 upper domain beneath the extension loop of the adjacent VP26 and interacts through charge and hydrophilic interactions (Fig. 5A). In the N-terminal domain, only αA interacts with the hexon-VP5 upper domain (Fig. 5A). Our structural analysis is consistent with a previously reported mutagenesis study of HSV-1 VP26, which showed that resi-

dues 50 to 112 are sufficient for binding hexons (31). To find out if there are any structural constraints that prevent VP26s from capping pentons, we superimposed the structure of the hexon-VP5 upper domain bound to VP26 onto the penton-VP5 upper domain. The analysis suggested a complete loss of interactions between VP26 and the adjacent VP26 and significantly reduced contacts with the adjacent VP5 (Fig. 5B). Therefore, VP26 can only cap hexons, but not pentons. Six copies of VP26 form a ring structure by end-to-end interactions, filling the gaps between the

heads of neighboring subunits in a hexon and further stabilizing hexons.

The triplex and its interactions with VP5s

The triplex, a structural feature of herpesvirus capsid shells, consists of two VP23 conformers (denoted as VP23-1 and VP23-2) and one copy of VP19C and lies among three adjacent capsomers, linking them together (Fig. 6A and Movie 3). From the bottom view, the triplex adopts a trimeric arrangement to match the quasi-threefold

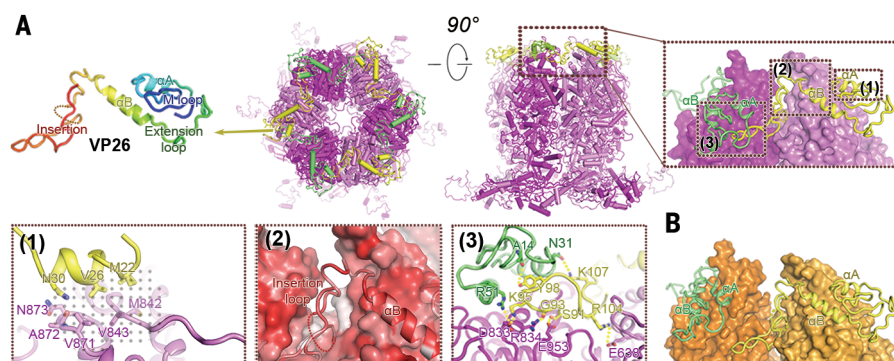


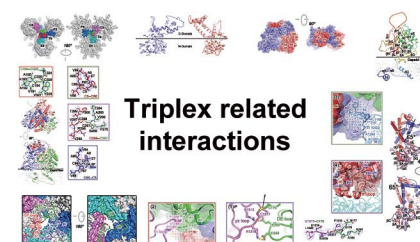
Fig. 5. VP26 structure and its interactions with VP5. (A) VP26s cap the hexon but not the penton. One set of VP5 and VP26 is colored in light tone; the adjacent set of VP5 and VP26 is colored in bright tone. The rainbow ribbon of VP26 is shown in the leftmost panel of the first row. Enlarged views of interactions (1) to (3) (boxed) are shown. Residues involved in the interactions are shown as sticks in (1) and (3), with VP5 colored in violet (light violet for the adjacent VP5) and VP26 colored in green (light green for the adjacent VP26). In (2), VP5s and VP26s are shown as surface representations and cartoons, respectively, which are colored by residues' hydrophobic characters: hydrophobic (red) to hydrophilic (white) gradient. **(B)** The superposed model of penton-VP26s based on the complex structure of hexon-VP26s. The penton is represented as surface, and VP26s are shown as cartoons. The secondary structural elements are colored and labeled. The neighboring VP5s are colored in brown and light brown, and the corresponding VP26s are colored in green and light green, respectively.

symmetrical environment (Fig. 6A). Overall, the triplex is relatively compact and rigid; the structure being reinforced by four pairs of disulfide bonds (C5-C86 within VP23-1 and VP23-2, C194-C325 within VP19C, and C267-C298 between VP19C and VP23-1) (Fig. 6B and fig. S10). The two copies of VP23 have an $\alpha\beta$ fold, comprising an N domain (residues 1 to 144 and 291 to 318) and a C domain (residues 145 to 290), which form the lower and the upper portions, respectively (Fig. 6C). VP23-1 and VP23-2 interact through a number of helices (αF - αJ) in the C domain (Fig. 6D). Interestingly, the conformations of VP23-1 and VP23-2 differ in the C domain due to a $\sim 65^\circ$ rotation of the αI (αI in VP23-1 becomes two helices, αI and αJ , in VP23-2) helix and a large rearrangement of the αF - αH region. However, the two N domains are very similar (Fig. 6E). VP19C, ~ 150 residues longer than VP23, makes up the third component of the trimeric fold. A disulfide bond (C267-C298 between VP19C and VP23-1) and helix bundle interactions (including αD and αI from VP19C, αE from VP23-1, and αJ , αD from VP23-2) between VP19C and two VP23 conformers integrates VP19C into the triplex (Fig. 6B). The N-terminal region (residues 1 to 105), comprising three helices, penetrates the capsid floor around the quasi-threefold axis, anchoring the triplex in the capsid. The structure also supports the location of a nuclear localization signal (32) in VP19C at its N terminus (residues 50 to 61), which is presumed to bind DNA in vitro (Fig. 6F) (33), albeit densities for DNA binding to the N-terminal arm of triplex in the C-capsid reconstruction have not been observed yet (23). A number of β strands of the N domains from VP23 and VP19C contact the capsid floor (fig. S11). These contacts contribute the majority of the triplex-capsid interactions. Additionally, triplex-capsid protrusion interactions further

fix the orientation of the triplex; these involve charge and hydrophobic interactions with the α helix, th, and yz loops of the buttress domain of three adjacent VP5s, as well as one intermolecular disulfide bond (C1317-C179 between C2 and VP19C) (Fig. 7A). Previous studies have reported that disulfide bond formation between triplex and VP5 contributes to HSV capsid stability and assembly (34, 35). The disulfide bonds observed in B capsids structurally support these results to some extent. However, the disulfide bonds observed in the structure of B capsids may not be representative of those found in C capsids. We show that covalent as well as non-covalent interactions between triplexes and surrounding VP5s further stabilize the capsid.

Implications for assembly

In the broader context of the capsid structure, six VP5s from three different capsomers are arranged around a central triplex and three of them form one lasso triangle, upon which the triplex sits (Fig. 7A). Notably, interactions between the central triplex and the lasso triangle (interaction area $\sim 4700 \text{ \AA}^2$) dominate the contacts with all six VP5s (with an interaction area of $\sim 5300 \text{ \AA}^2$). A disulfide bond (between the triplex and one VP5 from the lasso triangle) and these anchoring interactions integrate the triplex into the lasso triangle, forming a structurally rigid unit (Fig. 7, A and B). The lasso triangle is not an equilateral triangle (each center of the three VP5s shows variable distances to the other two centers), with an average of $\sim 10\%$ deviations among three sides, and each lasso triangle varies slightly, depending on the microenvironments (Fig. 7B). As suggested previously (36), the triplexes confer a pronounced directionality on assembly of capsid shell. Specifically, VP19C from Ta is oriented



Movie 3. Structure of the triplex and interactions with VP5s. An overview of a triplex and its surrounding VP5s is shown. Both the covalent and noncovalent interactions within the triplex and between the triplex and the surrounding VP5s are highlighted and labeled.

outward from the penton, and Ta-Tc, Tc-Tb, Tb-Td, and Td-Te exhibit twofold symmetry, albeit with no direct interactions between them (Fig. 7B). In the absence of scaffold proteins, VP5s and triplex proteins formed capsids with a $T = 7$ shell (37), suggesting that the internal scaffold proteins play a role in controlling the correct symmetry of the capsid shell. Moreover, increasing evidence indicates that the triplexes are essential for the correct assembly of the capsid (38–40). It is quite likely that a structurally rigid unit comprising a triplex, the VP5 lasso triangle, and probably including scaffold proteins, might act as an assembly unit to regulate sequential assembly. The twofold symmetric interactions between these assembly units result from VP5-VP5 interactions, which can explain the triplex directionality (Fig. 7B). One special case is that of the assembly unit Tc (the assembly units are named according to the triplex that they contain) and the assembly unit Td' from the neighboring asymmetric unit, which are not related by a strict twofold axis. However, due to capsid assembly forces, the neighboring sides (highlighted in light yellow color in Fig. 7B) of the assembly unit Tc and Td' are adjusted to approximately the same length in order to enhance the interactions and retain the quasi-equivalent twofold axis (Fig. 7B). The assembly unit Tf is another special case due to its location on the threefold axis, so that the imposition of icosahedral symmetry in the reconstruction averages the Tf density.

HSV B capsids structurally resemble C capsids

A feature of the infections caused by herpesviruses is the production of three different types of mature capsid forms (A, B, and C capsids) in the host cell nucleus. Whether A and B capsids are abortive forms or assembly intermediates is still debated (39, 41–43). Comparison of the low resolution cryo-EM structures of A, B, and C capsids indicates that except for the presence of capsid-associating tegument proteins in C capsids, structures of all three types of capsids are very similar (13, 44). A high-resolution structural analysis to verify this inference is lacking. To address this issue, we fitted our high-resolution HSV-2 B capsid coordinates with five rigid

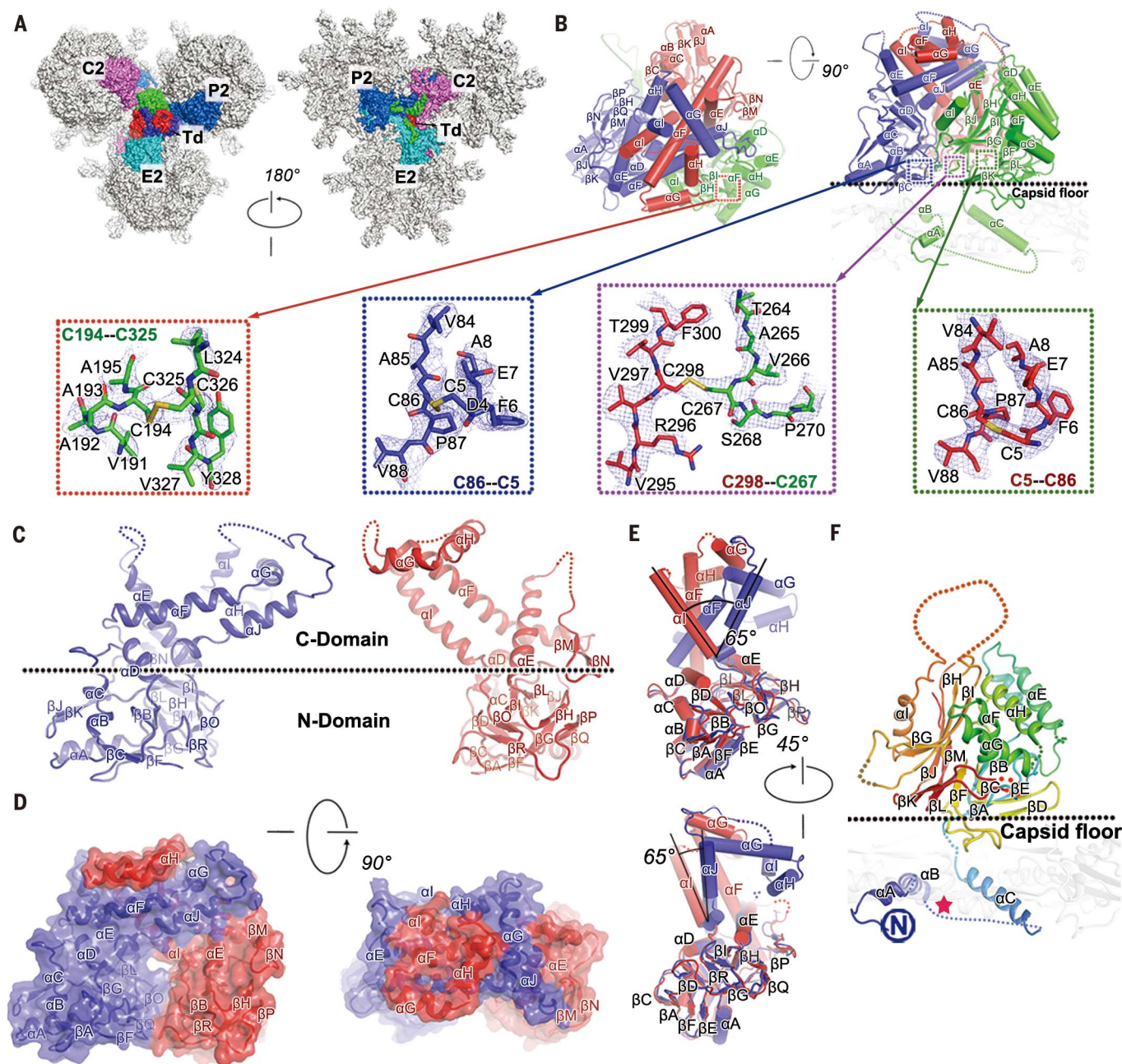


Fig. 6. Structural features of triplex. (A) Overview of Td triplex and its surrounding hexons. Td triplex and the subunits of the hexons that exhibit major interactions with Td triplex are highlighted with different colors (color scheme is the same as in Fig. 1C); the other subunits are shown in gray. (B) Overall structure of the triplex. VP23-1, VP23-2, and VP19C are colored in red, blue, and green, respectively. Electron density maps (blue mesh) for intramolecular and intermolecular disulfide bonds are shown in

zoomed-in boxes. (C) Ribbon diagrams of VP23-1 and VP23-2. (D) Surface representation of the dimer consisting of VP23-1 and VP23-2. Shown are the side view (left) and top view (right). The color scheme is the same as in Fig. 4C. (E) Superimposition of VP23-1 (red) over VP23-2 (blue), viewed from the side. (F) Ribbon diagram of VP19C, color ramped from the NH2 terminus (blue) to the COOH terminus (red). The reported nuclear localization signal (NLS) is labeled with a red star.

asymmetric units into the ~7-Å-resolution cryo-EM reconstruction of the HSV-1 virion (EMD-6386), which exhibits ~95%, ~93%, and 83% amino-acid identities in VP5, VP23, and VP19C, respectively, with HSV-2 (23). The fitting gave a correlation coefficient of 0.95, showing that all the capsid proteins, including their secondary

structural elements, were well aligned (Fig. 8). The structures and organization of VP5 assembled in the penton and hexons, together with the triplexes, showed no notable differences between the HSV-2 B capsid and the HSV-1 C capsid (Fig. 8). A striking feature of our HSV-2 B-capsid structure is a set of five helix pairs lining the inner

capsid surface beneath each penton, which perfectly match densities at equivalent positions of the HSV-1 virion (Fig. 8). Because of the low resolution of the reconstruction of C capsids, it is difficult to identify disulfide bonds of B capsids in C capsids with confidence. The primary sequences of HSV-2 capsid proteins share only

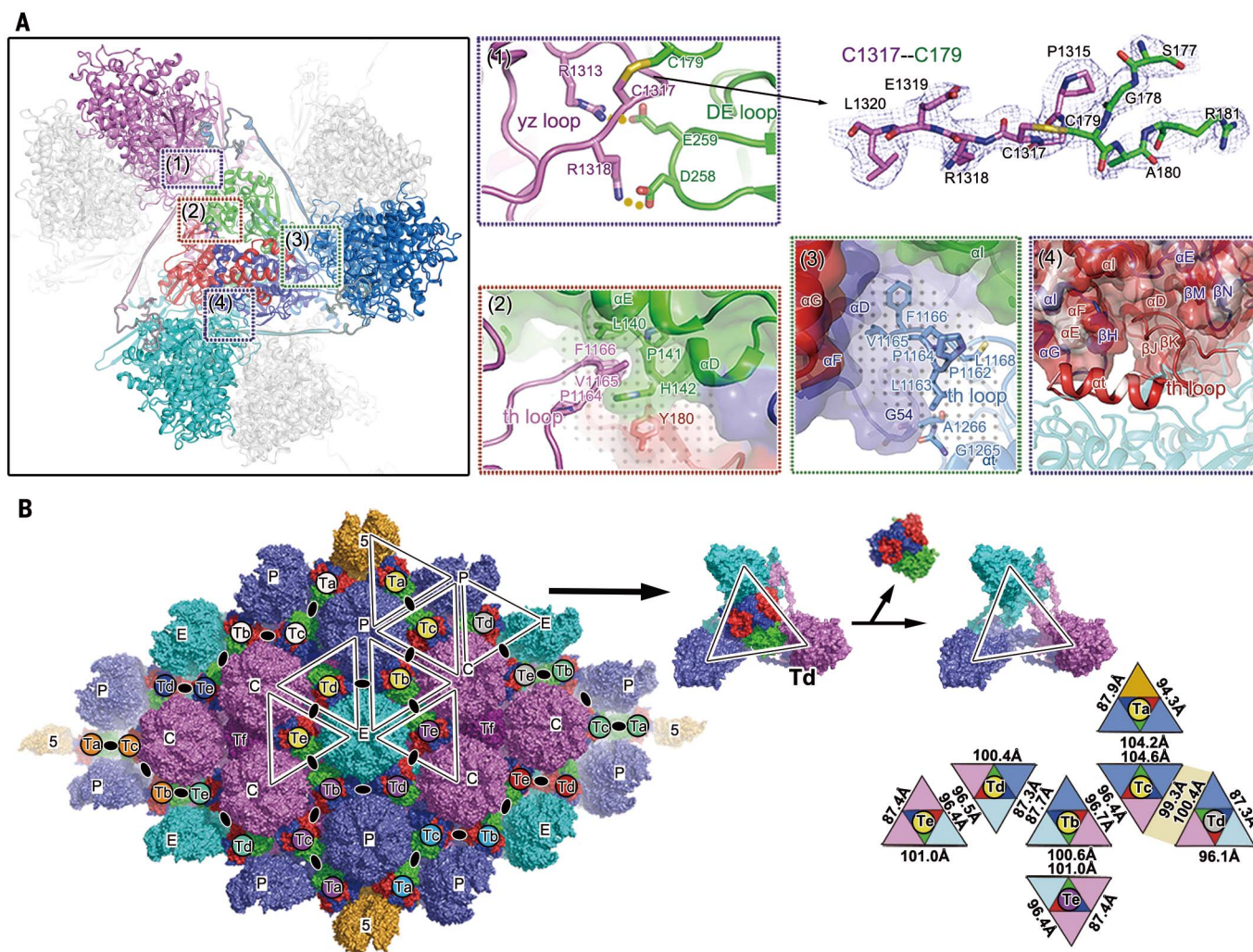


Fig. 7. Rigid unit interactions and global capsid organization.

(A) Overview of a triplex and its surrounding six VP5s (e.g., Td, top view). A triplex and its covalently linked lasso triangle comprise a structurally rigid unit. The color scheme is same as in Fig. 6A. Insets show the detailed topside interactions within a structurally rigid unit. Enlarged views of interactions (1) to (4) (boxed) are shown. (1) Charge and covalent interactions; the electron density map (blue mesh) for the intermolecular disulfide bond is shown. (2) to (4) Hydrophobic interactions, the triplex, and VP5s are shown as surface representation and cartoon, respectively. Residues involved in the interactions are shown as sticks in (1) to (3). (4) Regions involving hydrophobic interactions are colored by residues' hydrophobic characters: hydrophobic (red) to hydrophilic (white) gradient; other regions are colored as in Fig. 6A. (B) Two icosahedral facets are shown in surface representation at left with fivefold axis, C-Hex, E-Hex, and P-Hex labeled as 5, C, E and P, respectively, at the corresponding positions. The color scheme is the same as

in Fig. 1C. Triplexes (a few sets of Ta to Te) are labeled in different colors according to the asymmetric units they come from. The triplex Tf is colored in purple and labeled without a circle. The local quasi-equivalent twofold axes, where Ta-Tc, Tc-Tb, Tb-Td, and Td-Te exhibit twofold symmetry, are marked with black ellipses. The black triangles represent structurally rigid units (the centers of these three VP5s are connected by black lines). (Right) Pictorial representation of the rigid unit/rigid unit interactions. A triplex [drawn as an inner triangle with red (VP23-1), blue (VP23-2), and green (VP19C) colors and labeled by a circle] and its covalently linked lasso triangle (drawn as an external triangle with different colors according to which hexons the three VP5s come from: C-Hex, violet; E-Hex, cyan; P-Hex, slate) make up a putative assembly unit. The length for each side of the external triangle was calculated by measuring the distance between the centers of two VP5s within a lasso triangle. The associations between assembly units of Tc and Td' (from the neighboring asymmetric unit) are highlighted in light yellow.

~27% amino acid identity with those of the capsid proteins of HCMV. Despite this, a superposition of our structures of HSV-2 capsid proteins (VP5 and triplex) over the recently reported structure of HCMV reveals overall structural similarities. However, significant conformational differences between the capsids of the two viruses are observed, which is in line with the specific differences between the virus types

(fig. S12). Thus, conserved structural features may underlie similar mechanisms of capsid assembly across all herpesviruses.

Discussion

The herpesvirus capsid initially assembles as a precursor procapsid that subsequently matures during DNA packing (8–10). HSV procapsid assembly is a complex process requiring the or-

dered packing of some 4000 protein subunits (19). An in vitro assembly system based on a panel of recombinant baculoviruses encoding HSV procapsid proteins has revealed that VP5, triplex, and scaffold proteins are sufficient to produce a capsid with a correct $T = 16$ shell (8, 45). The imposition of icosahedral symmetry in the reconstruction of the whole capsid likely limited the resolution of the scaffold

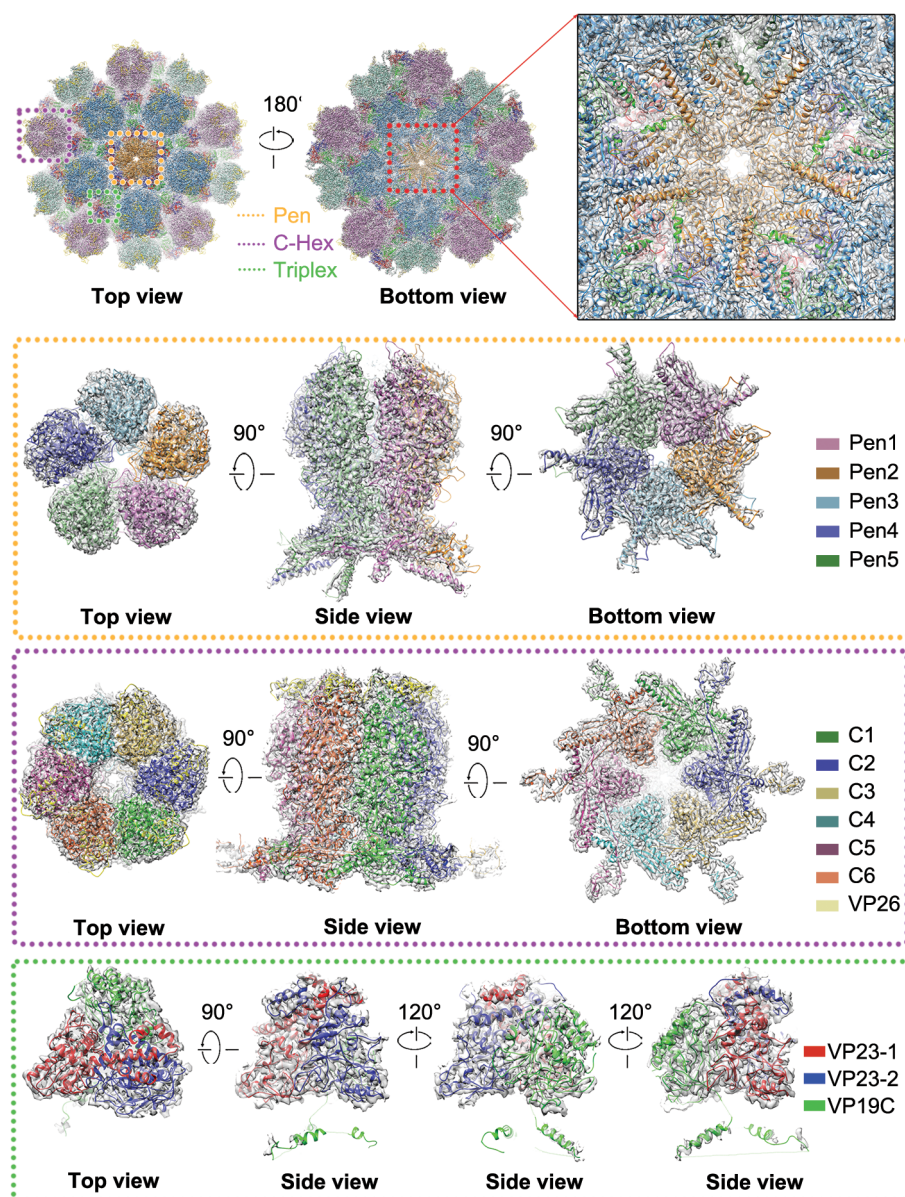


Fig. 8. Structural comparison of HSV-2 B capsid with HSV-1 virion. Fitting of HSV-2 B capsid coordinates with five asymmetric units into the ~ 7 -Å resolution cryo-EM reconstruction of HSV-1 virion (emd-6386) (23). The penton, C-Hex, P-Hex, and E-Hex are colored in orange, violet, slate, and cyan, respectively. The five helix pairs lining the inner capsid surface beneath the penton is marked, and a zoomed-in view is shown in the red inset. Zoomed-in views of the penton, C-Hex, and triplex are shown in orange, purple, and green insets, respectively. Each subunit within the penton and hexons is depicted in a different color.

core. The low-resolution map with a diameter of ~ 660 Å does not provide information on how scaffold proteins determine the correct symmetry of the particle (Fig. 1A). Together with previous studies on in vitro-assembled procapsids (11), these suggest that the scaffold may not need to adopt a specific organization to fulfill its function, on the condition that its overall dimensions are within the tolerance necessary to ensure the correct shell conformation. Although the portal structures of dsDNA bacteriophages have been extensively studied

(46, 47), it has proved difficult to study the portal structure of herpesviruses because there are no sentinel markers for the location of the portal in herpesviruses. Available evidence seems to indicate that the portal associates with scaffold proteins to initiate the capsid assembly in herpesviruses (48, 49). Due to the lack of detailed structural information on the portal and scaffold proteins, we are currently unable to use our model to speculate on the integration of the portal and scaffold proteins into the capsid. However, the observed pattern of directionality of the triplexes

and structural adaptations of the capsomers provide some insights into the mode of capsid assembly. A structurally rigid unit comprising a triplex together with its covalently linked lasso triangle might possibly act as one of the basic assembly units, which plays strategic roles in capsid assembly. Such a method of assembly of the capsid conforms to the efficient strategy of producing basic assembly units first, which then assemble into higher-order structures that ultimately lead to the formation of highly complex structures like the capsid of the HSV.

Despite the evolutionary and biological divergence of the eight human herpesviruses that have been classified into three subgroups (50), a large number of core gene products are highly conserved among these viruses (51). Moreover, all herpesviruses share a common virion (capsid) structure, a core genome replication process, and similar entry and egress pathways (52, 53). In summary, this work not only marks a substantial improvement in the resolution of the structure of herpesvirus capsid determined by cryo-EM but also is a step toward understanding the drivers of assembly of the capsid. We have identified extensive networks of intersubunit interactions, including intermolecular disulfide bonds, that underpin capsid stability. In line with structural analysis, B as well as C capsids were robust and could withstand heat treatment at 65°C for 10 min (54) (fig. S13). The structure of HSV described here could provide a basis for development of better antiviral drugs for treating infections caused by herpesviruses.

Materials and methods

HSV-2 capsid preparation

Vero cells were cultured in Dulbecco's Modified Eagle Medium (DMEM) plus 10% fetal bovine serum (FBS). Cells were grown to 90% confluence and infected with herpes simplex virus 2 strain MS at a multiplicity of infection (MOI) of 0.1–1. At 4 days post infection, the cells were collected, resuspended in PBS containing 1% NP-40 and lysed by three cycles of freezing and thawing. After lysis, the solution was centrifuged at 1500 g at 4°C for 15 min to remove large debris. A discontinuous 20% and 60% sucrose gradient (w/v in PBS) was used to further purify the capsids. Fractions containing the capsids at the interface of the two sucrose layers were collected after centrifugation. Crude HSV-2 capsids concentrate [~ 0.6 mg in 600 μL PBS (pH 7.4)] was loaded onto a continuous 20% to 50% (w/v in PBS) sucrose density gradient and centrifuged at 80,000 g for 1 hour. Three sets of fractions were collected and dialyzed against PBS buffer. Capsids from these fractions were imaged by negative staining electron microscopy and cryo-EM.

Analytical ultracentrifugation

Sedimentation velocity experiments were performed on a Beckman XL-I analytical ultracentrifuge at 20°C . HSV-2 capsids were diluted with PBS buffer to 400 μL with $A_{280\text{nm}}$ absorption of about 0.8. Samples were loaded into a

conventional double-sector quartz cell and mounted in a Beckman four-hole An-60 Ti rotor. Data were collected at 3000 rpm at a wavelength of 280 nm. Interference sedimentation coefficient distributions were calculated from the sedimentation velocity data using the SEDFIT software program (www.analyticalultracentrifugation.com).

Negative stain

For examination by negative staining, preparations of capsids were diluted in PBS (pH 7.4) to a suitable concentration, applied to a freshly glow-discharged grid, washed twice with PBS, and stained with 1% phosphotungstic acid (pH 7). All samples were examined on a 120-kV electron microscope.

Cryo-EM and data collection

For cryo-grid preparation, a 3- μ L aliquot of purified HSV-2 capsids was applied to a fresh glow-discharged 400-mesh holey carbon-coated copper grid (C-flat, CF-2/1-2C, Protochips). Grids were blotted for 3.5 s in 80% relative humidity for plunge-freezing (Vitrobot; FEI) in liquid ethane. Cryo-EM data sets were collected at 300 kV with a Titan Krios microscope (FEI). Movies (25 frames, each 0.2 s, total dose 25 e⁻Å⁻²) were recorded using a Falcon3 detector with a defocus range of 0.8 to 2.3 μ m. Automated single-particle data acquisition was performed with SerialEM, with a nominal magnification of 59,000 \times , which yields a final pixel size of 1.38 Å.

Image processing

A total of 5527 micrographs were recorded. Out of these, 4600 micrographs with visible CTF rings beyond 1/5 Å in their spectra were selected for further processing (fig. S1). The defocus value for each micrograph was determined using Gctf (55). More than 55,000 particles from the 4600 micrographs were boxed using EMAN package (56). The RELION (57) and jalign (58) were used to process the HSV capsid data, which led to a reconstruction of ~4-Å resolution with icosahedral symmetry imposed. There were two obstacles that limited the resolution of this 1250-Å-diameter virus. One was the structural complexity resulting from the fact that the capsid was not strictly following the icosahedral symmetry (59). The reason for this anomaly could be the intrinsic structural flexibility associated with the particle or some form of structural perturbation (local deformation) caused by ultracentrifugation during the purification process. The other was the Ewald sphere effect, which is equivalent to the consequence of the defocus gradient on this large virus. Conventional programs available for determining cryo-EM structures cannot deal with these two problems. We developed a reconstruction method named block-based reconstruction. In this method, the asymmetric unit of the icosahedral virus was divided into 4 blocks and each block was refined and reconstructed separately. During refinement, in each boxed cryo-EM image, there were 60 icosahedral-symmetry-related copies for each block. The initial orientation and center parameters for the copies could

be calculated based on the icosahedral symmetry virus reconstruction by RELION or jalign. A local search for better rotation and translation parameters of each copy was performed to overcome the capsid structure complexity. After 4 blocks being refined and reconstructed, a program was used to combine the 4 blocks into an asymmetric unit. The resolution as determined by Golden standard Fourier shell correlation was 3.6 Å using the 0.143 threshold. To solve the Ewald sphere problem, knowing the rotation and translation parameters of a virus, the distance d between the center of one copy in the 3D virus and the center of the virus along the z axis (parallel to the incident electron beam) was calculated. Assuming the defocus obtained by fitting the Thon ring representing the distance between the center of the virus and focused point of objective lens, the local defocus of each copy in the 3D virus was the sum of d and the defocus value. This local defocus of each copy instead of the uniform defocus obtained by fitting was used to reconstruct the blocks. After combining these blocks, the final resolution of HSV capsid approached 3.1-Å resolution. We used the program of post process in RELION (57) to evaluate the resolution and did the map sharpening (estimate the B-factor automatically).

Model building and refinement

The ab-initio atomic models of the C-Hex, P-Hex, Pen, VP26, and Triplex were built de novo into density using COOT (60). Among these, the crystal structure of the upper domain (61) was manually fitted into the maps of the capsomers using CHIMERA (62) and further manually corrected in COOT (60). Models were further improved by iterative positional and B-factor refinement in real space using Phenix (63), rebuilding in COOT (60), and evaluated by Molprobity (64) and Refmac (65). Refinement statistics are listed in table S1.

REFERENCES AND NOTES

1. P. Chayavichitsilp, J. V. Buckwalter, A. C. Krakowski, S. F. Friedlander, Herpes simplex. *Pediatr. Rev.* **30**, 119–130 (2009). doi: [10.1542/pir.30-4-119](https://doi.org/10.1542/pir.30-4-119); pmid: [19339385](https://pubmed.ncbi.nlm.nih.gov/19339385/)
2. R. J. Cohrs, D. H. Gilden, Human herpesvirus latency. *Brain Pathol.* **11**, 465–474 (2001). doi: [10.1111/j.1750-3639.2001.tb00415.x](https://doi.org/10.1111/j.1750-3639.2001.tb00415.x); pmid: [11556692](https://pubmed.ncbi.nlm.nih.gov/11556692/)
3. B. Grinde, Herpesviruses: Latency and reactivation - viral strategies and host response. *J. Oral Microbiol.* **5**, 22766 (2013). doi: [10.3402/jom.v5i0.22766](https://doi.org/10.3402/jom.v5i0.22766); pmid: [24167660](https://pubmed.ncbi.nlm.nih.gov/24167660/)
4. M. Ghebremichael, D. Habtzgi, E. Paintsil, Deciphering the epidemic synergy of herpes simplex virus type 2 (HSV-2) on human immunodeficiency virus type 1 (HIV-1) infection among women in sub-Saharan Africa. *BMC Res. Notes* **5**, 451 (2012). doi: [10.1186/1756-0500-5-451](https://doi.org/10.1186/1756-0500-5-451); pmid: [22909236](https://pubmed.ncbi.nlm.nih.gov/22909236/)
5. E. J. Mmbaga, G. H. Leyna, B. Stray-Pedersen, K. I. Klepp, Herpes simplex virus type-2 and human immunodeficiency virus infections in a rural population in Kilimanjaro Tanzania. *East Afr. J. Public Health* **8**, 28–32 (2011). pmid: [22066279](https://pubmed.ncbi.nlm.nih.gov/22066279/)
6. K. K. Venkatesh et al., The relative contribution of viral and bacterial sexually transmitted infections on HIV acquisition in southern African women in the Methods for Improving Reproductive Health in Africa study. *Int. J. STD AIDS* **22**, 218–224 (2011). doi: [10.1258/ijsa.2010.010385](https://doi.org/10.1258/ijsa.2010.010385); pmid: [21515755](https://pubmed.ncbi.nlm.nih.gov/21515755/)
7. P. M. Ojala, B. Sodeik, M. W. Ebersold, U. Kutay, A. Helenius, Herpes simplex virus type 1 entry into host cells: Reconstitution of capsid binding and uncoating at the nuclear pore complex in vitro. *Mol. Cell. Biol.* **20**, 4922–4931 (2000). doi: [10.1128/MCB.20.13.4922-4931.2000](https://doi.org/10.1128/MCB.20.13.4922-4931.2000); pmid: [10848617](https://pubmed.ncbi.nlm.nih.gov/10848617/)
8. W. W. Newcomb et al., Assembly of the herpes simplex virus capsid: Characterization of intermediates observed during cell-free capsid formation. *J. Mol. Biol.* **263**, 432–446 (1996). doi: [10.1006/jmbi.1996.0587](https://doi.org/10.1006/jmbi.1996.0587); pmid: [8918599](https://pubmed.ncbi.nlm.nih.gov/8918599/)
9. F. J. Rixon, D. McNab, Packaging-competent capsids of a herpes simplex virus temperature-sensitive mutant have properties similar to those of in vitro-assembled procapsids. *J. Virol.* **73**, 5714–5721 (1999). pmid: [10364322](https://pubmed.ncbi.nlm.nih.gov/10364322/)
10. W. W. Newcomb et al., Assembly of the herpes simplex virus procapsid from purified components and identification of small complexes containing the major capsid and scaffolding proteins. *J. Virol.* **73**, 4239–4250 (1999). pmid: [10196320](https://pubmed.ncbi.nlm.nih.gov/10196320/)
11. B. L. Trus et al., The herpes simplex virus procapsid: Structure, conformational changes upon maturation, and roles of the triplex proteins VP19c and VP23 in assembly. *J. Mol. Biol.* **263**, 447–462 (1996). doi: [10.1016/S0022-2836\(96\)80018-0](https://doi.org/10.1016/S0022-2836(96)80018-0); pmid: [8918600](https://pubmed.ncbi.nlm.nih.gov/8918600/)
12. M. L. Perdue, J. C. Cohen, M. C. Kemp, C. C. Randall, D. J. O'Callaghan, Characterization of three species of nucleocapsids of equine herpesvirus type-1 (EHV-1). *Virology* **64**, 187–204 (1975). doi: [10.1016/0042-6822\(75\)90091-4](https://doi.org/10.1016/0042-6822(75)90091-4); pmid: [1167720](https://pubmed.ncbi.nlm.nih.gov/1167720/)
13. R. Tandon, E. S. Mocarski, J. F. Conway, The A, B, Cs of herpesvirus capsids. *Viruses* **7**, 899–914 (2015). doi: [10.3390/v7030899](https://doi.org/10.3390/v7030899); pmid: [25730559](https://pubmed.ncbi.nlm.nih.gov/25730559/)
14. Z. H. Zhou et al., Seeing the herpesvirus capsid at 8.5 Å. *Science* **288**, 877–880 (2000). doi: [10.1126/science.288.5467.877](https://doi.org/10.1126/science.288.5467.877); pmid: [10797014](https://pubmed.ncbi.nlm.nih.gov/10797014/)
15. W. W. Newcomb et al., Structure of the herpes simplex virus capsid. Molecular composition of the pentons and the triplexes. *J. Mol. Biol.* **232**, 499–511 (1993). doi: [10.1006/jmbi.1993.1406](https://doi.org/10.1006/jmbi.1993.1406); pmid: [8393939](https://pubmed.ncbi.nlm.nih.gov/8393939/)
16. P. Desai, N. A. DeLuca, S. Person, Herpes simplex virus type 1 VP26 is not essential for replication in cell culture but influences production of infectious virus in the nervous system of infected mice. *Virology* **247**, 115–124 (1998). doi: [10.1006/viro.1998.9230](https://doi.org/10.1006/viro.1998.9230); pmid: [9683577](https://pubmed.ncbi.nlm.nih.gov/9683577/)
17. D. J. Owen, C. M. Crump, S. C. Graham, Tegument assembly and secondary envelopment of alphaherpesviruses. *Viruses* **7**, 5084–5114 (2015). doi: [10.3390/v7092861](https://doi.org/10.3390/v7092861); pmid: [26393641](https://pubmed.ncbi.nlm.nih.gov/26393641/)
18. W. Gibson, B. Roizman, Proteins specified by herpes simplex virus. 8. Characterization and composition of multiple capsid forms of subtypes 1 and 2. *J. Virol.* **10**, 1044–1052 (1972). pmid: [4344252](https://pubmed.ncbi.nlm.nih.gov/4344252/)
19. J. D. Baines, Herpes simplex virus capsid assembly and DNA packaging: A present and future antiviral drug target. *Trends Microbiol.* **19**, 606–613 (2011). doi: [10.1016/j.tim.2011.09.001](https://doi.org/10.1016/j.tim.2011.09.001); pmid: [22000206](https://pubmed.ncbi.nlm.nih.gov/22000206/)
20. P. E. Prevelige Jr., J. King, Assembly of bacteriophage P22: A model for ds-DNA virus assembly. *Prog. Med. Virol.* **40**, 206–221 (1993). pmid: [8438077](https://pubmed.ncbi.nlm.nih.gov/8438077/)
21. M. L. Baker, W. Jiang, F. J. Rixon, W. Chiu, Common ancestry of herpesviruses and tailed DNA bacteriophages. *J. Virol.* **79**, 14967–14970 (2005). doi: [10.1128/JVI.79.23.14967-14970.2005](https://doi.org/10.1128/JVI.79.23.14967-14970.2005); pmid: [16282496](https://pubmed.ncbi.nlm.nih.gov/16282496/)
22. R. H. Rochat, C. W. Hecksel, W. Chiu, Cryo-EM techniques to resolve the structure of HSV-1 capsid-associated components. *Methods Mol. Biol.* **1144**, 265–281 (2014). doi: [10.1007/978-1-4939-0428-0_18](https://doi.org/10.1007/978-1-4939-0428-0_18); pmid: [24671690](https://pubmed.ncbi.nlm.nih.gov/24671690/)
23. A. Huet et al., Extensive subunit contacts underpin herpesvirus capsid stability and interior-to-exterior allostery. *Nat. Struct. Mol. Biol.* **23**, 531–539 (2016). doi: [10.1038/nsmb.3212](https://doi.org/10.1038/nsmb.3212); pmid: [27111889](https://pubmed.ncbi.nlm.nih.gov/27111889/)
24. X. Dai et al., Cryo-EM and mutagenesis reveal that the smallest capsid protein cements and stabilizes Kaposi's sarcoma-associated herpesvirus capsid. *Proc. Natl. Acad. Sci. U.S.A.* **112**, E649–E656 (2015). doi: [10.1073/pnas.1420317112](https://doi.org/10.1073/pnas.1420317112); pmid: [25646489](https://pubmed.ncbi.nlm.nih.gov/25646489/)
25. X. Yu, J. Jih, J. Jiang, Z. H. Zhou, Atomic structure of the human cytomegalovirus capsid with its securing tegument layer of pp150. *Science* **356**, eaam6892 (2017). doi: [10.1126/science.aam6892](https://doi.org/10.1126/science.aam6892); pmid: [28663444](https://pubmed.ncbi.nlm.nih.gov/28663444/)
26. S. H. Scheres, S. Chen, Prevention of overfitting in cryo-EM structure determination. *Nat. Methods* **9**, 853–854 (2012). doi: [10.1038/nmeth.2115](https://doi.org/10.1038/nmeth.2115); pmid: [22842542](https://pubmed.ncbi.nlm.nih.gov/22842542/)
27. D. I. Stuart, M. Levine, H. Muirhead, D. K. Stammers, Crystal structure of cat muscle pyruvate kinase at a resolution of 2.6 Å. *J. Mol. Biol.* **134**, 109–142 (1979). doi: [10.1016/0022-2836\(79\)90416-9](https://doi.org/10.1016/0022-2836(79)90416-9); pmid: [537059](https://pubmed.ncbi.nlm.nih.gov/537059/)
28. W. R. Wikoff et al., Topologically linked protein rings in the bacteriophage HK97 capsid. *Science* **289**, 2129–2133 (2000). doi: [10.1126/science.289.5487.2129](https://doi.org/10.1126/science.289.5487.2129); pmid: [11000116](https://pubmed.ncbi.nlm.nih.gov/11000116/)

29. W. W. Newcomb, J. C. Brown, Structure of the herpes simplex virus capsid: Effects of extraction with guanidine hydrochloride and partial reconstitution of extracted capsids. *J. Virol.* **65**, 613–620 (1991). PMID: [1846187](#)
30. Z. H. Zhou, D. H. Chen, J. Jakana, F. J. Rixon, W. Chiu, Visualization of tegument-capsid interactions and DNA in intact herpes simplex virus type 1 virions. *J. Virol.* **73**, 3210–3218 (1999). PMID: [10074174](#)
31. P. Desai, J. C. Akpa, S. Person, Residues of VP26 of herpes simplex virus type 1 that are required for its interaction with capsids. *J. Virol.* **77**, 391–404 (2003). doi: [10.1128/JVI.77.1.391-404.2003](#); PMID: [12477844](#)
32. Y. Li, L. Zhao, S. Wang, J. Xing, C. Zheng, Identification of a novel NLS of herpes simplex virus type 1 (HSV-1) VP19C and its nuclear localization is required for efficient production of HSV-1. *J. Gen. Virol.* **93**, 1869–1875 (2012). doi: [10.1099/vir.0.042697-0](#); PMID: [22622329](#)
33. A. Bera, E. M. Perkins, J. Zhu, H. Zhu, P. Desai, DNA binding and condensation properties of the herpes simplex virus type 1 triplex protein VP19C. *PLOS ONE* **9**, e104640 (2014). doi: [10.1371/journal.pone.0104640](#); PMID: [25121591](#)
34. R. Szczepaniak *et al.*, Disulfide bond formation contributes to herpes simplex virus capsid stability and retention of pentons. *J. Virol.* **85**, 8625–8634 (2011). doi: [10.1128/JVI.00214-11](#); PMID: [21697480](#)
35. W. W. Newcomb, F. L. Homa, D. R. Thomsen, Z. Ye, J. C. Brown, Cell-free assembly of the herpes simplex virus capsid. *J. Virol.* **68**, 6059–6063 (1994). PMID: [8057482](#)
36. A. A. Aksyuk *et al.*, Subassemblies and asymmetry in assembly of herpes simplex virus procapsid. *mBio* **6**, e01525–e15 (2015). doi: [10.1128/mBio.01525-15](#); PMID: [26443463](#)
37. A. Saad, Z. H. Zhou, J. Jakana, W. Chiu, F. J. Rixon, Roles of triplex and scaffolding proteins in herpes simplex virus type 1 capsid formation suggested by structures of recombinant particles. *J. Virol.* **73**, 6821–6830 (1999). PMID: [10400780](#)
38. J. D. Tatman, V. G. Preston, P. Nicholson, R. M. Elliott, F. J. Rixon, Assembly of herpes simplex virus type 1 capsids using a panel of recombinant baculoviruses. *J. Gen. Virol.* **75**, 1101–1113 (1994). doi: [10.1099/0022-1317-75-5-1101](#); PMID: [8176371](#)
39. D. R. Thomsen, L. L. Roof, F. L. Homa, Assembly of herpes simplex virus (HSV) intermediate capsids in insect cells infected with recombinant baculoviruses expressing HSV capsid proteins. *J. Virol.* **68**, 2442–2457 (1994). PMID: [8139029](#)
40. H. S. Kim *et al.*, A domain in the herpes simplex virus 1 triplex protein VP23 is essential for closure of capsid shells into icosahedral structures. *J. Virol.* **85**, 12698–12707 (2011). doi: [10.1128/JVI.05791-11](#); PMID: [21957296](#)
41. P. M. Beard, C. Duffy, J. D. Baines, Quantification of the DNA cleavage and packaging proteins U(L)15 and U(L)28 in A and B capsids of herpes simplex virus type 1. *J. Virol.* **78**, 1367–1374 (2004). doi: [10.1128/JVI.78.3.1367-1374.2004](#); PMID: [14722291](#)
42. S. P. Weinheimer *et al.*, Autoproteolysis of herpes simplex virus type 1 protease releases an active catalytic domain found in intermediate capsid particles. *J. Virol.* **67**, 5813–5822 (1993). PMID: [8396657](#)
43. F. L. Homa *et al.*, Structure of the pseudorabies virus capsid: Comparison with herpes simplex virus type 1 and differential binding of essential minor proteins. *J. Mol. Biol.* **425**, 3415–3428 (2013). doi: [10.1016/j.jmb.2013.06.034](#); PMID: [23827137](#)
44. X. Yu *et al.*, Biochemical and structural characterization of the capsid-bound tegument proteins of human cytomegalovirus. *J. Struct. Biol.* **174**, 451–460 (2011). doi: [10.1016/j.jsb.2011.03.006](#); PMID: [21459145](#)
45. W. W. Newcomb, F. L. Homa, D. R. Thomsen, J. C. Brown, In vitro assembly of the herpes simplex virus procapsid: Formation of small procapsids at reduced scaffolding protein concentration. *J. Struct. Biol.* **133**, 23–31 (2001). doi: [10.1006/jsbi.2001.4329](#); PMID: [11356061](#)
46. R. K. Lokareddy *et al.*, Portal protein functions akin to a DNA-sensor that couples genome-packaging to icosahedral capsid maturation. *Nat. Commun.* **8**, 14310 (2017). doi: [10.1038/ncomms14310](#); PMID: [28134243](#)
47. L. Sun *et al.*, Cryo-EM structure of the bacteriophage T4 portal protein assembly at near-atomic resolution. *Nat. Commun.* **6**, 7548 (2015). doi: [10.1038/ncomms8548](#); PMID: [26144253](#)
48. J. B. Huffman, W. W. Newcomb, J. C. Brown, F. L. Homa, Amino acids 143 to 150 of the herpes simplex virus type 1 scaffold protein are required for the formation of portal-containing capsids. *J. Virol.* **82**, 6778–6781 (2008). doi: [10.1128/JVI.00473-08](#); PMID: [18417585](#)
49. K. Yang, J. D. Baines, Proline and tyrosine residues in scaffold proteins of herpes simplex virus 1 critical to the interaction with portal protein and its incorporation into capsids. *J. Virol.* **83**, 8076–8081 (2009). doi: [10.1128/JVI.00655-09](#); PMID: [19474093](#)
50. C. M. Fauquet, M. A. Mayo, J. Maniloff, U. Desselberger, L. A. Ball, *Virus Taxonomy: VIIIth Report of the International Committee on Taxonomy of Viruses*. (Academic Press, 2005).
51. E. S. Mocarski Jr., in *Human Herpesviruses: Biology, Therapy, and Immunopathogenesis*, A. Arvin *et al.*, Eds. (Cambridge Univ. Press, 2007).
52. K. E. Leigh *et al.*, Structure of a herpesvirus nuclear egress complex subunit reveals an interaction groove that is essential for viral replication. *Proc. Natl. Acad. Sci. U.S.A.* **112**, 9010–9015 (2015). doi: [10.1073/pnas.1511140112](#); PMID: [26150520](#)
53. C. Hagen *et al.*, Structural basis of vesicle formation at the inner nuclear membrane. *Cell* **163**, 1692–1701 (2015). doi: [10.1016/j.cell.2015.11.029](#); PMID: [26687357](#)
54. D. W. Bauer *et al.*, Exploring the balance between DNA pressure and capsid stability in herpesviruses and phages. *J. Virol.* **89**, 9288–9298 (2015). doi: [10.1128/JVI.01172-15](#); PMID: [26136570](#)
55. K. Zhang, Gctf: Real-time CTF determination and correction. *J. Struct. Biol.* **193**, 1–12 (2016). doi: [10.1016/j.jsb.2015.11.003](#); PMID: [26592709](#)
56. S. J. Ludtke, P. R. Baldwin, W. Chiu, EMAN: Semiautomated software for high-resolution single-particle reconstructions. *J. Struct. Biol.* **128**, 82–97 (1999). doi: [10.1006/jsbi.1999.4174](#); PMID: [10600563](#)
57. S. H. Scheres, A Bayesian view on cryo-EM structure determination. *J. Mol. Biol.* **415**, 406–418 (2012). doi: [10.1016/j.jmb.2011.11.010](#); PMID: [22100448](#)
58. F. Guo, W. Jiang, Single particle cryo-electron microscopy and 3-D reconstruction of viruses. *Methods Mol. Biol.* **1117**, 401–443 (2014). doi: [10.1007/978-1-62703-776-1_19](#); PMID: [24357374](#)
59. W. Jiang, L. Tang, Atomic cryo-EM structures of viruses. *Curr. Opin. Struct. Biol.* **46**, 122–129 (2017). doi: [10.1016/j.jsbi.2017.07.002](#); PMID: [28787658](#)
60. P. Emsley, K. Cowtan, Coot: Model-building tools for molecular graphics. *Acta Crystallogr. D Biol. Crystallogr.* **60**, 2126–2132 (2004). doi: [10.1107/S0907444904019158](#); PMID: [15572765](#)
61. B. R. Bowman, M. L. Baker, F. J. Rixon, W. Chiu, F. A. Quiocho, Structure of the herpesvirus major capsid protein. *EMBO J.* **22**, 757–765 (2003). doi: [10.1093/emboj/cdg086](#); PMID: [12574112](#)
62. E. F. Pettersen *et al.*, UCSF Chimera—a visualization system for exploratory research and analysis. *J. Comput. Chem.* **25**, 1605–1612 (2004). doi: [10.1002/jcc.20084](#); PMID: [15264254](#)
63. P. V. Afonine *et al.*, Towards automated crystallographic structure refinement with phenix.refine. *Acta Crystallogr. D Biol. Crystallogr.* **68**, 352–367 (2012). doi: [10.1107/S0907444912001308](#); PMID: [22505256](#)
64. V. B. Chen *et al.*, MolProbity: All-atom structure validation for macromolecular crystallography. *Acta Crystallogr. D Biol. Crystallogr.* **66**, 12–21 (2010). doi: [10.1107/S0907444909042073](#); PMID: [20057044](#)
65. A. A. Vagin *et al.*, REFMAC5 dictionary: Organization of prior chemical knowledge and guidelines for its use. *Acta Crystallogr. D Biol. Crystallogr.* **60**, 2184–2195 (2004). doi: [10.1107/S0907444904023510](#); PMID: [15572771](#)

ACKNOWLEDGMENTS

We thank X. Huang, B. Zhu, Z. Guo, and J. Lei for cryo-EM data collection; and the Center for Biological Imaging (CBI), Institute of Biophysics, and the Tsinghua University Branch of China National Center for Protein Sciences for EM work. **Funding:** Work was supported by the National Key Research and Development Program (2017YFC0840300, 2014CB542800, 2014CBA02003, 2016YFA0501100, and 2017YFA0504700), the Strategic Priority Research Program (XDB08000000), National Science Foundation of China (813300237, 31570717, 91530321, 31570742, and 81520108019), and Natural Science Foundation of Hunan Province (2017RS3033). X.W. was supported by Young Elite scientist sponsorship by CAST and program C of “One Hundred Talented People” of the Chinese Academy of Sciences. X.Z. received scholarships from the “National Thousand (Young) Talents Program” from the Office of Global Experts Recruitment in China. **Author contributions:** S.Y., J.-L.W., D.Z., N.W., Q.G., and X.W. performed experiments; X.W., H.L., X.Z., J.-Z.W., and Z.R. designed the study; all authors analyzed data; and X.W., H.L., X.Z., J.-Z.W., and Z.R. wrote the manuscript. **Competing interests:** All authors have no competing interests. **Data and materials availability:** Cryo-EM density map of HSV-2 B capsid has been deposited in the Electron Microscopy Data Bank under accession code EMD-6907, and the atomic coordinates of the asymmetric unit have been deposited in the Protein Data Bank under accession code 5ZAP.

SUPPLEMENTARY MATERIALS

www.sciencemag.org/content/360/6384/eaao7283/suppl/DC1
Figs. S1 to S13

Table S1

References (66–69)

21 August 2017; accepted 23 February 2018
10.1126/science.aao7283

RESEARCH ARTICLE SUMMARY

CELL BIOLOGY

Triggered recruitment of ESCRT machinery promotes endolysosomal repair

Michael L. Skowrya, Paul H. Schlesinger, Teresa V. Naismith, Phyllis I. Hanson*

INTRODUCTION: Lysosomes are degradative organelles that break down diverse materials delivered from inside and outside the cell by specialized vesicles called endosomes. Collectively, these membrane-enclosed compartments constitute the endolysosomal network. Endolysosomes can be ruptured or otherwise damaged by materials that they transport or accumulate. Damage can occur intentionally as in the case of incoming pathogens that seek to access the cytoplasm. Alternatively, damage can arise incidentally by membrane destabilizing molecules or by particulates such as crystals and protein aggregates that can puncture the lipid bilayer. To guard against these toxic or harmful substances and preserve pathway function, cells must be able to maintain and restore the integrity of their endolysosomal membranes. The mechanisms responsible for this vital function remain unclear.

RATIONALE: Extensively damaged compartments can be sequestered and degraded by

a form of selective autophagy called lysophagy, which is facilitated by cytosolic damage sensors such as galectins that bind to luminal glycans exposed on injured organelles. More limited damage is likely to require alternative responses for efficient resolution and repair. The endosomal sorting complex required for transport (ESCRT) machinery comprises a collection of proteins that form polymeric filaments to promote budding and fission of membranes in numerous contexts, notably during the formation of multivesicular endosomes. Recent studies highlight an additional role for ESCRT proteins in resolving small wounds on the plasma membrane and tears in the nuclear envelope. We investigated whether ESCRT machinery might also be recruited to damaged endolysosomes to promote their repair.

RESULTS: Using common peptide reagents that accumulate within acidic endolysosomes and selectively trigger their disruption, we demonstrate that ESCRT machinery rapidly and

coherently assembles on the limiting membrane of injured endolysosomal organelles. This response was observed in multiple types of cells, including phagocytes, and was especially prominent on endolysosomes damaged by internalized silica crystals. Notably, damage-triggered ESCRT recruitment required calcium as well as known ESCRT-nucleating factors including TSG101 and ALIX, and was distinct from lysophagy. To investigate the role played by ESCRT machinery on damaged endolysosomes, we used live-cell imaging of fluorescently tagged ESCRT proteins together with probes to dynamically monitor compartmental integrity. These

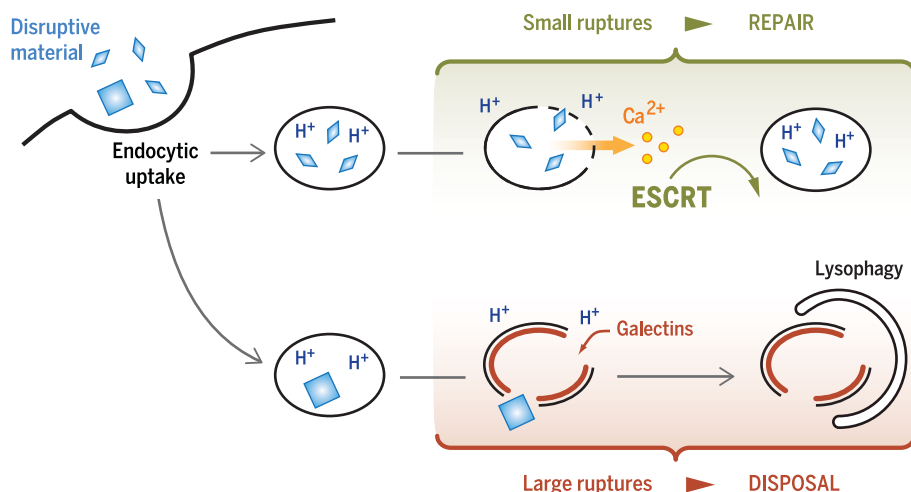
ON OUR WEBSITE

Read the full article at <http://dx.doi.org/10.1126/science.aar5078>

experiments established that ESCRT recruitment correlates with the onset of small perforations permeable to protons, but not with larger ruptures that allow exchange of

high molecular weight material, including internalized dextrans and cytoplasmic glycan-sensing galectins. Imaging ESCRT dynamics during a pulse of transient membrane disruption further revealed that ESCRT recruitment precedes recovery of compartmental function, monitored with a fluorogenic indicator of lysosomal protease activity. Accordingly, depleting cells of relevant ESCRT recruitment factors impaired both the reacidification and functional recovery of transiently injured organelles.

CONCLUSION: Our kinetic and functional data reveal a role for ESCRTs in the repair of small perforations in endolysosomes. This activity enables a restorative response to limited membrane damage that is likely to be protective in pathological contexts involving endolysosomal leakage and may help counter damage-induced inflammation. Transiently pacifying this response could additionally benefit efforts aimed at maximizing targeted drug and nanoparticle delivery through endocytosis. ESCRT participation in endolysosomal repair shares similarities with previously described roles for this machinery in mending nanometer-sized wounds at the plasma membrane and resealing the nuclear envelope, suggesting that ESCRT-promoted membrane repair may constitute a generic cellular response to limited membrane disruption. Based on the geometric constraints of endolysosomes and the type of damage they incur, we speculate that repair could proceed through closure of the membrane wound by ESCRT-containing filaments. ■



Alternative fates of damaged endolysosomes. Materials that are transported by or accumulate in endolysosomes can disrupt their membranes. Small disruptions trigger Ca^{2+} -dependent recruitment of ESCRT machinery to promote repair of the injured organelle. More extensively damaged compartments instead accumulate galectins and are degraded by lysophagy.

Department of Cell Biology and Physiology, Washington University School of Medicine, St. Louis, MO 63110, USA.
*Corresponding author. Email: phanson22@wustl.edu
Cite this article as M. L. Skowrya et al., *Science* **360**, eaar5078 (2018). DOI: 10.1126/science.aar5078

RESEARCH ARTICLE

CELL BIOLOGY

Triggered recruitment of ESCRT machinery promotes endolysosomal repair

Michael L. Skowyra, Paul H. Schlesinger, Teresa V. Naismith, Phyllis I. Hanson*

Endolysosomes can be damaged by diverse materials. Terminally damaged compartments are degraded by lysophagy, but pathways that repair salvageable organelles are poorly understood. Here we found that the endosomal sorting complex required for transport (ESCRT) machinery, known to mediate budding and fission on endolysosomes, also plays an essential role in their repair. ESCRTs were rapidly recruited to acutely injured endolysosomes through a pathway requiring calcium and ESCRT-activating factors that was independent of lysophagy. We used live-cell imaging to demonstrate that ESCRTs responded to small perforations in endolysosomal membranes and enabled compartments to recover from limited damage. Silica crystals that disrupted endolysosomes also triggered ESCRT recruitment. ESCRTs thus provide a defense against endolysosomal damage likely to be relevant in physiological and pathological contexts.

Endosomes and lysosomes together constitute the endolysosomal network that functions to sort, recycle, and degrade a wide range of substances from within and outside the cell. Endolysosomes are vulnerable to damage from diverse material such as incoming pathogens that seek to access the cytoplasm, molecules that intercalate into or otherwise destabilize the lipid bilayer, or particulate matter such as crystals that can puncture the membrane. Failure to promptly repair or sequester disrupted compartments can have deleterious consequences, including, in extreme cases, cell death.

Damaged endolysosomes can be isolated from the rest of the cell and degraded by a form of selective autophagy known as lysophagy. Lysophagy is promoted by recruitment of cytoplasmic proteins including galectins and glycoprotein-specific ubiquitin ligases to abnormally exposed luminal glycans on the afflicted compartment (1–6). Whether damaged endolysosomes can avoid autophagic degradation and instead be fully repaired is less clear but has been suspected (7–11). How this might work and how disrupted compartments would be triaged between these opposing fates is not known.

Membrane repair is known to occur elsewhere in the cell, particularly at the plasma membrane where coordinated responses counter mechanical and other disruptions (12, 13), but also at the nuclear envelope (14). In both of these contexts, recent studies highlight important roles played by ESCRT (endosomal sorting complex required for transport) machinery (15–19). ESCRT proteins are organized into several modular complexes des-

ignated ESCRT-0, -I, -II, and -III, in addition to the adenosine triphosphatase VPS4 and associated factors, that together help power such processes as intraluminal vesicle formation, viral budding, and cytokinetic abscission, in addition to membrane repair (20). All of these processes share the involvement of ESCRT-III proteins (including CHMPs 1–7 and IST1), which form filaments around membrane orifices that are thought to drive constriction and typically promote membrane fission (21, 22).

ESCRTs respond to endolysosomal damage

To investigate whether ESCRT machinery might participate in repairing damaged endolysosomes, we first asked whether ESCRT components are recruited to these compartments after selective membrane damage. The lysosomotropic compound LLOME (L-leucyl-L-leucine *O*-methyl ester) is commonly used to rupture endolysosomes (3, 23, 24). LLOME rapidly permeates cellular membranes and accumulates in the lumen of acidified organelles, where it is condensed into a membranolytic polymer by the lysosomal enzyme cathepsin C (9, 23). We confirmed LLOME-induced damage in HeLa cells by noting concentration of cytoplasmic GAL3 [a galectin frequently used to monitor damage (24)] on punctate structures (Fig. 1A). Immunostaining LLOME-treated cells for the ESCRT-III component CHMP4A revealed that this typically cytoplasmic protein also accumulated on intensely stained puncta throughout the cell (Fig. 1A). These CHMP4A-containing structures did not completely correspond to those marked by GAL3, but they did overlap with the known CHMP4A-interacting protein ALIX (Fig. 1B).

Multiple ESCRT-III proteins, including CHMP2B (Fig. 1C) as well as CHMP1A, CHMP1B, CHMP3,

CHMP4B, CHMP5, and IST1 (fig. S1), were co-recruited along with CHMP4A to LLOME-triggered puncta in U2OS cells, as were additional ESCRT-III interactors, including VPS4A and VTA1 (fig. S1). The extensive accumulation and coincidence of this large number of ESCRT-III proteins suggests that ESCRT mobilization constitutes a coherent response to LLOME. We detected similar LLOME-dependent redistribution of ESCRT proteins in several different cell types, including breast adenocarcinoma and glioblastoma cells as well as macrophage-like THP-1 cells commonly used in studies of pathogen uptake and endolysosomal escape (fig. S2), and in HeLa cells expressing fluorescently tagged ESCRT-III proteins (fig. S3).

We next confirmed that ESCRT recruitment correlated with LLOME-induced membrane damage. The effects of LLOME on ESCRTs were abolished by preincubating cells with the cathepsin inhibitor E64d (Fig. 1D), which prevents LLOME processing by cathepsin C and consequent membrane disruption (9). Accordingly, ESCRT-enriched structures induced by LLOME corresponded to late endosomes and lysosomes, coinciding well with LAMP1 but not with the early endosome protein EEA1 (Fig. 1E). ESCRT proteins localized to the limiting membrane of damaged endolysosomes (fig. S4). Closer inspection of ESCRT-labeled compartments by deep-etch electron microscopy confirmed that ESCRTs accumulated on vesicular structures (Fig. 1F and fig. S5). ESCRTs were seen to cluster in small domains on compartments exhibiting low immunolabel density, suggesting a role at discrete regions of the organelle membrane.

We next explored how ESCRT machinery might be targeted to damaged endolysosomes, using CHMP4A as a reporter of ESCRT recruitment. The ESCRT-I protein TSG101 is well known to nucleate ESCRT assembly in various contexts (20). TSG101 coaccumulated with CHMP4A on endolysosomes after LLOME-induced damage (fig. S6), and depleting cells of TSG101 delayed, but did not abolish, CHMP4A recruitment (fig. S7). TSG101 interacts with, and in certain contexts cooperates with, ALIX to recruit ESCRT-III machinery (25, 26). Although ALIX colocalized with CHMP4A and other ESCRT components on endolysosomes after damage (Fig. 1B and fig. S1), CHMP4A accumulation was unperturbed in LLOME-treated cells depleted of ALIX alone (fig. S7) despite efficient protein reduction (fig. S8). However, depleting both TSG101 and ALIX suppressed the response of CHMP4A to LLOME (Fig. 2A and figs. S7 and S8). Other ESCRT-III proteins were similarly attenuated, although some residual signal was observed that was potentially attributable to differential antibody sensitivity and/or incomplete knockdown (fig. S9). Because TSG101 is known to be important for ESCRT-mediated endosomal sorting, we wanted to be sure that the reduction in ESCRT recruitment was not caused by impaired LLOME processing. GAL3 accumulation in response to LLOME was, however, unchanged in cells co-depleted of TSG101 and ALIX (Fig. 2B), confirming comparable membrane damage.

TSG101 and ALIX direct ESCRT assembly to membranes in response to pathway-specific signals.

Department of Cell Biology and Physiology, Washington University School of Medicine, St. Louis, MO 63110, USA.

*Corresponding author. Email: phanson22@wustl.edu

Calcium is an established trigger of cellular responses to membrane damage at the plasma membrane (13) and is required to recruit ESCRTs to plasma membrane wounds (15, 16). Because endolysosomes are calcium-storing organelles and rupturing them increases intracellular calcium (27, 28), we wondered whether ESCRT recruitment to damaged endolysosomes might similarly be regulated by calcium. Preloading cells with the calcium chelator BAPTA-AM prevented accumulation of ESCRTs on LLOME-disrupted endolysosomes without impairing organelle damage, demonstrated again by GAL3 accumulation (Fig. 2C). Supporting a role for calcium, ESCRT machinery coaccumulated on damaged endolysosomes with ALG-2 (fig. S10), a protein previ-

ously implicated in calcium-dependent ESCRT assembly at plasma membrane wounds (16, 29).

ESCRT response is separable from lysophagy

Calcium-triggered responses are typically rapid, prompting us to inspect the timing of ESCRT recruitment to damaged compartments. In U2OS and HeLa cells treated with LLOME for varying durations, ESCRT components were detectable on LAMP1-containing organelles within a minute (Fig. 3A) and reached maximal accumulation shortly thereafter (Fig. 3, B to D). In contrast, GAL3-reactive structures were largely undetectable at these early times, instead appearing steadily over a prolonged period (Fig. 3, B and C), as

expected (3, 4). The delayed accumulation of GAL3 was accompanied by increasing amounts of ubiquitin-conjugated material (Fig. 3D and fig. S11) and the ubiquitin-dependent disaggregase VCP/p97 (fig. S12), consistent with known roles for ubiquitination and associated proteins in lysophagy (2, 5, 30). Early ESCRT recruitment and delayed accumulation of GAL3 and ubiquitinated material were also apparent in macrophage-like THP-1 cells (fig. S13), suggesting that the ESCRT response is distinct from lysophagy.

ESCRTs, however, have long been suspected to play a poorly defined role during autophagosome maturation (31), prompting us to further examine the relationship between lysophagy and ESCRT recruitment. Lysophagy involves engulfment of

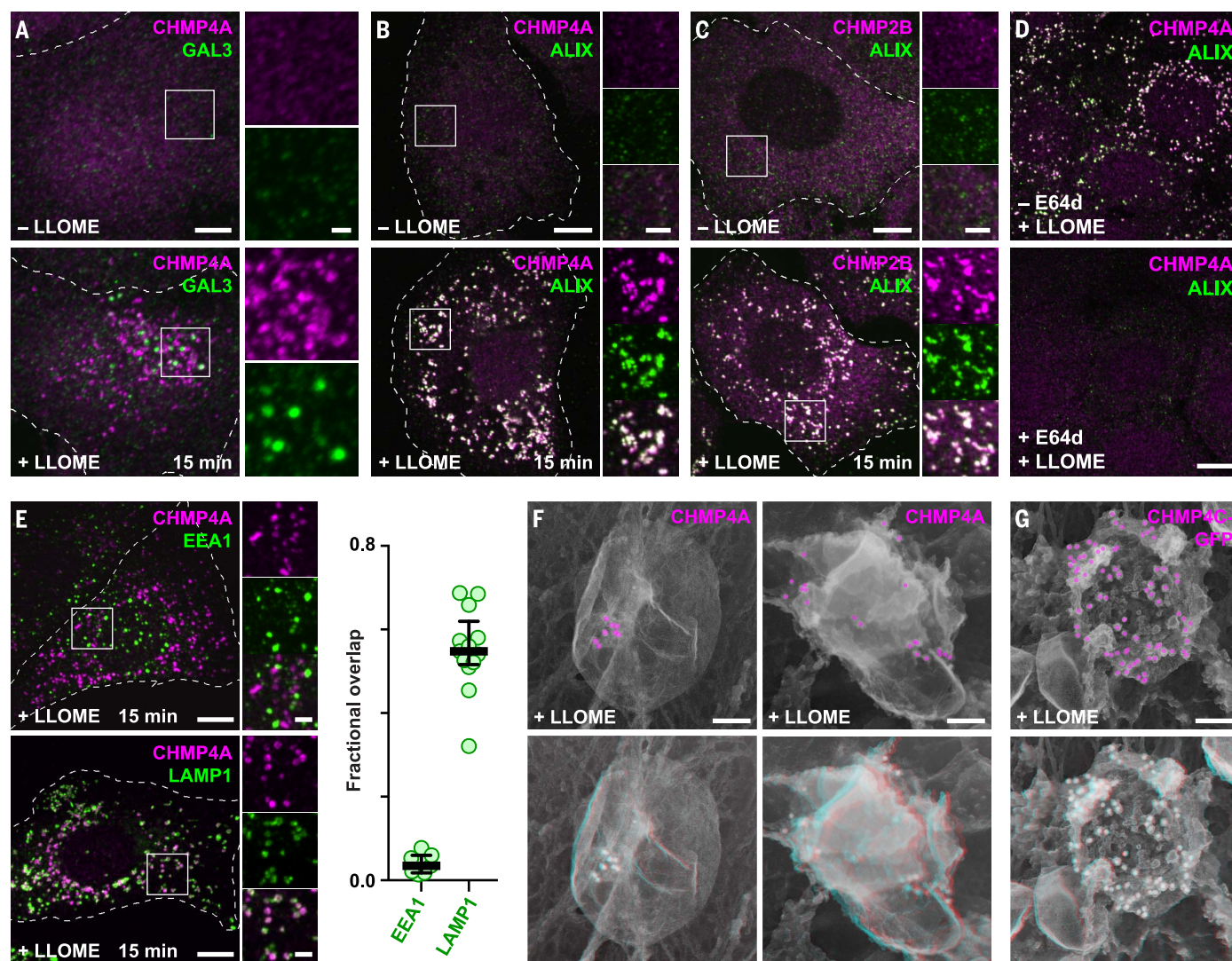


Fig. 1. Damaged endolysosomes recruit ESCRT machinery. (A) HeLa cells treated with or without LLOME were costained for CHMP4A and GAL3. (B and C) U2OS cells treated as above were costained for ALIX and the indicated ESCRT-III proteins. (D) U2OS cells preincubated for 5 min in the absence or presence of the cathepsin inhibitor E64d were exposed to LLOME and costained for CHMP4A and ALIX. (E) LLOME-treated U2OS cells were stained for CHMP4A and EEA1 or LAMP1. Fractional overlap between CHMP4A puncta and labeled compartments is shown at right ($n = 7$ cells for EEA1, 13

cells for LAMP1). (F) U2OS cells or (G) HeLa cells producing CHMP4C-GFP were treated with LLOME and immunolabeled as indicated before processing for deep-etch electron microscopy. Top panels depict two-dimensional views with pseudocolored immunogold; bottom panels show corresponding anaglyphs, to be viewed with dual-color glasses. In all fluorescence micrographs, representative cells are shown outlined by dashed white lines; boxed areas are magnified at right; and coincidence of green and magenta appears white. Scale bars, 10 μm [(A to E); 2 μm in magnified views]; 100 nm (F and G).

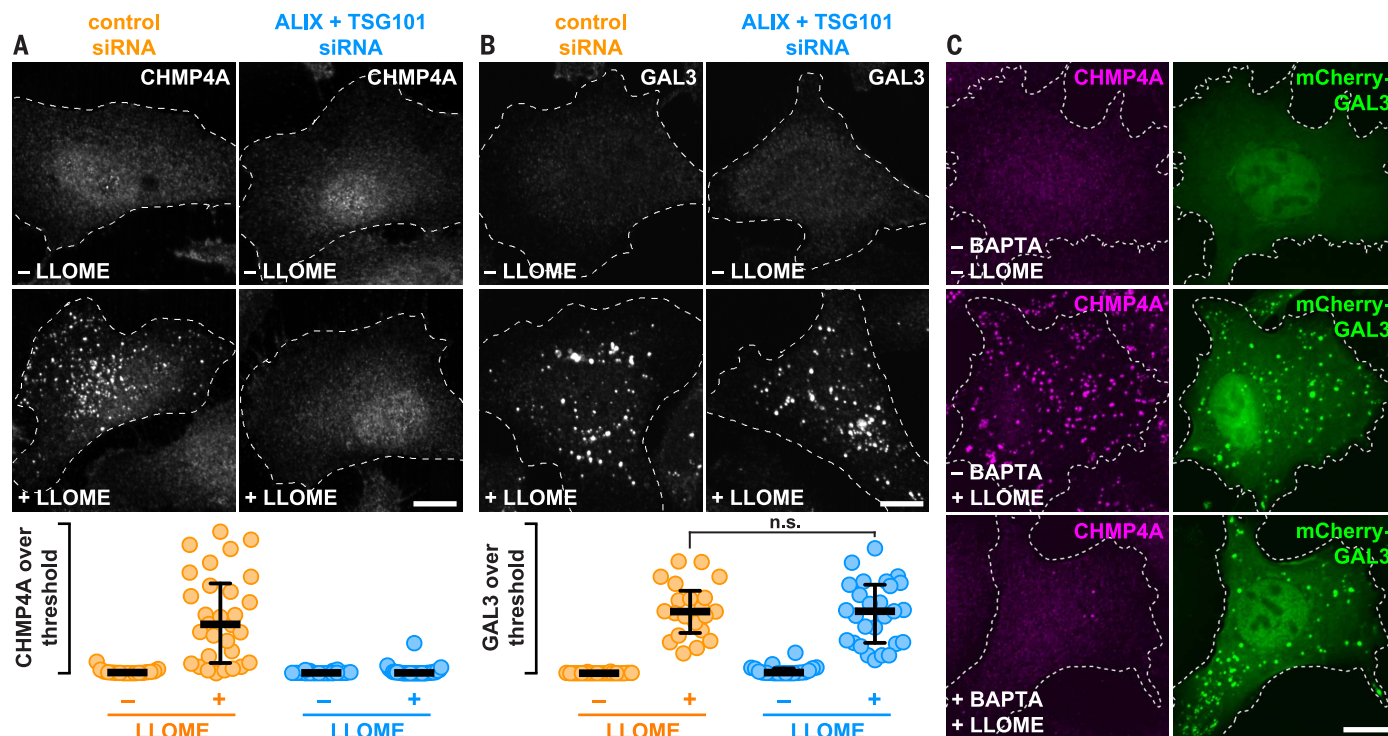


Fig. 2. TSG101 and ALIX, as well as calcium, are required for ESCRT assembly on damaged endolysosomes. (A and B) HeLa cells transfected with the indicated siRNAs were treated with or without LLOME and stained for CHMP4A (A) or GAL3 (B). The proportion of each stain that exceeded a starting threshold is quantified [in the order shown: $n = 20, 33, 21$,

and 33 cells in (A); and 20, 21, 20, and 27 cells in (B); n.s. denotes $P = 0.6319$ by Student's two-tailed unpaired t test]. Horizontal bars mark the median; whiskers span the interquartile range. (C) U2OS cells producing mCherry-GAL3 were preincubated for 1 hour with or without BAPTA-AM, then treated with or without LLOME and stained for CHMP4A. Scale bars, 10 μm .

the damaged organelle by an autophagosome, whose formation requires phosphatidylinositol 3-phosphate (PI3P) (Fig. 3E). The ESCRT response to LLOME was unaffected by treating cells with wortmannin (Fig. 3F), an inhibitor of PI3P synthesis, despite clear physiological changes associated with loss of PI3P elsewhere in the cell (fig. S14). Organelle engulfment also requires conjugation of LC3 to the expanding autophagosome membrane (3) by the autophagy elongation complex (32). Indeed, HeLa cells lacking ATG16L1 (33) failed to accumulate green fluorescent protein (GFP)-tagged LC3B in association with LLOME-damaged endolysosomes (fig. S15). Nevertheless, LLOME-induced ESCRT redistribution was unperturbed (Fig. 3G). GFP-LC3B association with LLOME-damaged organelles was also unaffected in cells depleted of TSG101 and ALIX (fig. S16). The presence of ESCRT machinery on LLOME-damaged endolysosomes could thus be uncoupled from autophagosome formation.

ESCRTs preferentially sense small ruptures in the endolysosomal membrane

We next examined why ESCRTs and factors involved in lysophagy respond differently to LLOME-induced damage. LLOME forms hydrophobic adducts that destabilize the lipid bilayer, causing damage that ranges from small perturbations permeable to protons and small molecules (9) to larger ruptures that allow exchange of higher

molecular weight material (24). Lysophagy of ruptured endolysosomes is directed in part by an influx of galectins, which bind to injury-exposed luminal β -galactosides (1, 2) and would thus require sufficiently large membrane disruptions to access the compartmental interior. ESCRTs, by contrast, would not be similarly constrained because they assemble on the cytoplasmic surface of organellar membranes.

We used live-cell imaging to assess whether the nature of membrane damage dictates whether and when ESCRTs or galectins are recruited. Fluorescently tagged ESCRT-III proteins, in this case CHMP4B-GFP (34), responded to LLOME earlier than did mCherry-GAL3 (Fig. 4A), as observed for their endogenous counterparts (Fig. 3, B to D). The proteins also did not always appear together, with some compartments only recruiting CHMP4B-GFP, some only recruiting mCherry-GAL3, and others accumulating both (see arrows in Fig. 4A). Dually labeled compartments were typically first surrounded by ESCRTs and only later acquired mCherry-GAL3, occasionally through what appeared to be a single breach of the limiting membrane (Fig. 4B), consistent with restricted access of GAL3 to the endolysosomal interior.

We clarified this behavior by loading endolysosomes with high molecular weight dextrans conjugated to pH-sensitive FITC (fluorescein isothiocyanate), enabling us to distinguish perturbations permeable to protons from larger ruptures that allow dextran escape. Adding LLOME

increased the fluorescence of dextran-loaded endolysosomes (Fig. 4C), indicating a dissipated pH gradient in an otherwise intact organelle. Most brightened dextran puncta were quickly surrounded by the ESCRT-III protein CHMP3-mCherry (Fig. 4C and fig. S17), whereas similar recruitment was not observed after raising luminal pH with ammonium chloride (fig. S18). We did not see much mCherry-GAL3 on brightened dextran puncta during the same early time period (Fig. 4D). There were, however, occasional events in which sudden loss of dextran coincided with rapid concentration of mCherry-GAL3 (see arrows in Fig. 4D), linking the galectin response to substantial membrane perforation. Similarly abrupt GAL3 accumulation accompanies adenoviral escape from endosomes (35). ESCRTs thus responded to proton-permeable disruptions on most afflicted compartments that GAL3 did not perceive (Fig. 4E). In support of this conclusion, treating cells with a low concentration of LLOME to limit damage redistributed ESCRTs onto LAMP1-reactive compartments, but only a few contained substantial GAL3 (fig. S19).

ESCRTs are transiently recruited after acute membrane damage

The preceding experiments were performed in the continuous presence of LLOME and thus reported on cumulative ESCRT recruitment to perturbed compartments. However, ESCRT machinery operates transiently in most contexts that use

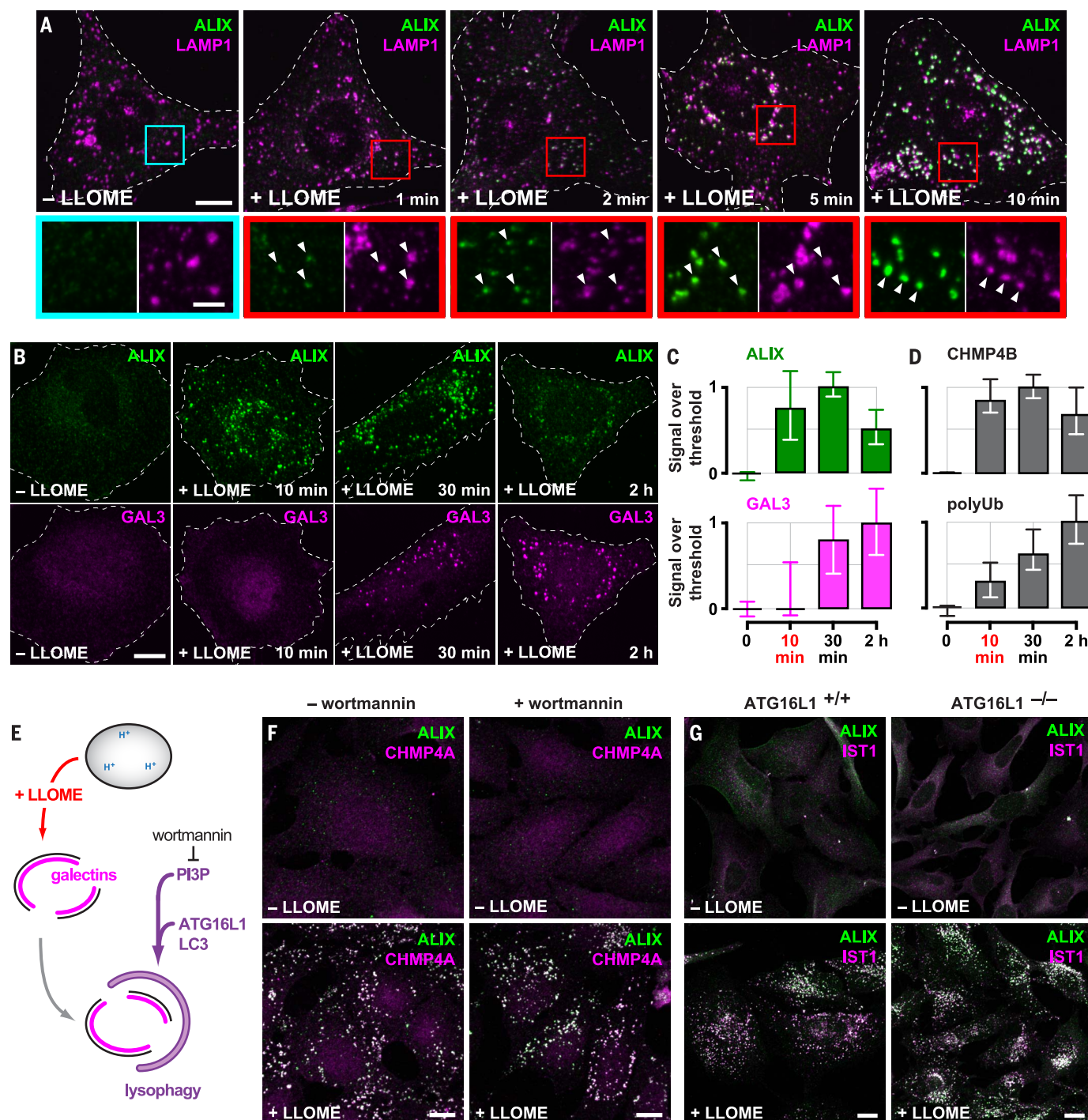


Fig. 3. ESCRT machinery is rapidly recruited to LLOME-damaged endolysosomes and is independent of lysophagy. (A) U2OS cells exposed to LLOME for the indicated times were costained for ALIX and LAMP1. Boxed areas are magnified below; arrows highlight LLOME-induced ESCRT puncta. (B) HeLa cells treated with LLOME for the indicated times were costained for ALIX and GAL3. The proportion of each stain that exceeded a starting threshold is plotted in (C). Shown are the median and interquartile range (in chronological order: $n = 3, 8, 10$ and 8 cells). (D) Quantitation of CHMP4B or ubiquitinated material (polyUb) (see

fig. S11) as in (C) (in chronological order: $n = 10, 11, 15$, and 16 cells for CHMP4B; $n = 19, 18, 25$, and 26 cells for polyUb). (E) Schematic depicting lysophagy and the role of factors targeted in adjacent experiments. (F) U2OS cells preincubated with or without wortmannin were treated with LLOME and costained for ALIX and CHMP4A. (G) HeLa cells expressing endogenous ATG16L1 (ATG16L1^{+/+}) or lacking ATG16L1 as a result of CRISPR-mediated gene deletion (ATG16L1^{-/-}) were treated with or without LLOME for 10 min and costained for ALIX and the ESCRT-III protein IST1. Scale bars, 10 μm (2 μm in magnified views).

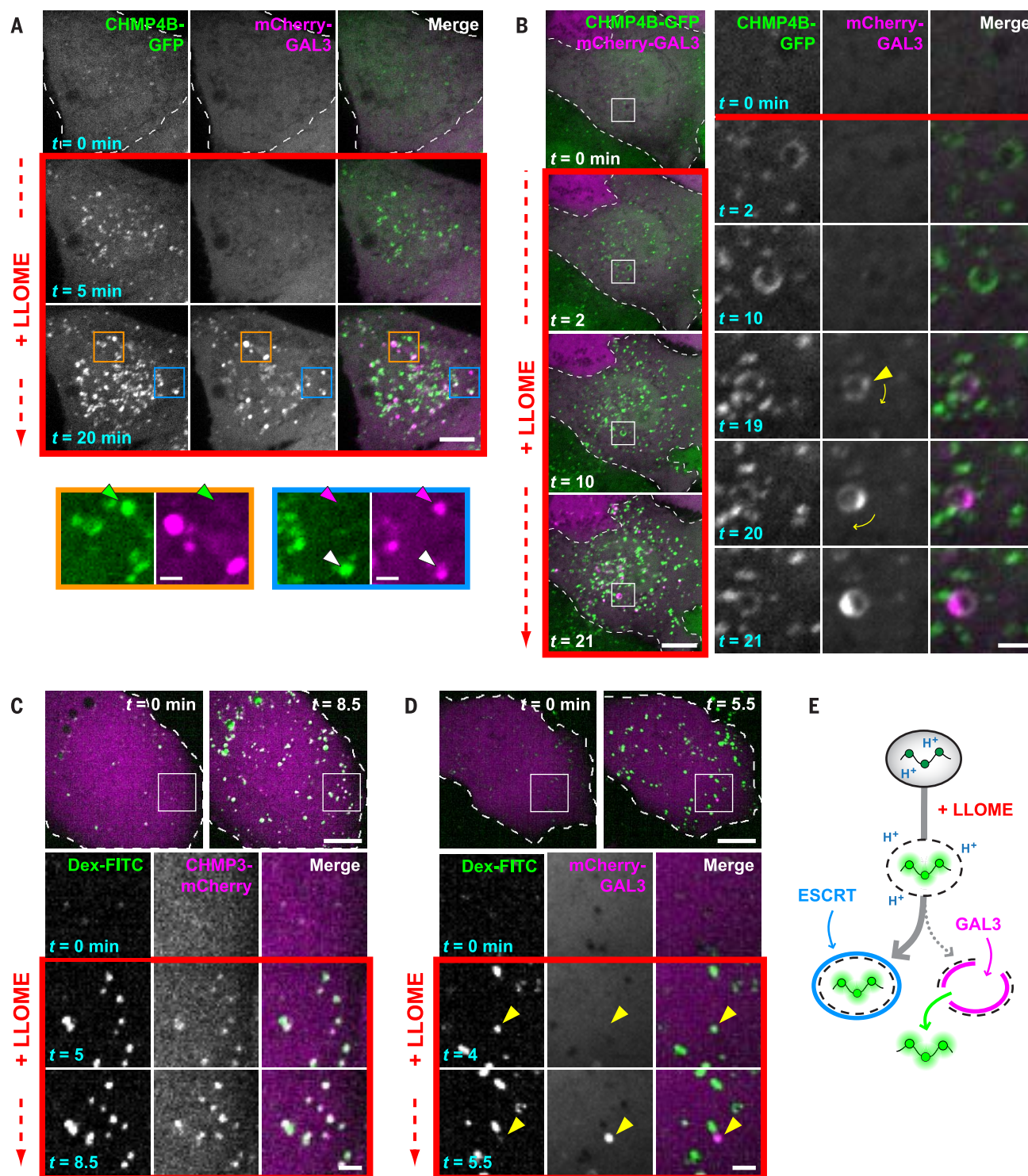


Fig. 4. ESCRT machinery preferentially responds to small membrane disruptions. (A) HeLa cells producing CHMP4B-GFP were additionally transfected with a plasmid encoding mCherry-GAL3 and imaged live before and after adding LLOME. Colored arrows in magnified views of boxed areas designate structures containing only CHMP4B-GFP (green), only mCherry-GAL3 (magenta), or both (white). (B) Cells imaged as in (A). Boxed areas are magnified at right, with the leftmost two columns showing each signal in grayscale; these are merged and colored in the third column. Arrowhead marks the initial appearance of GAL3. Note that this compartment rotates over

time, as denoted by the curved arrows. (C and D) U2OS cells were transfected with plasmids encoding CHMP3-mCherry (C) or mCherry-GAL3 (D) and loaded with 40-kDa pH-sensitive FITC-dextran chased into endolysosomes. Cells were imaged live before and after addition of LLOME. Boxed areas are magnified as in (B). Arrowheads in (D) indicate a dextran-laden compartment that rapidly acquires GAL3 after sudden loss of dextran. (E) Interpretive illustration of the different events seen in (C) and (D). In all panels, single planes of a representative cell are shown at the times indicated from each recording. Scale bars, $10 \mu\text{m}$ ($2 \mu\text{m}$ in magnified views).

GPN (glycyl-L-phenylalanine 2-naphthylamide) is an alternative rupturing agent that accumulates in endolysosomes like LLOME (11, 27). However, GPN is processed into metabolites thought



Fig. 6. Depleting ESCRT machinery impairs endolysosomal membrane repair.

(A) A ratiometric pH-sensing assay was used to monitor endolysosomal integrity. U2OS cells transfected with the indicated siRNAs were loaded with 40- to 70-kDa dextrans conjugated to pH-sensitive FITC and pH-insensitive rhodamine B fluorophores chased into endolysosomes. Loaded cells were imaged at 30-s intervals during and after a 1-min exposure to LLOME. Fluorescence micrographs show a representative field of endolysosomes from each cohort, depicting the changes in FITC fluorescence associated with key steps in the assay. Scale bars, 10 μ m. (B) Changes in the median ratio of FITC-to-rhodamine B fluorescence per cell at each time are plotted ($n = 97$ control and 85 knockdown cells from four experiments). Red line traces the response of a representative control cell. Blue lines designate two cells from the ESCRT-depleted cohort, one in which recovery was impaired and another in which recovery was similar to that of the control. Horizontal dashed line specifies a recovery threshold derived from the control population (see methods). In (C), the percentage of cells in each cohort that reached this threshold during recovery was counted, in each of four experiments. Lines connect the median; boxes and whiskers span the corresponding quartiles. (D to G) With the use of the same approach, the behavior of control and ESCRT-deficient cells was compared after a 3-min exposure to GPN [(D and E); $n = 99$ control and 91 knockdown cells from four experiments] or to 10 mM ammonium chloride [(F and G); $n = 43$ control and 29 knockdown cells from four experiments].

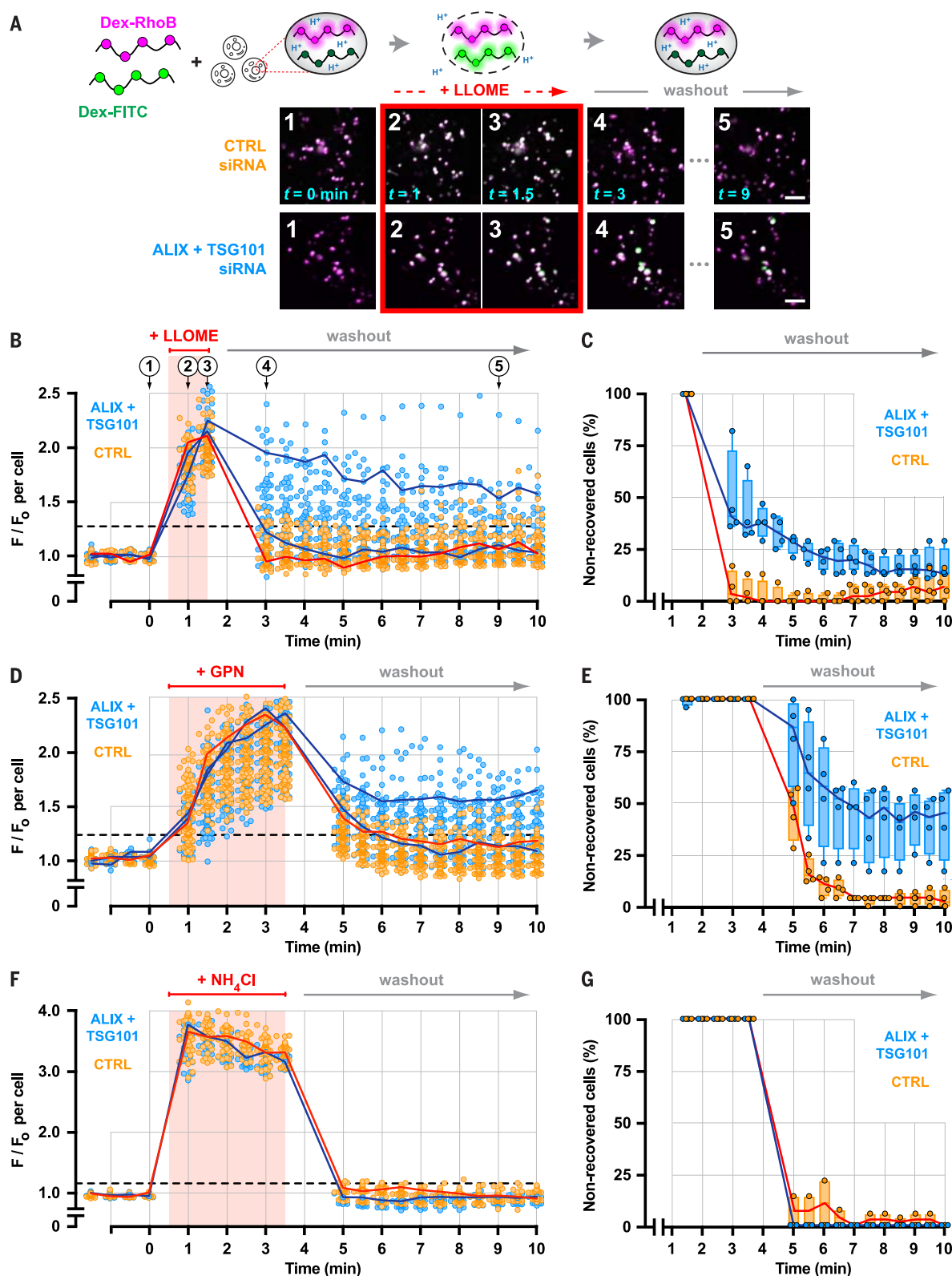
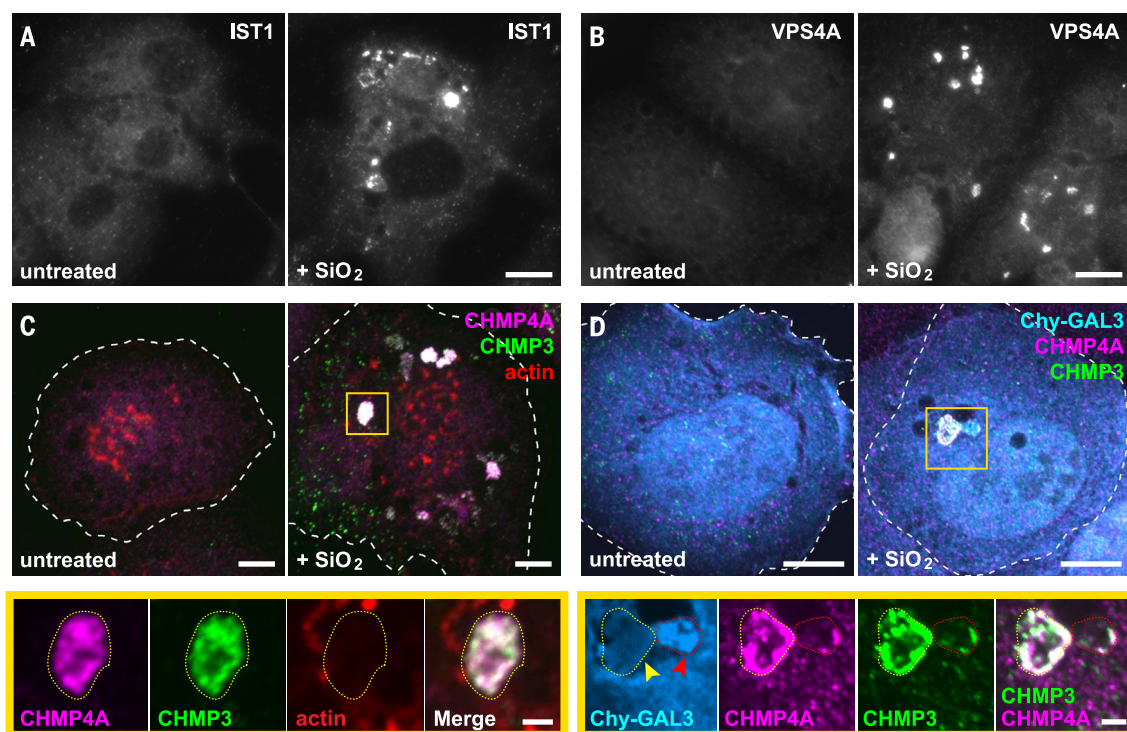


Fig. 7. ESCRTs are recruited to vacuolar compartments disrupted by silica nanocrystals. (A and B) PMA-differentiated THP-1 monocytes were treated with or without silica (SiO₂) (50 µg/ml) nanoparticles for 3 hours and stained for IST1 or VPS4A. Shown are widefield fluorescence images of representative cells from each cohort.

(C) THP-1 cells treated as above were co-stained for the indicated ESCRT-III proteins along with rhodamine-conjugated phalloidin. Note that the prominent actin-rich puncta correspond to podosomes characteristic of this cell type. Shown are maximum-intensity projections of representative cells. Magnified below are single planes corresponding to the boxed area, highlighting the type of compartment (outlined by yellow dotted lines) on which ESCRTs were predominantly observed in SiO₂-fed cells (see fig. S27 for a corresponding three-dimensional rendering). (D) U2OS cells producing mCherry-GAL3 (Chy-GAL3) were fed silica nanoparticles for 1.5 hours and costained for the indicated ESCRT-III



proteins. Shown are maximum-intensity projections and magnified single-plane views of the boxed area. Yellow arrow indicates a compartment (elsewhere encircled by a dotted yellow line) intensely stained for both ESCRT-III proteins but lacking Chy-GAL3; red arrow marks a compartment (elsewhere encircled by a dotted red line) that has accumulated Chy-GAL3 along with some ESCRT. Scale bars, 10 µm (2 µm in magnified views).

to promote osmotic rupture (27, 37) potentially similar to damage caused by materials that normally transit the endolysosomal network. On initial examination, ESCRT recruitment in GPN-treated cells was less pronounced than that seen with LLOME (fig. S22). However, similarly to LLOME, briefly treating cells with GPN caused ESCRT proteins to transiently accumulate on dextran-marked endolysosomes (fig. S23).

ESCRTs facilitate endolysosomal membrane repair

We next compared the timing of ESCRT recruitment with loss and recovery of endolysosomal function, using the Magic Red fluorogenic indicator of lysosomal protease activity (11). Magic Red fluorescence was lost after brief exposure to GPN as above, but returned after washing GPN away (Fig. 5B and movie S1). ESCRT puncta appeared transiently after Magic Red dissipation but before complete recovery (Fig. 5B, fig. S24, and movie S1). A similar relationship between transient ESCRT puncta and Magic Red was observed in cells treated briefly with LLOME (fig. S25) but not in mock-treated controls (fig. S26 and movie S2).

The temporal correlation between transient ESCRT recruitment and endolysosomal recovery suggested that ESCRTs might be involved in repairing damaged endolysosomal membranes, a hypothesis supported by known roles of ESCRT

proteins in resealing wounds at the plasma membrane and nuclear envelope (15–17). We thus implemented the protocol just described to examine endolysosomal recovery in cells depleted of TSG101 and ALIX. ESCRT-deficient cells and controls acquired Magic Red to a similar extent, and lost Magic Red fluorescence with similar kinetics after adding GPN (Fig. 5C), indicating comparable pathway function and GPN processing. However, reacquisition of Magic Red fluorescence after removing GPN was significantly delayed in ESCRT-deficient cells. In addition, ~20% fewer Magic Red structures recovered than were present at the start of the assay, revealing a net loss of functional endolysosomes when the ESCRT response was impaired.

Recovery of endolysosomal activity after damage is arguably a complex process, in which restoration of membrane integrity is an early but critical step. Endolysosomal pH is well known to be acutely sensitive to changes in membrane permeability (38). We thus adapted a ratiometric pH-reporting system as a readout of membrane integrity (Fig. 6A), loading endolysosomes with a mixture of 40- to 70-kDa dextrans conjugated to pH-sensitive FITC or pH-insensitive rhodamine B fluorophores. FITC fluorescence was initially quenched in the acidic endolysosomal environment but transiently increased during brief exposure to LLOME, revealing transient pH dissipation consistent with membrane disruption and re-

covery. Compartments in cells depleted of TSG101 and ALIX responded to LLOME-induced damage with increased FITC fluorescence comparable to that in controls (Fig. 6A). By plotting the median compartmental fluorescence ratio from individual cells over time, however, we noted that many ESCRT-deficient cells recovered organellar pH significantly more slowly than controls (Fig. 6, B and C) (39). Delayed recovery in ESCRT-deficient cells was also apparent after GPN-induced rupture (Fig. 6, D and E). Under both conditions, a significant proportion of knockdown cells failed to recover by the end of the assay, suggesting a greater number of irreparably damaged compartments. Notably, knockdown cells responded similarly to controls to pH modulation by the weak base ammonium chloride (Fig. 6, F and G). Thus, ESCRT activity is required in endolysosomal repair.

ESCRTs respond to membrane perforation by silica crystals

Previous studies have established that vesicular membranes can be damaged by particulate material such as crystals of silica, alum, and uric acid (10, 40, 41). In phagocytic cells, crystal-induced damage can lead to inflammasome activation that triggers secretion of proinflammatory cytokines and in dire cases activates cell death pathways. Although vesicles extensively damaged by silica are subject to lysophagy (3), silica-laden

vacuoles have also been seen to incur small and resolvable membrane disruptions (10).

To assess whether ESCRT machinery would respond to silica-induced damage, we examined ESCRT localization in macrophage-like THP-1 cells that had been fed silica nanoparticles. Multiple ESCRT-III proteins were heavily enriched on vacuolar as well as smaller structures in a majority of silica-treated cells, whereas comparable structures were not observed in mock-treated controls (Fig. 7, A to C). ESCRTs colocalized on silica-damaged compartments and covered a large portion of their surface area (Fig. 7C and fig. S27). Similar ESCRT accumulation was apparent in U2OS cells exposed to silica nanoparticles (Fig. 7D). We additionally noted that ESCRT-positive vacuoles only sometimes contained GAL3 (Fig. 7D), supporting our conclusion that ESCRT machinery responds to sublytic membrane damage independently of galectins.

Discussion

ESCRTs are best known—and named for—their involvement in endosomal trafficking and are essential for generating vesicles that bud into multivesicular endosomes. Here we have shown that ESCRT machinery plays an additional role on endolysosomal organelles, responding to and promoting the repair of damaged or perforated membrane. ESCRT proteins readily accumulate on compartments disrupted by lysosomotropic peptides or internalized silica crystals and are important for restoring compartmental pH and hydrolytic function in an experimental paradigm of acute and reversible membrane damage. Notably, ESCRTs are recruited to small disruptions in endolysosomes independently of factors involved in lysophagy such as galectins, which are preferentially engaged by more extensively damaged compartments. Together with earlier studies showing that ESCRTs respond to wounds at the plasma membrane (15–17) and nuclear envelope (18, 19), our study bolsters the idea that ESCRTs help to protect membrane integrity.

The need to protect endolysosomal integrity has broad implications for many situations, perhaps most critically in highly phagocytic cells that internalize and process substantial loads of potentially disruptive material. Much of what is currently understood about damage to endolysosomal compartments comes from studies of pathogen entry, which collectively reveal a wide variety of strategies for interacting with and modulating host endolysosomal membranes. Roles for ESCRT proteins in bacterial (42, 43) and viral (44–47) entry into cells have been reported, but never fully developed, because of challenges in reconciling them with trafficking functions classically associated with ESCRTs on endolysosomes. A role for ESCRTs in protecting endolysosomal integrity may provide an additional context for further understanding these connections.

Finally, central to this and previous studies of ESCRT function in membrane repair is the question of how this machinery acts to resolve membrane damage. Current thinking regarding ESCRT involvement in plasma membrane

repair envisions that ESCRTs package wounded membrane into vesicles for release from the cell surface (15–17). We propose an alternative although not mutually exclusive possibility in which ESCRT-III proteins and the filaments they form may repair damaged membranes on endolysosomes, and potentially elsewhere, by directly resealing wounds. Although clearly speculative, ESCRT-III filaments exhibit a propensity to assemble into spirals on membranes (21, 48) that can readily be envisioned to surround, constrict, and ultimately close an open hole.

Materials and Methods

Reagents and cell culture

All chemical reagents were purchased from Sigma-Aldrich (St. Louis, MO, USA) unless otherwise indicated. Compounds were used at the following concentrations unless explicitly stated: 25 μ M BAPTA-AM (no. 15551; Cayman Chemical, Ann Arbor, MI, USA); 200 μ M E64d (no. 13533; Cayman Chemical); 200 μ M GPN (no. sc-252858; Santa Cruz Biotechnology Dallas, TX, USA); 1 mM LLOME (no. L7393; Sigma-Aldrich); and 10 μ M wortmannin (no. W1628; Sigma-Aldrich). Concentrated stock solutions of all compounds were prepared in dimethyl sulfoxide (DMSO) and stored at -80°C in single-use aliquots.

The mammalian expression vector encoding mCherry-GAL3 was kindly supplied by C. Wehl at Washington University in St. Louis (MO, USA) and has been described (27). The vector for p97-GFP was previously described (44). The plasmid encoding CHMP3-mCherry was constructed by cloning the human CHMP3 coding sequence into pmCherry-N1 (Clontech, Mountain View, CA, USA) using restriction enzymes Xba I and Hind III.

All cells were maintained at 37°C and supplemented with 5% CO_2 . HeLa human cervical adenocarcinoma, U2OS human osteosarcoma, U-87 MG human glioblastoma, and MCF7 human breast adenocarcinoma cells originally from the American Type Culture Collection (ATCC; Manassas, VA, USA) were grown in Dulbecco's modified Eagle's medium (DMEM) (no. 11965-084; Gibco, Carlsbad, CA, USA) supplemented with 8% v/v fetal bovine serum (FBS; Atlanta Biologicals, Flowery Branch, GA, USA). HeLa cells constitutively producing C-terminal GFP-tagged CHMP1B, CHMP4B, or CHMP4C were a generous gift from S. Simon at Rockefeller University (New York, NY, USA) and have been previously described (49). HeLa cells lacking ATG16L1 as a result of genetic deletion (clone G9), as previously described (33), were kindly provided by R. Xavier at the Broad Institute (Boston, MA, USA) and H. Virgin at Washington University; these were maintained in DMEM supplemented with 10% v/v heat-inactivated FBS, 1 mM sodium pyruvate, and 10 mM HEPES (pH 7.4). The THP-1 (ATCC TIB-202) monocytic cell line was grown in suspension in Roswell Park Memorial Institute (RPMI) 1640 medium (R8758; Sigma-Aldrich) supplemented with 8% v/v FBS, 1 mM sodium pyruvate, and 50 μ M 2-mercaptoethanol. Prior to an experiment, 2×10^5 to 3×10^5 THP1 cells/ml were seeded over glass coverslips and differentiated into a macrophage-like state by

incubating for 3 to 4 days in growth medium additionally supplemented with 0.4 $\mu\text{g}/\text{ml}$ PMA (phorbol-12-myristate-13-acetate) (no. 524400; Calbiochem, San Diego, CA, USA).

Drug treatments for immunofluorescence

Cells were seeded over coverslips under the conditions appropriate for each cell line as described above. Growth media for all manipulations and drug dilutions were warmed to 37°C and equilibrated in 5% CO_2 before adding to cells. For experiments requiring continuous exposure to rupturing agents, coverslips were bathed in medium containing the appropriate agent, typically for 5 to 10 min unless otherwise indicated, then processed for immunofluorescence. For pulse-chase experiments, coverslips were immersed in medium containing the appropriate agent for the time indicated, rinsed in drug-free medium, and then incubated in excess drug-free medium as indicated before processing for immunofluorescence. For experiments assessing the effect of inhibitors or chelators on cellular responses to endolysosomal damage, cells were incubated in medium containing the inhibitor or chelator as specified, then switched to medium containing the inhibitor or chelator together with the indicated rupturing agent.

Crystal nanoparticle uptake

Silica nanoparticles (no. t1rl-sio; InvivoGen, San Diego, CA, USA) were suspended in ultrapure water according to the manufacturer's instructions and diluted in complete growth medium to 50 to 200 $\mu\text{g}/\text{ml}$. The resulting suspension was added to subconfluent cells on glass coverslips, and cells were incubated for the times indicated before being fixed and prepared for immunofluorescence.

RNA interference

Subconfluent cells were suspended by trypsinization and transfected using DharmaFECT 1 (Dharmacon, Lafayette, CO, USA) according to the manufacturer's instructions. The resulting cell suspension was diluted in growth medium to a final concentration of $\sim 1 \times 10^5$ cells/ml, 25 nM total siRNA, and 0.12% v/v transfection reagent, and dispensed into a well of a six-well plate and incubated as described above. Medium was replaced after ~ 12 hours. After 36 to 48 hours, cells were suspended by trypsinization, reseeded at an appropriate density for subsequent experiments and incubated for an additional 16 to 24 hours. Where indicated, cells were additionally transfected with plasmid DNA, as described below, before reseeding. The siRNA sequences used were against human ALIX (5' CCU GGA UAA UGA UGA AGG A), TSG101 (5' CCU CCA GUC UUC UCU CGU C), or firefly luciferase (5' AUG UAU UGG CCU GUA UUA G) as a nontargeting control. Each siRNA was synthesized with dideoxythymidine 3' overhangs by Dharmacon.

DNA transfections

Cells were suspended by trypsinization and transfected using Lipofectamine 2000 (Invitrogen,

Carlsbad, CA, USA) according to the manufacturer's instructions. The resulting cell suspension was diluted in growth medium to a final concentration of $\sim 1 \times 10^5$ cells/ml, 1 $\mu\text{g/ml}$ total DNA, and 0.14% v/v transfection reagent; dispensed into a culture vessel appropriate for the intended application; and incubated for 16 to 24 hours before use.

Immunoblotting

Cell lysates were electrophoretically resolved under denaturing and reducing conditions according to the method of Laemmli, and transferred to Protran nitrocellulose membranes (Amersham, Piscataway, NJ, USA) before immunoblotting with indicated antibodies against ALIX (mouse; no. 634502, Biolegend, San Diego, CA, USA), TSG101 (mouse; no. sc-7964, Santa Cruz), or α -tubulin (mouse; no. T-6199, Sigma-Aldrich), in Tris-buffered saline containing 0.01% v/v Tween 20 (Fisher Scientific, Waltham, MA, USA), and 3% w/v nonfat milk solids (Carnation, Vevey, Switzerland). Immunoblots were developed by chemiluminescence and captured on a ChemiDoc MP Imaging System (Bio-Rad Laboratories, Hercules, CA, USA).

Microscopy

The following imaging platforms were used where designated. Settings appropriate for individual applications are specified in each corresponding section in the methods.

Platform 1, widefield fluorescence: Images were acquired via Metamorph Advanced software (64-bit, v. 7.7.5.0; Molecular Devices, Sunnyvale, CA, USA) on an Olympus (Tokyo, Japan) IX-81 microscope, using a 60 \times 1.42 numerical aperture (NA) PLAPON Apochromat oil-immersion objective, an X-Cite 120Q excitation light source (Excelitas Technologies, Waltham MA, USA), an ORCA-Flash 2.8 scientific CMOS camera (Hamamatsu Photonics, Hamamatsu City, Japan), and the following Brightline filter sets (Semrock, Rochester, NY, USA): long-pass blue emission (no. DAPI-I1LP-A-000); single-band green emission (no. GFP-3035D-000); single-band red emission (no. mCherry-C-000); and single-band far-red emission (no. Cy5-4040C-000).

Platform 2, Olympus spinning disk confocal: This configuration utilized the same microscope and objective as in Platform 1, except that images were acquired via μ Manager (50) using a Yokogawa (Tokyo, Japan) CSU10 spinning disk confocal scanner; a two-line (488 and 561 nm) Sapphire laser module (Coherent, Santa Clara, CA, USA) equipped with an acousto-optic tunable filter (Gooch & Housego, Ilminster, UK); green emission (525 \pm 25 nm) and red emission (605 \pm 26 nm) ET series single-band bandpass filters (Chroma, Bellow Falls, VT, USA); and a Cascade 512B camera (Photometrics, Tucson, AZ, USA) in charge multiplication mode. For all time-lapse recordings, the Olympus IX3 Z-drift compensation module (IX3-ZDC2) was engaged to compensate for axial drift.

Platform 3, Nikon spinning disk confocal, single-camera mode: Images were acquired on a Nikon (Tokyo, Japan) spinning disk confocal system, com-

posed of a Nikon Ti-E inverted microscope, 60 \times 1.40 NA and 100 \times 1.45 NA CFI Plan Apochromat Lambda oil-immersion objectives, and a four-line (405, 488, 561, and 647 nm) laser module coupled to a Yokogawa CSU-X1 variable speed scanner through a filter wheel equipped with the following single-band bandpass filters (Chroma): blue emission ET455/50m (455 \pm 25 nm); green emission ET525/36m (525 \pm 18 nm); red emission ET605/70m (605 \pm 30 nm); and far-red emission ET700/75m (700 \pm 37.5 nm). Images were acquired via NIS-Elements AR software (version 4.51; Nikon) on a Zyla 4.2-megapixel scientific CMOS camera (Andor, Belfast, UK). For all time-lapse recordings, the Nikon Perfect Focus System (PFS) was used to compensate for axial drift. Where indicated, the camera was configured to use a 16-bit dual amplifier to improve the signal-to-noise ratio (SNR) yet preserve a sufficiently wide dynamic range to avoid pixel saturation. Binning was additionally employed to further improve the SNR as appropriate.

Platform 4, Nikon spinning disk confocal, dual-camera mode: Images were acquired on the same system as Platform 3, with the following modifications. For ratiometric pH assessment, samples were simultaneously illuminated with 488- and 561-nm excitation light, and emitted fluorescence was simultaneously directed through an Andor TuCam dual camera adapter to a pair of Andor Zyla 4.2-megapixel sCMOS cameras, using a 580 nm BrightLine dichroic beamsplitter (no. FF580-FD101; Semrock) coupled to red emission (617 \pm 36.5 nm; no. FF02-617/73) and green emission (514 \pm 15 nm; no. FF01-514/30) BrightLine single-band bandpass filters (Semrock). For all other experiments, samples were sequentially illuminated with 488- and then 561-nm excitation light, and only the green component of the 488-nm emission and the red component of the 561-nm emission (as determined by the above filter cut-offs) were retained.

Immunofluorescence

Cells grown over no. 1.5 round glass coverslips (Electron Microscopy Sciences, Hatfield, PA, USA) were fixed in \sim 4% w/v paraformaldehyde (Electron Microscopy Sciences) in PBS for 15 min at room temperature (RT), rinsed with phosphate-buffered saline (PBS), and permeabilized either in 0.1% v/v Triton X-100 (no. 28314; Pierce Biotechnology, Waltham, MA, USA) or, for all immunostains involving LAMP1, in 0.4% w/v saponin (no. 84510; Sigma-Aldrich), in PBS for 10 min at RT. Cells were next rinsed in PBS and blocked for 30 min in 5% v/v goat serum in PBS with or without 0.1% w/v saponin, as appropriate. Alternatively, cells were fixed by immersing the coverslips in cold methanol on dry ice for 30 min, then air-dried for 5 min before blocking.

Cells were immunolabeled in blocking solution for 1 hour at RT with antibodies against the following proteins: ALG-2 at a 200-fold dilution (rabbit; no. 12303-I-AP, ProteinTech Group, Rosemont, IL, USA); ALIX at 5 $\mu\text{g/ml}$ (mouse; no. 634502, Biolegend); CHMP1A at 1 $\mu\text{g/ml}$ (mouse; no. sc-271617, Santa Cruz); CHMP1B at 0.7 $\mu\text{g/ml}$ (rabbit;

no. 14639-I-AP, ProteinTech Group); CHMP2B at 5 $\mu\text{g/ml}$ (rabbit; no. ab33174, Abcam, Cambridge, United Kingdom); CHMP3 at 1 $\mu\text{g/ml}$ (mouse; no. sc-166361, Santa Cruz); CHMP4A at 1.3 $\mu\text{g/ml}$ (rabbit; (32)); CHMP4B at a 200-fold dilution (rabbit; clone 485, a generous gift from A. Shiels at Washington University); CHMP5 at 0.8 $\mu\text{g/ml}$ (rabbit; no. sc-67230, Santa Cruz); GAL3 at 1 $\mu\text{g/ml}$ (rabbit; no. sc-20157, Santa Cruz) or at 1 $\mu\text{g/ml}$ (mouse; no. sc-32790, Santa Cruz); IST1 at 0.4 $\mu\text{g/ml}$ (rabbit; no. 19842-I-AP, ProteinTech); EEA1 at 0.5 $\mu\text{g/ml}$ (mouse; no. 610456, BD Biosciences, Franklin Lakes, NJ, USA); LAMP1 at a 1000-fold dilution of ascites fluid (mouse; clone H4A3, the Developmental Studies Hybridoma Bank, Iowa City, IA, USA); TSG101 at 0.2 $\mu\text{g/ml}$ (mouse; no. sc-7964, Santa Cruz); VPS4A at 5 $\mu\text{g/ml}$ (mouse; no. SAB4200215, Sigma-Aldrich); or VTA1 at 3.7 $\mu\text{g/ml}$ (rabbit; no. GTX107286, GeneTex, Irvine, CA, USA).

After rinsing with PBS, goat secondary antibodies conjugated to Alexa Fluor 488, 555, or 647 fluorescent dyes (Molecular Probes, Carlsbad, CA, USA) were diluted to 1 $\mu\text{g/ml}$ in blocking solution together with 0.25 $\mu\text{g/ml}$ of 4',6-diamidino-2-phenylindole (DAPI; Molecular Probes) and added to immunolabeled cells for 30 min at RT. After rinsing with PBS, coverslips were mounted in a solution of 100 mM Tris (pH 8.5 at RT), 10.5% w/v polyvinyl alcohol, and 21% v/v glycerol and allowed to cure for 24 hours before imaging.

Images of fixed cells were acquired on the platform indicated in each figure legend. Where appropriate, multicolor images were computationally corrected for lateral and axial chromatic aberration using as a reference fluorescent microspheres (Invitrogen) imaged using identical parameters. Images to be compared were collected with identical acquisition settings, configured to maximize the dynamic range while avoiding saturation of relevant features.

Electron microscopy

Cells were grown to near confluence on polylysine-coated 12-mm no. 1 coverslips (BioCoat, no. 354085; Discovery Labware, Bedford, MA, USA), then incubated with LLOME for 10–15 min. Coverslips were next briefly rinsed in 0.3 \times KHMgE (at 1 \times : 30 mM Hepes pH 7.2 at RT, 70 mM KCl, 5 mM MgCl_2 , and 3 mM EGTA), unroofed by brief ultrasonication, and immediately immersed in KHMgE containing 2% w/v paraformaldehyde for \sim 1 hour. Antibody staining was performed as previously described (51) using 18-nm gold particles conjugated to goat anti-rabbit or anti-mouse (Jackson ImmunoResearch, West Grove, PA, USA) antibodies. The area of coverslip with the highest yield of plasma membranes was identified by phase contrast microscopy and trimmed with a diamond knife to \sim 3 \times 3 mm. Replicas were prepared as previously described (51) and viewed on a JEM-1400 transmission electron microscope (JEOL, Tokyo, Japan) at two different tilt angles (\pm 5 $^\circ$). Images were captured using an XR111 camera (Advanced Microscopy Techniques, Woburn, MA, USA). Digital image pairs were made into anaglyphs as described (51).

Sample preparation for time-lapse recordings

The following procedure was used to prepare cells for imaging in all time-lapse experiments; modifications and additional information specific to any given application are described in the corresponding sections below. Cells from a sub-confluent culture were seeded in a four-chamber, no. 1.5 glass-bottom dish (Cellvis, Mountain View, CA, USA) and cultured as appropriate for the intended experiment. Before imaging, medium was replaced with warmed imaging solution [composed of 20 mM HEPES (pH 7.4) at RT, 140 mM NaCl, 2.5 mM KCl, 1.8 mM CaCl₂, 1 mM MgCl₂, 10 mM D-glucose, and 5% v/v FBS], and the dish immediately transferred to a Tokai Hit (Fujinomiya City, Japan) INU series stage-top incubator pre-heated to 37°C. The dish was allowed to equilibrate for 20 min before initiating acquisition. Imaging solution intended for all manipulations and drug dilutions was warmed to 37°C in a separate vessel placed within the stage-top incubator together with the cells, to prevent slight differences in temperature and atmospheric conditions from influencing the cellular response.

Time-lapse recordings of fluorescently tagged proteins

U2OS cells transfected with plasmids encoding the indicated mCherry-tagged proteins, or HeLa cells constitutively producing the indicated GFP-tagged proteins, were seeded at $\sim 1 \times 10^4$ cells per chamber of a four-well dish and cultured for 16 to 24 hours. Where indicated, cells were additionally transfected with plasmids encoding mCherry-tagged proteins before seeding, or loaded with FITC-conjugated or rhodamine B-conjugated dextran (see section on ratiometric pH sensing below) before being prepared for imaging. Single-color recordings were acquired at 30-s intervals on 20 to 30 fields of cells using Platform 2. Dual-color recordings were acquired at 30-s intervals using Platform 4, with both cameras operating at a readout rate of 200 MHz and utilizing a 16-bit dual amplifier with binning. Acquisition was paused for 30 s after the first four timepoints to allow cells to be bathed in imaging solution containing rupturing agent or vehicle alone, and subsequently continued without interruption.

Time-lapse recordings using Magic Red

Stock solutions of Magic Red (no. 938; Immuno-Chemistry Technologies, Bloomington, MN, USA) were prepared in DMSO according to the manufacturer's instructions and stored at -80°C in single-use aliquots. A fresh aliquot was thawed for each experiment before use.

For imaging GFP-tagged ESCRT-III proteins in the presence of Magic Red, appropriate HeLa cells were cultured in four-well dishes and prepared for imaging. Magic Red was diluted 2000-fold in excess imaging solution and equilibrated in an additional vessel on the stage-top incubator together with the cells and regular imaging solution. Before each experiment, 0.5 ml of this labeling solution was added to cells. Compartments labeled with Magic Red began to be discernible by 2 min,

at which time 20 to 30 cells with ~ 10 or more bright puncta were selected for imaging; and by 10 min, the intensity of Magic Red-labeled compartments had stabilized and acquisition was initiated. Acquisition was paused for 30 s after the first four timepoints and the cells bathed in imaging solution containing Magic Red together with the rupturing agent or vehicle. Acquisition was then continued for the duration specified; paused again for 1 min as the cells were washed with 1 ml of fresh imaging solution and reimmersed in additional imaging solution containing only the Magic Red reagent; and subsequently continued without further interruption. Recordings were acquired at 30-s intervals using Platform 4.

For imaging Magic Red in cells depleted of TSG101 and ALIX, U2OS cells were seeded at no more than 5×10^4 cells per chamber of a four-well dish and cultured for 16 to 24 hours before labeling with Magic Red and imaging as above. Fields were imaged consecutively, for 100 msec each, at 30-s intervals on Platform 3, using 561-nm excitation and the 100 \times 1.45 NA objective, and the camera configured to operate at 200 MHz with the 16-bit dual amplifier and 4 \times 4 binning.

Ratiometric pH sensing

U2OS cells were seeded at no more than 5×10^4 cells per chamber of a four-well glass-bottom dish and allowed to adhere for ~ 12 hours. Medium was then replaced with fresh growth medium containing 0.5 mg/ml fluorescein isothiocyanate (FITC)-conjugated 40-kDa dextran (no. D-1844, Molecular Probes) and 0.2 mg/ml rhodamine B-conjugated 70-kDa dextran (no. D-1841, Molecular Probes). After 6 hours, cells were washed in excess medium and incubated for a further 6 hours in dextran-free medium to allow the dextrans to accumulate in late endosomes and lysosomes, before being prepared for imaging.

For each experiment, 20 to 30 fields were selected that consisted of a single cell containing ≥ 10 compartments with bright rhodamine B fluorescence and dim FITC fluorescence. Fields were imaged consecutively, for 100 ms each, at 30-s intervals on Platform 4 using the 100 \times 1.45 NA objective. Both cameras were configured to operate with a readout rate of 200 MHz using a 16-bit dual amplifier and 4 \times 4 binning. After the first four timepoints, the recording was paused for 30 s as cells were bathed in imaging solution containing an appropriate concentration of rupturing agent or other compound. The recording was continued for the duration indicated, paused again for 1 min as the cells were washed once with 1 ml of imaging solution and then bathed in 0.5 ml of imaging solution, and subsequently continued without interruption.

Image analysis

All analyses were performed on the original, unmodified image data using ImageJ (52) with the aid of custom-written scripts that are available on request. For time-lapse recordings, all fields in which cells detached or otherwise moved out of the focal plane at any time during imaging were omitted from analysis.

In Fig. 1D, fractional overlap between the ESCRT and endosomal marker immunostains was calculated as follows. Images were first automatically thresholded to generate regions of interest corresponding to the compartments that stained either for the ESCRT component or for each respective marker. Next, additional regions of interest were generated that corresponded to the intersection of the ESCRT compartments and those identified by each respective marker. Finally, the total pixel area of the intersecting set was calculated, and divided by the total pixel area occupied by the ESCRT compartments in each image.

In Fig. 2 (A and B) and Fig. 3 (C and D), the proportion of each indicated immunostain that exceeded a starting threshold was calculated as follows. Only images of individual cells, and in which the majority of the cellular area fit within the imaging field, were considered for analysis. The outlines of individual cells and the corresponding nuclei were manually traced to further limit the analysis to the pixels within the cytoplasmic area of each cell. A starting intensity threshold was first derived by extracting and pooling pixel intensity values from all images of untreated cells, and then calculating the corresponding 99th percentile for that cohort. Next, the proportion of total signal that exceeded this threshold (i.e., denoted as signal over threshold) was calculated for each image, and normalized to the median signal over threshold for the timepoint cohort with the maximal intensity.

In Fig. 5B, the number of Magic Red and ESCRT puncta was calculated as follows. For each channel, a mean background value was manually calculated by averaging, across several fields, the pixel intensity in an extracellular area at least 100 \times 100 pixels wide. This value was then subtracted from all pixels in the respective channel at every timepoint for each field. Background-corrected images were next linearly contrast-stretched to normalize the pixel intensity distribution: for each field, lower and upper intensity bounds were calculated that allowed 0.1% pixel saturation at the initial timepoint; the remaining timepoints were then adjusted to this range. Finally, puncta were identified in terms of local intensity maxima above an empirically determined threshold. (The same threshold was applied to all recordings of all samples analyzed within each experiment.) For Magic Red, the number of puncta identified at each timepoint was normalized to the initial number of puncta, calculated as the average of the first four timepoints. For fluorescent ESCRT-III proteins, the number of puncta identified at each timepoint was normalized to the initial puncta count as described above, as well as to the maximum number of puncta identified within the respective field at any timepoint during the recording.

In Fig. 5C, the number of Magic Red puncta was determined as follows. Images of Magic Red fluorescence were background-subtracted as above, and further corrected for local intensity variations using the Rolling Ball Background Subtraction algorithm in ImageJ. Compartments

containing Magic Red were then identified by calculating local intensity maxima above a predetermined threshold as above. For every cell, the number of compartments thus identified at each timepoint was normalized to the average number of compartments for that cell during the initial four timepoints.

In Fig. 6, relative changes in endolysosomal pH were extracted from time-lapse recordings of fluorescently-labeled dextrans. A mean background value was first manually calculated for each channel by averaging, across several fields, the pixel intensity in an area at least 100×100 pixels devoid of dextran puncta. This value was then subtracted from all pixels in the respective channel at every timepoint for each field. Dextran-loaded compartments were next computationally identified as follows, using the channel corresponding to the pH-insensitive fluorescence of the rhodamine B-conjugated dextran. At each timepoint, the background-subtracted rhodamine B image was first linearly contrast-stretched by allowing 0.1% pixel saturation to normalize the pixel intensity distribution, and then thresholded according to a predetermined value that preserved the majority of visible dextran-loaded compartments. (The same threshold was applied to all recordings of all samples analyzed within each experiment.) The brightest pixels within the image were next identified by calculating local intensity maxima, and every pixel thus identified was symmetrically enlarged by one pixel in each direction to yield a square region 3×3 pixels wide that encompassed the majority of the corresponding compartment. The total intensity within this region was measured from the original background-subtracted image for each channel, and reported as the ratio of the FITC intensity to the rhodamine B intensity for that compartment at that timepoint. For whole cell-based measurements, the median ratio for the respective field was calculated from the ratios of all compartments identified within that field at that timepoint, and normalized to the average ratio of the first four timepoints for that cell. The data were then filtered by first calculating the 5th and 95th percentiles of the control cohort at the timepoint immediately preceding washout, and then excluding from further analysis any cell from either cohort whose ratio value at this timepoint was less than the above 5th percentile or greater than the above 95th percentile. In addition, any cell whose ratio at any timepoint after washout exceeded the above 95th percentile was also rejected. The extent of recovery was then assessed as follows. A recovery threshold was first derived by pooling all whole cell values from the control cohort throughout the duration of washout and calculating the corresponding 95th percentile. For each cohort the number of cells was then counted that exceeded this threshold at every timepoint after washout and reported as a percentage of all cells analyzed.

Statistics

Statistical significance was calculated using Graphpad Prism 7.0c (La Jolla, CA, USA).

Image processing for publication

All digital images, including fluorescence and electron micrographs, immunoblots, and time-lapse recordings, were linearly contrast stretched in ImageJ to display relevant features. All frames within a movie, and all images and movies intended to be compared, were processed identically. For images of pH-sensitive fluorophores, background fluorescence was first subtracted as described above in the section on time-lapse recordings using Magic Red, before contrast stretching. In fig. S27, three-dimensional projections were rendered from spinning-disk confocal Z-stacks in NIS-Elements software using new engine in alpha blending mode. Data were plotted using Graphpad Prism 7.0c. Figures were assembled for publication using Adobe Illustrator CS4 (San Jose, CA, USA).

REFERENCES AND NOTES

1. Paz et al., Galectin-3, a marker for vacuole lysis by invasive pathogens. *Cell. Microbiol.* **12**, 530–544 (2010). doi: [10.1111/j.1462-5822.2009.01415.x](https://doi.org/10.1111/j.1462-5822.2009.01415.x); pmid: [19951367](https://pubmed.ncbi.nlm.nih.gov/19951367/)
2. T. L. Thurston, M. P. Wandel, N. von Muhlinen, A. Foeglein, F. Randow, Galectin 8 targets damaged vesicles for autophagy to defend cells against bacterial invasion. *Nature* **482**, 414–418 (2012). doi: [10.1038/nature10744](https://doi.org/10.1038/nature10744); pmid: [2246324](https://pubmed.ncbi.nlm.nih.gov/2246324/)
3. I. Maejima et al., Autophagy sequesters damaged lysosomes to control lysosomal biogenesis and kidney injury. *EMBO J.* **32**, 2336–2347 (2013). doi: [10.1038/emboj.2013.171](https://doi.org/10.1038/emboj.2013.171); pmid: [23921551](https://pubmed.ncbi.nlm.nih.gov/23921551/)
4. Y.-H. Hung, L. M.-W. Chen, J.-Y. Yang, W. Y. Yang, Spatiotemporally controlled induction of autophagy-mediated lysosome turnover. *Nat. Commun.* **4**, 2111 (2013). doi: [10.1038/ncomms3111](https://doi.org/10.1038/ncomms3111); pmid: [23817530](https://pubmed.ncbi.nlm.nih.gov/23817530/)
5. S. Chauhan et al., TRIMs and galectins globally cooperate and TRIM16 and galectin-3 co-direct autophagy in endomembrane damage homeostasis. *Dev. Cell* **39**, 13–27 (2016). doi: [10.1016/j.devcel.2016.08.003](https://doi.org/10.1016/j.devcel.2016.08.003); pmid: [27693506](https://pubmed.ncbi.nlm.nih.gov/27693506/)
6. Y. Yoshida et al., Ubiquitination of exposed glycoproteins by SCF^{FBX027} directs damaged lysosomes for autophagy. *Proc. Natl. Acad. Sci. U.S.A.* **114**, 8574–8579 (2017). doi: [10.1073/pnas.1702615114](https://doi.org/10.1073/pnas.1702615114); pmid: [28743755](https://pubmed.ncbi.nlm.nih.gov/28743755/)
7. M. J. Davis, B. Gregorka, J. E. Gestwicki, J. A. Swanson, Inducible renitence limits *Listeria monocytogenes* escape from vacuoles in macrophages. *J. Immunol.* **189**, 4488–4495 (2012). doi: [10.4049/jimmunol.1103158](https://doi.org/10.4049/jimmunol.1103158); pmid: [23002437](https://pubmed.ncbi.nlm.nih.gov/23002437/)
8. S. Kreibich et al., Autophagy proteins promote repair of endosomal membranes damaged by the *Salmonella* type three secretion system 1. *Cell Host Microbe* **18**, 527–537 (2015). doi: [10.1016/j.chom.2015.10.015](https://doi.org/10.1016/j.chom.2015.10.015); pmid: [26567507](https://pubmed.ncbi.nlm.nih.gov/26567507/)
9. U. Repnik et al., L-leucyl-L-leucine methyl ester does not release cysteine cathepsins to the cytosol but inactivates them in transiently permeabilized lysosomes. *J. Cell Sci.* **130**, 3124–3140 (2017). doi: [10.1242/jcs.204529](https://doi.org/10.1242/jcs.204529); pmid: [28754686](https://pubmed.ncbi.nlm.nih.gov/28754686/)
10. G. N. Hoshi, A. M. Goetjen, D. A. Knecht, Silica particles cause NADPH oxidase-independent ROS generation and transient phagolysosomal leakage. *Mol. Biol. Cell* **26**, 3150–3164 (2015). doi: [10.1091/mbc.E15-03-0126](https://doi.org/10.1091/mbc.E15-03-0126); pmid: [26202463](https://pubmed.ncbi.nlm.nih.gov/26202463/)
11. N. A. Bright, L. J. Davis, J. P. Luzio, Endolysosomes are the principal intracellular sites of acid hydrolase activity. *Curr. Biol.* **26**, 2233–2245 (2016). doi: [10.1016/j.cub.2016.06.046](https://doi.org/10.1016/j.cub.2016.06.046); pmid: [27498570](https://pubmed.ncbi.nlm.nih.gov/27498570/)
12. N. W. Andrews, P. E. Almeida, M. Corrotte, Damage control: Cellular mechanisms of plasma membrane repair. *Trends Cell Biol.* **24**, 734–742 (2014). doi: [10.1016/j.tcb.2014.07.008](https://doi.org/10.1016/j.tcb.2014.07.008); pmid: [25105093](https://pubmed.ncbi.nlm.nih.gov/25105093/)
13. S. T. Cooper, P. L. McNeil, Membrane repair: Mechanisms and pathophysiology. *Physiol. Rev.* **95**, 1205–1240 (2015). doi: [10.1152/physrev.00037.2014](https://doi.org/10.1152/physrev.00037.2014); pmid: [26336031](https://pubmed.ncbi.nlm.nih.gov/26336031/)
14. P. Isermann, J. Lammerding, Consequences of a tight squeeze: Nuclear envelope rupture and repair. *Nucleus* **8**, 268–274 (2017). doi: [10.1080/19491034.2017.1292191](https://doi.org/10.1080/19491034.2017.1292191); pmid: [28287898](https://pubmed.ncbi.nlm.nih.gov/28287898/)
15. A. J. Jimenez et al., ESCRT machinery is required for plasma membrane repair. *Science* **343**, 1247136 (2014). doi: [10.1126/science.1247136](https://doi.org/10.1126/science.1247136); pmid: [24482116](https://pubmed.ncbi.nlm.nih.gov/24482116/)
16. L. L. Scheffer et al., Mechanism of Ca²⁺-triggered ESCRT assembly and regulation of cell membrane repair. *Nat. Commun.* **5**, 5646 (2014). doi: [10.1038/ncomms6646](https://doi.org/10.1038/ncomms6646); pmid: [25534348](https://pubmed.ncbi.nlm.nih.gov/25534348/)
17. Y. N. Gong et al., ESCRT-III acts downstream of MLKL to regulate necroptotic cell death and its consequences. *Cell* **169**, 286–300.e16 (2017). doi: [10.1016/j.cell.2017.03.020](https://doi.org/10.1016/j.cell.2017.03.020); pmid: [28388412](https://pubmed.ncbi.nlm.nih.gov/28388412/)
18. C. M. Denais et al., Nuclear envelope rupture and repair during cancer cell migration. *Science* **352**, 353–358 (2016). doi: [10.1126/science.1247297](https://doi.org/10.1126/science.1247297); pmid: [27013428](https://pubmed.ncbi.nlm.nih.gov/27013428/)
19. M. Raab et al., ESCRT III repairs nuclear envelope ruptures during cell migration to limit DNA damage and cell death. *Science* **352**, 359–362 (2016). doi: [10.1126/science.1247611](https://doi.org/10.1126/science.1247611); pmid: [27013426](https://pubmed.ncbi.nlm.nih.gov/27013426/)
20. J. H. Hurley, ESCRTs are everywhere. *EMBO J.* **34**, 2398–2407 (2015). doi: [10.15252/emboj.201592484](https://doi.org/10.15252/emboj.201592484); pmid: [26311197](https://pubmed.ncbi.nlm.nih.gov/26311197/)
21. N. Chiaruttini, A. Roux, Dynamic and elastic shape transitions in curved ESCRT-III filaments. *Curr. Opin. Cell Biol.* **47**, 126–135 (2017). doi: [10.1016/j.cub.2017.07.002](https://doi.org/10.1016/j.cub.2017.07.002); pmid: [28728013](https://pubmed.ncbi.nlm.nih.gov/28728013/)
22. J. Schöneberg, I. H. Lee, J. H. Iwasa, J. H. Hurley, Reverse-topology membrane scission by the ESCRT proteins. *Nat. Rev. Mol. Cell Biol.* **18**, 5–17 (2017). doi: [10.1038/nrm.2016.121](https://doi.org/10.1038/nrm.2016.121); pmid: [27703243](https://pubmed.ncbi.nlm.nih.gov/27703243/)
23. D. L. Thiele, P. E. Lipsky, Mechanism of L-leucyl-L-leucine methyl ester-mediated killing of cytotoxic lymphocytes: Dependence on a lysosomal thiol protease, dipeptidyl peptidase I, that is enriched in these cells. *Proc. Natl. Acad. Sci. U.S.A.* **87**, 83–87 (1990). doi: [10.1073/pnas.87.1.83](https://doi.org/10.1073/pnas.87.1.83); pmid: [2296607](https://pubmed.ncbi.nlm.nih.gov/2296607/)
24. S. Aits et al., Sensitive detection of lysosomal membrane permeabilization by lysosomal galectin puncta assay. *Autophagy* **11**, 1408–1424 (2015). doi: [10.1080/15548627.2015.1063871](https://doi.org/10.1080/15548627.2015.1063871); pmid: [26114578](https://pubmed.ncbi.nlm.nih.gov/26114578/)
25. L. Christ et al., ALIX and ESCRT-III function as parallel ESCRT-III recruiters in cytokinetic abscission. *J. Cell Biol.* **212**, 499–513 (2016). doi: [10.1083/jcb.201507009](https://doi.org/10.1083/jcb.201507009); pmid: [26929449](https://pubmed.ncbi.nlm.nih.gov/26929449/)
26. S. Tang et al., ESCRT-III activation by parallel action of ESCRT-I/II and ESCRT-0/Bro1 during MVB biogenesis. *eLife* **5**, e15507 (2016). doi: [10.7554/eLife.15507](https://doi.org/10.7554/eLife.15507); pmid: [27074665](https://pubmed.ncbi.nlm.nih.gov/27074665/)
27. T. Haller, P. Dietl, P. Deetjen, H. Völkl, The lysosomal compartment as intracellular calcium store in MDCK cells: A possible involvement in InsP₃-mediated Ca²⁺ release. *Cell Calcium* **19**, 157–165 (1996). doi: [10.1016/S0143-4160\(96\)90084-6](https://doi.org/10.1016/S0143-4160(96)90084-6); pmid: [8689673](https://pubmed.ncbi.nlm.nih.gov/8689673/)
28. B. S. Kilpatrick, E. R. Eden, A. H. Schapira, C. E. Futter, S. Patel, Direct mobilisation of lysosomal Ca²⁺ triggers complex Ca²⁺ signals. *J. Cell Sci.* **126**, 60–66 (2013). doi: [10.1242/jcs.118836](https://doi.org/10.1242/jcs.118836); pmid: [23108667](https://pubmed.ncbi.nlm.nih.gov/23108667/)
29. M. Maki, T. Takahara, H. Shibata, Multifaceted roles of ALG-2 in Ca²⁺-regulated membrane trafficking. *Int. J. Mol. Sci.* **17**, 1401 (2016). doi: [10.3390/ijms17091401](https://doi.org/10.3390/ijms17091401); pmid: [2751067](https://pubmed.ncbi.nlm.nih.gov/2751067/)
30. C. Papadopoulos et al., VCP/p97 cooperates with YOD1, UBXD1 and PLAA to drive clearance of ruptured lysosomes by autophagy. *EMBO J.* **36**, 135–150 (2017). doi: [10.15252/emboj.201695148](https://doi.org/10.15252/emboj.201695148); pmid: [27753622](https://pubmed.ncbi.nlm.nih.gov/27753622/)
31. C. Lefebvre, R. Legouis, E. Culetto, ESCRT and autophagies: Endosomal functions and beyond. *Semin. Cell Dev. Biol.* **74**, 21–28 (2018). pmid: [28807884](https://pubmed.ncbi.nlm.nih.gov/28807884/)
32. N. T. Ktistakis, S. A. Tooze, Digesting the Expanding Mechanisms of Autophagy. *Trends Cell Biol.* **26**, 624–635 (2016). doi: [10.1016/j.tcb.2016.03.006](https://doi.org/10.1016/j.tcb.2016.03.006); pmid: [27050762](https://pubmed.ncbi.nlm.nih.gov/27050762/)
33. J. Begun et al., Integrated genomics of Crohn's disease risk variant identifies a role for CLEC12A in antibacterial autophagy. *Cell Rep.* **11**, 1905–1918 (2015). doi: [10.1016/j.celrep.2015.05.045](https://doi.org/10.1016/j.celrep.2015.05.045); pmid: [26095365](https://pubmed.ncbi.nlm.nih.gov/26095365/)
34. We used several fluorescently tagged ESCRT-III proteins interchangeably throughout this study and note that their recruitment to damaged endolysosomes was indistinguishable within the spatial and kinetic resolution of our assays.
35. O. Maier, S. A. Marvin, H. Wodrich, E. M. Campbell, C. M. Wiethoff, Spatiotemporal dynamics of adenovirus membrane rupture and endosomal escape. *J. Virol.* **86**, 10821–10828 (2012). doi: [10.1128/JVI.01428-12](https://doi.org/10.1128/JVI.01428-12); pmid: [22855481](https://pubmed.ncbi.nlm.nih.gov/22855481/)
36. B. E. Steinberg et al., A cation counterflux supports lysosomal acidification. *J. Cell Biol.* **189**, 1171–1186 (2010). doi: [10.1083/jcb.200911083](https://doi.org/10.1083/jcb.200911083); pmid: [20566682](https://pubmed.ncbi.nlm.nih.gov/20566682/)
37. M. Jadot, C. Colmant, S. Wattiaux-De Coninck, R. Wattiaux, Intralysosomal hydrolysis of glycyl-L-phenylalanine 2-naphthylamide. *Biochem. J.* **219**, 965–970 (1984). doi: [10.1042/bj2190965](https://doi.org/10.1042/bj2190965); pmid: [6743255](https://pubmed.ncbi.nlm.nih.gov/6743255/)
38. Y. Ishida, S. Nayak, J. A. Mindell, M. Grabe, A model of lysosomal pH regulation. *J. Gen. Physiol.* **141**, 705–720 (2013). doi: [10.1085/jgp.201210930](https://doi.org/10.1085/jgp.201210930); pmid: [23712550](https://pubmed.ncbi.nlm.nih.gov/23712550/)

39. The range of recovery defects observed could be influenced, among others, by incomplete protein depletion through RNA interference (RNAi) as noted in fig. S9; by the stochastic nature of membrane damage induced by the lysosomotropic compounds used here; or by additional undefined repair machinery.
40. V. Hornung *et al.*, Silica crystals and aluminum salts activate the NALP3 inflammasome through phagosomal destabilization. *Nat. Immunol.* **9**, 847–856 (2008). doi: [10.1038/ni.1631](https://doi.org/10.1038/ni.1631); pmid: [18604214](https://pubmed.ncbi.nlm.nih.gov/18604214/)
41. S. R. Mulay, H. J. Anders, Crystal nephropathies: Mechanisms of crystal-induced kidney injury. *Nat. Rev. Nephrol.* **13**, 226–240 (2017). doi: [10.1038/nrneph.2017.10](https://doi.org/10.1038/nrneph.2017.10); pmid: [28218266](https://pubmed.ncbi.nlm.nih.gov/28218266/)
42. L. W. Cheng *et al.*, Use of RNA interference in *Drosophila* S2 cells to identify host pathways controlling compartmentalization of an intracellular pathogen. *Proc. Natl. Acad. Sci. U.S.A.* **102**, 13646–13651 (2005). doi: [10.1073/pnas.0506461102](https://doi.org/10.1073/pnas.0506461102); pmid: [16157870](https://pubmed.ncbi.nlm.nih.gov/16157870/)
43. J. A. Philips, M. C. Porto, H. Wang, E. J. Rubin, N. Perrimon, ESCRT factors restrict mycobacterial growth. *Proc. Natl. Acad. Sci. U.S.A.* **105**, 3070–3075 (2008). doi: [10.1073/pnas.0707206105](https://doi.org/10.1073/pnas.0707206105); pmid: [18287038](https://pubmed.ncbi.nlm.nih.gov/18287038/)
44. G. Pasqual, J. M. Rojek, M. Masin, J. Y. Chatton, S. Kunz, Old world arenaviruses enter the host cell via the multivesicular body and depend on the endosomal sorting complex required for transport. *PLoS Pathog.* **7**, e1002232 (2011). doi: [10.1371/journal.ppat.1002232](https://doi.org/10.1371/journal.ppat.1002232); pmid: [21931550](https://pubmed.ncbi.nlm.nih.gov/21931550/)
45. D. Silva-Ayala *et al.*, Genome-wide RNAi screen reveals a role for the ESCRT complex in rotavirus cell entry. *Proc. Natl. Acad. Sci. U.S.A.* **110**, 10270–10275 (2013). doi: [10.1073/pnas.1304932110](https://doi.org/10.1073/pnas.1304932110); pmid: [23733942](https://pubmed.ncbi.nlm.nih.gov/23733942/)
46. O. Shtanko, R. A. Nikitina, C. Z. Altuntas, A. A. Chepurinov, R. A. Davey, Crimean-Congo hemorrhagic fever virus entry into host cells occurs through the multivesicular body and requires ESCRT regulators. *PLoS Pathog.* **10**, e1004390 (2014). doi: [10.1371/journal.ppat.1004390](https://doi.org/10.1371/journal.ppat.1004390); pmid: [25233119](https://pubmed.ncbi.nlm.nih.gov/25233119/)
47. B. Kumar *et al.*, ESCRT-III protein Tsg101 plays a role in the post-macropinocytic trafficking and infection of endothelial cells by Kaposi's sarcoma-associated herpesvirus. *PLoS Pathog.* **12**, e1005960 (2016). doi: [10.1371/journal.ppat.1005960](https://doi.org/10.1371/journal.ppat.1005960); pmid: [27764233](https://pubmed.ncbi.nlm.nih.gov/27764233/)
48. P. I. Hanson, R. Roth, Y. Lin, J. E. Heuser, Plasma membrane deformation by circular arrays of ESCRT-III protein filaments. *J. Cell Biol.* **180**, 389–402 (2008). doi: [10.1083/jcb.200707031](https://doi.org/10.1083/jcb.200707031); pmid: [18209100](https://pubmed.ncbi.nlm.nih.gov/18209100/)
49. N. Jouvenet, M. Zhadina, P. D. Bieniasz, S. M. Simon, Dynamics of ESCRT protein recruitment during retroviral assembly. *Nat. Cell Biol.* **13**, 394–401 (2011). doi: [10.1038/ncb2207](https://doi.org/10.1038/ncb2207); pmid: [21394083](https://pubmed.ncbi.nlm.nih.gov/21394083/)
50. A. D. Edelstein *et al.*, Advanced methods of microscope control using µManager software. *J. Biol. Methods* **1**, 10 (2014). doi: [10.14440/jbm.2014.36](https://doi.org/10.14440/jbm.2014.36); pmid: [25606571](https://pubmed.ncbi.nlm.nih.gov/25606571/)
51. A. G. Cashikar *et al.*, Structure of cellular ESCRT-III spirals and their relationship to HIV budding. *eLife* **3**, e02184 (2014). doi: [10.7554/eLife.02184](https://doi.org/10.7554/eLife.02184); pmid: [24878737](https://pubmed.ncbi.nlm.nih.gov/24878737/)
52. C. A. Schneider, W. S. Rasband, K. W. Eliceiri, NIH Image to ImageJ: 25 years of image analysis. *Nat. Methods* **9**, 671–675 (2012). doi: [10.1038/nmeth.2089](https://doi.org/10.1038/nmeth.2089); pmid: [22930834](https://pubmed.ncbi.nlm.nih.gov/22930834/)

ACKNOWLEDGMENTS

We thank C. Wehl and J. Philips for insightful discussions, reagents, and sharing unpublished data; K. Blumer, D. Kast, and D. Piston for helpful discussions; R. Roth for making deep-etch electron microscopy replicas; A. Ustione for microscopy assistance; and A. Clippinger and members of the Hanson laboratory for helpful discussions, reagents, microscopy assistance, and contributions to experimental design. **Funding:** This work was supported by R01 GM122434 from the National Institutes of Health (to P.I.H.). Imaging was performed in part through use of the Washington University Center for Cellular Imaging, partially supported by the Children's Discovery Institute at Washington University (CDI-CORE-2015-505). **Author contributions:** M.L.S., P.H.S., and P.I.H. designed research. All authors performed research and/or analyzed data. M.L.S. and P.I.H. wrote the manuscript. All authors discussed results and commented on the manuscript. **Competing interests:** The authors declare no competing financial interests. **Data and materials availability:** All data needed to evaluate the conclusions in the paper are present in the paper and/or the supplementary materials.

SUPPLEMENTARY MATERIALS

www.sciencemag.org/content/360/6384/eaar5078/suppl/DC1
Figs. S1 to S27
Movies S1 and S2

15 November 2017; accepted 16 February 2018
10.1126/science.aar5078

RESEARCH ARTICLE

NEUROSCIENCE

CRMP2-binding compound, edonerpic maleate, accelerates motor function recovery from brain damage

Hiroki Abe,^{1*} Susumu Jitsuki,^{1*} Waki Nakajima,^{1*} Yumi Murata,^{2*}
 Aoi Jitsuki-Takahashi,¹ Yuki Katsuno,¹ Hirobumi Tada,¹ Akane Sano,¹ Kumiko Suyama,¹
 Nobuyuki Mochizuki,^{1,3,4} Takashi Komori,^{1,3,4} Hitoshi Masuyama,^{1,3,4}
 Tomohiro Okuda,^{3,4} Yoshio Goshima,⁵ Noriyuki Higo,² Takuya Takahashi^{1†}

Brain damage such as stroke is a devastating neurological condition that may severely compromise patient quality of life. No effective medication-mediated intervention to accelerate rehabilitation has been established. We found that a small compound, edonerpic maleate, facilitated experience-driven synaptic glutamate AMPA (α -amino-3-hydroxy-5-methyl-4-isoxazole-propionic-acid) receptor delivery and resulted in the acceleration of motor function recovery after motor cortex cryoinjury in mice in a training-dependent manner through cortical reorganization. Edonerpic bound to collapsin-response-mediator-protein 2 (CRMP2) and failed to augment recovery in CRMP2-deficient mice. Edonerpic maleate enhanced motor function recovery from internal capsule hemorrhage in nonhuman primates. Thus, edonerpic maleate, a neural plasticity enhancer, could be a clinically potent small compound with which to accelerate rehabilitation after brain damage.

Brain damage mainly caused by stroke is a severe neurological condition that may lead to paralysis and compromise work capacity and self-care. No pharmacological intervention that could foster recovery and complement current rehabilitation has yet been established as effective. Restoration of motor impairment after brain damage is considered to be the result of compensative neural plasticity in intact brain regions, mediated by the reorganization of cortical motor maps (1–7). Experience-dependent synaptic AMPA (α -amino-3-hydroxy-5-methyl-4-isoxazole-propionic-acid) receptor (AMPA) delivery underlies behaviors that require neural plasticity such as learning (8–18). We have previously shown that synaptic AMPAR trafficking plays crucial roles in the compensative cortical reorganization of the sensory cortex (15). Thus, the facilitation of experience-dependent synaptic AMPAR delivery could result in rehabilitative training-dependent motor cortical reorganization and the acceleration of motor function recovery with rehabilitation after brain damage. Collapsin-

response-mediator-protein 2 (CRMP2) is a downstream molecule of semaphorin (19, 20) and is thought to be related to synaptic plasticity and learning (21, 22).

Results

Edonerpic maleate facilitates experience-dependent synaptic AMPAR delivery in the adult mice barrel cortex

Edonerpic maleate (T-817MA; 1-{3-[2-(1-benzothiophen-5-yl)ethoxy]propyl}azetidin-3-ol maleate) (Fig. 1A) protects neuronal cells and modifies their morphology (23). Edonerpic maleate has been the most characterized compound among this series of compounds. Further, phase I of a clinical trial of edonerpic maleate was successfully terminated, and the safety of edonerpic maleate has been proven. However, its clinical application has not been determined. In order to explore actions of edonerpic maleate on neuronal function, we focused on the roles of edonerpic maleate in experience-dependent synaptic plasticity, which has not been studied. To examine whether edonerpic maleate affects experience-dependent synaptic AMPAR delivery, we focused on layer 4–2/3 pyramidal synapses of adult mice barrel cortex, where natural whisker experience-dependent AMPAR delivery is not observed (Fig. 1, B and C). We administered edonerpic maleate orally, twice a day (30 mg/kg) for 3 weeks to 2-month-old adult mice. Then, we prepared acute brain slices and examined synaptic responses at layer 4–2/3 pyramidal synapses of the barrel cortex. We first recorded the ratio of evoked AMPAR- to NMDA

(*N*-methyl-D-aspartate) receptor (NMDAR)-mediated synaptic currents (AMPA/NMDA ratio). We found an increased AMPA/NMDA ratio in edonerpic maleate-administered compared with vehicle-administered mice (Fig. 1B). This effect was whisker experience-dependent because we detected no increase of the AMPA/NMDA ratio in edonerpic maleate-administered mice in the absence of whiskers (deprived for 2 or 3 days) (Fig. 1B). There was no difference in kinetics of NMDAR-mediated currents among these groups (fig. S1). We then replaced extracellular Ca^{2+} with Sr^{2+} in order to induce asynchronous transmitter release and analyzed the quantal EPSCs (excitatory postsynaptic currents) at layer 4–2/3 pyramidal synapses. We found increased amplitude of evoked miniature EPSCs (mEPSCs) in edonerpic maleate-administered mice, compared with vehicle-administered mice, in the presence but not in the absence of whiskers (Fig. 1C). Three days of treatment with edonerpic maleate exhibited the same effect (fig. S2). Consistent with this, the induction of long-term potentiation (LTP) at layer 4–2/3 barrel cortical synapses onto pyramidal neurons was facilitated by the presence of edonerpic maleate (fig. S3).

Edonerpic maleate binds to CRMP2

We prepared affinity columns of edonerpic-conjugated resin (edonerpic beads) (fig. S4A), only linker-conjugated resin (linker beads), or inactivated control resin (control beads). After the protein purification, we analyzed purified proteins and detected a band near 60 kDa specific to purified proteins by edonerpic beads (Fig. 1D). Mass spectrometry revealed that this band corresponded to CRMP2 (Fig. 1E). Immunoblotting of mice brain lysate pulled down by edonerpic beads (but not linker beads or control beads) also detected the CRMP2-specific band (Fig. 1F). To further examine the binding of edonerpic to CRMP2, we pulled down the brain lysate obtained from CRMP2-deficient mice with edonerpic beads (24). We did not observe detectable CRMP2-positive bands with CRMP2-deficient mice (fig. S4B). We performed isothermal titration calorimetry (ITC) with cell-free conditions and found that the dissociation constant (K_d) value of the edonerpic-binding to CRMP2 at $\sim 7.35 \times 10^{-4}$ M (Fig. 1G). To further investigate the effect of edonerpic on CRMP2, we mixed purified CRMP2 with edonerpic maleate in a cell-free condition and analyzed with native polyacrylamide gel electrophoresis. Edonerpic maleate significantly ($P < 0.05$) decreased the amount of monomeric CRMP2 (Fig. 1H), indicating that edonerpic maleate regulates multimerization of CRMP2 through direct interaction.

To examine whether CRMP2 mediates the edonerpic maleate-induced facilitation of synaptic AMPAR delivery in the adult mice barrel cortex, we used CRMP2-deficient mice (24). We administered edonerpic maleate as described above to 3-month-old CRMP2-deficient mice, measured the AMPA/NMDA ratio, and evoked mEPSC at layer 4–2/3 synapses onto pyramidal neurons of the barrel cortex. We observed a decreased

¹Yokohama City University Graduate School of Medicine, Department of Physiology, Yokohama, 236-0004, Japan.

²Human Informatics Research Institute, National Institute of Advanced Industrial Science and Technology, Ibaraki, 305-8568, Japan. ³Toyama Chemical Co., Tokyo, 160-0023, Japan. ⁴Fujifilm Corporation, Tokyo, 107-0052, Japan.

⁵Yokohama City University Graduate School of Medicine, Department of Molecular Pharmacology and Neurobiology, Yokohama, 236-0004, Japan.

*These authors contributed equally to this work.

†Corresponding author. Email: takahast@yokohama-cu.ac.jp

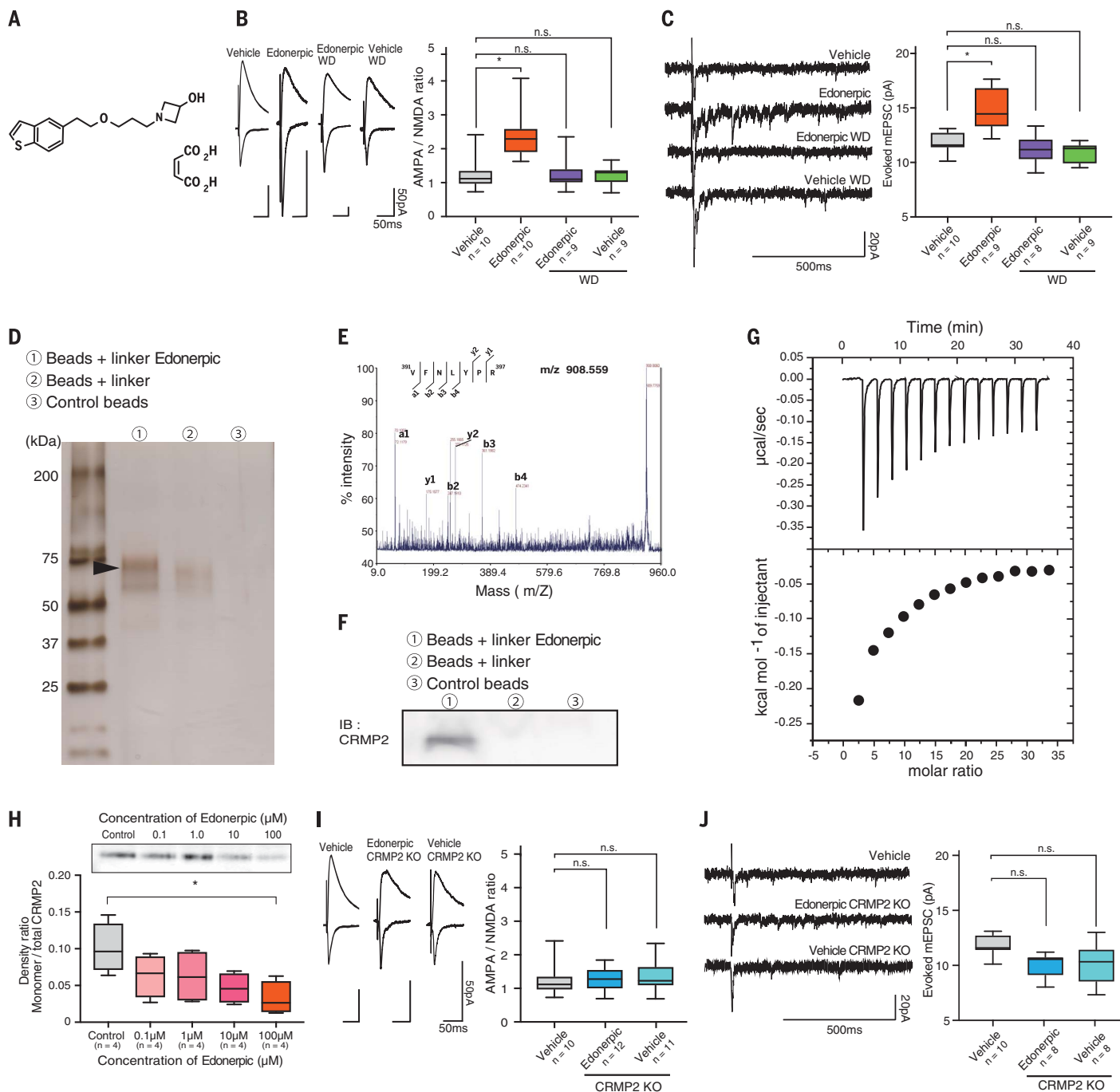


Fig. 1. Edonerpic maleate–induced facilitation of synaptic AMPAR delivery. (A) Chemical structure of edonerpic maleate. (B) (Left) Representative EPSCs in the barrel cortex treated with vehicle with intact whiskers, edonerpic with intact whiskers, edonerpic with whiskers deprived (WD), or vehicle with WD. (Right) Average AMPA/NMDA ratio. (C) (Left) Evoked mEPSC as in (B). (Right) Average amplitudes of evoked mEPSCs. (D) Silver-stained gel showing edonerpic-binding proteins. The black arrowhead indicates the protein selected for analysis with mass spectrometry. (E) Tandem mass spectra from tryptic digests of CRMP2. Fragment ions of the a, b, and y series identified in the tandem mass spectra from each peptide are shown. (F) Immunoblot of cortical lysate pulled down by indicated beads. (G) ITC-based measurements of

edonerpic fumarate binding to CRMP2. (Top) Raw thermogram. (Bottom) Integrated titration curve. (H) (Top) Immunoblot of purified CRMP2 reacted with edonerpic. (Bottom) Monomer-to-total CRMP2 ratio. Data were normalized to control. (I) (Left) Representative EPSCs in the barrel cortex in CRMP2 knockout mice. Data of WT mice treated with vehicle with intact whiskers were derived from Fig. 1B. (Right) Average AMPA/NMDA ratio. (J) (Left) Evoked mEPSC in the barrel cortex in CRMP2 knockout mice. Data of WT mice treated with vehicle with intact whiskers were derived from Fig. 1C. (Right) Average amplitudes of evoked mEPSCs. * $P < 0.05$. Data were analyzed with one-way ANOVA, with Dunnett's post hoc tests [(B), (C), (H), (I), and (J)]. The number of animals used for each experiment is indicated in the figure.

AMPA/NMDA ratio and the amplitude of evoked mEPSC in edonerpic maleate-administered CRMP2-deficient mice, compared with edonerpic maleate-administered wild-type (WT) mice, in the presence of whiskers [Fig. 1, I and J (and Fig. 1, B and C)]. The AMPA/NMDA ratio and the amplitude of evoked mEPSC in edonerpic maleate- or vehicle-administered CRMP2-deficient mice was comparable with that in vehicle-administered WT mice with whiskers and edonerpic maleate-administered WT mice in the absence of whiskers [Fig. 1, I and J] (and Fig. 1, B and C)]. There was no difference in kinetics of NMDAR-mediated currents among these groups (fig. S4C). We next knocked down the expression of CRMP2 of pyramidal neurons at layer 2/3 of the adult barrel cortex by means of lentivirus-mediated *in vivo* gene transfer of short hairpin RNA (shRNA) targeted to CRMP2 (25), examined the AMPA/NMDA ratio, and evoked mEPSC at layer 4–2/3 pyramidal synapses in the adult barrel cortex with whole-cell recordings. CRMP2 knockdown blocked edonerpic maleate-induced increase of the AMPA/NMDA ratio (fig. S4D) and the amplitude of evoked mEPSC at synapses formed from layer 4 to layer 2/3 pyramidal neurons (fig. S4E).

Edonerpic maleate accelerates motor function recovery from injury of the motor cortex

Recovery of motor function with rehabilitation after brain damage is considered to be a training-dependent plastic event in the nervous system. Edonerpic maleate, an enhancer of experience-dependent synaptic AMPAR delivery, could accelerate the effect of rehabilitation after brain damage of motor function recovery in a training-dependent manner. To assess this effect on forelimb movements, we trained mice to reach a forelimb for food pellets. Reaching forelimb movements were analyzed by the success rate of taking the food pellets (supplementary materials, materials and methods). As the mice were trained, the success rate improved (Fig. 2A). We first investigated whether the acquisition of the reaching task required synaptic AMPAR delivery. We overexpressed green fluorescent protein (GFP)-tagged cytoplasmic portion of GluA1 (a

subunit of AMPA receptors) or GFP only in layer 5 of the motor cortex and trained animals in the reaching task. This peptide (GluA1-ct) prevents synaptic GluA1 delivery (12). Expression of GFP-GluA1-ct prevented acquisition of the reaching task, whereas GFP expression did not (fig. S5).

In humans, brain damage such as stroke disrupts once-acquired motor skills and leads to severe impairments. For the induction of brain injury, we used the cryoinjury method (supplementary materials, materials and methods). We trained animals in the reaching task and then induced motor cortical cryoinjury. Cryoinjury in the motor cortex of trained animals impaired their success rate (Fig. 2, B and C). After mild cortical cryoinjury, the decreased success rate in the reaching task could be recovered through training. This recovery was synaptic AMPAR delivery-dependent because expression of GFP-GluA1-ct in layer 5 of the intact motor cortex prevented recovery after training (fig. S6).

Next, we produced a more severe motor cortical cryoinjury (Fig. 2B) in trained animals. In this condition, training was not sufficient for recovery (Fig. 2C). One day after the injury, we initiated oral administration of edonerpic maleate (30 mg/kg, twice a day) or vehicle. Three weeks later, we treated mice with or without training. Training was initiated 1 hour after oral administration of edonerpic maleate, based on pharmacokinetic results, in which the maximum concentration of edonerpic was observed in the plasma and the brain in rodents at 1 hour after the oral administration (fig. S7). Concomitant training with edonerpic maleate administration dramatically recovered the impaired success rate in the reaching task. There was no obvious recovery in either edonerpic maleate-administered animals without training or vehicle-administered animals with or without training (Fig. 2D and fig. S8A). We also examined the dose-dependent effect of edonerpic maleate. One day after the injury, we started oral administration of edonerpic maleate in lower doses (20, 5, and 1 mg/kg, once a day). Three days later, we initiated training. Double-blind examination revealed that edonerpic maleate-administered mice at the dose of 20 or 5 mg/kg,

but not 1 mg/kg, exhibited prominent recovery in reaching task performance in a rehabilitative training-dependent fashion (fig. S8B). We detected no significant difference ($P = 0.79$) of the injury size between vehicle-treated and edonerpic maleate-treated (20 mg/kg) mice during experiments (fig. S8C). Further, no behavioral abnormalities by the administration of edonerpic maleate have been observed (fig. S9). Neither SA4503 nor paroxetine, previously reported (26, 27) as potential accelerators of rehabilitation, showed effects on motor function recovery in this experimental design (fig. S10).

Edonerpic maleate drives AMPARs into synapses of peri-injured regions

We next examined whether functional cortical reorganization is accompanied by edonerpic maleate-induced recovery after cryoinjury of the motor cortex. We produced the motor cortical cryoinjury and administered edonerpic maleate (30 mg/kg, twice a day) for three weeks, as described above, and trained animals for a week when we detected the motor function recovery. Then, we introduced a second lesion at the peri-injured region (just rostral to the first-injured region) (Fig. 2E). A week later, the animals with the second lesion exhibited deterioration of once-recovered motor function compared with sham-operated animals (Fig. 2E). This indicates that edonerpic maleate-induced motor function recovery after cryoinjury results from functional reorganization of the cortex.

We examined whether synaptic AMPAR contents are altered by edonerpic maleate in the motor cortex of injured animals with recovered motor function. We produced the motor cortical cryoinjury and administered edonerpic maleate (30 mg/kg, twice a day) or vehicle for 3 weeks. Then, we treated animals with or without training and, 6 weeks later, prepared acute brain slices and recorded from layer 5 pyramidal neurons in the above detected peri-injured region of the motor cortex, which could compensate for lost cortical function (Fig. 2F). Edonerpic maleate-administered recovered animals exhibited increased amplitude of mEPSCs, compared with vehicle-administered unrecovered mice (Fig. 2F). Consistent with the dose-dependent effects of edonerpic maleate on motor function recovery, edonerpic maleate-administered mice at 20 or 5 mg/kg (recovered), but not 1 mg/kg (non-recovered), exhibited a prominent increase of the amplitude of mEPSC in the compensatory peri-injured region. In this experiment, 1 day after the injury, we started oral administration of edonerpic maleate at a reduced dose: 20, 5, and 1 mg/kg, once a day. Three days later, we initiated training. Four weeks after the start of training, we prepared acute brain slices and recorded from pyramidal neurons of layer 5 (fig. S11).

Next, we examined whether edonerpic maleate-induced recovery of motor function after cryoinjury of the motor cortex requires synaptic delivery of AMPARs in the cortical region, which was not primarily responsible for reaching task

Table 1. Monkeys used in the present study. Three monkeys were used in each treatment. There are no significant differences ($P = 0.2$ for weight, $P = 0.6$ for days of first reach) in body weight, age, or days of first reach.

	No.	Weight (kg)	Age (years)	Dominant hand	Days of first reach
Edonerpic	A	5.14	5	L	25
	B	4.94	5	R	8
	C	4.10	5	R	8
	Mean	4.73			13.7
Vehicle	D	4.41	5	L	9
	E	3.68	5	L	10
	F	4.05	6	R	12
	Mean	4.05			10.3

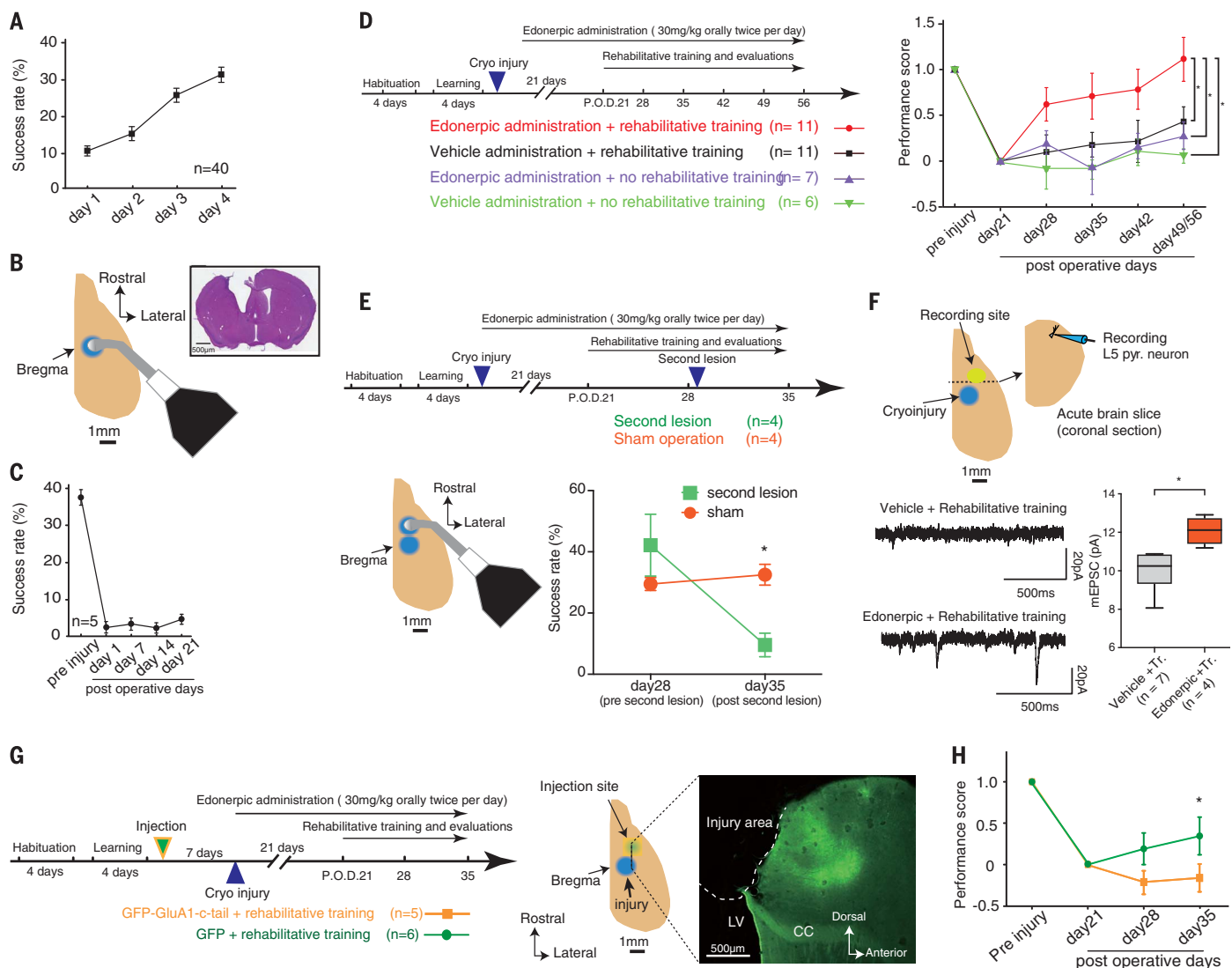


Fig. 2. Accelerated recovery of the motor function after functional cortical reorganization. (A) Average success rate (SR) in the reaching task. (B) (Left) Schema of cryoinjury. (Right) Hematoxylin-eosin-stained with severe cryoinjury. (C) Average SR after cryoinjury. (D) (Left) Experimental design of treatments. (Right) Average performance score (PS). (E) (Top) Experimental design for the evaluation with second lesion at the peri-injured cortex. (Bottom left) Schema of second lesion. (Bottom right) Average SR in day 28 (before second lesion) or 35 (after second lesion). (F) (Top) Representative mEPSC at layer 5 pyramidal neurons in the peri-injured region. (Bottom left) Representative mEPSC at layer 5 pyramidal neurons in the peri-injured cortex after day 56 [as in (D)].

Edonerpic with rehabilitative training or vehicle with rehabilitative training. (Bottom right) Average amplitudes of mEPSCs. (G) (Left) Experimental design for the evaluation with GFP-GluA1-ct or GFP expression by lentivirus in the peri-injured cortex. (Middle) Representative photomicrograph of the virus injection site. (Right) GFP-expressing cells in the peri-injured cortex. The dotted line represents the cryo-injured region. LV, lateral ventricle; CC, corpus callosum. (H) Average PS in mice with GFP-GluA1-c-tail or GFP expression. Data were analyzed with two-way ANOVA, followed by Bonferroni's post hoc tests in (D) and (H), or unpaired *t* test in (E) and (F). **P* < 0.05. The number of animals used in each experiment is indicated in the figure.

performance before the cryoinjury. We trained animals in the reaching task and expressed GFP-tagged GluA1-ct or GFP in the motor cortex by means of lentivirus-mediated *in vivo* gene transfer (Fig. 2G). Injected areas were wider than injured areas and covered potential compensatory areas detected in the previous experiments (Fig. 2E). We then introduced cryoinjury in the motor cortex as described above. One day after the injury, we started oral administration of edonerpic maleate (30 mg/kg, twice a day). Three weeks after the initiation of edonerpic maleate administration,

we initiated the training. One week after the beginning of the training, we began evaluating the recovery of motor function in the reaching task. Expression of GluA1-ct prevented edonerpic maleate-induced recovery of motor function (Fig. 2H).

CRMP2 mediates edonerpic maleate-induced acceleration of motor function recovery through rehabilitative training

We found that edonerpic bound to CRMP2 ($K_d = \sim 7.35 \times 10^{-4}$ M). To examine whether

edonerpic maleate-induced functional recovery is mediated by CRMP2, we produced the motor cortical cryoinjury in trained CRMP2-deficient mice in the reaching task, as described above. After the injury, we orally administered edonerpic maleate (30 mg/kg, twice a day) or vehicle. Three weeks later, we treated mice with or without training. During the training period, we evaluated the reaching task of these mice once a week as in the experiments described above. Training failed to recover reaching task performance in the mutant mice treated with

edonerpic maleate (Fig. 3A and fig. S8A). Consistent with this behavioral experiment, we detected no increase in the amplitude of mEPSCs of layer 5 pyramidal neurons of intact compensatory peri-injured motor cortical region of edonerpic maleate-administration CRMP2-

deficient mice 6 weeks after the beginning of the training (Fig. 3B).

Because abnormal neurological conditions could modulate CRMP2 (20, 28), we investigated the phosphorylation status of CRMP2 in the compensatory peri-injured region from edo-

nerpic maleate-treated injured mice that recovered with rehabilitative training. We detected decreased amount of phosphorylated CRMP2 in edonerpic maleate-treated recovered mice than vehicle-treated unrecovered mice with training (fig. S12A).

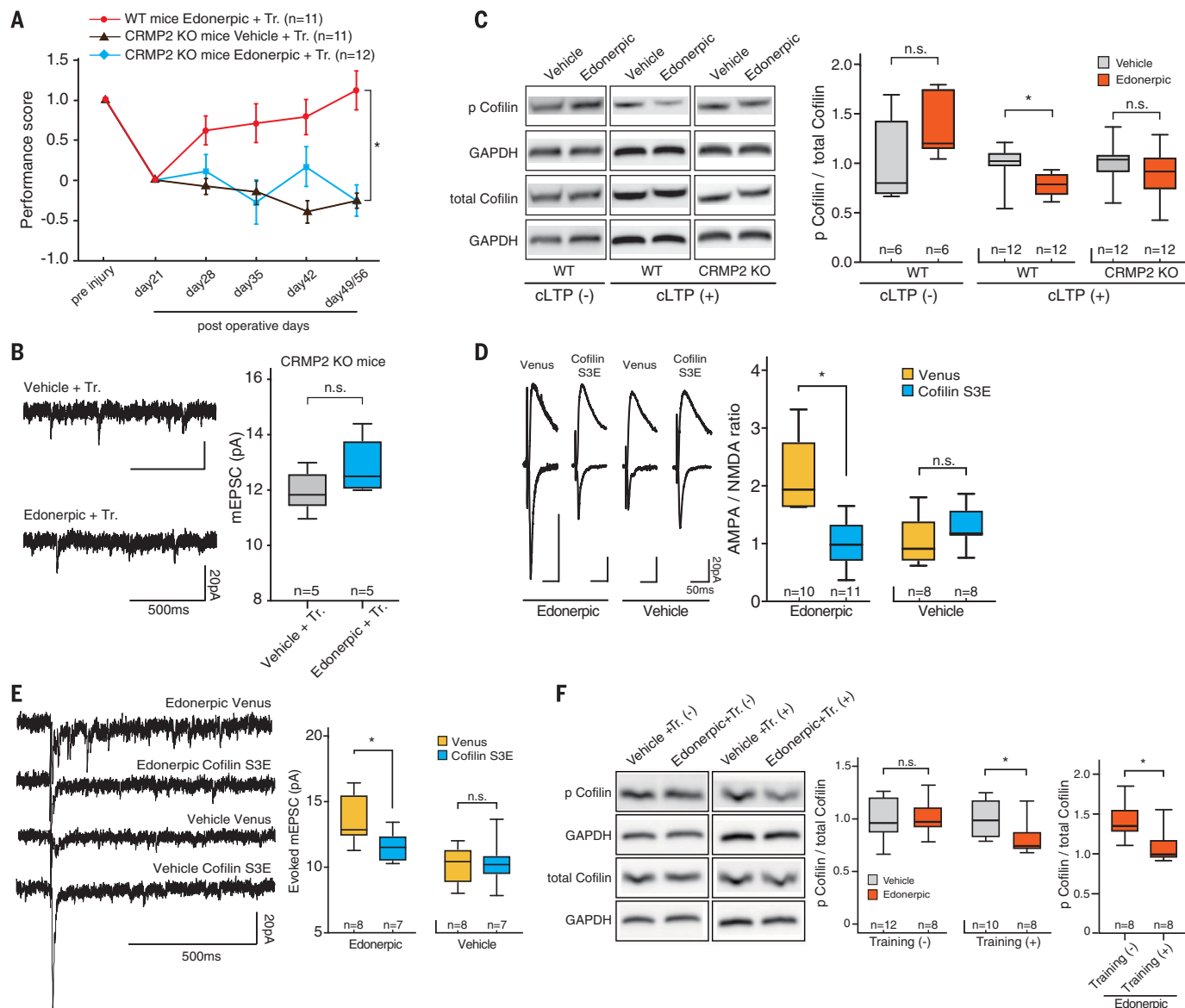


Fig. 3. CRMP2 mediates edonerpic-induced functional recovery via ADF/cofilin activation.

(A) Average performance score. WT mice data were derived from Fig. 2D. CRMP2 knockout data were added. (B) (Left) Representative mEPSC at layer 5 pyramidal neurons in the peri-injured region of CRMP2 knockout mice (Fig. 2F). Edonerpic + rehabilitative training (Tr.) / knockout or vehicle + Tr. / knockout. (Right) Average amplitudes of mEPSCs. (C) (Left) Immunoblots of Cofilin, phosphorylated Cofilin, and glyceraldehyde-3-phosphate dehydrogenase (GAPDH) obtained from cLTP-induced cortical slices of WT or CRMP2 knockout mice. (Right) The level of p-Cofilin. GAPDH was used as the reference. The data were normalized to the vehicle-treated group. (D) (Left) Representative EPSCs from Venus-expressing neurons or Cofilin S3E in the barrel cortex of mice administered with edonerpic or vehicle.

(Right) Average AMPA/NMDA ratio. (E) (Left) Evoked mEPSC as in (D). (Right) Average amplitudes of evoked mEPSCs. (F) (Left) Immunoblots of Cofilin, p-Cofilin, and GAPDH from peri-injured cortical region of mice at day 28 (Fig. 2D). (Middle) Phosphorylation level of Cofilin. GAPDH was used as the reference. The data were normalized to the vehicle-treated group. (Right) Phosphorylation level of Cofilin in the peri-injured regions of edonerpic maleate-administered mice (comparison between with and without training). GAPDH was used as the reference. Data were analyzed with two-way ANOVA, followed by Bonferroni's post hoc tests [(A); edonerpic + Tr. / WT versus other groups in day 35, 42, and 49/56], or unpaired *t* test [(B), (C), (D), (E), and (F)]. **P* < 0.05. n.s. indicates not significant. The number of animals used in each experiment is indicated in the figure.

CRMP2 mediates edonerpic maleate-induced activation of ADF/cofilin

To further elucidate the mechanisms of how edonerpic-CRMP2 interaction modifies synaptic function under the plasticity-inducing condition (29), we performed biochemical studies with chemical LTP-induced cortical slices. We prepared cortical slices of the motor cortex and chemically induced LTP (cLTP) by briefly exposing the slices to the potassium channel blocker tetraethylammonium (TEA) (30). The actin-depolymerizing factor (ADF)/cofilin mediates AMPAR trafficking during synaptic plasticity (30–32); thus, we focused on this molecule as a potential downstream effector of edonerpic-CRMP2 interaction. ADF/cofilin is inactivated by phosphorylation and activated by dephosphorylation at the serine-3 (Ser³) residue. To determine whether edonerpic-maleate activates ADF/cofilin in slices of the motor cortex under cLTP, we prepared the synaptoneurosomes from cLTP-treated acute motor cortical slices. We detected decreased phosphorylation of ADF/cofilin at Ser³ in the edonerpic maleate-treated slices, compared with vehicle-treated ones, under cLTP but not under the normal condition, suggesting that ADF/cofilin is activated by edonerpic maleate under cLTP (Fig. 3C and fig. S12B). Edonerpic maleate-induced activation of ADF/cofilin under cLTP was abolished in slices from CRMP2-deficient mice (Fig. 3C and fig. S12B). Further, the phosphorylation of ADF/cofilin at Ser³ was decreased in slices of WT mice than CRMP2-deficient mice in the presence of edonerpic maleate (fig. S12C). These results indicate that edonerpic maleate-induced activation of ADF/cofilin under cLTP is mediated by CRMP2.

To test whether the activation of ADF/cofilin mediates edonerpic-CRMP2-induced facilitation of synaptic AMPAR delivery, we overexpressed the dominant negative form of ADF/cofilin (S3E) together with Venus or Venus alone in the adult barrel cortex of edonerpic maleate-administered or vehicle-treated mice with lentivirus. Three weeks after the initiation of edonerpic maleate administration, we prepared acute brain slices and examined the AMPA/NMDA ratio and evoked mEPSC at layer 4–2/3 pyramidal synapses. We detected decreased AMPA/NMDA ratio and the amplitude of evoked mEPSC by the expression of ADF/cofilin S3E, compared with the expression of Venus alone, in edonerpic maleate-administered animals (Fig. 3, D and E). We detected no significant ($P > 0.20$) decrease of AMPA/NMDA ratio and the amplitude of mEPSC at layer 4–2/3 pyramidal synapses by the expression of ADF/cofilin S3E compared with the expression of Venus alone in vehicle-treated animals (Fig. 3, D and E).

Consistent with this, we found activation of ADF/cofilin (decreased phosphorylation of ADF/cofilin at Ser³) in the synaptoneurosomes fraction obtained from the compensatory peri-injured region of edonerpic maleate-administered recovered mice compared with vehicle-treated nonrecovered mice (Fig. 3F). We also found significant

($P < 0.01$) decrease of the phosphorylation levels of ADF/cofilin in edonerpic maleate-treated animals with training than in those without training (Fig. 3F).

Edonerpic maleate facilitates motor function recovery after ICH in nonhuman primates

Stroke such as hemorrhage and embolism in the internal capsule leads to severe paralysis of motor functions. The severity and outcome of motor impairments depend on the degree of damage to this region (33–36). To further show that edonerpic maleate facilitates training-dependent recovery from brain damage, we used an internal capsule hemorrhage (ICH) model in nonhuman primates. We trained macaque monkeys in two different tasks. A simple reach-to-grasp task aimed at evaluating the performance in both reaching and gross grasping (Fig. 4A). In nonhuman primates and humans, development of the corticospinal tract correlates with improvement in the index of dexterity, particularly in the ability to perform precision grip, holding a small object between the thumb and index finger tips (37). In the vertical-slit task, the performance of dexterous hand movements, typical of primates, were evaluated (Fig. 4B).

After monkeys learned to perform the tasks, we injected collagenase to the hemisphere contralateral to the preferred hand, under magnetic resonance imaging (MRI)–stereotaxic guidance. MRI scanning confirmed hemorrhage in the internal capsule (Fig. 4C). The area of the hyperintense signal expanded at days 3 to 7 after injection and then decreased (fig. S13A). Thereafter, the residual hypointense area was almost stable until the end of the experiment, 6 months after injection (fig. S13B). The lesion in the internal capsule was also histologically confirmed after the behavioral experiment ended (fig. S13C). Although there was a tendency that the decrease of lesion area in edonerpic maleate-treated animals during experiment is smaller than vehicle-treated monkeys, we did not detect statistical significance (fig. S13D).

Before ICH, all animals smoothly performed both tasks, and they used precision grip in the vertical-slit task (movie S1). Immediately after ICH, flaccid paralysis of the contralateral forelimb, almost complete paralysis of the hand digits, and incomplete but severe paralysis of the wrist, elbow, and shoulder were observed. Forelimb motor functions then gradually recovered. Some of the monkeys showed mild paralysis of the contralateral hindlimb immediately after ICH, but the paralysis disappeared within a few days. Although the average stroke volume of edonerpic maleate-administered monkeys was higher than that of vehicle-administered monkeys, the difference between the two groups was not statistically significant ($P = 0.90$, Mann-Whitney U test) (Fig. 4D). All monkeys were able to move the elbow and shoulder joints 1 to 2 weeks after ICH. On the day when the monkeys first reached for the piece of apple, presented in each task, rehabilitative training began (Fig. 4E and Table 1).

The rehabilitative training was initiated 15 min after the administration of edonerpic maleate, based on the results of the pharmacokinetic study (fig. S14).

During rehabilitative training, the performance of the simple reach-to-grasp task gradually recovered in both the edonerpic maleate- and vehicle-administered monkeys (Fig. 4, F, G, H, and I; and figs. S15 and S16). Two-way analysis of variance (ANOVA) revealed significant ($P < 0.001$) effects of edonerpic maleate administration on the recovery of time to retrievals, compared with the vehicle-administered group, for both near and far locations (Fig. 4, F and G, and movies S2 and S3). Although the effect of edonerpic maleate was significant ($P < 0.005$) for both locations in the early phase, the effect was significant ($P < 0.001$) only for far location in the late phase of the rehabilitative training period (Fig. 4, H and I). Retrieval from the far location required more coordination of forelimb muscles, including the proximal and distal parts, as compared with the near location. In the vertical slit task, a significant ($P < 0.001$) effect of edonerpic maleate administration was found for recovery of both the success rate and the time to retrieval, throughout the rehabilitative training period (Fig. 4, J, K, and L; and figs. S15 and S16). The edonerpic maleate-administered monkeys frequently showed dexterous hand movements, including precision grip after the rehabilitative training period (Fig. 4M and movie S4). On the other hand, precision grip was rarely observed in the vehicle-administered monkeys after ICH (Fig. 4M and movie S4).

Discussion

Although medication during the acute phase of brain damage exhibits some effectiveness, there is no small compound-mediated intervention to enhance the effect of later rehabilitation after functional loss due to brain damage (38). Previous experiments have shown that motor cortical reorganization in the intact regions of a damaged brain is crucial for functional recovery (4, 6, 7, 29, 39, 40). Here, we found that edonerpic maleate, a CRMP2-binding compound, accelerates functional recovery after brain damage in a rehabilitative training-dependent manner, which induces functional motor cortical reorganization. Thus, edonerpic maleate could provide a pharmacological solution for unmet medical needs. Although many compounds exhibit some effectiveness on motor function recovery in rodents, most fail to prove their efficacy in primates. In this study, we proved the prominent effect of edonerpic maleate on training-dependent motor function recovery in primates. Thus, edonerpic maleate may be a strong candidate for a small compound to accelerate rehabilitative training-dependent motor function recovery after brain damage, such as stroke, in humans.

CRMP2 can bind to actin, and its regulator proteins, which is crucial for synaptic AMPAR delivery (20, 31, 41, 42). Among them, the activation of ADF/cofilin drives trafficking of

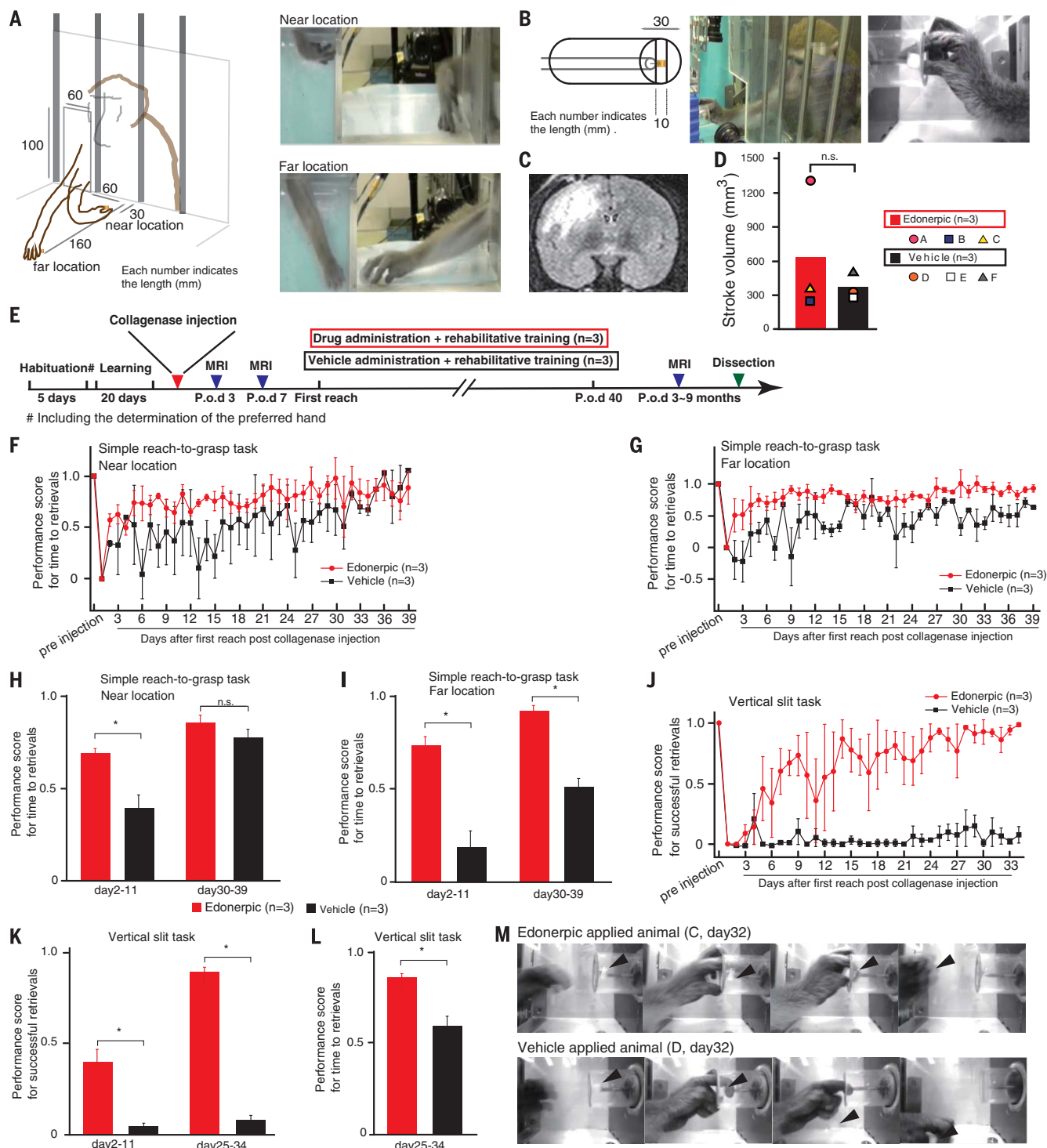


Fig. 4. Edonerpic maleate accelerates motor function recovery in nonhuman primates. (A) (Left) Simple reach-to-grasp task. (Right) Representative reaching and grasping for each location. (B) (Left middle) The vertical slit task. (Right) The finger-thumb grip in the vertical slit task before collagenase injection. (C) The fluid-attenuated inversion recovery images of MRI scanning (monkey D) 3 days after the collagenase injection into the right internal capsule. (D) Stroke volume of edonerpic maleate- or vehicle-administered monkeys. Each symbol indicates data from one monkey. There was no significant difference between the two groups (Mann-Whitney U-test, $P = 0.90$). (E) Experimental design. (F and G) Time course of the PS in the simple reach-to-grasp task. (H and I) Average PS in

the simple reach-to-grasp in the early (days 2 to 11) and in the late (days 30 to 39) phase of the training period. (J) Time course of the PS for successful retrievals in the vertical slit task. (K) The average PS in the vertical slit task in the early and in the late phase of the training period. (L) The average PS for time to retrievals in the late phase of the training period of the vertical slit task. (M) Sequential captures of the late phase (day 32) of the training period. Edonerpic maleate-administered monkeys could perform the task smoothly without dropping the piece of apple (black arrowheads indicate the apple's positions), whereas the vehicle-administered monkeys could not. Data were analyzed with two-way ANOVA [edonerpic-maleate, $P < 0.0001$; (F), (G), and (J)] and Mann-Whitney U-test [(H), (I), (K), and (L)]. * $P < 0.05$.

AMPA into the spine surface under plasticity-inducing conditions (31). The activation of ADF/cofilin is involved in synaptic AMPAR trafficking in various genetic and environmental conditions (30, 32). We detected CRMP2-dependent activation of ADF/cofilin by edonerpic maleate in the plasticity-inducing condition. We also found that edonerpic CRMP2-induced activation of ADF/cofilin mediates the facilitation of synaptic AMPAR trafficking. CRMP2 is required for the trafficking of N-type voltage-sensitive Ca^{2+} channels (43). Thus, edonerpic-CRMP2 interaction could facilitate synaptic AMPAR delivery through the regulation of actin dynamics. In addition to actin dynamics, neuromodulatory systems such as dopaminergic and serotonergic inputs could regulate synaptic AMPAR trafficking (15, 44). It will be crucial to examine whether edonerpic-CRMP2 complex affects dopaminergic and serotonergic signaling.

Although the decrease of lesion area in edonerpic maleate-treated monkeys during experiment tended to be smaller than that in vehicle-treated monkeys, we did not detect statistical significance (fig. S13D). We also did not find any difference of the change of lesion volume during experiments between edonerpic maleate-treated and vehicle-treated mice (fig. S8C). Further, the recovery of edonerpic maleate-treated mice with cryoinjury was blocked by the expression of GluA1-ct in the compensatory cortical area (Fig. 2H). Taken together, edonerpic maleate-mediated facilitation of motor function recovery after brain injury is primarily mediated by the augmented synaptic AMPA receptor delivery. It will also be crucial to further study whether edonerpic maleate promotes neuroregeneration.

Although the affinity of edonerpic binding to CRMP2 was moderate ($K_d = \sim 7.35 \times 10^{-4}$ M), we found that (i) a major band specific to the sample that was pulled down with edonerpic-conjugated beads from the lysate of mice cortical primary culture corresponded to CRMP2 (there existed a faint band near CRMP2-positive bands with the edonerpic beadspulldown preparation from CRMP2-deficient mice; this could be due to other isoforms of CRMP family), (ii) edonerpic maleate decreased the monomer of CRMP2 in the cell-free condition, (iii) edonerpic maleate-induced activation of ADF/cofilin in the plasticity-induced condition was blocked in the absence of CRMP2, (iv) edonerpic maleate-induced facilitation of synaptic AMPAR delivery was abolished in CRMP2-deficient mice, (v) edonerpic maleate-induced facilitation of synaptic AMPAR delivery was blocked by knocking down the expression of CRMP2 with shRNA, and (vi) edonerpic maleate-induced acceleration of motor function recovery was prevented in CRMP2-deficient mice. CRMP2 is an intracellular protein, and it is difficult to estimate the concentration of edonerpic maleate in the cortical neurons of treated animals. However, the evidence presented here suggests that CRMP2 is a primary target of edonerpic maleate for the rehabilitative training-dependent acceleration of motor function recovery from traumatic brain injury.

The efficacy of edonerpic maleate in humans should be evaluated in clinical trials because safety profiles of this compound have already been well established in clinical phase I studies. For stroke recovery, engineering technologies for rehabilitation, such as brain machine interface and robotics, are expected to be promising tools (45, 46). Other biological technologies, such as cell transplantation, may also be potential therapeutic alternatives, with distinct mechanisms from edonerpic maleate (47). Thus, the combination of these tools with the application of edonerpic maleate could induce synergistic effects and greatly increase the number of treatable patients with pathological brain damage.

REFERENCES AND NOTES

1. T. H. Murphy, D. Corbett, *Nat. Rev. Neurosci.* **10**, 861–872 (2009).
2. Y. Murata *et al.*, *J. Neurosci.* **35**, 84–95 (2015).
3. M. Nishibe, E. T. Urban 3rd, S. Barbay, R. J. Nudo, *Neurorehabil. Neural Repair* **29**, 472–482 (2015).
4. M. Nishibe, S. Barbay, D. Guggenmos, R. J. Nudo, *J. Neurotrauma* **27**, 2221–2232 (2010).
5. R. J. Nudo, *Curr. Opin. Neurobiol.* **16**, 638–644 (2006).
6. R. J. Nudo, *J. Commun. Disord.* **44**, 515–520 (2011).
7. R. J. Nudo, B. M. Wise, F. SiFuentes, G. W. Milliken, *Science* **272**, 1791–1794 (1996).
8. H. W. Kessels, R. Malinow, *Neuron* **61**, 340–350 (2009).
9. D. Mitsushima, K. Ishihara, A. Sano, H. W. Kessels, T. Takahashi, *Proc. Natl. Acad. Sci. U.S.A.* **108**, 12503–12508 (2011).
10. S. Rumpel, J. LeDoux, A. Zador, R. Malinow, *Science* **308**, 83–88 (2005).
11. D. Mitsushima, A. Sano, T. Takahashi, *Nat. Commun.* **4**, 2760 (2013).
12. T. Takahashi, K. Svoboda, R. Malinow, *Science* **299**, 1585–1588 (2003).
13. J. R. Whitlock, A. J. Heynen, M. G. Shuler, M. F. Bear, *Science* **313**, 1093–1097 (2006).
14. R. L. Clem, A. Barth, *Neuron* **49**, 663–670 (2006).
15. S. Jitsuki *et al.*, *Neuron* **69**, 780–792 (2011).
16. T. Miyazaki *et al.*, *J. Clin. Invest.* **122**, 2690–2701 (2012).
17. H. K. Lee *et al.*, *Cell* **112**, 631–643 (2003).
18. K. Takemoto *et al.*, *Nat. Biotechnol.* **35**, 38–47 (2017).
19. Y. Goshima, F. Nakamura, P. Strittmatter, S. M. Strittmatter, *Nature* **376**, 509–514 (1995).
20. K. Hensley, K. Venkova, A. Christov, W. Gunning, J. Park, *Mol. Neurobiol.* **43**, 180–191 (2011).
21. H. Nakamura *et al.*, *Genes Cells* **21**, 1059–1079 (2016).
22. K. Kadoyama *et al.*, *J. Neurosci. Res.* **93**, 1684–1692 (2015).
23. K. Hirata *et al.*, *J. Pharmacol. Exp. Ther.* **314**, 252–259 (2005).
24. H. Makiyama *et al.*, *Genes Cells* **21**, 994–1005 (2016).
25. J. P. Ip *et al.*, *Nat. Neurosci.* **15**, 39–47 (2011).
26. K. Ruscher *et al.*, *Brain* **134**, 732–746 (2011).
27. F. Chollet *et al.*, *Lancet Neurol.* **10**, 123–130 (2011).
28. J. N. Zhang *et al.*, *Sci. Rep.* **6**, 37050 (2016).
29. R. J. Nudo, *Front. Hum. Neurosci.* **7**, 887 (2013).
30. H. Tada *et al.*, *Proc. Natl. Acad. Sci. U.S.A.* **113**, E7097–E7105 (2016).
31. J. Gu *et al.*, *Nat. Neurosci.* **13**, 1208–1215 (2010).
32. S. Jitsuki *et al.*, *Cereb. Cortex* **26**, 427–439 (2016).
33. S. K. Schiemann, G. Kwakkel, M. W. Post, L. J. Kappelle, A. J. Prevo, *J. Rehabil. Med.* **40**, 96–101 (2008).
34. C. Rosso *et al.*, *Neuroradiology* **53**, 763–771 (2011).
35. R. Wenzelburger *et al.*, *Brain* **128**, 64–74 (2005).
36. Y. Murata, N. Higo, *PLOS ONE* **11**, e0154752 (2016).
37. G. Courtine *et al.*, *Nat. Med.* **13**, 561–566 (2007).
38. H. P. Adams Jr., R. J. Nudo, *Ann. Neurol.* **74**, 4–10 (2013).
39. S. Barbay *et al.*, *Stroke* **46**, 1620–1625 (2015).
40. R. J. Nudo, G. W. Milliken, W. M. Jenkins, M. M. Merzenich, *J. Neurosci.* **16**, 785–807 (1996).
41. K. Hensley *et al.*, *J. Neurosci.* **30**, 2979–2988 (2010).
42. Y. Kawano *et al.*, *Mol. Cell. Biol.* **25**, 9920–9935 (2005).
43. J. M. Brittain *et al.*, *Nat. Med.* **17**, 822–829 (2011).
44. D. S. Tukey, E. B. Ziff, *J. Biol. Chem.* **288**, 35297–35306 (2013).
45. M. D. Murphy, D. J. Guggenmos, D. T. Bundy, R. J. Nudo, *Front. Cell. Neurosci.* **9**, 497 (2016).
46. M. Aach *et al.*, *Spine J.* **14**, 2847–2853 (2014).
47. T. Yamashita *et al.*, *Cell Transplant.* **26**, 461–467 (2016).

ACKNOWLEDGMENTS

We thank Y. Kimura and T. Akiyama (Advanced Medical Research Center, Yokohama City University) for technical assistance in analysis of mass spectrometry. We thank M. Taguri (Department of Biostatistics, Yokohama City University) for useful advice in statistical analysis. We also thank Y. Katakai for polite assistance in nonhuman primate experience. **Funding:** This project was supported by Special Coordination Funds for Promoting Science and Technology (T.T.) and partially supported by the Strategic Research Program for Brain Sciences from Japan Agency for Medical Research and Development (AMED) (T.T.) and the Brain Mapping by Integrated Neurotechnologies for Disease Studies (Brain/MINDS) from AMED (T.T.). This project is also partially supported by Grants-in-Aid for Scientific Research in a Priority Area (grant 17082006) and Creation of Innovation Centers for Advanced Interdisciplinary Research Areas Program in the Project for Developing Innovation Systems (grant 42890001) from the Ministry of Education, Science, Sports and Culture (Y.G.). **Author contributions:** T.T. designed the project and experiments, interpreted and analyzed data, and wrote the manuscript. H.A. conducted behavioral experiments (mice and monkey) and biochemical experiments and wrote the manuscript. S.J. conducted electrophysiological and biochemical experiments and wrote the manuscript. W.N. and Y.M. conducted behavioral and histological experiments of monkey. A.J.-T. conducted electrophysiological experiments. Y.K. and N.M. conducted behavioral experiments (mice). H.T., K.S., H.M., and T.K. conducted biochemical experiments. A.S. conducted viral preparation. T.O., Y.G., and N.H. contributed to interpret the data. We shared the data with all authors who contributed to the analysis and interpretation of the data and to the design of the experiments. **Competing interests:** The authors of this publication include employees of Toyama Chemical Co., which holds intellectual property rights of edonerpic maleate (T-817MA) and funded Yokohama City University for the study using macaque monkeys. T.T. is one of the inventors of a patent application claiming the use of edonerpic maleate to enhance the functional recovery after brain damage [substance patent (WO03/035647, Alkyl ether derivatives or salts thereof) and use patent (WO2015/115582, Post nerve injury rehabilitation effect-enhancing agent comprising alkyl ether derivative or salt thereof)]. All the other authors declare that they have no competing interests. **Data and materials availability:** Edonerpic maleate is a compound under the clinical development stage. Thus, research use of edonerpic maleate requires the approval from Toyama Chemical Co. and Fujifilm Corporation. There is no fixed format of those requests. All data are available in the manuscript or the supplementary materials. Original data are kept on local hard drives (with backups). Processed data for this study are additionally kept and curated on local hard drives of the Yokohama City University (http://neurosci.med.yokohama-cu.ac.jp/ao2300_processed_data.html) and servers of Toyama Chemical Co.

SUPPLEMENTARY MATERIALS

www.sciencemag.org/content/360/6384/50/suppl/DC1
Materials and Methods
Figs. S1 to S16
References (48–67)
Movies S1 to S4

29 June 2017; accepted 1 February 2018
10.1126/science.aao2300

NITROGEN CYCLE

Convergent evidence for widespread rock nitrogen sources in Earth's surface environment

B. Z. Houlton,^{1,*} S. L. Morford,^{1,2*} R. A. Dahlgren¹

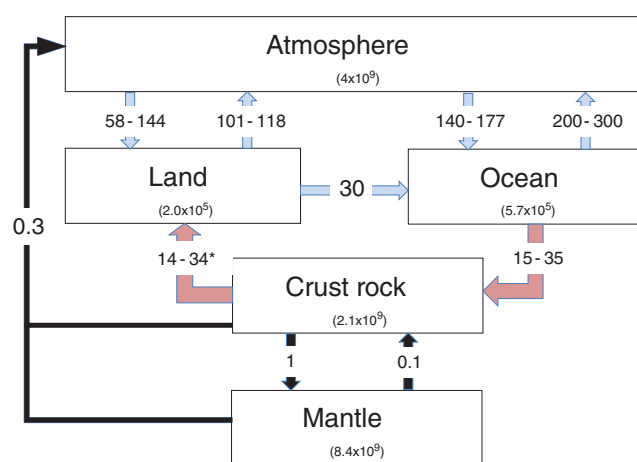
Nitrogen availability is a pivotal control on terrestrial carbon sequestration and global climate change. Historical and contemporary views assume that nitrogen enters Earth's land-surface ecosystems from the atmosphere. Here we demonstrate that bedrock is a nitrogen source that rivals atmospheric nitrogen inputs across major sectors of the global terrestrial environment. Evidence drawn from the planet's nitrogen balance, geochemical proxies, and our spatial weathering model reveal that ~19 to 31 teragrams of nitrogen are mobilized from near-surface rocks annually. About 11 to 18 teragrams of this nitrogen are chemically weathered in situ, thereby increasing the unmanaged (preindustrial) terrestrial nitrogen balance from 8 to 26%. These findings provide a global perspective to reconcile Earth's nitrogen budget, with implications for nutrient-driven controls over the terrestrial carbon sink.

Nitrogen (N) availability controls many aspects of ecosystem structure and function on land and in the sea (1, 2). This includes strong, N-driven effects on Earth's climate system and the size and sustainability of the terrestrial carbon (C) sink (3). Disagreements exist, however, over the biosphere's N balance and how natural sources of N could alter terrestrial C uptake patterns in the future (4). Textbook paradigms and global computational models assume that ecosystems rely principally on the atmosphere for N (5), yet N accumulation rates in vegetation and soil can greatly exceed inputs from biological N fixation and N deposition (6). Recent evidence has raised questions about the role of rock N sources in resolving this discrepancy (7), with potentially widespread implications, given the massive amount of fixed N in the global rock reservoir (8, 9).

We investigated rock N weathering rates in Earth's surface environment, where terrestrial plants, soils, and microbes interact. Over billions of years of Earth history, N has accumulated in rocks, largely as a product of N fixation by aquatic and terrestrial organisms that becomes trapped in sedimentary basins; this N has been traced back to ancient biogeochemical processes, as opposed to contemporary N fixation by free-living microbes and root-associated symbionts. The amount of N varies widely among general rock types; sedimentary and metasedimentary lithologies occupying ~75% of Earth's surface have concentrations of ~500 to 600 mg N kg⁻¹ rock, whereas more spatially restricted igneous rocks often have much lower values (<100 mg N kg⁻¹ rock) (9–11). Although N-rich sediments are globally widespread, such rock N concentrations do

Fig. 1. The preindustrial planetary nitrogen cycle. Fluxes (arrows) in teragrams per year and reservoir sizes in teragrams.

Maintenance of the atmospheric N reservoir requires a transfer of N from crustal rocks to land because degassing fluxes from the crust and mantle are unable to balance N transfer from the ocean to the crust. *Mass required to balance the marine N burial term minus mantle and volcanic degassing. Nitrogen fixation estimates are from (4, 13, 36, 47); preindustrial nitrogen deposition is from (37); denitrification, hydrologic N transport, and marine burial are from (13, 16); N transport to the mantle and volcanic N emissions are from (14); and N mass reservoirs are from (8, 9). Section 1 of the supplementary materials provides further details.



not translate directly to N inputs in Earth's surface environment. Rather, rock N availability to terrestrial soils and vegetation is determined by denudation (physical plus chemical weathering), which varies as a general function of geochemistry, relief, tectonic uplift, climate, and biology (12).

Therefore, we examined the mobility and reactivity of rock N sources in Earth's surface environment by means of three diverse and largely independent assessments: the planetary mass balance of N (case 1); global-scale denudation and chemical weathering proxy data (case 2); and a spatially explicit N weathering model that uses a statistical probability approach (case 3) (table S1). When combined, these approaches enable us to identify a hitherto unrecognized source of rock N that is ecologically important across Earth's diverse environments and at the planetary scale.

Rock N weathering and the missing N in the planetary balance (case 1)

A classical approach for gaining insight into the magnitude of Earth's biogeochemical transfers relies on the principle of mass and energy conservation. By accounting for N inputs and outputs among Earth system reservoirs, biogeochemists can draw coarse-scale inferences about N exchanges between the atmosphere, biosphere, hydrosphere, and geosphere, which can then be vetted against evidence from more direct approaches. Whereas traditional “box and arrow” models have emphasized N transfers between land, air, and water systems (13), recent quantitative advances in Earth system modeling point to sustained transport of sedimentary marine N through the deep Earth (i.e., the mantle) (14). Considering the geochemical and biological fluxes together illuminates a discrepancy in the planetary N balance, which can be resolved by considering the return of rock N to the land-surface environment (Fig. 1).

Models of the planet's N balance can be classed into two domains: (i) short-term models that emphasize N transformations and fluxes between the atmosphere, biosphere, and human activities (13) and (ii) longer-term models that consider N exchange between the atmosphere and mantle (15). Short-term perspectives emphasize how atmospheric N inputs are balanced by physical and microbial denitrification processes, which return N back to the atmosphere, and thereby ignore the return of N from rocks to land. Instead, these models treat marine sedimentary burial as a global N sink with an integrated flux of ~15 to 35 Tg N year⁻¹ (13, 16).

However, over the longer term, the amount of N entering marine sediments should reasonably balance the amount of N leaving this reservoir. Tectonic uplift forces sediments to Earth's surface over millions of years, a mass-transfer flux that is ultimately balanced by denudation. A fraction (<10%) of sedimentary N enters the mantle, where it can be stored or returned to the atmosphere via

¹Department of Land, Air and Water Resources, University of California, Davis, CA, USA. ²Terra Analytics, Helena, MT, USA.

*These authors contributed equally to this work.

†Corresponding author. Email: bzhoulton@ucdavis.edu

volcanic emissions [combined long-term average, $\sim 1.5 \text{ Tg N year}^{-1}$ (14)]. Hence, the evidence suggests that considerably more N is entering the rock N reservoir than can be accounted for by mantle exchange and volcanic emissions—what can explain this discrepancy?

One possibility involves non-steady-state conditions, wherein N accumulates in crustal rock and the mantle indefinitely. A simple calculation shows that this explanation is improbable: The atmospheric N_2 reservoir would have completely vanished after <300 million years in this case (17). Although variations in N transfers over geological epochs (e.g., the Deccan Traps) could alter this calculation, for much of the Phanerozoic eon, marine organic matter burial (and hence organic N burial) is estimated to have fluctuated by less than a factor of 2 (18); thus, long-term volcanic degassing and mantle advection fluxes would need to increase by a factor of 20 to 40 over modern rates to compensate for sedimentary N burial. Such increases are unlikely given that sustained volcanism of this magnitude would lead to mass extinctions on land and severe ocean acidification (19).

Instead, the most parsimonious explanation centers on mass-balance closure in which the substantial transfer of N from rocks to the land surface is balanced by N burial rates in the seafloor (Fig. 1). This alternative fits with evidence for a stable atmospheric N_2 reservoir over the Phanerozoic (2) and is aligned with Earth's dynamic rock cycle, whereby sediments are lithified and tectonically uplifted to replenish losses from continental erosion (Fig. 1). Although humans have both purposely and inadvertently increased the terrestrial biosphere's N balance (13), this modern-day perturbation is insubstantial vis-à-vis the cumulative N cycle transfers that have taken place over Earth history. Thus, the planetary-scale mass balance points to a nontrivial N weathering term from the continental rock reservoir of ~ 14 to $34 \text{ Tg N year}^{-1}$ (equation S2).

Evidence for rock N denudation and weathering based on global proxies (case 2)

The planet's N inventory provides coarse-scale evidence for substantial N weathering reactions in Earth's surface environment, but this approach is more impressionistic than direct. Likewise, our extensive sampling efforts (11) and other global-scale syntheses (9, 10) reveal widespread rock N sources in the near-surface environment (Fig. 2A); however, these results do not address global N weathering rates. We must place quantitative constraints on rock N denudation rates to draw more direct inferences about N chemical weathering inputs worldwide. This includes an analysis of the organic N that is bound in sedimentary rocks and the mineral N in silicates (largely as NH_4^+).

We first consider global-scale constraints on organic N denudation rates (physical plus chemical weathering) in sedimentary rock by combining data on organic C denudation rates with the C:N stoichiometry of sedimentary rock (11). Fossilized organic C denudation rates range between 100 and $143 \text{ Tg C year}^{-1}$ (20) and show

good agreement with estimates of global C burial in marine sediments [126 to $170 \text{ Tg C year}^{-1}$ (21–23)]. Dividing these fluxes by the average C:N ratio of sedimentary rock (8.13 by mass; supplementary materials) yields a N denudation flux between ~ 12 and $18 \text{ Tg N year}^{-1}$ and a marine burial rate of ~ 16 to $21 \text{ Tg N year}^{-1}$ (Table 1). These global N denudation values agree reasonably well with the planetary mass balance (discussed above), despite the very different data and techniques used in each case (table S1).

A second approach derives from basin-scale sediment and solute fluxes and cosmogenic radionuclide (CRN) denudation data, which collectively reflect the net movement of silicate rocks from the terrestrial to marine environment. This

approach addresses the N in mineral form. Using sediment and solute budgets, Milliman and Farnsworth (24) estimate that $\sim 23 \text{ Pg}$ of total silicate-rock mass is delivered to the global oceans annually. Combined with endorheic basins (environments not in contact with the ocean), the global land-to-sink mass flux of silicates is roughly 28 Pg year^{-1} . Applying our global mean N lithology concentration of 337 mg N kg^{-1} to the mass flux of silicates (supplementary materials) yields a N denudation flux of $\sim 9 \text{ Tg N year}^{-1}$ (Table 1) for silicate-bound N.

The results of this calculation are consistent with findings from catchment-scale CRN analysis, which suggest a global rock denudation flux of 28 Pg year^{-1} (25); however, grid-scale biases

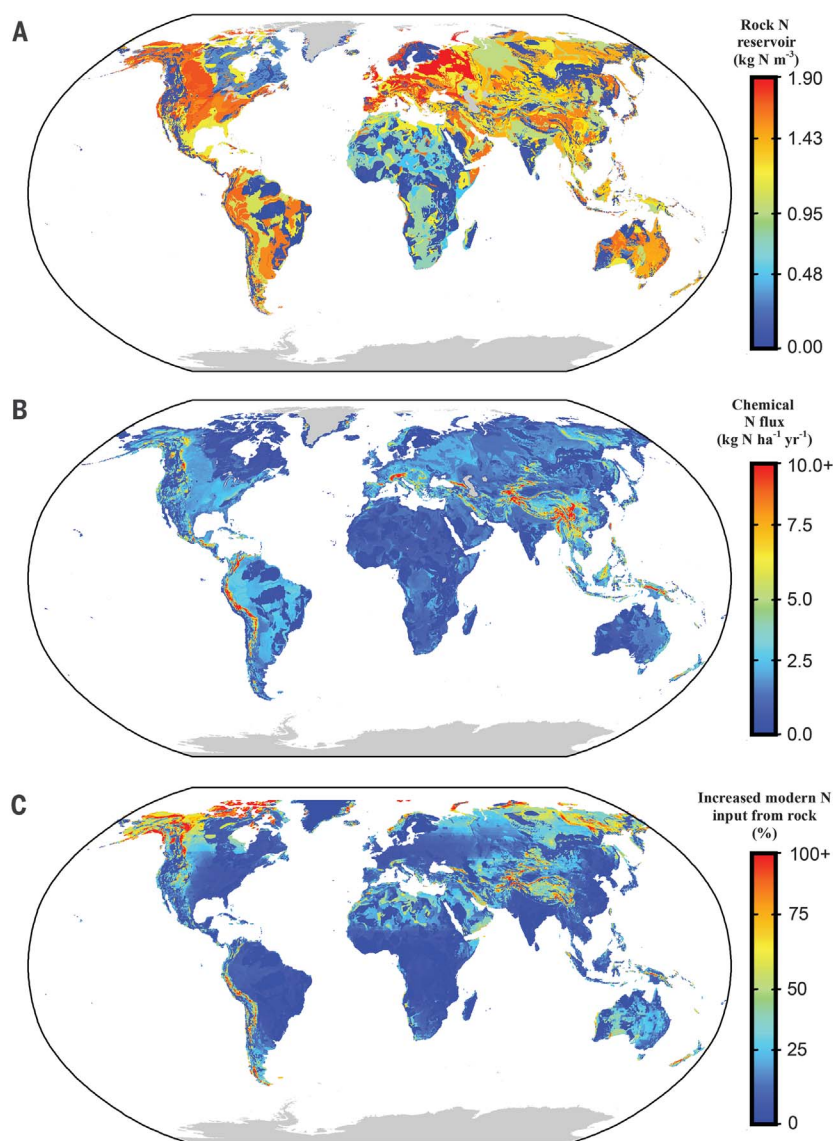


Fig. 2. Spatial patterns of rock N concentrations, weathering fluxes, and rock N contributions versus atmospheric sources of N. (A) Spatially explicit estimates of surface (top 1 m) rock N concentrations. (B) Nitrogen chemical weathering fluxes derived from our globally calibrated model. (C) Percent increase in the preindustrial terrestrial N balance with rock N inputs (i.e., rock N weathering divided by the sum of atmospheric N inputs). The model points to highest absolute (B) and relative (C) rock N input fluxes in mountainous regions and at higher latitudes.

Table 1. Estimates of global rock nitrogen reservoirs and fluxes.

	Case 2			Case 3
	Fossilized organic matter	Silicate solute and sediment yield	Catchment-scale CRN	Global spatial model
N reservoir (petagrams N in top 1 m of rock)	149	N/A	N/A	92–110
N denudation (teragrams N per year)	12–18	9	2–22	19–31
Marine burial (teragrams N per year)	16–21	N/A	N/A	N/A
Terrestrial chemical weathering (teragrams N per year)	5–12*	0.9–4.5	0.7–11†	11–18‡

*Range of organic nitrogen weathering. †Range of mineral nitrogen weathering. ‡Organic plus mineral nitrogen weathering from the spatial model.

and extrapolation (26) of catchment-scale studies to Earth’s surface produce a broad range of estimates at the global scale (6 to 64 Pg year^{−1}). On the basis of these end-members and the mean global N reservoir above, the silicate-rock N denudation flux may be as low as 2 and as high as 22 Tg N year^{−1}. Importantly, such CRN-derived estimates do not consider the acceleration of erosion and denudation rates through modern land-use practices, which have increased erosion by a factor of 10 to 100 (27).

The chemical weathering quotient of the total N denudation fluxes can be estimated from fossilized organic matter (FOM) weathering and chemical depletion of silicates. Chemical weathering of FOM occurs more completely than for silicate minerals, because the former is susceptible to oxidation as opposed to kinetically constrained acid-hydrolysis reactions. Globally, chemical (oxidative) weathering of C in FOM varies between 40 and 100 Tg C year^{−1} (20), which translates to an organic N weathering flux of 5 to 12 Tg year^{−1} (Table 1 and supplementary materials). In contrast, chemical weathering of silicate rocks is less certain; it varies across parent material, climate, relief, and biological communities. Chemical depletion of silicates in bulk rocks has been shown to vary from 10 to 16% (24, 28), which would imply a mineral N weathering flux between 0.2 and 3.5 Tg year^{−1} [i.e., the range of N denudation estimates (2 to 22 Tg N year^{−1}; Table 1) multiplied by 0.1 to 0.16].

However, this lattermost calculation does not consider the differential chemical reactivity of elements in rock, which can be particularly rapid for certain rock-derived elements, including N (7, 29). For example, chemical depletion of parent materials varies from virtually nil (e.g., zirconium and titanium) to relatively rapid (e.g., calcium) in common rock substrates and is biased by the presence of quartz, which is highly resistant to chemical weathering. Application of data from our field studies (29) in rapidly denuding mountains of the northern California Coast Ranges demonstrates a N chemical depletion of ~36 to 50%, which raises the silicate N weathering flux to 0.7 to 11 Tg N year^{−1} (range of weathering for catchment-scale CRN; Table 1).

These diverse geochemical proxies point to a global N denudation flux (organic plus mineral N) that varies between 14 and 40 Tg year^{−1}, with a chemical N weathering fraction between ~6 and 23 Tg N year^{−1} (weathering range of FOM plus catchment-scale CRN; Table 1). These estimates confirm expectations from the planetary mass-balance results (case 1) and derive from actual proxies of physical and chemical weathering within a given set of assumptions; however, neither case 1 nor case 2 address spatial patterns and environmental controls on N weathering rates across Earth’s surface—issues that we addressed with our spatial global weathering model.

A probabilistic modeling approach to N weathering inputs worldwide (case 3)

We developed a data-driven modeling approach to spatially quantify global N weathering fluxes. Our model incorporates topographic, climatological, and lithological factors to estimate N denudation and chemical weathering rates, and it is calibrated using solute sodium (Na⁺) fluxes from 106 large river basins across Earth (30). It differs from previous approaches in that we rely on machine-learning algorithms, quantile regression, and Monte Carlo simulations, as opposed to the more classical mean-field parameterization schemes. We applied our model at 1-km²-grid scales, using mass-balance equations developed at hillslope to small basin scales (31). The conservation-of-mass equations used in our model take the form

D_{N,Na} = (Q_D)(ρ)([N, Na]_{rock}) (1)

CDF_{Na} = 1 − [Na]_{soil} / [Na]_{rock} (2)

W_{Na} = (D_{Na})(CDF_{Na}) (3)

W_N = (D_N)(f_{OM-N})(CDF_{org-N}) + (D_N)(1 − f_{OM-N})(CDF_{Na}) (4)

where D_{N,Na} (mass × length^{−2} × time^{−1}) is the element-specific (N or Na⁺) denudation flux, Q_D is the denudation rate (length × time^{−1}), ρ is rock density (mass × length^{−3}), and [N, Na]_{rock} is the element-specific concentration in rock

(mass × mass^{−1}). Chemical depletion of Na⁺ from silicate rocks (CDF_{Na}) is applied to both Na⁺ and N weathering functions (section 3 of the supplementary materials). W (mass × length^{−2} × time^{−1}) is the element-specific (N or Na⁺) chemical weathering flux, and f_{OM-N} (dimensionless) is the fraction of total rock N in organic forms.

Briefly, our model relies on Monte Carlo methods to estimate probability values for Q_D, [N, Na]_{rock}, and CDF_{Na}, with 10,000 simulations per parameter per cell. We calibrated the model by minimizing residuals between the modeled and empirically observed basin-scale Na⁺ training set (W_{Na}). We estimated denudation (Q_D) by using a statistical model that incorporates catchment-scale CRN denudation rates (32) and digital topography. Rock N and Na⁺ concentrations ([N]_{rock} and [Na]_{rock}) were derived from our synthesis of measurements (11) and the U.S. Geological Survey geochemical database, respectively (33). We used a generalized additive model to estimate the chemical depletion fraction (CDF_{Na}). The factors in the model include topographic relief, evapotranspiration, and excess water (precipitation minus evapotranspiration) (supplementary materials). We parameterized the CDF model by using 41 separate observations of soil Na⁺ depletion rates collected from the primary literature (section 3 of the supplementary materials).

These simplifying assumptions capture generalized patterns of chemical weathering rates as a function of climate and topographic relief, as calibrated with salt-corrected riverine Na⁺ fluxes to the ocean (tables S5 and S6). The model’s reliance on soil-based chemical depletion rates is limited in low-relief landscapes, in areas where subwatershed measurements may be decoupled from larger-scale fluxes, and in recently deglaciated terrains (28). Yet our simulations are consistent with general global observations of soil development and weathering patterns (figs. S3 and S4) and the anticipated switch from supply-limited to transport-limited kinetics in chemical weathering that has been observed for high-relief landscapes (34). Further, total rock denudation rates predicted by our model (46 to 61 Pg year^{−1}) fall within the range of previous studies [20 to 64 Pg year^{−1} (25)].

At the global scale, our model simulates a large N denudation flux, consistent with cases 1 and 2. Specifically, we estimate that ~19 to 31 Tg N year⁻¹ is denuded from the land-surface environment, with a chemical weathering flux of 11 to 18 Tg N year⁻¹ (Table 1 and Fig. 2B). These results suggest that ~40 to 60% of rock N is chemically released to the terrestrial surface environment before export, consistent with field studies of mineral N depletion rates in mountainous areas (29); that is, ~50% of rock nitrogen is lost to physical erosion without entering terrestrial ecosystem pools in situ. We do not consider the fate of such physically eroded N in downslope ecosystems, which would likely increase the global N weathering flux in low-relief environments.

The scaled-up spatial N chemical weathering flux corresponds well with mean-field geochemical proxies (Table 1). Furthermore, our geospatial model indicates that as much as ~65% (7 to 12 Tg N year⁻¹) of the total rock N chemical flux is derived from organic N, similar to the FOM-based estimates (5 to 12 Tg N year⁻¹; Table 1). These results appear reasonable given our limited understanding of differences in weathering processes among FOM and silicate rocks.

Across the land surface, rock N weathering is relatively widespread, with variations in N geochemistry, relief, and climate determining the magnitude of rock N inputs to terrestrial ecosystems (Fig. 2B). For example, large areas of Africa are devoid of N-rich bedrock and have relatively low relief and arid climate conditions, which together substantially limit N weathering fluxes. In contrast, some of the highest rock N inputs are estimated for the northern latitudes (Fig. 2B), where N-rich rocks and high-relief landscapes are more prevalent. At regional scales, mountainous regions with high uplift and adequate moisture—for example, the Himalaya and

Andes mountains—are estimated to be large sources of N weathering inputs to land-surface environments, similar to the importance of these regions to global weathering rates and climate (35).

Context and implications

The body of evidence points to substantial rock N denudation and weathering rates at regional to global scales. Although each of our approaches is rooted in mass-balance principles, the diversity of techniques confers a reasonable degree of independence among the case studies (table S1); this adds robustness to the working conclusion of widespread rock N inputs in terrestrial surface ecosystems. Our geospatial model provides the most direct and geographically rich set of predictions, with the global range in fluxes largely driven by the calibration approach (basin- versus global-scale; supplementary materials). Results from the other case studies overlap with the spatial model, and we make conservative assumptions about rock N weathering rates in general (table S1). Future work could therefore cause the case studies to diverge, but with a tendency toward higher rather than lower overall rock N fluxes. We conclude that our findings extend previous plot-scale evidence for rock N weathering inputs in select ecosystems to a global biogeochemical paradigm, and that they indicate considerable limitations in contemporary models, which exclude the role of rock N sources in governing global-scale patterns of terrestrial N availability.

To further examine the importance of rock N weathering vis-à-vis the terrestrial N balance, we compare our geospatial model estimates with N fixation and deposition inputs to natural biomes (i.e., nonagrarian areas; Fig. 2C and Table 2). Isotopically constrained global terrestrial N fixation varies from 58 to 100 Tg N year⁻¹ (36), with

N deposition rates in preindustrial and modern nonagrarian environments varying from 11 to between 30 and 34 Tg N year⁻¹, respectively (37, 38). Thus, although anthropogenic activities have dramatically increased global N inputs through deposition, nearly half of this input is in agricultural and urban landscapes where rock is not likely to be a substantial component of ecosystem N cycling (table S6).

Our findings for rock N weathering rates increase the preindustrial terrestrial nitrogen budget by 8 to 26% (Table 2), with a modern-day rock N contribution to natural systems of 6 to 17% of total N inputs. These calculations point to rock inputs increasing the mean (midpoint) global N budget by 17 and 11% for preindustrial and modern periods, respectively, with more pronounced effects at the biome and regional scales.

Our results show that rock N inputs may be particularly important in montane ecosystems where denudation rates are rapid (Fig. 2C) and high-latitude ecosystems where high biological N fixation rates are temperature-limited (39). Spatially, our analysis suggests that rock N inputs can account for a substantial fraction of modern N inputs (including anthropogenic N deposition) to temperate and montane grasslands (8 to 32%), temperate and boreal forests (9 to 38%), tundra (23 to 51%), deserts (11 to 23%), and Mediterranean shrub- and woodlands (9 to 22%) (Table 2 and table S6). In contrast, rock N inputs constitute a substantially smaller fraction of N inputs to tropical grasslands (2 to 8%) and tropical forests (4 to 12%), where weathering is supply-limited and N fixation rates are naturally high.

Where N weathering occurs deep beneath the soil and regolith, some or all of the N may be released to groundwater and transported to fluvial systems (40–42). Under this scenario, the ability of terrestrial plant communities to use

Table 2. External nitrogen inputs from rock and atmospheric sources (teragrams per year). Values in parentheses show the range of estimates, where available. Biome areas are from World Wildlife Fund ecoregions. Biome-specific N fixation estimates are from (4, 40, 47). Atmospheric N deposition is derived for 1860 (preindustrial) and 1993 from (37) and for 2001 from (38). Global-scale estimates (bottom row) include N inputs from sources above and estimates from (36). N inputs to modern agrarian lands are not considered in these calculations; table S7 shows the agrarian influence.							
Biome	Rock weathering		Biological fixation		Atmospheric deposition		
					Preindustrial	Modern	
Tundra	0.7	(0.6–0.9)	0.6	(0.7–1.7)	0.1	0.3	(0.3–0.4)
Taiga (boreal forest)	1.3	(1–1.6)	1.2	(1.6–5.3)	0.6	1.9	(1.3–2.5)
Temperate forest	2.8	(2.1–3.4)	6	(8–8.9)	2.6	5.3	(5.2–5.4)
Temperate grassland	1.2	(0.9–1.4)	1.4	(1.8–3.8)	1	1.9	(1.8–2.0)
Montane grassland	1.2	(0.9–1.5)	1.2	(1.5–2)	0.4	1.9	(1.9–1.8)
Mediterranean	0.3	(0.3–0.3)	0.3	(0.5–1.1)	0.2	0.4	(0.4–0.4)
Deserts	2.1	(1.2–2.5)	7.7	(5.5–10.2)	1	4.7	(4.2–5.1)
Mangroves	0	(0–0)	0.3	(0.3–0.4)	0	0.1	(0.1–0.1)
Tropical forest	3.9	(3–4.7)	40.1	(25–53.1)	3.7	8.1	(7.6–8.7)
Tropical grassland	1.4	(1.1–1.7)	39.2	(14.6–51.9)	1.4	7.0	(6.6–7.3)
Tropical wet grassland	0.1	(0.1–0.1)	1.8	(0.7–2.4)	0.1	0.4	(0.4–0.4)
Rock/water	0.1	(0–0.1)	0.3	(0.2–0.4)	0.1	0.2	(0.2–0.2)
Global totals	15.1	(11.2–18.2)	100.1	(58.0–132.5)	11.2	32.2	(29.9–34.4)

deeply weathered N is dependent on plant-root proliferation into the deep subsurface (i.e., the depth of the critical zone). Woody plants can effectively penetrate deep regolith, with roots extending tens of meters below the terrestrial surface, in environments ranging from deserts to rainforests (43). Inferential work has pointed to the high mobility of rock N in ecosystems, which can be depleted from minerals at rates that exceed Na^+ and K^+ release from silicates (29). The role of microbes may be particularly important in this regard; so-called “rock-eating” fungi can accelerate weathering rates of minerals harboring biologically important nutrients, such as phosphorus (P), K^+ , and Ca^{2+} (44, 45).

Lastly, the availability of N singly and in combination with P profoundly limits terrestrial C storage, with nontrivial effects on global climate change (4, 46). Our previous work demonstrated a doubling of ecosystem C storage among temperate conifer forests residing on N-rich bedrock (7). Our model indicates that rock N inputs could make up >29% of total N inputs to boreal forests, which could help to explain the high C uptake capacity observed for this biome and partially mitigate the mismatch of C and N budgets in Earth system models (3). Historically, weathering has been viewed as responsive to CO_2 enrichment and climate change over deep geological time (millions of years) (35). The direct connections that we draw between tectonic uplift, N inputs, and weathering reactions therefore emphasize a role for rock-derived nutrients in affecting the 21st-century C cycle and climate system.

REFERENCES AND NOTES

- P. M. Vitousek, R. W. Howarth, *Biogeochemistry* **13**, 87–115 (1991).
- R. A. Berner, *Geology* **34**, 413–415 (2006).
- B. A. Hungate, J. S. Dukes, M. R. Shaw, Y. Luo, C. B. Field, *Science* **302**, 1512–1513 (2003).
- Y. P. Wang, B. Z. Houlton, *Geophys. Res. Lett.* **36**, L24403 (2009).
- F. S. Chapin III, P. A. Matson, H. A. Mooney, *Principles of Terrestrial Ecosystem Ecology* (Springer, 2002).
- D. Binkley, Y. Son, D. W. Valentine, *Ecosystems* **3**, 321–331 (2000).
- S. L. Morford, B. Z. Houlton, R. A. Dahlgren, *Nature* **477**, 78–81 (2011).
- G. E. Bebout, M. L. Fogel, P. Cartigny, *Elements* **9**, 333–338 (2013).
- B. Johnson, C. Goldblatt, *Earth Sci. Rev.* **148**, 150–173 (2015).
- J. M. Holloway, R. A. Dahlgren, *Global Biogeochem. Cycles* **16**, 65–1–65–17 (2002).
- S. Morford, B. Houlton, R. Dahlgren, *Global Biogeochem. Cycles* **29**, (2016).
- H. Jenny, *Factors of Soil Formation: A System of Quantitative Pedology* (McGraw-Hill, 1941).
- N. Gruber, J. N. Galloway, *Nature* **451**, 293–296 (2008).
- V. Busigny, P. Cartigny, P. Philippot, *Geochim. Cosmochim. Acta* **75**, 7502–7521 (2011).
- P. Cartigny, B. Marty, *Elements* **9**, 359–366 (2013).
- N. Gruber, “The marine nitrogen cycle: Overview and challenges,” in D. G. Capone, D. A. Bronk, M. R. Mulholland, E. Carpenter, Eds., *Nitrogen in the Marine Environment* (Academic Press, ed. 2, 2008), pp. 1–50.
- S. R. Boyd, *Chem. Geol.* **176**, 1–30 (2001).
- R. A. Berner, *Nature* **426**, 323–326 (2003).
- S. V. Sobolev et al., *Nature* **477**, 312–316 (2011).
- Y. Copard, P. Amiotte-Suchet, C. Di-Giovanni, *Earth Planet. Sci. Lett.* **258**, 345–357 (2007).
- J. I. Hedges, R. G. Keil, *Mar. Chem.* **49**, 81–115 (1995).
- R. W. Smith, T. S. Bianchi, M. Allison, C. Savage, V. Galy, *Nat. Geosci.* **8**, 450–453 (2015).
- R. A. Berner, *Am. J. Sci.* **282**, 451–473 (1982).
- J. D. Milliman, K. L. Farnsworth, *River Discharge to the Coastal Ocean* (Cambridge Univ. Press, 2013).
- I. J. Larsen, D. R. Montgomery, H. M. Greenberg, *Geology* **42**, 527–530 (2014).
- W. Zhang, D. R. Montgomery, *Water Resour. Res.* **30**, 1019–1028 (1994).
- L. Reusser, P. Bierman, D. Rood, *Geology* **43**, 171–174 (2015).
- J. L. Dixon, F. von Blanckenburg, *C. R. Geosci.* **344**, 597–609 (2012).
- S. L. Morford, B. Z. Houlton, R. A. Dahlgren, *Ecology* **97**, 54–64 (2016).
- M. Meybeck, A. Ragu, in *Freshwater Contamination*, B. Webb, Ed. (International Association of Hydrological Sciences, 1997), pp. 3–14.
- C. S. Riebe, J. W. Kirchner, R. C. Finkel, *Geochim. Cosmochim. Acta* **67**, 4411–4427 (2003).
- E. W. Portenga, P. R. Bierman, *GSA Today* **21**, 4–10 (2011).
- U.S. Geological Survey, National Geochemical Database: Rock; <https://mrdata.usgs.gov/ngdb/rock/>.
- A. J. West, A. Galy, M. Bickle, *Earth Planet. Sci. Lett.* **235**, 211–228 (2005).
- M. Raymo, W. F. Ruddiman, *Nature* **359**, 117–122 (1992).
- P. M. Vitousek, D. N. L. Menge, S. C. Reed, C. C. Cleveland, *Philos. Trans. R. Soc. London B Biol. Sci.* **368**, 20130119 (2013).
- F. Dentener et al., *Global Biogeochem. Cycles* **20**, GB4003 (2006).
- R. Vet et al., *Atmos. Environ.* **93**, 3–100 (2014).
- B. Z. Houlton, Y. P. Wang, P. M. Vitousek, C. B. Field, *Nature* **454**, 327–330 (2008).
- S. M. Strathouse, G. Sposito, P. J. Sullivan, L. J. Lund, *J. Environ. Qual.* **9**, 54–60 (1980).
- M. J. Hendry, R. G. L. McCready, W. D. Gould, *J. Hydrol.* **70**, 177–198 (1984).
- J. M. Holloway, R. A. Dahlgren, B. Hansen, W. H. Casey, *Nature* **395**, 785–788 (1998).
- J. Canadell et al., *Oecologia* **108**, 583–595 (1996).
- A. G. Jongmans et al., *Nature* **389**, 682–683 (1997).
- R. Landeweert, E. Hoffland, R. D. Finlay, T. W. Kuyper, N. van Breemen, *Trends Ecol. Evol.* **16**, 248–254 (2001).
- J. J. Elser et al., *Ecol. Lett.* **10**, 1135–1142 (2007).
- C. C. Cleveland et al., *Global Biogeochem. Cycles* **13**, 623–645 (1999).

ACKNOWLEDGMENTS

Funding: This work was supported by NSF grants EAR-1411368 and DEB-1150246 and the Andrew W. Mellon Foundation. **Author contributions:** B.Z.H. developed the concept and structure and wrote the initial text of the manuscript; S.L.M. and R.A.D. provided comments, edits, and feedback that improved the manuscript substantially. S.L.M. designed the global weathering model, parameterization scheme, and data-gathering techniques. All authors analyzed the results equally. **Competing interests:** None declared. **Data and materials availability:** The data are available in the text and supplementary materials.

SUPPLEMENTARY MATERIALS

www.sciencemag.org/content/360/6384/58/suppl/DC1
Materials and Methods
Figs. S1 to S4
Tables S1 to S7
References (48–75)

14 April 2017; resubmitted 8 September 2017
Accepted 21 February 2018
10.1126/science.aan4399

REPORT

TOPOLOGICAL MATTER

Observation of fractional Chern insulators in a van der Waals heterostructure

Eric M. Spanton,^{1*} Alexander A. Zibrov,^{2*} Haoxin Zhou,² Takashi Taniguchi,³ Kenji Watanabe,³ Michael P. Zaletel,⁴ Andrea F. Young^{2†}

Topologically ordered phases are characterized by long-range quantum entanglement and fractional statistics rather than by symmetry breaking. First observed in a fractionally filled continuum Landau level, topological order has since been proposed to arise more generally at fractional fillings of topologically nontrivial Chern bands. Here we report the observation of gapped states at fractional fillings of Harper-Hofstadter bands arising from the interplay of a magnetic field and a superlattice potential in a bilayer graphene-hexagonal boron nitride heterostructure. We observed phases at fractional filling of bands with Chern indices $C = -1, \pm 2$, and ± 3 . Some of these phases, in $C = -1$ and $C = 2$ bands, are characterized by fractional Hall conductance—that is, they are known as fractional Chern insulators and constitute an example of topological order beyond Landau levels.

Bands in electronic systems can be classified by their symmetry and topology (*1*). In two dimensions with no symmetries beyond charge conservation, for example, bands are characterized by a topological Chern number, C (*2*). The Chern number determines the Hall conductance contributed by a filled band, which takes quantized integer values, $\sigma_{xy} = t \frac{e^2}{h}$ with $t \in \mathbb{Z}$ (*2*) (here e is the charge of an electron, h is the Planck constant, and \mathbb{Z} is the set of all integers). Systems with an integer number of filled bands with nonzero C (Chern bands) thus show a quantized, nonzero Hall conductance and are known as Chern insulators (CIs). The first experimental examples of CIs are the integer quantum Hall (IQH) states, which have been observed in isotropic two-dimensional electron systems subjected to a large magnetic field (*3*). In the case of IQH states, a quantized Hall conductance is observed when an integer number of Landau levels (LLs) are filled, each with $C = 1$.

IQH systems are very nearly translation-invariant, in which case t is fixed by the magnetic field B and the electron density n , via $t = \frac{nh}{Be}$, with some disorder required for the formation of plateaus in the Hall conductance (*4*). Recently, there has been interest in a dif-

ferent class of CIs for which continuous translation invariance is strongly broken by a lattice, decoupling the Hall conductance from the magnetic field. CIs in which t is decoupled from $\frac{n}{B}$ have been observed in magnetically doped thin films with strong spin-orbit interactions (*5*) and in the Harper-Hofstadter (*2*) bands of graphene subjected to a superlattice potential (*6–8*). Haldane's staggered flux model (*9*), which has nonzero quantized Hall conductance even when the net magnetic field is zero, has been engineered with ultracold atoms in an optical lattice (*10*).

Interactions expand the topological classification of gapped states, allowing t to be quantized to a rational fraction. By Laughlin's flux-threading argument, an insulator with $t = \frac{p}{q}$ ($p, q \in \mathbb{Z}$) must have a fractionalized excitation with charge $\frac{e}{q}$ (*11*). A fractionally quantized Hall conductance in a bulk insulator is thus a smoking-gun signature of topological order, and fractional quantum Hall (FQH) effects have been observed in partially-filled continuum LLs in a variety of experimental systems (*12–15*). Can a fractional Chern insulator (FCI) arise from fractionally filling a more general Chern band (*16*)? Although a FQH effect in a LL may be considered a special case of an FCI, in this work we focus on FCIs that require a lattice for their existence.

The phenomenology of lattice FCIs differs from that of continuum LLs. Chern bands with $C \neq 1$ can arise, leading to different ground states than are allowed in $C = 1$ LL. In addition, unlike LLs, Chern bands generically have a finite, tunable bandwidth that competes with interactions, providing a new setting for the study of quantum phase transitions. Finally, FCIs might be found in experimental systems where Chern bands, but not LLs, are realizable. A large body of the-

oretical work has begun to investigate these issues (*17–24*).

Here we report the experimental discovery of FCIs in a bilayer graphene (BLG) heterostructure at high magnetic fields. The requirements to realize an FCI in an experimental system are, first, the existence of a Chern band, and, second, electron-electron interactions strong enough to overcome both disorder and band dispersion. We satisfied these requirements by using a high-quality BLG heterostructure in which the bilayer is encapsulated between hexagonal boron nitride (hBN) gate dielectrics and graphite top and bottom gates (Fig. 1, A and B). This geometry was recently demonstrated to markedly decrease disorder, permitting the observation of delicate FQH states (*25*). We generated Chern bands by close rotational alignment ($\sim 1^\circ$) between the BLG and one of the two encapsulating hBN crystals. Beating between the mismatched crystal lattices leads to a long-wavelength (~ 10 nm) moiré pattern that the electrons in the closest layer experience as a periodic superlattice potential (Fig. 1B) (*26*). At high magnetic fields, the single-particle spectrum of an electron in a periodic potential forms the Chern bands of the Hofstadter butterfly (*7–9*). These bands are formally equivalent to Chern bands proposed to occur in zero magnetic field; at any fractional flux, a finite-field lattice model can be converted to an equivalent zero-field model using gauge invariance (*16*).

We measured the penetration field capacitance (*27*) (C_p), which distinguishes between gapped (incompressible) and ungapped (compressible) states (*26*). Figure 1, C and D, shows C_p measured as a function of B and the electron density, $n \approx n_0 \equiv c(v_t + v_b)$, where v_t and v_b are the applied top and bottom gate voltages and c denotes the geometric capacitance to either of the two symmetric gates. We used a perpendicular electric field, parameterized by $p_0/c = v_t - v_b$ (where p_0 is the electron density imbalance between layers in the absence of screening), to localize the charge carriers onto the layer with a superlattice potential, e.g., adjacent to the aligned hBN flake. High- C_p features, corresponding to gapped electronic states, are evident throughout the experimentally accessed parameter space (Fig. 1, C and D), following linear trajectories in the nB plane. We estimated the area of the superlattice unit cell from zero-field capacitance data (*26*) and defined the electron density $n_e = N_e/N_S$ and flux density $n_\Phi = N_\Phi/N_S$ per unit cell. Here N_e , N_S , and N_Φ are the number of electrons, superlattice cells, and magnetic flux quanta ($\Phi_0 = h/e$) in the sample, respectively. The trajectories are parameterized by their inverse slope t and n -intercept s in the nB plane

$$N_e = tN_\Phi + sN_S, n_e = tn_\Phi + s \quad (1)$$

The Streda (*28*) formula, $t = \frac{\partial n_e}{\partial n_\Phi} \big|_{N_S} = \frac{h}{e^2} \sigma_{xy}$, shows that the Hall conductance of a gapped phase is exactly t . The invariant $s = \frac{\partial N_e}{\partial N_S} \big|_{N_\Phi}$ encodes the amount of charge “glued” to the unit cell; i.e., the charge that is transported if the lattice is dragged adiabatically (*29*). Nonzero s indicates that strong

¹California Nanosystems Institute, University of California, Santa Barbara, CA 93106, USA. ²Department of Physics, University of California, Santa Barbara, CA 93106, USA.

³Advanced Materials Laboratory, National Institute for Materials Science, Tsukuba, Ibaraki 305-0044, Japan.

⁴Department of Physics, Princeton University, Princeton, NJ 08544, USA.

*These authors contributed equally to this work.

†Corresponding author. Email: andrea@physics.ucsb.edu

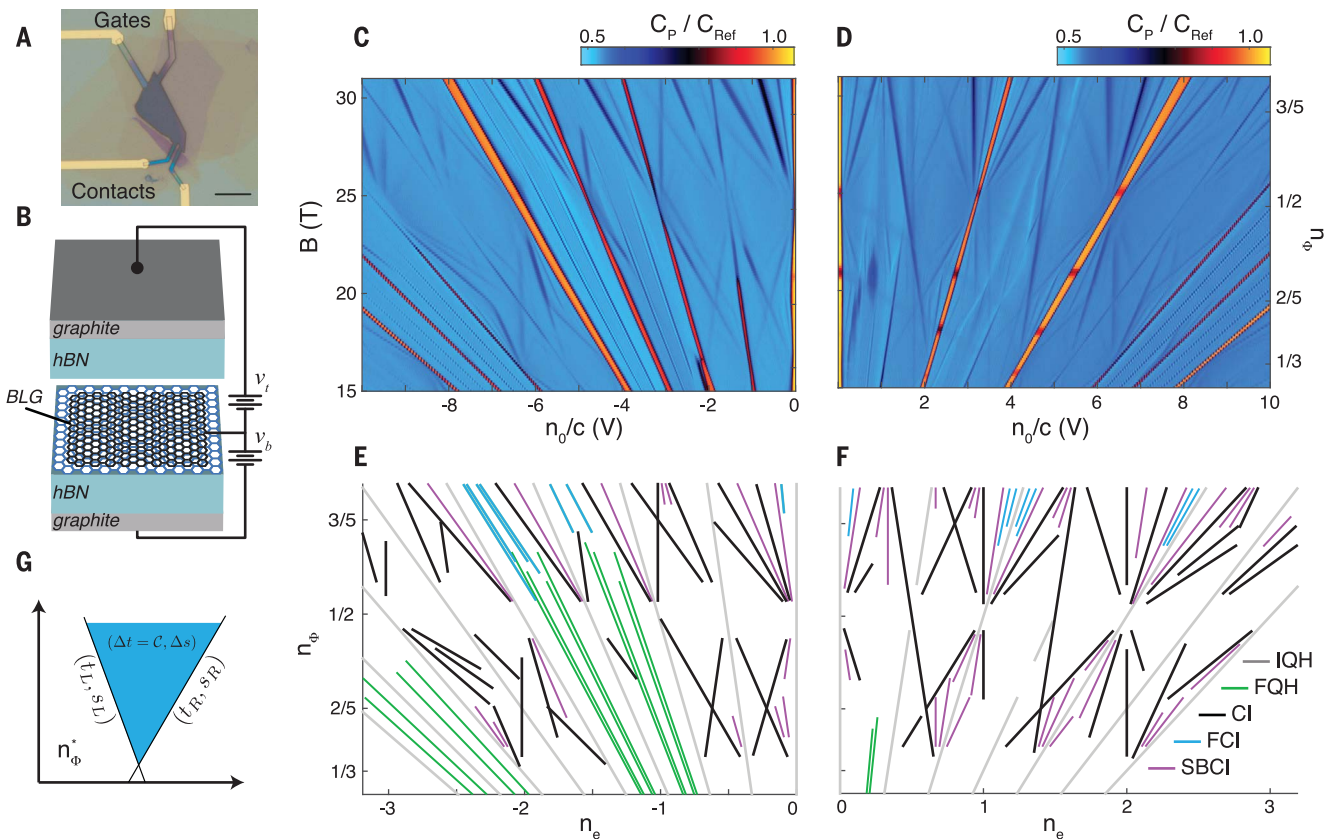


Fig. 1. Magnetocapacitance in a high-quality BLG moiré superlattice device. (A) Optical micrograph of the device. Scale bar, 10 μm . (B) Schematic of the device, with top and bottom graphite gates at potential v_t and v_b . A moiré potential is induced by alignment of the graphene bilayer with one of the encapsulating hBN crystals. (C) Penetration field capacitance (C_P) as a function of density $n_e \sim n_0 \equiv c(v_t + v_b)$ and magnetic field B for $n_0 < 0$. $T = 300$ mK, and C_{Ref} is a reference capacitance. A large electric field $p_0/c = (v_t - v_b) = 16$ V is applied to force the valence electrons onto the top layer, which is in contact with the aligned hBN. (D) C_P for $n_0 > 0$ with $v_t - v_b = -16$ V at $T = 300$ mK. (E and F) Linear gap trajectories observed in (C) and (D)

parameterized by $n_e = t \cdot n_\Phi + s \cdot n_\Phi$ and n_e are the magnetic flux quanta and number of electrons per moiré unit cell, respectively. $n_\Phi = \frac{\sqrt{3}\lambda^2 B}{24\phi_0} = 1/2$ (λ , wavelength) when $B = 24.3$ T and $n_e = 1$ when $n_0/c = 3.1$ V. Five trajectory classes are distinguished by color: Integer quantum Hall (gray; $s = 0, t \in \mathbb{Z}$), fractional quantum Hall (green; $s = 0, t$ fractional), Hofstadter Chern insulators (black; $s, t \in \mathbb{Z}, s \neq 0$), symmetry-broken Chern insulators (purple; fractional $s, t \in \mathbb{Z}$), and fractional Chern insulators (cyan; fractional s, t). (G) Schematic of a $(\Delta t, \Delta s)$ Chern band (see text).

lattice effects have decoupled the Hall conductance from the electron density. Within band theory, the invariants of a gap arise from summing the invariants $(\Delta t_j, \Delta s_j)$ of the occupied bands, $(t, s) = \sum_{j \in \text{occ}} (\Delta t_j, \Delta s_j)$ —in particular, the Hall conductance t is the sum of the occupied band Chern indices, $\Delta t_j = C_j$.

On the basis of the properties of t and s , we observed five classes of high- C_P trajectories, each of which corresponds to a distinct class of gapped state (Fig. 1, E and F). Free-fermion band gaps must have integer t and s : Trajectories with $s = 0$ correspond to gaps between LLs, i.e., IQH states. Trajectories with $s \neq 0$ indicate the formation of the non-LL Chern bands of the Hofstadter butterfly (6–8). Trajectories with fractional t or s are beyond the single-particle picture and thus indicate interaction-driven gapped phases. The conventional FQH states follow trajectories with fractional t and $s = 0$. Gap trajectories with integer t and fractional s [previously

observed in monolayer graphene (30)] must be either topologically ordered or have interaction-driven spontaneous symmetry breaking of the superlattice symmetry. The theoretical analysis below suggests that the latter case is most likely, so we refer to this class as symmetry-broken Chern insulators (SBCIs). Finally, there are trajectories with fractional t and fractional s , which are the previously unreported class of topologically ordered FCI phases.

To better understand states with fractional t or s , we first identified the single-particle Chern bands in our experimental data by identifying all integer- t , integer- s gapped states. We focused on adjacent pairs of gapped states with integer (t_L, s_L) and (t_R, s_R) (where L and R denote gapped states with lower and higher n_0 , respectively), which form the boundaries of a finite range of n_e in which no other single-particle gapped states appear (Fig. 1G). Adding charge to the left gapped state corresponds to filling a Chern band with invariants $(\Delta t, \Delta s) = (t_R - t_L, s_R - s_L)$. From

this criterion, we detected a variety of Chern bands with $\Delta t = \pm 1, \pm 2, \pm 3$, and ± 5 in the experimental data (26), each of which appears as a triangle between adjacent single-particle gapped states. These Chern bands are observed to obey certain rules expected from the Hofstadter problem: For example, Δt and Δs are always coprime, and Chern bands with Δt always emanate from a flux $n_\Phi^* = p/\Delta t$.

Interaction-driven phases occur at fractional filling ν_C of a Chern band, following trajectories $(t_{\nu_C}, s_{\nu_C}) = (t_L, s_L) + \nu_C(\Delta t, \Delta s)$. The Chern numbers of the bands in which some of the observed interaction-driven phases appear (Fig. 2, A to C) are depicted schematically in Fig. 2, D to F.

By combining a phenomenological description of the moiré potential with knowledge of orbital symmetry breaking in BLG (31), we were able to construct a single-particle model that closely matches the majority of the experimentally observed single-particle Chern bands (25). The

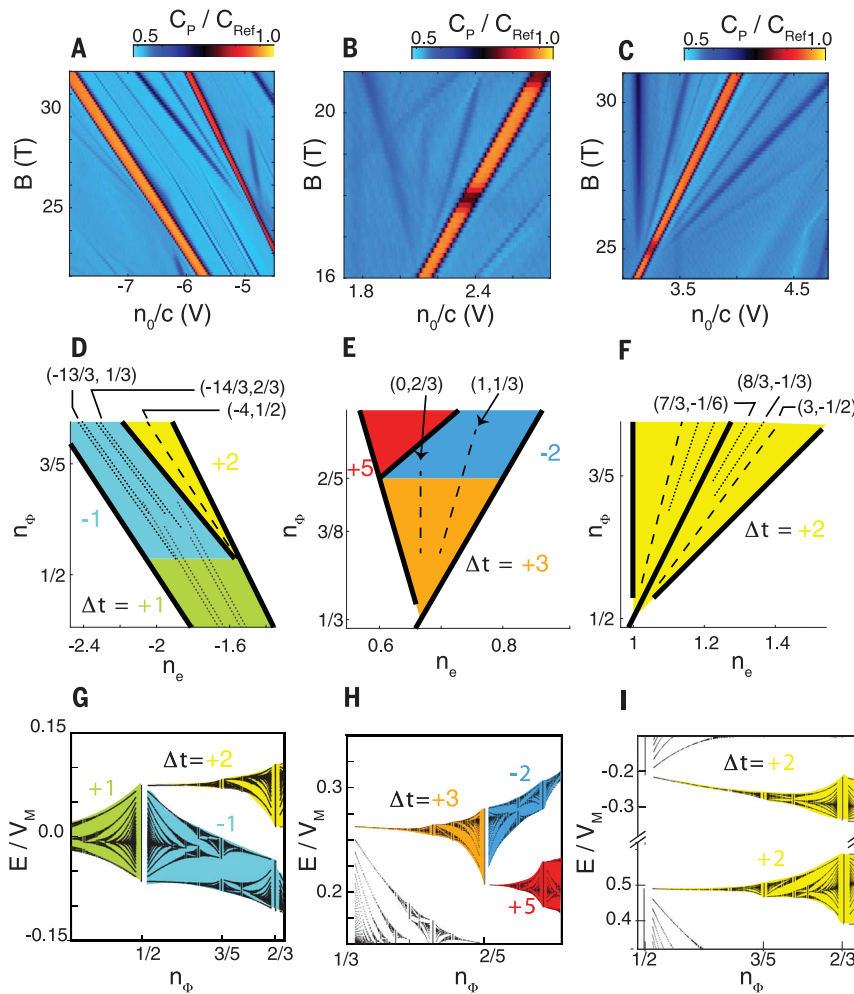


Fig. 2. Interaction-driven states at partial Chern-band filling. (A to C) Details of Fig. 1, C and D, showing (A) FCI states in a $\Delta t = -1$ band, (B) SBCI states in a $\Delta t = +3$ band, and (C) FCI and SBCI states in $\Delta t = 2$ bands. (D) Schematic of (A). FCI states (black dotted lines) with $(t, s) = (-13/3, 1/3)$, $(-22/5, 2/5)$, $(-23/5, 3/5)$, and $(-14/3, 2/3)$ occur at fractional filling of a $\Delta t = -1$ band (light blue). FQH states (gray dotted lines) occur at fractional filling of a conventional LL ($\Delta t = +1$, green) at low fields. (E) Schematic of (B). SBCI states (dashed lines) at $(t, s) = (0, 2/3)$ and $(1, 1/3)$ occur at $1/3$ and $2/3$ fractional filling of a $\Delta t = 3$ band (orange). (F) Schematic of (C). Both FCI and SBCI states (dotted and dashed lines, respectively) occur in the $\Delta t = 2$ bands. (G) Calculated Hofstadter energy spectrum (25) in the regime of (A), matching the observation that the LL splits into $C = -1, 2$ bands. (H) Calculated Hofstadter spectrum in the regime of (B), matching the observed splitting of a $C = 3$ band into $C = 5, -2$ bands. (I) Calculated Hofstadter spectrum in the regime of (C). The IQH gap at $v = 2$ separates the two single-particle bands and is much larger than v_M .

calculated energy spectra of the bands relevant to Fig. 2, A to C, are shown in Fig. 2, G to I. As is clear from the band structure, stable phases at fractional v_C are not expected within the single-particle picture: Instead, the encompassing Chern band splits indefinitely into finer Chern bands at lower levels of the fractal butterfly that depend sensitively on n_Φ .

The three columns of Fig. 2 represent instances of three general classes of fractional v_C states observed in our experiment. Figure 2A shows two gapped states within a $\Delta t = -1$ band at $v_C = \frac{1}{3}$ and $\frac{2}{3}$. These gapped states extend from $n_\Phi \approx 0.55$ to at least $n_\Phi \approx 0.8$ (26). Both are characterized by fractional t and s , and we identify them as FCI

states. As with FQH states, the fractionally quantized Hall conductance implies that the system has a charge $e/3$ excitation (11). The fractional s values of these states, being multiples of this fractional charge, do not require broken superlattice symmetry. Gapped states at $v_C = 1/3, 2/3$ in a $\Delta t = -1$ band are accompanied by comparatively weaker states at $v_C = 2/5, 3/5$ (Fig. 3B). These fillings match the odd-denominator composite fermion sequence observed for FQH states (Fig. 3C), in agreement with theoretical predictions (32).

Figure 2 shows gapped states with fractional s and integer t at $v_C = 1/3, 2/3$ in a $\Delta t = +3$ band (Fig. 2B) and at $v_C = 1/2$ in a $\Delta t = +2$ band (Fig.

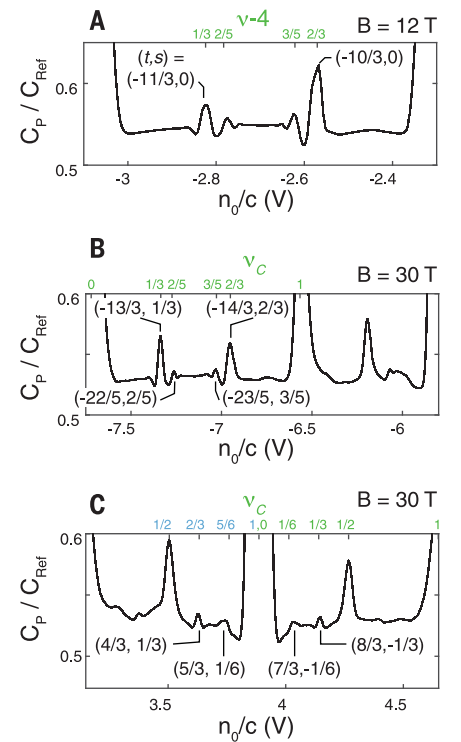


Fig. 3. Line cuts of C_P comparing FCI and FQH states. (A) Line cut of C_P versus n_0/c (bottom axis) and Chern band filling factor (v_C , top axis). The data are averaged over $p_0/c \sim 1.0$ to 4.0 V at $B = 12$ T, showing FQH states in a conventional LL. At low fields, the effective moiré potential is weak, and FQH states are observed at filling factors $v = -4 = 1/3, 2/3$ as well as $2/5, 3/5$ of the $\Delta t = +1$ LL. (B) Line cut averaged over $p_0/c \sim 4.0$ to 14.0 V at $B = 30$ T, showing FCI in the $\Delta t = -1$ band (also shown in Fig. 2A). Weaker features appear at $v_C = 2/5, 3/5$, similar to the composite fermion sequence in (A). (C) Line cut averaged over $p_0/c \sim -14.0$ to 9.0 V at $B = 30$ T, showing FCI in two $\Delta t = 2$ bands (also shown in Fig. 2C). Blue and green values indicate the filling of two distinct bands. The relative strength of the $v_C = 1/3$ state compared to the $v_C = 1/6$ state in the right $\Delta t = 2$ band is consistent with the former preserving the lattice symmetry.

2C). Filling a Chern- Δt band to a multiple of $v_C = \frac{1}{|\Delta t|}$ corresponds to integer t but fractional s . These states are unlikely to admit a simple interpretation as FCIs; however, we cannot exclude exotic fractionalized states. Absent fractional excitations, a gapped state with fractional $s = \frac{x}{y}$ implies broken superlattice symmetry: The unit cell of such a phase must contain an integral number of electrons, and the smallest such cell contains y superlattice sites. Theoretically, such symmetry breaking is expected to arise spontaneously as a result of electronic interactions, in a lattice analog of quantum Hall ferromagnetism (33). A Δt Chern band is similar to a Δt -component LL, but in contrast to an internal spin, translation acts by

cyclically permuting the components (33–35). Spontaneous polarization into one of these components thus leads to a t -fold increase of the unit cell (33). The observation of SBCIs is thus analogous to the observation of strong odd-integer IQHEs that break spin-rotational invariance. Some of the “fractional fractal” features recently described in monolayer graphene appear to be consistent with this explanation (30).

Further, we also observed fractional- t states within a $\Delta t = +2$ band (Fig. 3C); for example, at $v_C = 1/3$ ($t = 8/3$ and $s = -1/3$) and $v_C = 1/6$ ($t = 7/3$ and $s = -1/6$). FCIs in Chern- $\Delta t \neq \pm 1$ bands can either preserve or break the underlying lattice symmetry. Symmetry-preserving FCIs are expected (21, 32, 36) at fillings $v_C = \frac{m}{2lm\Delta t+1}$ for integers l and m . The state observed at $v_C = 1/3$ is consistent with this sequence ($l = 1$, $m = -1$); in contrast, the weaker state at $v_C = 1/6$ is not. For the $v_C = 1/6$ state, the observed $t = 7/3$ suggests a fundamental charge of $e/3$. As for SBCIs, the observed $s = -1/6$ implies that each unit cell binds only half a fundamental charge—i.e., the moiré unit cell is doubled and the $v_C = 1/6$ state is a symmetry-broken FCI state. A $\Delta t = 2$ Hofstadter band is similar to a spin-degenerate LL, with lattice symmetry taking the place of spin symmetry. In a spin-degenerate LL at $v_C = 1/6$ (i.e., LL filling $v_C = 1/3$), the system spontaneously spin polarizes, forming a single-component Laughlin state. In contrast, at $v_C = 1/3$ ($v_C = 2/3$) the system can either spin polarize (observed only for large Zeeman energy) or form a multicomponent FQH state that preserves spin rotation symmetry. The absence of an obvious analog of the Zeeman effect in our Hofstadter band makes a multicomponent state a more likely candidate for the feature observed at $v_C = 2/3$.

To assess the plausibility of FCI and SBCI ground states, we used the infinite density matrix renormalization group (iDMRG) to numerically compute the many-body ground state within a minimal model of the BLG (37). We first considered Coulomb interactions and a triangular moiré potential of amplitude V_M projected into a BLG $N = 0$ LL (38), matching the parameter regime in Fig. 2A (26). We focused on $n_\Phi = \frac{2}{3}$ at a density corresponding to $v_C = \frac{1}{3}$ filling of the $\Delta t = -1$ band.

If interactions are too weak compared with the periodic potential [as parameterized by V_M/E_C , where $E_C = e^2/(\epsilon\ell_B)$ is the Coulomb energy, $\ell_B = \sqrt{\frac{\hbar}{eB}}$ is the magnetic length, ϵ is the dielectric constant, and \hbar is the reduced Planck constant], the ground state at $n_\Phi = \frac{2}{3}$ is gapless, corresponding to a partially filled Chern band. If the interactions are too strong, the system forms a Wigner crystal that is pinned by the moiré potential. In the intermediate regime, however, the theoretical ground state of this model has a fractional t and s that match the experiment and hence is an FCI, with entanglement signatures that indicate a Laughlin-type topological order (26). The FCI is stable across a range of V_M/E_C (Fig. 4A) corresponding to $|V_M| \sim 14 - 38$ meV,

consistent with recent experiments (39) suggesting that $|V_M| \sim 25$ meV. Figure 4B shows that the real-space density of an FCI is strongly modulated by the potential but preserves all the symmetries of the superlattice.

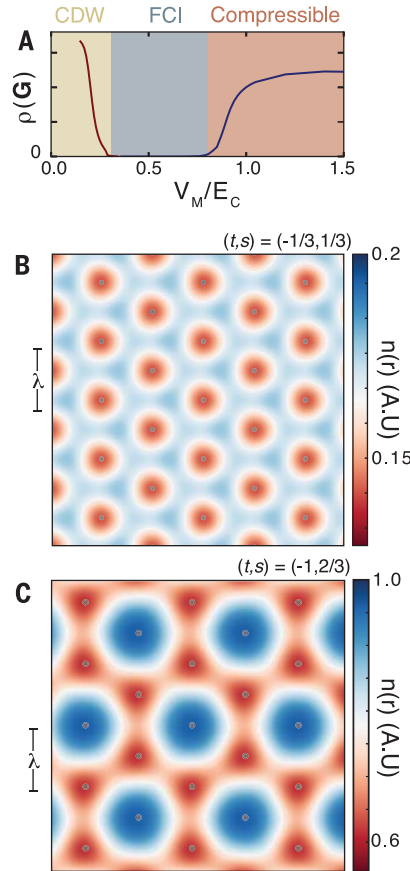


Fig. 4. iDMRG calculations showing the stability of FCI and SBCI states.

(A) Calculated iDMRG phase diagram at $v_C = 1/3$ filling of the $\Delta t = -1$ band shown in Fig. 2, A, D, and G ($n_\Phi = 2/3$). V_M is the moiré potential amplitude, E_C is the Coulomb energy, and $\rho(\mathbf{G})$ is the charge density at Bragg vector \mathbf{G} . The FCI competes with two other phases: a charge density wave (CDW) at low V_M and a compressible phase at high V_M . The competing phases are diagnosed by symmetry-breaking density waves at wave vector $\mathbf{G} = \mathbf{G}_0/3$ (red) and $\mathbf{G} = \mathbf{G}_0/2$ (blue), where \mathbf{G}_0 is a reciprocal vector of the moiré potential (25). (B) Calculated real-space electron density $n(r)$ of the FCI found in (A). $n(r)$ preserves the symmetry of the moiré potential, whose periodicity is indicated by the gray circles. Here $V_M/E_C = 0.7$. (C) Calculated real-space electron density $n(r)$ at $v_C = \frac{2}{3}$ filling of the $\Delta t = 3$ band shown in Fig. 2, B, E, and H ($n_\Phi = 3/8$). The result is consistent with an SBCI phase; $(t, s) = (-1, 2/3)$, and $n(r)$ spontaneously triples the unit cell of the underlying moiré potential, indicated by gray circles. Here $V_M/E_C = 0.6$ and $\Theta_M = \pi/8$.

We next conduct iDMRG calculations to assess the plausibility of the SBCI hypothesis. We focus on the well-developed Chern-3 band of Fig. 2, B, E, and H. As a minimal model, we project the moiré and Coulomb interactions into the $N = 1$ LL of the BLG, fixing $V_M = 21$ meV and $E_C(B = 17T) = 35$ meV, and take $n_\Phi = \frac{3}{8}$.

At $v_C = \frac{1}{3}$ filling, the electron density exhibits a modulation that spontaneously triples the superlattice unit cell (Fig. 4C). A similar tripling is observed at $v_C = \frac{2}{3}$. These are not merely density waves, however, as they have finite (t, s) invariants, in agreement with experimental observations.

The SBCI states are distinct from a second class of integer- t , fractional- s features, the moiré-pinned Wigner crystals (30, 40). In the latter case, starting from a LL-gap at $t, s = t_L, 0$, additional electrons form a Wigner crystal pinned by the moiré potential; the added electrons are electrically inert, leading to a state at $t, s = t_L, \frac{x}{y}$ that cannot be ascribed to fixed v_C of an encompassing band. These states are thus analogous to reentrant IQH effects, with the moiré potential playing the role of disorder. In contrast, although the electrons added to the SBCI spontaneously increase the unit cell, they also contribute an integer Hall conductance, which together corresponds to some v_C .

In summary, we find that instead of a self-repeating fractal structure, interactions mix Hofstadter-band wave functions to form stable, interaction-driven states at fractional filling of a Chern band. Among these are both SBCIs and topologically ordered FCIs, the latter of which constitute a lattice analog of the FQH effect. Lattice engineering can lead to increased experimental control. For example, multicomponent FCI states in bands with higher Chern numbers—as may be responsible for the $v_C = 1/3$ feature in Fig. 3C—have been predicted to host non-abelian defects at engineered lattice dislocations (34). A pressing experimental question, then, is whether FCI states can be realized in microscopically engineered superlattices.

REFERENCES AND NOTES

1. S. Ryu, A. P. Schnyder, A. Furusaki, A. W. W. Ludwig, *New J. Phys.* **12**, 065010 (2010).
2. D. J. Thouless, M. Kohmoto, M. P. Nightingale, M. den Nijs, *Phys. Rev. Lett.* **49**, 405–408 (1982).
3. K. Klitzing, G. Dorda, M. Pepper, *Phys. Rev. Lett.* **45**, 494–497 (1980).
4. S. M. Girvin, *Topological Aspects of Low Dimensional Systems* (Springer, 1999).
5. C.-Z. Chang et al., *Science* **340**, 167–170 (2013).
6. C. R. Dean et al., *Nature* **497**, 598–602 (2013).
7. L. A. Ponomarenko et al., *Nature* **497**, 594–597 (2013).
8. B. Hunt et al., *Science* **340**, 1427–1430 (2013).
9. F. D. M. Haldane, *Phys. Rev. Lett.* **61**, 2015–2018 (1988).
10. G. Jotzu et al., *Nature* **515**, 237–240 (2014).
11. R. B. Laughlin, *Phys. Rev. Lett.* **50**, 1395–1398 (1983).
12. D. C. Tsui, H. L. Stormer, A. C. Gossard, *Phys. Rev. Lett.* **48**, 1559–1562 (1982).
13. X. Du, I. Skachko, F. Duerr, A. Luican, E. Y. Andrei, *Nature* **462**, 192–195 (2009).
14. K. I. Bolotin, F. Ghahari, M. D. Shulman, H. L. Stormer, P. Kim, *Nature* **462**, 196–199 (2009).
15. A. Tsukazaki et al., *Nat. Mater.* **9**, 889–893 (2010).
16. We use the term “fractional Chern insulator” to denote any non-FQH, topologically ordered state

- at fractional filling of a Chern band, rather than a more restrictive definition requiring the states to occur at zero field.
17. S. A. Parameswaran, R. Roy, S. L. Sondhi, *C. R. Phys.* **14**, 816–839 (2013).
 18. E. J. Bergholtz, Z. Liu, *Int. J. Mod. Phys. B* **27**, 1330017 (2013).
 19. A. S. Sørensen, E. Demler, M. D. Lukin, *Phys. Rev. Lett.* **94**, 086803 (2005).
 20. R. N. Palmer, D. Jaksch, *Phys. Rev. Lett.* **96**, 180407 (2006).
 21. G. Möller, N. R. Cooper, *Phys. Rev. Lett.* **115**, 126401 (2015).
 22. D. N. Sheng, Z.-C. Gu, K. Sun, L. Sheng, *Nat. Commun.* **2**, 389 (2011).
 23. T. Neupert, L. Santos, C. Chamon, C. Mudry, *Phys. Rev. Lett.* **106**, 236804 (2011).
 24. N. Regnault, B. A. Bernevig, *Phys. Rev. X* **1**, 021014 (2011).
 25. A. A. Zibrov *et al.*, *Nature* **549**, 360–364 (2017).
 26. See supplementary materials.
 27. J. P. Eisenstein, L. N. Pfeiffer, K. W. West, *Phys. Rev. Lett.* **68**, 674–677 (1992).
 28. P. Streda, *J. Phys. C* **15**, L717–L721 (1982).
 29. A. H. MacDonald, *Phys. Rev. B* **28**, 6713–6717 (1983).
 30. L. Wang *et al.*, *Science* **350**, 1231–1234 (2015).
 31. B. M. Hunt *et al.*, *Nat. Commun.* **8**, 948 (2017).
 32. A. Kol, N. Read, *Phys. Rev. B* **48**, 8890–8898 (1993).
 33. A. Kumar, R. Roy, S. L. Sondhi, *Phys. Rev. B* **90**, 245106 (2014).
 34. M. Barkeshli, X.-L. Qi, *Phys. Rev. X* **2**, 031013 (2012).
 35. Y.-L. Wu, N. Regnault, B. A. Bernevig, *Phys. Rev. Lett.* **110**, 106802 (2013).
 36. A. Sterdyniak, C. Repellin, B. A. Bernevig, N. Regnault, *Phys. Rev. B* **87**, 205137 (2013).
 37. M. P. Zaletel, R. S. K. Mong, F. Pollmann, E. H. Rezayi, *Phys. Rev. B* **91**, 045115 (2015).
 38. X. Chen, J. R. Wallbank, M. Mucha-Kruczyński, E. McCann, V. I. Fal'ko, *Phys. Rev. B* **94**, 045442 (2016).
 39. M. Lee *et al.*, *Science* **353**, 1526–1529 (2016).
 40. A. M. DaSilva, J. Jung, A. H. MacDonald, *Phys. Rev. Lett.* **117**, 036802 (2016).

ACKNOWLEDGMENTS

We thank M. Barkeshli, A. Bernevig, C. Dean, and R. Mong for discussions and J. Jaroszynski and M. Yankowitz for experimental assistance. **Funding:** Numerical simulations were performed on computational resources supported by the Princeton Institute for Computational Science and Engineering using iDMRG code developed with R. Mong and the TenPy Collaboration. E.M.S. acknowledges the support of the Elings Fellowship. K.W. and T.T. acknowledge support from the Elemental Strategy Initiative conducted by the Ministry of Education, Culture, Sports, Science and Technology (MEXT) of Japan and Japan Society for the Promotion of Science KAKENHI grant JP15K2122. Measurements were performed at the

National High Magnetic Field Laboratory, which is supported by NSF Cooperative Agreement DMR-1157490 and the state of Florida. Magnetocapacitance measurements were funded by the NSF under grant DMR-1654186. A portion of the nanofabrication and transport measurements were funded by the U.S. Army Research Office under proposal 69188PHH. A.F.Y. acknowledges the support of the David and Lucile Packard Foundation. **Author contributions:** A.A.Z., E.M.S., and H.Z. performed the measurements. A.A.Z. fabricated the device. T.T. and K.W. provided hBN single crystals. M.P.Z. performed calculations. E.M.S., A.A.Z., M.P.Z., and A.F.Y. wrote the manuscript with input from all coauthors. **Competing interests:** None declared. **Data and materials availability:** Experimental data files are available from the Open Science Framework at <http://osf.io/7qckf/>.

SUPPLEMENTARY MATERIALS

www.sciencemag.org/content/360/6384/62/suppl/DC1
Materials and Methods
Supplementary Text
Figs. S1 to S14
Tables S1 and S2
References (41–62)

26 May 2017; accepted 13 February 2018
Published online 1 March 2018
10.1126/science.aan8458

SOLAR CELLS

Light-induced lattice expansion leads to high-efficiency perovskite solar cells

Hsinhan Tsai,^{1,2} Reza Asadpour,³ Jean-Christophe Blancon,¹ Constantinos C. Stoumpos,⁴ Olivier Durand,⁵ Joseph W. Strzalka,⁶ Bo Chen,⁷ Rafael Verduzco,^{2,8} Pulickel M. Ajayan,² Sergei Tretiak,⁹ Jacky Even,⁵ Muhammad Ashraf Alam,³ Mercouri G. Kanatzidis,⁴ Wanyi Nie,^{1*} Aditya D. Mohite^{1,8*}

Light-induced structural dynamics plays a vital role in the physical properties, device performance, and stability of hybrid perovskite-based optoelectronic devices. We report that continuous light illumination leads to a uniform lattice expansion in hybrid perovskite thin films, which is critical for obtaining high-efficiency photovoltaic devices. Correlated, in situ structural and device characterizations reveal that light-induced lattice expansion benefits the performances of a mixed-cation pure-halide planar device, boosting the power conversion efficiency from 18.5 to 20.5%. The lattice expansion leads to the relaxation of local lattice strain, which lowers the energetic barriers at the perovskite-contact interfaces, thus improving the open circuit voltage and fill factor. The light-induced lattice expansion did not compromise the stability of these high-efficiency photovoltaic devices under continuous operation at full-spectrum 1-sun (100 milliwatts per square centimeter) illumination for more than 1500 hours.

Recent breakthroughs in the power conversion efficiency (PCE) of hybrid perovskites have been achieved by compositional engineering of the ABX₃ structure, where A and B are cations and X is an anion, in mixed-cation mixed-halide perovskites. This approach allows the formation of a stable cubic phase with suppressed nonradiative recombination for exceptionally high open-circuit voltage (V_{OC}) and short-circuit current density (J_{SC}) (1–5). Similar strategies were also applied by Snaith and co-workers to achieve a near-ideal band-gap material to create perovskite-perovskite tandem cells (6). Nonetheless, several recent reports (7–11) have led to the realization that dynamic light-induced structural changes play a vital role in the observed optoelectronic properties, performances, and long-term stability of devices. Charge-carrier recombination can be altered by constant illumination, which was proposed to be closely linked with ionic movement, defect passivation, or local polarization triggered by light (12–15). Local cation

rotation or structural dynamics under light exposure can affect photophysical and electronic properties of methylammonium lead triiodide (MAPbI₃) (16–18). Wu and co-workers used ultrafast electron diffraction on MAPbI₃ thin films under illumination to experimentally elucidate the relationship between light-induced methylammonium (MA) rotation and the dynamics of hot carriers (19). Also, Zhou *et al.* indirectly attributed the post-illumination changes in the lattice to the weakening of the hydrogen bonding between MA and iodide (20).

Although these studies illustrate the importance of understanding these changes in the structure under light soaking, a direct and correlated in situ study monitoring the crystal structure transformations and their implications for photovoltaic (PV) performance, without invoking ionic migration, is still lacking. Such a study is also critical for understanding the microscopic origin of several reported light-induced changes in devices, such as ion migration near the interfaces, local polarization effects, and photoinduced degradation (21–25). Areas in need of research include mixed-cation halide perovskites, which offer the potential to approach the thermodynamic limit for a single-junction PV device with technologically relevant stability.

We report that continuous light soaking using a standard 1-sun (100 mW/cm²) source causes a large and uniform lattice expansion. In a stabilized mixed-cation pure-iodide system, the light-induced lattice expansion resulted in an increase in the average structural correlation length and relaxation of the local strain. Comprehensive device characterization coupled with quantitative device modeling suggests that lattice expansion leads to two effects that improve the PCE: namely, reduction in the energetic barrier near the

perovskite-contact interface and reduction in the nonradiative recombination, both in the bulk and in the interface. We observed a substantial improvement, from 18.5 to 20.5%, in the average PCE of a planar solar cell with a structure of fluorine-doped tin oxide–lithium-doped nickel oxide–formamidinium (FA)_{0.7}MA_{0.25}Cs_{0.05}PbI₃–fullerene–aluminum, with stability exceeding 1500 hours.

The FA_{0.7}MA_{0.25}Cs_{0.05}PbI₃ perovskite thin films were fabricated by mixing the precursors at desired stoichiometric ratios and spin-coated by our recently developed hot-casting method (26, 27) (see the methods section in the supplementary materials). Figure 1A shows the synchrotron grazing-incidence wide-angle x-ray scattering (GIWAXS) map (left panel) for the FA_{0.7}MA_{0.25}Cs_{0.05}PbI₃ perovskite and the line cut (right panel) taken from the GIWAXS map. The peaks were indexed based on the cubic phase of MAPbI₃ perovskites with larger lattice constants, indicating that FA was incorporated within the lattice forming the cubic structure (the supplementary text and fig. S1 provide detailed analysis of GIWAXS for various compositions). Moreover, the addition of 5% Cs stabilized the cubic phase, which otherwise undergoes phase segregation (fig. S2), at room temperature (6, 28). The band gap shifted from 1.66 eV for the MAPbI₃ thin film to 1.56 eV for the mixed-cation pure-iodide thin film (fig. S3), reflecting the incorporation of FA (28, 29).

To examine the structural transformation of the FA_{0.7}MA_{0.25}Cs_{0.05}PbI₃ thin films under constant illumination, we used in situ GIWAXS measurement under intermediate vacuum pressure (10^{−5} torr) at 25°C ± 0.5°C with a controlled cooling stage (Fig. 1, A to E). Figure 1A (right panel) shows the line cuts obtained from in situ GIWAXS maps of thin films with increasing illumination times from 0 to 180 min measured at 10-min intervals. No splitting or new Bragg peaks emerged after 180 min of continuous illumination, implying the absence of phase segregation or degradation under continuous 1-sun illumination. However, all of the diffraction peaks uniformly shifted toward lower values of scattering vector **q**, corresponding to an isotropic increase in lattice constant *d* (lattice expansion) from 6.290 ± 0.002 Å to 6.330 ± 0.004 Å (Fig. 1B). This 1.4% change in the FA_{0.7}MA_{0.25}Cs_{0.05}PbI₃ thin film was the same as the expansion seen in a complete PV device with contact layers (fig. S4). We also observed a similar response for pure MAPbI₃ thin films, which suggests that light-induced lattice expansion is a general property of hybrid perovskites (fig. S5).

Even after the films rested in the dark, the lattice expansion persisted for 30 min before the lattice relaxed back to its original, pre-light exposure value (dashed lines in Fig. 1, A and C). We could exclude heat-induced lattice expansion because *d* remained unchanged after films were heated to 50°C (fig. S6). We also observed an increase in main-peak intensities associated with sharpening of the peak widths after illumination (Fig. 1C), suggesting improved crystallinity. Indeed, the full width at half maximum (FWHM) of the peak as a function of illumination time (Fig. 1D)

¹Division of Materials Physics and Application, Los Alamos National Laboratory (LANL), Los Alamos, NM 87545, USA.

²Department of Materials Science and NanoEngineering, Rice University, Houston, TX 77005, USA. ³School of Electrical and Computer Engineering, Purdue University, West Lafayette, IN 47907, USA. ⁴Department of Chemistry and Department of Materials Science and Engineering, Northwestern University, Evanston, IL 60208, USA. ⁵Université de Rennes, Institut National des Sciences Appliquées (INSA) de Rennes, CNRS, Institut FOTON (Fonctions Optiques pour les Technologies de l'Information)—UMR 6082, F-35000 Rennes, France. ⁶Division of X-Ray Science, Argonne National Laboratory, Argonne, IL 60439, USA. ⁷Smalley-Curl Institute, Rice University, Houston, TX 77005, USA. ⁸Department of Chemical and Biomolecular Engineering, Rice University, Houston, TX 77005, USA. ⁹Division of Theoretical Chemistry and Molecular Physics, LANL, Los Alamos, New Mexico 87545, USA.

*Corresponding author. Email: wanyi@lanl.gov (W.N.); amohite@lanl.gov (A.D.M.)

decreased rapidly in the first 20 min and then more slowly during the next 2 hours. To evaluate the crystallite size (the coherent domain size of diffraction) and strain distribution, we performed a detailed structural analysis using a line profile (integral breadths) analysis of all of the diffraction planes on the basis of the Halder-Wagner equation (see the methods section in the supplementary materials and Fig. 1E). The coherence length, which describes the average crystallite size, was obtained from the slope of the linear fit of the Halder-Wagner plot. After light soaking, we observed a reduction in the y intercepts and thus a decrease in the microstrains, along with a reduction in the slope that resulted from an increase in the average crystallite size. The decrease in microstrains along with the increase in the crystallite size after illumination is indicative of the relaxation of the local strain in hybrid perovskites containing multiple cations. We propose a possible microscopic origin for the lattice expansion (Fig. 1F) as follows: The as-prepared thin film is strained because of the distorted nature of the lattice, which balances cations of different sizes. Upon illumination, it undergoes volumetric expansion in all directions. This process relaxes the local strain, reducing the mosaicity of the crystallites and sharpening the Bragg peaks.

We rationalize that on the microscopic scale, illuminating the hybrid perovskite films with photon energies greater than the band gap develops electron-hole pairs in the material. The photogenerated electrons in the conduction band can populate bonding states, whereas holes in the valence band vacate antibonding states. Both processes can weaken covalent bonds and lead to either less-distorted Pb–I–Pb bonds or elongation of the Pb–I bonds, which causes lattice expansion. From the photoluminescence (PL) measurements of the mixed-cation perovskite thin films before and after illumination, the emission peak undergoes a 5-meV red shift (fig. S10), which has been proposed for an enlarged unit cell caused by the increase of the Pb–I–Pb bond angle (30), whereas for Pb–I bond elongation, a blue shift should be expected (37). The lattice expansion observed did not originate exclusively from light-induced ion migration effects reported previously (21–23, 32). In fact, x-ray photoelectron spectroscopy (XPS) with depth profiling of mixed-cation thin films performed before and after illumination showed the absence of an ion migration mechanism (figs. S7 and S8). More precisely, change in the I/Pb chemical ratio after light illumination, a signature of the redistribution of the halide (iodide) (22), was absent in the $\text{FA}_{0.7}\text{MA}_{0.25}\text{Cs}_{0.05}\text{PbI}_3$ mixed-cation system.

Realizing that the reduced mosaicity and improved crystallinity (Fig. 1) may lead to highly efficient and reliable solar cells, we fabricated a set of planar PV devices with nickel oxide and fullerene as selective contacts on the hole and electron collector sides, respectively (see the methods section in the supplementary materials). We directly analyzed the effect of light-induced lattice expansion on the device behavior by in situ monitoring of the structure (through GIWAXS)

and PV figures of merit. We extracted the figures of merit from the current density–voltage (J - V) curve as a function of illumination time (Fig. 2A) and compared the change in those values with the change in the lattice constant (Fig. 2B). Figure 2A shows the time evolution of the V_{OC} , the fill factor (FF), and the J_{SC} . We observed an increase in the V_{OC} (Fig. 2A, top) from 0.73 to 0.9 V in the first 20 min, and then the V_{OC} gradually increased to 1.08 V during the next 120 min. The FF increased steadily from 60 to 74% with 2 hours of illumination, and the J_{SC} remained relatively unchanged.

Correlating the changes in device parameters ($\Delta V/V_0$ and $\Delta \text{FF}/\text{FF}_0$, where ΔV and ΔFF are the change in V and the change in FF, respectively, and V_0 and FF_0 are the initial values before illumination) (Fig. 2A) with the lattice constant difference ($\Delta d/d$) obtained from GIWAXS mapping (Fig. 1, A and B) as a function of illumination time (Fig. 2B) showed that the increase in the V_{OC} and FF and the increase in the lattice constant were synchronized. After 120 min of light soaking, both the lattice expansion and the V_{OC} and FF levels were saturated. Figure 2C illustrates the

typical dark (dashed lines) and light (solid lines) J - V curves measured before (blue) and after (red) 120 min of light soaking. The peak efficiency occurred after 2 hours of illumination, when the V_{OC} and FF reached their peak values. The efficiency of our best device, with 0.35 cm^2 of active area, was 20.5%, with a V_{OC} of 1.08 V, a J_{SC} of $24.35 \text{ mA}/\text{cm}^2$, and an FF of 76.6%, and the statistical average efficiency (over 30 devices) was 19.35% with negligible hysteresis (figs. S12 and S13). Figure 2D shows the corresponding external quantum efficiency (EQE) of a typical light-soaked device accompanied by an electroluminescence (EL) spectrum before and after light soaking. The EL spectrum showed a 10-meV red shift after light soaking. The red shift in the EL spectrum is twice that for PL (5 meV) after light soaking, implying that the influence of lattice expansion may be more magnified in a device configuration where the perovskite is interfaced with rigid contact materials.

To understand the correlated improvement in the V_{OC} and FF caused by light-induced lattice expansion, we conducted measurements in both thin-film and device structures. The PL intensity

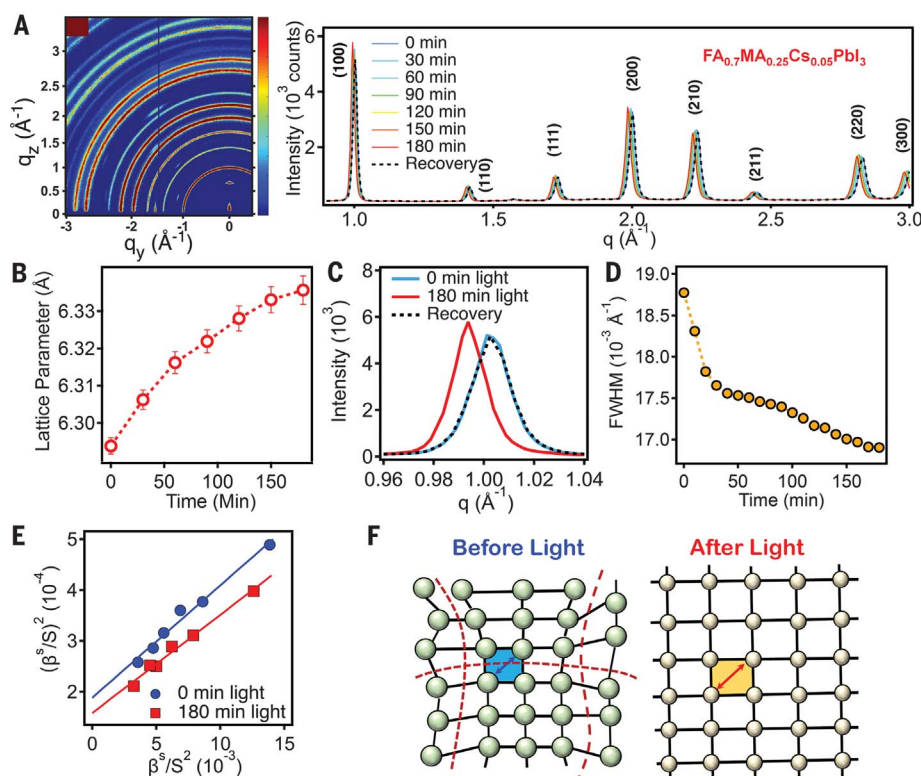


Fig. 1. Light-induced lattice expansion and structural analyses. (A) A typical synchrotron diffraction pattern (left) and the line cut of GIWAXS maps (right) for $\text{FA}_{0.7}\text{MA}_{0.25}\text{Cs}_{0.05}\text{PbI}_3$ (cubic phase) thin films under various illumination times and the recovery spectra obtained after the films were kept in the dark for 30 min. q_y , vector along in-plane direction, and q_z , vector along out-of-plane direction in reciprocal space with respect to the substrate. (B) Lattice constant as a function of illumination time. Error bars indicate the error from peak fitting. (C) Peak change before and after 180 min of illumination and recovery in the dark. (D) Full width at half maximum (FWHM) for peak as a function of illumination time. (E) Linear fit of integral-breadth analysis using Halder-Wagner plots, where β is the integral breadth of the diffraction peak and S is defined as $S = q/2\pi$. (F) Schematic describing the crystal structure change before illumination (local distortion) and after illumination (lattice expansion).

in the bulk film after light soaking increased by roughly a factor of 2 (fig. S10), suggesting passivation of trap states in the film. The PL intensity offers information on the radiative recombination efficiency in the thin film, which is correlated to the intrinsic quasi-Fermi level splitting without considering the contacts. However, such a small increase in the radiative efficiency corresponds to a gain of merely a few tens of millielectron volts in quasi-Fermi level splitting and does not account for the observed increase in V_{OC} of >200 mV after light soaking.

To understand the increase in the V_{OC} , we investigated the variations in the charge collection by performing a detailed analysis of the J - V curves coupled with a quantitative device model before and after illumination (Fig. 3, A and B; figs. S14 to S16; and tables S1 to S4). Examination of the slope of the J - V curves (obtained by taking the derivative of curves in Fig. 2C) as a function of applied voltage (Fig. 3A) revealed a slow rise near the low-field regime (0.5 to 0.7 V) before extended light soaking. The functional form converted to an S-shaped curve near the V_{OC} , indicative of field-dependent charge collection. Such behavior is also reflected in the crossover observed near the low-field regime in the dark and light J - V curves before light soaking (Fig. 2C). Both of these observations are signatures

for the presence of an energetic barrier at the perovskite-contact interface in a p-i-n junction device (33, 34).

Both the S-shaped curve and dark-light J - V crossing near the flat-band condition diminished after 2 hours of light soaking when lattice expansion occurred. We simulated the dark and light J - V curves and calculated the energy-band dispersion with a quantitative device model (Fig. 3B, red and blue solid lines). A good fit to the experimental J - V curves was obtained only by including a band misalignment (Fig. 3B) at the perovskite-contact interface for the device before light soaking (figs. S14 to S16). The band misalignment translates to a barrier for electrons injected from the electron-transporting material and holes injected from the hole-transporting material near the flat-band condition. The photo-generated carriers lose their energy through recombination, reducing the charge collection efficiency at low fields.

We experimentally confirmed the presence of such an energetic barrier before light soaking and its removal thereafter by directly probing the flat-band voltage ($V_{FLATBAND}$) of the PV device by measuring the amplitude of the electroabsorption (EA) signal at the band-edge energy (794 nm) as a function of applied direct current (DC) bias (V_{DC}) (Fig. 3C, the method section in the supplement-

tary materials, and fig. S17) (35). Briefly, the EA signal amplitude vanished at the absorber band edge once the applied bias compensated for the internal electric field when the device reached the flat-band condition. We observed a 200-mV increase in $V_{FLATBAND}$ after illumination, a direct indication of the reduction of the barrier after long-term light soaking (or lattice expansion). This increase resulted in efficient charge collection in the low-field (0.5 to 0.9 V) regime. The substantial reduction of the interfacial barrier was also consistent with the measured EL EQE (EQE_{EL}) and the forward injection current (J_{INJ}) as a function of applied voltage before and after light soaking (Fig. 3D). The EQE_{EL} measured when the device was driven at low voltage increased by 100 times after extended illumination. We attribute this increase to the reduced nonradiative recombination current and improved EL intensity. Before illumination, both the hole and the electron injection were mitigated by the barrier, which would be more pronounced at one of the contacts (Fig. 3B and fig. S16). This difference resulted in a high recombination current at low voltage.

Our experimental results presented in Fig. 2 and 3 suggest that the effect of light-induced lattice expansion is directly reflected in PV operation through the improvement in the band alignment,

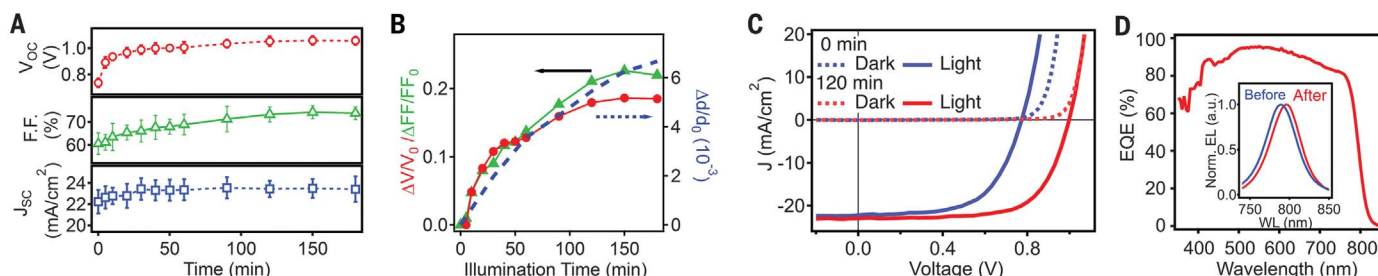


Fig. 2. Effect of light-induced lattice expansion on PV performance of $FA_{0.7}MA_{0.25}Cs_{0.05}PbI_3$ thin films. (A) Solar cell figures of merit as a function of illumination time. Error bars indicate statistical variation over 30 devices. (B) Changes in V_{OC} and FF ($\Delta V/V_0$ and $\Delta FF/FF_0$) correlated to the change in the lattice constant ($\Delta d/d_0$) as a function of light-soaking time, where

V_0 and FF_0 are the initial points before illumination. (C) J - V curves obtained in the dark and under AM1.5G (global standard spectrum air mass) solar simulator illumination. (D) EQE for a typical device and the corresponding EL spectrum for the same device before and after 120 min of illumination. Norm., normalized; a.u., arbitrary units; WL, wavelength.

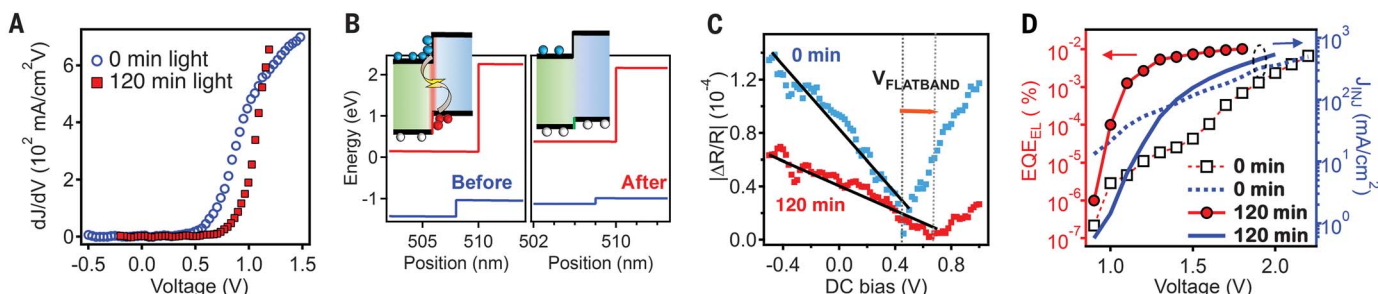


Fig. 3. Device and thin-film characteristics under constant illumination. (A) First-order derivative of the J - V curves (from Fig. 2C) before and after 2 hours of light soaking. (B) Calculated band alignment from the charge density profile based on the J - V fitting before and after light soaking, along with schematics illustrating the charge collection and recombination processes at

the interface. (C) Device flat-band voltage ($V_{FLATBAND}$) before and after light soaking for 2 hours, obtained by measuring the EA magnitude change as a function of DC bias. $\Delta R/R$, change in reflection (ΔR) normalized by the linear reflection. (D) EL characteristics for the same device before and after illumination, plotted as EQE_{EL} (left) and current density J_{INJ} (right) versus voltage.

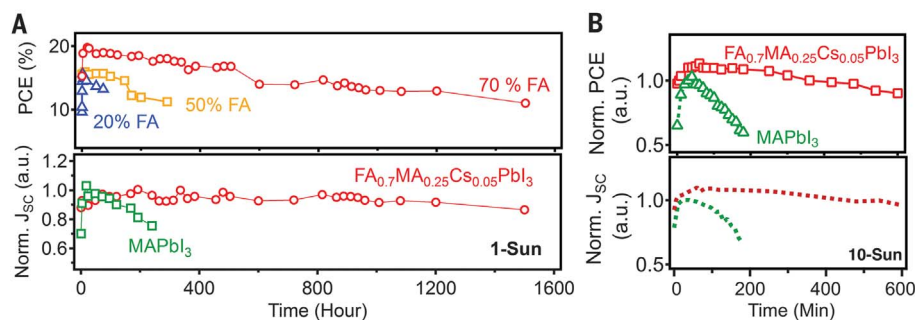


Fig. 4. Photostability studies. Long-term photostability test under constant 1-sun (A) and 10-sun (B) illumination, carried out by monitoring the time evolution of device PCE and J_{SC} .

which enhances the built-in voltage and suppresses the interfacial nonradiative recombination, as indicated by increases in the EL, the V_{OC} , and the FF. However, the J_{SC} remains largely unaffected because of the presence of a large internal field at short circuit, coupled with the long diffusion of mixed-cation perovskites (4, 6). These results also suggest that the influences of light-induced lattice expansion and strain relaxation are most magnified at one of the interfaces and facilitate the suppression of the energetic barrier.

Interface modification after light soaking was previously observed in a MAPbI₃ system (22, 24, 36) and was attributed to the iodide migration toward the contact that effectively doped the interface. To exclude this possibility in our system, two experiments were designed: XPS depth profiling (experiment one) and a control experiment of applying a bias in the dark (experiment two). Experiment one directly probed the ion (Pb²⁺ and I⁻) distribution before and after illumination. As no change in halide distribution occurred (fig. S7 and S8), we excluded halide redistribution in the mixed-cation system, a conclusion that is further supported by PL map measurements (figs. S10 and S11). In experiment two, we monitored V_{OC} and FF values for PV devices under constant bias in the dark to probe whether ion migration occurred under an applied electrical field. Given the data obtained (supplementary text and figs. S18 and S19), we did not observe any appreciable change in device performance after dark biasing with a constant current. These experimental results are direct proof of lack of ion migration in the system and unambiguously demonstrate that light-induced lattice expansion is the dominant mechanism responsible for lowering the interface barrier and improving the V_{OC} and FF. The lack of evidence for ion migration in the mixed cation is also consistent with some recent studies (6, 28) in which no degradation was observed, suggesting that ion migration does not dominate the properties in these systems. However, our observed mechanism can be correlated to the recently suggested local ionic movements activated by light (32, 36–39) and may provide insight into the structural origin for those observed phenomena. Moreover, lattice expansion-induced interfacial changes have also been observed in oxide perovskite interfaces (in SrTiO₃ and BiFeO₃),

silicon–silicon dioxide interfaces (40), and other classical semiconductors. However, in contrast to most reports on superconductors [for example, (41)], our study describes a beneficial effect from the light-induced lattice expansion.

Finally, we verified that the light-induced lattice expansion was not detrimental to device stability. We assessed our PV device under a wide range of operating conditions and external stresses (Fig. 4 and fig. S18). Figure 4 shows the long-term stability of encapsulated devices obtained by monitoring the PCE and J_{SC} under 1- and 10-sun illuminations (see the methods section in the supplementary materials). The PCE retained 85% of the peak value after 800 hours of continuous operation at the maximum power point. The J_{SC} did not undergo any observable photoinduced degradation during more than 1500 hours of continuous illumination. The drop in PCE results from a loss in FF, which we believe is consistent with the degradation of the Al contact and is a result of the fullerene-Al interface (3).

We also performed aggressive stability tests under 10-sun solar intensities (Fig. 4B). In contrast to MAPbI₃-based devices, which degrade within 30 min, the FA_{0.7}MA_{0.25}Cs_{0.05}PbI₃ devices maintained 95% of their efficiency for 300 min and then degraded to 80% over 600 min. The J_{SC} (Fig. 4B, bottom) maintained 96% of the original value even after 600 min of 10-sun illumination. We performed further stability tests by increasing the current injection in EL, the J_{SC} as a function of light intensity, and the time-dependent EQE (fig. S21 and supplementary text), which further demonstrated the technologically relevant durability of mixed-cation pure-halide perovskites for low-cost, high-efficiency optoelectronic applications. We believe that our results demonstrating light-induced lattice expansion independent of ion migration will motivate the exploration of new behaviors and structural phases in hybrid perovskites, analogous to those observed in complex oxides under nonequilibrium conditions and external stimuli.

REFERENCES AND NOTES

- W. S. Yang et al., *Science* **356**, 1376–1379 (2017).
- C. Yi et al., *Energy Environ. Sci.* **9**, 656–662 (2016).
- M. Saliba et al., *Science* **354**, 206–209 (2016).
- D. Bi et al., *Sci. Adv.* **2**, e1501170 (2016).
- N. J. Jeon et al., *Nature* **517**, 476–480 (2015).

- D. P. McMeekin et al., *Science* **351**, 151–155 (2016).
- S. Draguta et al., *Nat. Commun.* **8**, 200 (2017).
- K. Zheng et al., *J. Phys. Chem. Lett.* **7**, 4535–4539 (2016).
- M. Sendner et al., *Mater. Horiz.* **3**, 613–620 (2016).
- W. Nie et al., *Nat. Commun.* **7**, 11574 (2016).
- D. W. deQuilettes et al., *Science* **348**, 683–686 (2015).
- S. Chen et al., *Sol. RRL* **1**, 1600001 (2017).
- S. Shao et al., *Adv. Funct. Mater.* **26**, 8094–8102 (2016).
- S. Meloni et al., *Nat. Commun.* **7**, 10334 (2016).
- R. Gottesman et al., *J. Phys. Chem. Lett.* **5**, 2662–2669 (2014).
- M. Bokdam et al., *Sci. Rep.* **6**, 28618 (2016).
- A. M. A. Leguy et al., *Nat. Commun.* **6**, 7124 (2015).
- C. Eames et al., *Nat. Commun.* **6**, 7497 (2015).
- X. Wu et al., *Sci. Adv.* **3**, e1602388 (2017).
- Y. Zhou et al., *Nat. Commun.* **7**, 11193 (2016).
- I. Zarazua, J. Bisquert, G. Garcia-Belmonte, *J. Phys. Chem. Lett.* **7**, 525–528 (2016).
- D. W. deQuilettes et al., *Nat. Commun.* **7**, 11683 (2016).
- C. Zhao et al., *Adv. Energy Mater.* **5**, 1500279 (2015).
- Y. Deng, Z. Xiao, J. Huang, *Adv. Energy Mater.* **5**, 1500721 (2015).
- H.-W. Chen, N. Sakai, M. Ikegami, T. Miyasaka, *J. Phys. Chem. Lett.* **6**, 164–169 (2015).
- H. Tsai et al., *Nature* **536**, 312–316 (2016).
- W. Nie et al., *Science* **347**, 522–525 (2015).
- M. Saliba et al., *Energy Environ. Sci.* **9**, 1989–1997 (2016).
- G. E. Eperon et al., *Energy Environ. Sci.* **7**, 982–988 (2014).
- C. C. Stoumpos, M. G. Kanatzidis, *Adv. Mater.* **28**, 5778–5793 (2016).
- S. Boyer-Richard et al., *J. Phys. Chem. Lett.* **7**, 3833–3840 (2016).
- Y.-C. Zhao et al., *Light Sci. Appl.* **6**, e16243 (2017).
- R. V. K. Chavali et al., *IEEE J. Photovolt.* **5**, 865–873 (2015).
- J. E. Moore, S. Dongaonkar, R. V. K. Chavali, M. A. Alam, M. S. Lundstrom, *IEEE J. Photovolt.* **4**, 1138–1148 (2014).
- I. H. Campbell et al., *Polym. Adv. Technol.* **8**, 417–423 (1997).
- P. Calado et al., *Nat. Commun.* **7**, 13831 (2016).
- S. Ravishanker et al., *J. Phys. Chem. Lett.* **8**, 915–921 (2017).
- S. Shao et al., *Energy Environ. Sci.* **9**, 2444–2452 (2016).
- E. Mosconi, D. Meggiolaro, H. J. Snaith, S. D. Stranks, F. De Angelis, *Energy Environ. Sci.* **9**, 3180–3187 (2016).
- S. Nonomura et al., *J. Non-Cryst. Solids* **266–269**, 474–480 (2000).
- N. Poccia et al., *Nat. Mater.* **10**, 733–736 (2011).

ACKNOWLEDGMENTS

Funding: The work at LANL was supported by the Laboratory Directed Research and Development (LDRD) Directed Research (DR) project. The XPS analyses were done in Shared Equipment Authority (SEA) and were supported by Rice University. The GIWAXS maps were done at sector 8-ID-E of the Advanced Photon Source, a U.S. Department of Energy (DOE) Office of Science User Facility operated for the DOE Office of Science by Argonne National Laboratory under contract DE-AC02-06CH11357. Work at Northwestern was supported by the U.S. Department of Energy, Office of Science (grant SC0012541, structure characterization). A.D.M. acknowledges support by Office of Energy Efficiency and Renewable Energy grant DE-FOA-0001647-1544 for this work. **Author contributions:** W.N., H.T., and A.D.M. conceived the idea, designed experiments, and co-wrote the manuscript. H.T. fabricated and characterized the thin films and devices and analyzed data under the supervision of W.N. and A.D.M. C.C.S. and M.G.K. performed crystallography analysis of the powder diffraction and calculated the molecular structures. J.-C.B. conducted the optical spectroscopy measurements on the thin film and analyzed the data. R.A. performed device modeling simulations and analyzed simulation data with M.A.A., who conceived and supervised the device modeling. J.W.S. helped with GIWAXS experiment setup, and O.D. analyzed the GIWAXS data. B.C., R.V., and P.M.A. helped with XPS experiments and analyses. S.T. and J.E. were involved in discussion. All authors have read the manuscript and agree to its contents. **Competing interests:** None declared. **Data and materials availability:** All data needed to evaluate the conclusions in the paper are present in the supplementary materials.

SUPPLEMENTARY MATERIALS

www.sciencemag.org/content/360/6384/67/suppl/DC1
Materials and Methods
Supplementary Text
Figs. S1 to S21
Tables S1 to S9
References (42–75)

4 September 2017; resubmitted 15 December 2017
Accepted 9 February 2018
10.1126/science.aap8671

BIOCATALYSIS

Enzymatic construction of highly strained carbocycles

Kai Chen, Xiongyl Huang, S. B. Jennifer Kan, Ruijie K. Zhang, Frances H. Arnold*

Small carbocycles are structurally rigid and possess high intrinsic energy due to their ring strain. These features lead to broad applications but also create challenges for their construction. We report the engineering of hemeproteins that catalyze the formation of chiral bicyclobutanes, one of the most strained four-membered systems, via successive carbene addition to unsaturated carbon-carbon bonds. Enzymes that produce cyclopropenes, putative intermediates to the bicyclobutanes, were also identified. These genetically encoded proteins are readily optimized by directed evolution, function in *Escherichia coli*, and act on structurally diverse substrates with high efficiency and selectivity, providing an effective route to many chiral strained structures. This biotransformation is easily performed at preparative scale, and the resulting strained carbocycles can be derivatized, opening myriad potential applications.

In cyclic organic molecules, ring strain arises from distortions of bond angle and bond length, steric clashes of nonbonded substituents, and other effects (1). The simplest carbocycles, cyclopropanes and cyclobutanes, possess ring strains of 26 to 28 kcal/mol (2). Introducing carbon-carbon multiple bonds or bridges to these small ring systems induces additional strain as well as structural rigidity. For example, cyclopropenes with an *endo*-cyclic double bond bear a strain of 54 kcal/mol, whereas bicyclo[1.1.0]butanes, folded into puckered structures, distinguish themselves as one of the most strained four-membered systems, with strain of ~66 kcal/mol (fig. S1) (2). These carbocycles are particularly attractive intermediates in chemical and materials synthesis, because they can undergo strain-release transformations to furnish a myriad of useful scaffolds (3–6). The structural rigidity imparted by strained rings in supramolecular materials can lead to interesting physical properties, such as mechanical stability (7) and high glass transition temperature (8). The intrinsic energy of these strained structures can also be relieved in response to exogenous force, which leads to radical changes in physical properties (e.g., conductivity), a feature highly desirable for stimulus-responsive materials (9, 10).

High ring strain, however, greatly increases the difficulty of synthesis. A commonly used method for preparing bicyclobutanes starts from dibromo-2-(bromomethyl)cyclopropane substructures and uses organolithium reagents for lithium-halogen exchange, followed by nucleophilic substitution under rigorously anhydrous and cryogenic conditions (3). An alternative route relies on the double transfer of a carbene to alkynes, but the few examples in the literature are mostly limited to methylene carbene (11–13). Asymmetric bicyclobutane construction is particularly challeng-

ing, with multiple chiral centers generated at the same time (14, 15) (fig. S2). Cyclopropene synthesis through enantioselective single-carbene addition to alkynes also requires chiral transition metal catalysts based on rhodium (16, 17), iridium (18), and cobalt (19). Development of a sustainable catalytic system that performs with high efficiency and selectivity under ambient conditions would be a major advance for construction of these useful, highly strained carbocycles.

Enzymes, the catalytic workhorses of biology, are capable of accelerating chemical transformations by orders of magnitude while exhibiting exquisite control over selectivity (20). Although nature synthesizes various cyclopropane-containing products (21), cyclopropene or bicyclobutane fragments are extremely rare (fig. S3) (22, 23). This may be attributed to the lack of biological machinery for synthesizing these motifs and/or the instability of these structures under biological or natural product isolation/purification conditions. Nonetheless, we envisioned that existing enzymes could be repurposed to forge strained carbocycles by taking advantage of their catalytic promiscuity (24, 25) in the presence of non-natural substrates and by using directed evolution to optimize the activity and selectivity of these starting enzymes (26).

In the past several years, we and others have engineered natural hemeproteins to catalyze reactions not known in nature (27–32). We hypothesized that carbene transfer to triple bonds with a heme-dependent enzyme might afford highly strained cyclopropene and bicyclobutane structures and might do so enantioselectively. We anticipated several challenges at the outset, especially in chiral bicyclobutane formation, as it involves two sequential carbene additions to the alkyne substrate: (i) The enzyme would need to bind the alkyne in a specific conformation in order to transfer the carbene enantioselectively; (ii) the high-energy cyclopropene intermediate generated by the first carbene addition would need to be accepted and stabilized by the protein; (iii) relative to methylene carbene used previously, a substituted carbene (e.g., with

an ester group) might hinder access of the cyclopropene to the iron-carbenoid; and (iv) the protein would also need to exert precise stereocontrol over the second carbene transfer step, regardless of structural differences between the initial alkyne and the cyclopropene intermediate. Despite these challenges, we decided to investigate whether a starting enzyme with this unusual and non-natural activity could be identified, and whether its active site could be engineered to create a suitable environment for substrate binding, intermediate stabilization, and selective product formation.

We first tested whether free heme [with or without bovine serum albumin (BSA)], which is known to catalyze styrene cyclopropanation (27), could transfer carbene to an alkyne. Reactions using ethyl diazoacetate (EDA) and phenylacetylene (**1a**) as substrates in neutral buffer (M9-N minimal medium, pH 7.4) at room temperature, however, gave no cyclopropene or bicyclobutane product. Next, a panel of hemeproteins—including variants of cytochrome P450, cytochrome P411 (P450 with the axial cysteine ligand replaced by serine), cytochrome c, and globins in the form of *E. coli* whole-cell catalysts—were tested for the desired transformation under anaerobic conditions (32), but none were fruitful (fig. 1C and table S1). Interestingly, a P411 variant obtained in a previous cyclopropanation study, P411-S1 I263W (see supplementary materials for sources, sequences, and mutations), afforded a furan product (**3b**) with a total turnover number (TTN) of 210. Because other furan analogs have been identified as adducts of carbenes and alkynes (33), we were curious as to how furan **3b** was generated. Preliminary kinetic study of the enzymatic reaction suggested that the enzyme first synthesized an unstable cyclopropene (**3a**), which subsequently rearranged to the furan either spontaneously or with assistance from the enzyme (Fig. 1B and fig. S5). This result provided strong evidence that the P411 hemeprotein is capable of transferring a carbene to an alkyne, which is, to our knowledge, an activity not previously reported for any protein or even any iron complex.

To divert the enzymatic reaction to bicyclobutane formation, the enzyme would have to transfer a second carbene to cyclopropene intermediate **3a** before the cyclopropene rearranges to the undesired furan product (Fig. 1B). We thus tested P411 variants closely related to P411-S1 I263W. We reasoned that amino acid residue 263, which resides in the distal pocket above the heme cofactor, might modulate the rate of this step, and that the bulky tryptophan (Trp) side chain at this site may be blocking the second carbene transfer. A P411-S1 variant with phenylalanine (Phe) instead of Trp at this position (263F) in fact catalyzed bicyclobutane formation at a very low level (<5 TTN) (table S1). Variant **P4** with three additional mutations relative to P411-S1 I263F (V87A, A268G, and A328V) (28) synthesized the desired bicyclobutane **2a** with 80 TTN and with the formation of furan adduct substantially suppressed (**2a:3b** > 50:1; Fig. 1C). Another related P411 variant, **E10** (= **P4** A78V A82L F263L), which was

Division of Chemistry and Chemical Engineering 210-41, California Institute of Technology, Pasadena, CA 91125, USA.
*Corresponding author. Email: frances@chemo.caltech.edu

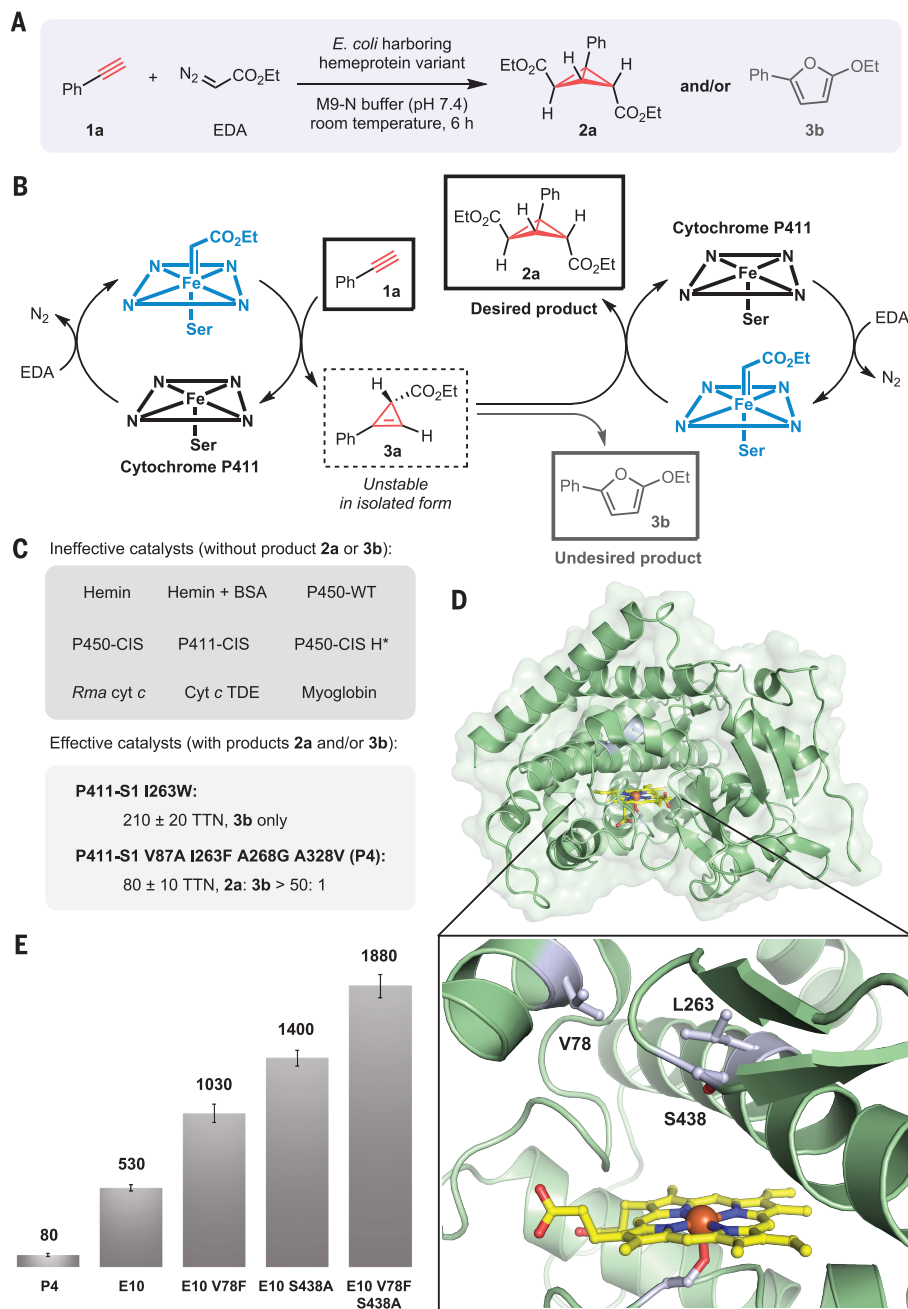


Fig. 1. Hemeprotein-catalyzed bicyclobutane formation. (A) Overall reaction of carbene transfer to an alkyne catalyzed by an engineered hemeprotein (Et, ethyl; Ph, phenyl). (B) Proposed catalytic cycle of carbene transfer to phenylacetylene to form cyclopropene and bicyclobutane structures. (C) Screening of hemein and hemeprotein catalysts for bicyclobutane formation (BSA, bovine serum albumin; WT, wild type; TDE, V75T M100D M103E; H*, C400H). See supplementary materials for sources, sequences, and mutations in *Bacillus megaterium* P411-S1 and other proteins. (D) X-ray crystal structure of P411-E10 (PDB ID: 5UCW) (29) and view of its distal heme region. The P411 heme axial ligand is S400; amino acid residues Val⁷⁸, Leu²⁶³, and Ser⁴³⁸ are shown as sticks. (E) Directed evolution of P411-E10 for bicyclobutane formation [using phenylacetylene and EDA as substrates; numbers refer to total turnovers to product (TTN) measured]. Experiments were performed at analytical scale using suspensions of *E. coli* expressing P411-E10 variants [optical density at 600 nm (OD₆₀₀) = 10 to 30], 10 mM phenylacetylene, 10 mM EDA, 5 vol % EtOH, and M9-N buffer (pH 7.4) at room temperature under anaerobic conditions for 6 hours. Reactions were performed in quadruplicate. TTN refers to the total desired product, as quantified by gas chromatography (GC), divided by total hemeprotein. (Note: Because bicyclobutane formation requires two carbene transfers, the number of carbene transfers the hemeprotein catalyzes is 2 × TTN in these reactions.) See supplementary materials for further details of reaction conditions and data analysis. Single-letter amino acid abbreviations (here or in Fig. 3): A, Ala; C, Cys; D, Asp; E, Glu; F, Phe; G, Gly; H, His; I, Ile; L, Leu; M, Met; P, Pro; S, Ser; T, Thr; V, Val; W, Trp; Y, Tyr.

engineered from **P4** for nitrene transfer reactions (29), catalyzed the desired transformation with a factor of >6 higher activity (530 TTN, Fig. 1E). Nuclear magnetic resonance (NMR) analysis revealed an *exo*, *endo*-configuration of the enzymatically produced bicyclobutane **2a**, which is distinct from the only reported achiral *endo*, *endo*-isomer, made using an osmium-porphyrin complex (34, 35). We chose this P411-E10 variant as the starting template for directed evolution of an even more efficient bicyclobutane-constructing enzyme.

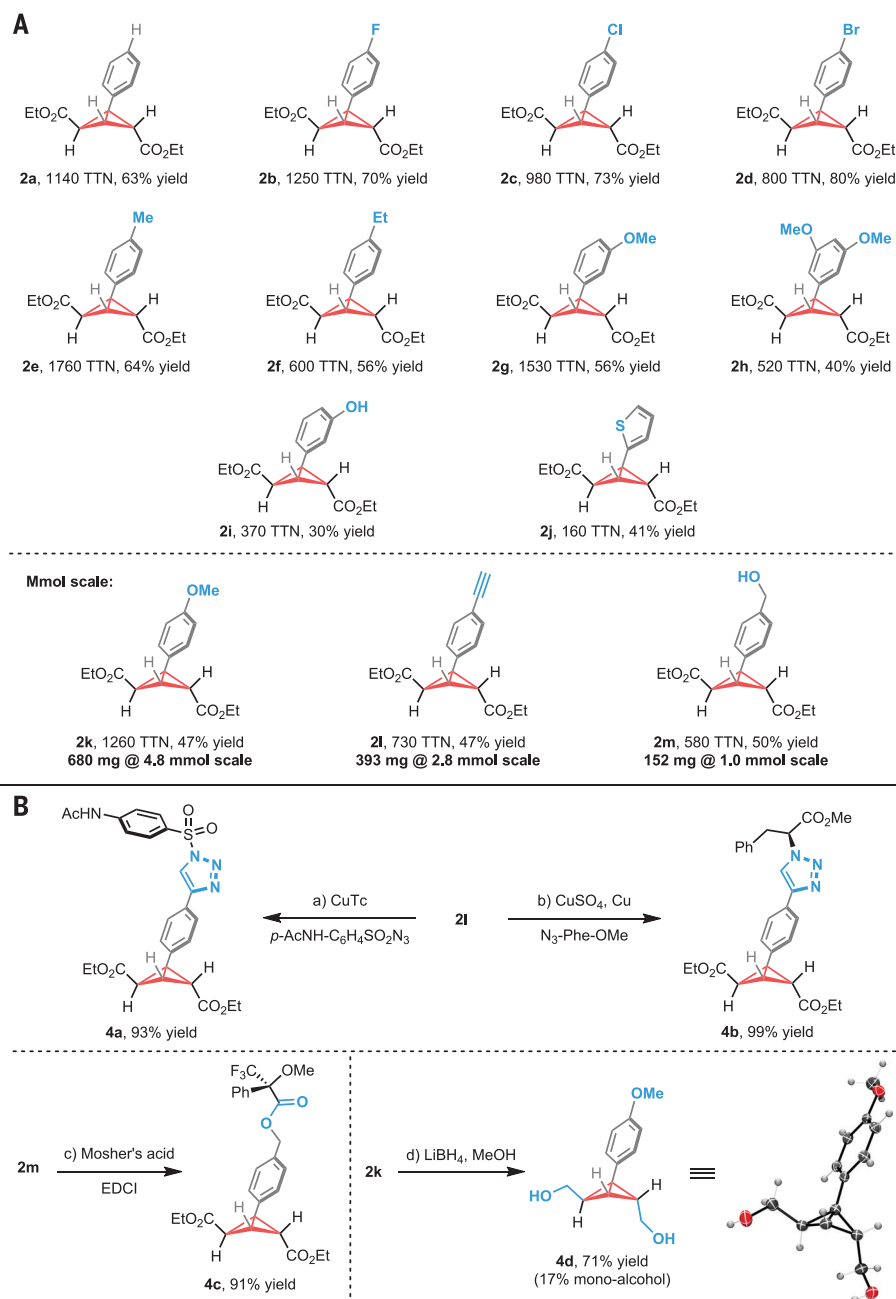
Because the side chain of residue 263 influenced formation of the bicyclobutane product, we performed site-saturation mutagenesis (SSM) of variant **E10** at position 263 and screened whole *E. coli* cells expressing the mutated proteins for improved production of bicyclobutane **2a**. The enzyme having leucine at this position (263L) was the most active; other amino acid residues either lowered the reactivity toward bicyclobutane formation and/or delivered more furan product. In parallel, two additional residues in **E10**, Val⁷⁸ and Ser⁴³⁸, were also targeted by SSM. Aromatic residues were found to be activating at position 78, with a phenylalanine or tyrosine mutation giving a factor of 1.5 to 2 improvement over **E10**. This beneficial effect may stem from a π - π stacking interaction between the side chain and the alkyne substrate or the cyclopropene intermediate. A single S438A mutation on a loop residing above the heme also increased the activity, giving a factor of >2.5 increase in turnover. Finally, recombination of V78F/Y and S438A mutations led to the discovery of even more powerful biocatalysts for bicyclobutane formation (e.g., 1880 TTN with **E10** V78F S438A) (Fig. 1E and fig. S9).

With the evolved **E10** V78F S438A variant in hand, we next assayed the bacterial catalyst against a panel of aromatic alkyne coupling partners. Bio-transformations with 10 different substrates were performed on a scale of 0.1 to 0.2 mmol. These preparative-scale reactions proceeded smoothly to furnish the corresponding bicyclobutanes with up to 1760 TTN and 80% yield (Fig. 2A). Additionally, three alkynes, **1k**, **1l**, and **1m**, were transformed at mmol scale, and bicyclobutanes were isolated in hundred-milligram quantities, demonstrating that the biocatalytic transformation is readily scalable. Among the 13 different substrates, the engineered P411 hemeprotein did not exhibit strong preference toward specific electronic or steric features. Electron-deficient halides (**2b–2d**), which can be used as prefunctionalities for further transformations, were accepted by the enzyme, as were electron-rich alkyl or alkoxy groups (**2e–2h** and **2k**) at the meta or para position of the phenyl group. Even heterocyclic substrates such as thiophene (**2j**) served as suitable alkyne partners, albeit with lower reactivity.

Free functionalities, including alcohols (**2i** and **2m**) and a second alkyne (**2l**), are well preserved, providing an additional opportunity for derivatization of these products. A terminal alkyne allows copper-catalyzed click chemistry, through which bicyclobutane **2l** can be modified with a simple sulfonyl azide (**4a**) or even decorated with

Fig. 2. Scope of bicyclobutane formation and derivatization.

(A) Scope of P411-**E10** V78F S438A-catalyzed bicyclobutane formation. Standard conditions of preparative-scale reactions (0.1- to 0.2-mmol scale unless otherwise indicated): suspension of *E. coli* (OD₆₀₀ = 15 to 20) expressing P411-**E10** V78F S438A, 1.0 equiv aromatic alkyne, 2.0 to 4.0 equiv EDA, 10 to 15 mM D-glucose, 1 to 5 vol % EtOH, and M9-N buffer (pH 7.4) at room temperature under anaerobic conditions for 12 hours. TTNs were determined on the basis of the isolated yields shown. **(B)** Derivatization of bicyclobutane products: (a) and (b), copper-catalyzed click cyclization of **2l** with azide substrates (Ac, acetyl; CuTc, copper(I) thiophene-2-carboxylate; EDCI, 1-ethyl-3-(3-dimethylaminopropyl)carbodiimide hydrochloride); (c), esterification of **2m** with Mosher's acid; (d), reduction of **2k** to diol with LiBH₄. See supplementary materials for further details of reaction conditions and data analysis.



biologically relevant fragments, such as a phenylalanine derivative (**4b**). An unprotected hydroxyl group could also offer the possibility of linkage to useful structures. Additionally, to probe the enantiopurity of bicyclobutane products, we derivatized **2l** and **2m** with *L*-azido-phenylalanine and (*R*)-Mosher's acid, respectively. The diastereomeric excess of these derivatized products would inform us of the enantiomeric ratio (e.r.) of the bicyclobutanes. In fact, we observed only one diastereomer of derivatized bicyclobutanes **4b** and **4c** by NMR. Furthermore, the dicarboxylic esters on the bicyclobutane structure can be reduced easily with a mild reducing reagent, LiBH₄, to give diol product **4d** with the strained ring structure preserved. The diol product **4d** allowed for

the unequivocal confirmation of the bicyclobutane structure and determination of the absolute configuration through x-ray crystallography.

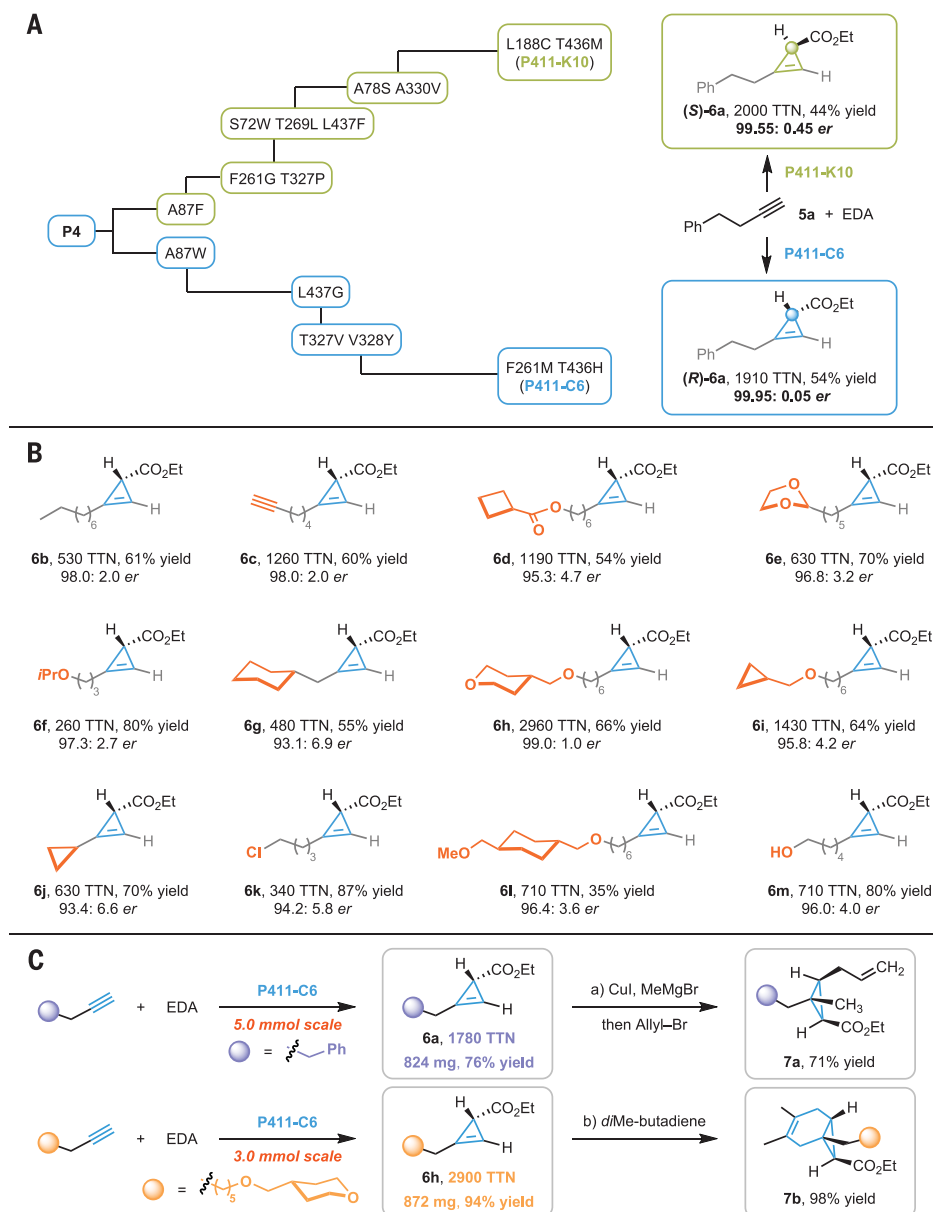
We next asked whether the enzyme could stop at the cyclopropene product if less reactive aliphatic alkynes were used. To this end, we examined enzyme variants from the P411-S1 lineage for cyclopropene formation, using phenylbutyne (**5a**) and EDA as starting reagents. We were encouraged to see that **P4** catalyzed the desired transformation with 260 TTN and 95.5:4.5 e.r. Further evolution was performed on **P4** to improve its catalytic efficiency. We first targeted position 87, known for its importance to substrate recognition in P450-catalyzed oxidations (**36**). A87F (290 TTN, 3.0:97.0 e.r.) and A87W

(240 TTN, 97.1:2.9 e.r.) were found to exert the opposite enantioselectivity, suggesting that residue 87 also controls substrate orientation for non-native carbene chemistry. Single- and double-site-saturation mutagenesis conducted sequentially on **P4** A87F and **P4** A87W improved both reactivity and selectivity (Fig. 3A and figs. S11 and S13). The final **K10** and **C6** variants performed with higher activity by a factor of >10 relative to the initial **P4** variant and with excellent stereocontrol (99.55:0.45 and 99.95:0.05 e.r., respectively).

To evaluate the substrate range of the evolved P411 variants for cyclopropene construction, we focused on P411-C6 and examined structurally diverse aliphatic alkynes. Enzymatic reactions with 12 alkynes at preparative scale (up to 5.0 mmol)

Fig. 3. Engineering P411 enzymes for stereodivergent cyclopropene formation: Scope and derivatization.

(A) Evolutionary trajectory of P411-P4 variants for stereodivergent cyclopropanation of aliphatic alkynes. **(B)** Scope of P411-C6-catalyzed cyclopropene formation. Standard conditions of preparative-scale reactions (0.08- to 0.4-mmol scale): suspension of *E. coli* (OD₆₀₀ = 10 to 32) expressing P411-C6 or K10, 1.0 equiv alkyne, 1.0 to 4.0 equiv EDA (6.0 equiv for **5m**), 10 to 15 mM D-glucose, 1 to 5 vol % EtOH, and M9-N buffer (pH 7.4) at room temperature under anaerobic conditions for 12 hours (iPr, isopropyl). TTNs were determined on the basis of the isolated yields shown; e.r. values were determined by chiral high-performance liquid chromatography (HPLC). **(C)** Enzymatic cyclopropanation at mmol scale and derivatization of corresponding products: (a), copper-catalyzed addition to cyclopropene **6a** for synthesizing a multisubstituted cyclopropane; (b), Diels-Alder reaction of cyclopropene **6h** with 2,3-diMe-buta-1,3-diene to form a fused-ring system. See supplementary materials for further details of reaction conditions and data analysis.



afforded the desired cyclopropenes, with TTNs ranging from hundreds to thousands and good to excellent stereoselectivities (Fig. 3, B and C). Alkynes with a linear carbon chain (**5b**) or cyclic fragments (**5g**, **5h**, and **5j**) all served as good substrates. Different functional groups, including ether (**5f**, **5i**, and **5l**), ester (**5d**), acetal (**5e**), chloride (**5k**), and free hydroxyl (**5m**), were well tolerated. Further optimization of reaction conditions with slow addition of EDA, for example, would likely improve the isolated yields, as we demonstrated for cyclopropene **6h** (66% yield, Fig. 3B; 94% yield, Fig. 3C).

Cyclopropenes are used as synthetic building blocks (4, 37), bio-orthogonal imaging precursors (38), and monomers in polymer synthesis (39). Our ability to construct these motifs using bacteria at scale allows us to further explore their potential utility in diverse fields. We carried out

two simple transformations of cyclopropenes to build a multisubstituted cyclopropane **7a** and a fused ring system, [4.1.0]heptene **7b** (Fig. 3C), both of which are substructures common in pharmaceutical candidates and bioactive natural products (21).

Our results constitute a biocatalytic platform for the construction of highly strained bicyclobutanes and cyclopropenes through directed evolution of a serine-ligated cytochrome P450 (P411) enzyme. That the protein could be quickly adapted to produce these highly strained structures (three to six rounds of mutagenesis and screening) highlights the evolvability of the P411 scaffold and its potential to direct the construction of complex motifs. The protein enabled the desired transformations through activation of iron-carbenoid for carbene addition to alkynes, stabilization of the reactive cyclopropene intermediate (in bicyclobutane formation), and precise stereocontrol

of the carbene transfer processes. Biotransformations with the evolved enzymes have a surprisingly broad substrate scope with high reactivity and selectivity, providing a route to more than 25 products in preparative scale. This biocatalytic system grants facile access to versatile molecular architectures rarely seen in nature, expanding the set of chemical structures available to biological systems.

REFERENCES AND NOTES

1. K. B. Wiberg, *Angew. Chem. Int. Ed.* **25**, 312–322 (1986).
2. E. V. Anslyn, D. A. Dougherty, *Modern Physical Organic Chemistry* (University Science, 2006), chap. 2.
3. M. A. A. Walczak, T. Krainz, P. Wipf, *Acc. Chem. Res.* **48**, 1149–1158 (2015).
4. I. Marek, S. Simaan, A. Masarwa, *Angew. Chem. Int. Ed.* **46**, 7364–7376 (2007).

5. A. de Meijere, S. I. Kozhushkov, H. Schill, *Chem. Rev.* **106**, 4926–4996 (2006).
6. R. Gianatassio *et al.*, *Science* **351**, 241–246 (2016).
7. A. M. Dilmac, E. Spuling, A. de Meijere, S. Bräse, *Angew. Chem. Int. Ed.* **56**, 5684–5718 (2017).
8. J. M. Longo, M. J. Sanford, G. W. Coates, *Chem. Rev.* **116**, 15167–15197 (2016).
9. T. M. Swager, D. A. Dougherty, R. H. Grubbs, *J. Am. Chem. Soc.* **110**, 2973–2974 (1988).
10. Z. Chen *et al.*, *Science* **357**, 475–479 (2017).
11. W. Mahler, *J. Am. Chem. Soc.* **84**, 4600–4601 (1962).
12. W. von E. Doering, J. F. Coburn Jr., *Tetrahedron Lett.* **6**, 991–995 (1965).
13. P. Wipf, C. R. J. Stephenson, K. Okumura, *J. Am. Chem. Soc.* **125**, 14694–14695 (2003).
14. R. Panish *et al.*, *J. Am. Chem. Soc.* **135**, 9283–9286 (2013).
15. C. Qin, H. M. L. Davies, *Org. Lett.* **15**, 310–313 (2013).
16. Y. Lou, M. Horikawa, R. A. Kloster, N. A. Hawryluk, E. J. Corey, *J. Am. Chem. Soc.* **126**, 8916–8918 (2004).
17. J. F. Briones, J. Hansen, K. I. Hardcastle, J. Autschbach, H. M. L. Davies, *J. Am. Chem. Soc.* **132**, 17211–17215 (2010).
18. M. Uehara, H. Suematsu, Y. Yasutomi, T. Katsuki, *J. Am. Chem. Soc.* **133**, 170–171 (2011).
19. X. Cui *et al.*, *J. Am. Chem. Soc.* **133**, 3304–3307 (2011).
20. S. J. Benkovic, S. Hammes-Schiffer, *Science* **301**, 1196–1202 (2003).
21. L. A. Wessjohann, W. Brandt, T. Thiemann, *Chem. Rev.* **103**, 1625–1648 (2003).
22. T. Itoh, C. Djerassi, *J. Am. Chem. Soc.* **105**, 4407–4416 (1983).
23. C. Schneider *et al.*, *Proc. Natl. Acad. Sci. U.S.A.* **104**, 18941–18945 (2007).
24. O. Khersonsky, D. S. Tawfik, *Annu. Rev. Biochem.* **79**, 471–505 (2010).
25. U. T. Bornscheuer, R. J. Kazlauskas, *Angew. Chem. Int. Ed.* **43**, 6032–6040 (2004).
26. H. Renata, Z. J. Wang, F. H. Arnold, *Angew. Chem. Int. Ed.* **54**, 3351–3367 (2015).
27. P. S. Coelho, E. M. Brustad, A. Kannan, F. H. Arnold, *Science* **339**, 307–310 (2013).
28. C. K. Prier, T. K. Hyster, C. C. Farwell, A. Huang, F. H. Arnold, *Angew. Chem. Int. Ed.* **55**, 4711–4715 (2016).
29. C. K. Prier, R. K. Zhang, A. R. Buller, S. Brinkmann-Chen, F. H. Arnold, *Nat. Chem.* **9**, 629–634 (2017).
30. P. Bajaj, G. Sreenilayam, V. Tyagi, R. Fasan, *Angew. Chem. Int. Ed.* **55**, 16110–16114 (2016).
31. O. F. Brandenburg, R. Fasan, F. H. Arnold, *Curr. Opin. Biotechnol.* **47**, 102–111 (2017).
32. P. S. Coelho *et al.*, *Nat. Chem. Biol.* **9**, 485–487 (2013).
33. H. M. L. Davies, K. R. Romines, *Tetrahedron* **44**, 3343–3348 (1988).
34. D. A. Smith, D. N. Reynolds, L. K. Woo, *J. Am. Chem. Soc.* **115**, 2511–2513 (1993).
35. C. G. Hamaker, J.-P. Djukic, D. A. Smith, L. K. Woo, *Organometallics* **20**, 5189–5199 (2001).
36. J. H. Capdevila *et al.*, *J. Biol. Chem.* **271**, 22663–22671 (1996).
37. P.-O. Delaye, D. Didier, I. Marek, *Angew. Chem. Int. Ed.* **52**, 5333–5337 (2013).
38. D. M. Patterson, L. A. Nazarova, B. Xie, D. N. Kamber, J. A. Prescher, *J. Am. Chem. Soc.* **134**, 18638–18643 (2012).
39. B. R. Elling, Y. Xia, *J. Am. Chem. Soc.* **137**, 9922–9926 (2015).

ACKNOWLEDGMENTS

We thank D. K. Romney, S. C. Hammer, and S.-Q. Zhang for helpful discussions and comments on the manuscript; C. K. Pier, O. F. Brandenburg, and A. M. Knight for sharing hemeprotein variants; K. Ding (D. J. Anderson Lab, Caltech) and J. Li (R. H. Grubbs Lab, Caltech) for generous donation of materials and reagents; S. C. Virgil and the Caltech Center for Catalysis and Chemical Synthesis, N. Torian and the Caltech Mass Spectrometry Laboratory,

and M. K. Takase, L. M. Henling, and the Caltech X-ray Crystallography Facility for analytical support; and B. M. Stoltz for use of polarimeter and chiral gas chromatography equipment. **Funding:** Supported by NSF Division of Molecular and Cellular Biosciences grant MCB-1513007; Ruth L. Kirschstein NIH Postdoctoral Fellowship F32GM125231 (X.H.); and NSF Graduate Research Fellowship grant DGE-1144469 and the Donna and Benjamin M. Rosen Bioengineering Center (R.K.Z.). R.K.Z. is a trainee in the Caltech Biotechnology Leadership Program. Any opinions, findings, and conclusions or recommendations expressed in this material are those of the author(s) and do not necessarily reflect the views of the funding organizations. **Author contributions:** conceptualization, K.C.; methodology, K.C.; validation, K.C. and X.H.; formal analysis, K.C., X.H., S.B.J.K., and R.K.Z.; writing (original draft), K.C. and F.H.A.; writing (review and editing), X.H., S.B.J.K., and R.K.Z.; funding acquisition, F.H.A.; supervision, F.H.A. **Competing interests:** K.C., X.H., and S.B.J.K. are inventors on patent application (CIT-7744-P) submitted by California Institute of Technology that covers biocatalytic synthesis of strained carbocycles. **Data and materials availability:** All data are available in the main text or the supplementary materials. Plasmids encoding the enzymes reported in this study are available for research purposes from F.H.A. under a material transfer agreement with the California Institute of Technology. Crystallographic coordinates and structure factors have been deposited with the Cambridge Crystallographic Data Centre (www.ccdc.cam.ac.uk) under reference number 1815089 for compound **4d**.

SUPPLEMENTARY MATERIALS

www.sciencemag.org/content/360/6384/71/suppl/DC1
Materials and Methods
Figs. S1 to S15
Tables S1 to S9
References (40–71)

8 November 2017; accepted 6 February 2018
10.1126/science.aar4239

ORGANIC CHEMISTRY

Modular radical cross-coupling with sulfones enables access to sp^3 -rich (fluoro)alkylated scaffolds

Rohan R. Merchant,^{1*} Jacob T. Edwards,^{1*} Tian Qin,^{1*} Monika M. Kruszyk,¹ Cheng Bi,¹ Guanda Che,² Deng-Hui Bao,² Wenhua Qiao,² Lijie Sun,² Michael R. Collins,³ Olugbeminiyi O. Fadeyi,^{4†} Gary M. Gallego,³ James J. Mousseau,⁴ Philippe Nuhant,⁴ Phil S. Baran^{1‡}

Cross-coupling chemistry is widely applied to carbon-carbon bond formation in the synthesis of medicines, agrochemicals, and other functional materials. Recently, single-electron-induced variants of this reaction class have proven particularly useful in the formation of $\text{C}(\text{sp}^2)\text{--C}(\text{sp}^3)$ linkages, although certain compound classes have remained a challenge. Here, we report the use of sulfones to activate the alkyl coupling partner in nickel-catalyzed radical cross-coupling with aryl zinc reagents. This method's tolerance of fluoroalkyl substituents proved particularly advantageous for the streamlined preparation of pharmaceutically oriented fluorinated scaffolds that previously required multiple steps, toxic reagents, and nonmodular retrosynthetic blueprints. Five specific sulfone reagents facilitate the rapid assembly of a vast set of compounds, many of which contain challenging fluorination patterns.

Cross-coupling proceeding through a single-electron transfer pathway to forge new carbon-carbon (C--C) bonds is complementary to the robust two-electron coupling paradigm of the venerable Heck, Suzuki, and Negishi reactions (1). In recent years, metal-catalyzed radical cross-coupling (RCC) has proven effective for forging bonds to sp^3 -hybridized secondary and tertiary carbon centers that remain challenging for the more widely applied two-electron palladium (Pd) catalysis (2). To realize the full potential of RCC strategies, functional groups more versatile than alkyl halides (3–8) are needed to expand the range of compatible coupling partners (Fig. 1A). In this regard, alkyl carboxylic acids (3, 4), alkylboron (5) and alkylsilicon (6) derivatives, olefins (7), alkyl pyridinium salts (derived from amines) (8), and alkyl dihydropyridines (9) have been identified as useful agents in RCC. Here, we show that readily available sulfones (specifically bearing the 1-phenyl-1*H*-tetrazol-5-yl group) can be directly used as an orthogonal redox-active functional group for RCC-based synthesis. The sulfones present three specific advantages. First, they toler-

ate powerful anionic chemistry (α -alkylation and fluorination) for functional elaboration before the cross-coupling event (Fig. 1, A and B) (10, 11); second, when attached to unsaturated systems, they enable facile cycloadditions and Michael/Giese-type additions (12); and last, their stability and crystallinity allow for convenient manipulation.

The literature is replete with examples of sulfones serving a variety of different roles in synthesis, from facilitating olefin formation and cycloadditions to their use in two-electron cross-couplings. In the latter regard, the independent work of the Crudden (13) and Li (14) research groups has stood out for their use of benzylic phenyl sulfones in a variety of Pd- and nickel (Ni)-catalyzed desulfonylative cross-coupling methodologies. The first systematic study of the use of an unactivated alkyl sulfone for RCC emerged in 2013 from the Denmark laboratory's report of iron (Fe)-catalyzed Kumada cross-coupling to forge $\text{C}(\text{sp}^2)\text{--C}(\text{sp}^3)$ bonds (15). These elegant studies pointed to the improvements needed for mainstream adoption of this chemistry. An ongoing medicinal chemistry project at Pfizer could have used this reaction, but the limited scope prevented its wide adoption [beyond the use of phenylmagnesium bromide (PhMgBr)]. Thus, first forays into this area centered on identifying a suitably substituted sulfone that would be susceptible to reduction under mild (for example, low-valent Ni) reaction conditions to generate an alkyl radical and unreactive sulfinate anion (4). We evaluated a variety of sulfones differing in relative reduction potential, electronegativity, and size under Ni-catalyzed Negishi-type conditions (Fig. 1C). In the case of aryl sulfone **3a**, used previously by

Denmark, starting material was recovered with only traces of formation of the desired product **5a**; sulfones **3b** to **3e** performed similarly. A primary breakthrough was the discovery that a redox-active phenyl-tetrazole (PT) sulfone **3f** was distinctly capable of delivering the desired RCC product **5a** (71% isolated yield). As outlined in tables S1 to S8, a variety of conditions were surveyed, and Ni proved an effective catalyst, whereas Fe did not; concurrent with our report, difluoromethyl 2-pyridyl sulfone was found to be a competent coupling partner under Fe catalysis (16). The use of a bipyridine-type ligand was also imperative because performing the reaction in the absence of ligand resulted in exclusive formation of the biaryl by-product; without the Ni precatalyst and bipyridine ligand, no reaction occurred.

From a pragmatic perspective, PT-sulfones can be easily derived from alcohols or alkyl halides by using Mitsunobu conditions or $\text{S}_{\text{N}}2$ displacement with inexpensive and odor-free thiol **6** followed by straightforward oxidation in order to produce stable products that are often crystalline (17). As shown below, the ability of PT-sulfones to enable modular synthesis strategies inspired the development of five reagents (two of which are new chemical entities).

The robustness of the optimized reaction conditions for the desulfonylative RCC reaction is illustrated in the synthesis of more than 60 products (Fig. 2, A to E). The scope of this methodology was initially evaluated with a variety of aryl zinc reagents (Fig. 2A). PT-sulfone **3f** reacted with 13 different organozinc reagents to produce a series of arylated piperidine derivatives (**5a** and **12** to **23**). *Ortho*-substituted arylzinc reagents could be used under the reaction conditions (**17** and **18**), and potential electrophilic coupling partners such as aryl chlorides were also tolerated on the arylzinc reagent (**21**). Both electron-rich and electron-deficient heterocyclic organozinc reagents proved competent coupling partners in this reaction manifold, as exemplified by indole **22** and pyridine **23**. To assess the disclosed method relative to the prior state of the art in the cross-coupling of unactivated alkyl sulfones, we conducted a direct comparison of substrates (**24** to **30**) previously evaluated under Fe catalysis. The conditions reported here compared favorably in all cases to literature-reported yields and allowed access to compounds that were previously inaccessible via a desulfonylative cross-coupling route (15). Arylzinc reagents can also be accessed through lithium-halogen exchange/transmetalation or magnesium (Mg)-halogen exchange/transmetalation and successfully used under the reaction conditions in yields comparable with those of arylzinc reagents derived via Mg insertion (71 versus 66% isolated yield for **5a**, for example).

Desulfonylative RCC is demonstrated in Fig. 2B as a means to synthesize a broad range of compounds from 18 different readily accessible sulfones. Primary (**31** to **35**, **47**, and **50**), secondary (acyclic and cyclic; **36** to **46**, **48**, **49**, **51**, and **52**),

¹Department of Chemistry, The Scripps Research Institute (TSRI), 10550 North Torrey Pines Road, La Jolla, CA 92037, USA. ²Asymchem Life Science (Tianjin), Tianjin Economic-Technological Development Zone, Tianjin 300457, China. ³Department of Chemistry, La Jolla Laboratories, Pfizer, 10770 Science Center Drive, San Diego, CA 92121, USA. ⁴Pfizer Medicinal Sciences, Eastern Point Road, Groton, CT 06340, USA.

*These authors contributed equally to this work. †Present address: Exploratory Science Center, Merck & Co., Cambridge, MA 02141, USA.

‡Corresponding author. Email: pbaran@scripps.edu

and benzylic (**47**) arylated products could be accessed from the corresponding sulfone. Alkyl chlorides (**35**) were tolerated under the reaction conditions despite their propensity to engage in single-electron chemistry under Ni catalysis, establishing the orthogonality of these two alkyl electrophiles. Moreover, desulfonylative RCC provides a straightforward means to access A-ring-modified steroids (**49** and **52**). As a testament to the mild reaction conditions, Roche ester-derived **47** was successfully synthesized with no erosion of enantiomeric excess. Because of the well-studied reactivity of vinyl sulfones in cycloaddition chemistry, **7** was treated with cyclohexadiene in a Diels-Alder reaction and subsequently cross-coupled to afford [2.2.2]-bicycle **51**. Compound **7** is known to react with dienes under mild and more selective conditions than those of acrylates or the corresponding phenyl vinyl sulfone (**12**).

The primary advantage of this chemistry lies in its ability to simplify the retrosynthetic analysis of complex sp^3 -rich organofluorine building blocks so that the C-C bond-forming disconnection used is the same regardless of fluorine content. Whereas methods to install fluoroalkyl groups via cross-coupling chemistry exist, they are limited by the lack of facile access to the corresponding fluoroalkyl electrophiles (a full listing is provided in fig. S24) (**18–20**). In the case of simple mono-fluoromethyl or difluoromethyl groups, many reagents are difficult to handle (for example, gaseous) or require additional steps to remove superfluous functionality (**21**). It is in this context that α -fluoroalkyl sulfones were evaluated; these are well regarded as stable reagents used in synthetic organic chemistry for a variety of applications (**22**), such as the installation of fluoroalkenes from carbonyl-containing compounds (**23**) as well as reacting as radical precursors under photoinduced electron transfer conditions (**24**). Redox-active α -fluoro-PT-sulfones were thus investigated in order to install fluorinated groups onto arenes by means of RCC (Fig. 2C). By using bathophenanthroline as the ligand with a 1:2 ratio of Ni precatalyst to ligand, Negishi-type arylation of mono- and difluorinated sulfones could be achieved.

Fluoromethyl reagent **8** and difluoromethyl reagent **9** were prepared in a straightforward manner according to literature procedures from inexpensive CF_3HCl and CF_2HCl , respectively (**25**). Difluoroethyl reagent **10** was accessed through anionic functionalization [deprotonation and quenching with *N*-fluorobenzenesulfonimide (NFSI)] of the parent ethyl PT-sulfone. Using other corresponding alkyl radical precursors (alkyl halides, alkyl carboxylic acids, alkylboron and alkylsilicon derivatives, olefins, alkyl pyridinium salts, and alkyl dihydropyridines), this anionic manipulation would not be possible; thus, redox-active PT-sulfones offer a distinct advantage to more traditional alkyl electrophiles in that they engender a modular solution for the installation of monofluoro- and difluoroalkyl groups onto an aryl group from a single sulfone starting material. These reagents were successfully used to

access mono- and difluoroalkyl arenes (**53** to **55**, **56–58**, **59**, and **60**) and could be used to shorten synthetic routes to compounds found in the literature (**55** and **58**) (**21**, **25**). Although CH_2F and CF_2H moieties can be installed from the corresponding halides, such procedures are inconvenient because they often require an excess of gaseous reagents. The synthesis of additional tertiary fluorides (**62** and **63**) was similarly achieved, presenting a useful alternative to traditional tertiary fluoride synthesis from the corresponding tertiary alcohol and treatment with

diethylaminosulfur trifluoride (DAST; a highly toxic and dangerous reagent), a transformation that often proceeds in low yield (**26**). A current limitation is that the trifluoromethyl group cannot be readily installed with this method (**64**).

Reagents such as **7** and **11** open up distinct possibilities for stepwise, successive RCC chemistry because the PT-sulfone is known to enhance the rate of Giese-type radical additions (**12**). A variety of olefin- and carboxylic acid-derived radicals could be smoothly intercepted with

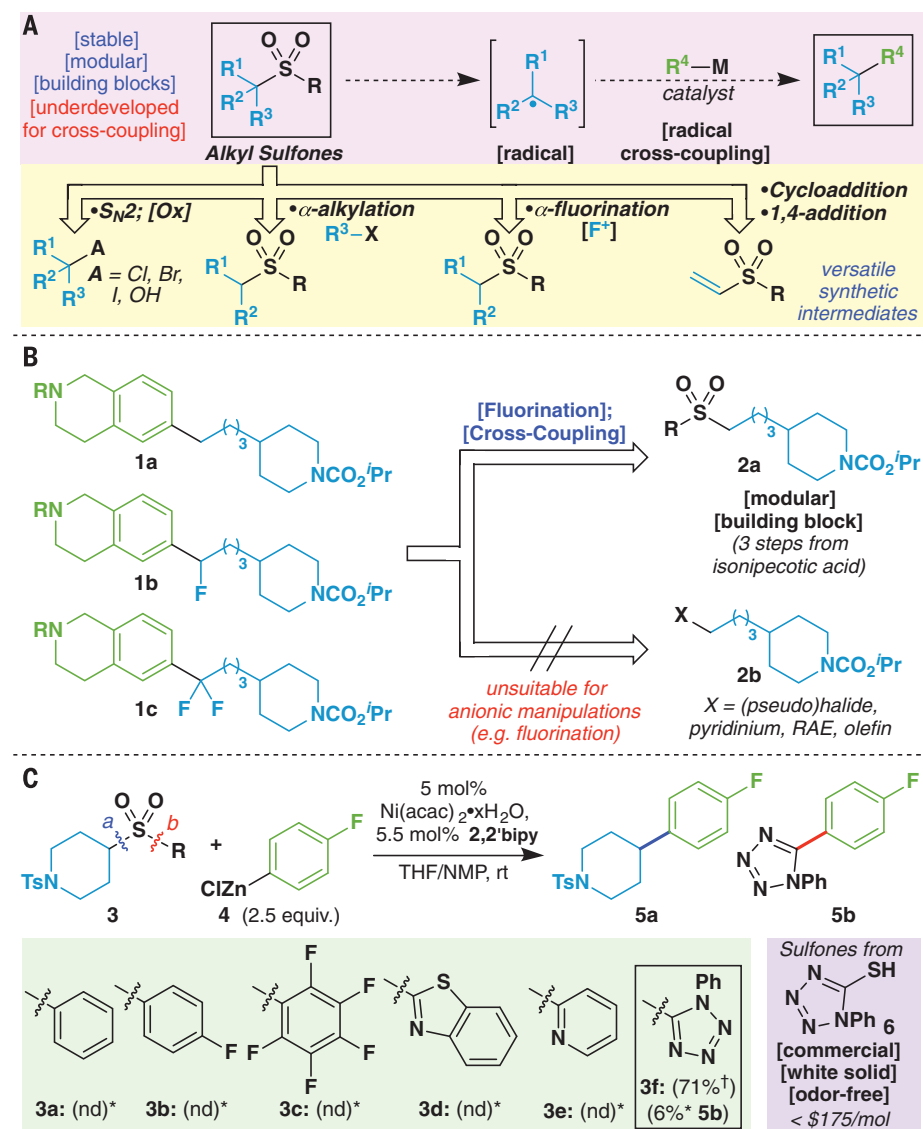


Fig. 1. Sulfone cross-coupling. (A) Alkyl sulfone: Modular electrophile for radical cross-coupling. Alkyl sulfones represent a promising and underexplored functional group for one-electron cross-coupling processes because of their distinct reactivity. (B) Alkyl sulfones: Ideal building blocks afford modular approach to druglike compounds. Described is the potential to achieve modular synthesis of fluorine-containing $C(sp^3)$ -rich architectures. (C) Initial investigations and optimization: Sulfones as radical cross-coupling electrophiles. Described is the identification of a redox-active sulfone and conditions in order to achieve selective cross-coupling under Ni-catalysis. *Yields determined by ^{19}F nuclear magnetic resonance (NMR) with 1-fluoronaphthalene as an internal standard. †Isolated yield. 2,2'-bipy, 2,2'-bipyridine; THF, tetrahydrofuran; NMP, 1-methylpyrrolidin-2-one; nd, not detected with ^{19}F NMR.

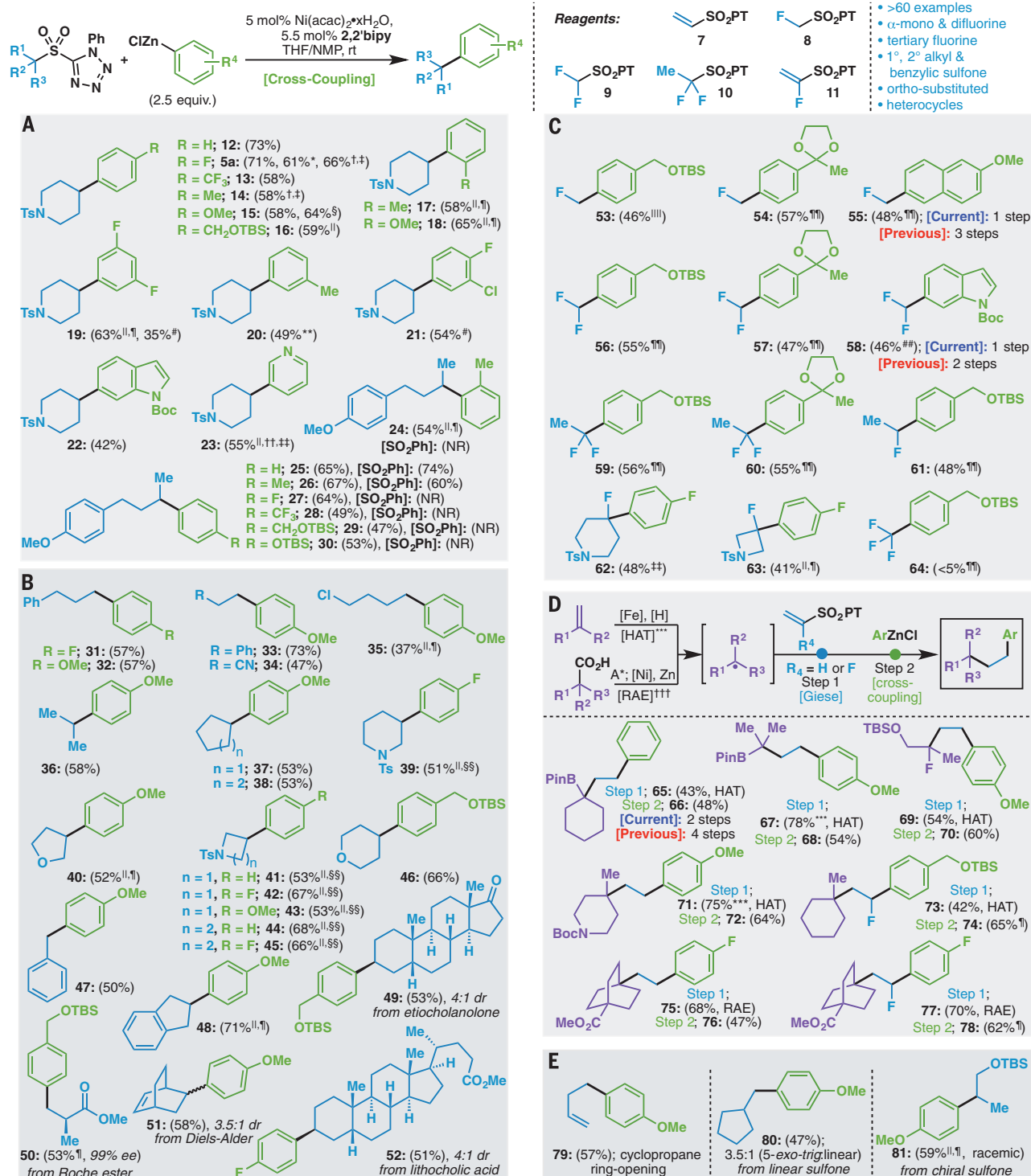


Fig. 2. Scope of the Ni-catalyzed cross-coupling of redox-active PT-sulfones. Experimental details are provided in the supplementary materials. **(A)** Aryl zinc reagents. **(B)** Sulfones. **(C)** Alkylfluorine sulfones. **(D)** Successive coupling. **(E)** Mechanistic studies. *2.5 mmol scale. †Arylzinc reagent prepared by means of lithium-halogen exchange with *n*-BuLi/transmetalation with ZnCl₂. ‡10 mole % (mol %) Ni(acac)₂·xH₂O, 11% 2,2'-bipy. §0.5 mmol scale. ||60°C. ¶20 mol % Ni(acac)₂·xH₂O, 22 mol % 2,2'-bipy, 3.0 equivalent arylzinc reagent. #Arylzinc reagent prepared by means of magnesium-halogen exchange with *i*PrMgCl·LiCl/transmetalation with ZnCl₂. **Arylzinc reagent was prepared by using commercial solution of ZnCl₂ in 2-MeTHF. ††*N,N'*-dimethylformamide (DMF) instead of NMP.

‡‡20 mol % Ni(acac)₂·xH₂O, 40 mol % 2,2'-bipy, 3.0 equivalent arylzinc reagent. §§30 mol % Ni(acac)₂·xH₂O, 33 mol % 2,2'-bipy, 4.0 equivalent arylzinc reagent. ||||30 mol % Ni(acac)₂·xH₂O, 60 mol % bathophenanthroline, 3.0 equivalent arylzinc reagent. ¶¶20 mol % Ni(acac)₂·xH₂O, 40 mol % bathophenanthroline, 3.0 equivalent arylzinc reagent. ###1.0 equivalent Ni(acac)₂·xH₂O, 1.1 equivalent bathophenanthroline, 6.0 equivalent arylzinc reagent. ***Experimental details and preparation are available in (27). †††Experimental details are available in (28). rt, room temperature; 2,2'-bipy, 2,2'-bipyridine; THF, tetrahydrofuran; NMP, 1-methylpyrrolidin-2-one; NR, no reaction; HAT, hydrogen atom transfer; A*, activation with NHPi; RAE, redox-active ester; DMF, *N,N*-dimethylformamide.

7 or **11** followed by desulfonylative RCC in order to generate structures that in some cases would be challenging to otherwise procure (27, 28). For example, **66** is prepared in the literature by using an elegant deborylative cyclization (29); the current modular approach starts with commercial cyclohexenyl boronic ester followed by olefin RCC and then desulfonylative RCC. Similarly, quaternary-center-bearing substrates **72**, **74**, **76**, and **78** are easily produced from either readily available acids or olefins through concurrent RCC chemistry, thus obviating the need for either deoxyfluorination or vexing cross-coupling challenges. Last, the success of this process points to the orthogonality of redox-active PT-sulfones both in the context of reductive chemistry (olefin HAT and acid Giese) and known radical precursors (boronic esters).

Mechanistically (fig. S9), alkyl radicals are posited intermediates under the reaction conditions, as evidenced by radical probe substrates **79** (cyclopropane ring-opening), **80** (5-*exo-trig* cyclization), and **81** (racemic product from a chiral sulfone), as shown in Fig. 2E (30).

In collaboration with Asymchem, **7**, **8**, **9**, and **10** have been prepared on a large scale (a graphical procedure is provided in the supplementary materials).

As illustrated in Fig. 3, the strategic impact of this chemistry shines in the preparation of complex, medicinally oriented building blocks that contain varying levels of fluorination. Traditionally, retrosynthetic analysis of these targets has centered around the installation of the fluorine atom; carbonyl chemistry and deoxyfluorination are therefore of prime importance. Moreover, such routes typically rely on highly toxic and dangerous reagents (such as DAST). Shown in Fig. 3, A to D, are examples from modern medicinal chemistry where this challenge is vividly displayed and contrasted with an RCC approach. In such contexts, fluorine atoms are often incorporated into scaffolds so as to alter solubility, efficacy, or metabolic properties. The often empirical nature of structure-activity relationships requires the targeting of multiple fluorinated variants as bioisosteric replacements (31), and such case studies are widespread in the medicinal chemistry literature. For instance (Fig. 3A), Schering scientists targeted building blocks **83a** and **83b**, differing only in the substitution at a single carbon (containing one or two fluorine atoms) (32). To access these simple structures, an eight-step sequence was devised from phenol **84**; only two of these steps are strategic and produce C–C bonds. In contrast, acetal **82** could be directly coupled with reagent **8**, **9**, or **10** to deliver **83a** and **83b** and a new analog **83c** after simple oxidation (the acetal is deprotected during the RCC workup with 1M HCl), thus avoiding tin-based reagents, ozonolysis, and deoxyfluorination steps.

A case study from a recent Merck campaign demonstrates the power of a concurrent RCC strategy for modularly generating C(sp³)-rich scaffolds (Fig. 3B) such as **87a** and **87b** (33, 34). In the original preparation, the absence or pres-

ence of fluorine atoms dictates the starting materials and methods used. In the preparation of the unfluorinated compound (five steps), an aryl aldehyde is used in concert with a Wittig reaction to forge the central C–C bond followed by hydrogenation to furnish **87a**. To access the latter, fluorine-substituted analog (**87b**, eight steps), a different route is required because the difluorinated carbon must be installed via deoxyfluorination of an aryl ketone, thus requiring a different starting material, protecting group swaps owing to harsh reagents (Boc → Cbz → Boc), thiols, and toxic HF. Using RCC-based logic, the same starting material can be used to make both **87a** and **87b** by using acid **85** ($n = 1$ CH₂ unit in the alkyl chain) in two successive RCC steps, the first of which uses the redox-active *N*-hydroxyphthalimide (NHPI) ester derived from the acid in a Giese-type addition to PT-sulfone reagent **7** to yield **86**. In the case of **87a**, redox-active PT-sulfone **86** is directly subjected to RCC to furnish **87a**, whereas for **87b**, anionic α -fluorination followed by RCC delivers **87b**. Both routes proceed in a fraction of the steps previously required and obviate the need for superfluous steps and/or toxic reagents.

A recent (2017) patent from the Shanghai Institute of Organic Chemistry (Fig. 3C) serves as a good example for the advantage of using the redox-active PT-sulfone over an alkyl halide for achieving the modular synthesis of a simple fluorinated scaffold (35). In the reported approach to **91** (six steps), an alkyl bromide is homologated with malonate and fluorinated with Selectfluor to produce a diester, which in turn undergoes decarboxylation and Hunsdiecker iodination to furnish a geminal-dihalide suitable for Ni-catalyzed Suzuki coupling. Alternatively, hydrocinnamic acid **92** could be homologated via the corresponding redox-active ester by using reagent **11** through Giese addition followed by RCC in order to deliver **91** in only two steps. In such a case, the fluorine atom in **91** was handled from a planning perspective as though it were any other substituent (methyl, aryl, or hydrogen), circumventing the fluorine-specific logic normally required.

The fourth case study (Fig. 3D), drawn from the patent literature (Novartis), demonstrates the advantage of a modular approach that diverges from the same intermediate even when the overall step count is similar (17). Targets **96a** to **96c** differ only in the presence or absence of benzylic fluorine atoms (0, 1, or 2), yet their preparation is guided not by the carbon skeleton (which comprises >90% of the molecular weight of **96b** and **96c**) but rather by fluorine atom incorporation. Whereas desfluoro analog **96a** is prepared from acid **97** via a Heck/hydrogenation sequence, mono- and difluoro analogs **96b** and **96c** require a pyridine-based starting material (**98**), which must be saturated, converted to a Grignard reagent, and added into an aryl subunit to afford a carbonyl group that serves as a gateway to introduce fluorine through deoxyfluorination. A very different blueprint emerges when using RCC. Thus, simple isonipecotic acid can be sub-

jected to decarboxylative alkyl-alkyl RCC with an alkyl-chloride-bearing zinc reagent followed by S_N2 displacement with **6** and oxidation to afford **95**, from which **96a** to **96c** can all be accessed. Similarly, direct RCC, α -fluorination/RCC, or α -difluorination/RCC affords **96a**, **96b**, or **96c**, respectively. Thus, the aforementioned case studies (Fig. 3, A to D) point to disconnection strategies that retain focus on the carbon skeleton during synthesis planning rather than allowing a single fluorine atom to completely alter the logic used.

In a final demonstration of the potential of RCC in synthesis (Fig. 3E), lithocholic acid was converted to a compound containing both a redox-active ester and sulfone, and controlled sequential RCC was demonstrated. Decarboxylative cross-coupling (DCC) proceeded selectively to afford products of Suzuki arylation (**101**) (36), Negishi arylation (**103**) (37), alkylation (**105**) (38), alkenylation (**107**) (39), and alkynylation (**109** and **111**) (40). Subsequently, those products underwent clean SCC arylation, delivering an array of useful diversity (**102**, **104**, **106**, **108**, and **110**). In the case of alkyne **111**, a classic two-electron cross-coupling (Sonogashira) could be conducted in an orthogonal manner before the final SCC to deliver **112**. Clearly, the choreography of both one- and two-electron-based cross-coupling protocols holds great potential not only for modular scaffold design but also for emerging programmed automated synthesis paradigms. Competition experiments suggest that the general order of reactivity in RCC chemistry correlates to the following qualitative trend: Cl/Br < SO₂PT < NHPI/TCNHPI [experiments run under SCC conditions with primary alkyl systems (fig. S1)].

It is worth reflecting on the complementarity of the sulfone and decarboxylative cross-coupling processes. The decarboxylative manifold has a distinct advantage in that the starting materials are ubiquitous, whereas the sulfone system stands out on the basis of privileged reactivity preceding the cross-coupling event and circumvention of prefunctionalization steps (ester hydrolysis and/or activation). Reagents **7** and **11**, stable crystalline solids, are illustrative of the practical advantage of PT-sulfones over analogous carboxy congeners that are not only toxic but also highly volatile. For example, the carboxy analog of reagent **8** (monofluoroacetic acid) is toxic, and the carboxy analog of reagent **9** does not currently participate in RCC. Anionic α -fluorination of esters is rare, and the common route to such α -substituted mono- and difluorinated systems involves α -oxidation and deoxyfluorination. In addition, crystalline and easily handled redox-active PT-sulfones can be used in concert with other single-electron and two-electron cross-coupling steps so as to enable another dimension of modular synthesis planning. Although there are some low-yielding substrates, most cross-couplings attempted reliably produced the desired cross-coupled product. The mass balance of reactions includes recovered starting material and biaryl products resulting from cleavage of

bond b (Fig. 1C). The safety profiles (thermal onset, friction, and shock sensitivity) of reagents **8** and **9** have been evaluated (table S20) and were found to be nonhazardous.

REFERENCES AND NOTES

1. M. Yan, J. C. Lo, J. T. Edwards, P. S. Baran, *J. Am. Chem. Soc.* **138**, 12692–12714 (2016).
2. G. C. Fu, *ACS Cent. Sci.* **3**, 692–700 (2017).
3. Z. Zuo *et al.*, *Science* **345**, 437–440 (2014).
4. J. Cornella *et al.*, *J. Am. Chem. Soc.* **138**, 2174–2177 (2016).
5. J. C. Tellis, D. N. Primer, G. A. Molander, *Science* **345**, 433–436 (2014).
6. M. Jouffroy, D. N. Primer, G. A. Molander, *J. Am. Chem. Soc.* **138**, 475–478 (2016).
7. S. A. Green, J. L. M. Matos, A. Yagi, R. A. Shenvi, *J. Am. Chem. Soc.* **138**, 12779–12782 (2016).
8. C. H. Basch, J. Liao, J. Xu, J. J. Piane, M. P. Watson, *J. Am. Chem. Soc.* **139**, 5313–5316 (2017).
9. K. Nakajima, S. Nojima, Y. Nishibayashi, *Angew. Chem. Int. Ed.* **55**, 14106–14110 (2016).
10. N. S. Simpkins, *Sulphones in Organic Synthesis* (Pergamon, 1993).
11. P. B. Alper *et al.*, U.S. patent US20100022515 A1 (2010).
12. E. Rodrigo, I. Alonso, J. L. García Ruano, M. B. Cid, *J. Org. Chem.* **81**, 10887–10899 (2016).
13. Z. T. Arik, Y. Maekawa, M. Nambo, C. M. Crudden, *J. Am. Chem. Soc.* **140**, 78–81 (2018).
14. J.-C. Wu *et al.*, *Angew. Chem. Int. Ed.* **51**, 9909–9913 (2012).
15. S. E. Denmark, A. J. Cresswell, *J. Org. Chem.* **78**, 12593–12628 (2013).
16. W. Miao *et al.*, *J. Am. Chem. Soc.* **140**, 880–883 (2018).
17. R. T. Taylor *et al.*, in *e-EROS Encyclopedia of Reagents for Organic Synthesis*, P. Fuchs, J. Bode, A. Charette, T. Rovis, Eds. (Wiley, 2015), pp. 1–4.
18. Y.-L. Xiao, Q.-Q. Min, C. Xu, R.-W. Wang, X. Zhang, *Angew. Chem. Int. Ed.* **55**, 5837–5841 (2016).
19. J. Sheng, H.-Q. Ni, G. Liu, Y. Li, X.-S. Wang, *Org. Lett.* **19**, 4480–4483 (2017).
20. L. An, Y.-L. Xiao, Q.-Q. Min, X. Zhang, *Angew. Chem. Int. Ed.* **54**, 9079–9083 (2015).
21. Y. Zhao *et al.*, *ACS Catal.* **3**, 631–634 (2013).
22. G. K. S. Prakash, J. Hu, *Acc. Chem. Res.* **40**, 921–930 (2007).
23. Y. Zhao, W. Huang, L. Zhu, J. Hu, *Org. Lett.* **12**, 1444–1447 (2010).
24. J. Rong *et al.*, *Angew. Chem. Int. Ed.* **55**, 2743–2747 (2016).
25. E. M. Woolridge, S. E. Rokita, *Tetrahedron Lett.* **30**, 6117–6120 (1989).
26. D. Sun *et al.*, *Bioorg. Med. Chem. Lett.* **19**, 1522–1527 (2009).
27. J. C. Lo *et al.*, *J. Am. Chem. Soc.* **139**, 2484–2503 (2017).
28. T. Qin *et al.*, *Angew. Chem. Int. Ed.* **56**, 260–265 (2017).
29. K. Hong, X. Liu, J. P. Morken, *J. Am. Chem. Soc.* **136**, 10581–10584 (2014).
30. S. Z. Tasker, E. A. Standley, T. F. Jamison, *Nature* **509**, 299–309 (2014).
31. N. A. Meanwell, *J. Med. Chem.* **54**, 2529–2591 (2011).
32. B. M. Baroudy *et al.*, U.S. patent US6391865 B1 (2002).
33. C. Caldwell *et al.*, U.S. patent US6265434 B1 (2001).
34. C. L. Lynch *et al.*, *Bioorg. Med. Chem. Lett.* **13**, 119–123 (2003).
35. X. Zhang, L. An, Chinese patent CN106278847A (2017).
36. J. Wang *et al.*, *Angew. Chem. Int. Ed.* **55**, 9676–9679 (2016).
37. F. Toriyama *et al.*, *J. Am. Chem. Soc.* **138**, 11132–11135 (2016).
38. T. Qin *et al.*, *Science* **352**, 801–805 (2016).
39. J. T. Edwards *et al.*, *Nature* **545**, 213–218 (2017).
40. J. M. Smith *et al.*, *Angew. Chem. Int. Ed.* **56**, 11906–11910 (2017).

ACKNOWLEDGMENTS

We thank D.-H. Huang and L. Pasternack (TSRI) for assistance with NMR spectroscopy; J. Chen (TSRI Automated Synthesis Facility); A. Rheingold, C. E. Moore, and M. A. Galella

(University of California, San Diego) for x-ray crystallographic analysis; J. J. Sabatini (U.S. Army Research Laboratory) for friction sensitivity testing of compounds **8** and **9**; and J. E. Spangler (Pfizer) and E.-X. Zhang (Asymchem) for helpful discussions. **Funding:** Financial support for this work was provided by Pfizer and the National Institutes of Health (grant GM-118176). Vividion Therapeutics supported a predoctoral fellowship to R.R.M., the U.S. Department of Defense supported a predoctoral fellowship to J.T.E. (National Defense Science and Engineering Graduate Fellowship Program), the Innovation Fund Denmark supported a predoctoral fellowship to M.M.K. (grant 4135-00085B), and Nankai University supported C.B. **Author contributions:** R.R.M., J.T.E., T.Q., and P.S.B. conceived the work. R.R.M., J.T.E., T.Q., M.M.K., C.B., and P.S.B. designed the experiments and analyzed the data. R.R.M., J.T.E., T.Q., M.M.K., C.B., M.R.C., O.O.F., G.M.G., J.J.M., and P.N. performed the experiments. G.C., D.-H.B., W.Q., and L.S. performed molescale experiments. P.S.B. wrote the manuscript. R.R.M., J.T.E., and T.Q. assisted in writing and editing the manuscript. **Competing interests:** Authors declare no competing interests. **Data and materials availability:** Experimental procedures, frequently asked questions, optimization data, ¹H NMR spectra, ¹³C NMR spectra, and mass spectrometry data are available in the supplementary materials. Crystallographic data are available free of charge from the Cambridge Crystallographic Data Centre under reference numbers CCDC 1590142–1590144, 1819895, and 1819896.

SUPPLEMENTARY MATERIALS

www.sciencemag.org/content/360/6384/75/suppl/DC1
Materials and Methods
Supplementary Text
Figs. S1 to S24
Tables S1 to S20
NMR Spectra
References (41–79)

12 December 2017; accepted 8 February 2018
Published online 18 February 2018
10.1126/science.aar7335

NEURODEVELOPMENT

Early emergence of cortical interneuron diversity in the mouse embryo

Da Mi,^{1,2*} Zhen Li,^{3*} Lynette Lim,^{1,2} Mingfeng Li,³ Monika Moissidis,^{1,2} Yifei Yang,⁴ Tianliyun Gao,³ Tim Xiaoming Hu,^{5,6} Thomas Pratt,⁴ David J. Price,⁴ Nenad Sestan,^{3†} Oscar Marín^{1,2†}

GABAergic interneurons (GABA, γ -aminobutyric acid) regulate neural-circuit activity in the mammalian cerebral cortex. These cortical interneurons are structurally and functionally diverse. Here, we use single-cell transcriptomics to study the origins of this diversity in the mouse. We identify distinct types of progenitor cells and newborn neurons in the ganglionic eminences, the embryonic proliferative regions that give rise to cortical interneurons. These embryonic precursors show temporally and spatially restricted transcriptional patterns that lead to different classes of interneurons in the adult cerebral cortex. Our findings suggest that shortly after the interneurons become postmitotic, their diversity is already patent in their diverse transcriptional programs, which subsequently guide further differentiation in the developing cortex.

The mammalian cerebral cortex contains more than two dozen GABAergic cell types (GABA, γ -aminobutyric acid) with particular morphological, electrophysiological, and molecular characteristics (1–3). Interneuron diversity has evolved to increase the repertoire of cortical computational motifs through a division of labor that allows individual classes of interneurons to control information flow in cortical circuits (4–6). Although a picture about cortical interneuron cell types is emerging (7, 8), the mechanisms that generate interneuron diversity remain controversial. One model proposes that interneurons acquire the potential to differentiate into a distinct subtype at the level of progenitors or shortly after becoming postmitotic, before they migrate; the competing model postulates that interneuron identity is established relatively late in development, after they have migrated to their final location, through interactions with the cortical environment (9).

To study cell diversity in the germinal regions of cortical interneurons (10), we dissected tissue from three regions in the mouse subpallium, the dorsal and ventral medial ganglionic eminence (dMGE and vMGE, respectively) and the caudal ganglionic eminence (CGE), across two stages that coincide with the peak of neurogenesis for

cortical interneurons [embryonic (E) days 12.5 and E14.5] (11) (Fig. 1A). We prepared single-cell suspensions and sequenced the transcriptome of individual cells, which, following quality control (fig. S1, A to E), led to a final data set of 2003 cells (fig. S1F), covering on average of about 3200 genes per cell. We performed regression analysis on these cells to remove the influence of cell cycle-dependent genes in cell type identification (fig. S1G).

We used principal components analysis (PCA) to identify the most prominent sources of variation. We found that developmental stage and anatomical source contribute to cell segregation (Fig. 1, B and C, and figs. S2 and S3). To distinguish between dividing and postmitotic cells, we conducted random forest (RF) feature selection and classification, starting with a list of established genes to sort cells into these categories (Fig. 1D). Subsequently, we reduced the dimensionality of our data using t-SNE (t-distributed stochastic neighbor embedding) to visualize the segregation of progenitor cells from neurons (figs. S4A and S5A). These analyses revealed gene expression patterns that distinguish progenitor cells and neurons at each developmental stage (figs. S4B and S5B).

We took a semisupervised clustering approach to explore variation across all progenitor cells and identified progenitor clusters with characteristic regional and developmental patterns (fig. S6, A to D). This analysis revealed a prominent temporal segregation of progenitor clusters (fig. S6, B and D), which suggests that progenitor cells in the ganglionic eminences (GE) may have a rapid turnover during embryonic development. To identify distinctive features of E12.5 and E14.5 progenitor cells, we further investigated progenitor cell diversity at each stage individually. We first used RF feature selection and classification, starting with a list of established genes to distinguish between ventricular zone (VZ) radial glial cells and

subventricular zone (SVZ) intermediate progenitors (12, 13) (fig. S7A). We then carried out semisupervised clustering and distinguished VZ and SVZ progenitor clusters at both developmental stages (Fig. 2A and fig. S7B), independent of their cell cycle state (fig. S8), and found characteristic patterns of gene expression (fig. S9). Cross-validation using MetaNeighbor (14) confirmed cluster robustness and identity (fig. S10A). Many progenitor clusters found at E12.5 did not seem to have a direct transcriptional equivalent at E14.5 (fig. S10B), which reinforces the notion that the GE contains highly dynamic pools of progenitor cells during development.

Analysis of progenitor cell clusters confirmed that radial glial cells and intermediate progenitors have distinct identities across different regions of the subpallium, with characteristic and often complementary expression of transcription factors (e.g., *Nkx2-1* and *Pax6* in VZ, *Lhx6* and *Foxp2* in SVZ) (Fig. 2B and figs. S11 and S12). Although the molecular diversity of VZ cells was more limited than anticipated (15, 16), this analysis revealed diversity among SVZ progenitors (Fig. 2B and figs. S11 to S14). Thus, based on transcriptomic signatures, the diversification of progenitor cells in the GE seems to emerge primarily within the highly neurogenic SVZ.

We next turned our attention to the neurons that are being generated in the GE during this temporal window of high progenitor cell diversity. The MGE and CGE generate different groups of cortical interneurons (17–19). Most parvalbumin (PV)-expressing and somatostatin (SST)-expressing interneurons are born in the MGE, whereas the CGE is the origin of vasoactive intestinal peptide (VIP)-expressing interneurons and neurogliaform (NDNF⁺) cells (20). We took a completely unsupervised approach to explore the emergence of neuronal diversity in the GE. Unbiased clustering of all neurons identified 13 groups of newborn neurons with distinctive gene expression profiles, as well as specific temporal and regional identities (figs. S15, A to D, and S16). This analysis revealed that regional identity segregates more clearly among E14.5 neuronal clusters (fig. S15C), which suggests that neurons become more transcriptionally heterogeneous over time. Similar results were obtained when neuronal clusters were identified for both stages separately (fig. S17).

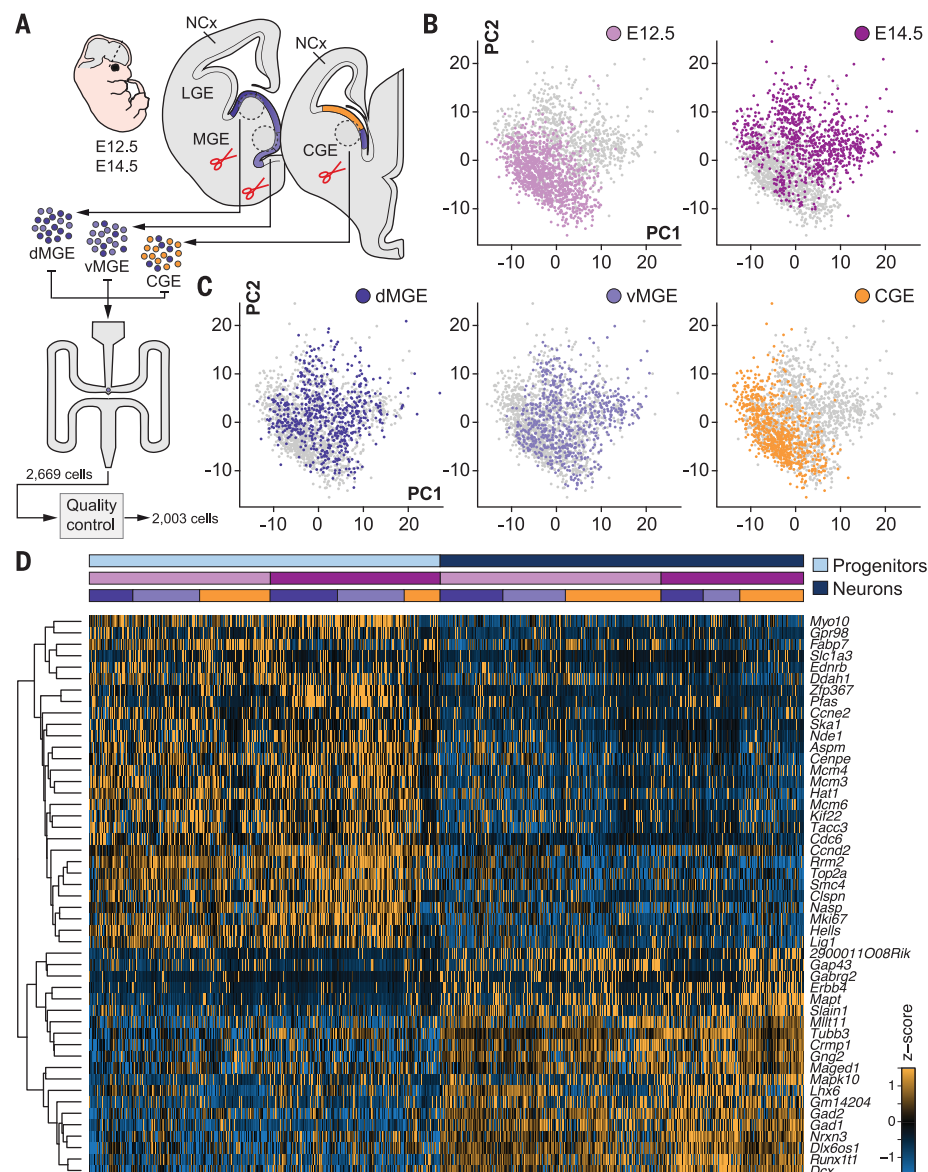
GO (Gene Ontology) enrichment analysis revealed different states of maturation across neuronal clusters (fig. S15E), which suggests that some aspects of this diversity might be linked to the differentiation of newborn neurons and not cell identity. Analysis of the expression of region- and cell type-specific genes revealed the emerging signature of the main groups of cortical interneurons (fig. S15F). For example, clusters primarily populated by MGE-derived cells can be further segregated into those with features of SST⁺ interneurons (N3 and N4) and those without (N1, N2, and N9), which presumably include neurons that will differentiate into PV⁺ interneurons. The profile of emerging CGE-specific interneuron classes, such as those characterized by the expression of *Meis2* (21), is also

¹Centre for Developmental Neurobiology, Institute of Psychiatry, Psychology, and Neuroscience, King's College London, London SE1 1UL, UK. ²Medical Research Council Centre for Neurodevelopmental Disorders, King's College London, London SE1 1UL, UK. ³Department of Neuroscience and Kavli Institute for Neuroscience, Yale School of Medicine, New Haven, CT 06510, USA. ⁴Biomedical Sciences, University of Edinburgh, Edinburgh EH8 9XD, UK. ⁵Department of Biomedical Informatics, Harvard Medical School, Boston, MA 02446, USA. ⁶Department of Physiology, Anatomy, and Genetics, University of Oxford, Oxford, UK.

*These authors contributed equally to this work.

†Corresponding author. Email: oscar.marin@kcl.ac.uk (O.M.); nenad.sestan@yale.edu (N.S.)

Fig. 1. Major sources of transcriptional heterogeneity among single cells from mouse MGE and CGE. (A) Schematic illustrating sample collection, sequencing, and single-cell RNA-seq analysis workflow. Single cells from E12.5 and E14.5 dMGE, vMGE, and CGE were isolated and subjected to cDNA synthesis using a Fluidigm C1 system and RNA-seq. (B and C) Visualization of stage and region of origin variation in single cells using PCA. (D) RF classification of cells into progenitor or neuronal identity. The heat map illustrates expression of genes selected by RF analysis that best represent progenitor or neuronal identity. Colored bars above the heat map indicate cell identity, stage, and region of origin.



delineated at this stage. This analysis also revealed that the CGE gives rise to neurons with molecular profile of SST⁺ interneurons (N13), which reinforces the view that this anatomical region contains a molecularly heterogeneous pool of progenitor cells (15).

The adult mouse cerebral cortex contains more than 20 distinct classes of interneurons with characteristic transcriptional profiles (7, 8). We asked whether any of these classes of interneurons would be identifiable shortly after becoming postmitotic in the GE. To this end, we used a publicly available single-cell RNA sequencing (RNA-seq) data set of 761 adult GABAergic interneurons from the adult mouse visual cortex (8) and identified highly variable genes in both adult and embryonic data sets. We employed the resulting data set to identify the features that best represent each of the 23 interneuron cell types found in the adult mouse cortex (8). We then carried out RF feature selection and classification based

on those features to assign the identity of adult interneurons into distinct cell types. We were unable to identify all cell types originally described in the adult data set (8), which suggests a difference in transcriptomic and cell-type diversity between embryo and adult. We then used the identified adult interneuron cell types to annotate the embryonic data set using the RF classification workflow and found six prospective interneuron subtypes among embryonic neurons (Fig. 3A and fig. S18). Cross-data set validation between the emerging embryonic subtypes and adult interneurons confirmed the robustness of these annotations (fig. S19).

We used a second, independent approach to assign embryonic neurons to adult interneuron subtypes. In brief, we conducted canonical correlation analysis (CCA) to identify the sources of variation that are shared between embryonic and adult neurons. To this end, we first reduced the dimensionality of both data sets onto the

same two-dimensional space using t-SNE, which allowed the identification of 11 clusters of adult interneurons based on the expression of variable genes shared between both data sets (Fig. 3B). These groups correspond to anatomically and electrophysiologically defined classes of cortical interneurons, including several types of PV⁺ basket cells, SST⁺ Martinotti and non-Martinotti cells, VIP⁺ basket and bipolar interneurons, and neurogliaform cells (8, 22). We then assigned prospective identities to embryonic neurons based on transcriptional similarity with adult interneurons. This analysis provided evidence for early cell type differentiation: All 11 classes of cortical interneurons were identified among embryonic neurons (Fig. 3C), which exhibit characteristic patterns of gene expression (Fig. 3D and fig. S20) and robustness in cross-validation analyses (fig. S21). Comparison between the two independent approaches identified eight conserved interneuron subtypes among the assigned

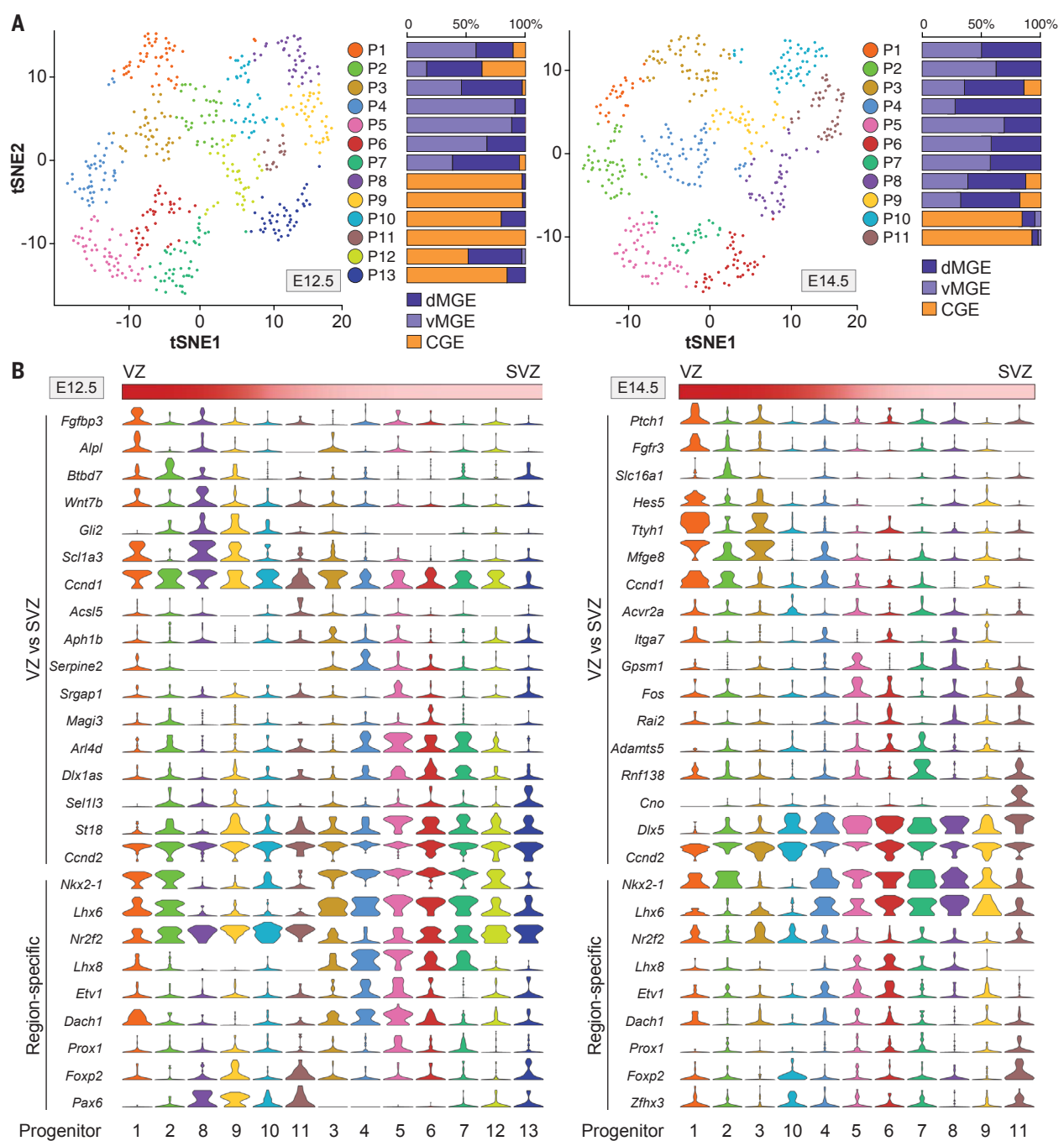


Fig. 2. Characterization of progenitor cell types in the embryonic germinal zones. (A) Visualization of progenitor cell diversity by t-SNE. Histograms illustrate the relative contribution of dMGE, vMGE, and CGE

cells to each progenitor cluster. (B) Violin plots depict the expression of marker genes that distinguish VZ/SVZ identities and patterning information in progenitor clusters.

embryonic neurons (Fig. 3E). Analysis of the contribution of E12.5 and E14.5 neurons to these identities revealed timing biases for the generation or maturation of some interneuron subtypes (Fig. 3F and fig. S22). Altogether, these results strongly suggested that interneurons exhibit a great diversity of transcriptional signatures shortly after becoming postmitotic in the GE.

We hypothesized that the patterns of gene expression identified in progenitor cells and

newborn neurons delineate specific lineages of cortical interneurons. To investigate this idea, we limited our analysis to embryonic neurons that were assigned to the same subtype identity by both RF and CCA methods, which we named “consensus” neurons and which belong to three interneuron subtypes: PV1, SST1, and SST2. We conducted MetaNeighbor analysis to identify possible links between progenitor cell clusters and consensus neurons. This analysis

revealed putative SST⁺ and PV⁺ progenitor cell clusters at E12.5 and E14.5 (Fig. 4A and fig. S23). We then carried out differential gene expression between E12.5 progenitor clusters P5 and P7 (Fig. 4B), which exhibited the highest association with PV1 and SST1, respectively (Fig. 4A). We found early PV (*Ccnd2* and *St18*) and SST (*Epha5*, *Cdk14*, and *Maf*) markers in these progenitor pools (Fig. 4, C and D), which are subsequently maintained in specific subtypes of

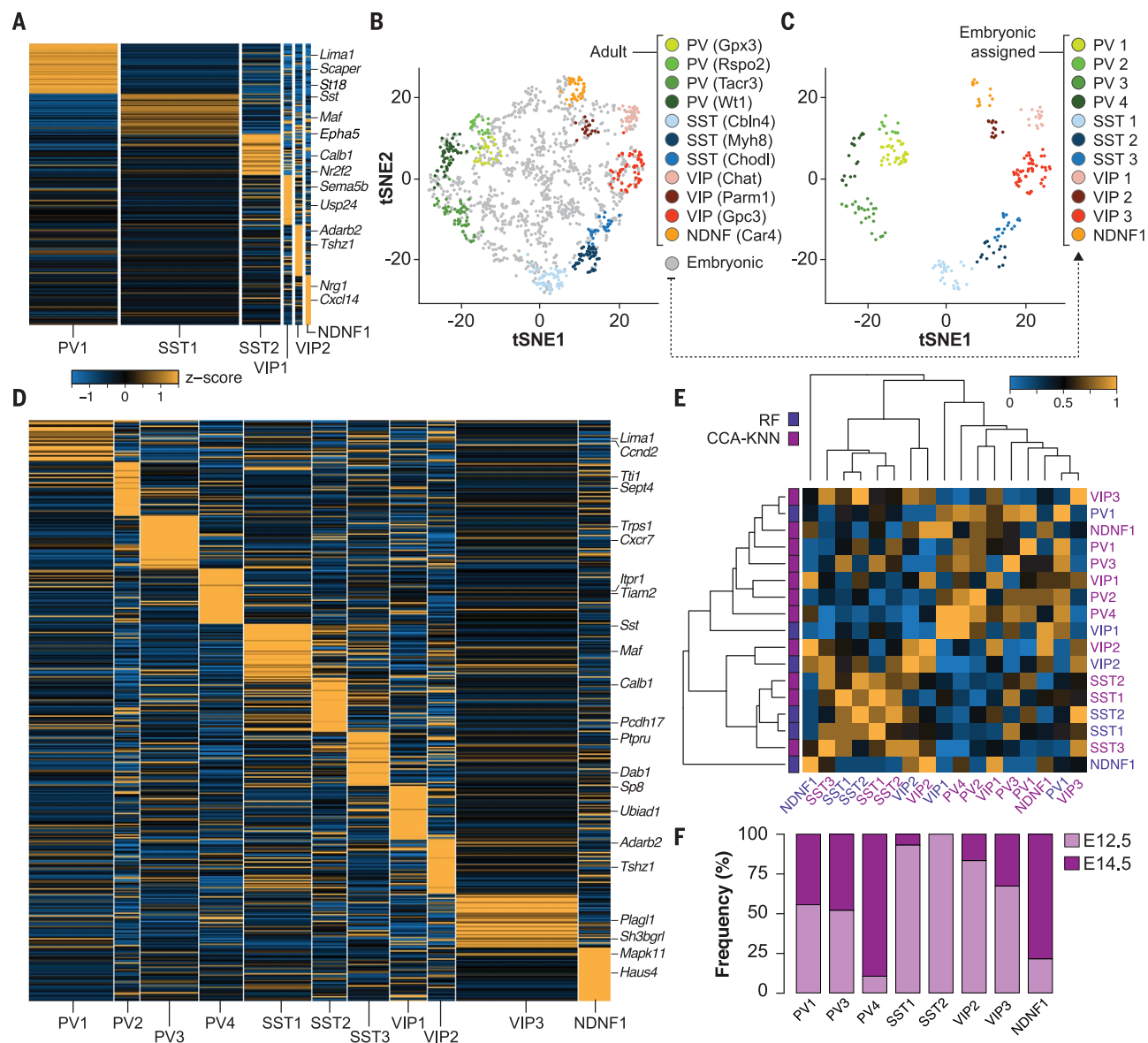


Fig. 3. Emergence of cortical interneuron diversity in the ganglionic eminences. (A) Heat map showing average expression of differentially expressed (DE) genes among six classes of interneurons identified by RF classification of embryonic neurons. (B) Integration of embryonic neurons and adult cortical interneurons in t-SNE space following canonical correlation analysis (CCA). (C) Embryonic neurons assigned to specific interneuron lineages by k-nearest neighbor (KNN) analysis are depicted in the same t-SNE space. Unassigned embryonic neurons are omitted. (D) Heat map illustrating the expression of DE genes among

newborn interneurons (Fig. 3, A and D). To validate these observations, we investigated the function of *Maf* in the delineation of MGE interneuron lineages. We infected progenitor cells in *Nkx2-1-Cre* embryos with conditional retroviruses expressing Cre-dependent control or *Maf* vectors during the period of SST⁺ interneuron production (E12.5) (23) and explored the identity of labeled interneurons in the cortex of young adult mice (Fig. 4E and fig. S24, A and B). We found that widespread expression of *Maf* in MGE progenitors increases the relative propor-

tion of SST⁺ interneurons at the expense of PV⁺ cells (Fig. 4F and fig. S24C). Conversely, conditional loss of *Maf* from MGE progenitor cells decreases the density of cortical SST⁺ interneurons (Fig. 4, G and H). We also observed that overexpression of *Maf* at the peak of PV neurogenesis (E14.5) (23) represses PV⁺ interneuron fates (fig. S24, D and E). Altogether, these results indicated that *Maf* regulates the potential of interneurons to acquire SST⁺ interneuron identity.

Our study reveals that GABAergic interneurons have a propensity toward a defined fate long

the 11 classes of interneurons identified by CCA. (E) Heat map of mean AUROC (area under the receiver operating characteristic curve) scores for assigned interneuron cell types using the two independent approaches (RF and CCA). AUROC scores of eight conserved interneuron subtypes: PV1_{RF}-PV1_{CCA} = 0.95; PV1_{RF}-PV3_{CCA} = 0.90; PV1_{RF}-PV4_{CCA} = 0.90; SST1_{RF}-SST1_{CCA} = 1; SST2_{RF}-SST2_{CCA} = 0.95; VIP2_{RF}-VIP2_{CCA} = 0.90; VIP2_{RF}-VIP3_{CCA} = 0.85; NDNF1_{RF}-NDNF1_{CCA} = 0.7. (F) Histogram illustrating the relative contribution of E12.5 and E14.5 neurons to conserved interneuron subtypes.

before they occupy their final position in the cerebral cortex during early postnatal development. This suggests that interneuron diversity does not emerge in response to activity-dependent mechanisms in the cortex (1, 9) but rather is established early, before these cells reach the cortex, by specific transcriptional programs that then unfold over the course of several weeks. Activity-dependent mechanisms undoubtedly influence development, maturation, and plasticity of cortical interneurons (24–26), but most aspects that are directly linked to the functional diversity of

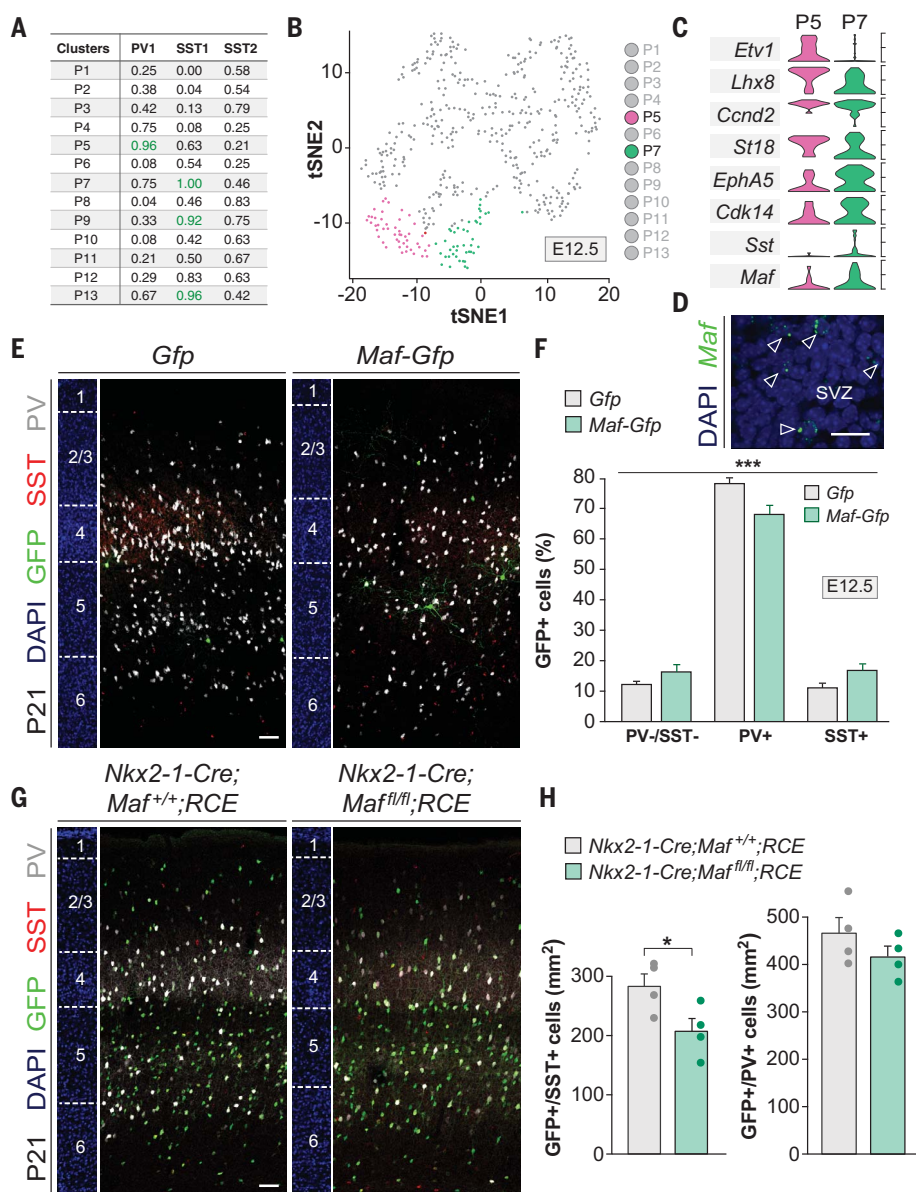


Fig. 4. *Maf* regulates SST⁺ interneuron fate. (A) AUROC values for putative lineages linking E12.5 progenitor clusters (P) with specific interneuron subtypes (AUROC scores above 0.9). (B) t-SNE plot illustrating progenitor cell clusters at E12.5. Two SVZ clusters, P5 and P7, are highlighted by color. (C) Violin plots for selected DE genes between P5 and P7 clusters. (D) RNAscope labeling of MGE SVZ progenitor cells with a *Maf* probe. (E) Coronal sections through the somatosensory cortex of P21 mice after viral infection with *Gfp* or *Maf*-P2A-*Gfp* retroviruses in the MGE at E12.5. (F) Quantification of the proportion of PV⁻/SST⁻, PV⁺, and SST⁺ interneurons; $n = 5$; χ^2 test, *** $P < 0.001$. Post-hoc analysis was performed with binomial pairwise comparison with adjusted P value by Bonferroni correction; PV⁻/SST⁻ versus PV⁺, *** $P < 0.001$; PV⁺ versus SST⁺, ** $P < 0.01$. (G) Coronal sections through the somatosensory cortex of P21 control and conditional *Maf* mutants. (H) Quantification of the density of GFP⁺/SST⁺ and GFP⁺/PV⁺ interneurons; $n = 4$, one-way analysis of variance with Tukey correction, * $P < 0.05$. Scale bars, 15 μ m (D) and 100 μ m [(E) and (G)].

cortical interneurons seem to be intrinsically determined (14, 27).

Our analysis identifies early markers for many different classes of cortical interneurons, whose functional validation may eventually illuminate the mechanisms regulating the differentiation of GABAergic interneurons into specific subtypes

and, through comparative analyses, inform the use of stem cell biology for the generation of distinct classes of human cortical interneurons (28, 29). Thus, core aspects of interneuron identity are drafted early in development, forming the foundation on which later interactions with other neurons must function.

REFERENCES AND NOTES

1. A. Kepecs, G. Fishell, *Nature* **505**, 318–326 (2014).
2. T. Klausberger, P. Somogyi, *Science* **321**, 53–57 (2008).
3. X. Jiang et al., *Science* **350**, aac9462 (2015).
4. W. Muñoz, R. Tremblay, D. Levenstein, B. Rudy, *Science* **355**, 954–959 (2017).
5. H. Hu, J. Gan, P. Jonas, *Science* **345**, 1255263 (2014).
6. H. J. Pi et al., *Nature* **503**, 521–524 (2013).
7. A. Zeisel et al., *Science* **347**, 1138–1142 (2015).
8. B. Tasic et al., *Nat. Neurosci.* **19**, 335–346 (2016).
9. B. Wamsley, G. Fishell, *Nat. Rev. Neurosci.* **18**, 299–309 (2017).
10. S. A. Anderson, D. D. Eisenstat, L. Shi, J. L. R. Rubenstein, *Science* **278**, 474–476 (1997).
11. G. Miyoshi, S. J. Butt, H. Takebayashi, G. Fishell, *J. Neurosci.* **27**, 7786–7798 (2007).
12. I. H. Smart, *J. Anat.* **121**, 71–84 (1976).
13. M. Götz, W. B. Huttner, *Nat. Rev. Mol. Cell Biol.* **6**, 777–788 (2005).
14. A. Paul et al., *Cell* **171**, 522–539.e20 (2017).
15. N. Flames et al., *J. Neurosci.* **27**, 9682–9695 (2007).
16. S. N. Silberberg et al., *Neuron* **92**, 59–74 (2016).
17. L. Sussel, O. Marin, S. Kimura, J. L. Rubenstein, *Development* **126**, 3359–3370 (1999).
18. S. Nery, G. Fishell, J. G. Corbin, *Nat. Neurosci.* **5**, 1279–1287 (2002).
19. H. Wichterle, J. M. Garcia-Verdugo, D. G. Herrera, A. Alvarez-Buylla, *Nat. Neurosci.* **2**, 461–466 (1999).
20. D. M. Gelman, O. Marin, *Eur. J. Neurosci.* **31**, 2136–2141 (2010).
21. S. Frazer et al., *Nat. Commun.* **8**, 14219 (2017).
22. R. Tremblay, S. Lee, B. Rudy, *Neuron* **91**, 260–292 (2016).
23. C. P. Wonders, S. A. Anderson, *Nat. Rev. Neurosci.* **7**, 687–696 (2006).
24. D. Bortone, F. Polleux, *Neuron* **62**, 53–71 (2009).
25. N. V. De Marco García, T. Karayannis, G. Fishell, *Nature* **472**, 351–355 (2011).
26. N. Dehorter et al., *Science* **349**, 1216–1220 (2015).
27. G. Bartolini, G. Ciceri, O. Marin, *Neuron* **79**, 849–864 (2013).
28. J. L. Close et al., *Neuron* **93**, 1035–1048.e5 (2017).
29. A. M. Maroof et al., *Cell Stem Cell* **12**, 559–572 (2013).

ACKNOWLEDGMENTS

We thank S. E. Bae for technical assistance and M. Fernández for general lab support. We are grateful to M. Zhong at Yale Stem Cell Center Genomics and Bioinformatics Core for conducting RNA sequencing; N. Flames and B. Rico for critical reading of the manuscript; S. Anderson, C. Birchmeier, F. Cage, and G. Fishell for reagents and mouse strains; and members of the Marin, Rico, and Sestan laboratories for stimulating discussions and ideas.

Funding: This work was supported by grants from the Wellcome Trust (103714MA) to O.M., the National Institutes for Health (NS095654 and MH106934) to N.S., and the Medical Research Council (N012291) and the Biotechnology and Biological Sciences Research Council (N006542) to D.J.P., Y.Y., and T.P. L.L. was supported by an EMBO postdoctoral fellowship. O.M. is a Wellcome Trust Investigator. **Author contributions:** D.M. and O.M. designed the study. Single-cell experiments were performed by D.M., Z.L., and T.G. Functional validation experiments were performed by L.L. and M.M. Data management and read processing was performed by M.L. Data analysis was performed by D.M., Z.L., L.L., M.M., Y.Y., and T.X.H. The study was supervised by D.M., Z.L., T.P., D.J.P., N.S., and O.M. The manuscript was prepared by D.M., Z.L., and O.M., with feedback from all authors. **Competing interests:** None declared. **Data and materials availability:** Sequencing data have been deposited at the National Center for Biotechnology Information BioProjects Gene Expression Omnibus and are accessible through GEO Series accession number GSE109796. c-*Maf* flox mice are available from C. Birchmeier under a material agreement with the Max-Delbrück-Centrum für Molekulare Medizin (Berlin). The supplementary materials contain additional data. All data needed to evaluate the conclusions in the paper are present in the paper or the supplementary materials.

SUPPLEMENTARY MATERIALS

www.sciencemag.org/content/360/6384/81/suppl/DC1
Materials and Methods
Figs. S1 to S24
Tables S1 to S4
References (30–44)

6 December 2017; accepted 14 February 2018
Published online 22 February 2018
10.1126/science.aar6821

PALEOANTHROPOLOGY

Environmental dynamics during the onset of the Middle Stone Age in eastern Africa

Richard Potts,^{1,2*} Anna K. Behrensmeyer,^{1,3} J. Tyler Faith,⁴ Christian A. Tryon,⁵ Alison S. Brooks,^{1,6} John E. Yellen,^{1,7} Alan L. Deino,⁸ Rahab Kinyanjui,² Jennifer B. Clark,¹ Catherine M. Haradon,⁹ Naomi E. Levin,¹⁰ Hanneke J. M. Meijer,^{1,11} Elizabeth G. Veatch,¹² R. Bernhart Owen,¹³ Robin W. Renaut¹⁴

Development of the African Middle Stone Age (MSA) before 300,000 years ago raises the question of how environmental change influenced the evolution of behaviors characteristic of early *Homo sapiens*. We used temporally well-constrained sedimentological and paleoenvironmental data to investigate environmental dynamics before and after the appearance of the early MSA in the Olorgesailie basin, Kenya. In contrast to the Acheulean archeological record in the same basin, MSA sites are associated with a markedly different faunal community, more pronounced erosion-deposition cycles, tectonic activity, and enhanced wet-dry variability. Aspects of Acheulean technology in this region imply that, as early as 615,000 years ago, greater stone material selectivity and wider resource procurement coincided with an increased pace of land-lake fluctuation, potentially anticipating the adaptability of MSA hominins.

Environmental drivers of African hominin evolution over the past several million years have been attributed to hydroclimate extremes (arid or moist conditions) and habitat variability (1–5). Testing for environment-evolution connections requires (i) evidence for geographic and temporal correspondence between novel hominin behaviors and shifts in climate, landscape, and overall biota, and (ii) an understanding of how those behaviors offered selective benefits to hominins as they foraged for resources affected by changing environmental parameters. Linkages between environmental change and evolution are anticipated because climate parameters, such as precipitation amount and variability, influence selection gradients globally (6), and because annual- and decadal-scale variability in climate has a demonstrable influence

on survival, reproduction, and demography (7). In human hunter-gatherers, environmentally induced variability and unpredictability in food return rates tend to favor wider mobility, information gathering, and investment in social resource exchange networks—a combination that promotes foraging efficiency, reduces risk, and thus improves fitness (8–10). Largely unexplored in human origins research are the environmental conditions and adaptive context in which a substantial technological shift and resource exchange networks emerged, as evidenced in the early Middle Stone Age (MSA) (11).

Long sequences of African middle Pleistocene strata that yield multiproxy environmental data associated with a dense archeological archive are rare. The Olorgesailie basin (Fig. 1), containing sedimentary strata dated between 1.2 million years (1.2 Ma) and 499,000 years (499 ka) ago and between 320 and 36 ka ago, preserves an archeological record that spans the Acheulean and MSA. The basin thus presents an opportunity to investigate the environmental context of this behavioral transition and to consider its evolutionary implications in relation to changes in landscape dynamics, climate, flora, and fauna.

MSA technologies are characterized by small points including weapon armatures, increased reliance on prepared core technologies requiring greater planning depth (12), and procurement of rocks from distant sources, among other traits indicative of complex symbolic, technological, and socioeconomic behaviors (13–15). By contrast, in addition to handaxes and other distinctive large tools (16), the 700-ka Acheulean sequence of the Olorgesailie Formation (Fm) exhibits highly localized use of stone material; 98% of rock used in tool manufacture was accessed within 5 km (table

S6) (17). The well-documented Acheulean technology of Olorgesailie (29 stratigraphic levels; Fig. 1A) is entirely replaced by MSA technology by ~320 ka ago (18), with evidence for long-distance obsidian exchange networks and previously unknown use of coloring materials (11). This represents a substantial revision in African hominin behavior at or near the time of origin of *Homo sapiens* (19, 20).

Evidence from Olorgesailie enables direct comparison between the environments associated with Acheulean and MSA technology (21). A ~180-ka erosional hiatus between 499 and ~320 ka ago in the Olorgesailie sequence precludes direct examination of the transitional stages, but the environmental and faunal differences before and after this time interval indicate a marked increase in climatic variability, landscape instability, and aridity. The rich Acheulean sequence of the Olorgesailie Fm is preserved in aggrading lacustrine floodplains and low-energy channels and paleosols representing relatively stable depositional conditions for ~700 ka (i.e., 1.2 Ma to 500 ka ago) (22, 23). However, an increasing pace of environmental change is recorded in the upper Olorgesailie Fm beginning ~800 ka ago, including more frequent land-lake oscillations and fire-reddened siliceous zones that reflect intense moist-arid fluctuation (Fig. 1, A and C) (24). Novel elements of Acheulean technology, some of which resemble innovations seen in the later MSA record, are recorded in this environmentally dynamic upper portion of the Olorgesailie Fm (text S2 and S3). Reliance on smaller artifacts is apparent, and the proportion of artifacts made from nonlocal stone (e.g., chert, obsidian, quartzite) is 3 to 6 times that observed in older Acheulean sites, and within the range found at the later MSA sites (Fig. 1D and tables S5 and S6).

Sedimentation of the Olorgesailie Fm came to an end ~499 ka ago, the age of the last recorded Acheulean technology in the basin (Fig. 1A and fig. S7). Approximately 180 ka of landscape dissection caused by major structural changes in the basin was followed by deposition of the Oltulelei Fm, signifying a basin-wide shift in depositional regime (25). In its oldest unit (Olkesititi Member), the early MSA is recorded in strata dated ~320 to 295 ka ago (18) in a sequence of diverse superposed lithologies indicative of rapidly shifting fluvial channel, floodplain, and spring deposition. The first records of the Olorgesailie MSA are therefore associated with dynamic paleolandscapes in which linked but semi-independent basins were subjected to repeated erosion and deposition across an area of ~60 km² north and northwest of Mt. Olorgesailie. Multiple phases of channel cutting and filling within the lower Olkesititi Member of the Oltulelei Fm further indicate repeated shifts in local base level, likely related to a combination of faulting and arid-moist climate variability (25).

MSA horizons at BOK (sites BOK-1E/BOK-3, BOK-2, and BOK-4, from lowest to highest), dated ~320 to 295 ka ago (18), occur in a succession of sedimentary fills of cross-cutting channels incised 2 to 4 m deep, indicating repeated cycles

¹Human Origins Program, National Museum of Natural History, Smithsonian Institution, Washington, DC 20013, USA.

²Department of Earth Sciences, National Museums of Kenya, P.O. Box 40658-00100, Nairobi, Kenya. ³Department of Paleobiology, National Museum of Natural History, Smithsonian Institution, Washington, DC 20013, USA.

⁴Natural History Museum of Utah and Department of Anthropology, University of Utah, Salt Lake City, UT 84108, USA. ⁵Department of Anthropology, Harvard University, Cambridge, MA 02138, USA. ⁶Department of Anthropology, George Washington University, Washington, DC 20052, USA.

⁷Archaeology Program, National Science Foundation, Alexandria, VA 22314, USA. ⁸Berkeley Geochronology Center, Berkeley, CA 94709, USA. ⁹Department of Earth Science, Santa Monica College, Santa Monica, CA 90405, USA.

¹⁰Department of Earth and Environmental Sciences, University of Michigan, Ann Arbor, MI 48109, USA.

¹¹University Museum, Department of Natural History, University of Bergen, Bergen, Norway. ¹²Department of Anthropology, Emory University, Atlanta, GA 30322, USA.

¹³Department of Geography, Hong Kong Baptist University, Kowloon Tong, Hong Kong. ¹⁴Department of Geological Sciences, University of Saskatchewan, Saskatoon, SK S7N 5E2, Canada.

*Corresponding author. Email: potts@si.edu

of erosion, filling, and development of floodplains (Fig. 2A). Silicified plant stems, roots, and siliceous tuffs are associated with the largest archeological assemblage at site BOK-2 (11) and are interpreted as evidence for localized springs and associated moist habitats during the artifact-rich channel-filling phase (25). The BOK sites are located within tens of meters of a confluence where the main drainage flowed toward a

gap in a nearby lava ridge. This confluence and nearby springs were a likely water source for hominins and other organisms. Site GOK-1 occurs below an erosional unconformity on top of a 5-m-thick red soil, and the eroded top of this soil is at least 1 m below a tuff dated ~277 ka ago (18). Thus, GOK-1 is possibly as old as or older than the BOK sites. The red paleosol interfingers with tufa deposits, indicating associated spring

activity, shallow ponds, and wetlands; subsequent MSA archeological levels at GOK occur in overlying floodplain deposits and paleosols (11, 25).

Coinciding with the large-scale change in depositional regime, the mammalian fauna associated with the Ologresailie MSA indicates substantial turnover [Jaccard distance = 0.85; i.e., only seven taxa (15%, $n = 46$) shared between the Acheulean

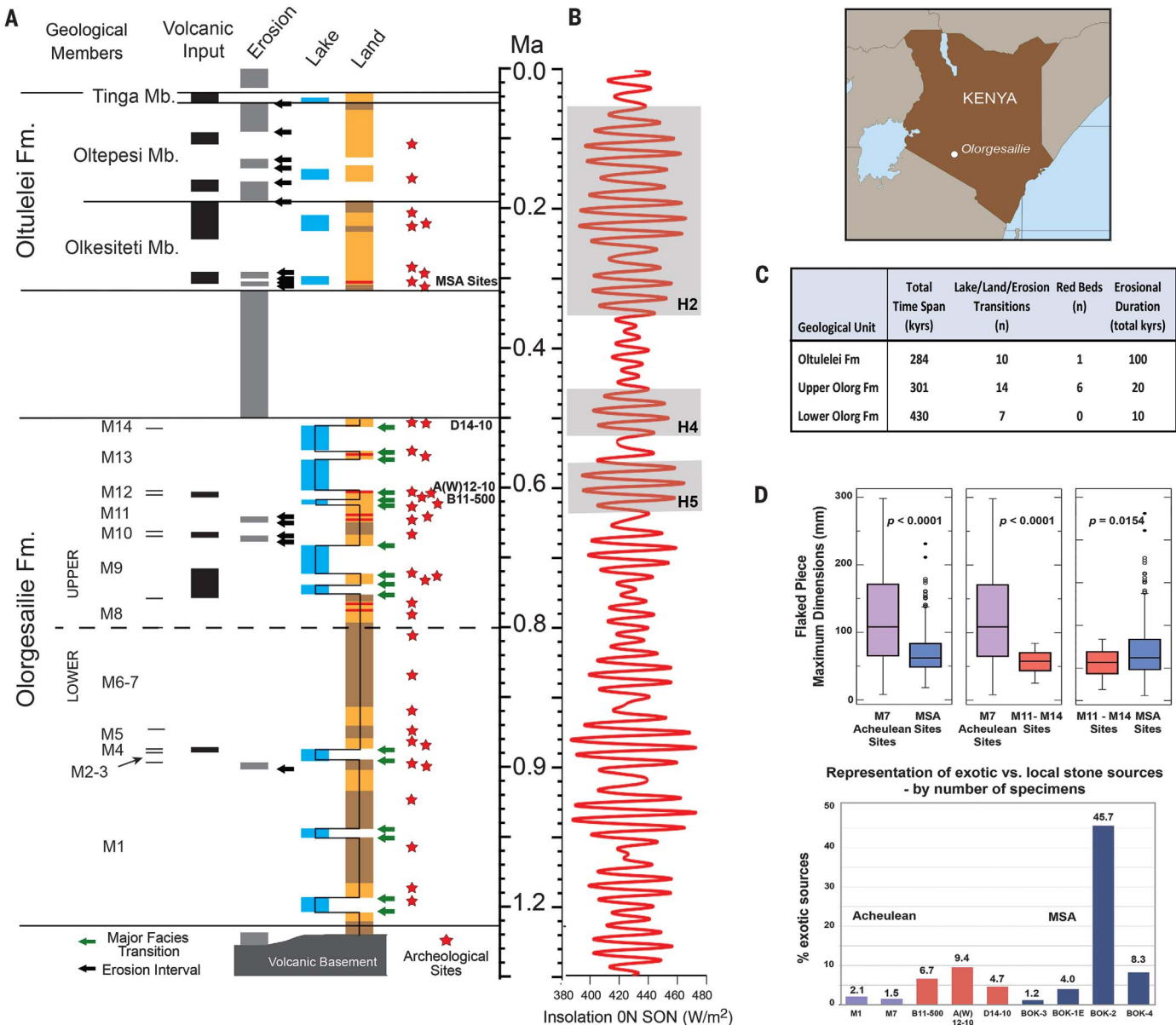


Fig. 1. Context of the Acheulean-to-MSA transition in the Ologresailie basin. (A) Sequence of major periods of erosion and deposition with inferred paleoenvironments in the Ologresailie and Oltulelei Formations, associated with Acheulean and MSA archeological sites, respectively. Color code: orange, aggrading sediment; brown, stable land surface; red, burned zone. (B) Insolation during the interval of Acheulean and MSA sites in the Ologresailie basin. Shaded areas are the three intervals of prolonged (>72 ka), highly variable climate predicted by eccentricity pertaining to the late Acheulean and oldest MSA sites in the basin

[climate variability phases H5, H4, and H2 (5)]. (C) Summary of land-lake oscillations and erosional phases associated with Ologresailie Acheulean and MSA sites. (D) Comparison of earlier Acheulean (purple), later Acheulean (red), and MSA (blue) sites in terms of (top) maximum size of flaked pieces (values for one-tailed t test) and (bottom) percentage of distant stone materials (exotic) relative to local rock sources (exotic stone counts for earlier versus later Acheulean, $\chi^2 = 448.93$, $P < 0.001$; for later Acheulean versus MSA, $\chi^2 = 535.30$, $P < 0.001$; see table S6).

and MSA assemblages] (Fig. 3). This impressive biotic shift included local extinction of previously dominant large-bodied specialized grazing lineages (e.g., *Paleoaloxodon recki*, *Equus oldowayensis*, *Theropithecus oswaldi*) prevalent in the Olororgesailie Acheulean sequence, their replacement by related taxa of smaller body size (Fig. 3) (26), and an example (springbok, *Antidorcas marsupialis*, known from Florisbad, South Africa ~100 to 400 ka ago) of apparent range extension covering as much as 2800 km (table S1 and fig. S5). The springbok's temporary presence in eastern Africa supports phylogeographic evidence that this region's dynamic environmental history contributed to elevated turnover, which included local extinctions and recolonization from southern African sources (27). This reorganization of the large mammalian community, which was more extensive than other examples of Pleistocene faunal turnover in eastern Africa [e.g., (28)], is first recorded in southern Kenya between ~330 and 320 ka ago (26, 29) (Fig. 3), roughly contemporaneous with the onset of the MSA sequence and consistent with the last appearances of extinct middle Pleistocene large-bodied mammals in eastern Africa (29).

The hyper-grazer alcelaphin *Damaliscus hypsodon* became prominent in the southern Kenya rift by ~330 ka ago (29) and is also found in fauna dated >305 ka ago in Olororgesailie MSA sites. *Equus*, including a previously unidentified large species that we attribute to *Equus* aff. *E. capensis*, and the bovids *Oryx* and *D. hypsodon* indicate arid, open terrain suitable for grazing; *Tragelaphus*, *Diceros*, and *Madoqua* indicate the presence of bush/shrubland; and *Hippopotamus* and *Crocodylus* attest to perennial bodies of water (text S1, tables S1 and S2, and figs. S3 and S4). Chord distance measures of dissimilarity to mammalian faunas from modern African wildlife reserves show that the BOK fauna most closely matches modern faunas from open, arid settings (Fig. 2D and fig. S2). BOK small mammal taxa (e.g., *Pedetes*) also imply semi-arid, open grassland to bushland habitats with little woody cover, and the presence of ostrich and francolin at the BOK sites indicates an open, dry, and grassy component of the Olororgesailie paleolandscape (text S1).

Carbon isotope data from the limited number of pedogenic carbonate horizons preserved at Olororgesailie point to the development of grasslands spanning the transition between the latest Acheulean and the earliest MSA. In accord with paleosol data from elsewhere in eastern Africa, Olororgesailie $\delta^{13}\text{C}$ values show a steady increase in grassy environments during the past 800 ka (Fig. 2B and text S1). The pedogenic carbonate isotope data are consistent with the presence of arid grassland-adapted fauna but do not show a sharp shift in vegetation commensurate with the faunal turnover. We consider it likely that the faunal change was a response to a combination of aridity and food/water resource variability that resulted, for example, from shifting rainfall seasonality and tectonically caused increases in topographic diversity (25)—factors that may have had

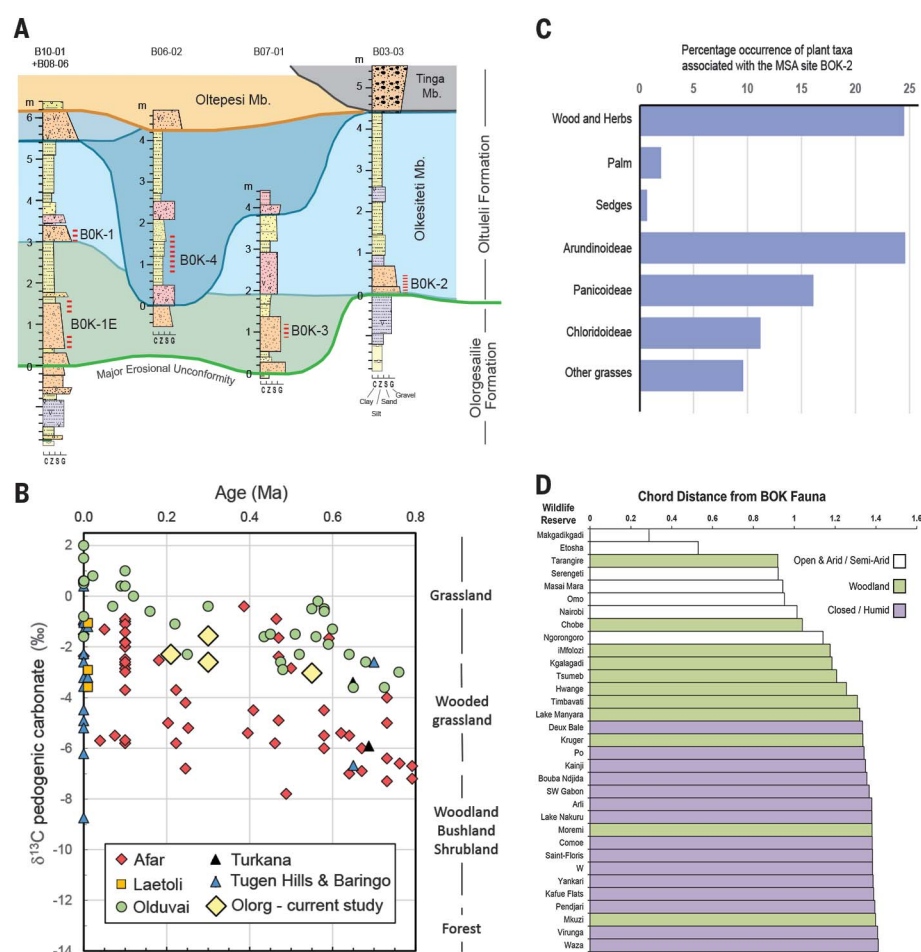


Fig. 2. Landscape and environmental setting of the >300,000-year-old MSA sites at Olororgesailie.

(A) Simplified stratigraphic panel showing superposed channel deposits (Olkesititi Member of the Oltulelei Fm: blue-green to blue-gray) that preserve the archaeological record in Locality B (BOK archaeological sites), viewed toward approximately west-southwest (toward the drainage outlet). White, Olororgesailie Fm; overlying orange and gray, channels of the upper members of the Oltulelei Fm. (B) Carbon isotope values of pedogenic carbonates from Olororgesailie paleosols (this study) and from elsewhere in eastern Africa [compiled in (37)] over the past 800 ka; vegetation cover categories are from (38). (C) Percentage of phytolith morphotypes of woody and herbaceous taxa, grass subfamilies, and palm and sedge (Cyperaceae) taxa associated with the MSA site BOK-2. (D) Chord distance, a measure of faunal dissimilarity for taxonomic abundance data (33), between the BOK fauna and census counts from 33 modern African wildlife reserves [data from (34)]. Modern faunas are arranged from lowest chord distance (top: most similar to BOK fauna) to highest chord distance (bottom: least similar to BOK fauna). Color coding of modern wildlife reserves: white, open and arid/semi-arid; green, woodland; purple, closed/humid (34–36). The BOK fauna is most similar to those from the open and arid settings of Makgadikgadi (Botswana) and Etosha (Namibia).

little influence on the carbon isotopic composition of vegetation in the local soils. A phytolith assemblage obtained from the BOK archaeological sites, however, indicates a local habitat that was more moist and vegetated. The BOK phytolith sample (Fig. 2C and text S1) contains short-grass (Chloridoideae) forms, consistent with the faunal and carbon isotope data, but also a high proportion of woody, herbaceous, and moisture-associated tall grass (Panicoideae) and sedge morphotypes, indicative of the vegetation at or adjacent to the focus of hominin activity. Together,

the environmental and geomorphological evidence implies that the MSA sites at BOK were situated in a predominantly grassland habitat near a reliable water source that also supported woody vegetation.

The Olororgesailie MSA coincided with a predicted interval of prolonged wet-dry climate oscillation for eastern Africa (climate variability stage H2; Fig. 1B) (5). Basin lithofacies document an increased tempo of erosional phases and volcanic input to the Olororgesailie region (Fig. 1, A and C) as tectonic activity created semi-independent

Taxonomic Group	Ologesailie Basin Mammalian Fauna	Ologesailie Fm Taxa (Acheulean-associated)	Olkesiteti Mbr Taxa (MSA-associated)
Bovidae	<i>Madoqua</i> sp.		X
	<i>Antidorcas marsupialis</i>		X
	<i>Gazella</i> sp./ <i>Gazella thomsoni</i>	X	X
	<i>Aepyceros</i> sp.	X	
	<i>Megalotragus</i> sp.	X	
	Alcelaphin size 3a cf. <i>Alcelaphus</i>	X	
	<i>Connochaetes</i> sp.	X	
	<i>Damaliscus hypsodon</i>		X
	<i>Oryx gazella</i> - Hippotragin oryx size		X
	Hippotragin - roan size		X
	<i>Taurotragus</i> sp./ <i>Taurotragus oryx</i>	X	X
	<i>Tragelaphus</i> sp./ <i>Tragelaphus strepsiceros</i>	X	X
	<i>Tragelaphus</i> cf. <i>T. imberbis</i>		X
Giraffidae	<i>Syncerus (Pelorovis)</i> cf. <i>S. antiquus</i>	X	
	<i>Kobus</i> sp.	X	
	<i>Redunca</i> sp.	X	
	<i>Giraffa</i> sp.	X	
Suidae	<i>Metridiochoerus</i> cf. <i>M. hopwoodi</i>	X	
	<i>Metridiochoerus</i> cf. <i>M. compactus</i>	X	
	<i>Kolpochoerus majus</i>	X	
	<i>Phacochoerus</i> sp.	X	X
Hippopotamidae	<i>Hippopotamus</i> cf. <i>H. gorgops</i>	X	
	<i>Hippopotamus</i> cf. <i>H. amphibius</i>		X
Equidae	<i>Equus</i> cf. <i>E. quagga</i>	X	X
	<i>Equus</i> cf. <i>E. grevyi</i>	X	
	<i>Equus oldowayensis</i>	X	
	<i>Eurygnathohippus</i> sp.	X	
	<i>Equus</i> aff. <i>E. capensis</i>		X
Rhinocerotidae	<i>Ceratotherium simum</i>	X	
	<i>Diceros bicornis</i>	X	X
Elephantidae	<i>Palaeoloxodon (Elephas)</i> <i>recki</i>	X	
	<i>Elephantidae</i> cf. <i>Loxodonta africana</i>		X
Carnivora	<i>Crocota</i> sp. nov.	X	
	<i>Crocota crocuta</i> /cf. Hyenidae	X	X
	<i>Canis</i> cf. <i>mesomelas</i>	X	
	<i>Canis</i> sp. - size 1b1c		X
	cf. <i>Panthera</i> sp.	X	
	<i>Felis</i> sp. indet.		X
	<i>Genetta</i> sp.	X	
	<i>Otocyon megalotis</i>		X
Primates	<i>Theropithecus oswaldi</i>	X	
	<i>Homo</i> cf. <i>H. erectus</i>	X	
	<i>Homo</i> sp. (MSA artifacts)		X
Rodentia	<i>Hystrix cristata</i>		X
	<i>Pedetes</i> sp.		X
	<i>Lepus</i> sp.		X

Fig. 3. Acheulean-associated and MSA-associated mammalian taxa of the Ologesailie basin.

depositional zones during the past ~320 ka of Ologesailie basin history (25). Tectonics also contributed to the topographic heterogeneity of the southern Kenya rift (30, 31). Because spatial and temporal habitat variability strongly influences resource patchiness and predictability, rapidly shifting environments at the outset of the Oltulelei Fm imply strong selective pressures on resource acquisition by hominins. Both the faunal turnover and MSA replacement of the Acheulean took place in this dynamic setting. Evidence of grassland expansion associated with the Ologesailie MSA further implies that MSA hominins encountered periods of intensified resource uncertainty. Foraging

unpredictability, with increased potential for resource scarcity, describes the conditions in which human hunter-gatherers broaden the spatial scale of the landscape they encounter through a combination of wider mobility, information and resource sharing, and the maintenance of resource exchange networks (8, 10, 32). These responses also characterize the Ologesailie MSA, in contrast to the behavioral record associated with the older Acheulean of the region (11). We thus hypothesize that the emergence of the MSA and its wholesale replacement of the Acheulean in the Kenya rift by ~320 ka ago represents an evolutionary response to resource landscapes that were less predictable in time (as a result of

amplified climate variability throughout eastern Africa) and were also more heterogeneous in space (as a result of local tectonic activity). Although we are not claiming that MSA technology originated in the Ologesailie basin, the changing conditions and depositional sequence there document the environmental correlates associated with its appearance in southern Kenya.

Although immediate MSA precursors in the Ologesailie basin cannot be investigated because of the erosional gap from 499 to 320 ka ago, recovery of Acheulean materials from intervals of enhanced climate oscillation recorded in Members 11, 12, and 14 of the upper Ologesailie Fm (Fig. 1A: sites B11-500, AW12-10, and D14-10) indicate that Acheulean toolmakers between 615 and 499 ka ago (18) produced smaller cores and flakes, and also increased their access to distant stone sources and were more selective of stone material than earlier in the Acheulean (Fig. 1D and text S3 and S4). These aspects of foraging technology suggest that, at least in periods of strong environmental variability, Acheulean hominins broadened their mobility and range of resource acquisition within the limits of a technology typified by the manufacture of large cutting tools. These incipient similarities to the MSA point to variation within the Acheulean that, by 615 ka ago, appears to have laid a foundation for the later evolution of adaptable behaviors distinctive of *H. sapiens*.

REFERENCES AND NOTES

1. P. B. deMenocal, *Science* **270**, 53–59 (1995).
2. M. H. Trauth, M. A. Maslin, A. Deino, M. R. Strecker, *Science* **309**, 2051–2053 (2005).
3. R. Potts, *Science* **273**, 922–923 (1996).
4. P. B. deMenocal, *Science* **331**, 540–542 (2011).
5. R. Potts, J. T. Faith, *J. Hum. Evol.* **87**, 5–20 (2015).
6. A. M. Siepielski et al., *Science* **355**, 959–962 (2017).
7. D. P. Vázquez, E. Gianoli, W. F. Morris, F. Bozinovic, *Biol. Rev. Camb. Philos. Soc.* **92**, 22–42 (2017).
8. R. L. Kelly, *The Lifeways of Hunter-Gatherers: The Foraging Spectrum* (Cambridge Univ. Press, 2013).
9. J. Yellen, H. Harpending, *World Archaeol.* **4**, 244–253 (1972).
10. R. Dyson-Hudson, E. A. Smith, *Am. Anthropol.* **80**, 21–41 (1978).
11. A. S. Brooks et al., *Science* **360**, 90–94 (2018).
12. E. Boeda, in *The Definition and Interpretation of Levallois Technology*, H. Dibble, O. Bar-Yosef, Eds. (Prehistory Press, Madison, WI, 1995), pp. 41–68.
13. S. McBrearty, A. S. Brooks, *J. Hum. Evol.* **39**, 453–563 (2000).
14. D. Richter et al., *Nature* **546**, 293–296 (2017).
15. C. A. Tryon, J. T. Faith, *Curr. Anthropol.* **54**, S234–S254 (2013).
16. G. L. Isaac, *Ologesailie: Archeological Studies of a Middle Pleistocene Lake Basin in Kenya* (Univ. of Chicago Press, 1977).
17. M. P. Noll, thesis, University of Illinois at Urbana-Champaign (2000).
18. A. L. Deino et al., *Science* **360**, 95–98 (2018).
19. J.-J. Hublin et al., *Nature* **546**, 289–292 (2017).
20. I. McDougall, F. H. Brown, J. G. Fleagle, *J. Hum. Evol.* **55**, 409–420 (2008).
21. See supplementary materials.
22. A. Deino, R. Potts, *J. Geophys. Res.* **95**, 8453–8470 (1990).
23. A. K. Behrensmeier, R. Potts, A. Deino, P. Ditchfield, in *Sedimentation in Continental Rifts*, R. W. Renaut, G. M. Ashley, Eds. (SEPM Special Publication 73, 2002), pp. 97–106.
24. W. G. Melson, R. Potts, *J. Archaeol. Sci.* **29**, 307–316 (2002).
25. A. K. Behrensmeier, R. Potts, A. Deino, *Bull. Geol. Soc. Am.* **10.1130/B31853.1** (2018).
26. R. Potts, A. Deino, *Quat. Res.* **43**, 106–113 (1995).
27. E. D. Lorenzen, R. Heller, H. R. Siegmund, *Mol. Ecol.* **21**, 3656–3670 (2012).
28. A. K. Behrensmeier, N. E. Todd, R. Potts, G. E. McBrinn, *Science* **278**, 1589–1594 (1997).

29. J. T. Faith *et al.*, *Palaeogeogr. Palaeoclimatol. Palaeoecol.* **361–362**, 84–93 (2012).
30. M. Marsden, thesis, McGill University (1979).
31. A. Guth, J. Wood, *Geology of the Magadi Area, Kenya* (Geological Society of America, 2013).
32. B. Winterhalder, *J. Anthropol. Archaeol.* **5**, 369–392 (1986).
33. Ø. Hammer, D. A. T. Harper, *Paleontological Data Analysis* (Blackwell, 2006).
34. D. J. de Ruiter, M. Sponheimer, J. A. Lee-Thorp, *J. Hum. Evol.* **55**, 1015–1030 (2008).
35. E. S. Vrba, in *Fossils in the Making*, A. K. Behrensmeyer, A. P. Hill, Eds. (Univ. of Chicago Press, 1980), pp. 247–272.
36. Z. Alemseged, *J. Hum. Evol.* **44**, 451–478 (2003).
37. N. E. Levin, *Compilation of East Africa Soil Carbonate Stable Isotope Data* (Interdisciplinary Earth Data Alliance, 2013).
38. T. E. Cerling *et al.*, *Nature* **476**, 51–56 (2011).

ACKNOWLEDGMENTS

We thank the National Museums of Kenya and M. Kibunja, I. O. Farah, F. K. Manthi, E. N. Mbua, M. Muungu, E. Ndiema, P. Kiura,

C. M. Kilonzi, S. M. Musyoka, J. N. Mativo, A. M. Kioko, B. L. Pobiner, J. Moerman, and K. Meshida for support. J. M. Nume, B. Kanunga, and C. M. Kilonzi managed the excavation teams. We acknowledge Kenya Government permission granted by the Ministry of Sports, Culture and the Arts, and by NACOSTI permit P/14/7709/683.

Funding: Supported by the Peter Buck Fund for Human Origins Research, Smithsonian Institution (R.P.), NSF HOMINID Program grant BCS-0218511 (R.P.), and NSF Archaeometry grant EAR-1322017 (A.L.D.). **Author contributions:** R.P. was principal author and directed the project; A.K.B. and A.L.D. led the geological research; A.S.B., J.E.Y., R.P., and C.A.T. led the excavations and recovery of archeological and fossil materials; R.P., J.T.F., J.B.C., C.M.H., and H.J.M.M. conducted faunal analysis; R.P. conducted the lithic analysis, reviewed by A.S.B. and C.A.T.; R.K. conducted phytolith sampling and analysis; N.E.L. carried out carbonate sampling and stable isotopic analysis; J.B.C. composed the figures; E.G.V. and J.B.C. drew and photographed the stone artifacts; R.B.O. and R.W.R. carried out analysis of spring deposits; and all authors contributed to the writing and review of the manuscript.

Competing interests: The authors have no competing interests.

J.E.Y. contributed to this article in his personal capacity; any opinions, findings, and conclusions or recommendations expressed in this material are those of the authors and do not reflect the views of the NSF. **Data and materials availability:** All data are available in the paper and supplementary materials, and all archeological and paleontological collections and field records are archived in the Department of Earth Sciences, National Museums of Kenya.

SUPPLEMENTARY MATERIALS

www.sciencemag.org/content/360/6384/86/suppl/DC1
Materials and Methods
Supplementary Text S1 to S4
Figs. S1 to S10
Tables S1 to S6
References (39–69)

27 June 2017; accepted 14 February 2018
Published online 15 March 2018
10.1126/science.aao2200

PALEOANTHROPOLOGY

Long-distance stone transport and pigment use in the earliest Middle Stone Age

Alison S. Brooks,^{1,2*} John E. Yellen,^{2,3} Richard Potts,^{2,4*} Anna K. Behrensmeyer,⁵ Alan L. Deino,⁶ David E. Leslie,⁷ Stanley H. Ambrose,⁸ Jeffrey R. Ferguson,⁹ Francesco d'Errico,^{10,11} Andrew M. Zipkin,⁸ Scott Whittaker,¹² Jeffrey Post,¹³ Elizabeth G. Veatch,¹⁴ Kimberly Foecke,¹ Jennifer B. Clark²

Previous research suggests that the complex symbolic, technological, and socioeconomic behaviors that typify *Homo sapiens* had roots in the middle Pleistocene <200,000 years ago, but data bearing on human behavioral origins are limited. We present a series of excavated Middle Stone Age sites from the Olorgesailie basin, southern Kenya, dating from $\geq 295,000$ to $\sim 320,000$ years ago by argon-40/argon-39 and uranium-series methods. Hominins at these sites made prepared cores and points, exploited iron-rich rocks to obtain red pigment, and procured stone tool materials from ≥ 25 - to 50-kilometer distances. Associated fauna suggests a broad resource strategy that included large and small prey. These practices imply notable changes in how individuals and groups related to the landscape and to one another and provide documentation relevant to human social and cognitive evolution.

The Middle Stone Age (MSA) comprises a diverse group of African industries characterized by the absence or rarity of large cutting tools (LCTs, such as Acheulean handaxes and cleavers), the presence of prepared core (Levallois) technologies, and regional and/or temporal variation in weapon armatures (1–3). Later MSA industries contain varying frequencies of small retouched bladelets and geometric artifacts (4), small unifacially and bifacially worked points, and larger lanceolate and bone points (5, 6). African MSA sites are associated with the oldest known fossils attributed to *Homo sapiens*, which date between ~ 195 and ~ 350 thousand years

(ka) ago (7–9). After 130 ka ago, late Pleistocene MSA sites, mostly from the north and south temperate zone extremities of the continent, document some of the oldest beads (10, 11), complex geometric designs (12, 13), lithic projectile armatures interpreted as arrow or dart tips (14, 15), paint production (16), heat treatment of lithics (17), and expanded resource use, including fishing and shellfish collecting (18, 19).

Although these late Pleistocene behaviors are thought to reflect advanced cognitive abilities for learning, imitation, working memory, planning, and recursive technological innovation, their middle Pleistocene or earlier antecedents have remained obscure. Evolutionary explanations for the middle Pleistocene enlargement of relative brain size, largely overlapping the modern *H. sapiens* range, include a shift to larger social groups or networks (20); greater foraging, technological, and social adaptability in the face of more rapid and unpredictable climate fluctuations (21); and the development of symbolic expression (22).

Middle Pleistocene evidence from >200 ka ago for the emergence of these new cognitive and social behaviors is limited to a small number of isolated sites and site complexes, mostly in tropical and subtropical Africa and also in the northwest (8, 23–26). The most extensive record in both chronological coverage and individual excavations is from the Kapthurin Formation in Kenya (27–30).

Olorgesailie is a $\sim 65\text{-km}^2$ paleolake basin in the southern Kenya rift where more than 75 years of research have documented Acheulean sites in the Olorgesailie Formation, dating from 1.2 million years ago to 499 ka ago (31, 32). From 2001 to 2011, the Smithsonian team investigated sites in the younger Oltulelei Formation (33, 34). Seventeen excavations were conducted in Localities B and G in the Oltulelei Formation, including 11

in the Olkesititi Member (Fig. 1). The five oldest sites are described here (35). The oldest (~ 305 to 320 ka old) and the youngest (between ~ 295 and ~ 298 ka old) (32) yielded some of the earliest evidence for MSA lithic industries lacking LCTs (Fig. 2 and fig. S5).

These MSA sites occur in a topographically complex paleolandscape marked by repeated channel erosion and filling, periodic influxes of volcanics, tectonic shifts, and spring-deposited tufas (33, 34). The oldest MSA sites in Locality B (BOK-1E and BOK-3; Fig. 1) directly overlie channel-deposited gravels representing initial aggradation after the long (~ 180 ka) erosional hiatus between the Olorgesailie and Oltulelei Formations. These gravels postdate the ~ 499 -ka capping age of the former and predate the ~ 305 -ka-old tephra overlying the BOK-1E occupations (32). Site BOK-2 is slightly higher stratigraphically and underlies the ~ 305 -ka-old tephra and a ~ 302 -ka-old tuff, whereas BOK-4 is, as noted above, slightly younger (between ~ 295 and ~ 298 ka old) (Fig. 1).

In eastern Locality G, the Olorgesailie Formation is absent in most outcrops. We infer that the well-developed red paleosol containing the GOK-1 lithic industry formed after Olorgesailie Formation deposition ceased <500 ka ago. Archaeological site formation in the GOK-1 red soil was followed by a widespread erosional unconformity. A U-series date of 277 ± 1.8 ka old in deposits overlying the unconformity provides an upper limit for the age of GOK-1. Subsequent volcanoclastic units above the unconformity at GOK-1 are dated at ~ 220 ka ago (32). The lithic industry shares comparable percentages of diagnostic MSA elements (table S3) with the two oldest sites in Locality B. No LCTs were found in the extensive GOK-1 excavations. Together, the stratigraphic context and flaked stone artifacts suggest that the age of GOK-1 is comparable to or possibly older than that of the early Locality B MSA sites (Fig. 1).

All early Locality B sites are in fine-grained silty or sandy sediments that represent low-energy sedimentation in channel-fill settings above the basal gravels. The absence of preferential orientation of long axes and abundance of artifacts <2 cm in maximum dimension (table S2), together with large cores, grindstones, and hammerstones (table S3), indicate that the artifact assemblages were deposited by hominins in or near inactive channels, followed by only minor postdepositional sorting or winnowing. Sets of refitted obsidian artifacts at BOK-2 and BOK-4 (figs. S3 and S4 and table S2) further indicate the integrity of the artifact assemblages.

Most artifacts at all but one of the Olkesititi Member sites were made on local volcanic rocks with 1 to 8% nonlocal obsidian and chert (table S4). The small amount (0 to 2%) of green, brown, and white chert has not been sourced but is not available locally. Even within the lavas, a preference for fine-grained rocks is evidenced by the predominance of Mt. Olorgesailie basalt, which lacks visible phenocrysts and was available at outcrops within 2 km.

At BOK-2, however, 42% of the plotted artifacts (table S5) are obsidian, which has no known local

¹Center for the Advanced Study of Human Paleobiology, Department of Anthropology, George Washington University, Washington, DC 20052, USA. ²Human Origins Program, National Museum of Natural History, Smithsonian Institution, Washington, DC 20013-7012, USA. ³Archaeology Program, National Science Foundation, Alexandria, VA 22314, USA. ⁴Department of Earth Sciences, National Museums of Kenya, Post Office Box 40658-00100, Nairobi, Kenya. ⁵Department of Paleobiology, National Museum of Natural History, Smithsonian Institution, Washington, DC 20013-7012, USA. ⁶Berkeley Geochronology Center, Ridge Road, Berkeley, CA 94709, USA. ⁷Department of Anthropology, University of Connecticut, Storrs, CT 06269, USA. ⁸Department of Anthropology, University of Illinois at Urbana-Champaign, Urbana, IL 61801, USA. ⁹University of Missouri Research Reactor Center, Columbia, MO 65211, USA. ¹⁰Centre National de la Recherche Scientifique, UMR 5199-Dé la Préhistoire à l'Actuel: Culture, Environnement et Anthropologie (PACEA), Université de Bordeaux, 33615 Pessac, France. ¹¹Senter for Fremragende Forskning (SFF) Centre for Early Sapiens Behaviour (SapienCE), University of Bergen, Postboks 7805, 5020 Bergen, Norway. ¹²Laboratory of Analytical Biology, National Museum of Natural History, Smithsonian Institution, Washington, DC 20013-7012, USA. ¹³Department of Mineral Sciences, National Museum of Natural History, Smithsonian Institution, Washington, DC 20013-7012, USA. ¹⁴Department of Anthropology, Emory University, Atlanta, GA 30322, USA. *Corresponding author. Email: abrooks@gwu.edu (A.S.B.); potts@si.edu (R.P.)

usable outcrop or conglomerate source. Compositional analysis of 688 obsidian artifacts from BOK-2 and BOK-4 was carried out by several techniques, including portable x-ray fluorescence (pXRF) and neutron activation analysis (NAA), to determine probable sources, based on a large database of known provenience. About 78% of the Olorgesailie samples are attributed to seven source groups located in direct lines from 25 to 50 km from the BOK sites in five different directions. A small number of samples were from more distant sources (Fig. 3). Given the rugged terrain of the southern Kenya rift, the walking distance would have been considerably longer

than the straight-line distance. For four occupation horizons at BOK-2, the source diversity and distance are smallest in the oldest level and largest in the youngest (Fig. 3, bottom panels).

Large obsidian flakes and cores weighing 60 to 90 g, refit sequences (figs. S3 and S4), low cortex ratios, and the presence of >46,000 obsidian pieces <2 cm in size at BOK-2 and 226 pieces at BOK-4 (tables S2 and S4) indicate that obsidian was brought in as raw material and worked on-site rather than imported as finished artifacts. Average cortex ratios on whole flakes are low (0 to 25%) for both local and exotic common materials in the Locality B sites (table S4). Long-

distance obsidian transport at Olorgesailie precedes previously documented occurrences (30) by ~80 to 100 ka.

The distinct artifact levels at BOK-2 represent multiple reoccupations, also evident at BOK-1E and GOK-1, indicating repeated visits to focal landscape points in the basin, likely related to resource availability.

Analysis of lithic technology (Fig. 3, fig. S5, and table S3) at all five sites supports attribution to the MSA rather than to the Acheulean. First, no large cutting tools were recovered in the excavations, although a few surface finds of core axes and picks with trihedral points and unfinished bases were recovered on a red-soil surface below GOK-1; such artifacts are typical of early post-Acheulean industries of middle Pleistocene age in eastern and central Africa (36) (fig. S1). Second, diverse technological sequences recovered in situ included prepared cores, especially Levallois, or asymmetrical cores (Fig. 2, H and I, and fig. S5); other core strategies included the production of blade and bladelet cores (Fig. 2G), bipolar cores on small chert and obsidian nodules, and discoidal and multiplatform cores. Third, the desired end products were predominantly small- to medium-sized flakes (<5-cm average length), especially flakes that were relatively thin (table S4). Fourth, flat invasive retouch was used to shape some of the points and the more rounded “ovates.”

Classic MSA end products at the Locality B sites reflect innovation and standardization that were not present earlier. These include pointed forms (Fig. 2 and table S3) both unretouched and retouched at BOK-2, BOK-4, and BOK-1E. Retouched points were preferentially made on obsidian at BOK-2 and on chert at BOK-4. The bases of some points have been thinned or modified in a manner typical of hafting (Fig. 2, D and F). Perforators, side and end scrapers, notched and denticulate pieces, and other retouched forms are present at all three sites. At BOK-2, a series of short end scrapers on obsidian flakes occur, as well as very small scrapers on flakes (fig. S2). In summary, the industries of these early sites fit within the scope of African industries grouped as MSA in the diversity of artifact forms and technological approaches to tool manufacture.

More than 2000 faunal remains of 23 larger (>2 kg) mammalian taxa, micromammals, reptiles, birds, and fish were recovered from the Locality B sites in association with the lithics; these remains carry implications for reconstructing both human behavior and paleoenvironments and are presented in detail in (34). Surface markings document human use. Carnivore remains are rare and do not suggest a den concentration, and dens or burrows were not present in the excavated sediments. The most common taxa include equids, suids, eland, kudu, an extinct alcelaphin (*Damaliscus hypsodon*), springbok, bat-eared fox, springhare, and root rat. The presence of many relatively smaller taxa suggests direct predation by humans rather than scavenging, as small taxa remains are unlikely to survive initial consumption by primary predators. Comparable recent

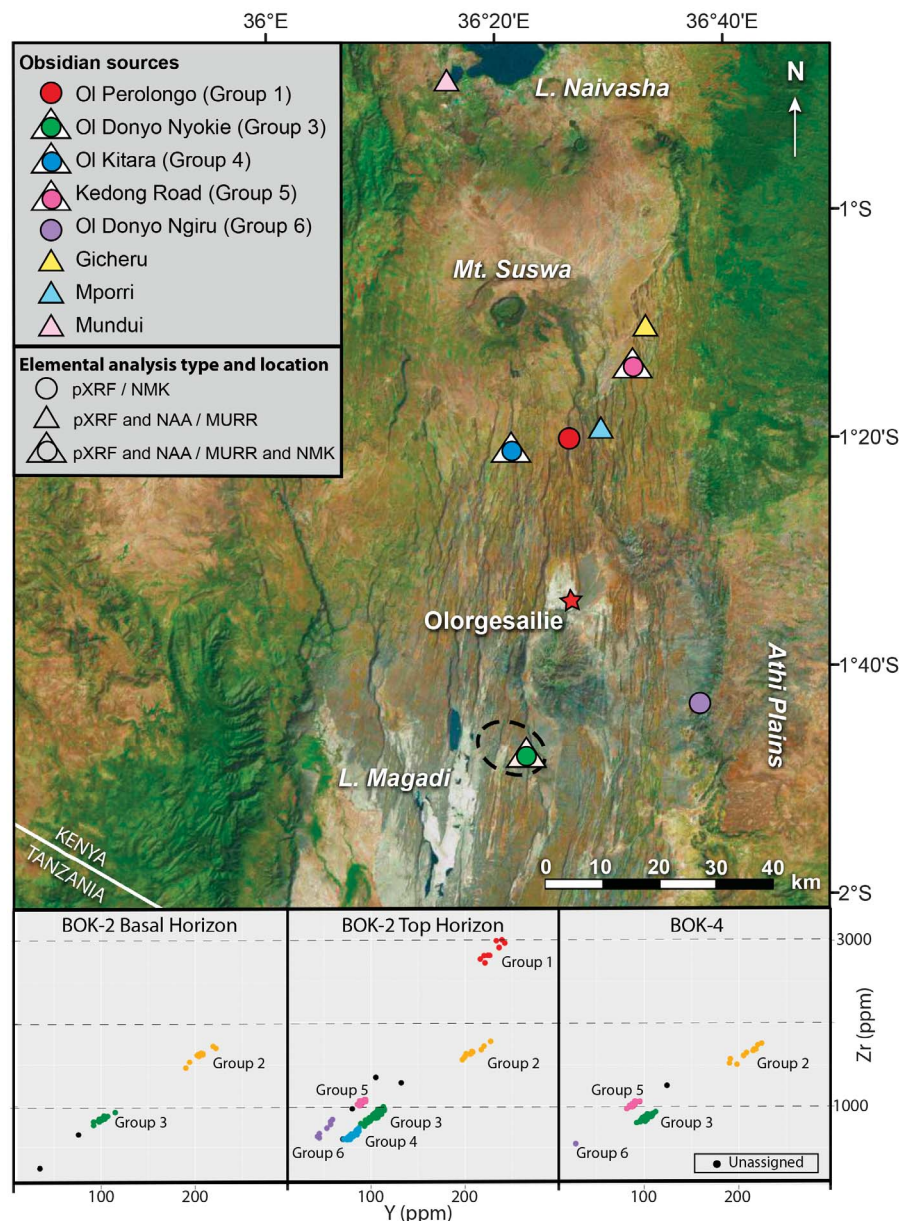


Fig. 3. Location of major obsidian sources. Sources matched chemically to Olorgesailie MSA artifacts by pXRF and NAA at the University of Missouri Research Reactor (MURR) and/or by pXRF at the National Museums of Kenya (NMK). The bottom panels are chemical plots that show the use of multiple sources in basal and upper levels at BOK-2 and BOK-4. Source group 2 is an unknown source. ppm, parts per million.

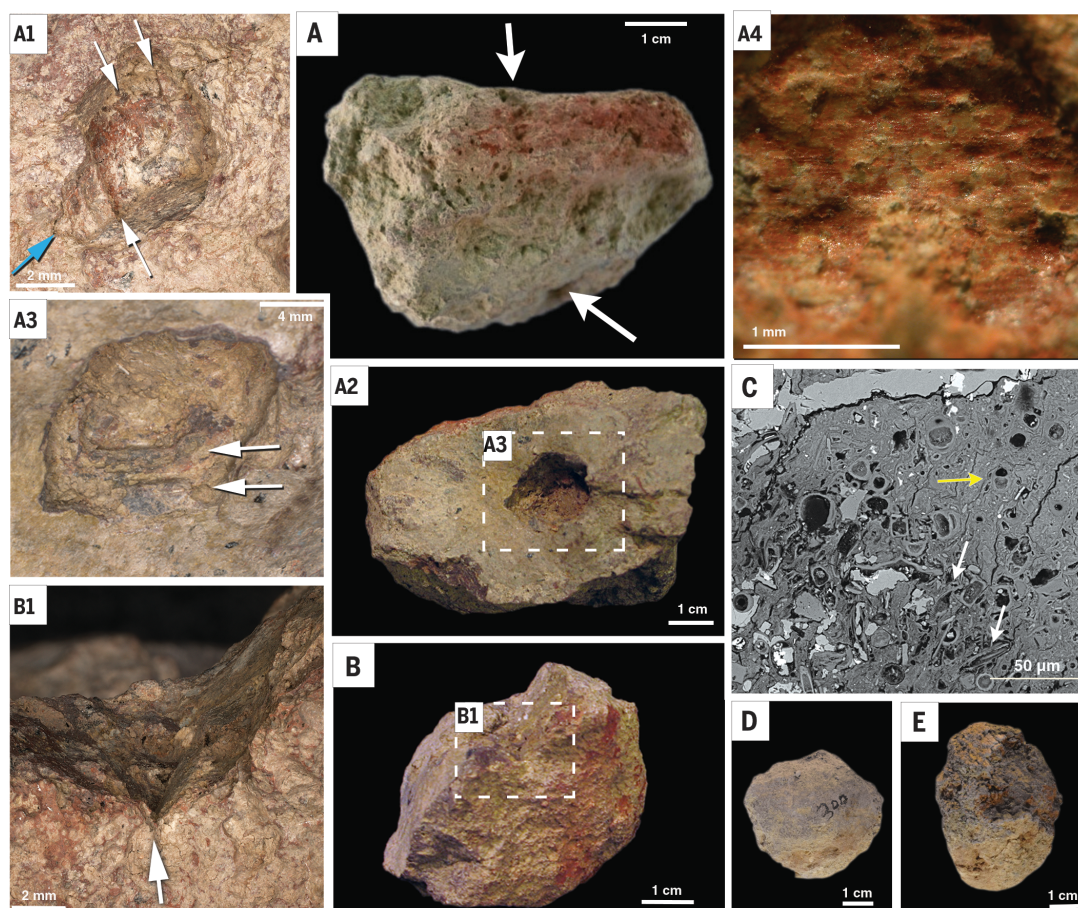


Fig. 4. MSA pigments from Olorgesailie. (A) From GOK-1, large ochre block (specimen 6) with two opposing holes (white arrows) and abraded red area. (A1) Smaller lower hole with chop marks made by sharp, straight-edged tool (white arrows), a gouge mark (blue arrow) in lower left corner, and vertical walls left and right. (A2) Top view of the large ochre block. (A3) Magnified view of area enclosed by dashed rectangle in (A2). Larger upper hole with chop marks (white arrows) and gouge mark (lower left). (A4) Magnified view of abraded red area showing striations. (B) From GOK-1, smaller block with red streaks and notch in upper left (specimen 7). (B1) Magnified view of notch showing chop mark (white arrow). (C) Surface section of a BOK-1E lump, showing diatoms (white arrows), possible cyanobacterium (yellow arrow), and manganese infillings. (D and E) Pigment examples from BOK-1E.

African forager reliance on small mammals, including small carnivores, is documented in table S15.

Given the age of the sites, of particular interest are mineral pigments from two of the five sites: BOK-1E and GOK-1. Within the upper artifact horizon at BOK-1E, were 86 rounded concretionary lumps of soft dark mineral. One nodule analyzed by scanning electron microscopy energy-dispersive x-ray spectroscopy consists mainly of calcite with fluorite inclusions and veins of manganese oxide, a dark brown-to-black potential pigment, whereas the nodule's surface layer contains diatoms and possibly cyanobacteria, indicating formation in water (Fig. 4C) (supplementary text S6). Test squares extending both north and south from the excavation indicated that, although the sediment enclosing the artifacts continues in both directions, the dark mineral lumps occur only in association with artifacts. This association, together with the lack of evidence for standing water around the artifact horizon, suggests that these specimens were collected and brought to the site by hominins, although they were too friable to preserve grinding striations (supplementary text S6).

In the GOK-1 excavation, two rocks that have bright red streaks and patches were recovered in the red soil, one (specimen 7) in the uppermost unit and one (specimen 6) in the middle unit. Specimen 6 has two opposing holes, initially

thought to be of geological origin. Microscopic examination revealed that the red streaks on this stone are grinding striations (Fig. 4, panel A4), and geochemical analysis of the rock by laser ablation inductively coupled plasma mass spectrometry (LA-ICPMS) (fig. S8, A and B) indicated that it is mainly composed of iron mineral. Rather than a grindstone that was used to produce pigment, this is interpreted as a lump of ochre pigment that had been ground. Further visual examination with a free-angle zoom microscope documented chop marks in the two opposing holes, one large and one small, as well as in the notches of the second rock (specimen 7), indicating that the holes and notches are anthropogenic (Fig. 4). Geochemical comparison of the GOK-1 red rocks with potential local sources indicates that the rocks are exotic to the immediate region and not derived from the nearest potential source located on Mt. Olorgesailie (fig. S9). Although earlier ochre has been occasionally reported, evidence of anthropogenic transport and utilization is rarely documented [but see (1, 37)]. The GOK-1 rocks are thus among the oldest-known clearly worked pigments and the oldest evidence of a possible attempted perforation. Although ochre can have utilitarian functions, experimental data have shown that these functions can also be satisfied by less-brightly colored minerals (38), suggesting that transport of exotic bright red and black rocks may have been valued for their bright

color and used as symbolic communicators of identity or status.

The evidence from the five oldest MSA sites at Olorgesailie has multiple implications for understanding human behavioral evolution. First, this evidence indicates that distinctive technological features of the African MSA reflecting innovation, standardization, and new cognitive abilities had already been developed in eastern Africa before 300 ka ago. Second, the repeated occurrence of exotic raw materials from multiple distant sources as cores, knapping products, and finished artifacts and the quantities involved suggest a new behavior in the human repertoire: the formation of networks of exchange or procurement over a substantial area. At least two sources were used in the oldest level at BOK-2, and four to six sources were used in the later horizons of this site and at BOK-4 (Fig. 3). The formation of extended networks and social connections is an important universal aspect of ethnographically documented hunter-gatherer adaptations to unpredictable environments and is effective strategy for risk mitigation (39, 40). Expanded social networks are one possible explanation for the middle Pleistocene increase in relative brain size (20), although evidence supporting this social expansion >300 ka ago was not previously available. Along with improved lithic technology, particularly stone-tipped weapons, and a more diverse economic strategy suggested

by the faunal remains, larger-scale social relationships would have provided a buffer against increased climate variation and resource unpredictability (34, 39, 40).

In a Kalahari environment comparable to that implied by the BOK sites, fauna, isotopes, and other indicators (34), modern hunter-gatherer families maintain contacts with exchange partners up to a 100-km distance but generally range over only a 20-km radius annually (39). Thus, the distances implied by the range of obsidian procurements somewhat exceeds the likely home range in the Olorgesailie environment of a small family-based band but are consistent with exchange-network sizes of modern people in a similar environment. The absence of this pattern from the underlying Acheulean levels (34) indicates that this major transition in human social and cognitive behavior occurred before 300 ka ago but postdated 500 ka ago. Finally, the apparent association of early pigment use and expanded social networks implied by the repetitive use of exotic raw materials from multiple sources suggests that the pigment itself may also have been of social and symbolic importance.

REFERENCES AND NOTES

1. S. McBrearty, A. S. Brooks, *J. Hum. Evol.* **39**, 453–563 (2000).
2. C. A. Tryon, J. T. Faith, *Curr. Anth.* **54** (S8), S234–S254 (2013).
3. E. M. Scerri, *Quat. Int.* **300**, 111–130 (2013).
4. S. Wurz, *Curr. Anth.* **54** (S8), S305–S319 (2013).
5. C. S. Henshilwood, F. d'Errico, C. W. Marean, R. G. Milo, R. Yates, *J. Hum. Evol.* **41**, 631–678 (2001).
6. J. J. Shea, *J. Hum. Evol.* **55**, 448–485 (2008).
7. D. Richter *et al.*, *Nature* **546**, 293–296 (2017).
8. J.-J. Hublin *et al.*, *Nature* **546**, 289–292 (2017).
9. K. Kuman, M. Inbar, R. Clarke, *J. Archaeol. Sci.* **26**, 1409–1425 (1999).
10. A. Bouzouggar *et al.*, *Proc. Natl. Acad. Sci. U.S.A.* **104**, 9964–9969 (2007).
11. F. d'Errico, C. Henshilwood, M. Vanhaeren, K. van Niekerk, *J. Hum. Evol.* **48**, 3–24 (2005).
12. P.-J. Texier *et al.*, *J. Archaeol. Sci.* **40**, 3412–3431 (2013).
13. C. S. Henshilwood *et al.*, *Science* **295**, 1278–1280 (2002).
14. A. S. Brooks, L. Nevell, J. E. Yellen, G. Hartman, in *Transitions Before the Transition*, E. Hovers, S. L. Kuhn, Eds. (Springer, 2006), pp. 233–255.
15. M. Lombard, M. N. Haidle, *Camb. Archaeol. J.* **22**, 237–264 (2012).
16. C. S. Henshilwood *et al.*, *Science* **334**, 219–222 (2011).
17. K. S. Brown *et al.*, *Science* **325**, 859–862 (2009).
18. A. S. Brooks *et al.*, *Science* **268**, 548–553 (1995).
19. C. W. Marean *et al.*, *Nature* **449**, 905–908 (2007).
20. R. I. Dunbar, *Annu. Rev. Anth.* **32**, 163–181 (2003).
21. R. Potts, *Quat. Sci. Rev.* **73**, 1–13 (2013).
22. T. W. Deacon, *The Symbolic Species: The Co-evolution of Language and the Brain* (Norton, 1998).
23. L. Barham, *The Middle Stone Age of Zambia, South Central Africa* (Western Academic & Specialist Press, 2000).
24. S. McBrearty, C. Tryon, in *Transitions Before the Transition*, E. Hovers, S. L. Kuhn, Eds. (Springer, 2006), pp. 257–277.
25. N. Porat *et al.*, *J. Arch. Sci.* **37**, 269–283 (2010).
26. Y. Sahle, L. E. Morgan, D. R. Braun, B. Atnafu, W. K. Hutchings, *Quat. Int.* **331**, 6–19 (2014).
27. A. L. Deino, S. McBrearty, *J. Hum. Evol.* **42**, 185–210 (2002).
28. C. A. Tryon, S. McBrearty, *Quat. Res.* **65**, 492–507 (2006).
29. D. E. Leslie, S. McBrearty, G. Hartman, *Palaeogeogr. Palaeoclimatol. Palaeoecol.* **449**, 27–40 (2016).
30. N. Blegen, *J. Hum. Evol.* **103**, 1–19 (2017).
31. A. Deino, R. Potts, *J. Geophys. Res. Solid Earth* **95** (B6), 8453–8470 (1990).
32. A. L. Deino *et al.*, *Science* **360**, 95–98 (2018).
33. A. K. Behrensmeier, R. Potts, A. Deino, *GSA Bull.* 10.1130/B31853.1 (2018).
34. R. Potts *et al.*, *Science* **360**, 86–90 (2018).
35. Materials and methods are available as supplementary materials.
36. J. D. Clark, *Kalambo Falls Prehistoric Site* (Cambridge Univ. Press, 2001), vol. 3, pp. 234–285.
37. I. Watts, M. Chazan, J. Wilkins, *Curr. Anth.* **57**, 287–310 (2016).
38. A. M. Zipkin, M. Wagner, K. McGrath, A. S. Brooks, P. W. Lucas, *PLOS ONE* **9**, e112560 (2014).
39. J. Yellen, H. Harpending, *World Archaeol.* **4**, 244–253 (1972).
40. P. Wiessner, Risk, in *Politics and History in Band Societies*, E. Leacock, R. Lee, Eds. (Cambridge Univ. Press, 1982), pp. 61–84.

ACKNOWLEDGMENTS

We are grateful to the National Museums of Kenya (NMK) and the Ministry of Sports, Culture, and the Arts for support of this project. Special thanks to M. Kibunja, I. O. Farah, F. K. Manthi, E. N. Mbua, M. Muungu, J. Mwangi, C. Ogola, E. Ndiema, P. Kiura, C. M. Kilonzi, S. M. Musyoka, J. N. Mativo, A. M. Kioko, C. Kirwa, J. M. Munyiri, and F. Bante for their contributions at the NMK. J. M. Nume, B. Kanunga, and C. M. Kilonzi were in charge of the excavation teams. We thank S. Nchilalo, E. ole Keri, and S. ole Keri for guidance to obsidian and ochre sources, D. Wawrzyniak for assistance with obsidian compositional tables, J. Watson and N. Little for initial analysis of the pigments, and L. Dussubieux for laboratory assistance and use of facilities at The Field Museum of Natural History (Chicago) for ochre compositional studies. The following individuals also contributed to field and laboratory research: W. G. Sharp, J. T. Faith, C. M. Haradon, C. A. Tryon, E. M. Williams, K. Ranhorn, N. E. Levin, A. G. Henry, F. Gomez, A. Bauernfeind, R. Biermann, R. Kinyajui, R. B. Owen, and R. W. Renaut. **Funding:** Kenya field and Kenya and U.S. laboratory work were supported by the Peter Buck Fund for Human Origins research (Smithsonian Institution) (R.P.) and by NSF Human Origins: Moving in New Directions (HOMINID) award BCS-0218511 (R.P.). Field and laboratory work by A.M.Z. on obsidian and ochre

sourcing was supported by NSF Graduate Research Fellowship 2011116368 (A.M.Z.), NSF Doctoral Dissertation Research Improvement Grant BCS-1240694 (A.S.B. and A.M.Z.), NSF Integrative Graduate Education and Research Traineeship (IGERT) award DGE-0801634 to George Washington University, and Wenner-Gren Foundation Dissertation Fieldwork Grant 8623 (A.M.Z.). Laboratory analyses on dating samples were funded by NSF grant EAR-1322017 to A.L.D. Field and laboratory research on Kenya obsidian sourcing was funded by NSF awards to the University of Missouri Research Reactor Center (BCS-0802757) and to J.R.F. and S.H.A. for the Kenya obsidian project (BCS-0814304). Laboratory work on the ochre by F.d'E. was funded by the Research Council of Norway (SFF Centre SapienCE), project number 262618, and the Université de Bordeaux LaScArBx research program (ANR-10-LABX-52). J.E.Y. was supported by the NSF and by the Smithsonian Institution Olorgesailie project. **Author contributions:** A.S.B. and J.E.Y. led the survey, excavation, and analysis of the MSA sites and preparation of relevant tables and figures; R.P. directed the overall Olorgesailie Project and analyzed the fauna and nonobsidian volcanic materials; A.K.B. and A.L.D. conducted the geological study and sampling of the Olutielele Formation; A.L.D. conducted ⁴⁰Ar/³⁹Ar dating; J.E.Y. identified artifact raw materials and carried out pXRF analysis at the NMK; D.E.L. conducted the refitting studies; S.H.A. led the Kenyan field study of obsidian sources and participated in the source chemistry analysis; J.R.F., S.H.A., and K.F. conducted geochemical studies of sources and artifacts; F.d'E. conducted the first microscopy that demonstrated grinding striations on the ochre; A.M.Z. assisted with the excavations and led the study of ochre sources, including geochemical compositional study of the ochre pieces by LA-ICPMS at the Field Museum of Natural History (Chicago); S.W. conducted microscopy on the anthropogenic modifications of the ochre pieces; J.P. analyzed dark pigment in polished section; E.G.V. produced the lithic drawings; and J.B.C. conducted the microfauna study and prepared the figures, including artifact photography and computer assembly. A.S.B. was the principal author, with major sections contributed by A.K.B., S.H.A., A.M.Z., and K.F., and R.P. edited the paper. **Competing interests:** The authors declare no competing interests. J.E.Y. contributed to this article in his personal capacity; any opinions, findings, and conclusions or recommendations expressed in this material are those of the authors and do not reflect the views of the NSF. **Data and materials availability:** All data are available in the paper and supplementary materials, and all archaeological, paleontological, and obsidian-source reference collections and field records are archived in the NMK, Department of Earth Sciences.

SUPPLEMENTARY MATERIALS

www.sciencemag.org/content/360/6384/90/suppl/DC1
Materials and Methods
Supplementary Text
Figs. S1 to S10
Tables S1 to S15
References (41–76)

30 June 2017; accepted 14 February 2018
Published online 15 March 2018
10.1126/science.aao2646

PALEOANTHROPOLOGY

Chronology of the Acheulean to Middle Stone Age transition in eastern Africa

Alan L. Deino,^{1*} Anna K. Behrensmeyer,² Alison S. Brooks,^{3,4} John E. Yellen,^{5,4} Warren D. Sharp,¹ Richard Potts^{4,6*}

The origin of the Middle Stone Age (MSA) marks the transition from a highly persistent mode of stone toolmaking, the Acheulean, to a period of increasing technological innovation and cultural indicators associated with the evolution of *Homo sapiens*. We used argon-40/argon-39 and uranium-series dating to calibrate the chronology of Acheulean and early MSA artifact-rich sedimentary deposits in the Olorgesailie basin, southern Kenya rift. We determined the age of late Acheulean tool assemblages from 615,000 to 499,000 years ago, after which a large technological and faunal transition occurred, with a definitive MSA lacking Acheulean elements beginning most likely by ~320,000 years ago, but at least by 305,000 years ago. These results establish the oldest repository of MSA artifacts in eastern Africa.

The earliest development of the Middle Stone Age (MSA) has been obscure because stratigraphic records that span from the Acheulean, which is characterized by distinctive large cutting tools (LCTs), to the early MSA are rare and poorly constrained in time. Here we present precise geochronology based on ⁴⁰Ar/³⁹Ar and U-series dating of middle Pleistocene archaeological sites in the Olorgesailie basin, southern Kenya rift (detailed site stratigraphy is shown in Fig. 1; composite stratigraphy is shown in fig. S8), that document the stone technology, fauna, and environments of the Acheulean-to-MSA sequence (1, 2).

As originally defined (3), the MSA lacked LCTs and bladelet technologies, although more recent work recognizes the presence of LCTs in some early MSA assemblages and of bladelets especially after 70,000 years (70 ka) ago. For much of the 20th century, the MSA was considered irrelevant to human evolution and dispersal, largely because the chronometric techniques and climate correlations used in African contexts placed it at the end of the Pleistocene,

contemporary with the richer record of European cave art and elaborate lithic tool kits. Human behavioral evolution during the middle Pleistocene (780 to 130 ka ago) and into the late Pleistocene before 30 ka ago was thus poorly understood (4).

Based on newer techniques, the well-constrained oldest MSA sites in eastern and eastern-central Africa now have estimated ages of ≥286 to ≤182 ka (Table 1), whereas the earliest fossils attributable to *Homo sapiens sensu stricto* in eastern Africa have ages of ~160 to 200 ka [Table 1 and table S4; all K-Ar and ⁴⁰Ar/³⁹Ar ages are recalculated for consistency with K decay constants and revised standard ages (5)]. Although recent investigations in northern Africa suggest the coeval evolution of *H. sapiens sensu lato* and the MSA in the middle Pleistocene (6, 7), the earliest MSA predates current evidence for the first appearance of *H. sapiens sensu stricto* in eastern Africa and likely constitutes the context in which the anatomical and behavioral characteristics of our species evolved.

A summary of dates (Table 1) shows that Acheulean and transitional industries incorporating large tools (Sangoan and Fauresmith) disappeared in Kenya before 285 ka ago or earlier but persisted in areas of Ethiopia, Sudan, and southern Africa into the end of the middle Pleistocene, after the first appearance of *H. sapiens sensu stricto*. Although dates have been published for 12 middle Pleistocene South African sites, only Florisbad, Kathu Pan, and possibly Sterkfontein and Wonderwerk—all in northern South Africa—have dated MSA horizons older than marine isotope stage 6 (MIS6; ~191 ka ago) (8), and six lack LCTs. Coastal MSA cave horizons older than MIS6 appear in north-

western Africa but are absent from the rich later record of coastal South African caves.

After our team's investigations of the Acheulean sites, fossil remains, and geology of the Olorgesailie Formation, dated at ~1.2 to 0.5 million years (Ma) old (9–12), research since 2002 has extended into the Oltulelei Formation (13), which has rich accumulations of MSA artifacts. In this work, we set out the chronostratigraphic controls for the end of the Acheulean and its replacement by MSA sites in the Olorgesailie basin, which contains the longest stratigraphic sequence of Acheulean and overlying MSA sites in eastern Africa. Other recent and concurrent manuscripts establish the stratigraphic and regional geological context of strata younger than 500 ka at Olorgesailie (13), characterize the MSA sites (1), and examine the paleoenvironmental setting, faunal turnover, and landscape dynamics associated with the MSA in the Olorgesailie basin (2).

The MSA sites of Olorgesailie are exposed within a ~65-km² early to late Pleistocene sedimentary basin in the southern Kenya rift, north of the deeply eroded late Pliocene–early Pleistocene central volcano of Mt. Olorgesailie (14) (Fig. 1, inset). The Pleistocene deposits lie on older lavas dated at 2.66 ± 0.06 Ma old (all chronologic uncertainties are reported at the 2σ level) (9) and the regionally extensive Magadi Trachyte (1.4 to 0.8 ka old) (15). Normal fault movement contemporaneous with sedimentation has resulted in the separation of the Olorgesailie basin into three sub-basins with shifting histories of terrigenous and lacustrine sedimentary environments (13).

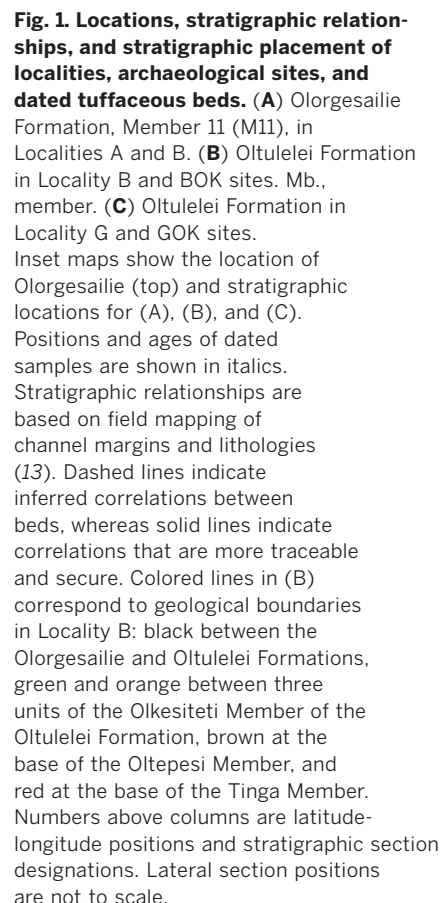
The basin strata consist of the older, areally extensive and horizontally stratified Olorgesailie Formation, overlain unconformably by channel fills and sheet deposits of the Oltulelei Formation. The latter formation has an upper age limit of <36 ka (13) and a lower age limit established here of ~320 ka. The ~180-ka hiatus between the formations was a time of deep erosion (>60-m-deep valley formation) and transport of basin materials into the Koora Graben.

Members 1 to 14 of the Olorgesailie Formation encompass the longest series of excavated Acheulean sites in Africa. Members 8 to 14 fall in the early part of the middle Pleistocene and contain Acheulean industries characterized by bold percussion flaking and varying percentages of LCTs. Recently discovered sites in Members 11 and 12 provide evidence of variations in the Acheulean that are relevant to MSA origins (2). Here we provide evidence establishing the age of the Member 11 Acheulean sites and of the oldest MSA sites that lack LCTs, which have been excavated in the Olkesititi Member of the Oltulelei Formation (1).

The chronological constraints on the MSA sites at Olorgesailie are mainly based on the ⁴⁰Ar/³⁹Ar dating technique applied to single phenocrysts of K-feldspar from volcanoclastic deposits. Two variants of the ⁴⁰Ar/³⁹Ar method were used; an early phase of the dating effort

¹Berkeley Geochronology Center, Ridge Road, Berkeley, CA 94709, USA. ²Department of Paleobiology, National Museum of Natural History, Smithsonian Institution, Washington, DC 20013-7012, USA. ³Department of Anthropology, George Washington University, Washington, DC 20052, USA. ⁴Human Origins Program, National Museum of Natural History, Smithsonian Institution, Washington, DC 20013-7012, USA. ⁵Archaeology Program, National Science Foundation, Alexandria, VA 22314, USA. ⁶Department of Earth Sciences, National Museums of Kenya, P.O. Box 40658-00100, Nairobi, Kenya.

*Corresponding author. Email: adeino@bgc.org (A.L.D.); potts@si.edu (R.P.)



The latest known Acheulean archaeological sites in the Olorgesailie Formation and the remains of the distinctive large-bodied grazing fauna associated with these sites are located in Members 11, 12, and 14 (2). Previous $^{40}\text{Ar}/^{39}\text{Ar}$ ages constrained Member 11 to a 62-ka interval between underlying Member 10 at 671 ± 8 ka old and overlying Member 12 at 609 ± 6 ka old, with an age of 499 ± 2 ka for Member 14 (9). New $^{40}\text{Ar}/^{39}\text{Ar}$ age determinations for Member 11 tuffaceous deposits further constrain the archaeological materials in Member 11' to the lower part of the 6-ka interval from 615 to 609 ka ago (Fig. 1A). The 615-ka-old constraint is based on two

Table 1. Eastern African MSA and Acheulean middle Pleistocene sites with published K-Ar or $^{40}\text{Ar}/^{39}\text{Ar}$ age estimates from ~600 to ~180 ka, excluding new Olorgesailie Formation (Member 11) analyses reported in this paper. Ages are recalculated using revised K decay constants (17) and astronomically calibrated standard ages [Fish Canyon Tuff sanidine, 28.201 Ma (18); Alder Creek Rhyolite sanidine, 1.1848 Ma (19)].

	Age estimate (thousands of years $\pm 2\sigma$)	Industry	LCTs present	Pigment present	References	Country
MSA sites						
Omo Kibish KHS levels 2 and 3, AHS, Member I	197 \pm 4	MSA	X		(20, 21)	Ethiopia
Gademotta (Kulkuletti unit 15) 72-1	$\leq 182 \pm 10$	early MSA	X		(22, 23)	Ethiopia
Gademotta (unit 12) ETH72-7B	$< 274 \pm 2$	early MSA	X		(22, 23)	Ethiopia
Gademotta (units 9 and 10) ETH72-8B	$\geq 274 \pm 2$	early MSA			(22, 23)	Ethiopia
Kapthurin, Kampi ya Samaki beds (upper K4)	237 \pm 4	MSA			(24, 25)	Kenya
Kapthurin, Sibilo School Road/Koimolot (upper bed K4)	~250 to 200*	MSA			(26)	Kenya
Kapthurin, K4	286 \pm 24	MSA			(24, 25)	Kenya
Kapthurin, upper K3/lower K4; GnJh-15, -17 (upper), -63; GnJi-28	512 \pm 18 to 286 \pm 24	Acheulean with blades/MSA?			(24, 25)	Kenya
Olduvai Ndutu Beds, upper	230 \pm 10, 220 \pm 90, 380 \pm 20, > 260 †	MSA			(27, 28)	Tanzania
Acheulean sites						
Herto, lower	262 \pm 32	Acheulean	X		(29)	Ethiopia
Andalee	$< 554 \pm 61$ ‡	Acheulean/Sangoan	X		(30, 31)	Ethiopia
Bodo	$< 554 \pm 61$ §	Acheulean	X		(30)	Ethiopia
Mieso	208 \pm 16	Acheulean	X		(32)	Ethiopia
Kapthurin, upper K3; GnJh-17 (lower); GnJh-15, -03, -05	512 \pm 18 to 286 \pm 24	Acheulean, with blades		X	(24, 25)	Kenya
Kapthurin; GnJh-41, -42, -57 (lower K3')	556 \pm 15 to 546 \pm 8	Core and flake/Acheulean?	X		(24, 25)	Kenya
Kapthurin K2	610 \pm 80 to 546 \pm 8	Acheulean	X		(24, 25)	Kenya
Olorgesailie Member 10	671 \pm 8	Acheulean	X		(9)	Kenya
Olorgesailie Member 12	609 \pm 6	Acheulean	X		(9)	Kenya
Olorgesailie Member 14	499 \pm 2	Acheulean	X		(9)	Kenya
Lainyamok, Khaki 2	397 \pm 8 to 334 \pm 12	MSA? (indeterminate)	X		(33)	Kenya

*Not directly dated; estimated on the basis of chemical compositional trends and reference to (24). †Not peer-reviewed; complicated dating situation subject to reinterpretation. ‡Age assigned by stratigraphic correlation with Bodo sequence. §Recalculated from sample 90-20 of (30). ||Acheulean sites below and above dated tuff.

ages obtained on pumice from a poorly sorted silty sandstone containing and underlying the artifacts (615.7 \pm 6.9 ka from Locality A and 614.7 \pm 5.2 ka from Locality B; a third result of 626.6 \pm 7.7 ka from Locality A was rejected as being too old; supplementary text S3).

Archaeological sites that we dated in the Olkesiteti Member of the Oltulelei Formation in Locality B occur within a 4- to 6-m-thick sequence of siltstones, sandstones, and conglomerates, with occasional pumice gravels and vitric tuffs (Fig. 1B). The stratigraphically lowest MSA sites lie above an eroded surface

of Member 9 of the Olorgesailie Formation (757 to 671 ka old). $^{40}\text{Ar}/^{39}\text{Ar}$ ages were obtained from three sites (BOK-1E, BOK-2, and BOK-4; Fig. 1B) (1), all within a lateral distance of 130 m.

MSA site BOK-1E underlies a succession of vitric tuffs with concordant ages of 303.7 \pm 8.4, 306.1 \pm 9.5, and 264.1 \pm 1.3 ka (section B10-01/B08-06, Fig. 1B). These are in turn overlain unconformably by much younger pumice gravel of the Oltepesi Member of the Oltulelei Formation, which yielded an age of 158.5 \pm 3.8 ka. Although the minimum age of the site is

established by these dated tuffs at > 305 ka, the maximum age is not similarly constrained and must be estimated through sedimentological arguments. We suggest an estimate of ~320 ka, based on considerations of fluvial sedimentology. This stratigraphic interval consists of a single upward-fining cycle with intervals of pedogenesis, and, for this fluvial system, ~10 to 20 ka (i.e., 15 ka) of accumulation is considered a reasonable estimate (16).

Site BOK-2 (section B03-03, Fig. 1B) is similarly constrained by an overlying pair of vitric tuffs, which are potentially correlative to those

above BOK-1E. Their ages are 305.2 ± 6.8 and 302.2 ± 6.3 ka. The lowest dated tuff lies less than a meter above the BOK-2 artifact levels, without indication of a major unconformity. Site BOK-4 occurs within a filled channel incised into the BOK-1E/BOK-2 stratigraphy (section B06-02, Fig. 1B). $^{40}\text{Ar}/^{39}\text{Ar}$ ages were obtained on seven pumice gravels intercalated with the artifact horizons within a ~2.5-m interval. For convenience, we grouped the gravels into a lower bed, a middle sequence of five dated gravels, and a capping gravel with ages of 297.0 ± 3.2 , 298.4 ± 1.5 , and 295.1 ± 6.4 ka, respectively. The entire episode of more than 4 m of channel cutting and filling at BOK-4 was completed in just ~6 to 7 ka after deposition of sites BOK-1 and BOK-2. In brief, the BOK sites began accumulating as early as ~320 ka ago and terminated by ~295 ka ago.

MSA sites in Locality G are distributed in a roughly north-south orientation over a distance of ~1.1 km in strata of the Olkesititi Member of the Oltulelei Formation (Fig. 1C). Most of the tuff samples that date these sites also are from this member. Six pumiceous tuff units were analyzed by the $^{40}\text{Ar}/^{39}\text{Ar}$ method, with additional age control from U-series dating.

The U-series sample, consisting of silica and carbonate replacing roots or stems in the oldest tuff unit in Locality G, yielded the precise age of 277.1 ± 1.8 ka (unit G-T1 in section G06-08, Fig. 1C). This tuff occurs in strata that overlie an erosional unconformity above the MSA archaeological material at GOK-1, which occurs in a thick (~2.5 m), well-developed reddish paleosol (section G08-01, Fig. 1C). Several factors suggest that this site is considerably older than the U-series date: its occurrence in a thick paleosol, the presence of an erosional unconformity at the top of the paleosol marking a cut-and-fill sedimentary cycle, and >1 m of strata beneath the dated tuff in section G06-08. These elements suggest that GOK-1 may be of antiquity equal to or greater than the BOK MSA sites.

Multiple $^{40}\text{Ar}/^{39}\text{Ar}$ results from pumice tuffs in Locality G above the level of the U-series date tightly constrain the age of the prolific MSA site GOK-1s (Fig. 1C). This site occurs within a few tens of centimeters of fine siltstone between the upper pair of a widespread group of three closely spaced tuffs, informally called the “Triple Tuffs” and assigned to the Oltulelei Tuffs (13). These tuffs yielded indistinguishable mean ages from 219.5 ± 3.6 to 221.8 ± 3.5 ka (Fig. 1C). Using a Bayesian chronology model for the Locality G samples (fig. S7), we estimate that the duration of the stratigraphic interval of GOK-1s was ≤ 1.5 ka.

MSA artifact sites GOK-3 and GOK-4 in Locality G are also constrained by the underlying Triple Tuffs and by two overlying pumice horizons within ~1.5 m of the artifact levels: a 3- to 10-cm pumice tuff unit at 215.3 ± 2.3 ka old (G-T6) and pumice gravel within the erosional base of a channel deposit at 207.1 ± 4.4 ka old (G-T7) (Fig. 1C).

This sequence of precise dates from the Olorgesailie basin in the southern Kenya rift, relying primarily on the $^{40}\text{Ar}/^{39}\text{Ar}$ technique but also using innovative U-series methodologies, provides secure chronostratigraphic constraints on the early establishment of MSA lifeways in eastern Africa and on the end of the Acheulean, which must have occurred by ~320 ka ago. Although the latest Acheulean site is found in Member 14 of the Olorgesailie Formation at ~499 ka old, earlier variations in the Acheulean showing a greater degree of stone raw material selectivity for toolmaking—including rocks from distant sources, thus potentially anticipating aspects of MSA behavior (2)—occur in Member 11 at ~615 to 609, Member 12 at ~609, and Member 14 at ~499 ka old. After a period of deep erosion at Olorgesailie between ~499 and ~320 ka ago, MSA technological innovations, including important cultural markers such as long-distance obsidian transport and pigment processing (7), were preserved in the Oltulelei Formation, beginning most likely by 320 and no later than 305 ka ago. These ages also imply that a major shift in the landscapes and mammalian biota of the southern Kenya rift (2) had occurred by 320 ka ago.

Our newly calibrated archaeological sequence provides a secure basis for comparison with the limited sample of other well-dated Acheulean and MSA occurrences in Kenya and elsewhere in Africa. Evidence for an increased pace of environmental change that now is well documented in the Olorgesailie sequence suggests that eastern Africa was important to the development of MSA technological, social, and cognitive innovations in human behavior before 300 ka ago, as a key region fostering the development of a more widespread set of behavioral changes related to the emergence of *H. sapiens*.

REFERENCES AND NOTES

1. A. S. Brooks *et al.*, *Science* **360**, 90–94 (2018).
2. R. Potts *et al.*, *Science* **360**, 86–90 (2018).
3. A. J. H. Goodwin, *S. Afr. J. Sci.* **25**, 410–418 (1928).
4. G. L. Isaac, in *After the Australopithecines*, K. W. Butzer, G. L. Isaac, Eds. (Mouton, 1975), pp. 875–887.
5. Materials and methods are available as supplementary materials.
6. J.-J. Hublin *et al.*, *Nature* **546**, 289–292 (2017).
7. D. Richter *et al.*, *Nature* **546**, 293–296 (2017).
8. L. E. Lisiecki, M. E. Raymo, *Paleoceanography* **20**, PA1003 (2005).
9. A. Deino, R. Potts, *J. Geophys. Res.* **95**, 8453–8470 (1990).
10. R. Potts, A. K. Behrensmeyer, P. Ditchfield, *J. Hum. Evol.* **37**, 747–788 (1999).
11. R. Potts, A. K. Behrensmeyer, A. Deino, P. Ditchfield, *J. Clark, Science* **305**, 75–78 (2004).
12. A. K. Behrensmeyer, R. Potts, A. Deino, P. Ditchfield, in *Sedimentation in Continental Rifts*, R. W. Renaut, G. M. Ashley, Eds. (SEPM Special Publication 73, SEPM Society for Sedimentary Geology, 2002), pp. 97–106.
13. A. K. Behrensmeyer, R. Potts, A. Deino, *Bull. Geol. Soc. Am.* **10.1130/B31853.1** (2018).
14. B. H. Baker, L. A. J. Williams, J. A. Miller, F. J. Fitch, *Tectonophysics* **11**, 191–215 (1971).

15. A. Guth, J. Wood, “Geology of the Magadia Area, Kenya” (Geological Society of America Digital Map and Chart Series DMCH016, Geological Society of America, 2013); www.geosociety.org/maps/2014-DMCH016/DMCH016_S3e_Magadi.pdf.
16. J. S. Bridge, *Rivers and Floodplains: Forms, Processes, and the Sedimentary Record* (Blackwell Science, 2003).
17. K. W. Min, R. Mundil, P. R. Renne, K. R. Ludwig, *Geochim. Cosmochim. Acta* **64**, 73–98 (2000).
18. K. F. Kuiper *et al.*, *Science* **320**, 500–504 (2008).
19. E. M. Niespolo, D. Rutte, A. L. Deino, P. R. Renne, *Quat. Geochronol.* **39**, 205–213 (2017).
20. J. J. Shea, *J. Hum. Evol.* **55**, 448–485 (2008).
21. I. McDougall, F. H. Brown, J. G. Fleagle, *Nature* **433**, 733–736 (2005).
22. L. E. Morgan, P. R. Renne, *Geology* **36**, 967–970 (2008).
23. Y. Sahle, L. E. Morgan, D. R. Braun, B. Atnafu, W. K. Hutchings, *Quat. Int.* **331**, 6–19 (2014).
24. A. L. Deino, S. McBrearty, *J. Hum. Evol.* **42**, 185–210 (2002).
25. C. A. Tryon, *Curr. Anthropol.* **47**, 367–375 (2006).
26. N. Blegen, *J. Hum. Evol.* **103**, 1–19 (2017).
27. M. I. Eren, A. J. Durant, M. Prendergast, A. Z. P. Mabulla, *Quat. Int.* **322–323**, 292–313 (2014).
28. P. C. Manega, thesis, University of Colorado, Boulder, CO (1993).
29. J. D. Clark *et al.*, *Nature* **423**, 747–752 (2003).
30. J. D. Clark *et al.*, *Science* **264**, 1907–1910 (1994).
31. J. Kalb, M. Jaegar, C. P. Jolly, B. Kana, *J. Archaeol. Sci.* **9**, 349–363 (1982).
32. A. Benito-Calvo, D. N. Barfod, L. J. McHenry, I. de la Torre, *J. Hum. Evol.* **76**, 26–38 (2014).
33. R. Potts, A. Deino, *Quat. Res.* **43**, 106–113 (1995).

ACKNOWLEDGMENTS

We thank the National Museums of Kenya and the Kenya Government for permission granted by the Ministry of Sports, Culture and the Arts and NACOSTI (National Commission for Science, Technology and Innovation) permit P/14/7709/683. We thank J. Clark for assistance in preparation of the manuscript. **Funding:** Laboratory analyses were supported by National Science Foundation grant EAR-1322017 (A.L.D.). Fieldwork was funded by the Peter Buck Fund for Human Origins Research, the Human Origins Program (Smithsonian), and NSF HOMINID program grant BCS-0218511 (R.P.). **Author contributions:** A.L.D. contributed $^{40}\text{Ar}/^{39}\text{Ar}$ geochronology; W.D.S. contributed U-series geochronology; A.K.B. led stratigraphic studies, with input from A.L.D., R.P., and W.D.S.; and archaeological data were contributed by A.S.B., J.E.Y., and R.P. **Competing interests:** The authors have no competing interests. J.E.Y. contributed to this article in his personal capacity; any opinions, findings, and conclusions or recommendations expressed in this material are those of the authors and do not necessarily reflect the views of the NSF. **Data and materials availability:** All geochronological data are available in the paper or in the supplementary materials. Samples and field notes are archived at the Berkeley Geochronology Center.

SUPPLEMENTARY MATERIALS

www.sciencemag.org/content/360/6384/95/suppl/DC1
Materials and Methods
Supplementary Text
Figs. S1 to S8
Tables S1 to S10
References (34–65)

27 June 2017; accepted 14 February 2018
Published online 15 March 2018
10.1126/science.aao2216

STEM CELLS

Cell cycle heterogeneity directs the timing of neural stem cell activation from quiescence

L. Otsuki and A. H. Brand*

Quiescent stem cells in adult tissues can be activated for homeostasis or repair. Neural stem cells (NSCs) in *Drosophila* are reactivated from quiescence in response to nutrition by the insulin signaling pathway. It is widely accepted that quiescent stem cells are arrested in G₀. In this study, however, we demonstrate that quiescent NSCs (qNSCs) are arrested in either G₂ or G₀. G₂-G₀ heterogeneity directs NSC behavior: G₂ qNSCs reactivate before G₀ qNSCs. In addition, we show that the evolutionarily conserved pseudokinase Tribbles (*Trbl*) induces G₂ NSCs to enter quiescence by promoting degradation of Cdc25^{String} and that it subsequently maintains quiescence by inhibiting Akt activation. Insulin signaling overrides repression of Akt and silences *trbl* transcription, allowing NSCs to exit quiescence. Our results have implications for identifying and manipulating quiescent stem cells for regenerative purposes.

Neural stem cells (NSCs) in *Drosophila*, like those in mammals, proliferate during embryogenesis, become quiescent in the late embryo, and then proliferate again (reactivate) postembryonically to produce neurons and glia (Fig. 1A and fig. S1A) (1, 2). A nutritional stimulus induces reactivation (3); specifically, dietary amino acids induce glial cells in the blood-brain barrier to secrete *Drosophila* insulin-like peptides (dILPs) (4, 5). dILPs activate the insulin signaling pathway in neighboring quiescent NSCs (qNSCs), prompting the NSCs to exit quiescence (4, 6).

Quiescent stem cells are widely accepted to be arrested in G₀, a poorly understood state characterized by a 2n DNA content and a lack of expression of cell cycle progression factors (7). We assessed whether *Drosophila* qNSCs are arrested

in G₀. As expected, we did not detect the M phase marker phospho-histone H3 (pH3) in qNSCs (fig. S1B). Previous studies demonstrated that qNSCs do not express the G₁ marker cyclin E or incorporate the S phase marker 5-bromo-2'-deoxyuridine (BrdU) or 5-ethynyl-2'-deoxyuridine (EdU) (1, 3, 6, 8). However, we found that 73% of qNSCs expressed the G₂ markers cyclin A (CycA) and cyclin B (CycB) (Fig. 1B and fig. S1C). This finding suggests that most qNSCs are arrested in G₂ and that qNSCs are arrested heterogeneously in the cell cycle.

We verified that ~75% of qNSCs were arrested in G₂ by comparing the fluorescent ubiquitination-based cell cycle indicator (FUCCI)-pH3 profiles of qNSCs and proliferating NSCs (Fig. 1, C and D, and fig. S1D) (9, 10). CycA-positive (CycA⁺) qNSCs had twice the DNA content of CycA-negative (CycA⁻) qNSCs (Fig. 1E) and larger nuclei [30.5 ± 0.66 μm³

versus 18.1 ± 0.32 μm³; *n* = 10 thoracic ventral nerve cords (tVNCs), with ~75 NSCs each] than CycA⁻ qNSCs. Thus, qNSCs exhibited two types of stem cell quiescence: The majority were arrested in G₂, and a minority were arrested in G₀ (Fig. 1F). G₂ quiescence has not been reported previously for stem cells in mammals or *Drosophila*.

The choice of G₂ or G₀ arrest could be stochastic or preprogrammed. We found seven G₀ qNSCs in the first thoracic hemisegment, T1, and eight G₀ qNSCs each in T2 and T3. A consistent subset of qNSCs were always arrested in G₀, namely, NB2-2, NB2-4, NB2-5, NB3-4, NB5-3, and NB7-4 (cells are named according to their spatial origin in the neuroectoderm) (Fig. 2, A and B; fig. S2; and table S1). Of these qNSCs, NB2-4 disappears from T1 during embryogenesis (11, 12), explaining why fewer qNSCs are arrested in G₀ in T1 than in T2 and T3. NB5-4 and NB5-7 were arrested in G₂ in 50% of hemisegments but were not always arrested in the same cell cycle phase on either side of the midline (fig. S2F). We conclude that, with the exception of NB5-4 and NB5-7, the choice of G₂ or G₀ quiescence is entirely invariant.

Is G₂-G₀ heterogeneity in qNSCs significant? We assessed the reactivation of G₂ and G₀ qNSCs by tracking the expression of the reactivation marker *wormiu* (*wor*) (fig. S3). More than 86% of G₂ qNSCs reactivated by 20 hours after larval hatching (ALH), compared with 20% of G₀ qNSCs (*n* = 10 tVNCs, ~150 NSCs each) (Fig. 2C). For example, NB3-4, a G₀ qNSC, reactivated in fewer than 7% of hemisegments (*n* = 10 tVNCs, six hemisegments each) (Fig. 2D). All NSCs reactivated by 48 hours ALH (fig. S3C). Thus, G₂ qNSCs are faster-reactivating stem cells than G₀ qNSCs.

We next profiled gene expression in qNSCs using targeted DamID (TaDa) (13), identifying

The Gurdon Institute and Department of Physiology, Development and Neuroscience, University of Cambridge, Tennis Court Road, Cambridge CB2 1QN, UK.
*Corresponding author. Email: a.brand@gurdon.cam.ac.uk

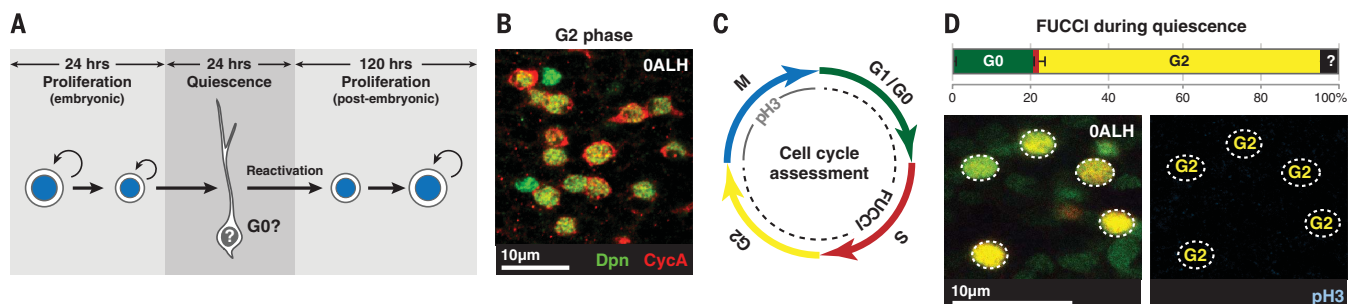


Fig. 1. qNSCs are arrested in G₀ or G₂. (A) qNSCs are smaller than proliferating NSCs and extend a primary process, which is retracted upon activation from quiescence. Proliferating NSCs in the embryo do not exhibit a primary process before entering quiescence. The cell cycle status of qNSCs is not known (as indicated by a question mark). (B) Among qNSCs (green), 73% ± 0.79% of cells expressed CycA (red). *n* = 10 tVNCs, ~150 NSCs each. (C) Cell cycle phase assessment with FUCCI and pH3. (D) Percentages of NSCs (outlined in bottom panels) in each cell cycle phase during quiescence. Colors correspond to phases as shown in (C). *n* = 5 tVNCs, ~150 NSCs each. ?, undetermined. (E) DAPI (4',6-diamidino-2-phenylindole) intensities of CycA⁺ and CycA⁻ qNSC nuclei were significantly different (*P* = 2.20 × 10⁻¹⁶, Kolmogorov-Smirnov test). *n* = 10 tVNCs, ~75 NSCs each. Arbitrary units (A.U.) were defined such that 1 A.U. equals the mean DAPI intensity of the CycA⁻ population. Error bars indicate SEM. (F) Features of G₂ and G₀ qNSCs. Images are single-section confocal images, unless indicated otherwise, and anterior is up in this and all subsequent figures.

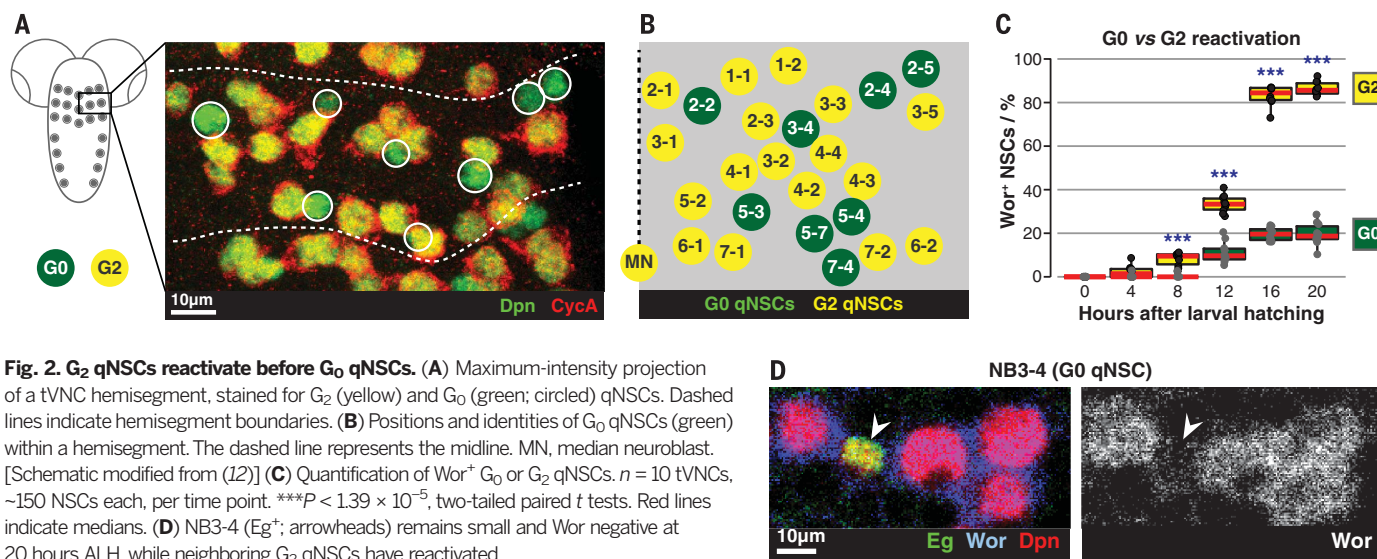
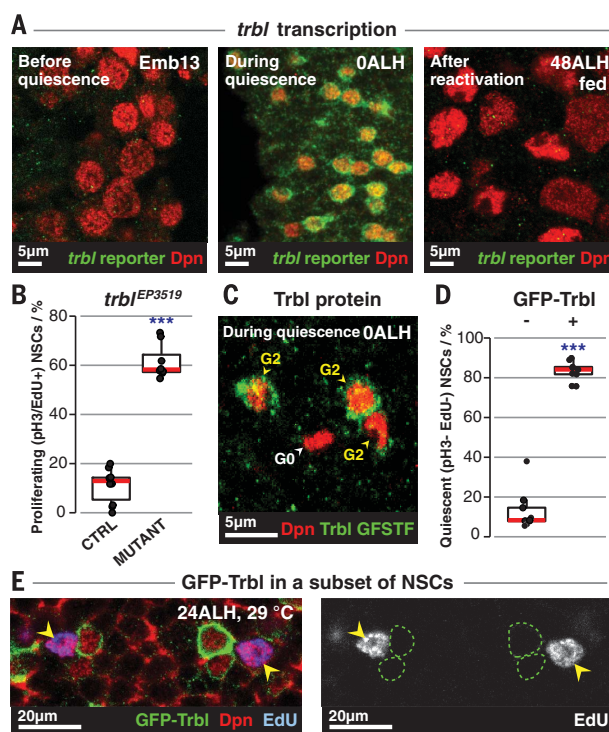


Fig. 3. *trbl* regulates G₂ qNSCs. (A) *trbl* reporter expression (green) in NSCs (red) before, during, and after quiescence. Emb, embryonic stage. (B) Quantification of proliferating NSCs in control (CTRL) tVNCs (*n* = 10 tVNCs) versus *trbl*^{EP3519} mutant tVNCs (*n* = 8 tVNCs), with ~120 NSCs per tVNC. ****P* = 7.06 × 10⁻¹⁴, Student's *t* test. (C) Trbl protein expression (green) in G₂ (CycA⁺) or G₀ (CycA⁻) qNSCs (red). Trbl GFSTF, Trbl tagged with EGFP-FlAsH-StreptII-TEV-3×Flag. (D) Quantification of qNSCs in tVNCs with GFP-Trbl expression driven by *grh*-GAL4 (*grh*-GAL4>GFP-Trbl tVNCs). “–” and “+” denote GFP-Trbl[–] and GFP-Trbl⁺ NSCs, respectively. *n* = 9 tVNCs, ~150 NSCs each. ****P* = 3.90 × 10⁻⁴, Wilcoxon signed-rank test. Red lines in (B) and (D) indicate medians. (E) In *grh*-GAL4>GFP-Trbl brains, GFP-Trbl⁺ NSCs (indicated by green outlines) do not incorporate EdU, but control NSCs (indicated by yellow arrowheads) do.



1656 genes. Corresponding Gene Ontology (GO) terms included “nervous system development” (35 genes; corrected *P* value, 2.70 × 10⁻⁶) and “neuroblast [NSC] development” (10 genes; corrected *P* value, 8.40 × 10⁻⁴) (tables S2 and S3). To identify quiescence-specific genes, we eliminated genes common to quiescent and proliferating NSCs (13), such as *deadpan* (*dpn*) (fig. S4, A and B). *tribbles* (*trbl*) is one of the most significantly expressed protein-encoding genes specific to qNSCs (fig. S4C). *trbl* encodes an evolutionarily conserved pseudokinase with three human homologs that have been implicated in insulin and mitogen-

activated protein kinase signaling [reviewed in (14)]. We confirmed that *trbl* labels quiescent but not proliferating NSCs in vivo (Fig. 3A and fig. S4, D to F). To date, no other gene that labels qNSCs specifically has been identified.

trbl is necessary for quiescence entry, as NSCs continued to divide during late embryogenesis in *trbl* hypomorphic mutants or when *trbl* was knocked down specifically in NSCs (Fig. 3B and fig. S5, A to D). *trbl* regulates quiescence entry specifically, without affecting division mode or cell viability (fig. S5, E and F). The ectopically dividing NSCs in the *trbl*^{EP3519} mutant were G₂,

not G₀, qNSCs (fig. S5G). G₂ but not G₀ qNSCs also became significantly smaller in *trbl*^{EP3519} mutants (fig. S5, H to J). As embryonic NSCs do not regrow between cell divisions (15), the size reduction is consistent with excessive divisions. Consistent with a function in G₂ quiescence, *Trbl* was expressed primarily in G₂ qNSCs (Fig. 3C and fig. S5K).

Trbl is also required to maintain quiescence. RNA interference-mediated knockdown of *trbl* in qNSCs caused NSCs to leave quiescence and divide (fig. S5, L and M). We generated transgenic flies carrying upstream activation sequence–green fluorescent protein (GFP)–*Trbl* and drove expression with *grainyhead* (*grh*)–GAL4 (4) to assess whether *Trbl* is sufficient to maintain G₂ quiescence. *grh*-GAL4 expression is initiated at quiescence entry and occurs in ~67% of NSCs, allowing comparison between neighboring GFP-*Trbl*-expressing and nonexpressing NSCs. Almost all (91.8 ± 0.88%; *n* = 10 tVNCs, ~120 NSCs each) GFP-*Trbl*-expressing NSCs remained in G₂ quiescence and expressed CycA (Fig. 3, D and E, and fig. S6). GFP-*Trbl*-expressing NSCs retained the primary process that is extended specifically by quiescent NSCs (Fig. 1A), unlike control NSCs, which had begun to divide (fig. S6, B and C) (1, 4, 16). Thus, *Trbl* is sufficient to maintain G₂ quiescence.

In the embryonic mesoderm, *trbl* induces G₂ arrest by promoting Cdc25^{String} protein degradation (17–19). We found that Cdc25^{String} protein was reduced in NSCs at quiescence entry but that *cdc25*^{String} mRNA was maintained (Fig. 4A). Therefore, Cdc25^{String} is regulated posttranscriptionally at quiescence entry. Significantly more NSCs were positive for Cdc25^{String} protein in *trbl*^{EP3519} mutants than in controls (Fig. 4B and fig. S7, A and B). This increase in Cdc25^{String} is sufficient to explain the excessive NSC proliferation in *trbl* mutants (fig. S7, C and D). Thus, *Trbl* initiates quiescence entry by promoting Cdc25^{String} protein degradation during late embryogenesis.

Trbl also maintains NSC quiescence postembryonically; however, it must act through another mechanism, as Cdc25^{String} is no longer expressed

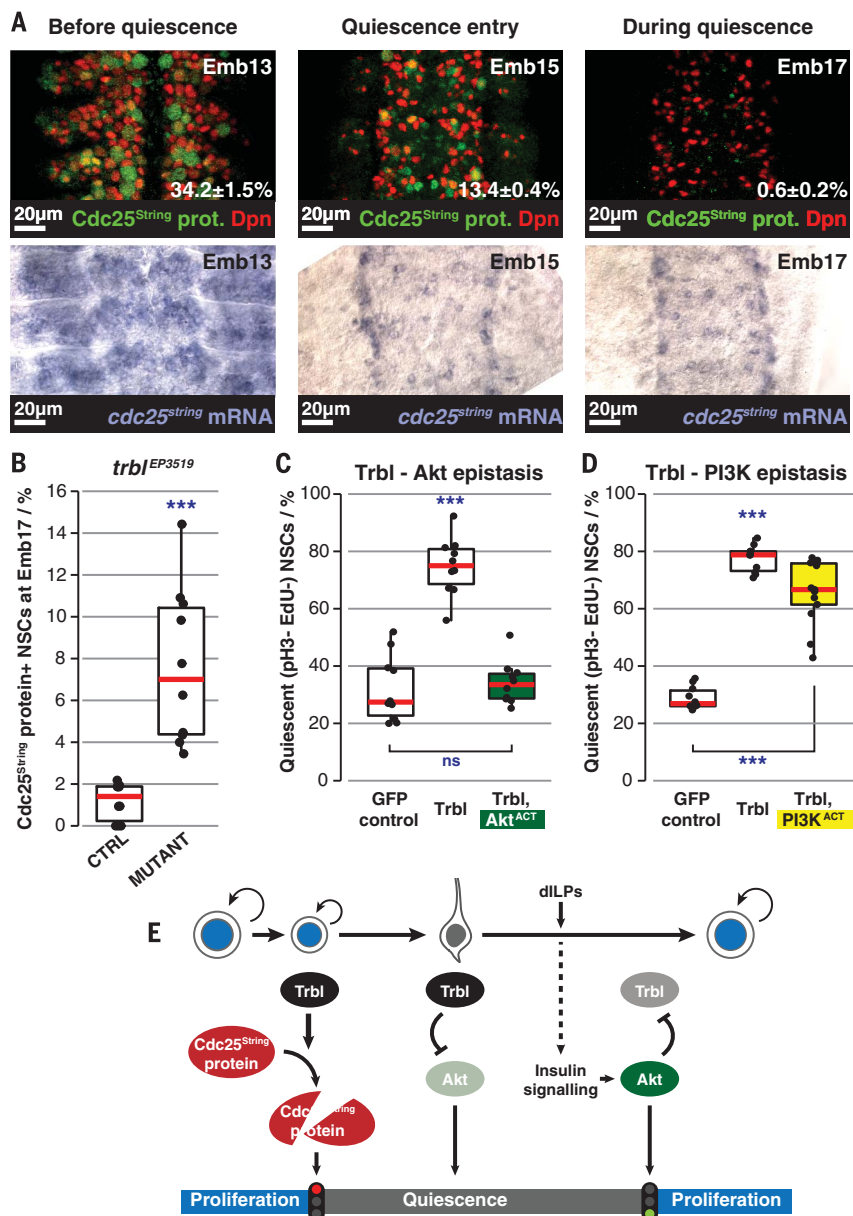


Fig. 4. Trbl induces and maintains quiescence through different mechanisms. (A) (Top) Maximum-intensity projections showing Cdc25^{String} protein (prot.) (green) expression in NSCs (red) before and during quiescence (percentages are means ± SEM). $n = 10$ tVNCs, ~130 NSCs each, per time point. (Bottom) In situ hybridization against *cdc25^{String}* mRNA at the same stages. (B) Percentages of Cdc25^{String} protein⁺ NSCs in control (*trbl*^{EP3519} heterozygote) tVNCs versus mutant tVNCs. $n = 10$ tVNCs, ~110 NSCs each, per genotype. *** $P = 9.08 \times 10^{-5}$, Kolmogorov-Smirnov test. (C and D) Quantification of qNSCs in epistasis experiments between GFP-Trbl and Akt^{ACT} (C) or PI3K^{ACT} (D). $n > 10$ tVNCs, ~80 NSCs each, per condition. *** $P < 3.39 \times 10^{-9}$; ns, not significant ($P > 0.05$), one-way analysis of variance (ANOVA) followed by Tukey's post hoc test. In (D), there is no significant difference between GFP-Trbl alone and GFP-Trbl plus PI3K^{ACT}. Red lines in (B) to (D) indicate medians. (E) Three-step model for Trbl activity.

in postembryonic qNSCs (fig. S8A). Trbl is known to inhibit insulin signaling by binding Akt and preventing its phosphorylation (fig. S8B) (20). Consistent with this, Trbl-expressing NSCs had less phosphorylated translation initiation factor 4E-binding protein (p4E-BP) than control NSCs (fig. S8C). If Trbl inhibits Akt to maintain quiescence, constitutively active Akt (myr-Akt; here-

after Akt^{ACT}) (21) should counteract Trbl-induced quiescence. Akt^{ACT} fully rescued NSC reactivation (Fig. 4C and fig. S8D). In contrast, as Trbl is thought to act downstream of phosphatidylinositol 3-kinase (PI3K) (20), constitutively active PI3K (dp110^{CAAX}, hereafter PI3K^{ACT}) (22) should not rescue reactivation, which it did not (Fig. 4D and fig. S8D). Thus, Trbl maintains quiescence by

blocking activation of Akt. This role is specific to postembryonic NSCs, as embryonic NSCs do not depend on insulin signaling to proliferate (fig. S8E).

trbl expression must be repressed to allow NSC reactivation. We found that insulin signaling is necessary and sufficient to repress *trbl* transcription. NSCs misexpressing phosphatase and tensin homolog (PTEN), an insulin pathway inhibitor, failed to down-regulate *trbl* transcription (fig. S8F). In contrast, activating the insulin pathway by expressing Akt^{ACT} in NSCs was sufficient to switch off *trbl* transcription (fig. S8G).

We have discovered the mechanisms by which *Drosophila* NSCs enter, remain in, and exit quiescence in response to nutrition (Fig. 4E). First, Trbl pseudokinase promotes degradation of Cdc25^{String} protein to induce quiescence; second, it blocks insulin signaling by inhibiting Akt in the same NSCs to maintain quiescence; and third, it is overridden by nutrition-dependent secretion of dILPs from blood-brain barrier glia, which activate insulin signaling in qNSCs, repress *trbl* expression, and enable reactivation.

We found that qNSCs are preprogrammed for arrest in G₂ or G₀, contrary to accepted doctrine. G₂ qNSCs are the first to reactivate and generate neurons; this is followed by reactivation of G₀ qNSCs. This pattern may ensure that neurons form the correct circuits in the appropriate order during brain development. G₂ arrest also enables high-fidelity homologous recombination-mediated repair in response to DNA damage, preserving genomic integrity during quiescence. Quiescent stem cells in mammals may also arrest in G₂, with implications for isolating and manipulating quiescent stem cells for therapeutic purposes.

REFERENCES AND NOTES

1. J. W. Truman, M. Bate, *Dev. Biol.* **125**, 145–157 (1988).
2. A. Prokop, G. M. Technau, *Development* **111**, 79–88 (1991).
3. J. S. Britton, B. A. Edgar, *Development* **125**, 2149–2158 (1998).
4. J. M. Chell, A. H. Brand, *Cell* **143**, 1161–1173 (2010).
5. P. Spéder, A. H. Brand, *Dev. Cell* **30**, 309–321 (2014).
6. R. Sousa-Nunes, L. L. Yee, A. P. Gould, *Nature* **471**, 508–512 (2011).
7. T. H. Cheung, T. A. Rando, *Nat. Rev. Mol. Cell Biol.* **14**, 329–340 (2013).
8. S.-L. Lai, C. Q. Doe, *eLife* **3**, e03363 (2014).
9. A. Sakaue-Sawano et al., *Cell* **132**, 487–498 (2008).
10. N. Zielke et al., *Cell Rep.* **7**, 588–598 (2014).
11. J. W. Truman, H. Schuppe, D. Shepherd, D. W. Williams, *Development* **131**, 5167–5184 (2004).
12. H. Lacin, J. W. Truman, *eLife* **5**, e13399 (2016).
13. T. D. Southall et al., *Dev. Cell* **26**, 101–112 (2013).
14. P. A. Evers, K. Keeshan, N. Kannan, *Trends Cell Biol.* **27**, 284–298 (2017).
15. V. Hartenstein, E. Rudloff, J. A. Campos-Ortega, *Roux Arch. Dev. Biol.* **196**, 473–485 (1987).
16. K. Narbonne-Reveau et al., *eLife* **5**, e13463 (2016).
17. J. Mata, S. Curado, A. Ephrussi, P. Rørth, *Cell* **101**, 511–522 (2000).
18. J. Großhans, E. Wieschaus, *Cell* **101**, 523–531 (2000).
19. T. C. Seher, M. Leptin, *Curr. Biol.* **10**, 623–629 (2000).
20. R. Das, Z. Sebo, L. Pence, L. L. Dobens, *PLOS ONE* **9**, e109530 (2014).
21. J. S. Britton, W. K. Lockwood, L. Li, S. M. Cohen, B. A. Edgar, *Dev. Cell* **2**, 239–249 (2002).
22. S. J. Leevers, D. Weinkove, L. K. MacDougall, E. Hafen, M. D. Waterfield, *EMBO J.* **15**, 6584–6594 (1996).

ACKNOWLEDGMENTS

We thank P. Callaerts, F. Diaz-Benjumea, J. Dods, C. Q. Doe, B. Edgar, E. Higginbotham, Y. Kimata, J. Ng, J. Urban, U. Walldorf,

E. Wieschaus, Bloomington *Drosophila* Stock Centre, and the Developmental Studies Hybridoma Bank (DSHB) for generously providing reagents; T. Southall and O. J. Marshall for updating the TaDa microarray data to Release 6 of the *Drosophila* genome and for gene expression analysis; and F. Doetsch, A. C. Delgado, F. J. Livesey, D. St. Johnston, and the Brand laboratory members for discussion. **Funding:** This work was funded by the Royal Society Darwin Trust Research Professorship, Wellcome Trust Senior Investigator award 103792, and Wellcome Trust Programme grant 092545 to A.H.B. and by Wellcome Trust

Ph.D. Studentship stipend 097423 to L.O. A.H.B. acknowledges core funding to the Gurdon Institute from the Wellcome Trust (grant 092096) and Cancer Research UK (CRUK) (grant C6946/A14492). **Author contributions:** L.O. and A.H.B. designed the experiments, analyzed the data, and wrote the manuscript. L.O. performed the experiments. **Competing interests:** The authors declare no conflict of interest. **Data and materials accessibility:** Microarray data have been deposited with the Gene Expression Omnibus under accession number GSE81745.

SUPPLEMENTARY MATERIALS

www.sciencemag.org/content/360/6384/99/suppl/DC1
Materials and Methods
Figs. S1 to S8
Tables S1 to S3
References (23–41)

1 June 2017; resubmitted 27 November 2017
Accepted 7 February 2018
10.1126/science.aan8795

MOLECULAR BIOLOGY

Real-time imaging of DNA loop extrusion by condensin

Mahipal Ganji,¹ Indra A. Shaltiel,^{2*} Shveta Bisht,^{2*} Eugene Kim,¹ Ana Kalichava,¹ Christian H. Haering,^{2†} Cees Dekker^{1†}

It has been hypothesized that SMC protein complexes such as condensin and cohesin spatially organize chromosomes by extruding DNA into large loops. We directly visualized the formation and processive extension of DNA loops by yeast condensin in real time. Our findings constitute unambiguous evidence for loop extrusion. We observed that a single condensin complex is able to extrude tens of kilobase pairs of DNA at a force-dependent speed of up to 1500 base pairs per second, using the energy of adenosine triphosphate hydrolysis. Condensin-induced loop extrusion was strictly asymmetric, which demonstrates that condensin anchors onto DNA and reels it in from only one side. Active DNA loop extrusion by SMC complexes may provide the universal unifying principle for genome organization.

The spatial organization of chromosomes is of paramount importance to cell biology. Members of the SMC (structural maintenance of chromosomes) family of protein complexes, including condensin, cohesin, and the SMC5/6 complex, play vital roles in restructuring genomes during the cellular life cycle (1–3). The principles by which SMC complexes achieve these fundamental tasks are still incompletely understood. Models based on random cross-linking of DNA by pairwise interactions or conformational changes in the DNA superhelicity have been proposed (4, 5). An alternative hypothesis suggested that SMC protein complexes processively enlarge small loops in the genome (6), which would elegantly explain how condensin mediates the formation of mitotic chromosome structures observed in electron micrographs and deduced from Hi-C chromosome conformation mapping experiments (7, 8). Indeed, polymer simulations showed that loop extrusion can, in principle, result in the efficient disentanglement and compaction of chromatin fibers (9–11). The recent discovery that condensin exhibits DNA translocase activity (12) was consistent with, but did not provide conclusive evidence for (13), DNA loop extrusion.

Here, we visualized the formation of DNA loops by the *Saccharomyces cerevisiae* condensin complex in real time (Fig. 1A). We tethered both ends of a double-stranded 48.5-kilobase pair (kbp) λ -DNA molecule to a passivated surface (14, 15), using the buffer flow rate to adjust the DNA end-to-end length to a distance much shorter than its contour length (Fig. 1B). We then imaged DNA after staining with Sytox Orange (SxO; Fig. 1C and movie S1). Upon flushing in 1 nM condensin (12) and 5 mM adenosine triphosphate (ATP), we observed the accumulation of fluorescence density at one spot along the length of the DNA (Fig. 1,

D and E, fig. S1, and movie S2). This finding shows that condensin induces local compaction of DNA.

To visualize the compacted DNA structures in the imaging plane of the microscope, we applied flow at a large angle with respect to the double-tethered DNA. This revealed that the bright spots were made up of extended pieces of DNA, consistent with single large DNA loops (Fig. 1, F and G, fig. S2, and movie S3). We observed no DNA loop formation by wild-type condensin in the absence of either ATP or Mg^{2+} , nor when we replaced ATP by the nonhydrolyzable analogs ATP γ S or AMPPNP, nor when we used a mutant condensin that is unable to bind ATP. Condensin hence creates DNA loops in a strictly ATP hydrolysis-dependent manner, either by gradually extruding DNA or by randomly grabbing and linking two DNA loci.

To distinguish between these two possibilities, we monitored the looping process by real-time imaging of the DNA while applying constant flow. This revealed the gradual appearance of an initially weak increase in fluorescence intensity at a local spot that grew into an extended loop over time (Fig. 2A, fig. S3, and movies S4 and S5), providing direct visual evidence of loop extrusion and ruling out the random cross-linking model. The extruded loops were in general stable (fig. S4), although they occasionally disrupted spontaneously in a single step (Fig. 2A and movie S6). Such a single-step disruption suggests that the DNA loop had been extruded by a single condensin unit that spontaneously let go of the loop, instead of a multistep relaxation of the loop due to multiple units. Imaging at higher temporal resolution allowed us to resolve the two individual DNA strands in the extruded loop in consecutive time frames. This demonstrated that condensin had extruded an actual loop rather than an intertwined, supercoiled, or otherwise connected structure (Fig. 2B, fig. S5, and movie S7).

To quantify the kinetics of loop extrusion, we returned to imaging in the absence of flow. We constructed kymographs from movies where the loop first nucleated as a single weak fluorescent spot that subsequently expanded in size over time (Fig. 3, A and B, and movie S8). We divided each

line of the kymograph into the regions outside the loop (I and III) and the DNA loop region itself (II) and calculated, for every frame, the DNA lengths from the fluorescence intensity in each region (Fig. 3C and fig. S6A). This revealed the extrusion of sizable amounts of DNA into the loop (region II), ranging from 5 to 40 kbp (the upper limit of our assay) before reaching a plateau (fig. S6, B and C). Simultaneously, the DNA content of one of the two outside regions (III) decreased by the same amount, whereas the DNA content of the other outside region (I), surprisingly, did not change at all during the loop extrusion process (Fig. 3, D to F). This result was consistent in all loop extrusion events that we analyzed quantitatively ($N = 36$; fig. S6, B to D) and shows that the loop extrusion process is asymmetric—a finding that is in stark contrast to theoretical loop extrusion models that have so far been based on two linked motor domains that translocate along the DNA in opposite directions, thereby reeling in DNA symmetrically from both sides (9–11).

The asymmetry can be explained if one site in the condensin complex remains stably anchored to the DNA while its motor site translocates along the same DNA. A candidate for such a DNA anchor site is the charged groove formed by the Ycg1 HEAT-repeat and Brn1 kleisin subunits (16). When we repeated the loop extrusion experiments with a mutant condensin that is unable to firmly entrap DNA within the groove, the extruded loops no longer remained stable over time, but instead changed size and frequently changed position (Fig. 3G and fig. S7), resulting in a DNA decrease in one outside region and an increase in the other outside region (compare the green curves in Fig. 3, C to G). Furthermore, when we increased the NaCl and Mg^{2+} concentrations of the buffer, we observed unidirectional motion of the extruded loop (fig. S8). The weakening of a stable anchoring point in both experiments is consistent with slippage of DNA through the safety belt. The latter finding also explains the observation of condensin translocation on DNA under the same buffer conditions (12).

We can estimate the speed of DNA loop extrusion from the slopes of the initial linear part of the extrusion curves, which yield an average rate of 0.6 kbp/s. As expected, this rate depends on the concentration of ATP (fig. S9) and the ability of condensin to bind and hydrolyze ATP (Fig. 3H). Correlation with the end-to-end lengths of individual DNA molecules showed that the speed and efficiency of loop extrusion strongly depended on the relative extension of the DNA, with rates of up to ~1.5 kbp/s and >80% of all DNA molecules displaying loop extrusion at lower DNA extensions (Fig. 3I and fig. S10). Although a direct comparison with Hi-C experiments is impeded by the complexity of chromosomes in cells, it is nonetheless remarkable that condensation rates calculated by this method for condensin II (0.1 to 0.2 kbp/s) (17) or a bacterial SMC complex (0.9 kbp/s) (18) are of the same order of magnitude. We note that our assay provides a direct measurement of the condensation rate by individual condensin molecules, as it avoids any ambiguity about roadblocks or multiple condensin units working

¹Department of Bionanoscience, Kavli Institute of Nanoscience Delft, Delft University of Technology, Delft, Netherlands. ²Cell Biology and Biophysics Unit, Structural and Computational Biology Unit, European Molecular Biology Laboratory, Heidelberg, Germany. *These authors contributed equally to this work. [†]Corresponding author. Email: christian.haering@embl.de (C.H.H.); c.dekker@tudelft.nl (C.D.)

in series or in parallel at different positions on the DNA.

The dependence of the extrusion rate on the DNA end-to-end length can be understood as a force dependence: As the loop is extruded, the amount of DNA between the two attachment points (excluding the loop) decreases correspondingly, thus continuously increasing the tension within the DNA (19) (to 1.2 ± 0.5 pN; $N = 23$; see supplementary materials) until the loop extrusion process stalls (see, for example, Fig. 3D). We used the known force-extension relation for DNA to plot the loop extrusion rate versus force, which revealed a steep dependence on force (Fig. 3J and fig. S11). This very strong force dependence, where the loop extrusion rate drops substantially near 0.4 pN, is consistent with previous magnetic tweezer experiments (20–22), which also reported condensation rates that match the loop extrusion rates that we measured at similar forces (Fig. 3J). Together, these findings show that condensin is a fast, yet weak, loop-extruding motor that rapidly stalls against a modest force applied to the DNA.

We measured an ATP hydrolysis rate of ~ 2 molecules/s for condensin in the presence of DNA (fig. S12A). Notably, such a bulk estimate only provides a lower limit of the adenosine triphosphatase (ATPase) activity of condensin complexes in the active loop extrusion process, because non-DNA-bound condensin molecules and complexes that

have stalled on the DNA are included in these assays. If we nonetheless assume, for the sake of argument, that condensin hydrolyzes two ATP molecules in the course of extruding ~ 110 nm (~ 0.6 kbp) of the folded DNA every second, it would take discrete condensation steps on the order of the 50-nm size of a single condensin complex. Scenarios that explain such large steps must be very different from those for conventional DNA motor proteins that move in single-base pair increments (23). An accurate model would need to take into account the flexibility of DNA, such that for low forces, condensin can reach nearby spots on the folded DNA to occasionally capture and extrude much longer stretches of DNA than the condensin size itself (12, 24, 25). This would be consistent with the very strong force dependence of the extrusion rate that we observe.

Finally, we labeled purified condensin holocomplexes with a single ATTO647N fluorophore (fig. S12) and co-imaged them with SxO-labeled DNA in a HILO (highly inclined and laminated optical) sheet mode (26). As expected, ATTO647N-condensin frequently localized to the stem of the extruded DNA loop (Fig. 4A, fig. S13, and movies S9 and S10). Using real-time monitoring, we consistently observed DNA binding of condensin in a single-step appearance, followed by DNA loop extrusion and finally single-step bleaching (Fig. 4B and figs. S14 and S15; $N = 20$). This sequence of events un-

ambiguously demonstrates that the DNA loop was extruded by a single condensin complex. Kymographs also revealed another class of condensin binding and unbinding events with a short dwell time that did not lead to DNA loop extrusion (fig. S16A). These were the only DNA binding events in the absence of ATP (fig. S16B). Furthermore, we observed events where a DNA loop disrupted while condensin stayed bound to the DNA and later started to extrude a new DNA loop (fig. S14, D and E). Hence, during the process of loop disruption, condensin spontaneously releases the extruded loop rather than dissociating from the DNA.

Quantification of the ATTO647N-condensin intensity provided further evidence that it is a single condensin complex that locates to the stem of the DNA loop. We compared the fluorescence intensity for three cases: (i) condensin binding events that led to DNA loop extrusion, (ii) condensin bleaching events, and (iii) temporary binding events that did not lead to loop extrusion. All three cases revealed the same change in intensity (Fig. 4C), showing that a single condensin complex localizes to the stem of the DNA loop (Fig. 4D). If two condensin complexes had assembled at the loop stem, the expected result would be a bimodal intensity distribution with two peaks of similar height for single- and double-labeled condensin dimers (based on a labeling efficiency of 60 to 85%; see supplementary materials). Instead, we observed

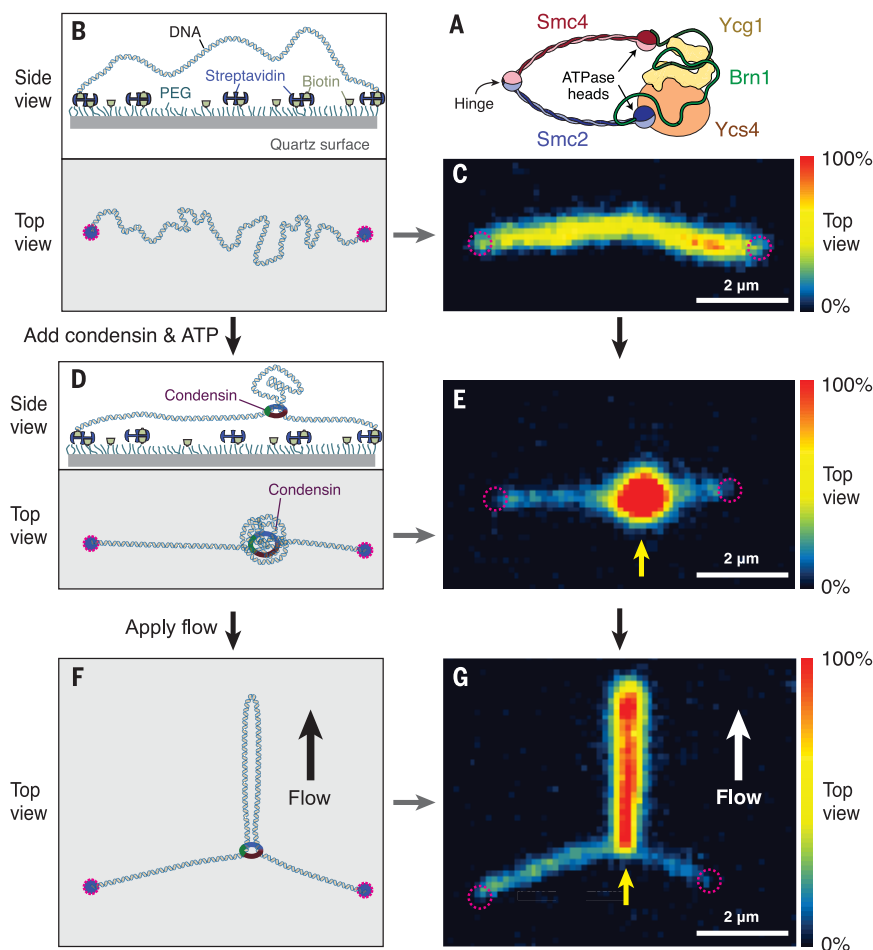
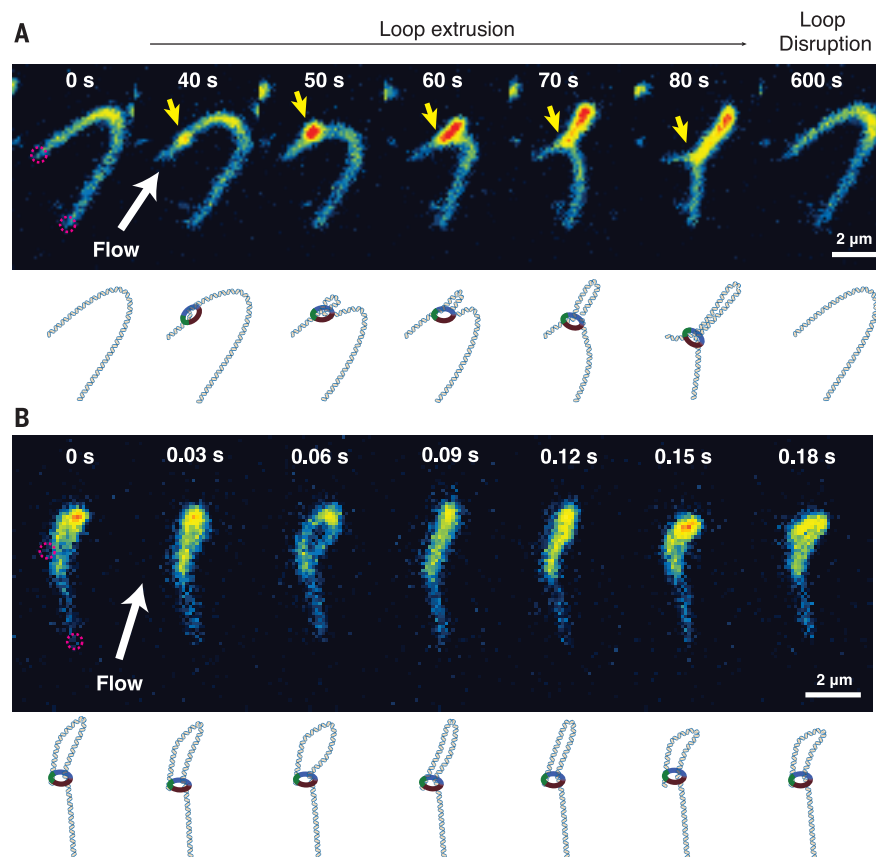


Fig. 1. Single-molecule assay for the visualization of condensin-mediated DNA looping. (A) Cartoon representation of the *S. cerevisiae* condensin complex.

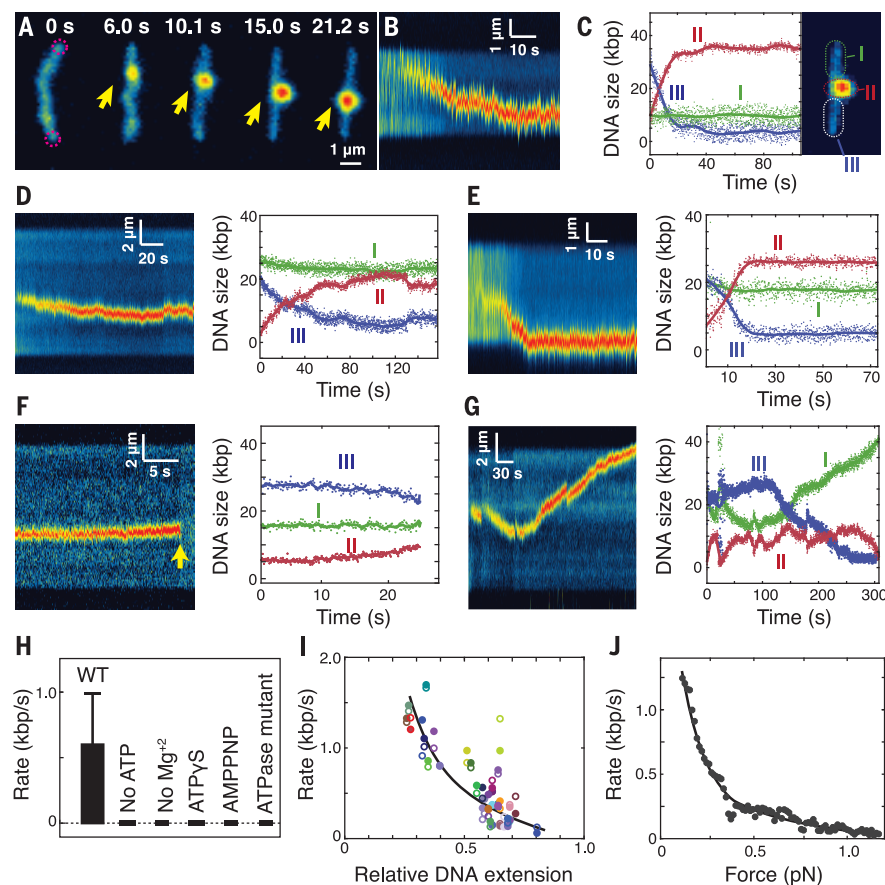
(B) Side- and top-view schematics of DNA that is doubly tethered to a polyethylene glycol (PEG)-passivated quartz surface via streptavidin-biotin linkage. (C) Snapshot of a double-tethered λ -DNA molecule (exposure, 100 ms) visualized by Sytox Orange (SxO) staining. Note the homogeneous fluorescence intensity distribution along the DNA. Dashed magenta circles indicate the surface attachment sites of the DNA. (D) Side- and top-view diagrams showing DNA loop formation on double-tethered DNA by condensin. (E) Snapshot of condensin-mediated DNA loop formation at one spot (indicated by the yellow arrow) along a SxO-stained DNA molecule. (F) Strategy to visualize DNA loops. Application of flow perpendicular to the axis of the immobilized DNA extends the loop within the imaging plane. (G) Snapshot of an extended DNA loop that is stretched out by flow (white arrow) perpendicular to the DNA, as illustrated in (F).

Fig. 2. Real-time imaging of DNA loop extrusion by condensin.

(A) Series of snapshots showing DNA loop extrusion intermediates created by condensin on a SxO-stained double-tethered λ -DNA (movie S3). A constant flow at a large angle to the DNA axis (white arrow) maintains the DNA in the imaging plane and stretches the extruded loop. A yellow arrow indicates the position of the loop base. At ~40 s, a small loop appears that grows over time until ~80 s, consistent with the loop extrusion model. A random linkage model would instead have predicted the sudden appearance of a loop that remains stable in size over time. After ~600 s, the loop suddenly disrupted. Schematic diagrams under each snapshot are for visual guidance. **(B)** Imaging at high time resolution reveals the splitting of the two DNA strands in the extruded loop in adjacent time frames.

**Fig. 3. Loop extrusion is asymmetric and depends on ATP hydrolysis.**

(A) Snapshots showing the gradual extension of a DNA loop (yellow arrow) on a double-tethered λ -DNA molecule. **(B)** Kymograph of SxO fluorescence intensities shown in (A). **(C)** DNA lengths calculated from the integrated fluorescence intensities and the known 48.5-kbp length of the λ -DNA in the kymograph of (B) for regions outside the loop (I and III) and the loop region itself (II). **(D to F)** Fluorescence kymographs (left) and intensity plots (right) of a more stretched DNA molecule (end-to-end distance 9.1 μ m) where the DNA loop stalls midway (D), of a DNA molecule where loop extrusion starts in the center and continues until reaching the physical barrier at the attachment site (E), and of a loop extrusion event that abruptly disrupts in a single step. **(G)** Kymograph and intensity plot for loop extrusion by a safety-belt condensin mutant complex, which displays dynamic changes of all three DNA regions and of the loop position. **(H)** Average loop extrusion rates (mean \pm SD) under various conditions; WT, wild type. **(I)** Rate of loop extrusion versus relative DNA extension in relation to its 20- μ m contour length. Solid circles are calculated from region II, open circles from region III; the line serves as a visual guide. **(J)** Rate of loop extrusion plotted versus the force exerted within the DNA as a result of increased DNA stretching upon increase of the loop size. The line serves as a visual guide.



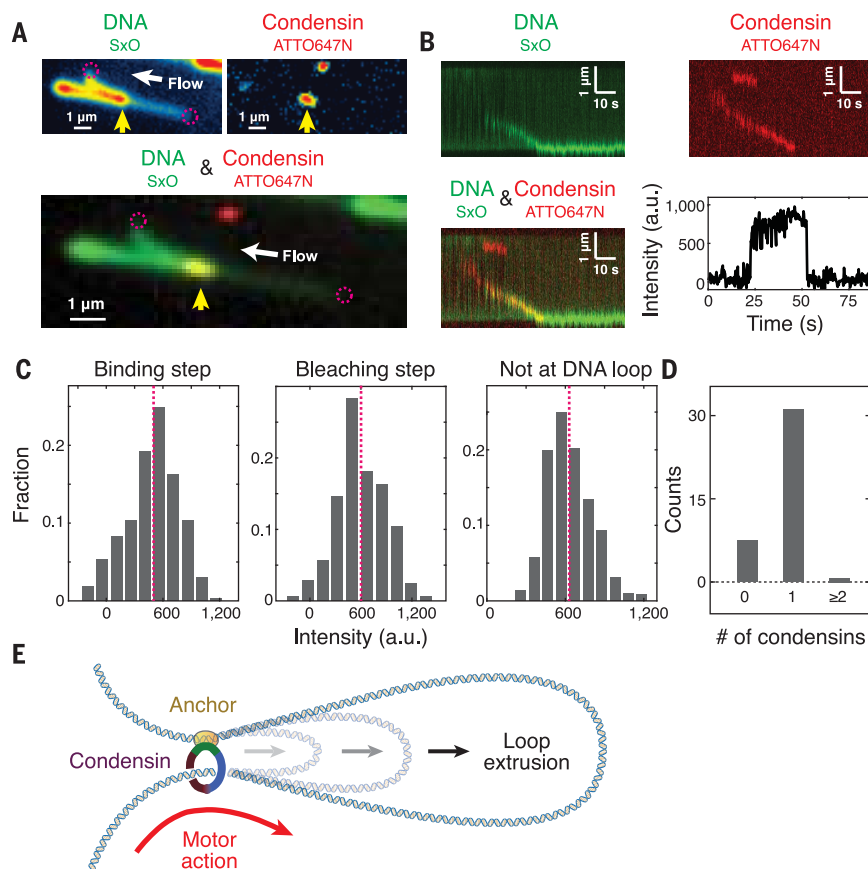


Fig. 4. Loop extrusion is induced by a single condensin complex. (A) Images of the same field of view of SxO-stained DNA (top left), ATTO647N-labeled condensin (top right), and their merge (bottom) reveal condensin at the stem of an extruded DNA loop (yellow arrow). Images are integrated over 2 s of a movie. (B) Kymographs of SxO-stained DNA (top left), ATTO647N-labeled condensin (top right), and their merge (bottom left) of a real-time movie of DNA loop extrusion. The corresponding ATTO647N fluorescence time trace (bottom right) shows single-step binding and single-step photobleaching events of the DNA-bound condensin. (C) Fluorescence intensity distributions for condensin binding events that led to DNA-loop extrusion (left), condensin bleaching in such events (center), and binding events that did not lead to loop extrusion (right) measured under similar optical conditions. (D) Histogram of the number of condensin complexes that show loop extrusion activity, as counted from the fluorescence steps. (E) Model for DNA loop extrusion by condensin. One strand of DNA is anchored by the kleisin and HEAT-repeat subunits (yellow-orange) of the condensin complex, which extrudes a loop of DNA.

no two-step bleaching events, a majority fraction (33/40) of single-step bleaching events, and a small fraction of DNA molecules (7/40) that showed DNA loop extrusion without any visible fluorescence (fig. S17), as expected for a labeling efficiency of 82%.

Although SMC complexes are vital for chromosome organization in all domains of life, the molecular basis for their action had remained largely speculative. Our experiments unambiguously demonstrate that condensin exhibits DNA loop extrusion

activity. Our real-time single-molecule dual-color movies of condensin and DNA reveal that loops are extruded by a single condensin complex at the stem of the loop in a manner that is ATP hydrolysis-dependent, strictly asymmetric, and highly sensitive to forces applied to the DNA. These properties can be explained by a model (Fig. 4E) where condensin makes stable contact with DNA at a binding site and then reels in DNA from only one side. The visual proof that condensin is a loop-extruding enzyme reveals the key principle that underlies the orga-

nization of genome architecture by condensin and most likely all other SMC protein complexes.

REFERENCES AND NOTES

1. L. Aragon, E. Martinez-Perez, M. Merkenschlager, *Curr. Opin. Genet. Dev.* **23**, 204–211 (2013).
2. F. Uhlmann, *Nat. Rev. Mol. Cell Biol.* **17**, 399–412 (2016).
3. K. Jeppsson, T. Kanno, K. Shirahige, C. Sjögren, *Nat. Rev. Mol. Cell Biol.* **15**, 601–614 (2014).
4. T. Hirano, *Cell* **164**, 847–857 (2016).
5. R. Thadani, F. Uhlmann, S. Heeger, *Curr. Biol.* **22**, R1012–R1021 (2012).
6. K. Nasmyth, *Annu. Rev. Genet.* **35**, 673–745 (2001).
7. J. R. Paulson, U. K. Laemmli, *Cell* **12**, 817–828 (1977).
8. N. Naumova et al., *Science* **342**, 948–953 (2013).
9. A. Goloborodko, M. V. Imakaev, J. F. Marko, L. Mirny, *eLife* **5**, e14864 (2016).
10. E. Alipour, J. F. Marko, *Nucleic Acids Res.* **40**, 11202–11212 (2012).
11. A. Goloborodko, J. F. Marko, L. A. Mirny, *Biophys. J.* **110**, 2162–2168 (2016).
12. T. Terakawa et al., *Science* **358**, 672–676 (2017).
13. K. Nasmyth, *Science* **358**, 589–590 (2017).
14. M. Ganji, S. H. Kim, J. van der Torre, E. Abbondanzieri, C. Dekker, *Nano Lett.* **16**, 4699–4707 (2016).
15. S. H. Kim, M. Ganji, J. van der Torre, E. Abbondanzieri, C. Dekker, DNA sequence encodes the position of DNA supercoils. *bioRxiv* 2017/08/24/180414 (2017).
16. M. Kschonsak et al., *Cell* **171**, 588–600.e24 (2017).
17. J. H. Gibcus et al., *Science* **359**, eaao6135 (2018).
18. X. Wang, H. B. Brandão, T. B. K. Le, M. T. Laub, D. Z. Rudner, *Science* **355**, 524–527 (2017).
19. C. Bustamante, S. B. Smith, J. Liphardt, D. Smith, *Curr. Opin. Struct. Biol.* **10**, 279–285 (2000).
20. J. M. Eeftens et al., *EMBO J.* **36**, 3448–3457 (2017).
21. J. Eeftens, C. Dekker, *Nat. Struct. Mol. Biol.* **24**, 1012–1020 (2017).
22. T. R. Strick, T. Kawaguchi, T. Hirano, *Curr. Biol.* **14**, 874–880 (2004).
23. W. Yang, *Annu. Rev. Biophys.* **39**, 367–385 (2010).
24. J. Lawrimore, B. Friedman, A. Doshi, K. Bloom, *Cold Spring Harb. Symp. Quant. Biol.* **10.1101/sqb.2017.82.033696** (2017).
25. M.-L. Diebold-Durand et al., *Mol. Cell* **67**, 334–347.e5 (2017).
26. M. Tokunaga, N. Imamoto, K. Sakata-Sogawa, *Nat. Methods* **5**, 159–161 (2008).

ACKNOWLEDGMENTS

We thank M. Kschonsak for providing the safety-belt mutant condensin complex, J. Kerssemakers and J. van der Torre for technical support, and J. Eeftens, A. Katan, J.-K. Ryu, and E. van der Sluis for discussions.

Funding: Supported by ERC grants SynDiv 669598 and CondStruct 681365, the Netherlands Organization for Scientific Research (NWO/OCW) as part of the Frontiers of Nanoscience program and a Rubicon Grant, and the European Molecular Biology Laboratory. **Author contributions:** M.G. and C.D. designed the single-molecule visualization assay, M.G., E.K., and A.K. performed the imaging experiments, I.A.S. and S.B. developed condensin fluorescence labeling strategies and purified protein complexes, I.A.S. performed ATPase assays, C.D. and C.H.H. supervised the work, M.G., C.H.H., and C.D. wrote the manuscript with input from all authors.

Competing interests: All authors declare that they have no competing interests. **Data and materials availability:** Original imaging data and protein expression constructs are available upon request.

SUPPLEMENTARY MATERIALS

www.sciencemag.org/content/360/6384/102/suppl/DC1
Materials and Methods
Figs. S1 to S17
Movies S1 to S10
References (27, 28)

17 December 2017; accepted 6 February 2018
Published online 22 February 2018
10.1126/science.aar7831

STEM CELLS

Hepatic thrombopoietin is required for bone marrow hematopoietic stem cell maintenance

Matthew Decker, Juliana Leslie, Qingxue Liu, Lei Ding*

Hematopoietic stem cell (HSC) maintenance depends on extrinsic cues. Currently, only local signals arising from the bone marrow niche have been shown to maintain HSCs. However, it is not known whether systemic factors also sustain HSCs. We assessed the physiological source of thrombopoietin (TPO), a key cytokine required for maintaining HSCs. Using *Tpo*^{DsRed-CreER} knock-in mice, we showed that TPO is expressed by hepatocytes but not by bone marrow cells. Deletion of *Tpo* from hematopoietic cells, osteoblasts, or bone marrow mesenchymal stromal cells does not affect HSC number or function. However, when *Tpo* is deleted from hepatocytes, bone marrow HSCs are depleted. Thus, a cross-organ factor, circulating TPO made in the liver by hepatocytes, is required for bone marrow HSC maintenance. Our results demonstrate that systemic factors, in addition to the local niche, are a critical extrinsic component for HSC maintenance.

Hematopoietic stem cells (HSCs) reside primarily in the bone marrow and are maintained by extrinsic cues that arise from supporting niche cells (1). Endothelial cells (2, 3) and perivascular mesenchymal stromal cells (2–6) are critical components of the bone marrow niche. Growing functional genetic evidence suggests that HSCs are maintained largely through signals arising directly from, or mediated

through, these local niche cells (7). However, olfaction maintains hematopoietic progenitors through systemic γ -aminobutyric acid (GABA) levels in *Drosophila* (8), suggesting that long-range signals may be able to directly maintain mammalian HSCs.

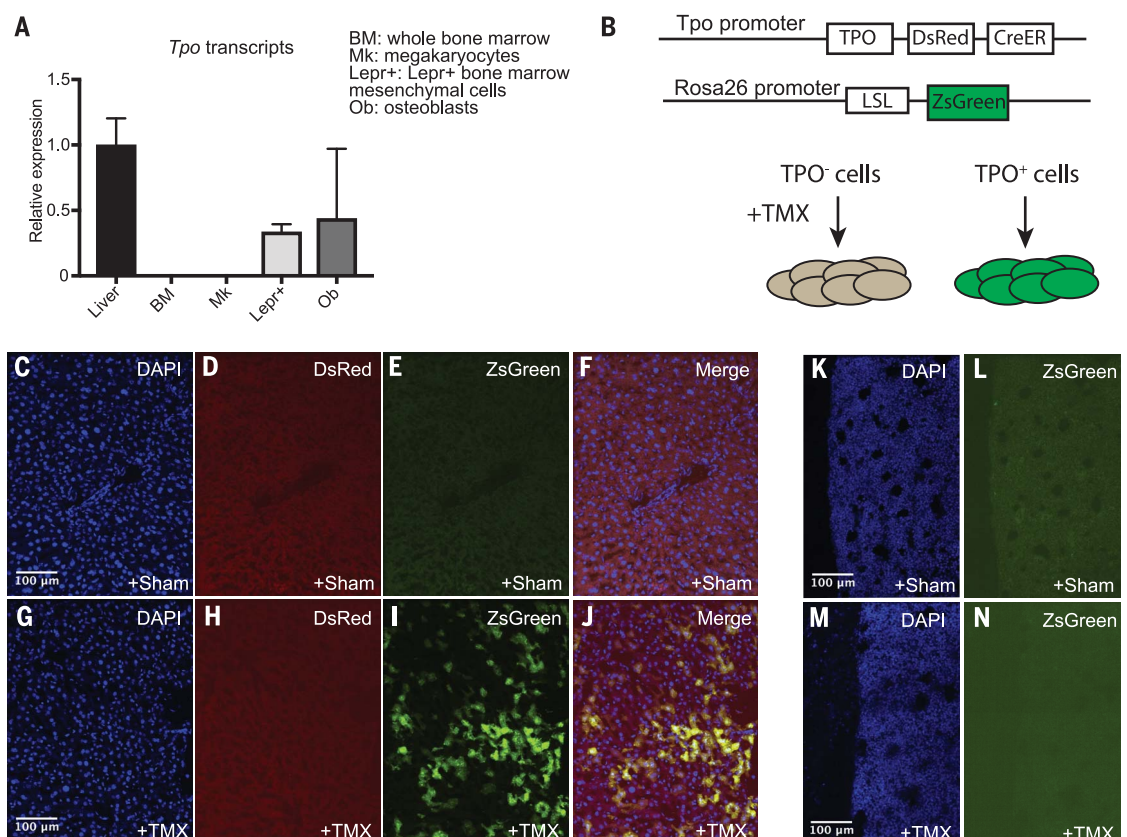
No such distal maintenance factors have yet been identified in the mammalian hematopoietic system, although long-range cues,

such as estrogen from the ovaries and erythropoietin from the kidneys, can acutely stimulate HSC proliferation and dictate HSC and progenitor differentiation (9, 10). Neurotransmitters from the nervous system can mobilize HSCs, but this effect is mediated through mesenchymal stromal cells in the niche (11). Therefore, evidence indicates roles for long-range cues that modify HSC behavior, but direct evidence for constant maintenance of HSCs by a cross-organ long-range systemic factor is lacking.

Signaling of the hematopoietic cytokine thrombopoietin (TPO) through its receptor c-MPL is essential for thrombopoiesis (12–14) and HSC maintenance (15–17). Patients with loss-of-function mutations in c-MPL or TPO develop congenital amegakaryocytic thrombocytopenia and subsequent bone marrow failure (18–20). *Tpo* mRNA is expressed by multiple cell types, including hepatocytes (14, 21), osteoblasts (17), megakaryocytes (22, 23), and stromal cells (21, 24). However, *Tpo* is under stringent translational control by inhibitory elements in the 5' untranslated region (25), so it is not clear whether any of the above-mentioned cell types actually synthesize TPO protein. *Tpo* has not

Fig. 1. TPO is expressed by hepatocytes but not by bone marrow cells.

(A) qRT-PCR analysis of *Tpo* transcript levels ($n = 3$ mice; error bars indicate SD). (B) Schema of TPO expression analysis in *Tpo*^{DsRed-CreER}, *loxpZsGreen* mice. LSL, *loxp-Stop-loxp*. (C to J) Confocal images of liver sections from sham-treated (+Sham) or TMX-treated *Tpo*^{DsRed-CreER}, *loxpZsGreen* mice. DAPI, 4',6-diamidino-2-phenylindole. (K to N) Confocal images of femur sections from sham- or TMX-treated *Tpo*^{DsRed-CreER}, *loxpZsGreen* mice.



Columbia Stem Cell Initiative, Department of Rehabilitation and Regenerative Medicine, and Department of Microbiology and Immunology, Columbia University Medical Center, New York, NY 10032, USA.

*Corresponding author. Email: ld2567@cumc.columbia.edu

been conditionally deleted from any cell types to assess its source for HSC maintenance. Thus, it is not clear how TPO maintains bone marrow HSCs in vivo. Loss of hepatic TPO leads to low platelet counts (26), showing that TPO from the liver regulates thrombopoiesis.

Using quantitative reverse transcription polymerase chain reaction (qRT-PCR) analysis, we found that *Tpo* transcripts were enriched in osteoblasts, mesenchymal stromal cells, and the liver (Fig. 1A and fig. S1, A and B), consistent with previous reports (14, 17, 21, 27). To systemically assess the expression of TPO protein, we generated *Tpo*^{DsRed-CreER} knock-in mice by replacing the stop codon of *Tpo* with a P2A-DsRed-P2A-CreER cassette (fig. S1, C to F). The P2A elements allow the translation of TPO, DsRed, and CreER recombinase under the control of *Tpo* endogenous regulatory elements. This arrangement enabled us to monitor the translational expression of TPO in vivo. We then generated *Tpo*^{DsRed-CreER}; *loxpZsGreen* mice (Fig. 1B). Consistent with the low expression level of *Tpo* in vivo (25), no DsRed fluorescence was detected (Fig. 1, C to F). However, upon tamoxifen (TMX) administration to 8-week-old mice, we detected broad and specific expression of ZsGreen in hepatocytes (Fig. 1, G to J, and fig. S1, G to O). We also observed rare ZsGreen⁺ cells in the kidney (fig. S1P). However, no ZsGreen⁺ bone marrow cells could be detected (Fig. 1, K to N, and fig. S1Q). Thus, TPO is generated by hepatocytes but not by cells in the bone marrow.

We generated a loss-of-function allele of *Tpo* (*Tpo*^{gfp}) by recombining a gene encoding enhanced green fluorescent protein (*gfp*) into the start codon of *Tpo* (fig. S2, A to C). As expected, *Tpo* transcripts were depleted from *Tpo*^{gfp/gfp} mouse livers (fig. S2D). Consistent with earlier reports (28, 29), whole-body loss of TPO led to reduced platelet counts (fig. S3, A to C) and reduced numbers of megakaryocytes (fig. S3, D to J). Bone marrow from *Tpo*^{gfp/gfp} mice had normal cellularity, but CD150⁺CD48⁺Lin[−]Sca1⁺cKit⁺ HSC frequency (the percentage of live whole bone marrow cells) decreased about 70-fold compared with the frequency in *Tpo*^{+/+} controls (fig. S3, K to M). CD150⁺CD48⁺Lin[−]Sca1⁺cKit⁺ multipotent progenitor (MPP) (30) and Lin[−]Sca1⁺cKit⁺ (LSK) hematopoietic progenitor frequencies declined by 10- and 3-fold, respectively (fig. S3, N and O). Lineage-restricted hematopoietic progenitors appeared normal, except that CD34⁺FcγR[−]Lin[−]Sca1⁺cKit⁺ common myeloid progenitors (CMPs) were reduced (fig. S3P). Bone marrow and spleen cells from *Tpo*^{gfp/gfp} mice formed fewer colonies in methylcellulose (fig. S3Q). Spleen cellularity did not change, but spleen HSC frequency was reduced (fig. S3, R and S). *Tpo*^{+/gfp} heterozygous mice displayed intermediate phenotypes (fig. S3). Thus, TPO is a major factor required for HSC maintenance.

We generated a floxed allele of *Tpo* (*Tpo*^{fl}) by inserting *loxp* sequences flanking exons 2 to 4 of *Tpo* (fig. S4, A to C). Recombination of the *loxp* sites will lead to the deletion of the start codon and the generation of a frameshift. We recombined the *Tpo*^{fl} allele in the germ line to

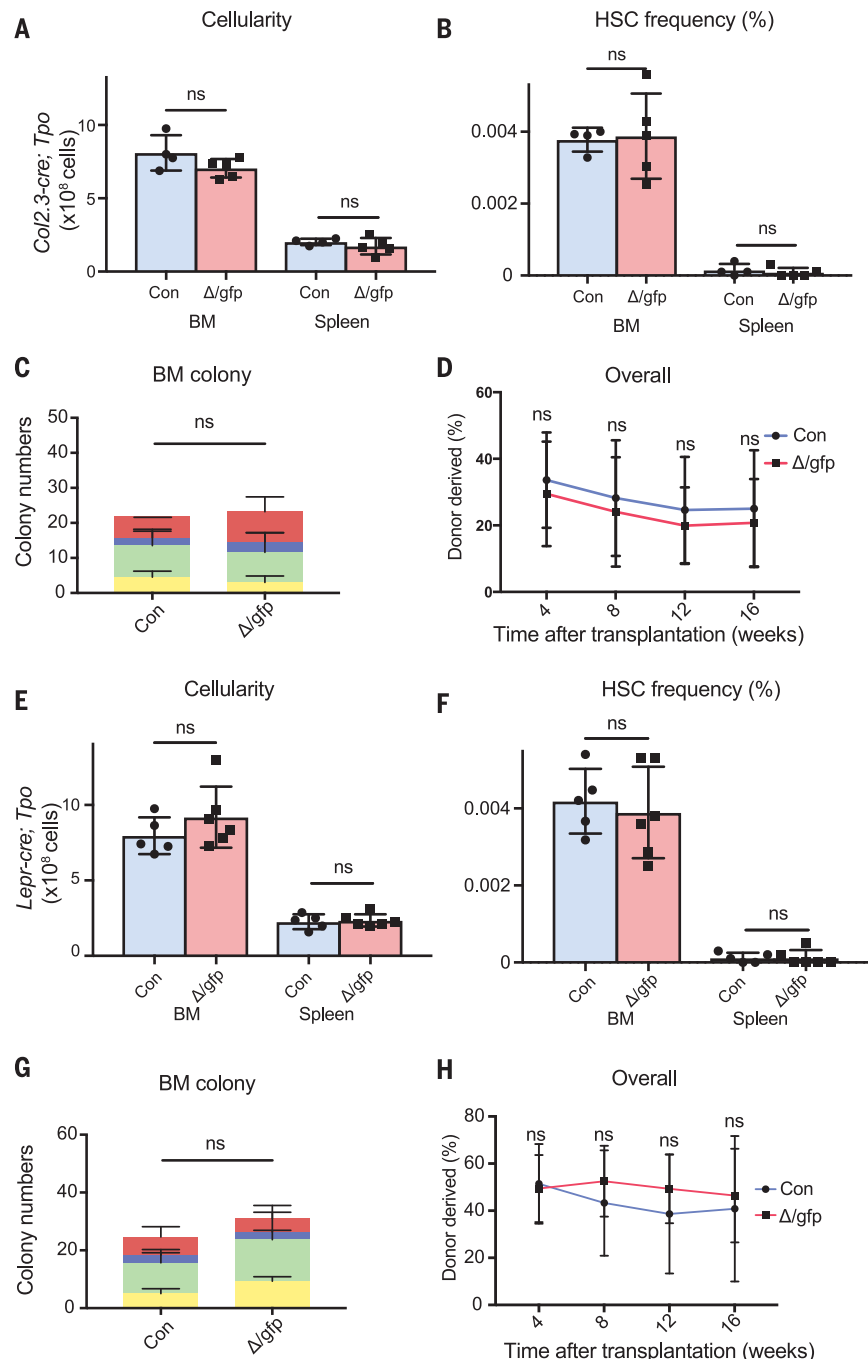


Fig. 2. Osteoblasts and mesenchymal stromal cells are not critical sources of TPO for HSC maintenance. (A to C) Cellularity (A), HSC frequency (B), and bone marrow colony-forming cell frequency (C) were normal in *Col2.3-cre;Tpo*^{fl/gfp} mice ($n = 4$ to 5 mice). (D) Bone marrow cells (5×10^5) from *Col2.3-cre;Tpo*^{fl/gfp} mice gave normal donor cell reconstitution compared to controls (in two experiments with a total of eight to nine recipient mice per genotype). (E to G) Cellularity (E), HSC frequency (F), and bone marrow colony-forming cell frequency (G) were normal in *Lepr-cre;Tpo*^{fl/gfp} mice ($n = 5$ to 6 mice). (H) Bone marrow cells (5×10^5) from *Lepr-cre;Tpo*^{fl/gfp} mice gave normal levels of donor cell reconstitution compared to controls (in two experiments with a total of eight recipient mice per genotype). Controls (Con), *Col2.3-cre;Tpo*^{+/gfp}, *Lepr-cre;Tpo*^{+/gfp}, or *Tpo*^{fl/gfp} mice. Δ /gfp, *Col2.3-cre;Tpo*^{fl/gfp} or *Lepr-cre;Tpo*^{fl/gfp} mice. Data are means \pm SD. ns, not significant ($P > 0.10$).

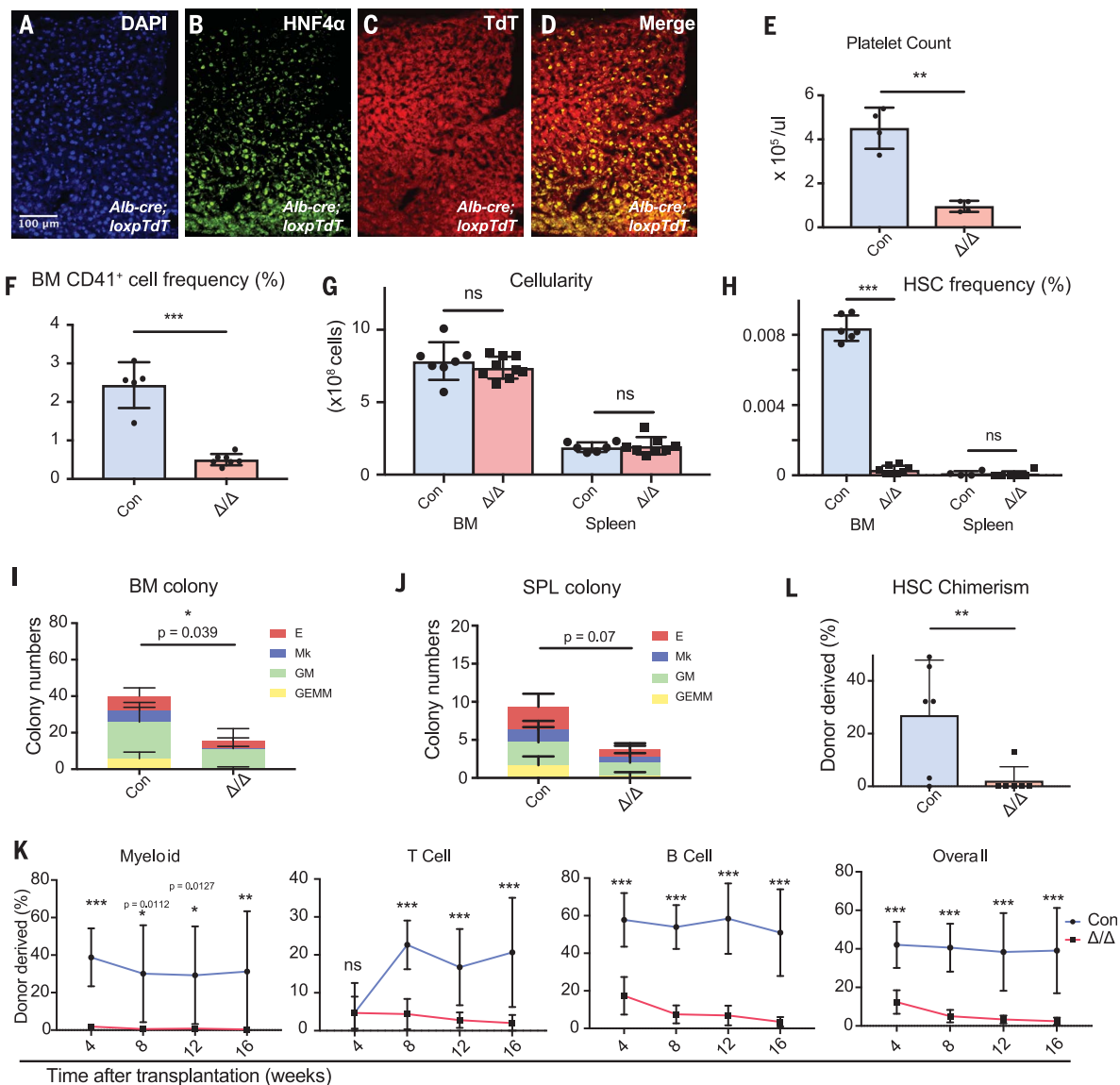


Fig. 3. Hepatocyte-derived TPO is required for HSC maintenance.

(A to D) Confocal images of liver sections from *Alb-cre;loxpTdTomato* (*Alb-cre;loxpTdT*) mice. HNF4 α , hepatocyte nuclear factor 4- α . (E) Platelet counts were decreased in *Alb-cre;Tpo^{fl/fl}* mice ($n = 4$). (F) Bone marrow CD41⁺ cell frequency was decreased in *Alb-cre;Tpo^{fl/fl}* mice ($n = 5$ to 7). (G) Cellularity was normal in the bone marrow and spleens from *Alb-cre;Tpo^{fl/fl}* mice ($n = 5$ to 6). (H) HSCs were depleted in the bone marrow but not in spleens from *Alb-cre;Tpo^{fl/fl}* mice ($n = 6$ to 8). (I and J) Colony-forming cell numbers were decreased in the bone marrow and trended lower in spleens (SPL) from *Alb-cre*;

Tpo^{fl/fl} mice ($n = 5$ to 6). E, erythroid burst-forming unit; Mk, megakaryocyte; GM, granulocyte-macrophage; GEMM, granulocyte-erythrocyte-monocyte-megakaryocyte. (K) Bone marrow cells (5×10^5) from *Alb-cre;Tpo^{fl/fl}* mice gave lower levels of donor cell reconstitution (in two experiments with a total of eight to nine recipient mice per genotype). (L) Recipient mice from (K) showed significant decrease in donor bone marrow HSC chimerism 16 weeks posttransplant ($n = 6$ mice per genotype). Con, *Alb-cre;Tpo^{+/+}*, *Tpo^{fl/fl}*, or *Tpo^{fl/+}* mice; Δ/Δ , *Alb-cre;Tpo^{fl/fl}* mice. Data are means \pm SD. ns, not significant ($P > 0.10$). * $P < 0.05$, ** $P < 0.01$, *** $P < 0.001$.

generate *Tpo^{-/-}* through mating with *Elia-cre* mice (fig. S4D). As expected, *Tpo* transcripts were absent from homozygous *Tpo^{-/-}* mice (fig. S4E). *Tpo^{-/-}* mice had significant reduction of HSCs, MPPs, and megakaryocytes (fig. S4, F to H) to levels nearly identical to those in the *Tpo^{slf/slf}* mice (fig. S3). Recombination of the *Tpo^{fl}* allele therefore gave a strong loss of *Tpo* function.

Megakaryocytes have been proposed to be a major source of TPO for HSCs (22, 23). However,

we did not detect any *Tpo* expression in megakaryocytes by qRT-PCR (Fig. 1A) or by using reporter mice (Fig. 1, K to N). Nonetheless, we directly tested whether megakaryocytes (or any hematopoietic cells) are sources of TPO for HSC maintenance in vivo by generating *Vav1-cre;Tpo^{fl/slf}* mice. *Vav1-cre* efficiently deleted *Tpo* from the hematopoietic system (fig. S5A). Eight-week-old *Vav1-cre;Tpo^{fl/slf}* mice had normal blood cell counts (fig. S5B), cellularity, and HSC frequency (fig. S5, C and D) and normal re-

stricted hematopoietic progenitors in the bone marrow (fig. S5, E to H). Spleen cellularity, HSC frequency, and megakaryocytic cells were also unaffected (fig. S5, I to K). Bone marrow cells from *Vav1-cre;Tpo^{fl/slf}* mice formed normal numbers of colonies in methylcellulose and reconstituted irradiated recipients normally (fig. S5, L and M). Thus, hematopoietic cells, including megakaryocytes, are not a critical source of TPO for HSC maintenance.

Osteoblasts have also previously been proposed to be the main source of TPO in the

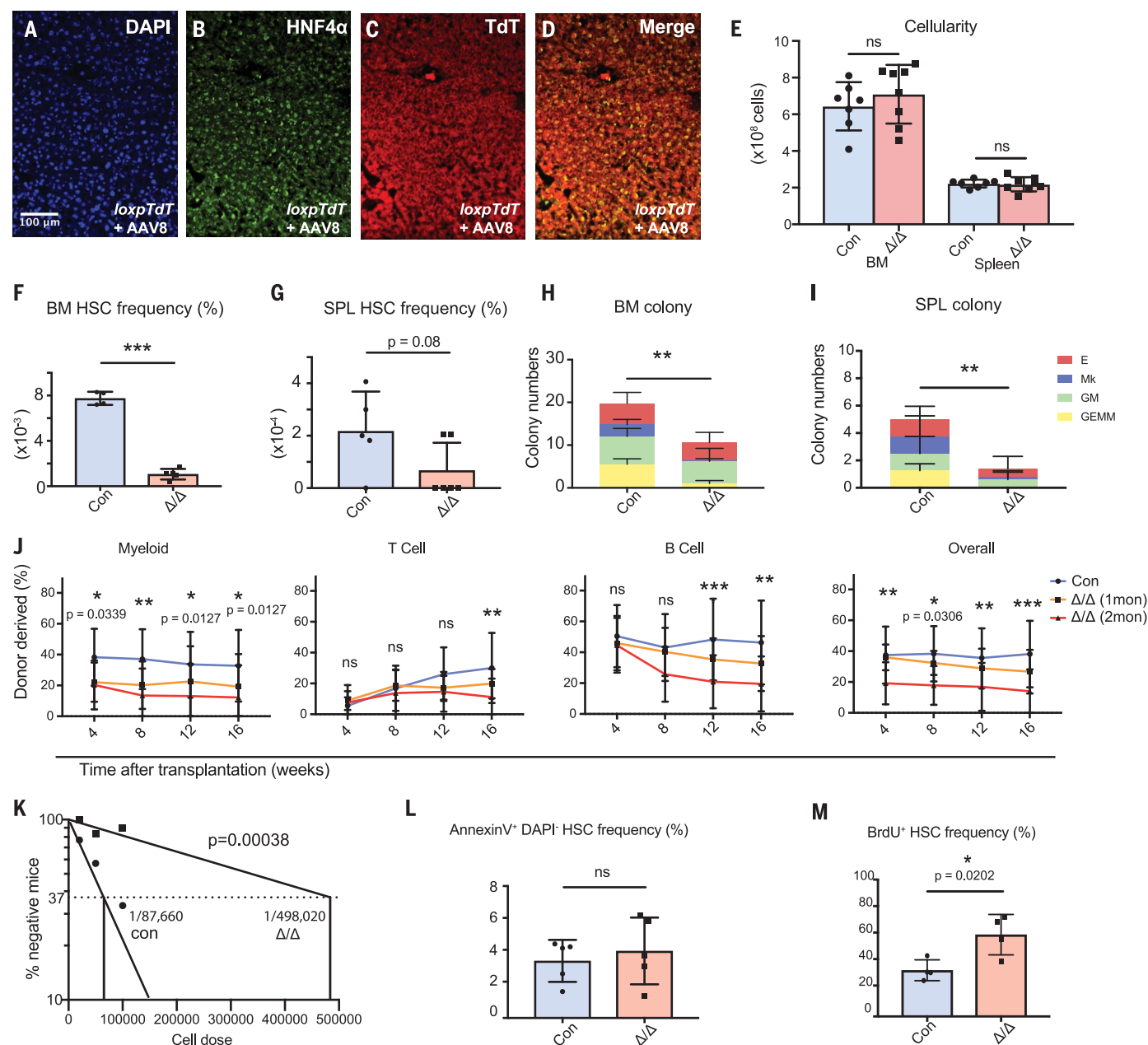


Fig. 4. TPO from adult hepatocytes regulates bone marrow HSC maintenance and quiescence. (A to D) Confocal images of liver sections from AAV8-TBG-cre-treated *loxpTdTomato* mice. (E) Bone marrow and spleen cellularity was normal in *Alb-cre;Tpo^{fl/fl}* mice ($n = 7$ to 8). (F) Bone marrow HSCs were depleted in AAV8-TBG-cre-treated *Tpo^{fl/fl}* mice ($n = 4$ to 5). (G) Spleen HSC frequency tended to decrease in AAV8-TBG-cre-treated *Tpo^{fl/fl}* mice. (H and I) Bone marrow and spleen colony-forming cell frequencies decreased in AAV8-cre; *Tpo^{fl/fl}* mice ($n = 6$ to 7). (J) Bone marrow cells (5×10^5) from AAV8-cre; *Tpo^{fl/fl}* mice gave lower levels of donor cell reconstitution than controls (in two to three experiments with a total of $n = 16$ for controls,

$n = 9$ for 1 month after AAV8 treatment, and $n = 14$ for 2 months after AAV8 treatment). (K) Limit dilution assays showed a 6-fold reduction in functional HSCs in the bone marrow from AAV8-cre; *Tpo^{fl/fl}* mice compared with those in controls (in two independent experiments). (L) Annexin V⁺ DAPI⁻ bone marrow HSC frequency was not affected in AAV8-cre; *Tpo^{fl/fl}* mice ($n = 5$). (M) Bone marrow HSCs incorporated more bromodeoxyuridine (BrdU) in AAV8-cre; *Tpo^{fl/fl}* mice ($n = 4$). Con, *Tpo^{+/+}* mice treated with AAV8-TBG-cre or *Tpo^{fl/fl}* mice treated with phosphate-buffered saline; Δ/Δ , *Tpo^{fl/fl}* mice treated with AAV8-TBG-cre. Data are means \pm SD. ns, not significant ($P > 0.10$). * $P < 0.05$, ** $P < 0.01$, *** $P < 0.001$.

bone marrow (17), and osteoblasts express *Tpo* transcripts (Fig. 1A); however, we could not detect any *Tpo* translational activity in osteoblasts from our reporter mice (Fig. 1, K to N). We directly tested whether deletion of *Tpo* from osteoblasts affects HSCs. Consistent with

previous reports (2, 3), *Col2.3-cre* recombined efficiently in bone-lining osteoblasts (fig. S6, A to G). Eight-week-old *Col2.3-cre;Tpo^{fl/fl}* mice had normal blood cell counts (fig. S6H), cellularity, and HSC frequency in the bone marrow and spleens (Fig. 2, A and B). Re-

stricted hematopoietic progenitors were also normal (fig. S6, I to L). Spleen megakaryocytic cells were unaffected (fig. S6M), as were the capacities of bone marrow and spleen cells to form colonies in methylcellulose (Fig. 2C and fig. S6N). *Col2.3-cre;Tpo^{fl/fl}* bone marrow

cells had normal capacities to reconstitute irradiated recipients (Fig. 2D and fig. S6, O and P). Thus, osteoblasts are not a critical source of TPO for HSC maintenance.

Bone marrow *Lepr*⁺ mesenchymal stromal cells are a critical source of HSC niche factors, including stem cell factor (SCF) and CXCL12 (2, 3). These cells express *Tpo* transcripts (Fig. 1A), although we could not detect *Tpo* translational activity (Fig. 1, K to N). We conditionally deleted *Tpo* from mesenchymal stromal cells by generating *Lepr-cre; Tpo*^{fl/ΔP} mice. *Tpo* was efficiently deleted from these cells (Fig. S7, A to G). Eight-week-old *Lepr-cre; Tpo*^{fl/ΔP} mice had normal blood cell counts (fig. S7H), cellularity, and HSC frequency in the bone marrow and spleens (Fig. 2, E and F). Restricted hematopoietic progenitors were also normal (fig. S7, I to L). Spleen megakaryocytic cells were unaffected (fig. S7M). Bone marrow and spleen cells from *Lepr-cre; Tpo*^{fl/ΔP} mice formed normal numbers of hematopoietic colonies in methylcellulose (Fig. 2G and fig. S7N). Bone marrow cells from *Lepr-cre; Tpo*^{fl/ΔP} mice reconstituted irradiated recipients normally (Fig. 2H and fig. S7, O and P). Thus, bone marrow mesenchymal stromal cells are not a critical source of TPO for HSC maintenance.

The above data suggest that TPO produced locally by osteoblasts or mesenchymal stromal cells is not required for HSC maintenance. To test whether systemic TPO generated by the liver is important for HSC maintenance, we generated *Alb-cre; Tpo*^{fl/ΔP} mice. As expected (31), *Alb-cre* recombined specifically and efficiently in hepatocytes but not in the bone marrow (Fig. 3, A to D, and fig. S8, A to D). Eight-week-old *Alb-cre; Tpo*^{fl/ΔP} mice had a fivefold reduction in platelet count (Fig. 3E and fig. S8E) and a fivefold reduction in megakaryocytic cells in the bone marrow (Fig. 3F). *Alb-cre; Tpo*^{fl/ΔP} mice exhibited normal bone marrow and spleen cellularity (Fig. 3G). The frequency of bone marrow HSCs was reduced by a factor of 24 compared with that in controls (Fig. 3H). LSK progenitors and MPPs were similarly reduced (fig. S8, F and G). CMPs were reduced in the bone marrow, whereas other restricted hematopoietic progenitors appeared normal (fig. S8H). Bone marrow and spleen cells from *Alb-cre; Tpo*^{fl/ΔP} mice formed fewer colonies in methylcellulose (Fig. 3, I and J). Spleen HSC frequency was normal in *Alb-cre; Tpo*^{fl/ΔP} mice (Fig. 3H), suggesting that there was no compensatory extramedullary hematopoiesis. Spleen CD41⁺ cell frequency decreased (fig. S8I). Bone marrow cells from *Alb-cre; Tpo*^{fl/ΔP} mice had severe defects in their ability to reconstitute irradiated recipients (Fig. 3, K and L). Overall, these data show that hepatic TPO is critical for the maintenance of bone marrow HSCs.

During development, HSCs transiently reside in the fetal liver (32), where *Alb-cre* recombines (33). Thus, it is possible that bone marrow HSCs in *Alb-cre; Tpo*^{fl/ΔP} mice acquire a persistent defect during development, although global deletion of *Tpo* has no impact on fetal liver HSCs (16). Nonetheless, we con-

ditionally deleted *Tpo* from adult hepatocytes by administering the hepatotropic Cre-bearing virus AAV8-TBG-cre (34). Consistent with a prior report (34), we observed specific and efficient recombination in hepatocytes after a single intravenous administration of AAV8-TBG-cre to adult mice (Fig. 4, A to D, and fig. S9, A to D).

We administered AAV8-TBG-cre virus once to 8-week-old *Tpo*^{fl/ΔP} mice and wild-type littermate control mice and analyzed the mice 4 to 8 weeks later. AAV8-TBG-cre-treated wild-type mice had phenotypes identical to those of buffer-treated *Tpo*^{fl/ΔP} mice. These mice were pooled together as controls. Deleting *Tpo* from adult hepatocytes (*AAV8-cre; Tpo*^{fl/ΔP}) significantly reduced platelet counts (fig. S9E). Bone marrow and spleen cellularity did not change (Fig. 4E). However, *AAV8-cre; Tpo*^{fl/ΔP} mice had significant reductions in bone marrow HSC, LSK, MPP, CMP, and CD41⁺ cell frequencies (Fig. 4F and fig. S9, G to I). The colony-forming capacities of bone marrow and spleen cells were also reduced (Fig. 4, H and I). Spleen HSC and CD41⁺ megakaryocytic cell frequencies trended lower (Fig. 4G and fig. S9J). Bone marrow cells from *AAV8-cre; Tpo*^{fl/ΔP} mice 2 months after the virus treatment had a significant decrease in their ability to reconstitute irradiated recipients, whereas bone marrow cells from *AAV8-cre; Tpo*^{fl/ΔP} mice 1 month after the virus treatment had an intermediate phenotype (Fig. 4J and fig. S9K). To quantify the frequency of functional HSCs, we performed limit dilution assays. In these assays, the frequencies of long-term multilineage reconstituting cells in bone marrow cells from control and *AAV8-cre; Tpo*^{fl/ΔP} mice were 1/87,660 and 1/498,020, respectively, corresponding to a 6-fold reduction (Fig. 4K). *AAV8-cre; Tpo*^{fl/ΔP} mice had no significant difference in Annexin V⁺ bone marrow HSCs compared with controls (Fig. 4L and fig. S9L), but HSCs from *AAV8-cre; Tpo*^{fl/ΔP} mice cycled more (Fig. 4M and fig. S9M). These data indicate that adult HSCs lacking hepatocyte-derived TPO signal are depleted through loss of quiescence.

Tpo transcription is up-regulated in the bone marrow during hematopoietic stress (21). We injected TMX-treated *Tpo*^{ΔRed-CreER}; *LoxPZsGreen* mice with 5-fluorouracil but failed to detect ZsGreen expression in the bone marrow (fig. S10), suggesting that bone marrow is not a major source of TPO in stress, at least under the conditions we tested. Our data show that hepatocytes are the major functional source of systemic TPO for bone marrow HSC maintenance under steady-state conditions. Further studies are required to determine the role of local and systemic TPO in nonhomeostatic conditions.

REFERENCES AND NOTES

1. S. J. Morrison, D. T. Scadden, *Nature* **505**, 327–334 (2014).
2. L. Ding, T. L. Saunders, G. Enikolopov, S. J. Morrison, *Nature* **481**, 457–462 (2012).
3. L. Ding, S. J. Morrison, *Nature* **495**, 231–235 (2013).

4. T. Sugiyama, H. Kohara, M. Noda, T. Nagasawa, *Immunity* **25**, 977–988 (2006).
5. S. Méndez-Ferrer et al., *Nature* **466**, 829–834 (2010).
6. A. Greenbaum et al., *Nature* **495**, 227–230 (2013).
7. D. T. Scadden, *Cell* **157**, 41–50 (2014).
8. J. Shim et al., *Cell* **155**, 1141–1153 (2013).
9. D. Nakada et al., *Nature* **505**, 555–558 (2014).
10. A. Grover et al., *J. Exp. Med.* **211**, 181–188 (2014).
11. S. Méndez-Ferrer, D. Lucas, M. Battista, P. S. Frenette, *Nature* **452**, 442–447 (2008).
12. K. Kaushansky et al., *Nature* **369**, 568–571 (1994).
13. S. Lok et al., *Nature* **369**, 565–568 (1994).
14. F. J. de Sauvage et al., *Nature* **369**, 533–538 (1994).
15. S. Kimura, A. W. Roberts, D. Metcalf, W. S. Alexander, *Proc. Natl. Acad. Sci. U.S.A.* **95**, 1195–1200 (1998).
16. H. Qian et al., *Cell Stem Cell* **1**, 671–684 (2007).
17. H. Yoshihara et al., *Cell Stem Cell* **1**, 685–697 (2007).
18. M. Ballmaier, M. Germeshausen, S. Krukemeier, K. Welte, *Ann. N.Y. Acad. Sci.* **996**, 17–25 (2003).
19. A. Seo et al., *Blood* **130**, 875–880 (2017).
20. M. J. Dasouki et al., *Blood* **122**, 3440–3449 (2013).
21. R. Sungar, B. Markovic, B. H. Chong, *Blood* **89**, 101–107 (1997).
22. A. Nakamura-Ishizu, K. Takubo, M. Fujioka, T. Suda, *Biochem. Biophys. Res. Commun.* **454**, 353–357 (2014).
23. A. Nakamura-Ishizu, K. Takubo, H. Kobayashi, K. Suzuki-Inoue, T. Suda, *J. Exp. Med.* **212**, 2133–2146 (2015).
24. B. McIntosh, K. Kaushansky, *Exp. Hematol.* **36**, 799–806 (2008).
25. N. Ghilardi, A. Wiestner, R. C. Skoda, *Blood* **92**, 4023–4030 (1998).
26. S. Qian, F. Fu, W. Li, Q. Chen, F. J. de Sauvage, *Blood* **92**, 2189–2191 (1998).
27. A. Guerrieri et al., *Blood* **90**, 3444–3455 (1997).
28. W. S. Alexander, A. W. Roberts, N. A. Nicola, R. Li, D. Metcalf, *Blood* **87**, 2162–2170 (1996).
29. A. L. Gurney, K. Carver-Moore, F. J. de Sauvage, M. W. Moore, *Science* **265**, 1445–1447 (1994).
30. M. J. Kiel et al., *Cell* **121**, 1109–1121 (2005).
31. C. Postic et al., *J. Biol. Chem.* **274**, 305–315 (1999).
32. H. K. A. Mikkola, S. H. Orkin, *Development* **133**, 3733–3744 (2006).
33. C. M. Weisend, J. A. Kundert, E. S. Suvorova, J. R. Prigge, E. E. Schmidt, *Genesis* **47**, 789–792 (2009).
34. K. Yanger et al., *Genes Dev.* **27**, 719–724 (2013).

ACKNOWLEDGMENTS

We thank V. Lin at the Columbia University transgenic core for helping generate *Tpo*^{fl/ΔP}, *Tpo*^{ΔRed-CreER}, and *Tpo*^{fl} mice. We thank S. Ho at the Columbia Center for Translational Immunology, A. Figueroa at the Columbia University Department of Microbiology and Immunology, and M. Kissner at the Columbia Stem Cell Initiative for flow cytometry. **Funding:** This work was supported by the Rita Allen Foundation and the National Heart, Lung, and Blood Institute (grant R01HL132074). M.D. was supported by the Columbia Medical Scientist Training Program and the NIH (grant 1F30HL137323). **Author contributions:** M.D., J.L., and L.D. performed experiments. Q.L. helped generate the targeting vectors. M.D. and L.D. designed the experiments, interpreted the results, and wrote the manuscript. **Competing interests:** The authors declare no competing interests. **Data and materials availability:** All data are available in the manuscript or the supplementary materials. The AAV8-TBG-cre virus is available from the Penn Vector Core under a material transfer agreement with the University of Pennsylvania.

SUPPLEMENTARY MATERIALS

www.sciencemag.org/content/360/6384/106/suppl/DC1
Materials and Methods
Figs. S1 to S10
References (35–40)

6 September 2017; accepted 8 February 2018
10.1126/science.aap8861

ANCIENT GENOMES

Ancient genomes revisit the ancestry of domestic and Przewalski's horses

Charleen Gauntitz,^{1*} Antoine Fages,^{1,2*} Kristian Hanghøj,^{1,2} Anders Albrechtsen,³ Naveed Khan,^{1,4} Mikkel Schubert,¹ Andaine Seguin-Orlando,^{1,2,5} Ivy J. Owens,^{6,7} Sabine Felkel,⁸ Olivier Bignon-Lau,⁹ Peter de Barros Damgaard,¹ Alissa Mittnik,¹⁰ Azadeh F. Mohaseb,^{11,12} Hossein Davoudi,^{12,13,14} Saleh Alquraishi,¹⁵ Ahmed H. Alfarhan,¹⁵ Khaled A. S. Al-Rasheid,¹⁵ Eric Crubézy,² Norbert Benecke,¹⁶ Sandra Olsen,¹⁷ Dorcas Brown,¹⁸ David Anthony,¹⁸ Ken Massy,¹⁹ Vladimir Pitulko,²⁰ Aleksei Kasparov,²⁰ Gottfried Brem,⁸ Michael Hofreiter,²¹ Gulmira Mukhtarova,²² Nurbol Baimukhanov,²³ Lembi Lõugas,²⁴ Vedat Onar,²⁵ Philipp W. Stockhammer,^{10,19} Johannes Krause,¹⁰ Bazartseren Boldgiv,²⁶ Sainbileg Undrakhbold,²⁶ Diimaajav Erdenebaatar,²⁷ Sébastien Lepetz,¹¹ Marjan Mashkour,^{11,12,13} Arne Ludwig,²⁸ Barbara Wallner,⁸ Victor Merz,²⁹ Ilja Merz,²⁹ Viktor Zaitbert,³⁰ Eske Willerslev,^{1,31,32} Pablo Librado,¹ Alan K. Outram,^{6†} Ludovic Orlando^{1,2†}

The Eneolithic Botai culture of the Central Asian steppes provides the earliest archaeological evidence for horse husbandry, ~5500 years ago, but the exact nature of early horse domestication remains controversial. We generated 42 ancient-horse genomes, including 20 from Botai. Compared to 46 published ancient- and modern-horse genomes, our data indicate that Przewalski's horses are the feral descendants of horses herded at Botai and not truly wild horses. All domestic horses dated from ~4000 years ago to present only show ~2.7% of Botai-related ancestry. This indicates that a massive genomic turnover underpins the expansion of the horse stock that gave rise to modern domesticates, which coincides with large-scale human population expansions during the Early Bronze Age.

Horses revolutionized human mobility, economy, and warfare (1). They are also associated with the spread of Indo-European languages (2) and new forms of metallurgy (3) and provided the fastest land transport until modern times. Together with the lack of diachronic changes in horse morphology (4) and herd structure (5, 6), the scarce archaeological record hampered the study of early domestica-

tion. With their preponderance of horse remains, Eneolithic sites (fifth and fourth millennia BCE) of the Pontic-Caspian steppe (2, 7) and the northern steppe of Kazakhstan (6, 8) have attracted the most attention.

We reconstructed the phylogenetic origins of the Eneolithic horses associated with the Botai culture of northern Kazakhstan, representing the earliest domestic horses (6, 8). This culture was

characterized by a sudden shift from mixed hunting and gathering to an extreme focus on horses and larger, more sedentary settlements (5). Horse dung on site (6), as well as evidence for poleaxing and against selective body-part transportation, suggests controlled slaughter at settlements rather than hunting (9). Tools associated with leather thong production, bit-related dental pathologies (7, 10), and equine milk fats within ceramics support pastoral husbandry, involving milking and harnessing (8).

Geological surveys at the Botai culture site of Krasnyi Yar, Kazakhstan, described a polygonal enclosure of ~20 m by 15 m with increased phosphorus and sodium concentrations (6), likely corresponding to a horse corral. We revealed a similar enclosure at the eponymous Botai site, ~100 km west of Krasnyi Yar (Fig. 1A), that shows close-set post molds, merging to form a palisade trench, and a line of smaller parallel postholes inside (Fig. 1B). Radiocarbon dates on horse bones from these postholes are consistent with the Botai culture (11). The presence of enclosures at Krasnyi Yar and Botai builds on the evidence supporting horse husbandry.

We sequenced the genomes of 20 horses from Botai and 22 from across Eurasia and spanning the past ~5000 years (table S1). With the published genomes of 18 ancient and 28 modern horses, this provided a comparative panel of 3 wild archaic horses (~42,800 to 5100 years ago), 7 Przewalski's horses (PH, 6 modern and 1 from the 19th century), and 78 domesticates (25 Eneolithic, including 5 from Borly4, Kazakhstan, ~5000 years ago; 7 Bronze Age, ~4100 to 3000 years ago; 18 Iron Age, ~2800 to 2200 years ago; 1 Parthian and 2 Roman, ~2000 to 1600 years ago; 3 post-Roman, ~1200 to 100 years ago; and 22 modern from 18 breeds).

The 42 ancient-horse genomes, belonging to 31 horse stallions and 11 mares, were sequenced to an average depth of coverage of ~1.1 to 9.3X

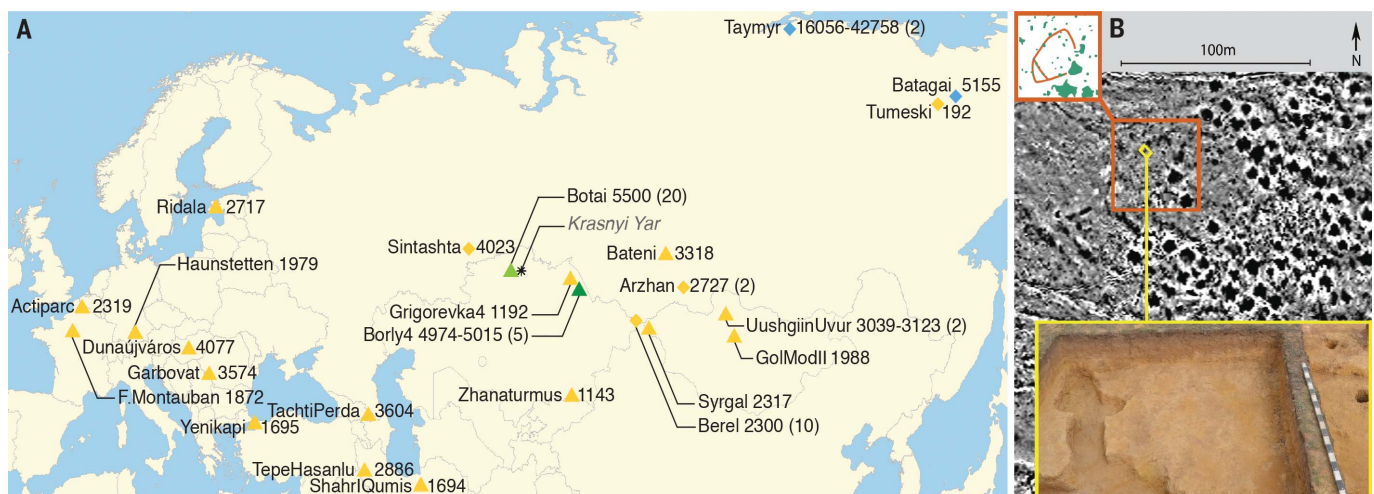


Fig. 1. Sample location and corral enclosure at Botai. (A) Archaeological sites. The age (years ago) of the genomes considered is reported to the right of each site name. The number of genomes sequenced per site is reported between parentheses if greater than one. Triangles refer to the ancient genomes characterized here, whereas diamonds indicate those previously published. Blue refers to wild ancient individuals, light and dark green to the

first domestic clade (Botai and Borly4), and yellow to individuals of the second domestic clade (DOM2). The Botai culture site of Krasnyi Yar is indicated with an asterisk, although no samples were analyzed from this site. (B) Magnetic gradient survey and excavation at Botai, with interpretation. The enclosure and its excavated boundary are indicated by red and yellow squares, respectively. Round black circles correspond to pit houses.

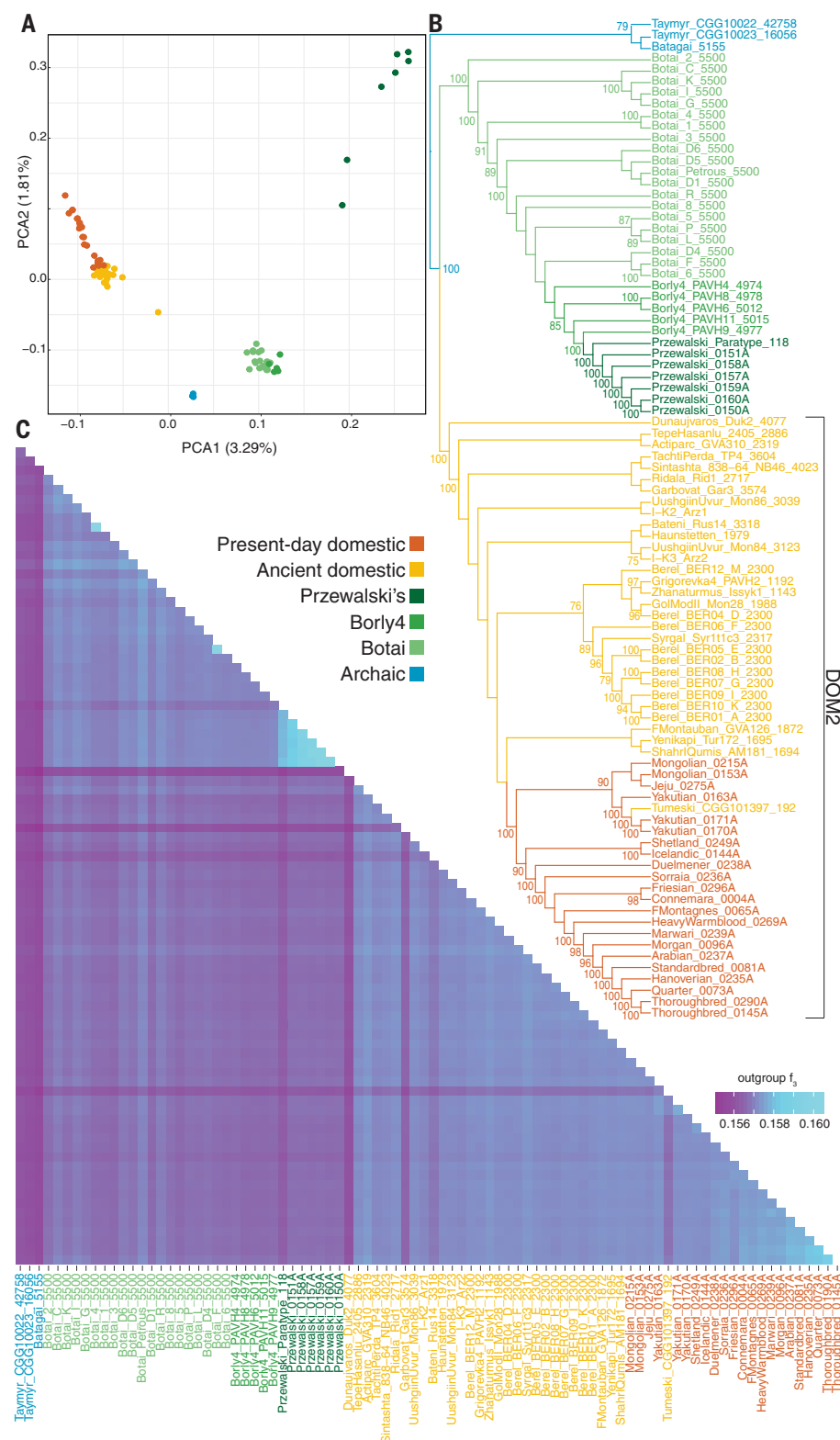


Fig. 2. Horse genetic affinities. (A) PCA of the genome variation present in 88 ancient- and modern-horse genomes. Only the first two principal components (PCA1 and PCA2) are shown. (B) Phylogenetic relationships. The tree was reconstructed on the basis of pairwise distances calculated with ~14.1 million transversion sites. Node supports derive from 100 bootstrap pseudoreplicates. The archaeological site and age (years ago) of ancient specimens are indicated in the first and last fields of the sample name. (C) Outgroup *f3*-statistics showing the pairwise genetic affinities.

(median = 3.0X). Damage patterns indicative of ancient DNA were recovered (figs. S8 and S9). Base-quality rescaling and termini trimming resulted in average error rates of 0.07 to 0.14% per site (tables S13 and S14).

Principal component analysis (PCA) revealed PH and the archaic horses as two independent clusters (Fig. 2A). Within domesticates, all 25 Botai-Borly4 Eneolithic specimens grouped together to the exclusion of all remaining horses.

Phylogenetic reconstruction confirmed that domestic horses do not form a single monophyletic group as expected if descending from Botai (Fig. 2B). Instead, PH form a highly drifted, monophyletic

¹Centre for GeoGenetics, Natural History Museum of Denmark, 1350K Copenhagen, Denmark. ²Laboratoire d'Anthropobiologie Moléculaire et d'Imagerie de Synthèse UMR 5288, Université de Toulouse, CNRS, Université Paul Sabatier, France. ³Bioinformatics Center, Department of Biology, University of Copenhagen, 2200N Copenhagen, Denmark. ⁴Department of Biotechnology, Abdul Wali Khan University, Mardan 23200, Pakistan. ⁵National High-Throughput DNA Sequencing Center, 1353K Copenhagen, Denmark. ⁶Department of Archaeology, University of Exeter, Exeter EX4 4QE, UK. ⁷The Charles McBurney Laboratory for Geoarchaeology, Department of Archaeology, University of Cambridge, Cambridge CB2 3DZ, UK. ⁸Institute of Animal Breeding and Genetics, University of Veterinary Medicine Vienna, 1210 Vienna, Austria. ⁹Équipe Ethnologie préhistorique, ArScAn, CNRS, UMR 7041, Maison de l'Archéologie et de l'Ethnologie (MAE) René-Ginouvès, 92023 Nanterre Cédex, France. ¹⁰Department of Archaeogenetics, Max Planck Institute for the Science of Human History, 07745 Jena, Germany. ¹¹Centre National de la Recherche Scientifique, Muséum National d'Histoire Naturelle, Archéozoologie, Archéobotanique, Sociétés, Pratiques et Environnements, UMR 7209, 75005 Paris, France. ¹²Archaeozoology section, Archaeometry Laboratory, University of Tehran, Tehran CP1417634934, Iran. ¹³Osteology Department, National Museum of Iran, Tehran 1136918111, Iran. ¹⁴Department of Archaeology, Faculty of Humanities, Tarbiat Modares University, Tehran 14115, Iran. ¹⁵Zoology Department, College of Science, King Saud University, Riyadh 11451, Saudi Arabia. ¹⁶German Archaeological Institute, Department of Natural Sciences, 14195 Berlin, Germany. ¹⁷Biodiversity Institute—Museum of Natural History, University of Kansas, Lawrence, KS 66045, USA. ¹⁸Anthropology Department, Hartwick College, Oneonta, NY 13820, USA. ¹⁹Institute for Pre- and Protohistoric Archaeology and Archaeology of the Roman Provinces, Ludwig-Maximilians-University Munich, 80799 München, Germany. ²⁰Institute for the History of Material Culture, Russian Academy of Sciences, St. Petersburg 191186, Russia. ²¹Institute for Biochemistry and Biology, Faculty of Mathematics and Natural Sciences, University of Potsdam, 14476 Potsdam, Germany. ²²Issyk State Historical-Cultural Reserve Museum, 040400 Almaty Region, Enbekshikazak District, Kazakhstan. ²³Shejire DNA Project, 050046 Almaty, Kazakhstan. ²⁴Archaeological Research Collection, Tallinn University, 10130 Tallinn, Estonia. ²⁵Osteoarchaeology Practice and Research Center and Department of Anatomy, Faculty of Veterinary Medicine, Istanbul University, 34320 Aviclar Istanbul, Turkey. ²⁶Ecology Group, Department of Biology, School of Arts and Sciences, National University of Mongolia, Ulaanbaatar 14201, Mongolia. ²⁷Department of Archaeology, Ulaanbaatar State University, Ulaanbaatar 51, Mongolia. ²⁸Department of Evolutionary Genetics, Leibniz Institute for Zoo and Wildlife Research, 10315 Berlin, Germany. ²⁹S.Toraihyrov Pavlodar State University, Joint Research Center for Archeological Studies, 637000 Pavlodar, Kazakhstan. ³⁰Scientific Research Institute of Archaeology and Steppe Civilizations, Al Farabi Kazakh National University, 050040 Almaty, Kazakhstan. ³¹Department of Zoology, University of Cambridge, Cambridge CB2 3EJ, UK. ³²Wellcome Trust Genome Campus, Hinxton CB10 1SA, UK.

*These authors contributed equally to this work.

†Corresponding author. Email: a.k.outtram@exeter.ac.uk (A.K.O.); ludovic.orlando@univ-tlse3.fr (L.O.)

group, unambiguously nested within Botai-Borly4 horses. All remaining domesticates cluster within a second, highly supported monophyletic group (DOM2). Applying TreeMix (12) to the 60 genomes with minimal 3.0X average depth of coverage confirmed this tree topology (fig. S23).

Outgroup f_3 - and D -statistics (13) support PH as genetically closer to Botai-Borly4 individuals than any DOM2 member (Fig. 2C and figs. S25 and S26). Finally, ancestry tests (14) confirmed Botai horses as the direct ancestors of Borly4 horses, and the Borly4 as ancestral to the only PH in our data set predating their massive demographic collapse and introgression of modern domestic genes (15).

Outgroup f_3 - and D -statistics also revealed that Dunaújváros_Duk2 (Duk2), the earliest and most basal specimen within DOM2, was divergent to all other DOM2 members. This is not due to sequencing errors, because the internal branch that splits from Duk2 and leads to the ancestor of all remaining DOM2 horses is long (Fig. 2B). This suggests instead shared ancestry between Duk2 and a divergent ghost population. We thus excluded Duk2 in admixture graph reconstructions (16) to avoid bias due to contributions from unsampled lineages (Fig. 3).

In the absence of admixture, the best admixture graph matched the trees reconstructed above. We also reconstructed admixture graphs for five additional scenarios with one or two admixture event(s), including between PH and domesticates (15). Bayes factors best supported a horse domestication history in which a first lineage gave rise to Botai-Borly4 and PH horses, whereas a second lineage founded DOM2 and provided the source of domestic horses during at least the past ~4000 years, with minimal contribution from the Botai-Borly4 lineage [95% confidence interval (CI) = 2.0 to 3.8%].

The limited Botai-Borly4 ancestry among DOM2 members concurs with slightly significant negative D -statistics in the form of $\{[(\text{DOM2_ancient}, \text{DOM2_modern}), \text{Botai-Borly4}], \text{donkey}\}$ for some DOM2 members, spanning a large geographical (Western Europe, Turkey, Iran, and Central Asia) and temporal range (from ~3318 to ~1143 years ago; fig. S28). This suggests that sporadic introgression of Botai ancestry into multiple DOM2 herds occurred until 1000 years ago. This gene flow was mediated not only through females, because 15 Botai-Borly4 individuals carried mitochondrial haplotypes characteristic of DOM2 matriline (figs. S12 and S13), but also through males, given the persistence of Botai-Borly4-related patriline within DOM2 (figs. S15 to S18).

PH are considered to be the last remaining true wild horses, which have never been domesticated (15). Our results reveal that they represent instead the feral descendants of horses first herded at Botai. It appears that their feralization likely involved multiple biological changes.

Metacarpal measurements in 263 ancient and 112 modern horses indicate that PH have become less robust than their Botai-Borly4 ancestors (Fig. 4A). One Botai individual likely showed limited unpigmented areas and leopard spots,

as it was heterozygous for four mutations at the *TRPM1* locus associated with leopard spotting and carried the ancestral allele at the *PATN1* modifier (17, 18) (Fig. 4B). Individuals homozygous for *TRPM1* mutations are generally almost completely unpigmented and develop congenital stationary night blindness (17). First maintained at Botai by human management, the haplotype associated with leopard spotting was likely selected against and lost once returning wild, leading to the characteristic PH Dun dilution coloration (19). Genomic regions with signatures of positive selection along the phylogenetic branch separating Borly4 and PH showed functional enrichment for genes associated, in humans, with cardiomyopathies ($P \leq 0.0496$), melanosis and hyperpigmentation ($P \leq 0.0468$), and skeletal abnormalities ($P \leq 0.0594$) (table S18), suggesting that at least some of the morpho-anatomical changes associated with feralization were adaptive.

Additionally, significantly negative D -statistics in the form of $\{[(\text{DOM2_PH}), \text{archaic}], \text{donkey}\}$ previously suggested that the extinct, archaic lineage formed by ~5100- to 42,700-year-old horses from Taymyr and Yakutia contributed to the genetic ancestry of modern domesticates (20, 21). Although we could confirm such D -statistics (fig. S29), almost all other D -statistics in the form of $\{[(\text{DOM2_Botai-Borly4}), \text{archaic}], \text{donkey}\}$ were not different from zero (fig. S30). This indicates selection against the archaic an-

cestry between ~4977 and ~118 years ago (the time interval separating the youngest Borly4 individual and the earliest PH sequenced). Alternatively, the PH lineage admixed with a divergent population of horses, both unrelated to the archaic lineage and the ghost population that contributed ancestry to Duk2, because D -statistics revealed Duk2 as closer to Borly4 than to PH (fig. S31).

Lastly, although the genetic load of PH and Botai-Borly4 genomes was equivalent until ~118 years ago, it drastically increased in modern animals (Fig. 4C). This accumulation of deleterious variants was thus not associated with PH feralization but with the recent introgression of deleterious variants from modern domesticates and demographic collapse, which hampered purifying selection.

That none of the domesticates sampled in the past ~4000 years descend from the horses first herded at Botai entails another major implication. It suggests that during the third millennium BCE, at the latest, another unrelated group of horses became the source of all domestic populations that expanded thereafter. This is compatible with two scenarios. First, Botai-type horses experienced massive introgression capture (22) from a population of wild horses until the Botai ancestry was almost completely replaced. Alternatively, horses were successfully domesticated in a second domestication center and incorporated minute amounts of Botai ancestry during their expansion.

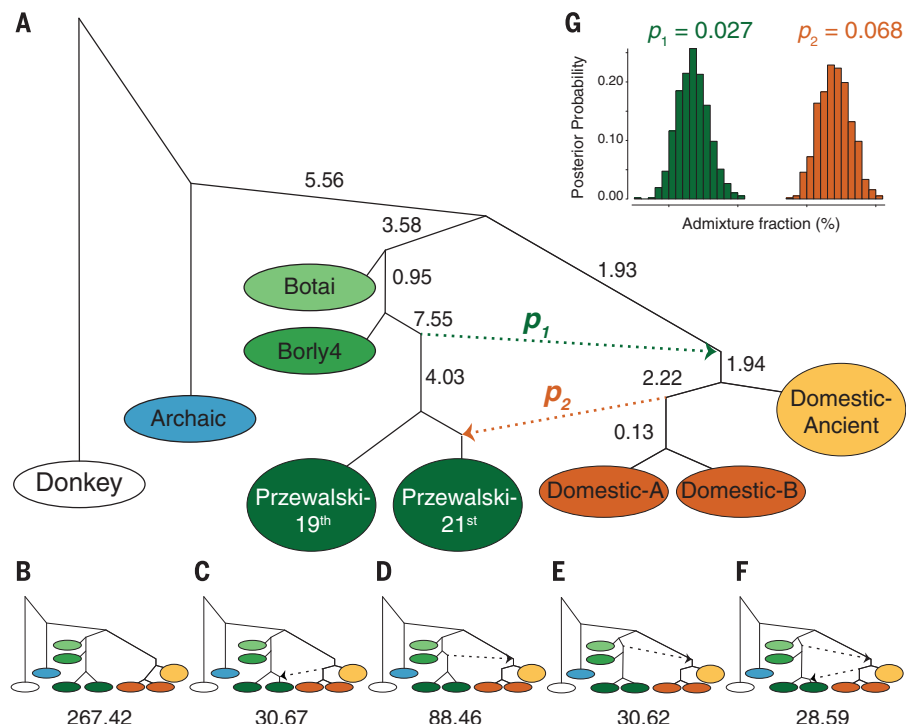
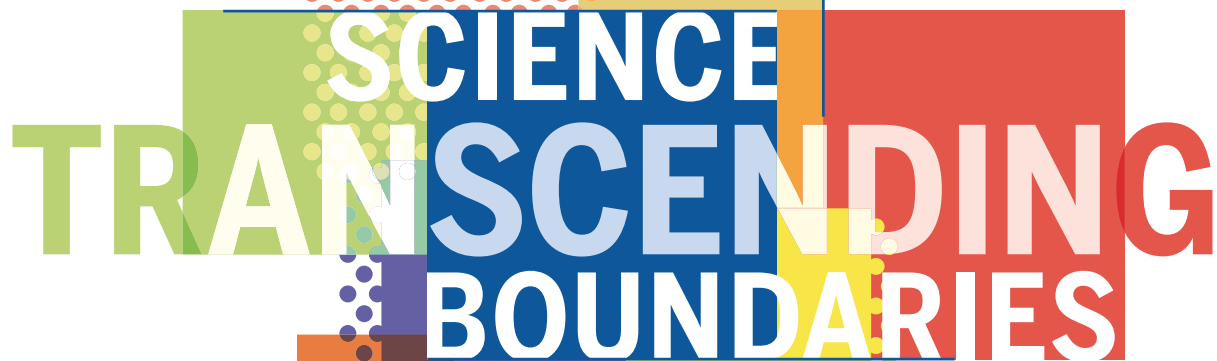


Fig. 3. Admixture graphs. (A to F) The six scenarios tested. The scenario in panel (A) received decisive Bayes factor support, as indicated below each corresponding alternative scenario tested. Domestic-Ancient and Domestic-A or -B refer to three phylogenetic clusters identified within DOM2 (excluding Duk2): ancient individuals; modern Mongolian, Yakutian (including Tumeski_CGG101397), and Jeju horses; and all remaining modern breeds. (G) Posterior distributions of admixture proportions. p_1 and p_2 represent admixture proportions along the dotted branches in the best-supported scenario.



SCIENCE TRANSCENDING BOUNDARIES

Call for Session Proposals

Session proposals for the 2019 AAAS Annual Meeting are now being solicited.
Deadline for submission: **April 19, 2018**

aaas.org/meetings



AAAS
ANNUAL MEETING
Feb. 14–18, 2019 | Washington, DC

How can science help address the many divisions in our communities, in global society, and in science itself? Science plays a unique and important role in how people see and understand the world, and how lines and distinctions are drawn. At this Annual Meeting, we look for ways science is bringing together people, ideas, and solutions from across real and artificial borders, disciplines, sectors, ideologies, and traditions. How can science working across boundaries improve its ability to find solutions to the pressing problems of our age? How can scientists, wherever they work, more effectively engage with the broader society? How can we find better ways to engage the public, especially in expanding access to science and scientific careers? At the international level, science diplomacy builds bridges between countries. How can we encourage more of this, and utilize science as a common ground more locally as well? Can science contribute information that might reduce or mitigate the starkly divergent interests of different populations and demographics, such as urban and rural communities? What boundaries most impede your research or your career? While acknowledging that some boundaries are useful and necessary, the meeting theme considers how research can be applied to problematic separations in the world, and how unhelpful boundaries within science are being addressed.



Global Ocean Summit 2018 (GOS2018), as the 2nd Global Ocean Summit, will be scheduled at Qingdao, China during 3-5 July 2018 and hosted jointly by Qingdao National Laboratory for Marine Science and Technology (QNLN) and Science/AAAS. It will follow the spirit of Building the Partnerships on Ocean Observation and Research which was widely recognized by the 1st Global Ocean Summit held in Qingdao, China during 26-28 Sept 2016, and invite the leaders and scientists from global marine research institutions, universities, and international organizations and programs including Woods Hole Oceanographic Institution, Scripps Institution of Oceanography, French Research Institute for Exploitation of the Sea, Russian Academy of Sciences, Japan Agency for Marine-Earth Science and Technology, North Pacific Marine Science Organization, Group on Earth Observation etc. We warmly welcome more leaders and scientists interested in marine science and technology join in the world-class grand event and register in the conference website www.gos2018.cn, and the accommodation with meal will be provided by QNLN.

QNLN, as one of the co-hosts to GOS2018, is approved by Ministry of Science and Technology in December, 2013, jointly supported by the national ministries and departments, Shandong Province and Qingdao Municipal Government. Being committed to build a world-class comprehensive research center of marine science and technology as well as an open platform for collaborative innovation, QNLN brings in resources and professional teams for the original researches, and jointly constructs the international Laboratories and centers with world-class institutes, such as the Centre for Southern Hemisphere Oceans Research, the International Laboratory for High Resolution Earth System Prediction, and the being constructed international joint center with Woods Hole Oceanographic Institute. More information about QNLN can be referred to www.qnlm.ac.

The 1st GOS had gathered nearly 70 leaders and heads from the marine research institutions, universities and international organizations and programs. It has released the “Qingdao Declaration” advocating jointly to commit to Building Partnership for Ocean Observation and Research to address the challenges arising from socio-economic development and global climate change, and to create opportunities for collaboration in marine research, observation, prediction, to inform use and sustainability. More information can browse to the link <http://gos2016.qnlm.ac/index>.

The 2nd GOS will uphold the Qingdao Declaration and continually delve deeper into “Building the Partnerships on Ocean Observation and Research”, focusing on: (1) ocean observation and prediction, (2) deep-sea research, (3) polar seas research, and (4) ocean sustainable, exchanging the development strategy on marine research institutions, discussing the sharing of knowledge, education resources, and infrastructure, and exploring solutions to challenges in marine science and technology resulted from economic development and global change.

Looking forward to your participation in Global Ocean Summit 2018!

CALL FOR PAPERS



SciencePartnerJournals.org/research

Research

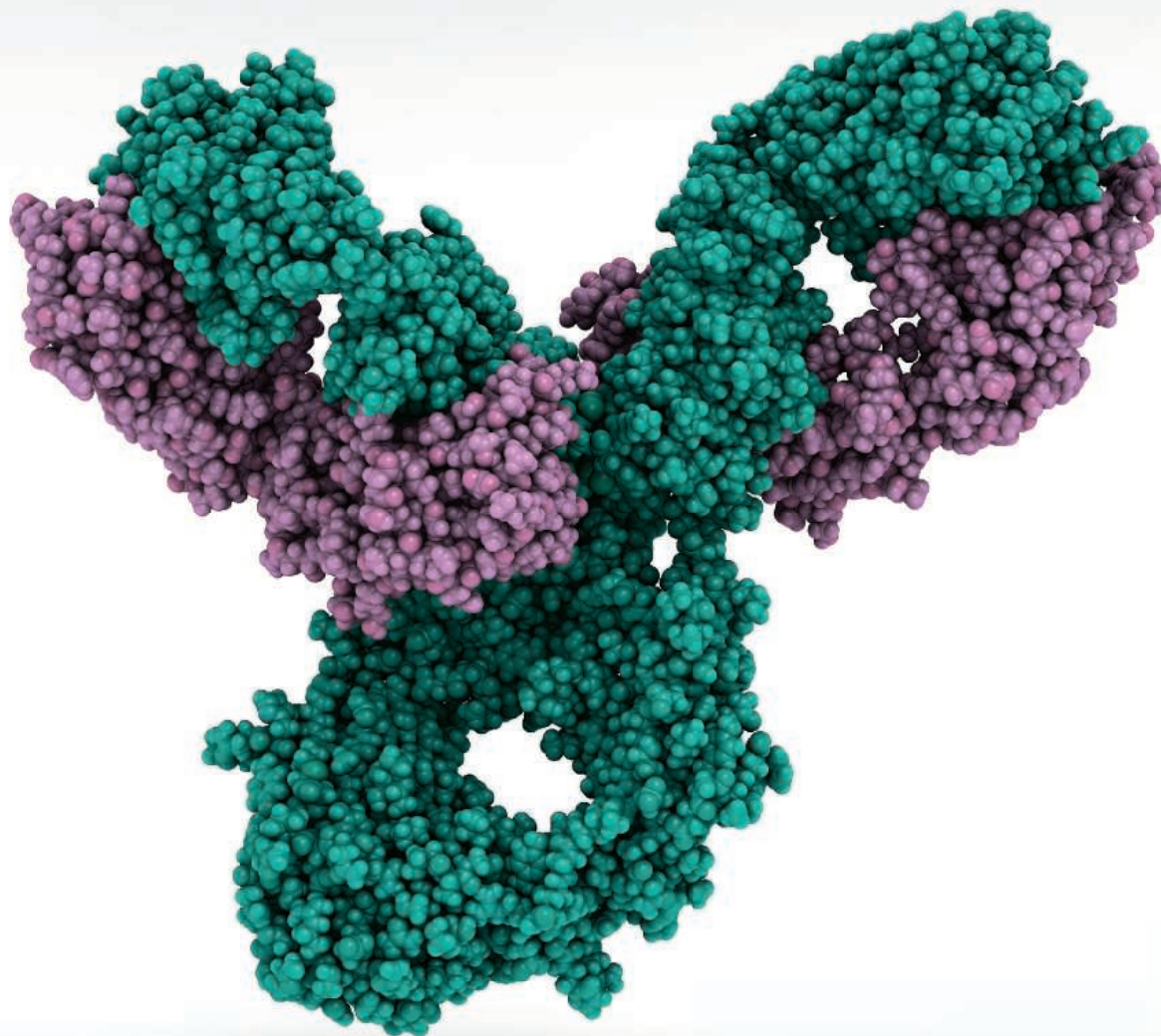
OFFICIAL JOURNAL OF CAST

An Open Access Journal

Research is a comprehensive, interdisciplinary, and selective **Open Access journal from the China Association of Science and Technology (CAST)**, published quarterly and distributed by the **American Association for the Advancement of Science (AAAS)**. *Research* provides an international platform for academic exchange, research collaboration, and technological advancements. The journal will publish fundamental research in the life and physical sciences as well as important findings or issues in engineering and applied science.

The **Science Partner Journals (SPJ)** program was established by AAAS, the nonprofit publisher of the *Science* family of journals. The SPJ program features high-quality, online-only open access publications produced in collaboration with international research institutions, foundations, funders and societies. Through these collaborations, AAAS expands its efforts to communicate science broadly and for the benefit of all people by providing top-tier international research organizations with the technology, visibility and publishing expertise that AAAS is uniquely positioned to offer as the world's largest international science society.

Publish your research in ***Science Immunology***



Science Immunology publishes original, peer-reviewed, science-based research articles that report critical advances in all areas of immunological research, including important new tools and techniques.

For more information: ScienceImmunology.org

Science
Immunology
AAAS

2017 Winner
Flavio Donato, Ph.D.
Kavli Institute
Norwegian University of
Science and Technology

For research on how neural
networks mature during
development to represent
space in the brain



Call for Entries

Application Deadline
June 15, 2018

Eppendorf & Science Prize for Neurobiology

The annual Eppendorf & Science Prize for Neurobiology is an international award which honors young scientists for their outstanding contributions to neurobiological research based on methods of molecular and cell biology. The winner and finalists are selected by a committee of independent scientists, chaired by *Science's* Senior Editor, Dr. Peter Stern. To be eligible, you must be 35 years of age or younger.

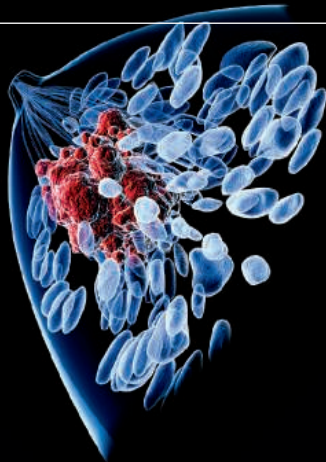
As the Grand Prize Winner, you could be next to receive

- > Prize money of US\$25,000
- > Publication of your work in *Science*
- > Full support to attend the Prize Ceremony held in conjunction with the Annual Meeting of the Society for Neuroscience in the USA
- > 10-year AAAS membership and online subscription to *Science*
- > Complimentary products worth US\$1,000 from Eppendorf
- > An invitation to visit Eppendorf in Hamburg, Germany

It's easy to apply! Learn more at:

www.eppendorf.com/prize

DOES YOUR LAB SEEK TO UNDERSTAND MECHANISMS OF DRUG RESISTANCE OR DISEASE PATHOLOGY?



Leslie K. Ferrarelli, "Focus Issue: Refining the War on Cancer", *Sci. Signal.* 7, 318eg2 (2014). Image: Raycat/iStockphoto

ScienceSignaling | AAAS
CELL SIGNALING IN PHYSIOLOGY AND DISEASE

Find out more about the scope of the journal and submit your research today. ScienceSignaling.org

AAASTravels



NEW ZEALAND Expedition

November 15-30, 2018

Explore New Zealand with outstanding naturalist Lloyd Esler, from Christchurch to Westland, Milford Sound to Stewart Island, Dunedin to Rotorua & Auckland!

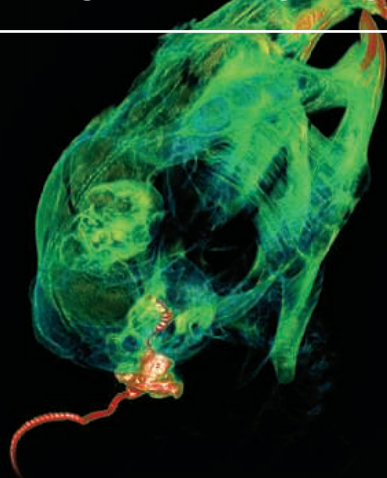
For a detailed brochure, call (800) 252-4910

All prices are per person twin share + air



BETCHART EXPEDITIONS Inc.
17050 Montebello Rd, Cupertino, CA 95014
Email: AAASInfo@betchartexpeditions.com
www.betchartexpeditions.com

CALL FOR PAPERS! DOES YOUR LAB TRANSLATE BIOMEDICAL RESEARCH INTO NEW CLINICAL APPLICATIONS?



Jeremy L. Pinyon *et al.* (Gary D. Housley), "Close-Field Electroporation Gene Delivery Using the Cochlear Implant Electrode Array Enhances the Bionic Ear", *Sci. Transl. Med.* 6, 233ra54 (2014) Credit: T. Hung, A. Kwek, J. Pinyon, and G. Housley/UNSW Australia and the National Imaging Facility of Australia

Challenge your thinking with the leading online journal of high-impact, peer-reviewed translational research that matters most for human health.

Part of the Science family of journals, *Science Translational Medicine* publishes weekly and showcases findings on interdisciplinary topics driving preclinical and clinical applications, including immunology, cancer, infectious disease, drug discovery, genomic medicine, and bioengineering.

Learn more and submit your research today.

ScienceTranslationalMedicine.org

**Science
Translational
Medicine**
AAAS



Bioreactor Range

The BIOSTAT STR is a fully scalable, single-use bioreactor family based on a conventional stirred-tank design. This new bioreactor range features upgraded hardware and software, as well as a fully integrated new design for Flexsafe STR single-use bags—all of which ensure quick and easy bioprocess scale-up of biologics and vaccines. The series consists of five systems in different sizes, and offers working volumes from 12.5 L to 2,000 L. Linear scale-up and

process transfer from 250 mL to 2,000 L can be achieved in weeks rather than months. The bioreactor's fully self-contained design, with its single-use bag, prevents product cross-contamination and saves time in setup, validation, clean-in-place procedures, and sterilize-in-place operations. Designed for efficient oxygen transfer, mixing, and CO₂ stripping, the system ensures excellent cell-culture performance with reproducible high-density growth even for sensitive cell lines.

Sartorius Stedim Biotech

For info: +49-(0)-551-308-0

www.sartorius.com/biostat-str

RNAi Services

The professional technical services provided by GenePharma's RNAi service team can help clients get the most out of their RNA interference (RNAi) technology and avoid some experimental errors. Our research team will work with you to develop more extensive and effective solutions. We offer two types of RNAi services: chemical-synthesis and vector-based services. Our RNAi services can be applied in areas such as functional genomics, gene therapy, drug-target screening, cellular-signal pathway analysis, and protein interaction. We also provide custom RNAi synthesis, including small interfering RNA (siRNA) oligos, predesigned siRNAs, short hairpin RNA (shRNA) plasmid vectors, and predesigned shRNA vectors.

GenePharma

For info: 400-690-0195

en.genepharma.com/en

Flow Cytometer System

NovoCyte is a high-performance benchtop flow cytometer designed for all levels of users and all types of laboratories. This budget-friendly instrument can detect up to 15 parameters with enhanced sensitivity and resolution. NovoCyte's customizable laser and optical configurations offer a high degree of flexibility while providing complex cell-analysis capabilities. The NovoExpress software facilitates easy, intuitive sample acquisition and analysis. Automation of multiple fluidic functions eliminates cumbersome and time-consuming procedures. User hands-on time is minimized by the flexible NovoSampler Pro, which can automatically analyze samples in single tubes, multitube racks, or 24-, 48-, or 96-well plates.

ACEA Biosciences

For info: 858-724-0928

www.aceabio.com/products/novocyte

Reporter Lentivirus for Signaling Pathway Studies

AMS Biotechnology (AMSBIO) has introduced a range of ready-to-use reporter lentiviruses for assessing cell-signaling activities in virtually any mammalian cell type. These premade products use a unique combination of transcription-factor reporter technology coupled with lentiviral delivery to provide a simple, highly sensitive method capable of operating over a large dynamic range. By measuring the activities of a reporter, AMSBIO Reporter Lentivirus can be used for performing gene regulation studies in living mammalian cells, and for functional genomics as well as drug-screening cell-signaling assays. It can also be used for generating your own pathway-screening assay cell lines. Options include androgen and estrogen receptors, JNK, NF-κB, Notch, and Wnt signaling pathways.

AMS Biotechnology

For info: +44-(0)-1235-828-200

www.amsbio.com/lentiviral-vector-systems.aspx

T-Cell Reagents

Ready to take your T-cell therapy research from bench to bedside? STEMCELL Technologies has a series of Current Good Manufacturing Practice-grade T-cell isolation, activation, and expansion reagents. The EasySep Release Human CD3 Positive Selection Kit is designed to positively select particle-free CD3⁺ cells from fresh or previously frozen peripheral blood mononuclear cells or washed leukapheresis samples, using a column-free immunomagnetic selection. ImmunoCult Human CD3/CD28 T-Cell Activator and ImmunoCult Human CD3/CD28/CD2 T-Cell Activator are soluble antibody complexes that recognize and crosslink CD3 and costimulatory molecules for robust activation and expansion of human T cells without using magnetic beads, feeder cells, or antigen. ImmunoCult-XF T-Cell Expansion Medium is a serum-free, xeno-free medium optimized for rapid, consistent expansion of human T cells. This medium supports robust T-cell expansion at levels comparable to serum-containing media and eliminates performance variability, with no serum supplementation needed.

STEMCELL Technologies

For info: 800-667-0322

www.stemcell.com/t-cell-therapy#section-products

Protein A Kit

The Gyrolab Protein A Kit offers increased efficiency and throughput for quantification of residual Protein A ligands. Two ready-to-use versions of the kit—Native Protein A and MabSelect Sure—are designed for use with Gyrolab systems, and include an enhanced protocol for automated acid pretreatment of harvested samples from downstream purification of biotherapeutics. Determination of residual Protein A is an essential regulatory requirement for the safety evaluation of biotherapeutics. During purification of biotherapeutics, Protein A can leach from the chromatography support and coelute with the therapeutic antibody product. If bound to immunoglobulins, Protein A can increase the risk of adverse reactions.

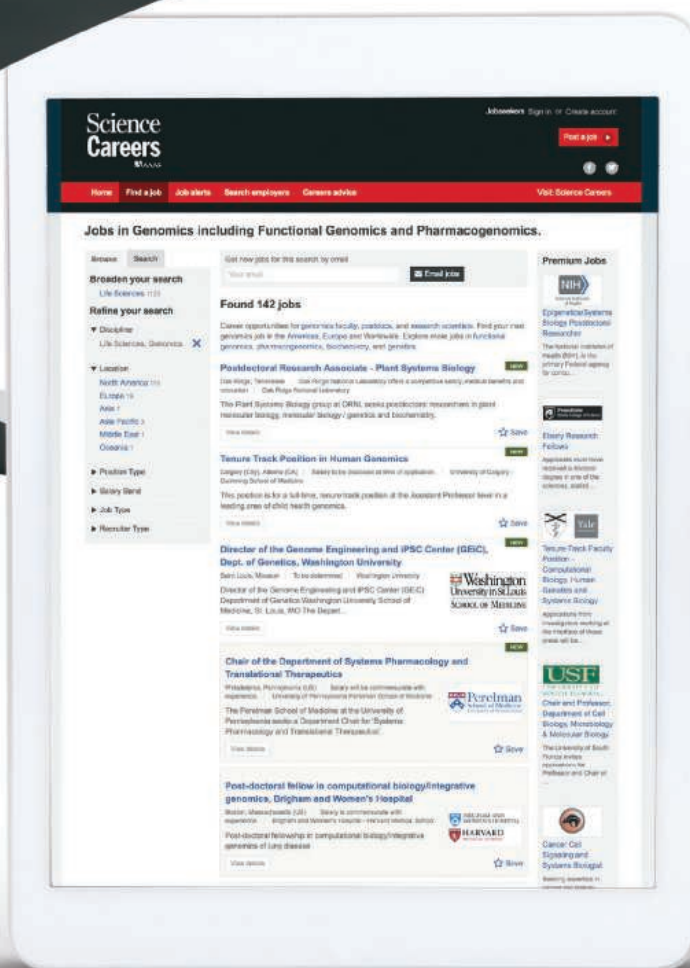
Gyros Protein Technologies

For info: +46-(0)-18-56-63-00

www.gyrosproteintechnologies.com

Electronically submit your new product description or product literature information! Go to www.sciencemag.org/about/new-products-section for more information.

Newly offered instrumentation, apparatus, and laboratory materials of interest to researchers in all disciplines in academic, industrial, and governmental organizations are featured in this space. Emphasis is given to purpose, chief characteristics, and availability of products and materials. Endorsement by *Science* or AAAS of any products or materials mentioned is not implied. Additional information may be obtained from the manufacturer or supplier.



Step up your job search with *Science Careers*

- Access thousands of job postings
- Sign up for job alerts
- Explore career development tools and resources



Search jobs on **ScienceCareers.org** today

Did you get the message?

In recent years, the discovery of new classes and modifications of RNA has ushered in a renaissance of RNA-focused research. Did you know that NEB[®] offers a broad portfolio of reagents for the purification, quantitation, detection, synthesis and manipulation of RNA? Experience improved performance and increased yields, enabled by our expertise in enzymology.



FEATURED PRODUCTS *for* RNA RESEARCH:

NEW Monarch[®] Total RNA Miniprep Kit –

rapidly purify up to 100 µg of high quality total RNA from multiple sample types

Luna[®] One-Step RT-qPCR kits –

improve RT-qPCR performance with our novel, Luna WarmStart[®] Reverse Transcriptase

NEW NEBNext[®] Ultra[™] II RNA Library Prep kits –

generate high quality RNA-seq libraries, even with limited amounts of RNA

HiScribe[®] *in vitro* transcription kits –

rapidly synthesize high yields of high quality RNA

Let NEB help streamline your **RNA-related workflows**.
Get started at **NEB[®]rna.com**



THE COLLEGE OF ENVIRONMENTAL SCIENCES AND ENGINEERING

is devoted to cutting-edge fundamental research
and clean technologies for a sustainable future

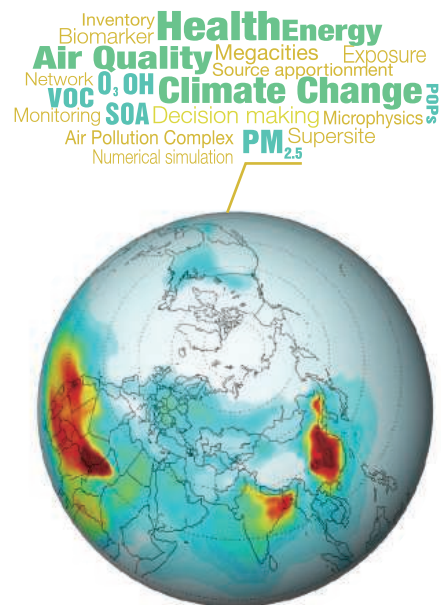
To improve the environment in the midst of rapid development is a major challenge facing China. As one of China's earliest programs dedicated to environmental research and talent cultivation, the College of Environmental Sciences and Engineering (CESE) of Peking University (PKU) takes it as its mission to tackle Chinese and global environmental challenges. CESE has built a whole-process research system, integrating science, engineering and public policies. In line with the pursuit of **Excellence** and **Relevance**, CESE endeavors to establish a world-class environmental discipline and research platform, cultivate high-level talents with global vision, and become a top environment policy think tank. According to the latest ESI data, PKU Environmental Sciences program ranks in the top 0.2% in the world. In the latest U.S. News & World Report and Quacquarelli Symonds discipline lists, environmental sciences at PKU ranks 44th and 26th globally.

CESE has 67 faculty members with national and international reputations, including one academician of the Chinese Academy of Sciences and two academicians of the Chinese Academy of Engineering. CESE also boasts two Creative Research Groups of the National Natural Science Foundation, one State Key Laboratory, one Ministry of Education Key Laboratory and one International Joint Laboratory. The faculty members have held over 40 positions as associated editors or members of editorial boards for international journals, 26 positions in international academic associations/societies and won many international awards. Currently,

CESE consists of the Department of Environmental Sciences, the Department of Environmental Engineering and the Department of Environmental Management. There are six research fields, including: Atmospheric Pollution and Climate Change, Environment and Human Health, Water Treatment and Microbial-Technology, Water Pollution Control and Integrated Watershed Management, Environmental and Resources Economics, Environmental Planning, Management and Sustainable Development. In recent years, CESE has successfully developed the environmental-media (atmosphere and hydrosphere)-based whole-process research system and the international-treaty-compliance-oriented global environmental governance studies. Building on solid basic research, CESE aims to promote policy implementation and technology application.

The development of new knowledge on atmospheric chemistry and physics is the key to the mitigation of China's severe air pollution. To meet this pressing need, CESE took the lead by proposing the 'Air Pollution Complex model' as well as the concept of 'Environmental Civilization'. Moreover, PKU discovered new mechanisms for the maintenance of the atmospheric oxidation capacity with global importance. The relevant findings were published in prestigious journals like *Science*, *Nature Geoscience* and *PNAS*. A comprehensive air pollution control technology system has been established, which integrates field observation, numerical simulation and pollution control strategy development so as to discover the formation mechanisms of air

pollution complex and achieve the technological innovation of regional air pollution control. Using the newly developed system, CESE has conducted a series of major observational research campaigns over the Pearl River Delta (PRIDE-PRD) and promoted the establishment of a regional monitoring network and an early warning system for air pollution control. Approved and adopted by the government, the monitoring network results have become instrumental to decision making in both PRD and Hong Kong. It is the first one of its kind in China and helps PRD to be the first polluted region in China for compliance of PM_{2.5} air quality standard. The air pollution in megacities and surrounding regions is of global importance. One typical case is the North China Plain, which is the largest territory covering many different provincial areas including Beijing. The coordinated provincial air pollution control thus has become a key strategic option. Based on a good understanding of the formation mechanism of air pollution, CESE developed strategies and methodologies for regional coordinated air pollution control, which successfully ensured the air quality during the 2008 Beijing Olympic Games in six provinces and cities. The theories and control technology system of complex air pollution developed by CESE also guaranteed the air quality for the Guangzhou Asian Games and the Shanghai World Expo, promoting the implementation of National Air Pollution Prevention and Control Action Plan. At present, CESE is organizing the country's best experts to explore the formation mechanism and source identification of the heavy air pollution around Beijing.





The focus of China's Clean Water Action Plan is on its major basins. CESE was the first to propose the concept of "All Materials Flux (AMF)" and has conducted the world's largest AMF monitoring in the Yangtze and the Yellow River. Such research has successfully identified the lateral transport of soil carbon and land-atmosphere CO₂ flux induced by water erosion in China. The relevant findings were published in *PNAS*. CESE has developed a series of water pollutants removal techniques and integrated watershed simulation-optimization models, especially for nitrogen pollution, the most urgent problem in China. Several breakthroughs on the nitrogen water pollution control and treatment have been achieved in the past several years, including advanced nitrogen removal technology for municipal sewage, efficient nitrogen removal techniques for industrial wastewater, ecological treatment of sewage in rural area, and the control of non-point (distributed) sources of regional nitrogen contamination. The heterotrophic nitrification and aerobic denitrification microorganisms have been successfully isolated and cultured to solve the key problems of advanced nitrogen removal in municipal wastewater treatment plants. To facilitate the degradation of highly toxic organic pollutants from industrial wastewater, the macroporous functional carriers, which could enhance the microbial tolerance to toxic substances and high ammonia nitrogen, have been fabricated. The proposed biological-ecological multi-medium techniques greatly improve the abundance of denitrification functional bacteria and have been successfully used to treat the sewage in rural areas. The developed techniques have provided core technical support for the improvement of

major basins in China, such as the South-North Water Diversion Project, the National Rural Safe Drinking Water Initiative, the Xiangjiang River heavy metal pollution treatment, the sediment treatment of the Yellow River and the Lake Dianchi eutrophication control.

CESE is concerned about public health risks due to environmental exposure. In view of the increasingly severe urban and regional environmental pollution in China, CESE takes full advantage of the many established disciplines of social, natural, and medical sciences at PKU, and promotes research in the field of environment and health by leading key research projects in collaboration with other disciplines, so as to establish the linkage between environmental exposure, internal exposure and health effect markers. Because of the palpable improvement of the air quality in Beijing during 2008 Olympic Games, CESE designed a "quasi-control" experiment by monitoring the biomarkers of inflammation, oxidative stress, immunity and vascular damage in order to find out the effect and mechanism of atmospheric pollution on human health. The results show that the oxidative effects among children, the cardiovascular system indicators among the elderly and cardiovascular function effects in healthy people are associated with atmospheric pollutants, especially the chemical composition of PM₁₀ and PM_{2.5}. Based on the measurements of multiple organic pollutants in the placenta as an indicator of the fetus's in utero exposure in a case-control study, pollutants such as PAHs were found to be the risk factor with a significant dose-response relationship. Such studies have been published in *JAMA*, *Lancet* and *PNAS*.

It is PKU's tradition to work out China's global environmental strategies. Directly involved in treaty negotiation, signing and compliance, CESE served as the technical team leader in the development of China's Plan for the Montreal Protocol and the relevant Industry-Wide Solution and Control System, setting a benchmark for developing countries. CESE also took the lead in developing China's National Implementation Plan of the Stockholm Convention, which has been adopted by the State Council and contributed greatly to the all-out ban on the production, importation and consumption of controlled POPs. A number of international awards were bestowed on CESE, such as the Gold Award from SEPA, UNEP/WMO Vienna Convention Award, Best-of-the Best Awards from US EPA, Twentieth Anniversary Ozone Protection Award from UNEP, Special Commendation Award and Technical Leadership Award from the secretariat of the Montreal Protocol.

CESE has been proactive in promoting international cooperation by designing major research programs and promoting joint research. As the site of the International Program Office, CESE has facilitated the implementation of the Monsoon Asia Integrated Research on Sustainability (MAIRS), one of the core projects under the framework of Future Earth. In addition, CESE has mobilized dozens of world-renowned research institutes to participate in such major research programs as CAREBEIJING, PRIDE-PRD and AMF, and taken the lead in drafting the report on the Impacts of Megacities on Air Pollution and Climate for the WMO and IGAC.

CESE at PKU aims to cultivate high-level interdisciplinary talents in environmental discipline and to train pro-active leaders with a solid academic foundation, a strong sense of social responsibility, and global vision. The guideline for talent cultivation incorporates healthy personality, diversity, environmental concern, self-actualization, responsibility, independent thinking, innovation and team work. Graduates from CESE have made great contributions to sustainable development in and outside China. Many of them hold important positions in UN organizations, NGOs, the Chinese government, and the world's first-class universities and institutes.

CESE cordially welcomes job applicants and visiting scholars with expertise in related areas such as environmental science, engineering, health and management. Feel free to contact us:

Website: <http://cese.pku.edu.cn>

Email: huiliu@pku.edu.cn

Tel: +86-10-62754126

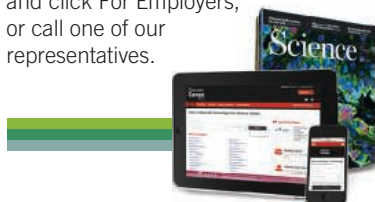
Fax: +86-10-62751480

Address: Environmental Building, Peking University, No.5 Yiheyuan Road, Beijing, China. 100871

Science Careers

SCIENCE CAREERS ADVERTISING

For full advertising details, go to ScienceCareers.org and click For Employers, or call one of our representatives.



AMERICAS

+1 202 326-6577
+1 202 326-6578
advertise@sciencecareers.org

EUROPE, INDIA, AUSTRALIA, NEW ZEALAND, REST OF WORLD

+44 (0) 1223 326527
advertise@sciencecareers.org

CHINA, KOREA, SINGAPORE, TAIWAN, THAILAND

+86 131 4114 0012
advertise@sciencecareers.org

JAPAN

+81 3-6459-4174
advertise@sciencecareers.org

CUSTOMER SERVICE

AMERICAS

+1 202 326-6577

REST OF WORLD

+44 (0) 1223 326528

advertise@sciencecareers.org

All ads submitted for publication must comply with applicable U.S. and non-U.S. laws. *Science* reserves the right to refuse any advertisement at its sole discretion for any reason, including without limitation for offensive language or inappropriate content, and all advertising is subject to publisher approval. *Science* encourages our readers to alert us to any ads that they feel may be discriminatory or offensive.

Science Careers

FROM THE JOURNAL SCIENCE AAAS

ScienceCareers.org

Advance
your career
with expert
advice from
Science
Careers.



Download Free Career Advice Booklets!
ScienceCareers.org/booklets

Featured Topics:

- Networking
- Industry or Academia
- Job Searching
- Non-Bench Careers
- And More



Science Careers

FROM THE JOURNAL SCIENCE AAAS



Nanjing Agricultural University Welcomes Talents from All Over the World

Nanjing Agricultural University (NAU) sincerely invites you to join us in teaching and research.

About us

Nanjing Agricultural University is a university under the administration of the Ministry of Education and has been selected and included in the National "Double World-Class" University Construction Initiative. In the fourth-round national first-level discipline evaluation in 2017, it had four disciplines listed in Class A+, ranking itself the 11th of the top universities in China. In the ESI rankings, it had seven disciplines ranked among the top 1% worldwide, and two of the disciplines, Agricultural Science and Plant & Animal Science, among the top 1‰. The US News 2018 has listed NAU the top 9 among the Best Global Universities of Agricultural Sciences.

Fields of research

The fields of research you are invited to join in are:

Agricultural Sciences including :

Crop Science, Horticulture, Agricultural Resources & Environment, Plant Protection, Animal Husbandry, Veterinary Science, Fisheries Science, and Grass Science;

Science and Technology including :

Biology, Ecology, Environmental Science & Engineering, Food Science & Engineering, Landscape Architecture, Agricultural Engineering, Bioinformatics, and Computer Science & Technology;

Humanities and Social Sciences including :

Management, Economics, Sociology, Legal Science, History, Literature, and Linguistics.

You are also welcome to join us in the following **Interdisciplinary Subjects :**

Genomics & Phenomics, Microorganism-Botany-Pest Interactions, Food Nutrition and Human Health, Agricultural Equipment Engineering, Agricultural Informatics, and so on.

Position requirements

Doctorate recipients from world famous universities; post-doctor researchers from famous research institutes; and talents with professional titles of associate professor, professor or other higher titles, from world-famous higher institutions or research institutes, and with outstanding teaching and research achievements.

NAU will offer you a benefits package which is competitive among the universities in the local area and which will be negotiated in person.

Talent introduction policy

You will enjoy a talent allowance equivalent to those for the Zhongshan Scholars of NAU who are Zhongshan Distinguished Professor, Zhongshan Professor, Zhongshan Fellow, and Zhongshan Young Scholar, according to your qualities for recruitment; or we may talk and agree on your annual salary.

Specific conditions of your research team, laboratory, graduate students to supervise, accommodation, and employment of your spouse are to be discussed in person.

Note: The Zhongshan Scholars is an NAU-developed open initiative to support career development and

academic innovation for leading scientists of today and tomorrow, and it is a major initiative to construct a world-class university and to establish world-class disciplines, so as to realize NAU's strategy of rejuvenation by talents. Recruitment is divided into four categories: Zhongshan Distinguished Professor, Zhongshan Professor, Zhongshan Fellow and Zhongshan Young Scholar. Special talent allowance is provided for these outstanding scientists.

Application documents

Please prepare and email to rcb@njau.edu.cn the following documents for your qualification:

- a detailed CV, starting from your undergraduate education till the time of your application, including periods of continuous education, working experience, publications, research projects hosted or participated in, and certificates of awards.
- photocopies of diplomas, certificate of doctor's degree, and certificate of current employment
- Full texts of five representative papers published in the past five years.

Contacts:

Ms. Liu Hongmei

Telephone:

+86-25-84399039

Email address:

rcb@njau.edu.cn



Global Talents Recruitment Program of Huaqiao University

Established in 1960, Huaqiao University (HQU) is one of China's renowned institutions of higher education. With its two campuses strategically located in two famous hometowns of overseas Chinese, Xiamen and Quanzhou in Fujian province, HQU is a national key comprehensive university directly affiliated to the Overseas Chinese Affairs Office of the State Council of the People's Republic of China.

We sincerely welcome topnotch talents from home and abroad to join us!

1. Vacancies

Key Disciplines: Mechanical Engineering, Materials Science and Engineering, Architecture, Civil Engineering, Chemical Engineering and Technology, Chemistry, Applied Economics, Philosophy, Software Engineering (Computer Science and Technology), Optical Engineering, Business Administration and Chinese Linguistics.

Other Disciplines: Instrumentation Science and Technology, Electrical Engineering, Biology, Mechanics, Electronics Science and Technology, Information and Communication Engineering, Control Science and Engineering, Urban and Rural Planning, Landscape Architecture, Environmental Science and Engineering, Biomedical Engineering, Pharmacy, Horticulture, Marine

Science, Management Science and Engineering, Mathematics, Statistics, Physics, Public Administration, Law, Political Science, Sociology, Marxist Theory, Sports Science, Foreign Languages and Literature, Chinese Philology, Journalism and Communication, Art, Design and History.

2. Qualifications

2.1 Basic Qualifications

Applicants are expected to be disciplined, honest, responsible, physically and psychologically healthy and dedicated to work.

2.2 Specific Qualifications

2.2.1 First Level

Applicants should be academicians of Chinese Academy of Sciences (CAS), academicians of Chinese Academy of Engineering (CAE), top-notch talents of the "State Special Support Plan", or talents from home and abroad of the same level.

2.2.2 Second Level

Applicants should be valid candidates of the Chinese Academy of Sciences (CAS) and Chinese Academy of Engineering (CAE), leading talents of the "State Special Support Plan", Distinguished Professors of Chang Jiang Scholars, winners of National Science Fund for Distinguished Young Scholars, selected candidates of long-term state level talent projects like the

Thousand Talents Plan, first person in charge of national key disciplines or key laboratories, chief scientists of major national projects, winners of National Science and Technology Award (ranking first), first-prize winners (ranking first) of Social Science Achievement Award for Higher Education of Ministry of Education.

Applicants should be no more than 55 years old.

2.2.3 Third Level

Applicants should be state-level selected candidates of the Hundred, Thousand and Ten Thousand Talents Plan, top-notch young talents of the "State Special Support Plan", or selected candidates of the Innovative Talents Promotion Plan of the Ministry of Science and Technology, the New Century Excellent Talents Supporting Project of the Ministry of Education, the National Science Foundation for Excellent Youth, the state-level Thousand Youth Talents Plan, the Young Project of Chang Jiang Scholars Program, or the National Outstanding Young Talents.

Applicants should be no more than 45 years old.

2.2.4 Fourth Level

Applicants should be young talents who display the potential to be selected into high-level young talents projects like the National Science Foundation for Excellent Youth,

the Thousand Youth Talents Plan, the Youth Project of Chang Jiang Scholars Program and National Outstanding Young Talent. Talents who are candidates of the above national youth projects will be directly recruited.

Or applicants should be associate professors or above from domestic renowned universities with academic achievements exceeding HQU's requirements for exceptional promotion to professor (if the associate professor has served for more than 5 years, his or her performance of the past five years will be mainly assessed). For applicants from abroad, his/her papers and works and representative achievements in his/her own academic field in the past five years should be submitted for assessment; in principle, he/she should have published papers that's equivalent to 1.5 times of HQU's requirements for exceptional promotion to professor, or have published one full academic paper in journals of the Nature, Science or Cell publishing groups with impact factor (IF) over 20 as the first author or the first corresponding author in the past five years, or seven papers on SCI TOP journals as the first author or the first corresponding author in the past five years. Applicants should be no more than 40 years old.

3. Benefits

Full-time talents recruited will enjoy the following benefits.

3.1 Funding Support

Level	Annual Salary		Housing Benefits		Scientific Research Allowances	
	Natural Science	Humanities & Social Sciences	Settling-in Allowances	Housing Subsidies	Natural Science	Humanities & Social Sciences
1	Negotiable					
2	≥90		60	200	300-500	80-120
3	60-90	50-70	40	140	100-300	60-100
4	35-50	30-40	20	80	80-200	40-60

Note: 1. Unit: 10,000 RMB, all before taxes.

2. The above funds do not contain subsidies for projects supported by national, provincial or municipal programs, or the university's awards for high-level achievements of over fulfilled scientific research task.

3.2 Working and Living Supports

3.2.1 Office, laboratory and related equipment will be furnished.

3.2.2 The talents who meet the HQU requirements for supervisors will be recommended and appointed as graduate students supervisors.

3.2.3 Temporary housing (or rent subsidies) will be provided in prior to housing subsidies.

3.2.4 HQU will also help with the job arrangement of the spouse as well as their children's schooling.

4. How to apply

This global talents recruitment program is valid in the long run. Applicants are supposed to fill in the "Approval Form of Huaqiao University for Recruiting Distinguished Professor" (available via <http://rsc.hqu.edu.cn/info/1039/2995.htm>). Please send your word document to our talents recruitment email: hqursc@126.com with the subject "name + disciplines applied+ position level".

5. Contact Information

Contact: Mr. Hong, Mr. Wang

Tel: 86-592-6161099,

86-595-22692370

Email: hqursc@126.com



Hibbitt Early Career Fellows Program

The Marine Biological Laboratory invites applications to its Hibbitt Early Career Fellows Program, designed to allow exceptional early career scientists the opportunity to establish their own research programs as an alternative to traditional postdoctoral positions. Postdoctoral scientists or recent Ph.D. graduates with proven research excellence will be given space, resources, and support needed to run independent labs under the mentorship of a network of scientists. Fellows will not have formal teaching or administrative responsibilities, but will be eligible to teach in MBL courses and workshops.

Fellows will take advantage of MBL's unique research environment and resources, in the context of a collaborative and interdisciplinary network of investigators, and will be able to apply for external funding as P.I. or co-P.I. to add strength to their research programs.

Applications are encouraged in research areas that can benefit from and contribute to MBL's strategic strengths in ecology and biological sciences (mbl.edu/strategic-themes).

MBL is especially committed to consideration of candidates from historically underrepresented talent pools, including women and minority candidates.

Applications will be accepted starting
March 15, 2018

For information and application:
mbl.edu/hibbittfellows

The MBL is an independent research institution located in Woods Hole, MA and is an affiliate of the University of Chicago.



The University of Texas Medical Branch

MOLECULAR BACTERIOLOGY AND IMMUNOLOGY FACULTY POSITIONS

The Department of Microbiology & Immunology at the University of Texas Medical Branch (UTMB), Galveston, is seeking to recruit tenure-track faculty at the academic rank of Assistant, Associate or Full Professor with MD, PhD, DVM or equivalent degrees. The preferred research areas of **bacteriology** include bacterial genomics, virulence, antibiotic resistance, and microbiomes. The preferred research areas of **immunology** include the molecular basis of innate and adaptive immunity to pathogen infection and autoimmune diseases. The successful candidates should be highly productive with an established record of extramural funding or the potential to establish robust, funded research programs in the desired research areas. The successful applicants should be amenable to collaborative studies with other investigators studying the pathogenesis of infectious diseases, as well as teaching and mentoring graduate and medical students. Salary and academic rank are commensurate with experience, and an excellent benefits and start-up package is offered.

UTMB has several highly interactive research centers, biomedical institutes, and a national biocontainment laboratory with excellent infrastructure to conduct research at BSL2, -3 and -4 on diverse animal models of infectious diseases. The Department, with 31 full-time faculty members, is ranked among the top of its peer departments in NIH funding. Interested candidates should apply to **Job id #59447, Professor** via the UTMB careers website at <https://www.utmb.edu/careers/>

UTMB Health strives to provide Equal Opportunity Employment without regard to race, color, national origin, sex, age, religion, disability, sexual orientation, gender identity or expression, genetic information or veteran status. As a VEVRAA Federal Contractor, UTMB Health takes affirmative action to hire and advance women, minorities, protected veterans and individuals with disabilities.



सत्यमेव जयते

Government of India Ministry of Science & Technology Department of Biotechnology

RAMALINGASWAMI RE-ENTRY FELLOWSHIP : 2017-2018

Applications are solicited from Indian nationals working in overseas research institutions for the "**Ramalingaswami Re-entry Fellowship**", a Re-entry scheme of the Department of Biotechnology (DBT), Ministry of Science & Technology, Government of India.

Aim of the Fellowship

The scheme is conceptualized with the aim of attracting highly skilled researchers (Indian Nationals) working overseas in various cutting edge disciplines of biotechnology (agriculture, health sciences, bio-engineering, energy, environment, bioinformatics and other related areas), by providing them an attractive avenue to pursue their R&D interests in Indian institutions.

Who is eligible to apply ?

The applicant should possess a Ph.D., /M.D., or equivalent degree with an outstanding track record as reflected in publications and other recognitions and with at least three years of post-doctoral research experience of which last two years should be from overseas laboratory.

Only candidates (Indian nationals) working overseas are eligible to apply. **Those who have already returned to India within one year of the closing date of this advertisement but without a job are also eligible.**

Researcher's upto 45 years of age as determined on closing date of application are eligible to apply.

Incentives of being a Ramalingaswami fellow

- This is a senior fellowship programme, and awardees are to be considered equivalent to Assistant Professor/Scientist-D level officer. Fellows selected are entitled to take up teaching/research assignments and supervising Doctoral/MS students.
- The scheme provides a consolidated monthly remuneration of Rs. 1,00,000/- p.m. In addition, a House Rent Allowance of Rs. 18,500/- p.m. is given to fellows. In case host institute provides accommodation to the fellow, no house rent allowance is admissible. The fellowship is taxable as per Govt. of India rules.
- Fellows will receive a research/contingency grant of Rs. 10.00 lakhs for the 1st & 2nd year; Rs. 7.50 lakhs for 3rd & 4th year; Rs. 5.00 lakhs for 5th year for purchase of consumables, minor equipment, international and domestic travel, engaging manpower and other contingent expenditure to be incurred for the implementation of research proposal which is a part of fellowship and Institutional overhead Rs. 50,000/ year.
- DBT encourages host institutions to provide medical benefits, transport allowance, leave travel allowance and other benefits as per their prevailing norms as applicable to their employees of the rank equivalent to Assistant Professor/Scientist D out of their own resources/ funds.
- Fellows retain an option for drawing either the fellowship or salary if they are appointed at a suitable permanent scientific position. Fellows opting for salary can continue to avail the research /contingency grant with prior approval of DBT.
- Ramalingaswami Re-entry Fellows could take up fellowship at any of the scientific institutes/ universities in the country. However, application should be duly forwarded by the competent authority of the host Institute. Fellows/Awardee can change his/her host institute only once during the tenure of the fellowship with the prior no objection certificate from the host institute who has forwarded the application (Director/Registrar/Vice-Chancellor/Dean as the case may be). Only one nomination will be considered.
- Awardees are eligible to apply for research grant/s to any of the funding agencies provided Co-PI is a permanent employee of the host institution.

Tenure of fellowship

Fellows can draw fellowship for a term of five years. Fellowship is further extendable for another two years on a fresh appraisal of performance of the fellow; only fellowship & HRA will be admissible during extension period. No research/contingency grant will be provided during the extension period. Those who are able to secure permanent positions will not be considered for 2nd term.

How to apply

Applications may be sent as per proforma downloadable from DBT website (www.dbtindia.nic.in) and duly forwarded by the competent authority to **Dr. Meenakshi Munshi, Adviser/Scientist "G" Department of Biotechnology, Block-2, 7th Floor, CGO Complex, Lodhi Road, New Delhi -110 003**, both as a hard copy as well as **Soft copy**. The applications not forwarded by the host institution will not be considered. **Soft copy to be mailed at Email :- rsfellowship.dbt@nic.in only as a single pdf file latest by 15th May, 2018**

No one is an island

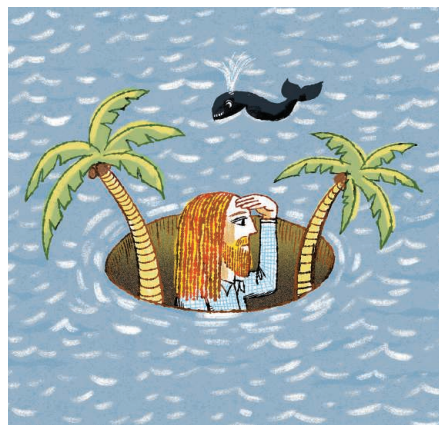
My supervisor waved goodbye and boarded a plane. I had just started my Ph.D. studying invasive species on a remote oceanic island, where I would be spending most of the next 3 years bashing through rainforest to count invertebrates. My supervisor had done his own Ph.D. here on Christmas Island in the Indian Ocean 2 decades earlier. He had found me a place to stay and introduced me to the handful of other ecologists who were managing the national park or conducting their own research, but I wasn't working directly with them. Everyone else attached to my project was more than 5000 kilometers away—and so were my friends, family, and entire support network. I told myself I could manage on my own.

Despite my enthusiasm about my research, it wasn't long before I began to feel lonely. At times, I struggled to find the motivation to get out into the field. I was suffering from a sense of isolation that is not uncommon for Ph.D. students, which in my case was amplified by literal isolation.

I hesitated to reach out to the locals—a small community that developed after the island was first settled at the end of the 19th century. I was worried that socializing would distract from my work, and I was nervous that the locals might not welcome an “outsider.” But I eventually realized that the only way I would get through my remote Ph.D. was to reach out and create a new support network.

My first move was to visit the epicenter of any small remote community: the local pub. One afternoon, after a long day in the field, I finally dropped in for a beer. Almost immediately, someone asked how long I had been working at the power station. I was confused, but then I realized I was wearing a work shirt bearing the company logo, which I had gotten at the secondhand shop. We both had a laugh after I explained who I was and what I was doing. This shirt confusion turned out to be a great conversation starter: I ended up having that same introductory chat with a bunch of people over the next few weeks. Soon, each visit to the pub involved catching up with friends and talking about different aspects of my research, which helped keep me motivated about my work.

Connecting with the community helped with more than just my emotional well-being. When I asked a new friend to help me assemble some fences I needed for my experiments, for example, he said he was more than happy to—



“The only way I would get through my remote Ph.D. was to reach out.”

but not if he needed to do it the way I had planned. My friend, who was a builder, suggested a bunch of practical improvements to the design, and together we were able to get the fences up with much less trouble. I don't think I would have been able to get the experiment done without him.

My final step in becoming a full member of the Christmas Island community was to give something back. Quite a few people on the island played music, and afternoon acoustic guitar shows were not uncommon, but rock 'n' roll gigs at the pub were unacceptably rare. So along with some friends, I sniffed out equipment scattered around the island; helped organize musicians into bands; and headlined the show with a raucous set of White

Stripes songs, complete with my own blues guitar stylings (although attendees were far more impressed by the drummer's skills). It felt like everyone on the island attended the show, and some were still talking about it years later.

Since finishing my Ph.D., I have moved twice for research positions, and each time I have found myself in new communities. The surroundings haven't been as extreme, but again, in the beginning, I was tempted to ignore any feelings of isolation and focus solely on work. But I knew better. I remembered how reaching out to the welcoming and supportive local community during my Ph.D. not only helped me get through the isolation, but also improved the quality of my work. And whenever I felt like a stranger, I made a point of visiting the pub. ■

Luke O'Loughlin is a postdoctoral fellow at the Australian National University in Canberra. Do you have an interesting career story? Send it to SciCareerEditor@aaas.org.